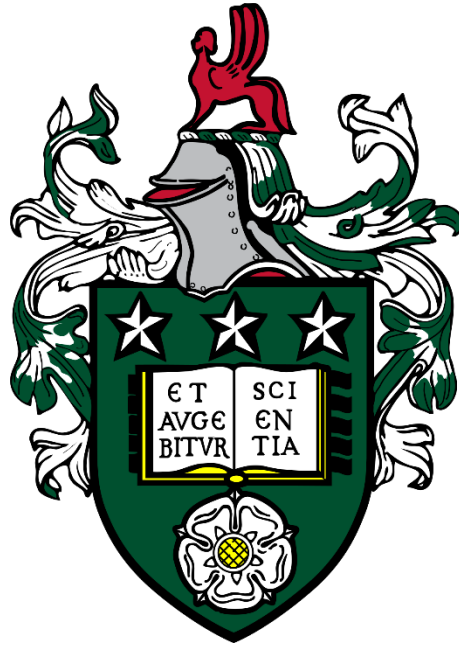


**Computational and experimental research for improved low  
NO<sub>x</sub> burner designs with application to gas turbines and  
process heaters**



José Ramón Quiñonez Arce

Submitted in accordance with the requirements for the degree of  
Doctor in Philosophy

The University of Leeds  
School of Chemical and Process Engineering

Prof. Gordon E. Andrews

Dr. Herodotos Phylaktou

April 2022

The candidate confirms that the work submitted is his own, except where work which has formed part of jointly-authored publications has been included. The contribution of the candidate and the other authors to this work has been explicitly indicated below. The candidate confirms that appropriate credit has been given within the thesis where reference has been made to the work of others.

*Quinonez Arce, JR, Al-Dabbagh, N.A., Andrews, G.E. and Burns, A. "Aerodynamics and Mixing in Grid Plate Flame Stabilizers" Proc. 12th ECCRIA, Cardiff, UK, 2018.*

*Quiñonez Arce JR, Al-Dabbagh NA., Burns AD, Andrews; GE. Aerodynamics of grid plate flame stabilisers. Proc. HEFAT14. 14th Int. Conf. Heat Transf. Fluid Mech. Thermodyn. [Internet] 2019; Available from:*

*<https://na.eventscloud.com/ehome/349879/program/>*

*Quiñonez Arce JR, Andrews GE, Burns AD, Al-Dabbagh N. Grid Plate Flame Stabilizer for High Intensity Gas Turbine Combustion: The Influence of the Method of Fuel Injection on Mixing, Flame Development and NOx Emissions" Proceedings of the ASME Turbo Expo 2021: Turbomachinery Technical Conference and Exposition. Volume 3B: Combustion, Fuels, and Emissions. Virtual, Online. June 7–11, 2021. V03BT04A032. ASME. <https://doi.org/10.1115/GT2021-60105>*

*Quinonez Arce, JR, Andrews, G.E., Phylaktou, H. "FGM Applied to Grid Plate Flame Stabilisers for Nox Prediction in Non-Premixed Gas Turbine Combustion" ASME Turbo Expo 2022. GT2022-82150. This paper has been pre-reviewed and accepted for the conference taking place in Rotterdam, The Netherlands, June 13-17, 2022*

This copy has been supplied on the understanding that it is copyright material and that no quotation from the thesis may be published without proper acknowledgement.

The right of José Ramón Quiñonez Arce to be identified as Author of this work has been asserted by him in accordance with the Copyright, Designs and Patents Act 1988.

## **Acknowledgements**

A special thank goes to my partner Aidan for all his love and unconditional support during this journey. To my parents, Hilda and Jose Ramon, and siblings, Luis Rodolfo, Paris and Monica, for all their encouragement and support when I needed it the most. Special thanks to my supervisors Prof. Gordon Andrews and Dr. Herodotos Phylaktou, for all their help, patience and guidance through this project.

I would like to thank my sponsor Consejo Nacional de Ciencia y Tecnologia and the Secretaria de Energia (CONACYT-SENER) for the financial support.

I carried out this research under the supervision of Dr Alan D. Burns, Prof Gordon E. Andrews and Dr Herodotos Phylaktou. My work is fully and explicitly indicated in the thesis. In summary, it mainly involved validating numerical models for experimental results for gas turbine combustor grid plate flame stabilisers; the equilibrium and adiabatic flame temperature calculation for glass melting furnaces (Glass Futures BEIS fuel switching contract.), and the development of experiments and simulation for domestic fires (BEIS funded Hy4Heat project).

The other members of the group and their contributions have been as follows:

The late Dr Alan Burns provided lots of help in the predictions of the aerodynamics of the flame stabilisers. He also gave valuable assistance in developing meshes for most studied geometries.

Prof. Gordon provided me with the direction and support on most aspects of the combustion theory required for the development of the project. In addition, he offered me the research assistant positions for the Hy4Heat project and Glass Futures, which research teams he was part of. Prof. Andrews was the Technical Lead on the Hy4Heat project. He was also the supervisor of the Dr Naman Al-Dabbagh Ph.D. project, who produced the experimental Grid Mix flame stabiliser results that I modelled in Chapters 5 and 6. The experimental work is included in this thesis so as to understand the difficulties in the experimental gas analysis traverse measurements that I modelled. Finally, he provided me with important feedback for the development of this thesis.

Dr. Herodotos gave me valuable feedback during the aerodynamics study stage for the stabilisers. He was also a co-investigator on the Hy4Heat project and on the Glass Futures work, where he taught me how to use Gaseq. Finally, he gave shape to this thesis and provided important feedback.

I would like to thank Dr. Naman Al-Dabbagh for the development of the experiments, which were the basis of the gas turbine chapters in this thesis. Also, for his help with the ASME papers.

Special thanks to my fellow research student Dr. Christian Michelbach who worked with me in the development of the experiments for the domestic fires explained in Chapter 7. Two people were needed to operate the fires, and Dr. Michelbach and I were employed as research assistants on the Hy4Heat contract to undertake the tests for hydrogen and natural gas fuels

I would also like to thank Prof. Alison Tomlin and Dr. Valerie Dupont, who were part of the BEIS Hy4Heat team and gave me the research assistant position for the project.

Prof. Tomlin provided me with the propane and hydrogen mechanisms needed to simulate combustion for some flame stabilisers. Prof. Tomlin was also my line manager under the Hy4Heat employment. She also provided very valuable feedback for calculating equilibrium in the Glass Futures employment.

Dr. Valerie Dupont provided valuable feedback for the calculations of some fuels studied under the Glass Futures project.

Thanks to Prof. Michael Fairweather provided me with feedback on flame stabilisers' pressure loss and  $\text{NO}_x$  calculation.

Thanks to Dr. Inna Gorbatenko gave me vital feedback when setting the parameters for the combustion simulation of flame stabilisers.

Thanks to Prof. Heinz Pitsch provided essential feedback on the combustion theory.

Thanks to Prof. Alexander Konnov provided the hydrogen-air mechanism needed for the hydrogen combustion simulations for the flame stabilisers.

Thanks to Prof. Christopher Decik provided with a detailed mechanism for propane-air combustion needed for the combustion study for flame stabilisers.

Special thanks to Pravin Nakod taught me a new and efficient meshing technique and introduced me to the flamelet generated manifold for simulation of combustion of the flame stabilisers. His valuable help led to much-improved  $\text{NO}_x$  predictions.

MSc. Harry Ford was my coworker during some tests carried out for Hy4Heat, and his work was essential in the Innovative project.

In addition, I would like to acknowledge valuable feedback from several referees of the papers that were accepted for publication and valuable discussions on my presentations with interested academics and industrialists:

The work in Chapter 7 was funded by BEIS Hy4Heat with an industrial consortia as detailed below:

Clean Combustion Systems (CBS): Jim Maxfield – project lead

Richard Wakeman – project manager

Steve Smith – Company managing director

Focal Point Fires – Andrew Lester – technical manager

The Late Duncan Spodes – Consultant on Gas Regulations

Legend Fires - Steve Stone – Managing Director

Ray Massey – Technical Manager

Bryan Waring- Designer

Birmingham Burners – Chris McGlone – Managing Director

I would like to thank these industrial partners for manufacturing the fires and burners used in Chapter 7 and all the required new design modifications, without which the work in Chapter 7 could not have been undertaken.

Manufacturing the very narrow slots for the hydrogen injection was rather challenging, and I thank the companies for their significant effort in making these. CBS, Focal Point Fires and Legend Fires were responsible for taking the fire designs developed in this work to full approval for use with the legislated tests at KIWA. All three fire designs are now fully approved for use with hydrogen and referred to as 'hydrogen ready' fires. They have not yet been approved as dual fuel fires, but the results in Chapter 7 show that this is possible, and CBS has intended to proceed to get this approval in the future.

The work in Chapter 7 and part of Chapter 4 was supported by three BEIS Hy4Heat contracts:

The Hy4Heat CBS led consortia has 3 Hy4Heat WP4 contracts.

1. DHOFAP: Domestic Hydrogen Open Fire: Adapted (dual fuel option)

Reference Fire: Focal Point Blenheim Slimline

2. 2HyBaFF: Dual Fuel Glass Fronted Balanced Flue

Reference Fire: Legend Evora

3. IDHA: Innovative domestic hydrogen appliance – Dual Fuel

The adiabatic flame temperature calculations in Chapter 4 were supported by the BEIS Fuel Switching Decarbonisation Programme:

Alternative Fuel Switching Technologies for the Glass Sector: Phase 3. Awarded to the Glass Futures consortia that Leeds University was part of, including Prof. Andrews and Dr. Phylaktou. The consortia was led by Aston Fuller and Rob Ireson was our primary contact on the work in Chapter 4.

Special thanks to all my PhD and master fellows: Jessica Quintana, Jaime Borbolla, Ana Encino, Konstantinos Drosos, Rodrigo Ortega, Thalia Amezcua, Flora Brocza, Myrna Pérez, Gabriela Reyna, Pebble Arrambi, Luis Garcia, Quiahuitl Sanches, Mario Vidaña, Jorge Jiménez, Erik Resendiz, Kun Li, Alejandro Barba, Alejandra Zazueta, Francis Omotola, Alejandra Figueroa, Nereida Oriz, Vicente Miron, Afrah AL-Shamery, Daisy Thomas, Nicola Wood, Charlotte Weaver, Richard Birley, Poppy Cooney, Jaime Nieto, and any other research and non research fellow that I met in this journey.

## **Abstract**

*Low NO<sub>x</sub> burner designs for gas turbines, process heaters and domestic fires have been numerically and experimentally investigated. All the technologies were suitable for operation on hydrogen, and this was a particular theme of the work on domestic fires. All the designs were studied for diffusion flames (non-premixed). Hydrogen premixed flames will always flash back, and a solution to this problem must be found if hydrogen is the zero-carbon fuel of the future. This work shows viable solutions to the problem for all the investigated applications. Hydrogen diffusion flame designs for domestic fires were a rather difficult design problem, as all current fires operate partially premixed.*

*Equilibria software was used for the investigation of hydrogen operation at the same flame temperature conditions as for propane and natural gas for gas turbines and domestic fires. This showed that hydrogen has to burn leaner. Equilibrium modelling was also used for predicting the operating conditions with fuel switching for glass melting furnaces that use large diffusion flames injected into high velocity very high air temperature jets. The aim here was to predict changes in the composition of the gases above the glass melt for hydrogen compared with natural gas and other renewable fuels.*

*Gas turbine low NO<sub>x</sub> grid plate flame stabilisers with four axial air jets were investigated using CFD. The fuel injection location relative to the air injection was studied for its influence on fuel/air mixing, flame development, and NO<sub>x</sub> emissions for rapid fuel and air mixing downstream of the flame stabiliser. The geometries aerodynamics, mixing, combustion and NO<sub>x</sub> were studied with RANS models, which were compared against the mean exit plane and with axial profiles previously obtained experimentally on propane fuel in a design called Grid Mix. The CFD work was carried out at modern high firing temperature low NO<sub>x</sub> gas turbine flow conditions, with 100% of the combustion air passing through the flame stabiliser at a combustor reference Mach number of 0.047 for a heat release of 28MW/m<sup>2</sup>bar. Reasonable agreement was shown between experimental data and simulation for this very high flame stretch combustion condition. This is the first time CFD has been applied to these GT combustion conditions. One of the GM designs was investigated for hydrogen combustion, and its application on a commercial burner showing good agreement.*

*Domestic fires for dual fuel-lean low NO<sub>x</sub> combustion operation on natural gas and hydrogen were investigated in new diffusion flame designs for three different natural draught fires. Fuel and air mixing was enhanced using impingement of*

*fuel jets on ceramic surfaces. Rich/lean combustion, internal gas recirculation and fuel staging were all shown to be effective in producing low NO<sub>x</sub> emissions.*

## Table of Contents

<b>Acknowledgements</b> .....	<b>iii</b>
<b>Abstract</b> .....	<b>vii</b>
<b>Table of Contents</b> .....	<b>ix</b>
<b>List of Tables</b> .....	<b>xvi</b>
<b>List of Figures</b> .....	<b>xx</b>
<b>Acronyms and abbreviations</b> .....	<b>xxxv</b>
<b>Chapter 1. INTRODUCTION</b> .....	<b>1</b>
1.1 The Role of Hydrogen in achieving Net Zero Greenhouse Gas Emissions.....	1
1.2 Considerations for hydrogen combustion.....	3
1.3 Equilibrium predictions.....	7
1.4 Grid plate flame stabilisers for gas turbines.....	9
1.5 Computational fluid dynamics for low NO <sub>x</sub> combustion.....	11
1.6 Innovative domestic fires for dual fuel applications.....	12
1.6.1 Open fires.....	13
1.6.2 Glass fronted coal effect fires.....	14
1.6.3 Flame effect or Innovative Fire.....	14
1.7 Combustion pollution and its effects.....	15
1.8 Legal framework and requirements for process burners.....	18
1.9 Research gaps.....	19
1.10 Aims and objectives.....	21
1.11. Thesis plan.....	22
<b>Chapter 2. LITERATURE REVIEW</b> .....	<b>24</b>
2.1 Nitrogen oxides (NO <sub>x</sub> ) emission types.....	24
2.1.1 Thermal NO <sub>x</sub> kinetics.....	26
2.2 Low-NO <sub>x</sub> technologies.....	27
2.2.1 Principles for low NO <sub>x</sub> .....	27
2.2.2 Rich-lean combustion.....	29
2.2.3. Two Staged Combustion (Lean/lean).....	30
2.2.4 Internal exhaust gas recirculation (IEGR).....	33
2.2.5 NO <sub>x</sub> reduction by impingement.....	35
2.2.6 NO <sub>x</sub> reduction by water injection.....	36
2.2.7 Premixed low-NO <sub>x</sub> combustion.....	37
2.2.8 Non-premixed low-NO <sub>x</sub> combustion.....	38

2.2.9 Hydrogen combustion .....	42
2.2.10 Grid plate flame stabilisers.....	44
2.2.10.1 Pressure loss in grid plate flame stabilisers.....	48
2.2.11 Pressure dependence of NO <sub>x</sub> .....	52
2.2.12 Ultra-low NO <sub>x</sub> levels by working at the lean flammability limit .....	53
2.3 Computational Fluid Dynamics for turbulent combustion .....	55
2.3.1 Turbulence modelling for 3D incompressible steady flows .....	56
2.3.1.1 Reynolds Number.....	56
2.3.2 Transport phenomena.....	57
2.3.2.1 Mass conservation .....	57
2.3.2.2 Momentum conservation .....	58
2.3.2.3 Conservation of Energy.....	59
2.3.2.4 Chemical Species Conservation equation. ....	60
2.3.3 Turbulence Models.....	61
2.3.3.1 Reynolds Average Navier Stokes (RANS) for incompressible flow .....	61
2.3.4 Mesh generation.....	66
2.3.5 Discretisation. ....	67
2.3.6 Solution of equations.....	68
2.3.7 Turbulent combustion.....	68
2.3.7.1 Non premixed turbulent combustion.....	70
2.3.7.2 Governing equations for non-premixed combustion.....	70
2.3.7.3 Combustion turbulent models for non-premixed combustion.....	72
2.3.8 Reaction rates and mechanisms.....	76
2.3.9 NO <sub>x</sub> modelling using CFD.....	77
2.4 Equilibrium software .....	78
<b>Chapter 3. METHODOLOGY.....</b>	<b>80</b>
3.1 Computational setup for thermodynamic equilibrium analysis.....	81
3.1.1. Equilibrium calculations for natural gas .....	84
3.1.1.1 Equilibrium calculations for natural gas in domestic fires .....	85
3.1.1.2 Equilibrium calculations for natural gas in the glass melting industry .....	85
3.1.2 Equilibrium calculations for hydrogen .....	86

3.1.2.1	Equilibrium calculations for hydrogen in domestic fire .....	86
3.1.2.2	Equilibria for the glass melting industry.....	87
3.1.3	Equilibrium calculations con biodiesel blend for glass melting industry.....	89
3.1.4	Equilibrium calculations for glycerol for the glass melting industry.....	90
3.1.5	Equilibrium calculations for European diesel blend for glass melting industry .....	91
3.1.6	Equilibrium calculations for ethanol for the glass melting industry.....	92
3.2	Computational setup for gas turbine combustor flame stabilisers for high combustion intensity.....	93
3.2.1	Grid Mix flame stabilisers.....	94
3.2.1.1	CFD study of aerodynamics for Grid Mix stabilisers ...	102
3.2.1.2	CFD study of non-reacting fuelling methods for Grid Mix flame stabiliser .....	106
3.2.1.3	CFD study of combustion for Grid Mix.....	110
3.2.1.3.1	Validation of turbulence and combustion models for combustion for GM2 using a propane/air mixture ..	111
3.2.1.3.2	Validation of turbulence and combustion models for combustion for GM1 using a propane/air mixture ..	119
3.2.1.4	CFD study of reacting fueling methods for Grid Mix flame stabilisers.....	121
3.2.1.4.1	Numerical combustion analysis for GM1 using a hydrogen/air mixture.....	123
3.3	Experimental setup for domestic fires .....	126
3.3.1	Rig concept.....	126
3.3.1.1	Leak testing.....	130
3.3.1.2	Pilot ignition test .....	130
3.3.1.3	Thermocouple Cut-off test.....	132
3.3.1.4	User-touchable surfaces temperature tests.....	132
3.3.2	Open fronted fire.....	133
3.3.3	Glass fronted fire (LEGEND).....	135
3.3.4	Innovative fire.....	138
3.4	Computational setup for domestic fires.....	141
3.4.1	Slot-shape hole geometry .....	142
3.4.2	Round hole geometry .....	143

<b>Chapter 4. EQUILIBRIA AND ADIABATIC TEMPERATURE CALCULATIONS FOR VARIOUS FUELS FOR PROCESS HEATERS.....</b>	<b>145</b>
4.1 Introduction.....	145
4.2 Equilibrium study for natural gas flame.....	145
4.2.1 Equilibrium study for natural gas for domestic fires.....	145
4.2.2 Equilibrium study for a cooled natural gas flame for domestic fires .....	146
4.2.3 Equilibrium study for natural gas for the glass melting industry.....	146
4.2.4 Equilibrium study for a cooled natural gas flame for the glass melting industry.....	147
4.3 Equilibrium study for hydrogen flame.....	147
4.3.1. Equilibrium study for hydrogen for domestic fires.....	147
4.3.2. Equilibrium study for a cooled hydrogen flame for domestic fires .....	148
4.3.3. Equilibrium study for glass melting industry (hydrogen).....	149
4.3.4 Equilibrium study for glass melting industry for a cooled flame (hydrogen) .....	150
4.4 Equilibrium study for biodiesel composition flame.....	151
4.4.1 Equilibrium study for biodiesel composition for a cooled flame .....	151
4.5 Equilibrium study for glycerol flame .....	152
4.5.1 Equilibrium study for glycerol flame for a cooled flame .....	153
4.5.2 Equilibrium study for glycerol/water composition flame.....	153
4.6 Equilibrium study for European diesel composition flame.....	155
4.6.1 Equilibrium study for European diesel composition for a cooled flame .....	155
4.7 Equilibrium study for ethanol flame .....	156
4.7.1 Equilibrium study for ethanol/air for a cooled flame .....	156
4.8 Conclusions .....	157
<b>Chapter 5. CFD STUDY FOR AERODYNAMICS FOR GAS TURBINE GRID PLATE FLAME STABILISERS .....</b>	<b>159</b>
5.1 Introduction .....	159
5.2 Modelling of pressure loss for single hole flame stabiliser .....	159
5.2.1 Single air hole 22.44mm flame stabilizer .....	159
5.2.2 Single 19.27mm air hole flame stabiliser.....	161
5.3 Modelling of pressure loss for four holes flame stabilisers .....	163
5.3.1 Four 22.44mm air hole stabiliser .....	164

5.3.2 Four 19.27mm air hole stabiliser .....	167
5.4 The influence of stabiliser thickness over fluid aerodynamics.....	170
5.5 The influence of welded inlet of grid plate flame stabiliser over fluid aerodynamics.....	174
5.6 Mesh sensitivity for flame stabiliser aerodynamics .....	178
5.6.1 Single hole geometries.....	178
5.6.2 Four hole geometries .....	179
5.7 Conclusions .....	181
<b>Chapter 6. CFD STUDY FOR NON-PREMIXED COMBUSTION GAS TURBINE GRID PLATE FLAME STABILISERS.....</b>	<b>182</b>
6.1 Introduction.....	182
6.2 Isothermal analysis of air/fuel mixing for grid plate flame stabiliser.....	182
6.3 Combustion analysis of grid plate flame stabiliser GM2 .....	185
6.3.1 GM2 studied with EDM and Chemical equilibrium combustion models.....	185
6.3.2 GM2 studied with SDF combustion model.....	187
6.3.3 GM2 studied with FGM combustion model.....	202
6.4 Combustion analysis for GM1 grid plate flame stabiliser .....	212
6.5 Combustion study for GM1, GM2 and GM3 .....	218
6.5.1 GM1 flame stabiliser for a hydrogen/air flame.....	223
6.5.2 Effect of a thicker stabiliser length on NO <sub>x</sub> emissions for a hydrogen flame.....	227
6.6 Conclusions .....	231
<b>Chapter 7. EXPERIMENTAL AND CFD ANALYSIS OF DOMESTIC HEATERS</b>	<b>234</b>
7.1 Introduction .....	234
7.2 Open fronted fire.....	234
7.2.1 Single-stage combustion .....	234
7.2.2. Two-stage combustion .....	240
7.3 Glass fronted fire .....	243
7.4 Innovative Fire .....	255
7.4.1 Numerical analysis for innovative fire .....	255
7.4.2 Experimental tests for innovative fire.....	259
7.4.2.1 M4 Design for a more attractive flame (fire box 150mm tall).....	260
7.5 Conclusions .....	265

<b>Chapter 8. CONCLUSIONS AND FUTURE WORK .....</b>	<b>266</b>
8.1 Equilibrium Flame Temperature and Composition.....	266
8.1.1 Ambient Temperature Burner Operation for Domestic Heat Application.....	267
8.1.2 Glass Furnace Prediction of the Composition of the Hot Gases above the Glass in the Float Glass Process for NG and hydrogen.....	268
8.1.3 Biofuels at glass melting conditions.....	269
8.2. CFD Predictions of Grid Mix Flame Stabilisers .....	270
8.2.1 Prediction of Flame Stabiliser Pressure Loss and $C_D$ .....	270
8.2.2 CFD prediction of Propane Grid Mix combustion .....	270
8.2.3 Prediction of the importance of fuel injection location on fuel and air mixing in Grid Mix burners .....	271
8.2.4 Predicted mean burner exit conditions. ....	271
8.3 Domestic Fires.....	272
8.4 Future work .....	274
8.4.1. Equilibrium study.....	274
8.4.2. Aerodynamics for grid plate flame stabilisers .....	275
8.4.3 Combustion for grid plate flame stabilisers .....	275
8.4.4 Combustion study for domestic fires on NG.....	275
<b>APPENDIX A. ....</b>	<b>294</b>
A.1 Navier Stokes equations .....	294
A.2 Realisable $k \epsilon$ model coefficients .....	295
A.3 SST $k-\omega$ model coefficients .....	295
A.4 Turbulence combustion regimes for premixed combustion .....	296
A.5 Turbulence combustion regimes for premixed combustion.....	297
<b>APPENDIX B. ....</b>	<b>299</b>
<b>APPENDIX C.....</b>	<b>305</b>
<b>APPENDIX D. ....</b>	<b>309</b>
<b>APPENDIX E.....</b>	<b>314</b>
<b>APPENDIX F.....</b>	<b>319</b>
<b>APPENDIX G. ....</b>	<b>324</b>
<b>APPENDIX H. ....</b>	<b>329</b>
H.1 Detailed Mechanism developed by Peters for propane/air combustion.....	329

<b>APPENDIX I.....</b>	<b>344</b>
I.1 Reduced Mechanism developed by Konnov for hydrogen/air combustion.....	344
<b>APPENDIX J.....</b>	<b>349</b>
J.1 Thin slots for dual fuel applications.....	349
J.1.1 Flow characteristics for thin slots.....	351
<b>APPENDIX K. ....</b>	<b>352</b>
K.1 Open fronted fire single-stage injection calculations.....	352
K.2 Open fronted fire two-stage design.....	353
<b>APPENDIX L.....</b>	<b>356</b>
L.1 Flow calculations for glass-fronted fire.....	356
<b>APPENDIX M.....</b>	<b>357</b>
M.1 Flow calculations for the Innovative fire.....	357
M.1.1 First fire configuration (LB4-LB5).....	357
M.1.2 Second fire configuration (Long burner).....	357

## List of Tables

Table 1-1. Local, Regional and Global Effects of 10 main pollutants [65].....	16
Table 2-1. CCGT combustor conditions for different turbine classes for a primary zone at 1800K. [30], [100]–[102].....	28
Table 2-2. Influence of $A_2/A_1$ on the contraction coefficient $C_c$ [173] for a sharp-edged orifice.....	51
Table 2-3. Influence of inlet temperature on lean flammability for various critical flame temperatures for methane and propane [99].....	54
Table 3-1 Comparison of Burcat/CEA thermodynamic polynomials considering enthalpy of formation for $H_2$ equilibrium products at 298K.....	83
Table 3-2: National Grid plc averaged natural gas composition over a two days period. ....	85
Table 3-3: Components of biodiesel fuels [253] .....	89
Table 3-4. Original C/H and O/C composition for FAME blend for soybean oil.....	90
Table 3-5. Approximation of the desired CHO composition for FAME blend for soybean oil .....	90
Table 3-6. Composition of diesel surrogate [252].....	91
Table 3-7. H/C calculation for diesel surrogate .....	92
Table 3-8. European diesel H/C approach using Excel Solver .....	92
Table 3-9 Gas analysis mean exhaust concentration % compared with that for the metered mean $\phi$ from equilibrium calculations for a metered $\phi= 0.69$ .....	96
Table 3-10: Studied flame stabiliser geometries using CFD for a 76mm combustor .....	98
Table 3-11. Boundary conditions for CFD simulations of aerodynamics.....	104
Table 3-12. Boundary conditions for CFD simulations of air/fuel mixing.....	107
Table 3-13. Under-relaxation factors for combustion simulation for GM2 using EDM and Chemical equilibrium.....	113
Table 3-14. Boundary conditions used for combustion simulations for GM2 using SDF .....	115
Table 3-15. Under-relaxation factors for combustion simulation for GM2 using SDF .....	116
Table 3-16. Element sizes used for structured hexahedral mesh used in combustion simulation with FGM for GM2 .....	117
Table 3-17. Boundary conditions used for combustion simulations for GM2 using FGM .....	118
Table 3-18. Under-relaxation factors for combustion simulation for GM2 using FGM.....	118

Table 3-19. Element sizes used for structured hexahedral mesh used in combustion simulation for GM1 .....	119
Table 3-20. Boundary conditions used for the combustion simulation of GM1.....	120
Table 3-21. Under-relaxation factors for combustion simulation for GM1.....	121
Table 3-22. Under-relaxation factors for combustion simulation for GM1 using FGM.....	122
Table 3-23. Under-relaxation factors for combustion simulation for GM3 using SDF .....	123
Table 3-24. Boundary conditions used for combustion simulations for GM1 for a hydrogen/air flame .....	124
Table 3-25. Under-relaxation factors for combustion simulation for GM1 for a hydrogen/air flame.....	125
Table 3-26. Safety temperature requirements for operating surfaces for relevant materials.....	132
Table 3-27. Safety temperature requirements for surfaces likely to be touched for relevant materials .....	132
Table 3-28: Boundary conditions for numerical study for Innovative fire. ....	142
Table 4-1. $T_{adiab}$ for NG mixture at an inlet temperature of 300K.....	145
Table 4-2. Equilibrium products for natural gas GOOLE mixture at 1.2% excess $O_2$ at 300K inlet temperature .....	146
Table 4-3: $T_{adiab}$ for NG mixture at an inlet temperature of 1500K.....	146
Table 4-4. Equilibrium products for natural gas GOOLE mixture at 1.0% excess $O_2$ at 1500K inlet temperature .....	147
Table 4-5. Equilibrium products for pure hydrogen mixture at 1.0% excess $O_2$ at 300K inlet temperature .....	149
Table 4-6: $T_{adiab}$ for $H_2$ mixture at 1500K inlet temp .....	149
Table 4-7: Equilibrium products for a mixture of pure hydrogen and air at 1.0% excess $O_2$ at 1500K inlet temperature.....	150
Table 4-8: $T_{adiab}$ for biodiesel mixture at 1500K inlet.....	151
Table 4-9: Equilibrium products for a cooled mixture of biodiesel from $T_{adiab}$ at 1.0% excess $O_2$ at 1500K inlet temperature.....	152
Table 4-10: $T_{adiab}$ for crude glycerol mixture at 1500K inlet .....	152
Table 4-11: Equilibrium products for a cooled mixture of crude glycerol from the adiabatic flame temperature at 1.0% excess $O_2$ at 1500K inlet temperature .....	153
Table 4-12: $T_{adiab}$ for 50% glycerol/50% water mixture at 1500K inlet temp.....	154
Table 4-13. Equilibrium products for a cooled mixture of 50% glycerol/50% water from the $T_{adiab}$ at 1.0% excess $O_2$ at 1500K inlet temperature .....	154

Table 4-14: $T_{adiab}$ for European diesel mixture at 1500K inlet temp .....	155
Table 4-15: Equilibrium products for a cooled mixture of European diesel from $T_{adiab}$ at ~1.0% excess $O_2$ at 1500K inlet temp .....	155
Table 4-16: $T_{adiab}$ for crude ethanol mixture at 1500K inlet temp.....	156
Table 4-17: Equilibrium products for a cooled mixture of ethanol/air from $T_{adiab}$ at 1% excess $O_2$ at 1500K inlet temperature .....	157
Table 4-18. Comparison of studied fuels for glass melting furnaces (Reference $NG=0.946$ $T_{in}=1500K$ ) .....	158
Table 5-1. $C_D$ and $C_C$ for single 22.44mm air hole flame stabilizer for the investigated mesh sizes .....	161
Table 5-2. $C_D$ and $C_C$ for single 19.27mm air hole flame stabilizer for the investigated mesh sizes .....	163
Table 5-3. $C_D$ and $C_C$ for a four 22.44mm air hole flame stabilizer for the investigated mesh sizes .....	164
Table 5-4 . $C_D$ and $C_C$ for a four 19.27mm air hole flame stabilizer for the investigated mesh sizes .....	168
Table 5-5. $C_D$ and $C_C$ for a four 19.62mm air hole flame stabilizer for the investigated mesh sizes .....	171
Table 5-6. $C_C$ and $C_D$ values for grid plate geometries featuring thin and thick blockages compared with the measured experimental values.....	171
Table 5-7. $C_D$ and $C_C$ for a four 19.62mm air hole flame stabilizer featuring various plate inlet weld slopes .....	175
Table 6-1. Experimental $NO_x$ results compared with simulation for GM2 $\emptyset=0.624$ .....	210
Table 6-2. Comparison of the CFD predicted mean composition at 330mm combustor length with two chemical equilibrium codes for GM2.....	212
Table 6-3. Experimental mean exit $NO_x$ levels compared with simulation for GM1 at $\emptyset=0.6$ .....	217
Table 6-4 Comparison of the CFD predicted mean composition at 330mm combustor length with two chemical equilibrium codes for GM1.....	218
Table 6-5. Comparison of the CFD predicted mean composition at 330mm combustor length with two chemical equilibrium codes for GM1-H2. ....	225
Table 6-6. Comparison of mean exit $NO_x$ levels between GM1-H2 and GM1-H2-7D.....	231
Table 6-7. Comparison of the CFD predicted mean composition at 330mm combustor length with two chemical equilibrium codes for GM1-H2 and GM1-H2-7D .....	231
Table 6-8. $NO_x$ level comparison for $C_3H_8$ and $H_2$ for GM1 .....	233
Table 7-1: Studied burner configurations for the open-fronted fire .....	235
Table 7-2: Steady-state emissions for FPB2 no coals $H_2$ .....	236
Table 7-3: Steady state emissions for FPB2 all coals NG.....	237

Table 7-4: Steady-state emissions for FPB2 no coals H <sub>2</sub> .....	237
Table 7-5: Steady-state emissions for FPB3 all coals NG and H <sub>2</sub> .....	239
Table 7-6: Steady-state emissions for FPB3 all coals two-stage combustion H <sub>2</sub> flame.....	241
Table 7-7: Studied burner configurations for the glass-fronted fire.....	244
Table 7-8: Steady-state results for LB2 with all coals tested for NG and H <sub>2</sub> .....	246
Table 7-9: Steady-state emissions for Innovative fire featuring LB4 and LB5 burners. 15.6 mbar H <sub>2</sub> .....	260
Table 7-10: Tests developed for the Innovative fire to improve the visual effect.....	261
Table 8-1. Comparison of adiabatic and cooled flame compositions for domestic heat applications for measured oxygen of about 1% .....	266
Table 8-2. NG and Hydrogen composition for adiabatic and cooled (1850K) flames for NG and H <sub>2</sub> at 1500K air inlet temperature. ....	268

## List of Figures

Figure 1-1. Final energy consumption from 1990-2020 [4] .....	2
Figure 1-2. Electricity energy source variation from 1998 to 2021 [6].....	2
Figure 1-3. Intermittent operation of NG CCGT to balance the Grid [7] .....	3
Figure 1-4. Wobbe Index and heating value variation for NG/H <sub>2</sub> blends .....	4
Figure 1-5. CFD output for temperature prediction (a) compared with measurements (b) from King et al. [46] .....	12
Figure 1-6. European mass distribution of NO <sub>x</sub> in ambient air [71]......	17
Figure 1-7. Estimated annual emissions of NO <sub>x</sub> in the UK in kt 1990- 2019[71] .....	18
Figure 2-1. Thermal NO <sub>x</sub> as a function of the flame temperature for residence times 5, 10 and 20ms. NO <sub>x</sub> ppm corrected to 15% oxygen. Calculations at 623K air temperature at 12.3 bar, typical industrial gas turbine conditions[97]......	26
Figure 2-2. Equilibrium NO <sub>x</sub> and adiabatic flame temperature vs equivalence ratio for different air temperatures (edited [107]).....	29
Figure 2-3: Lean/ lean stage combustor [109]......	31
Figure 2-4. Lean/lean two-stage combustors: a) Zenger et al [109]. b) Siemens [57] . .....	31
Figure 2-5. Designs of low NO <sub>x</sub> combustors from the NASA programme[112]-[115]. .....	32
Figure 2-6. NO <sub>x</sub> emissions vs flame temperature [119]......	33
Figure 2-7. 1700° C-class Gas Turbine Combined Cycle (GTCC) plant with exhaust gas recirculation [101]......	34
Figure 2-8. Adiabatic flame temperatures with various levels of intake oxygen at different fuel-air equivalence ratios [124] .....	35
Figure 2-9. Diagram of low pressure IEGR low NO <sub>x</sub> combustor [123]......	35
Figure 2-10 Effect of water/steam injection over NO <sub>x</sub> emissions [126] .....	36
Figure 2-11. Comparison of diffusion and premixed burners considering an equivalence ratio of 0.55 [130]......	37
Figure 2-12. NO <sub>x</sub> progression with premixed systems [136]. .....	38
Figure 2-13. FLOX burner with 12 single nozzles. [37] Edited. ....	39
Figure 2-14. CH <sub>4</sub> contours obtained with CFD for FLOX burner showing recirculating flow [81] .....	39
Figure 2-15. NO <sub>x</sub> and CO emissions for FLOX technology for two fuels [41].....	40
Figure 2-16. (A) Fuel staged cluster nozzle burner of HITACHI in a 3MW Gas Turbine. (B) NO <sub>x</sub> levels at different values of A/F [138]......	40
Figure 2-17. Micromix principle showing the recirculation areas inside the combustor using CFD (Edited [139], [140]) .....	41

Figure 2-18. NO <sub>x</sub> emissions vs $\phi$ for different combustors configurations. [139].....	41
Figure 2-19. Development and testing of a low NO <sub>x</sub> Hydrogen Combustion System for HDGT [43].....	42
Figure 2-20. NO <sub>x</sub> comparison for experimental and simulation values for Micromix hydrogen combustor [151].....	43
Figure 2-21. Flame temperature vs NO <sub>x</sub> levels for MT mixer [43].....	44
Figure 2-22. Comparison of NO <sub>x</sub> corrected to 15% oxygen as a function of $\phi$ at 400K [21]–[23] .....	46
Figure 2-23. Plate stabilizer geometries [157].....	47
Figure 2-24. Emission measurements for different grid plates [158].....	47
Figure 2-25. Four hole Grid Mix air jet configuration and jet shear layer hole shapes .....	48
Figure 2-26. Photographs of a diffusion pilot tip and the multi-tube [27] .....	55
Figure 2-27. Free shear flow showing laminar, transition and turbulent phases [179].....	56
Figure 2-28. $k$ - $\epsilon$ modelling a Jet in a crossflow [188].....	63
Figure 2-29. Gas flow streamlines in a grid plate using $k$ - $\omega$ SST [197].....	66
Figure 2-30. Different mesh types used. a) Structured with Ogrid. b) Unstructured. c) Hexahedral. d) Polyhedral.....	67
Figure 2-31. NO prediction comparison A) kinetic mechanism with NO, B)ANSYS FLUENT model [46]. .....	78
Figure 3-1: Adiabatic flame temperature for hydrogen flame comparison between CEA and Gaseq .....	84
Figure 3-2: CEA results for an H <sub>2</sub> composition at 295K and 1 ATM. A) Adiabatic temperature in K vs initial H <sub>2</sub> in vol % in air and equilibrium NO in ppm; b) Adiabatic temperature in °C vs $\phi$ and equilibrium NO in mg/kWh. ....	86
Figure 3-3: Thermal NO and adiabatic temperature vs H <sub>2</sub> vol% for 100 ms.....	87
Figure 3-4: Comparison of adiabatic flame temperature vs $\phi$ for pure and real H <sub>2</sub> compositions.....	88
Figure 3-5: a) Comparison of adiabatic flame temperature vs $\phi$ for pure and real H <sub>2</sub> mixtures showing the error between them; b) Calculated error between both mixtures. ....	88
Figure 3-6. Experimental rig used for grid mix flame stabilisers [157]. ....	94
Figure 3-7. Internal traverse water-cooled gas sample probe 15mm OD with 1mm gas sample hole inlet.....	97
Figure 3-8. Traverse locations of GA and TC for 2 different positions.....	98
Figure 3-9: Fuel injection methods for a) GM1; and b) GM2.....	99
Figure 3-10. Flame stabiliser GM2 featuring an annular injection.....	100

Figure 3-11. Flame stabiliser GM1 featuring eight radial inward fuel nozzles per air hole .....	100
Figure 3-12. Fuel injection methods for a) GM3; b) GM1-GE.....	101
Figure 3-13. Computational model used for single-hole simulations (aerodynamics).....	102
Figure 3-14. Computational model used for four-hole simulations.....	104
Figure 3-15. Y plus values for four 19.27mm hole flame stabiliser.....	105
Figure 3-16: GM2 showing 13° weld at the stabiliser upstream air inlet .....	105
Figure 3-17. Mesh statistics for GM2 tetrahedral unstructured mesh: LHS) Flat plate; RHS) Welded inlet plate. A) Quality, B) Determinant, C) Aspect ratio.....	106
Figure 3-18. Mesh statistics for radial injection GM1 for 19.62mmhole stabiliser. A) determinant, B) aspect ratio .....	108
Figure 3-19. Mesh statistics for radial injection GM2 for 19.62mmhole stabiliser. A) determinant, B) quality, C) aspect ratio.....	109
Figure 3-20. Mesh statistics for radial injection GM3 for 19.62mmhole stabiliser. A) determinant, B) quality, C) aspect ratio.....	110
Figure 3-21. Statistics for unstructured tetrahedral mesh used for preliminary combustion simulations for GM2.....	112
Figure 3-22. Hexahedral structured mesh used in combustion simulation for GM2.....	114
Figure 3-23. Inflation layer at fuel injection for hexahedral mesh used in combustion simulation with SDF for GM2 .....	114
Figure 3-24. Statistics for structured hexahedral mesh used in combustion simulation for GM2. A) Determinant, B) Aspect ratio.....	114
Figure 3-25. Hexahedral unstructured mesh used for the simulation of GM1.....	119
Figure 3-26. Schematics for: A) Hydrogen line; B) Natural gas line installed in G.03. H=hydrogen; NG=natural gas; IV=isolation valve; PR=pressure regulator; FV=flow valve; FM=flow meter .....	128
Figure 3-27. Rig set up in lab G.03f Energy building used in Hy4Heat project.....	129
Figure 3-28. Prototype pilot used for the fires in the Hy4Heat project.....	131
Figure 3-29. A) Reference open fronted fire. B) Slot-shape fuel holes burner configuration for open-fronted fire single-staged .....	134
Figure 3-30: Burner design for open-fronted fire two-stage injection.....	135
Figure 3-31. Location of single-stage fuel injection in the glass-fronted fire.....	136
Figure 3-32. Construction of the Legend Glass Fronted Fire .....	137
Figure 3-33: External flue/air pipe for the glass-fronted fire .....	137

Figure 3-34: Manometer for plenum pressure in the glass-fronted fire. ....	138
Figure 3-35: Innovative fire gas recirculation concept. ....	139
Figure 3-36: Preliminary prototype for Innovative fire .....	140
Figure 3-37: An approved design for Innovative fire tests.....	140
Figure 3-38: Innovative fire model used for the numerical analysis featuring a slot-shaped hole.....	142
Figure 3-39: Mesh used for numerical analysis of Innovative fire (slot- shaped hole).....	143
Figure 3-40: Mesh statistics for slot-shape fuel injection geometry of Innovative fire: a) quality; B) determinant.....	143
Figure 3-41: Mesh statistics for round fuel hole fuel injection geometry of Innovative fire: a) quality; B) determinant.....	144
Figure 4-1: Adiabatic flame temperatures for H <sub>2</sub> mixture (temps 298- 600K) .....	148
Figure 4-2: a) Exhaust dry H <sub>2</sub> vol % vs Ø for H <sub>2</sub> mixture (temps (298- 600K); b) NO ppm vs Ø for H <sub>2</sub> mixture at inlet temps 298-600K.....	148
Figure 5-1. Mesh qualities for wall pressure loss for one hole flame stabiliser 22.44mm diameter considering $k-\epsilon$ compared with the experimental results [157].....	160
Figure 5-2 Mesh qualities for wall pressure loss for one hole flame stabiliser 22.44mm diameter considering $SST$ compared with the obtained experimental results [157].....	160
Figure 5-3. Mesh qualities for wall pressure loss for one hole flame stabiliser 19.27mm diameter considering $k-\epsilon$ compared with the obtained experimental results [157].....	162
Figure 5-4. Mesh qualities for wall pressure loss for one hole flame stabiliser 19.27mm diameter considering $SST$ compared with the obtained experimental results [157].....	162
Figure 5-5. Mesh qualities for wall pressure loss for four hole flame stabiliser 22.44mm diameter considering $k-\epsilon$ compared with the obtained experimental results [157].....	164
Figure 5-6. Velocity contours for flame stabiliser 22.44mm diameter A) four holes 2.7M elements, B) one hole 6M elements.....	165
Figure 5-7. TKE contours for hole stabiliser 22.44mm diameter A) four holes, B) one hole. ....	166
Figure 5-8. TKE contours 55 mm downstream the stabiliser for flame stabiliser 22.44 mm diameter. A) one hole combustor. B) 4 holes combustor. ....	166
Figure 5-9. Mesh qualities for wall pressure loss for four hole flame stabiliser 19.27mm diameter considering $k-\epsilon$ compared with the obtained experimental results [157].....	167

Figure 5-10. Axial velocity contours for flame stabiliser 19.27mm diameter. A) one hole combustor. B) 4 holes combustor .....	168
Figure 5-11. TKE contours for flame stabiliser 19.27mm diameter. A) one hole combustor. B) 4 holes combustor .....	169
Figure 5-12. TKE contours 60mm downstream the stabiliser for flame stabiliser 19.27mm diameter. A) one hole combustor. B) 4 holes combustor .....	169
Figure 5-13. Mesh qualities for wall pressure loss for four-hole flame stabiliser 19.62mm diameter compared with 19.27mm stabiliser hole and the experimental results considering $k-\epsilon$ [157].....	170
Figure 5-14. Axial velocity contours for four-hole flame stabiliser. A) one hole 19.27mm diameter. B) 19.62mm diameter.....	172
Figure 5-15. Closeup for stabiliser region showing the flow separation and recirculation zone. ....	173
Figure 5-16. TKE contours for four-hole flame stabiliser. A) one hole 19.27mm diameter. B) 19.62mm diameter .....	174
Figure 5-17. Enclosure of 19.62mm airhole grid plate flame stabiliser: A) Flat inlet face, B) inlet face with welding slope .....	174
Figure 5-18. Mesh qualities for wall pressure loss for four-hole flame stabiliser 19.62mm diameter considering $k-\epsilon$ comparing various plate inlet weld slopes and the experimental results [157]. ....	175
Figure 5-19. Turbulence Kinetic energy comparison for 19.62mm four hole flame stabiliser: A) Welded inlet. B) Flat inlet. ....	176
Figure 5-20. Closeup for stabiliser region showing the TKE for 19.62mm stabiliser hole geometry. A) Welded inlet, B) Flat inlet. ....	177
Figure 5-21. TKE contours for GM2 using the SDF. A) Flat plate, B) Plate with the welded inlet. ....	178
Figure 5-22. Simulation/experiment error variance between mesh qualities for single hole geometries .....	179
Figure 5-23. Simulation/experiment error variance between mesh qualities for four hole geometries .....	180
Figure 5-24. Simulation/experiment error variance between mesh qualities for grid mix 19.62mm geometries. ....	180
Figure 6-1. Simulation of fuel injection methods for A) GM1, B) GM2, and C) GM3. ....	182
Figure 6-2. Equivalence ratio contours for non-reacting simulation A) GM1, B) GM2, I GM3 .....	183
Figure 6-3. Closeup of grid plate air hole for GM2 showing velocity vectors...	184
Figure 6-4. Equivalence ratio contours 100mm downstream of the stabiliser for a non-reacting simulation. A) GM1, B) GM2, C) GM3 .....	184

Figure 6-5. Comparison of temperature plot obtained with the gas analysis at the combustor centreline between experimental results [157] and simulation using EDM and chemical equilibrium.....	186
Figure 6-6. Comparison of temperature plot obtained with gas analysis 2.6mm from the combustor wall between experimental results [157] and simulation using EDM and chemical equilibrium.....	186
Figure 6-7. Temperature contours for combustion simulation for GM1. A)EDM, B) Chemical equilibrium .....	187
Figure 6-8. Internal combustor planes used for the obtention of combustion contours using SDF for GM2 A) Inline with the holes, B) in offset with the holes.....	188
Figure 6-9. Axial velocity contours for GM2 for SDF simulation. A) Inline with the holes, B) In offset with the holes.....	188
Figure 6-10. Axial TKE contours for GM2 for SDF simulation. A) Inline with the holes, B) In offset with the holes.....	189
Figure 6-11. Axial temperature contours for GM2 for SDF simulation. A) Inline with the holes, B) In offset with the holes.....	189
Figure 6-12. Axial equivalence ratio contours for GM2 for SDF simulation. A) Inline with the holes, B) In offset with the holes.....	190
Figure 6-13. Axial oxygen mass fraction contours for GM2 for SDF simulation. A) Inline with the holes, B) In offset with the holes.....	190
Figure 6-14. Axial CO mass fraction contours for GM2 for SDF simulation. A) Inline with the holes, B) In offset with the holes.....	191
Figure 6-15. Z velocity contours across combustor for axial distances 0, 25, 50, 75, 100, 150 and 300mm from GM2 downstream face (SDF simulation).....	192
Figure 6-16. TKE contours across combustor for axial distances 0, 25, 50, 75, 100, 150 and 300mm from GM2 downstream face (SDF simulation).....	192
Figure 6-17. Temperature contours across combustor for axial distances 0, 25, 50, 75, 100, 150 and 300mm from GM2 downstream face (SDF simulation).....	193
Figure 6-18. Contours of $\emptyset$ across combustor for axial distances 0, 25, 50, 75, 100, 150 and 300mm from GM2 downstream face (SDF simulation).....	194
Figure 6-19. O <sub>2</sub> contours across combustor for axial distances 0, 25, 50, 75, 100, 150 and 300mm from GM2 downstream face (SDF simulation).....	194
Figure 6-20. CO <sub>2</sub> contours across combustor for axial distances 0, 25, 50, 75, 100, 150 and 300mm from GM2 downstream face (SDF simulation).....	194

Figure 6-21. CO contours across combustor for axial distances 0, 25, 50, 75, 100, 150 and 300mm from GM2 downstream face (SDF simulation).....	195
Figure 6-22. Comparison of GA based temperature [157] with simulation using SDF for GM2 for the gas analysis probe located at the combustor airhole centreline .....	196
Figure 6-23. Comparison of gas analysis based temperature [157] with simulation using SDF for GM2 with the probe located 7.5mm away from the combustor wall.....	196
Figure 6-24. Comparison of thermocouple based temperature [157] with simulation using SDF for GM2 with the probe located 5mm in offset from the combustor centreline.....	197
Figure 6-25. Comparison of thermocouple based temperature [157] with simulation using SDF for GM2 with the probe located 29mm away from the wall.....	198
Figure 6-26. Comparison of combustion efficiency profiles obtained experimentally [157] and with simulation using SDF for GM2 with the gas analysis probe located at the hole centreline .....	198
Figure 6-27. Comparison of combustion efficiency profiles obtained experimentally [157] and with simulation using SDF for GM2 with the gas analysis probe located 7.5mm away from the wall .....	199
Figure 6-28. Comparison of $\emptyset$ profiles obtained experimentally [157] and with simulation using SDF for GM2 for the gas analysis probe 5mm offset from the combustor centreline .....	200
Figure 6-29. Comparison of $\emptyset$ profiles obtained experimentally [157] and with simulation using SDF for GM2 for the gas analysis probe located 7.5mm from the wall.....	200
Figure 6-30. Residuals for SDF simulation for GM2 .....	201
Figure 6-31. Temperature report definition for SDF simulation of GM2 .....	201
Figure 6-32. NO <sub>x</sub> contours for SDF simulation for GM2 .....	202
Figure 6-33. Simulation results for FGM and unstructured hexahedral mesh for GM2 A) Velocity contours, B)TKE contours.....	203
Figure 6-34. Comparison of equivalence ratio contours for GM2 A) FGM, B) SDF .....	204
Figure 6-35. Comparison of $\emptyset$ profiles obtained experimentally [157] and with simulation using FGM and SDF for GM2 for the gas analysis probe located 5mm in offset with the combustor centreline .....	204
Figure 6-36. Comparison of $\emptyset$ profiles obtained experimentally [157] and with simulation using FGM and SDF for the gas analysis probe located 7.5mm from the combustor wall.....	205
Figure 6-37. Comparison of temperature contours for GM2 A) FGM, B) SDF .....	206

Figure 6-38. Comparison of temperature profiles obtained experimentally [157] and with simulation using FGM and SDF for gas analysis probe located at the stabiliser hole centreline .....	206
Figure 6-39. Comparison of temperature profiles obtained experimentally [157] and with simulation using FGM and SDF for gas analysis probe located 7.5mm away from the combustor wall.....	207
Figure 6-40. Comparison of temperature profiles obtained experimentally [157] and with simulation using FGM and SDF for thermocouple located 5mm in offset from the combustor centreline.....	208
Figure 6-41. Comparison of temperature profiles obtained experimentally [157] and with simulation using FGM and SDF for thermocouple 29mm away from the combustor wall.....	208
Figure 6-42. Cross-sectional area-averaged mean flame temperature predicted with FGM as a function of axial distance from the stabiliser position for GM2.....	209
Figure 6-43. NO <sub>x</sub> contours for FGM simulation for GM2.....	209
Figure 6-44. Comparison of NO <sub>x</sub> profiles obtained experimentally [157] and with simulation using FGM for the gas analysis probe located 5mm in offset of the combustor centreline.....	210
Figure 6-45. Comparison of CO contours for GM2 A) FGM, B) SDF.....	211
Figure 6-46. Comparison of CO <sub>2</sub> contours for GM2 A) FGM, B) SDF.....	211
Figure 6-47. Axial velocity contours for FGM simulation for GM1 .....	212
Figure 6-48. Velocity vectors for GM1 simulation.....	213
Figure 6-49. TKE contours for GM1 simulation .....	213
Figure 6-50. Equivalence ratio contours for GM1 simulation .....	214
Figure 6-51. Equivalence ratio plots at the combustor centreline and at the centreline of the airholes for GM1. ....	214
Figure 6-52. Temperature contours for GM1 simulation.....	215
Figure 6-53. Temperature plots at the combustor centreline and at the centreline of the airholes for GM1.....	215
Figure 6-54. CO <sub>2</sub> contours for GM1 simulation .....	216
Figure 6-55. CO contours for GM1 simulation .....	216
Figure 6-56. NO <sub>x</sub> contours for GM1 simulation.....	216
Figure 6-57. NO <sub>x</sub> levels for GM1 at 5mm offset of combustor centreline. ....	217
Figure 6-58 GM1 flame at 400K, M=0.047, $\varnothing = 0.6$ compared with simulation .....	218
Figure 6-59. Comparison of axial velocity contours for reacting mixture A)GM1, B)GM2, C)GM3.....	219
Figure 6-60. Closeup of TKE contours for reacting mixture for GM1 showing no fuel penetration.....	220

Figure 6-61. TKE contours for reacting mixture GM3 .....	220
Figure 6-62. Comparison of equivalence ratio contours for reacting mixture A)GM1, B)GM2, C)GM3.....	221
Figure 6-63. Comparison of temperature contours for reacting mixture A)GM1, B)GM2, C)GM3.....	222
Figure 6-64. Comparison of NO <sub>x</sub> contours for reacting mixture A)GM1, B)GM2 .....	222
Figure 6-65. Flame aerodynamics for GM1 evaluated for hydrogen/air flame. A) Axial velocity, B) TKE .....	223
Figure 6-66. Equivalence ratio contours for GM1 evaluated for hydrogen/air flame .....	224
Figure 6-67. Temperature contours for GM1 evaluated for hydrogen/air flame.....	224
Figure 6-68. Oxygen contours for GM1 evaluated for hydrogen/air flame.....	225
Figure 6-69. NO <sub>x</sub> contours for GM1 for a hydrogen/air mixture A) Inline with the air holes B) 45° offset with the airholes.....	226
Figure 6-70. Comparison of NO <sub>x</sub> levels at the combustor centreline for GM1 for a hydrogen a propane flame.....	226
Figure 6-71. Axial velocity contours for GM1 with 7D stabiliser thickness for hydrogen/air flame .....	227
Figure 6-72. Velocity vectors at stabiliser region for GM1 with 7D stabiliser thickness for hydrogen/air flame .....	228
Figure 6-73. TKE contours for GM1 with 7D stabiliser thickness for hydrogen/air flame .....	228
Figure 6-74. TKE contours at stabiliser region for GM1 with 7D stabiliser thickness for hydrogen/air flame.....	228
Figure 6-75. Equivalence ratio contours for GM1 with 7D stabiliser thickness for hydrogen/air flame.....	229
Figure 6-76. Temperature contours for GM1 with 7D stabiliser thickness for hydrogen/air flame .....	229
Figure 6-77. Oxygen mole fraction contours for GM1 with 7D stabiliser thickness for hydrogen/air flame.....	230
Figure 6-78. NO <sub>x</sub> ppm contours for GM1 with 7D stabiliser thickness for hydrogen/air flame .....	230
Figure 6-79. NO <sub>x</sub> ppm contours at wall region for GM1 with 7D stabiliser thickness for hydrogen/air flame.....	230
Figure 7-1: Open fronted reference fire NG.....	236
Figure 7-2: FPB2 burner NO <sub>x</sub> levels for H <sub>2</sub> and NG .....	238
Figure 7-3: Open fronted fire FPB2 10 mbar: a) NG; b) H <sub>2</sub> .....	238
Figure 7-4: Open fronted fire FPB3 13.6 mbar: a) NG; b) H <sub>2</sub> .....	239

Figure 7-5: Steady-state emissions for FPB2 and FPB3 all coals NG and H <sub>2</sub> ....	239
Figure 7-6: Open fronted fire FPB3 for dual fuel H <sub>2</sub> 20 mbar.....	240
Figure 7-7: NO <sub>x</sub> emissions for FPB3 two-stage combustion 20 mbar, obtained in a 60 minutes test, H <sub>2</sub> flame.....	241
Figure 7-8: Steady-state NO <sub>x</sub> emissions for different powers for FPB3 for single-stage and two-stage combustion H <sub>2</sub> flame.....	242
Figure 7-9: Open fronted fire FPB3 for dual fuel NG 20 mbar.....	242
Figure 7-10: CO and NO <sub>x</sub> values for FPB3 two-stage burner full loading NG ...	243
Figure 7-11: Secondary injection showing cracks and notoriously worn. ....	243
Figure 7-12: Glass fronted reference fire LB1 natural gas.....	245
Figure 7-13: LB2 15mbar . a) Natural gas; b) Hydrogen .....	246
Figure 7-14: Glass fronted fire LB5 all coals NG 20mbar .....	247
Figure 7-15: Glass fronted fire LB5 all coals H <sub>2</sub> 3mbar .....	248
Figure 7-16: Glass fronted fire LB13 natural gas 20mbar .....	249
Figure 7-17: Glass fronted fire LB13 natural gas 5mbar .....	249
Figure 7-18: Glass fronted fire LB13 H <sub>2</sub> 6mbar .....	250
Figure 7-19: Temperature and NO <sub>x</sub> vs test duration for LB13 with H <sub>2</sub> 7mbar.....	250
Figure 7-20: Measurement of burner plate LB5 slot using Alicona infinite focus .....	251
Figure 7-21: Comparison of measured dimensions obtained with Alicona infinite focus device vs the designed dimensions for LB15 and LB6.....	251
Figure 7-22: LB17-FRONT-ALLC-D-NG; a) 10 mbar, b)20 mbar .....	252
Figure 7-23: Glass fronted fire LB17 H <sub>2</sub> full power (3.4kW): a) lights off, b) lights on .....	253
Figure 7-24: Glass fronted fire LB17 H <sub>2</sub> half power (3.4kW) .....	253
Figure 7-25: LB17 burner performance on hydrogen for different coal config.....	254
Figure 7-26: LB17 burner performance NO <sub>x</sub> for H <sub>2</sub> and NG.....	254
Figure 7-27: Velocity contours for A) Round hole; B) Slot-shaped hole for numerical analysis of Innovative fire prototype.....	256
Figure 7-28: Turbulence kinetic energy contours for A) Round hole; B) Slot-shaped hole for numerical analysis of Innovative fire prototype .....	256
Figure 7-29: Equivalence ratio contours for A) Round hole; B) Slot-shaped hole for numerical analysis of Innovative fire prototype.....	257
Figure 7-30: Temperature contours for A) Round hole; B) Slot-shaped hole for numerical analysis of Innovative fire prototype .....	257
Figure 7-31: NO <sub>x</sub> contours for A) Round hole; B) Slot-shaped hole for numerical analysis of Innovative fire prototype.....	258

Figure 7-32. Flame shape comparison for NG. A) Experiment; B) Simulation .....	258
Figure 7-33: Flame for Innovative fire using LB4 (LHS) and LB5 (RH) 15 mbar, H <sub>2</sub> .....	259
Figure 7-34: Test 31 Innovative fire appearance study 20 mbar.....	263
Figure 7-35: NO <sub>x</sub> emissions vs test duration for M6 Innovative fire test 31 ...	263
Figure 7-36: Thermal efficiency vs test duration for M6 Innovative fire test 31 .....	264
Figure 7-37. Final commercial design for the Innovative fire .....	264
Figure A-1. Regimes in non-premixed turbulent combustion [177].....	298
Figure B-1. Adiabatic flame temperature for Goole NG/air mixture(inlet temperatures 298-1600K) .....	299
Figure B-2. Exhaust CO molar fraction for Goole NG/air mixture (inlet temperatures 298-1600K) .....	300
Figure B-3. Exhaust H <sub>2</sub> molar fraction for Goole NG/air mixture (inlet temperatures 298-1600K) .....	301
Figure B-4. Exhaust H <sub>2</sub> O molar fraction for Goole NG/air mixture (inlet temperatures 298-1600K) .....	302
Figure B-5. Exhaust O <sub>2</sub> molar fraction for Goole NG/air mixture (inlet temperatures 298-1600K) .....	303
Figure B-6. Exhaust NO ppm for Goole NG/air mixture (inlet temperatures 298-1600K) .....	304
Figure C-1. Adiabatic flame temperature for pure H <sub>2</sub> mixture(inlet temperatures 298-1600K) .....	305
Figure C-2. Exhaust NO ppm for pure H <sub>2</sub> /air mixture (inlet temperatures 298-1600K) .....	306
Figure C-3. Exhaust H <sub>2</sub> O molar fraction for pure H <sub>2</sub> /air mixture (inlet temperatures 298-1600K) .....	307
Figure C-4. Exhaust O <sub>2</sub> molar fraction for pure H <sub>2</sub> /air mixture (inlet temperatures 298-1600K) .....	308
Figure D-1. Adiabatic flame temperature for biodiesel/air mixture(inlet temperatures 300-1600K) .....	309
Figure D-2. Exhaust CO molar fraction for biodiesel/air mixture (inlet temperatures 300-1600K) .....	310
Figure D-3. Exhaust H <sub>2</sub> molar fraction for CH <sub>1.88</sub> O <sub>0.11</sub> /air mixture (inlet temperatures 300-1600K) .....	311
Figure D-4. Exhaust H <sub>2</sub> O molar fraction for CH <sub>1.88</sub> O <sub>0.11</sub> /air mixture (inlet temperatures 300-1600K) .....	312
Figure D-5. Exhaust NO ppm for CH <sub>1.88</sub> O <sub>0.11</sub> /air mixture (inlet temperatures 300-1600K) .....	313

Figure E-1. Adiabatic flame temperature for pure glycerol/air mixture(inlet temperatures 300-1600K) .....	314
Figure E-2. Exhaust CO molar fraction for pure glycerol/air mixture (inlet temperatures 300-1600K) .....	315
Figure E-3. Exhaust H <sub>2</sub> molar fraction for pure glycerol/air mixture (inlet temperatures 300-1600K) .....	316
Figure E-4. Exhaust H <sub>2</sub> O ppm for pure glycerol/air mixture (inlet temperatures 300-1600K) .....	317
Figure E-5. Exhaust NO ppm for pure glycerol/air mixture (inlet temperatures 300-1600K) .....	318
Figure F-1. Adiabatic flame temperature for European diesel composition/air mixture (inlet temperatures 300-1600K) .....	319
Figure F-2. Exhaust CO molar fraction for European diesel composition/air mixture (inlet temperatures 300-1600K) .....	320
Figure F-3. Exhaust H <sub>2</sub> molar fraction for European diesel composition/air mixture (inlet temperatures 300-1600K) .....	321
Figure F-4. Exhaust H <sub>2</sub> O molar fraction for European diesel composition/air mixture (inlet temperatures 300-1600K).....	322
Figure F-5. Exhaust NO ppm for European diesel composition/air mixture (inlet temperatures 300-1600K) .....	323
Figure G-1. Adiabatic flame temperature for pure ethanol/air mixture (inlet temperatures 300-1600K) .....	324
Figure G-2. Exhaust CO molar fraction for pure ethanol/air mixture (inlet temperatures 300-1600K) .....	325
Figure G-3. Exhaust H <sub>2</sub> molar fraction for pure ethanol/air mixture (inlet temperatures 300-1600K) .....	326
Figure G-4. Exhaust H <sub>2</sub> O molar fraction for pure ethanol/air mixture (inlet temperatures 300-1600K) .....	327
Figure G-5. Exhaust NO ppm for pure ethanol/air mixture (inlet temperatures 300-1600K) .....	328
Figure K-1. Two-stage design for open-fronted fire.....	355
Figure M-1. Fuel plenum with different slot sizes used for the innovative fire tests featuring a single burner. ....	358

**List of equations**

Equation (1).....	24
Equation (2).....	25
Equation (3).....	25
Equation (4).....	26
Equation (5).....	26
Equation (6).....	26
Equation (7).....	50
Equation (8).....	50
Equation (9).....	50
Equation (10).....	50
Equation (11).....	50
Equation (12).....	51
Equation (13).....	51
Equation (14).....	51
Equation (15).....	52
Equation (16).....	52
Equation (17).....	52
Equation (18).....	53
Equation (19).....	56
Equation (20).....	57
Equation (21).....	58
Equation (22).....	58
Equation (23).....	58
Equation (24).....	59
Equation (25).....	59
Equation (26).....	60
Equation (27).....	60
Equation (28).....	60
Equation (29).....	61
Equation (30).....	62
Equation (31).....	64
Equation (32).....	64
Equation (33).....	64
Equation (34).....	64

Equation (35).....	64
Equation (36).....	64
Equation (37).....	65
Equation (38).....	65
Equation (39).....	65
Equation (40).....	70
Equation (41).....	70
Equation (42).....	70
Equation (43).....	70
Equation (44).....	71
Equation (45).....	71
Equation (46).....	71
Equation (47).....	71
Equation (48).....	73
Equation (49).....	73
Equation (50).....	73
Equation (51).....	73
Equation (52).....	74
Equation (53).....	75
Equation (54).....	75
Equation (55).....	75
Equation (56).....	76
Equation (57).....	76
Equation (58).....	76
Equation (59).....	76
Equation (60).....	79
Equation (61).....	79
Equation (62).....	79
Equation (63).....	79
Equation (64).....	79
Equation (65).....	79
Equation (66).....	86
Equation (67).....	107
Equation (68).....	107
Equation (69).....	111

Equation (70).....	127
Equation (71).....	127
Equation (72).....	127
Equation (73).....	127
Equation (74).....	130
Equation (75).....	294
Equation (76).....	294
Equation (77).....	294
Equation (78).....	294
Equation (79).....	296
Equation (80).....	296
Equation (81).....	296
Equation (82).....	296
Equation (83).....	296
Equation (84).....	297
Equation (85).....	297
Equation (86).....	297
Equation (87).....	297
Equation (88).....	297
Equation (89).....	297
Equation (90).....	297
Equation (91).....	353
Equation (92).....	353
Equation (93).....	354
Equation (94).....	354
Equation (95).....	354

## Acronyms and abbreviations

<b>Abbreviation</b>	<b>Definition</b>
CCGT	Combined Cycle Gas Turbines
BEIS	Department for Business Energy and Industrial Strategy
TET	Turbine Entry Temperature
NO <sub>x</sub>	Nitrogen oxides
GM1	Grid Mix one (radial injection)
GM2	Grid Mix two (annular feed)
GM3	Grid Mix three (central injection)
GM1-7D	Grid Mix one with a thicker stabiliser
IEGR	Internal exhaust gas recirculation
CFD	Computational fluid dynamics
RANS	Reynolds Averaged Navier Stokes
TKE	Turbulence kinetic energy
PDF	Probability density function
EDM	Eddy dissipation model
SDF	Steady diffusion model
FGM	Flamelet generated manifold
DO	Discrete ordinates

## Nomenclature

Symbol	Definition	SI Unit
$m'$	Mass fraction	kg/s
$C_D$	Discharge coefficient	-
$C_c$	Contraction coefficient	-
$Re$	Reynolds number	-
$\Delta P$	Pressure loss	-
$P$	Pressure	N/m <sup>2</sup>
$\rho$	Density	kg/m <sup>3</sup>
$\mu$	Dynamic viscosity	Ns/m <sup>2</sup>
$L/D$	Length to diameter ratio	-
$D_H$	Hydraulic Diameter	m
$\emptyset$	Equivalence ratio	-
$T_{adiab}$	Adiabatic temperature	K
$\beta$	Porosity = $\frac{\pi N d^2}{4A}$	-
$d$	Diameter of orifice	m
$K$	Pressure loss coefficient	-
$A$	Cross-sectional area of the combustor	m <sup>2</sup>
$N$	Number of orifices	-
$u$	Velocity	m/s
$M$	Mach number	-
$k$	Turbulence kinetic energy	m <sup>2</sup> /s <sup>2</sup>

# Chapter 1. INTRODUCTION

## 1.1 The Role of Hydrogen in achieving Net Zero Greenhouse Gas Emissions

The Kyoto Protocol was an international treaty that extended the 1997 United Nations Framework Convention on Climate Change, it was adopted in 1997 to reduce emissions of gases that cause of global warming, mostly CO<sub>2</sub> [1], and human energy consumption is responsible for most of the increase in CO<sub>2</sub> emissions. The Paris Protocol in 2015 established that an increase of more than 2°C would bring catastrophic damage. A long-term temperature goal is to keep the rise in temperature below that number but prefer to limit that rise to 1.5°C. This agreement also stated that emissions should be reduced as soon as possible, targeting a 50% CO<sub>2</sub> reduction by 2030 and reaching net-zero values by 2050 [2]. According to the Glasgow COP26 [3], 55 Billion metric tons of CO<sub>2</sub> are being released into the atmosphere every year. The agreement aims to reduce more than 7% of the greenhouse gases every year for the next decade.

Figure 1-1 shows the UK's reduction in energy use and hence CO<sub>2</sub> emissions since 1990. The total final energy consumption came down 13% in 2020 compared to 2019 due to the impact of the Covid-19 pandemic. The transport sector was affected 29% and the industry sector 6.2%. The overall final energy consumption adjusted to temperature was 11% was lower than the year before in 2020 [4]. Electricity generation went down in 2019 similar to the financial crisis in 2010. At approximately 6300 TWh gas turbines generated 24% of the total global power by 2020 [5] 43% in the UK (Check DUKES 2021 numbers). Figure 1-1 also illustrates the significant contribution of domestic and industrial energy use, which are addressed in this research. Green electricity through hydrogen-fuelled CCGT (Chapters 5 and 6), decarbonisation of industry heat through process burners operated on hydrogen (Chapters 5 and 6), with fuel switching to hydrogen and biofuels in the Glass Futures project in Chapter 4. Decarbonisation of domestic heat using hydrogen gas fires is the theme of Chapter 7.

Figure 1-2 shows the source of fuels for electricity production, where in the UK, natural gas (NG) is the only significant fossil fuel used today in the combined cycle gas turbines (CCGT). If hydrogen is to be produced by electrolysis from renewables such as nuclear, wind or solar plants, fuel switching to hydrogen for CCGTs enables net zero to be achieved in electricity supply. The increasing proportion of renewable energy requires an energy source counterbalancing

the intermittent nature of solar and wind energies. Currently, this is NG for CCGT, as illustrated in Figure 1-2. Natural gas in CCGT must continue being used for the grid to operate with a large proportion of intermittent wind and solar, as illustrated in Figure 1-3. Currently, no replacement technologies are being developed to balance the grid demand. Thus, if the electricity supply is to be zero greenhouse gas (GHG) emissions, a solution is needed to tackle this problem, and fuel switching to hydrogen in CCGTs is the solution.

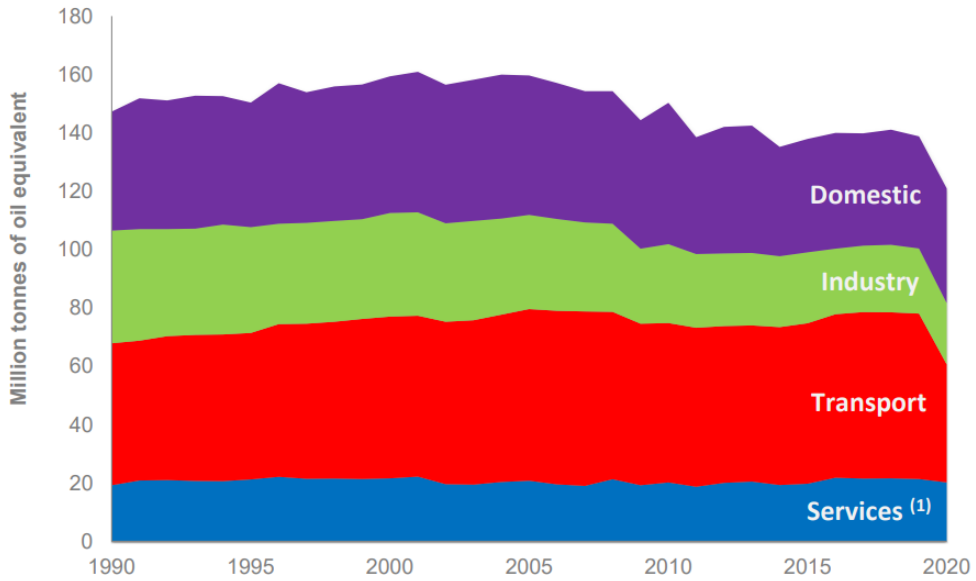


Figure 1-1. Final energy consumption from 1990-2020 [4]

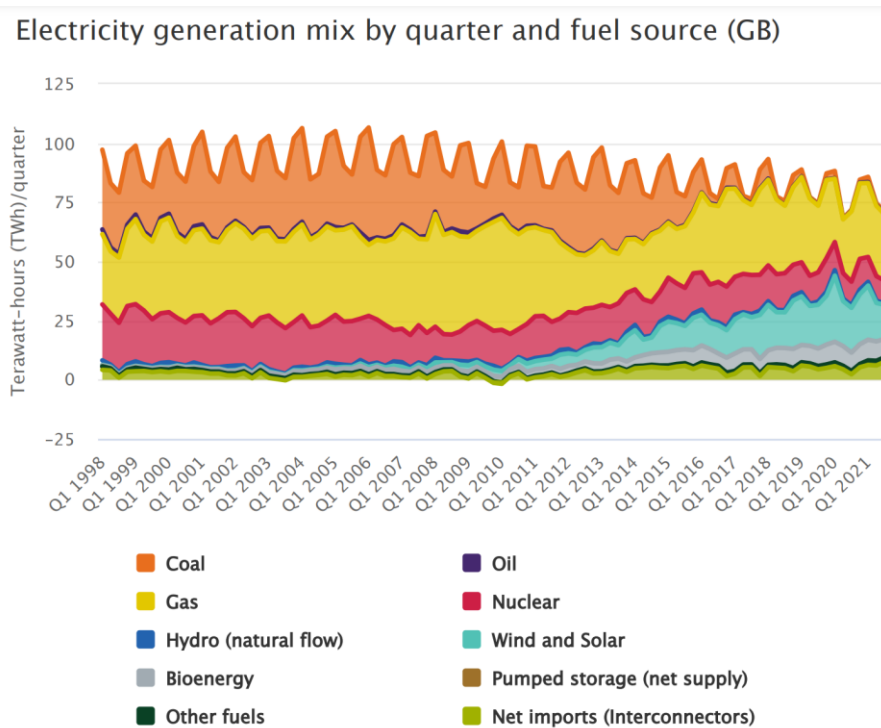
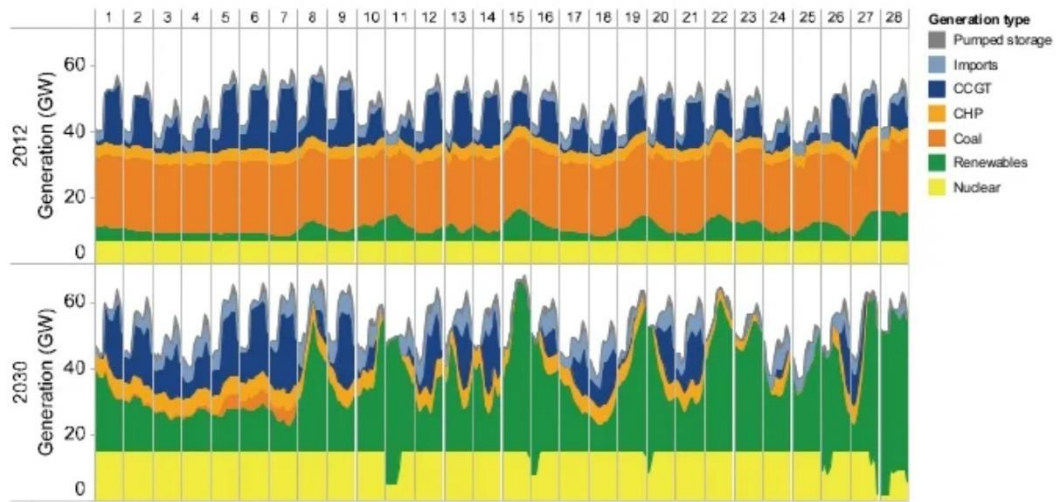


Figure 1-2. Electricity energy source variation from 1998 to 2021 [6]

Hydrogen also offers the possibility of energy storage by electrolysis which can absorb surplus renewable energy by using it to generate hydrogen for energy storage.



**Figure 1-3.** Intermittent operation of NG CCGT to balance the Grid [7]

One of the main routes to zero GHG emissions is the fuel switching to green hydrogen, which is part of the UK Government's strategy [8]. This fuel switching to hydrogen can be achieved using nuclear or renewable electricity to generate hydrogen by electrolysis. However, no gas turbines, process burners, or domestic fires operate with hydrogen currently other than experimentally. The UK government is closing this gap by providing funds for demonstration projects, and this research is part of four BEIS funded fuel-switching programmes, as detailed in the acknowledgements.

## 1.2 Considerations for hydrogen combustion.

The Wobbe Index (WI) is a parameter recently used to compare interchangeability of two different fuel blends defined as the ratio of the ground calorific value to the square of the specific gravity of the gas mixture. In the 1920s the concept of heating value over square root of density was used for fuel interchangeability, where the Wobbe index predecessor, or the C-index was established [9]. The WI is expressed in the same units as the gross calorific value ( $\text{MJ}/\text{m}^3$ ). In the UK the WI for natural gas is kept in the range of  $47.2\text{-}51 \text{ MJ}/\text{m}^3$  [10].

If two fuels have identical Wobbe Indices, for the same pressure and valve setup the thermal energy input will be also the same. However, the pressure and WI are not the only parameters needed to achieve a successful combustion. Burning velocities and flame temperatures are also important [11], [12].

Figure 1-4 shows the heating value and Wobbe Index variation for different concentrations of hydrogen in a NG blend. As observed the heating value follows a linear trend whereas the WI has an inflection point at 80%. Also it is possible to observe that the WI will be identical for a 100% H<sub>2</sub> compared to a 35% H<sub>2</sub>/65% NG blend.

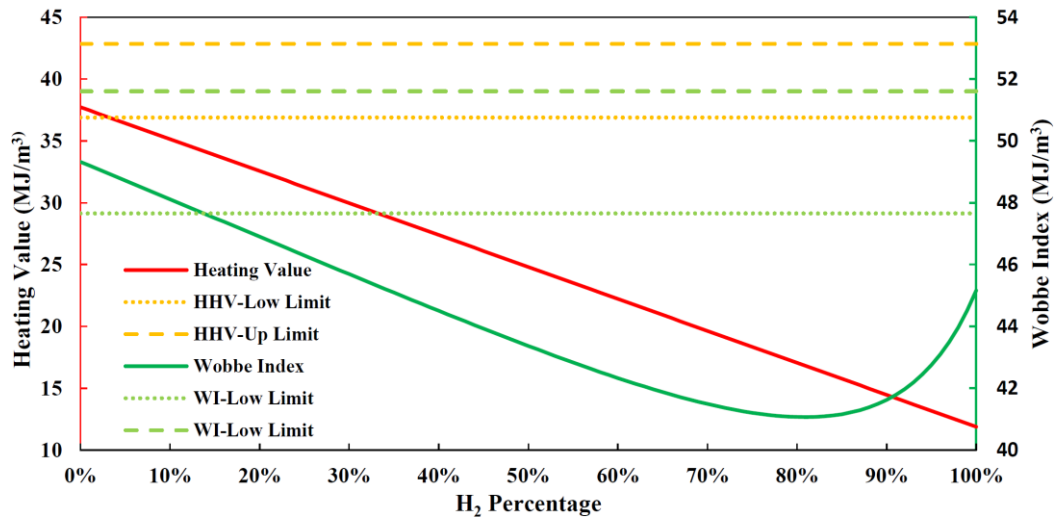


**Figure 1-4.** Wobbe Index and heating value variation for NG/H<sub>2</sub> blends

A dual fuel burner using hydrogen and natural gas is possible since the Wobbe Index for hydrogen is 48.5 MJ/m<sup>3</sup> [13]. Same burner holes for both fuels allow the passing of approximately the same amount of energy [14]. More detail can be found in Appendix H.

Gas turbines and process heaters can't be operated with hydrogen for a premixed flame since there is a risk of flame flashback given the reduced quench distance of hydrogen of 0.6mm compared to methane of 2.2mm [15], [16]. The flammability limit of hydrogen is 4-75%, wider to other gases such as methane (5-15%) [17]. Diffusion systems are usually employed for safety purposes given their reduced propagation speed. The burning velocity of hydrogen is 2.65 m/s compared to 0.4 m/s of methane for stationary gases. But at turbulent conditions faster velocities are achieved. And this increases the pressure [15]. However, hydrogen combustion is dependant on the concentration of hydrogen in the fuel, the burning velocities are slow for example if the concentration are below 8%. For a concentration above 20% intense combustion is achieved [18].

The phenomena of acoustic pressure oscillations has been a problem in the development of ultra low NO<sub>x</sub> gas turbine combustors. This problem is common in premixed systems and arises by having all the combustion air passing

through the stabiliser at an intense heat release above 1900K [19], where the frequency of the vortex shedding triggers the resonance, making in some cases the flame stabiliser essentially unstable. Operating too rich in the primary zone is another factor that generates resonance [20], and this is why premixed systems usually present this problem. The solution to resonance is the adequate design of the flame stabiliser in order to alter the turbulence production, or operating at lower pressure drop, and running at lower equivalence ratios. However, the present work for GT is for a low  $\text{NO}_x$  non-premixed combustor at a  $T_{\text{exit}}=1800\text{K}$  for both hydrogen and propane which is just under acoustic resonance.

For the three applications: gas turbines, process burners, and domestic gas fires, increased  $\text{NO}_x$  emissions are expected with hydrogen due to the higher peak flame temperature than NG (as shown in Chapter 4). A major topic of this research is the development of hydrogen flame stabilisers with low  $\text{NO}_x$  emissions. Increasing the  $\text{NO}_x$  emissions standards to facilitate the use of hydrogen for green heat and green electricity will not be permitted. This research's experimental and CFD parts concentrate on developing burners with low  $\text{NO}_x$  emissions, as hydrogen is not a viable green fuel unless low  $\text{NO}_x$  can be achieved.

This project predicted  $\text{NO}_x$  emissions for hydrogen combustion for grid plate type flame stabilisers that had previously been shown to have ultra-low  $\text{NO}_x$  for gas turbine application using propane fuel. These were referred to as Grid Mix (GM) [21]–[25] and were similar to the hydrogen designs used by York et al. [26], [27], which were well predicted in this work. The development of three types of domestic fires for low  $\text{NO}_x$  hydrogen combustion is also presented, which use several low- $\text{NO}_x$  design techniques reviewed in Chapter 2.

In the Glass Futures fuel switching BEIS project, the safe operation of a furnace at glass melting conditions was demonstrated on hydrogen. However, it showed a large increase in  $\text{NO}_x$  emissions compared with NG, as the burner design used the same location of the fuel lances and only changed the injection hole diameter to achieve the same flame length [28]. This has also been observed by Dreizler, et al [29]. They used external EGR to reduce the  $\text{NO}_x$  levels in their combustor. In the present work, we demonstrate burner designs for achieving low  $\text{NO}_x$  with hydrogen that do not require the use of external EGR. This thesis shows that burners can be designed to have low  $\text{NO}_x$  on hydrogen for gas turbines, process burners and gas fires. However, simply operating the existing NG burner on hydrogen may result in a significant

increase in  $\text{NO}_x$ , which the above examples indicate could be an increase in a factor of 2 – 10, which will never be permitted.

Process burners operate closer to stoichiometric to achieve the best thermal efficiency, which makes reducing  $\text{NO}_x$  difficult due to the high mean temperature near stoichiometric combustion. The classic method of reducing  $\text{NO}_x$  in these circumstances is to stage the air injection to achieve rich/lean combustion (as reviewed in Chapter 2). This has modest  $\text{NO}_x$  reduction, and a better method to achieve low  $\text{NO}_x$  is to use axial staged fuel injection, with the first stage operating very lean, as for low  $\text{NO}_x$  industrial gas turbine, and thus the low- $\text{NO}_x$  design techniques for lean combustion can be applied. The second stage fuel injection occurs after completing the first stage combustion with axially staged fuel injection. This second stage fuel burns in the combustion products of the upstream lean combustion, which is effectively a method of achieving very high internal gas recirculation. In future work (Chapter 8), this design will be developed as a low  $\text{NO}_x$  hydrogen burner for the zero-carbon operation of Whisky distilleries. Currently, there are no commercial applications of axially stage fuel combustion in the open literature, apart from that used in some gas turbine designs for lean overall combustion explained in 2.2.3.

Modern power generating gas turbines operate at the highest possible exit temperature to work at the highest possible thermal efficiency and lowest  $\text{CO}_2$ . State of the art is the current operation at 1800K-1900K in the J class CCGT plants first developed by MHI in Japan[30]. These high firing temperature plants can only achieve Ultra-low  $\text{NO}_x$  if all the combustion air passes through the flame stabiliser. However, in the MHI work, they could not deliver low  $\text{NO}_x$  on natural gas at these high firing temperatures and used 35% external exhaust gas recirculation (EGR) into the air compressor inlet to achieve the legislated required  $\text{NO}_x$  [30]. This illustrates the difficulty of a lean burning flame stabiliser design solution to low  $\text{NO}_x$  emissions for high turbine entry temperatures. Chapters 5 and 6 show that low  $\text{NO}_x$  can be achieved at these high temperature operating conditions with the Grid Mix flame stabilisers using an internal grid plate fuelling each air hole.

It is common to develop low  $\text{NO}_x$  gas turbine combustors at atmospheric pressure. There is no thermal  $\text{NO}_x$  generation for combustor exit temperatures up to 1800-1900K, resulting in no pressure influence (as reviewed in Chapter 2). However, only successful low  $\text{NO}_x$  combustors are tested at high pressure due to the elevated cost. Process burners for heat applications obviously

operate at atmospheric pressure. So the present experimental and CFD work is equally relevant to low NO<sub>x</sub> process burners and gas turbines.

### **1.3 Equilibrium predictions**

CFD predictions of combustion should, if the combustor is long enough (residence time high enough), reach equilibrium. The gas composition should be the adiabatic equilibrium if the combustion is complete prior to any heat removal, as in gas turbines and the proposed process burners. Thus, knowing the adiabatic equilibrium flame temperature and gas composition helps validate CFD predictions. Also, to demonstrate that the distance to reach equilibrium is the flame development length, which should be shorter than the combustor length.

Several pieces of equilibrium software have been developed in the past, where the most common are Gaseq and CEA. They have been widely used for combustion purposes, including gas turbines[31]–[33]. However, they have not been used to study domestic fires or the glass melting sector. The equilibrium software can predict the adiabatic flame temperature and product composition, including equilibrium NO emissions.

Equilibrium programmes also predict the equilibrium NO<sub>x</sub>, which is the NO<sub>x</sub> for infinite residence time. Usually, combustors are not long enough to reach NO<sub>x</sub> equilibrium, but in glass melting float glass furnaces, the gas temperatures are so hot that equilibrium is achieved in a relatively short distance. Thus, equilibrium codes can predict trends in equilibrium NO<sub>x</sub>, such as the influence of inlet air temperature, equivalence ratio, water addition, etc. All these trends were explored in Chapter 4.

In addition, equilibrium software can take an adiabatic composition in the near stoichiometric high-temperature region and predict the change in gas composition as the mixture is cooled. This feature of equilibrium codes is rarely investigated but was used in this work as cooling is a feature of all combustion systems. Additionally, operation at low excess oxygen is required for process heating burners for the highest thermal efficiency. In this application, cooling in boilers or water heaters reduces the CO due to re-association chemical reactions. This feature is shown in Chapter 4 to be critical in predicting the gas composition above the glass melt in glass melting float glass furnaces. This was used to predict the change in the product composition using hydrogen. A matter of concern was the water content of the product gases, particularly hydrogen, where an increase could influence the glass quality. The predictions

in Chapter 4 were shown to effectively predict the gas composition above the glass melt for natural gas and hydrogen.

Gas turbine combustors operate at elevated air temperatures, and chemical equilibria are required for different air temperatures up to 800K in gas turbines. In addition, some process heat applications use thermal heat exchange between the exhaust gases and the inlet air to generate very high air temperatures. This is the glass melting industry situation where regenerative heat exchange between the outgoing burnt gases and incoming air is used to create air temperatures up to 1600K. The equilibrium composition for air temperatures from 300 to 1600K in intervals of 100K was part of this work.

This thesis is concerned with fuel switching from NG to hydrogen. Still, the BEIS fuel-switching programme includes switching to biofuels, and so in this work, the adiabatic flame temperature and gas composition have been predicted for several fuels. Fuel switching aims to operate a burner or system such as glass melting furnaces (Glass Futures project) using an alternative fuel at the equivalent flame temperature as natural gas. Higher excess oxygen is required for hydrogen and less for biomass fuels, as shown in Chapter 4.

Biofuel diesel (biodiesel) offers an expensive but effective solution to reducing fossil fuels and decarbonisation. A generic blend of biodiesel was studied with the equilibria software. The Glass Futures fuel-switching programme has successfully operated a glass furnace on biodiesel.

Glycerol is the cheapest biofuel available which offers a viable solution for decarbonizing heat. Roughly 11% of the vegetable oil used to produce biodiesel is rejected as crude glycerol [34]. This fuel is often overlooked and disposed of as a waste product. This was why it was investigated for the glass melting industry and is currently being investigated for applications in the distillery industry. As an additional contribution, this fuel was investigated for a mixture of water/glycerol for water removal in the Whisky distillation process. Water is sometimes used for NO<sub>x</sub> reduction in combustion systems, as explained in 2.2.6. Still, contaminated water is a big waste product in distilleries, so destruction in the burners is a cost-effective waste disposal method.

Ethanol is an alternative to achieving zero carbon. It is available with immediate effect as it is obtained directly from biofuels for adding to gasoline. Currently, 10% ethanol in gasoline is requested [35]. Pure ethanol and ethanol/gasoline burn cleanly and make a good SI engine fuel [35]. Ethanol was a possible fuel switching for the glass melting industry and is a green fuel for use in the distillery heating process.

Methane and natural gas were studied as methane is not a practical fuel and natural gas is a complex mixture of methane with higher hydrocarbons and inerts. A natural gas composition provided from records at the Guardian Glass plant at Goole was used for the average of a month's supply. In this thesis, only natural gas results are presented. The methane equilibrium calculations were undertaken and the results obtained were very similar to those for natural gas.

The pipeline hydrogen composition was assumed to be obtained from the steam methane reformer for natural gas. Whereas pure hydrogen is obtained from electrolysis. So pure hydrogen and pipeline hydrogen (from Hy4Heat WP2 – BEIS) were predicted.

Finally, the CFD simulations in Chapter 6 using propane were validated with the equilibria software. This activity was undertaken because the experimental work with internal gas composition traverses was undertaken with propane.

#### **1.4 Grid plate flame stabilisers for gas turbines**

Perforated plates, also known as grid plates, are flame stabilisers used in some low  $\text{NO}_x$  gas turbine combustors. These technologies create interacting shear layers that are used to rapidly mix fuel and air, with the fuel injected into each air hole in the grid plate, achieving low  $\text{NO}_x$  emissions. Grid plate flame stabilisers were the first premixed system to achieve low  $\text{NO}_x$  emissions [22], [36]. Andrews et al. [21]–[25] have demonstrated the principle of direct fuel injection in grid plates by fuelling the air jets passing through the stabiliser holes. Also, several companies have shown the use of grid plates in their combustion systems, and there has been a renewed interest in using these grid plate technologies for hydrogen combustors. The FLOX burner, originally a process burner, includes a grid plate with central axial fuel injection in each grid plate air hole [37]. The Hitachi Multicluster burner features an array of various grid plate airholes with a central fuel injection [38]. Some studies have also shown grid plates in hydrogen combustion [26], [39], [40]. Lastly, some process burner designs have demonstrated the use of grid plate burners. More detail about these technologies is provided in Chapter 2.

The Grid Mix flame stabilisers were fuelled with two methods of injecting the fuel into the air: radially inward using eight fuel jets per air hole (GM1) and as an annulus around each hole (GM2). This was achieved using hollow grid plates, which acted as a fuel plenum to feed fuel into each air hole. All the air needed for combustion passed through the Grid Mix flame stabiliser. The combustion process must be carried out as lean as possible to achieve low  $\text{NO}_x$ .

Also, a good lean flame stability margin is required to achieve low lean  $\text{NO}_x$ . This was shown experimentally in previous work by Andrews and a co-worker [21]–[25] to have good flame stability so that operation in the lean low  $\text{NO}_x$  region could be achieved. The GM2 design had better flame stability than the GM1 design but higher  $\text{NO}_x$ . This was the database where the CFD prediction procedures were validated in Chapters 5 and 6.

A combustor with all the airflow through the stabiliser operates at a reference Mach number,  $M_1$ , of typically 0.05 based on the combustor flow area at the air inlet temperature. In Andrews's work,  $M$  was 0.047, and the heat release was  $28 \text{ MW/m}^2\text{bar}$ . Modern low  $\text{NO}_x$  combustors designed for high firing temperatures should have a heat release of around  $25 \text{ MW/m}^2\text{bar}$ . Still, most low  $\text{NO}_x$  combustor work has operated at conditions around  $15 \text{ MW/m}^2\text{bar}$  or lower in many cases.  $15 \text{ MW/m}^2\text{bar}$  represents 60% of the combustor airflow passing through the flame stabiliser. In the present work, all the combustion air has to pass through the flame stabiliser and operation at  $28 \text{ MW/m}^2\text{bar}$  is necessary for 1800-1900k flame temperature operation at low  $\text{NO}_x$ . This is a new application for CFD as no previous application of CFD has been applied to such high-intensity combustion for gas turbine applications.

Axial central fuel injection on each stabiliser airhole has been experimentally and numerically investigated for FLOX burners [37], [41], [42]. A large central burnt gas recirculation zone between an annular ring of air holes has been demonstrated to create high IEGR. This alternative method of fuelling each air hole in a grid plate has been modelled using CFD in this work, called GM3, as it uses the same grid geometry as for GM1 and 2.

York et al. [43], [44] showed the use of a grid plate flame stabiliser, similar to GM1 but with elongated mixing tubes, achieved ultra-low  $\text{NO}_x$  levels for hydrogen combustion. These results were modelled in the present work using GM1 with the hole length extended in proportion to the geometry of York et al.

Pressure loss is an important aspect of low  $\text{NO}_x$  gas turbine combustion that can influence low  $\text{NO}_x$  gas turbine combustor fuel and air mixing as it controls the turbulent energy generated by the flow, which also controls the turbulent burning velocity. The burner blockage or porosity which directly affects the contraction coefficient of the flow through the flame stabiliser holes, it is the flow expansion from the vena contracta that controls the pressure loss.

The experiments and predictions were carried out at a  $\Delta P/P$  of 2 and 4%, which are the typical range used in gas turbines. Any higher pressure loss

deteriorates the cycle thermal efficiency and lower pressure loss lead to poor flame stability and poor combustion efficiency.

Gas turbines combustors operate at high pressure, but for lean well mixed combustors with primary zone temperatures below about 1900K, pressure has little effect on NO<sub>x</sub> which is why the present experimental work was carried out at atmospheric pressure. This is for several reasons: for lean mixtures pressure has no effect on flame temperature below about 1900K as dissociation is insignificant and this leads to very low levels of atomic oxygen, which is a key part of the thermal NO<sub>x</sub> formation. Pressure does have an influence on thermal NO<sub>x</sub> for richer mixtures with higher flame temperatures and experimental studies show that this is a square root dependence. Also, pressure reduces dissociation so the availability of atomic oxygen in the thermal NO<sub>x</sub> generation is reduced for flames with temperatures above 1900K. Pressure will increase NO<sub>x</sub> if the mixing of fuel and air is poor so that even though lean mixtures with <1900K is used, the unmixedness creates local hot zones that give rise to a pressure dependence of NO<sub>x</sub>. This is why in the present work CFD predictions of isothermal fuel and air mixing were made, as operating a primary zone lean for low NO<sub>x</sub> is not sufficient, as it must also be well mixed. Hence, the work on isothermal mixing predictions for different methods of fuel injection into the same grid plate aerodynamics was undertaken. The worst fuel and air mixing fuelling positions were shown, by CFD and experimental measurements, to have the highest NO<sub>x</sub>.

This thesis shows the use of validated CFD to parametrically investigate and improve existing gas turbine and process heaters designs and apply it to low carbon combustion such as hydrogen. The work is directed at the latest gas turbine's highest firing temperature conditions, which require all the air to pass through the grid plate. This leads to very demanding high turbulence and high-velocity jet flames, as reviewed in Chapter 2. Experimentally, for GM1 and GM2 no resonance was encountered, so this was not modelled with CFD. The richest equivalence ratio investigated by Andrews and Al Dabbagh was just at the onset of resonance, but these parameters are not part of the scope of this thesis.

## **1.5 Computational fluid dynamics for low NO<sub>x</sub> combustion**

In recent years computational fluid dynamics (CFD) has been widely used by academia and industry to improve combustion systems and understand the flame structure in low NO<sub>x</sub> flame stabilisers. For example, CFD has been able to predict temperatures and NO<sub>x</sub> formation. Additionally, it has allowed the prediction of fuel and air mixing, which is very useful given that the flame

unmixedness is usually the problem of high NO<sub>x</sub> emission. So once correct prediction of the mixing, it is possible to predict the flame temperature and NO<sub>x</sub> emissions.

Using different combustion models, various researchers have successfully investigated turbulent combustion for premixed [32–36] and non-premixed combustion [37–39]. NO<sub>x</sub> modelling is strongly dependent on temperature prediction and mixing quality. Phil King studied combustion and NO<sub>x</sub> prediction for non-premixed combustion radial swirlers with radial vane passage fuel injection [45]–[47] at a Mach number 0.03, 40% less than the conditions studied in this thesis. Figure 1-5 compares the CFD prediction for flame temperature with experimental measurements from gas composition measurements using radial gas sample traverses at different axial distances. The bottom of each diagram is the combustor centre-line and the top the combustor wall.

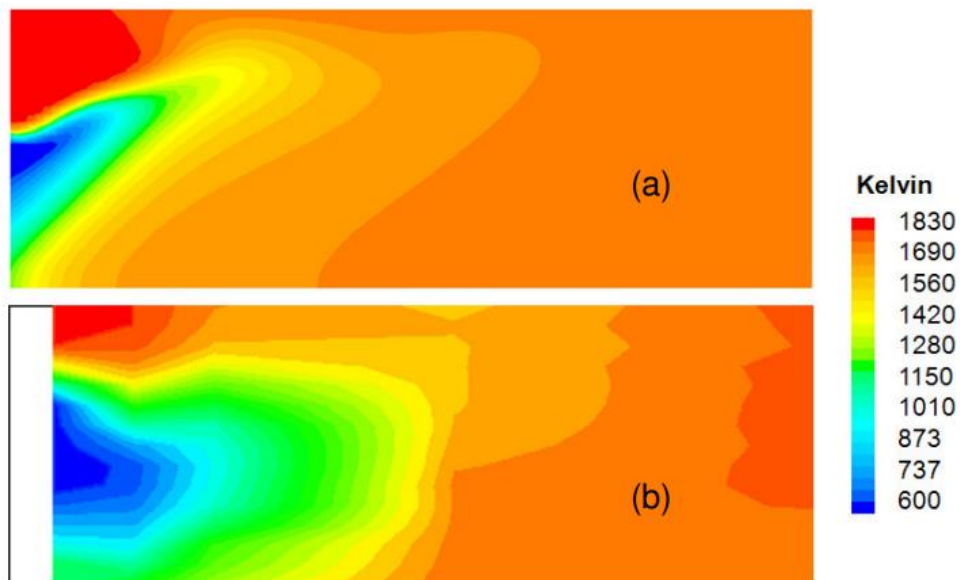


**Figure 1-5.** CFD output for temperature prediction (a) compared with measurements (b) from King et al. [46]

One of the main contributions of this thesis is the achievement of predicting combustion at high combustion intensities of 28 MW/m<sup>2</sup>bar for low lean NO<sub>x</sub> at high turbine entry temperatures, which has not been done previously.

## 1.6 Innovative domestic fires for dual fuel applications

Domestic fires are the lowest cost domestic heating appliance with a capital cost of around £300 and simple user heat controls. Because of their low price, they are used by the poorest in society. Unless these can be developed to work

on hydrogen, low-cost decarbonised heat will be unavailable, increasing fuel poverty and deaths due to hypothermia.

By 2022 the estimated UK domestic space heating market was worth £338 million, with gas space heating having a 33% share, supported by an ever-increasing number of UK homes on the gas grid [48]. In terms of Units for Fuel Effect fires, this means some 230,000 per year [49], but with the diversity in product specifications and prices, this needs treating with caution, though the overall position is one of consistent growth. The market size for domestic space heating has been growing at a steady 3% per annum which is expected to continue [50]. Fuel Effect Fires account for around 44% of the space heating market, supported by product innovation and higher value aspirational designs [51].

The BEIS Hy4Heat project was developed by a group of companies led by Arup LTD commissioned by the Department for Business, Energy and Industrial Strategy (BEIS) to demonstrate the safe use of hydrogen for heating in UK households. The main goal was to establish whether it was possible to replace the natural gas supply with hydrogen for homes and gas appliances. Nine work packages were developed to do so, starting from the technical management to the demonstration of the technologies. One funded area was 'coal-effect' fires, with a contract for three fires awarded to a consortium led by Clean Combustion System (CBS) Ltd with the University of Leeds leading on the technology. Chapter 7 of this thesis is the results of this research.

Three types of "coal effect" gas fires were investigated in this work: open fires, glass-fronted fires and flame effect innovative fires.

### **1.6.1 Open fires.**

Open fires are the cheapest domestic heating and are designed to look like coal fires with ceramic 'coals' heated by premixed gas/air flames, giving glowing ceramics and some post ceramic gas flames. The ceramics do not get consumed by the fire. The air supply to the premixed flame is controlled by an orifice in the base of the fire. Open fires have the front of the fire open to external air from the room and entrain large amounts of air above the fire zone so that the oxygen level in the flue is at 19-20%. These fires are rich lean in their operation with axially stage air with rich premixed combustion below the fire and lean air admission above the fire. These fires can leak CO into the room, which would not happen with a hydrogen flame as CO cannot be produced. This is a significant advantage of hydrogen fires, as many more people die of CO poisoning from gas heating than gas explosions [52].

The industrial link for this fire was with Focal Point using their appliance as the fire to be demonstrated on hydrogen. The model used was the Focalpoint Blenheim Slimline fire with a heat output of 3.2kW and 1.8kW on low heat. This is one of the UK's top-selling open gas fires (70,000 units sold since 2011)[53]. The NO<sub>x</sub> emissions are 128 mg/kWh at high heat, which is below the EU Ecodesign requirement for these fires of 130 mg/kWh [54].

### **1.6.2 Glass fronted coal effect fires.**

Glass-fronted coal-effect fires have the air supply to the fire controlled by the size of an air inlet below the fire, and the front of the fire is sealed with a glass door so that there is no entrainment of air above the firebase. These operate at flue gas oxygen levels in the 8-10% region. The use of ceramic coals is similar to the glass-fronted fire but manufactured of different shapes.

The Legend fires Evora balanced flue fire was the reference appliance, one of the UK's top-selling glass-fronted gas fires, currently selling 1000 units per year [55].

This appliance is available with Class 1 brick built chimneys, Class 2 twin wall systems and concentric balanced flue. The fire fits in a standard 16"x22" opening. The fire heat output is 3.8kW, and the heat input is 4.5kW gross and 4.1 kW net. This gives thermal efficiencies of 84% gross and 93% net, one of the best efficiencies for this type of fire. This appliance has been designed, tested and manufactured to BS EN613:2001 +A1: +C1:2008 relating to balanced flue appliances. Ignition is carried out by a piezo spark. Legend has currently sold 7500 units in the UK alone, making this award-winning fire one of the UK's best-selling glass fronted fires[55]. This reference fire was suitable for developing a dual fuel hydrogen/NG appliance with a standard burner and fuel system, where hydrogen burned over a broader range of equivalence ratios ( $\phi$ ) than NG. Hence, power turndown was not a problem for hydrogen.

### **1.6.3 Flame effect or Innovative Fire**

The BEIS funding awarded for this work was for a hydrogen fire with innovative features, and the CBS consortia funding was for a fire that did not use ceramic coal effects. However, ceramics could be used for heating without having a coal-like effect. A class of NG fires uses visible diffusion flames that flicker in a relatively large volume. The present work presents this appliance for a diffusion flame against a near-vertical ceramic wall to generate an attractive flame. At the time, BEIS advice [56] was that this would be impossible

as hydrogen flames had poor visibility. Hydrogen diffusion flames are non-luminous, given the lack of soot radiation but not invisible. One of the oldest references on hydrogen diffusion flames [57] reported the visible flame length, confirmed in more recent work [58]. The consultants who advised BEIS were clearly unaware of this [56]. They advocated that BEIS should fund a programme on making hydrogen flames visible and stated that the lack of flame visibility could make hydrogen use impossible for domestic applications, including cookers and fires.

The innovative aspect of the work in Chapter 7 was that the fire compartment was made so the air supply was as far as possible from the fuel injection holes to give the best rich/lean combustion for low NO<sub>x</sub> and with internal reverse flow so that the diffusion flames burnt in a reduced oxygen atmosphere which reduced the NO<sub>x</sub> emissions further giving enhanced colour to the flame. NO<sub>x</sub> reduction for hydrogen flames was at the heart of the burner design process.

## **1.7 Combustion pollution and its effects**

NO<sub>x</sub> emissions are the critical factor in hydrogen burners, given the severe health and environmental effects NO<sub>x</sub> emissions cause. NO<sub>2</sub> impairs lung function, forms ozone with volatile organic compounds (VOC) emissions, sunlight [59] [60] and heat creating acid rain [61], which deteriorates plant and tree growth.

After diffusion to the stratosphere, it also causes ozone depletion, increasing skin cancer from increased UV reaching the earth's surface. This is why hydrogen will not be allowed to be operated unless the burners meet current and future NO<sub>x</sub> standards. It was shown in s.1.2 that all current hydrogen burners increase NO<sub>x</sub> relative to the equivalent NG burner by a factor of 3 or more. A significant achievement of this research is to design hydrogen-fuelled fires that are well inside the current standard for gas fires of 130 mg/m<sup>3</sup>.

The ozone formation from NO<sub>x</sub> emissions has two impacts: ozone is a potent greenhouse gas, two thousand times more active than CO<sub>2</sub> for the same ppmv [62]. Also, ozone reduces lung function and irritates the eyes.

Carbon monoxide indirectly affects the climate forcing since it elevates concentrations of direct greenhouse gases such as methane (CH<sub>4</sub>) and tropospheric ozone [63]. In addition, CH<sub>4</sub> combined with CO depletes the hydroxyl radical (OH), minimising its function in removing O<sub>3</sub> [64].

Table 1-1 shows the effects of the 10 primary air pollutants. First, the local impact covers the emissions that harm directly human's health, followed by

regional consequences like acid rain and ozone. Lastly, the global effects like the ones produced by O<sub>3</sub>.

Some of the discussed pollutants can directly affect human health, such as carbon monoxide (CO), reducing blood capacity to transport oxygen [66]. Or the ozone that can cause asthma, bronchitis, and other cardiopulmonary problems[66], [67].

**Table 1-1.** Local, Regional and Global Effects of 10 main pollutants [65]

Impact	PM	Lead	SO <sub>2</sub>	NO <sub>x</sub>	VOC	CO	CH <sub>4</sub>	CO <sub>2</sub>	N <sub>2</sub> O	CFC's
<b>Local (Health and welfare)</b>	✓	✓	✓	✓	✓	✓				
<b>Regional -Acidification</b>			✓	✓						
<b>-Photochemical oxidants</b>				✓	✓	✓				
<b>Global -Indirect greenhouse effect</b>				✓	✓	✓	✓			✓
<b>-Direct greenhouse effect</b>							✓	✓	✓	✓
<b>-Stratospheric O<sub>3</sub> depletion</b>				✓					✓	✓

Interim effects of exposure to NO<sub>2</sub> are susceptibility to respiratory infections and inflammation of respiratory airways. But it can also worsen symptoms of those suffering from heart or lung disease [68]. Additionally, nitric acid vapour droplets can penetrate lung tissue and cause emphysema, bronchitis, or even cardiac infarction [69].

NO<sub>x</sub> emissions have dropped 76% since 1970 to 702,000 tonnes in 2020. This reduction has been caused due to progressive removal of fossil fuels for energy generation and improvements in the automotive industry [68], [70]

In Europe, the most important sources of NO<sub>x</sub> emissions by 2019 were road transport, with 39%, energy production and distribution, with 16%, and the commercial, institutional and households sectors with 14% [71]. Figure 1-6 shows the total NO<sub>x</sub> production by different sectors. The composition of the exhaust gases generated by the combustion processes depends on the fuel type and the conditions under which the combustion is carried out. Since some of the gas components are air pollutants, therefore, should be eliminated before releasing the gas into the atmosphere. Special extremely slow and expensive cleaning procedures are required, such as the Selective Catalytic Reduction (SCR) process and special measurements related to combustion, like the provision of air by stages, are used to reduce nitric oxides in the combustion stage [72].

The NO<sub>x</sub> production in the UK has also been reduced for the most critical sectors. The implementation of SCR and more stringent regulations have dropped the NO<sub>x</sub> levels to less than a quarter of the produced in 1990, as shown in Figure 1-7. However, 42% of the emissions in Figure 1-7 are from the areas addressed in this research, electricity generation (NG CCGT), industrial heat and domestic heat. This is why the use of hydrogen in these sectors will not be allowed to compromise the reductions achieved in NO<sub>x</sub> emissions over many years, as summarised in Figure 1-7 [65].

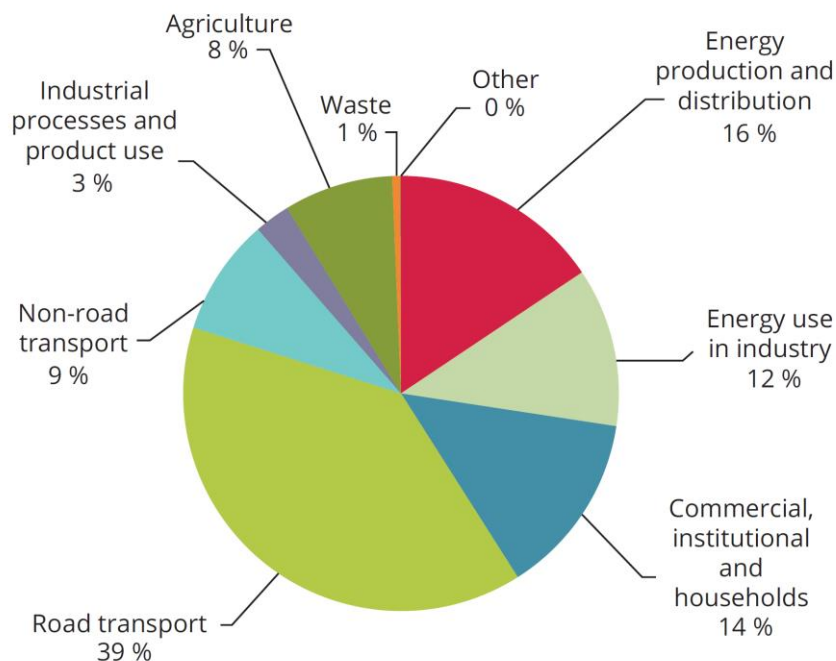


**Figure 1-6.** European mass distribution of NO<sub>x</sub> in ambient air [71].

Emissions from energy plants and industrial process burners have dropped considerably, given the constant development of new renewable energies and the reduction of carbon-based energy sources [68]. As an additional fact,

heating production accounts for almost half of the total energy consumed in the UK [73].

Approximately 760TWh are produced in the UK to provide heat, and roughly 60% of this heat is used for domestic heating purposes [73]. With over 280 thousand km of gas pipe around the country, the UK gas grid feeds around 24M customers [74]. Fuel switching the gas grid to hydrogen is the most cost-effective way of decarbonising heat and electricity and is crucial to the achievement of net-zero.

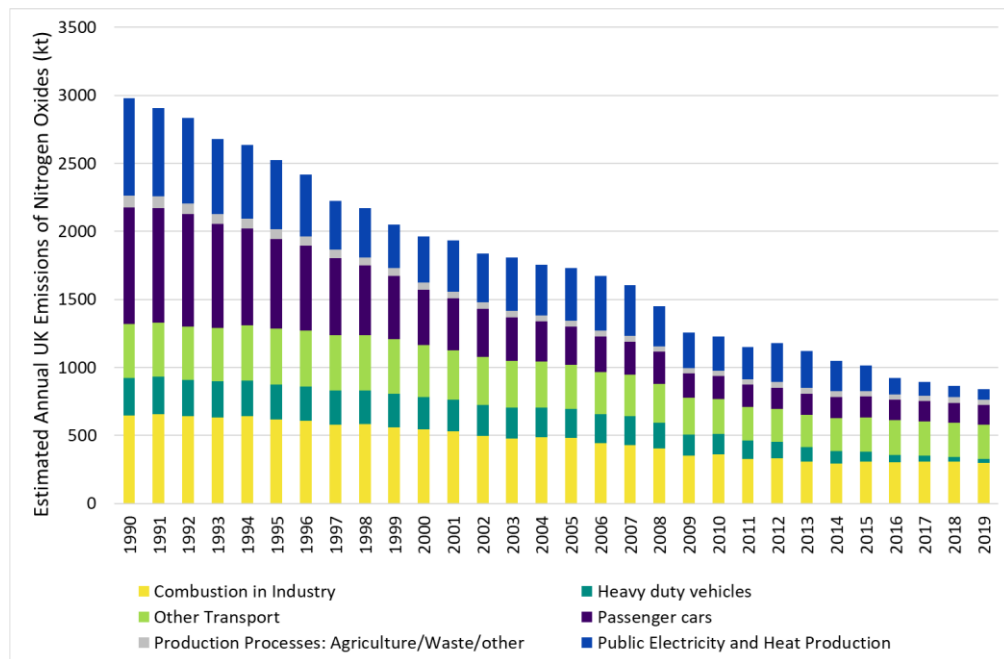


**Figure 1-7.** Estimated annual emissions of NO<sub>x</sub> in the UK in kt 1990-2019[71]

### 1.8 Legal framework and requirements for process burners

In most areas of the world, boilers are required to achieve what's known as ultra-low NO<sub>x</sub> levels. For example, the EU Ecodesign regulations [54] for small residential gas boilers demanded no more than 56 mg<sub>NO<sub>x</sub></sub>/kWh levels from 2018. For gas fires, 130 mg<sub>NO<sub>x</sub></sub>/kWh is allowed [75]. For natural gas (NG) with a calorific value of 50MJ/kg, the requirement is 13.9 g<sub>NO<sub>x</sub></sub>/GJ for an emission index of 0.78 g<sub>NO<sub>x</sub></sub>/kg<sub>fuel</sub>, which gives 27ppm at 0% O<sub>2</sub>. The demand for California USA is 5ppm at 0% O<sub>2</sub> [76].

The European Industrial Emissions Directive sets the regulations for industrial burners, which the UK still complies with. They established in 2016 a limit of 50 mg/m<sup>3</sup> or 25 ppm NO<sub>x</sub> at 15% oxygen in mass concentration for combustion plants of thermal input above 50MW. For plants with thermal input below

1MW, the equivalent limit was  $200\text{mg}/\text{m}^3$  at 3%  $\text{O}_2$  [77]. There is currently no regulation for thermal heating plants or power generation plants between the eco standard regulations (at 0% oxygen) and 1 MW. However, Europe is working on the development of regulations for this sector.

$\text{NO}_x$  regulations for electric power generation gas turbines have been less than 25 ppm at 15%  $\text{O}_2$  for decades. Nevertheless, current requirements are less than 10ppm in many world areas [78]. And in some places like California, USA, the demand is less than 2.5 ppm[79], given the smog problem that arose in the 70's [80]. All regulations for  $\text{NO}_x$  emissions for industrial gas turbines are referenced to 15% of oxygen level.

The use of reference oxygen corrections for  $\text{NO}_x$  in electricity generation CCGT plants and process and domestic heat (15%, 3% and 0%, respectively) is not sensible as the oxygen reference level was set in 1970s technology, and there is no reward for gains in thermal efficiency. This is mainly a problem for domestic fires that operate at much higher oxygen levels than 0% oxygen, resulting in a significant correction. It would be preferable to legislate in mass emissions per unit of work, power or heat produced as is done in road transport and aircraft emissions. Aero-engine emissions regulations are in  $\text{gNO}_x/\text{KGfuel}$ , and road transport emissions are in units of g/km for passenger vehicles or g/kWh for truck engines. There is no correction to a reference oxygen level. If the thermal efficiency is improved, less fuel is used, resulting in lower mass emissions. Hence, g/kWh units are preferable to g/km. Unfortunately, mass-based units are not used in Europe for electricity production and heat production, and only Canada has sensible units of  $\text{gNO}_x/\text{MWh}_{\text{electric}}$ .

## 1.9 Research gaps

1. Fuel switching to hydrogen in CCGT offers a viable solution for electricity supply if the aim is to be zero greenhouse gas (GHG) emissions, which is part of the UK Government's strategy [8]. Currently, no gas turbines are operating on hydrogen for zero-carbon electricity, and part of the reason is concern over increased  $\text{NO}_x$  emissions. So there is a research gap on hydrogen combustors with low  $\text{NO}_x$  for CCGTs. This is a larger research gap the higher the firing temperature of the gas turbines, with the J class 63% thermal efficiency CCGTs the most difficult due to the combustor outlet temperature being 1900K or higher.

2. For modern gas turbines with a high firing temperature of 1900K or higher there is a research gap as dry low  $\text{NO}_x$  designs are very difficult to achieve low

NO<sub>x</sub> with NG, as the mixing of fuel and air has to be near perfect. In the first J Class 2000K gas turbine it was assumed that this could not be achieved. For the MHI J class 2000K 35% external EGR was used via a water cooler into the compressor inlet to oxygen concentration, which reduced the flame temperature and the NO<sub>x</sub>. However, the use of EGR in the compressor deteriorates the cycle thermal efficiency, as the compressor is not designed for air plus 35% EGR.

3. No dry low NO<sub>x</sub> combustor is available with all the combustion air passing through the flame stabiliser with a very high heat release of 28 MW/m<sup>2</sup>bar. This is a requirement for achieving low NO<sub>x</sub> in high temperature gas turbines as the only way for a 1900K gas turbine to have low NO<sub>x</sub> is for the primary zone to be at 1900K with no dilution or wall cooling air, which requires all the compressor air flow to pass through the flame stabiliser, which is the condition used in the present work experimentally and using CFD.

4. The 28 MW/m<sup>2</sup>bar condition of future high-efficiency CCGTs also has had no previous CFD studies, which is another research gap. The work on the Grid Mix design is a solution to this gap. York et al. [26], [44] have shown for a grid mix type of design that ultra-low NO<sub>x</sub> emissions could be achieved on hydrogen, and these results were well predicted by the CFD procedures shown to be effective for the high combustion intensity of 28 MW/m<sup>2</sup>bar.

5. All current publications for hydrogen process burners for heat have substantially higher NO<sub>x</sub> emissions with hydrogen compared to NG, and the increase reviewed earlier is in the range of 3 – 10. Process and domestic heater burners work near stoichiometric at 1% excess O<sub>2</sub>. This is a major research gap as these will not be allowed for use in industrial process heat. This work has shown that perforated grid plates with each air hole directly fuelled can achieve ultra-low NO<sub>x</sub> levels without external EGR [21]–[25]. Various manufacturers and academics have investigated the principle used by these technologies [13,18,25,29,30], which have also improved their systems using CFD [43], [81].

6. A significant process heat application is in glass melting, where very high air temperatures up to 1600K are used, due to regenerative heat recovery from the high temperature furnace exit gases. The consequences of fuel switching from NG to hydrogen on glass quality and NO<sub>x</sub> emissions is a research gap. Equilibrium predictions were used to predict the cooled gas composition at 1850K glass melting furnace conditions. This enabled the increase in water vapour when firing with hydrogen at 1850K to be predicted, and these had good agreement with flue gas measurements on NG for CO.

7. Domestic heat using fuel switching to hydrogen is a research gap as no work has been published on this application. However, open fires and glass fronted fires are a significant part of domestic heat used by the poorest families, so a solution must be found for domestic heat's hydrogen decarbonisation. Chapter 7 shows that this research gap has been filled in this work, where certified fires on hydrogen have been developed.

### **1.10 Aims and objectives**

The key aim of the research was to contribute to hydrogen combustion technology to enable the decarbonisation of domestic and industrial heat and of electricity generated by NG CCGTs. The increase in  $\text{NO}_x$  emissions with hydrogen combustion is the main problem area that has to be solved for all hydrogen applications for decarbonisation. Therefore, a significant research aim was CFD techniques to assist in the decarbonisation design process.

This research investigates the latest gas turbine's highest firing temperature conditions, which requires all the air to pass through the grid plate for a heat release of  $28 \text{ MW/m}^2\text{bar}$  and  $M=0.047$ .

The objectives of the research are:

1. Investigation of fuel switching for decarbonisation of the glass melting industry that can replace NG and operate at the same flame temperature. The objective was to predict the gas composition above the glass melt using equilibrium modelling. Hydrogen and biofuels were investigated.
2. Using CFD prediction flame stabiliser aerodynamics for the pressure loss using adequate RANS parameters.
3. Prediction of combustion and  $\text{NO}_x$  results for two ultra-low  $\text{NO}_x$  grid plate flame stabilises using RANS CFD.
4. Comparison of fuel injection methods featured by GM1, GM2 and GM3.
5. The study of GM2 for its use on hydrogen for high combustion intensity using RANS CFD and comparison with experimental results.
6. The experimental development of hydrogen domestic gas fires with low  $\text{NO}_x$  emissions that meet the regulations for NG. This objective is for three types of domestic fires:

6.1 Experimental analysis of a low cost open fronted fire showing dual-fuel capabilities for NG and H<sub>2</sub>.

6.2 Experimental study of a glass-fronted fire appliance for dual-fuel applications.

6.3 Numerical and experimental study of an innovative fire for its use on hydrogen.

## **1.11. Thesis plan**

### **Chapter 1**

This chapter provides an introduction and general information regarding process heaters and gas turbines. Aims and objectives for the project are also presented

### **Chapter 2**

A literature review of the relevant areas for the project is provided, focusing on NO<sub>x</sub> production, mainly for gas turbines and process heaters. In addition, a detailed section for Computational Fluid Dynamics (CFD) is provided.

### **Chapter 3**

A detailed description is given of the methods and procedures followed for equilibrium calculations, CFD simulations and experimental work.

### **Chapter 4**

The obtained results for calculating the adiabatic flame temperature and product composition for various fuel blends used in domestic fires and glass melting sectors using existing equilibria software are presented. The cooling of adiabatic equilibrium composition to predict the composition after heat transfer has been developed for application to glass furnaces and process heaters.

### **Chapter 5**

The aerodynamics results obtained for different Grid Mix geometries of flame stabilisers for low NO<sub>x</sub> gas turbine combustion are presented. The fuel injection location internally in the Grid Mix design was a key variable investigated. The study was carried out using RANS simulation with no combustion.

### **Chapter 6**

Mixing, combustion and NO<sub>x</sub> results for existing technologies of Grid Mix flame stabilisers are investigated using RANS CFD. Variations of the geometries are

also presented, evaluating and comparing different methods of fuel injection and the different applications of GM (Grid Mix) in hydrogen combustion.

### **Chapter 7**

The experimental results obtained for three different models of domestic fires are presented. In addition, the simulation results obtained for one of the fires are also presented, where different fuel hole shapes are evaluated and compared for temperature distribution and NO<sub>x</sub>.

### **Chapter 8**

General conclusions and future work are presented.

## Chapter 2. LITERATURE REVIEW

### 2.1 Nitrogen oxides (NO<sub>x</sub>) emission types

Nitrogen oxides or NO<sub>x</sub> (NO + NO<sub>2</sub>) are a group of gases formed mainly from fossil fuel combustion. The nitrogen in the fuel reacts with oxygen to form nitrogen oxide (NO) in the first instance, which is later converted to nitrogen dioxide (NO<sub>2</sub>) when it meets the air in the atmosphere. Both oxides are toxic; NO<sub>2</sub> is a dangerous respiratory poison and, when reacting with VOC by using daylight [59], contributes to photochemical smog formation, a secondary greenhouse gas that is the main compound of ozone (O<sub>3</sub>) [60]. Murray et al [82] was a pioneer in measuring NO<sub>x</sub> in the stratosphere aided with infrared spectroscopy. In 1970 it was discovered that O<sub>3</sub> was destroyed in the stratosphere by nitrogen oxides [83]. NO is the main gas emitted from gas turbines, although there are routes in the flame to convert NO to NO<sub>2</sub>, which involves the HO<sub>2</sub> radical, in the main NO<sub>2</sub> in the atmosphere is formed by reaction of NO with ozone [84]. This leads to depletion of O<sub>3</sub> in the lower atmosphere. In atmospheric air quality monitoring this can be seen through low O<sub>3</sub> in the morning as traffic emits NO which consumes O<sub>3</sub> as it is converted to NO<sub>2</sub>. Later in the day the NO<sub>2</sub> reacts with VOCs in the presence of sunlight to reform ozone.



Resulting in  $O_3 + O \rightarrow 2O_2$  [83], [85]

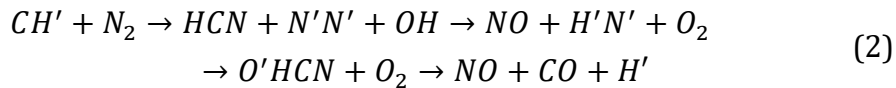
NO<sub>x</sub> is the sum of NO and NO<sub>2</sub> as potentially all the NO will end up as NO<sub>2</sub>. However, it is only NO<sub>2</sub> that is a health hazard. In NO<sub>x</sub> measurement the chemiluminescence analyser has a catalyst that converts NO<sub>2</sub> to NO so that the total NO<sub>x</sub> can be measured, as well as the NO separately, by bypassing the catalytic converter.

When any NO<sub>x</sub> compounds react with ammonia and are mixed with water, they create nitric acid (HNO<sub>3</sub>) [61], which forms the phenomenon known as acid rain. The other component of acid rain is sulphuric acid from sulphur dioxide (SO<sub>2</sub>) emissions, which are negligible in NG fired CCGTs as there is no sulphur in the fuel. Acid rain acidifies bodies of water, deteriorates ecosystems, and results in economic losses due to infrastructural damage [86].

There are three types of nitrogen oxide emissions: Thermal NO<sub>x</sub>, prompt NO<sub>x</sub>, and fuel NO<sub>x</sub> [87].

In most gaseous and liquid fuels thermal NO<sub>x</sub> is the primary source of NO<sub>x</sub> since it is created in high-temperature regions above 1800K. It is created by the reaction of nitrogen and oxygen by Equations 6-8 [87]. To minimize the thermal NO<sub>x</sub> formation, it is usual to reduce the flame temperature, but reduced O<sub>2</sub> using EGR is also helpful [88].

Fenimore first discovered Prompt NO<sub>x</sub> in 1970 when studying laminar premixed ethylene-air flames [89]. The source of this NO<sub>x</sub> remains after thermal and fuel bound nitrogen are eliminated in the combustion. For lean well-mixed combustion, it is usually less than 5 ppm [90]. Fenimore recognized this NO<sub>x</sub> was due to the atmospheric nitrogen reaction with combustion hydrocarbons radicals arising in the initial stages of combustion following the next mechanism [91]:



This mechanism does not depend on temperature and it becomes significant when thermal and fuel NO<sub>x</sub> have been removed. Which makes this kind of NO<sub>x</sub> rather important since it is the cause to avoid reaching zero NO<sub>x</sub> values.

Fuel bound nitrogen (FBN) or Fuel NO<sub>x</sub> needs the fuel to contain organic nitrogen compounds like pyridine or NPAH. Almost 100% efficiency is reached when converting fuel bound nitrogen to NO for lean mixtures, and this can be avoided using rich/lean combustion as in rich zones the FBN is converted to N<sub>2</sub> [87].

There are some similarities and differences between these three types of NO<sub>x</sub> sources described by Toff in 1986 and whose model can predict the different NO<sub>x</sub> emissions from combustion turbines [92]. The present work did not use any fuels with FBN and so FBN NO<sub>x</sub> was ignored.

Nitrogen oxides emissions are given in mg/Nm<sup>3</sup>. However, legislators first require NO<sub>x</sub> to be converted into a reference O<sub>2</sub>, which removes part of the actual emissions mass, as shown in Equation (3). Therefore, these new corrected NO<sub>x</sub> levels are not the whole mass passing through the flue.

$$NO_{xc} = NO_x \text{ ppm} \left[ \frac{20.9\% - O_2 \text{ Ref}}{20.9\% - O_2\% \text{ Actual}} \right] \quad (3)$$

Gas turbines work at an O<sub>2</sub> reference level of 15%, whilst furnaces operate at 3-6% using oil, coal, or natural gas.

Some burners and domestic boilers work at zero oxygen levels.

### 2.1.1 Thermal NO<sub>x</sub> kinetics.

The main objective of ultra-low NO<sub>x</sub> gas turbine combustor designs is to eliminate thermal NO<sub>x</sub>, which is achieved by burning lean with well-mixed fuel and air. Thermal NO<sub>x</sub> is determined by the Zeldovich mechanism [93]. Where Equation (4) is the dominant reaction and Equation (6) corresponds solely to rich mixtures, so it can be avoided in low lean NO<sub>x</sub> [94]. More detail on this mechanism can be found in the works of Lefebvre and Siegel [95], [96].



$$k_{f1} = 1.8 \times 10^{14} \exp[-38370/T]$$



$$k_{f2} = 1.8 \times 10^{10} T \exp[-4680/T]$$



$$k_{f3} = 7.1 \times 10^{13} \exp[-450/T]$$

The thermal NO<sub>x</sub> creation rate goes up exponentially as temperature increases. Some oxygen is required to generate NO<sub>x</sub> and this results in NO<sub>x</sub> formation peaking at an equivalence ratio of about 0.9 [92]. Combustion is always lean in gas turbines, and NO<sub>x</sub> should not be created at firing temperatures less than 1800K [62]. It can be seen in Figure 2-1 that thermal NO<sub>x</sub> is less than 10ppm at 2000K and less than 1ppm at 1800K, considering a typical 5ms of residence time [94].

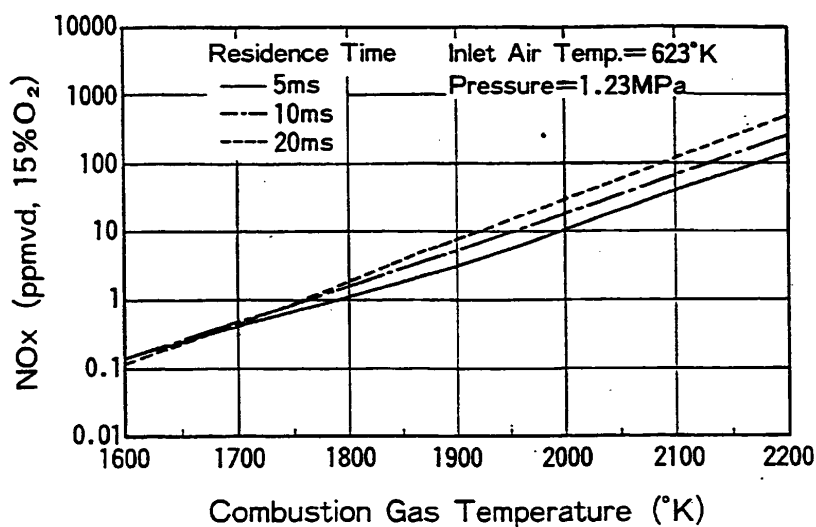


**Figure 2-1.** Thermal NO<sub>x</sub> as a function of the flame temperature for residence times 5, 10 and 20ms. NO<sub>x</sub> ppm corrected to 15% oxygen. Calculations at 623K air temperature at 12.3 bar, typical industrial gas turbine conditions[97].

It is possible to achieve this single digit NO<sub>x</sub> for burner temperatures up to 2000K, which is the operational temperature of J class gas turbines, for which a lean low NO<sub>x</sub> combustor design should be possible but is not offered by the manufacturers MHI. Thick, turbulent flames are characteristic of lean low NO<sub>x</sub> combustion, and the heat release usually occurs over about one third or a half of the burner length.

Residence time for thermal NO<sub>x</sub> is the time after combustion finishes, after heat release is complete. Low NO<sub>x</sub> lean combustion zones have a long flame development with a thick flame which for a fixed length combustor leaves a small residence time in the burnt gases for thermal NO<sub>x</sub> to be generated. On the other hand, this is a drawback for prompt NO<sub>x</sub> formation because prompt NO<sub>x</sub> occurs in the flame development region [93].

## **2.2 Low-NO<sub>x</sub> technologies**

### **2.2.1 Principles for low NO<sub>x</sub>**

Some important principles for obtaining the lowest NO<sub>x</sub> will be summarised in the following lines[93]:

- In gas turbine combustors, all the combustion air must pass through the flame stabiliser. This means that there isn't dilution or cooling air, and just a little amount of air has to be used to cool blades. Moreover, the primary zone must be stable at the overall equivalence ratio.

This will allow the flame stabiliser flow area to be larger than designs that do not meet this requirement, considering the same pressure loss.

There must be continuous cooling regeneration in the combustor, with a low-pressure loss, by first cooling the outer wall with the combustor air.

- Future high compression rate engines must be used considering outlet temperatures at 750-1000k.
- Pressure does not influence NO<sub>x</sub> emissions for lean well-mixed mixtures, and then it is possible to work with atmospheric pressure.
- There will be flashback and auto-ignition problems and low calorific value compatibility designs for future liquid fuel. These issues can be solved if no conventional premix passage is employed. This characteristic also avoids any acoustic matter. Finally, low NO<sub>x</sub> through direct fuel injection into the shear layers can obtain a good mixing [98].
- The flame stabilizer should reach a weak extinction similar to or better than the fundamental flammability limit. In other words, the stabilizer has to operate at a temperature not less than 1500K. Unfortunately, it is

not common to achieve this requirement, and just a few systems can do it [99].

- A fuel pilot cannot be used if the requirement is ultra-low NO<sub>x</sub> levels. However, this can be useful for lower powers.
- It is compulsory to achieve better than 10% of unmixedness for a fuel-air mixture, where the main heat release occurs in the flame instead of the outlet of the mixing duct. It is possible to employ the shear layer turbulence to mix the fuel and air.

Over the last 40 years, the combined cycle gas turbine (CCGT) power generators have reduced their CO<sub>2</sub> levels and improved their thermal efficiency by increasing the turbine entry temperature (TET), as shown in Table 2-1 [30], [100]–[102]. This table illustrates the development of the primary zone for low NO<sub>x</sub> combustion for a TET of 1800K, at which all the combustion air should enter the primary zone with no film cooling or dilution zone [87]. For higher entry temperatures, two techniques have been developed for NO<sub>x</sub> control: The use of axial staged fuel injection described in 2.2.3 and firstly studied by Willis et al. [103], Okuto et al. [104] and applied in the GE DLN 2.6 [105]; and the use of external EGR as explained in 2.2.4. However, an increasing turbine inlet temperature has been needed for the reduction of CO<sub>2</sub> levels and to improve thermal efficiency, which makes achieving ultra-low NO<sub>x</sub><sup>1</sup> levels even harder.

**Table 2-1.** CCGT combustor conditions for different turbine classes for a primary zone at 1800K. [30], [100]–[102]

Class	First Year	~TET	CCGT η%	Primary Mref	Primary airflow %	Primary MW/m <sup>2</sup> bar
D	1965	~1300K	48	0.025	50	7.5
E	1972	~1500K	52	0.03	60	12
F	1986	~1600K	56	0.04	80	18
G	1998	~1700K	58	0.045	90	22
H	2004	~1800K	62	0.05	100	28
J	2010	~1900K	64	0.05	100	30

---

<sup>1</sup> Ultra low NO<sub>x</sub> levels are less than 10ppm at a corrected 10% oxygen level.

### 2.2.2 Rich-lean combustion

The difference between gas turbine burners and process / domestic heaters is the operating equivalence ratio and the total excess oxygen level at which they run [106]. The turbine components affect the gas turbine's high temperatures, which must be considered in the design. A gas turbine burner operates well under stoichiometric conditions, and well-mixed lean combustion requires low  $\text{NO}_x$ . Well-mixed lean combustion will result in high  $\text{NO}_x$  levels under process conditions. Process burners can't be operated under lean conditions since the overall thermal efficiency gets compromised. In contrast, running a gas turbine combustor at stoichiometric or richer conditions would give better thermal efficiency than lean operation, but this could also result in very high temperatures, leading to blade melt-up.

For these reasons, advances in gas turbines are highly related to the firing temperature. Figure 2-2 shows the equilibrium  $\text{NO}_x$  and adiabatic flame temperature for a methane mixture as a function of the equivalence ratio for gas turbines operating at different inlet air temperatures. The peak  $\text{NO}_x$  is reached at  $\phi=0.85-0.9$ . As previously stated, the highest  $\text{NO}_x$  levels are achieved near stoichiometric levels, and ultra-low  $\text{NO}_x$  levels can be obtained running at very lean or very rich conditions, as shown in Figure 2-2. However, given that the peak adiabatic flame temperature is achieved just above stoichiometric, a rich operation would produce very high temperatures. This image also shows that peak  $\text{NO}_x$  is not at peak temperature since oxygen is needed to achieve the peak  $\text{NO}_x$ .

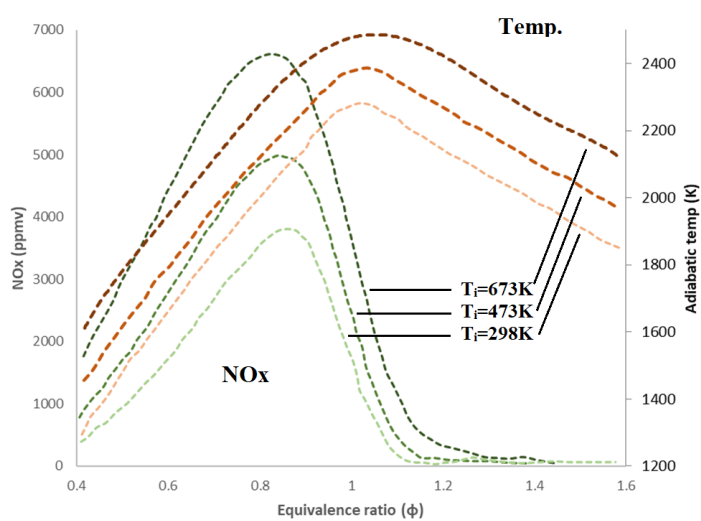


**Figure 2-2.** Equilibrium  $\text{NO}_x$  and adiabatic flame temperature vs equivalence ratio for different air temperatures (edited [107])

In terms of burning design, an increase in the excess air in a flow-mixed burner or premixed burners will increase the NO<sub>x</sub> levels. The peak would be located at the well-mixed region for this case scenario. In a process, a burner near stoichiometric levels is needed to not compromise the thermal efficiency, which changes the burner design [108].

Burning the fuel in a rich zone so the organic nitrogen compounds can be reduced to N<sub>2</sub> and then adding air producing a well-mixed zone is called rich/lean or staged combustion and can help solve problems such as FBN formation.[87]

Domestic fires share the same nature as process burners, and they can be treated as such. However, these devices operate at very lean conditions in terms of the flue gases, and they usually burn at ambient temperature unless a heat recovery system is adapted in contrast to gas turbines which can run at variable inlet temperatures thanks to the compressor. This concept is applied to a domestic fire appliance in Chapter 7.

### **2.2.3. Two Staged Combustion (Lean/lean)**

Thermal and prompt NO<sub>x</sub> dominate the aero-engine fuels[93]. Lean combustion in the primary zone and temperatures below 1900K can aid destroy thermal NO<sub>x</sub>. However, this temperature is too high for most civil engines at idle, so ultra-low NO<sub>x</sub> levels are only possible for a well-mixed lean primary zone. A lean well-mixed primary zone can help reduce prompt NO<sub>x</sub> and eliminate carbon emissions [108]. To achieve this at high turbine entry temperatures, most of the air is needed in the dilution zone, but additional air supply in the primary zone.

A common problem in single-stage well mixed primary zones is that to achieve low NO<sub>x</sub> at high power conditions, the stability gets compromised, and low power turn down is usually encountered [108].

The technique of axial staged lean/lean combustion has been used by various authors. One of the primary examples is the FLOX combustor presented by Zenger et al. [109] (Figure 2-3), which will be described in 2.2.7. The radial swirler with vane passage fuel injection by Andrews et al. [108] is shown in Figure 2-4a). Several of the ultra-low NO<sub>x</sub> process burners of Hamworthy and John Zink feature axial staged lean/lean combustion, where the fuel is injected in high-velocity air jets penetrating into the flame downstream of the central fuel [110]. Commercial combustors brands such as GE [105] shown in 2.2.6., KHI, Siemens [111] and RR have also used this concept. Figure 2-4b) shows the

Siemens fire where the central baffle is, in reality, a cone for the H class gas turbine. This baffle keeps the premixed pilot away from the other swirl flow at low powers, allowing a richer and hotter zone than the main combustion zone.

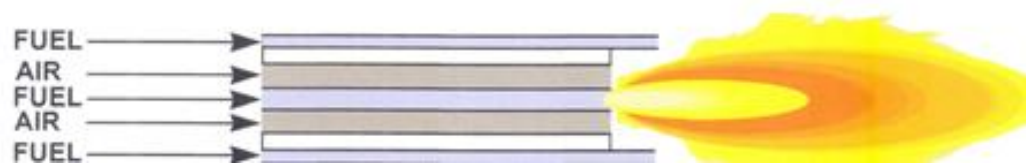


**Figure 2-3:** Lean/lean stage combustor [109].

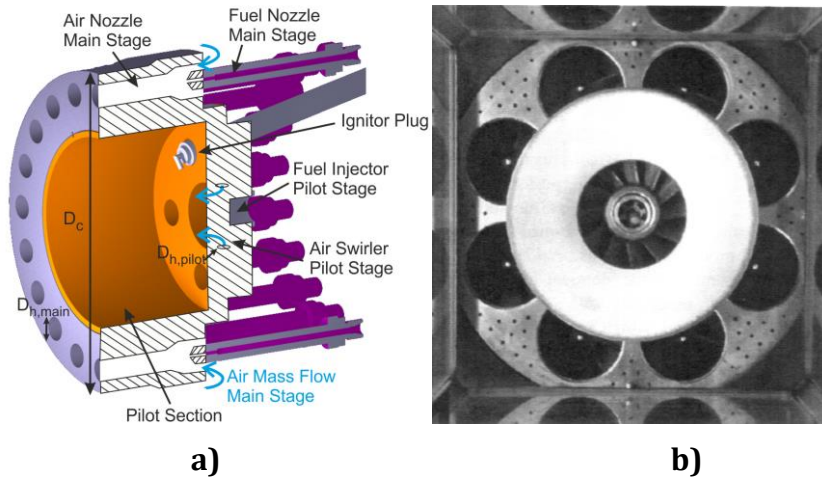


**Figure 2-4.** Lean/lean two-stage combustors: a) Zenger et al [109]. b) Siemens [57].

This technology is not only beneficial for the aero-engine sector, but its applications in the heating sector like domestic fires or biomass gasification are currently being studied in the UK. This concept has also been applied in domestic fires in Chapter 7.

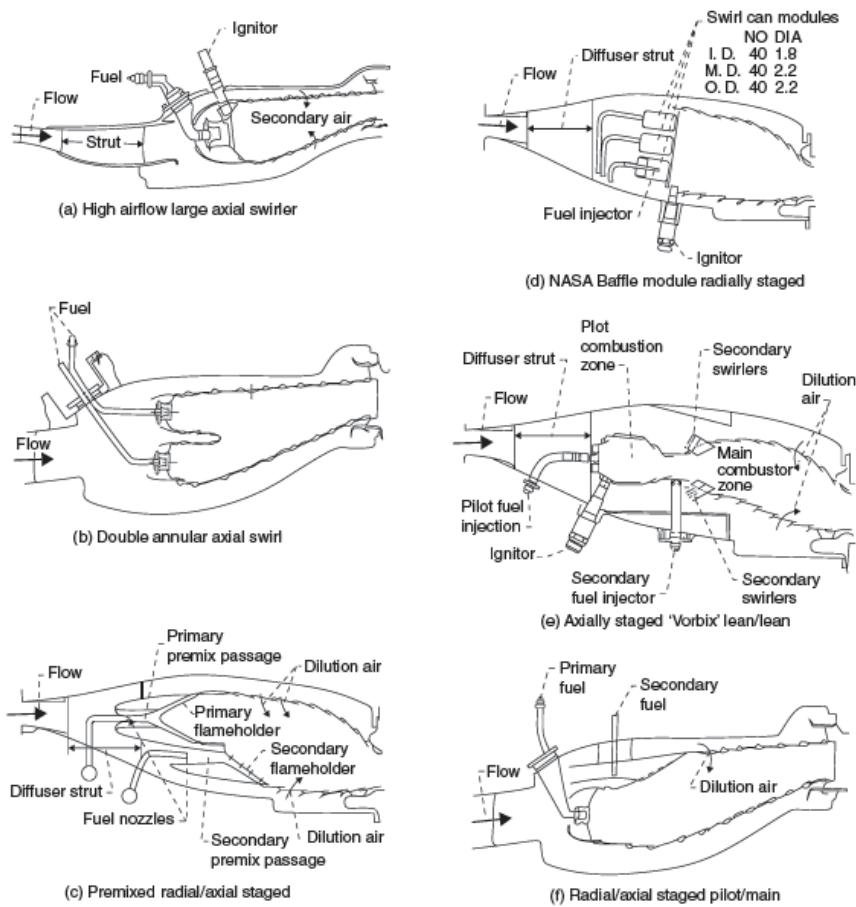


**Figure 2-5.** Designs of low NO<sub>x</sub> combustors from the NASA programme [112]–[115].

The aero-engine Clean Combustor Programme was created by NASA in the 1970s in which low NO<sub>x</sub> gas turbine combustor design technology was shown. Most of the designs in Figure 2-5 feature axial swirlers featuring lean/lean combustion. Image (a) in that same picture illustrates the high airflow large axial swirler can achieve lean combustion by allowing much air supply to the primary zone. This design has been applied in some industrial low NO<sub>x</sub> combustion turbines [116]–[118].

Figure 2-6 illustrates the lowest NO<sub>x</sub> emissions published in the literature for a gas turbine. These correspond to Leonard and Stegmaier [119], whose work presents the development of a new aero-derivative premixed combustion system which reduces NO<sub>x</sub> emissions by 90% from the original aircraft engine system, less than 25ppm each of NO<sub>x</sub>, CO and UHC. In their work, recirculation increases the concentration of CO<sub>2</sub> in the escape gases from 3-4% to 7-8%, making the absorption process more efficient and reduces the carbon capture plant size required. However, one big issue is the requirement to cool the recirculated burnt gases to environment temperature. This process enhances

the secondary losses of the cycle. In some instances, this process is avoided [120].

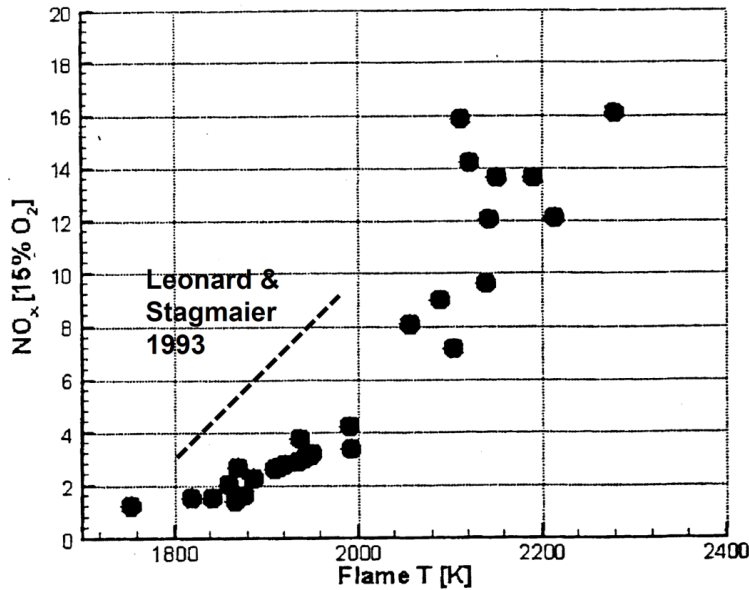


Figure 2-6. NO<sub>x</sub> emissions vs flame temperature [119].

#### 2.2.4 Internal exhaust gas recirculation (IEGR)

The introduction to Exhaust Gas Recirculation (EGR) has been required to achieve good levels of NO<sub>x</sub> for the development of gas turbines that work at 1700°C [101]. An example of this concept can be seen in Figure 2-7. Internal EGR (IEGR) inside the combustor reduces NO<sub>x</sub> formation. However, this process doesn't change the exhaust CO<sub>2</sub> emissions. FLOX (flameless oxidation) technology features high IEGR.

However, lean burning low NO<sub>x</sub> gas-turbine combustion is already flameless because the temperature of the flames is low and the colour light blue due to lean burning.

The process of flameless oxidation burning was developed for near stoichiometric process combustors, for which the presence of high local temperatures near stoichiometric allows a very effective reduction of NO<sub>x</sub> emissions by the internal burnt gas recirculation [121], [122].

The heat capacity of internal gases in EGR permits the decline of the flame temperature. Besides, there is associated air dilution that allows the O<sub>2</sub> to be reduced. This can be seen in Figure 2-8, where roughly 20% results in very small thermal NO<sub>x</sub>.

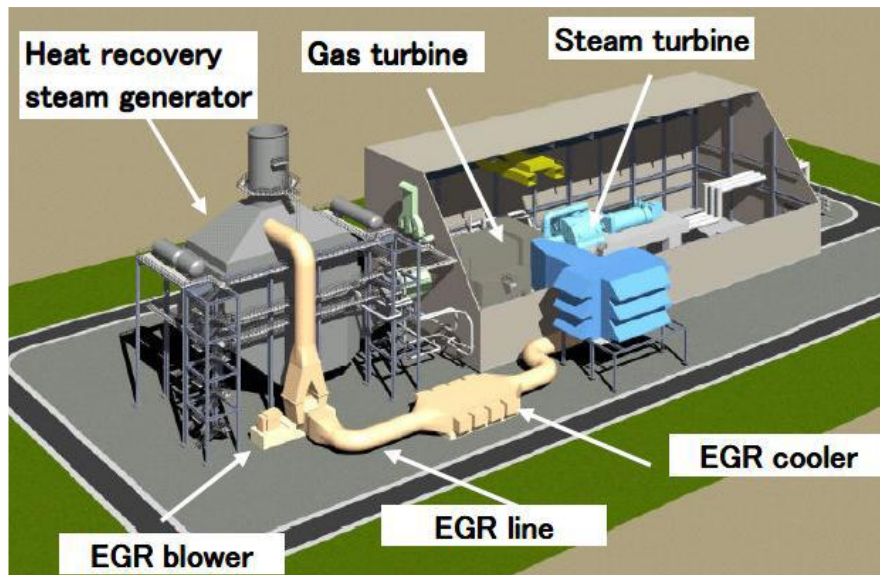


**Figure 2-7.** 1700° C-class Gas Turbine Combined Cycle (GTCC) plant with exhaust gas recirculation [101].

Flue gas recirculation (EGR or FGR) in gas turbines allows air displacement while the average operating temperature remains constant for the same power. EGR affects flame stability and the increase in equilibrium because both are controlled by the equivalence ratio and the mean temperature. The reduction of  $\text{NO}_x$  in gas turbines due to external EGR will occur if there is any thermal  $\text{NO}_x$  generation through local unmixedness and local near stoichiometric high-temperature zones. The EGR puts the peak temperature down in those zones; thus, the  $\text{NO}_x$  is reduced. EGR possesses the best  $\text{NO}_x$  reduction for both premixed and well-mixed gas flames near stoichiometric. Moreover, it has the most negligible  $\text{NO}_x$  reduction for rich/lean flames near stoichiometric [62].

MHI suppressed  $\text{NO}_x$  emissions in their low  $\text{NO}_x$  combustor using IEGR[123] by recirculating low-pressure exhaust gases from an engine turbocharger outlet to a turbocharger inlet after being treated by a scrubber. Figure 2-9 shows a diagram of the hydrogen combustor developed by MHI.

Huber et al. [29] showed in their NG 44MW Marathon series burners  $85 \text{ mg/m}^3$   $\text{NO}_x$  for 100% fuel. The same burner was used for hydrogen featuring a central baffle with eight fuel injection nozzles in the periphery of the baffle. They termed this principle “hollow flame technology”. This hydrogen burner achieved  $230 \text{ mg/m}^3$  at 3% oxygen for full hydrogen.

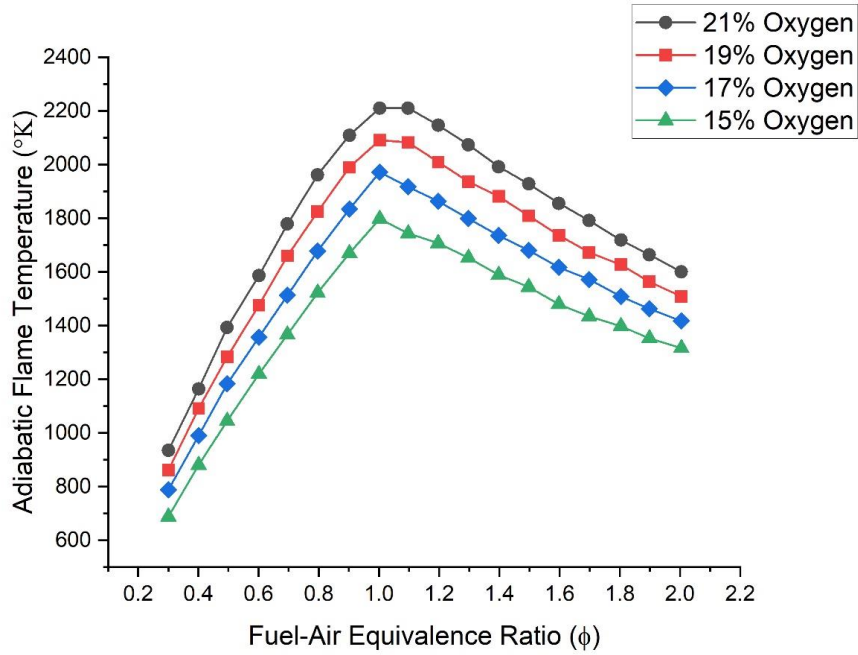


**Figure 2-8.** Adiabatic flame temperatures with various levels of intake oxygen at different fuel-air equivalence ratios [124]

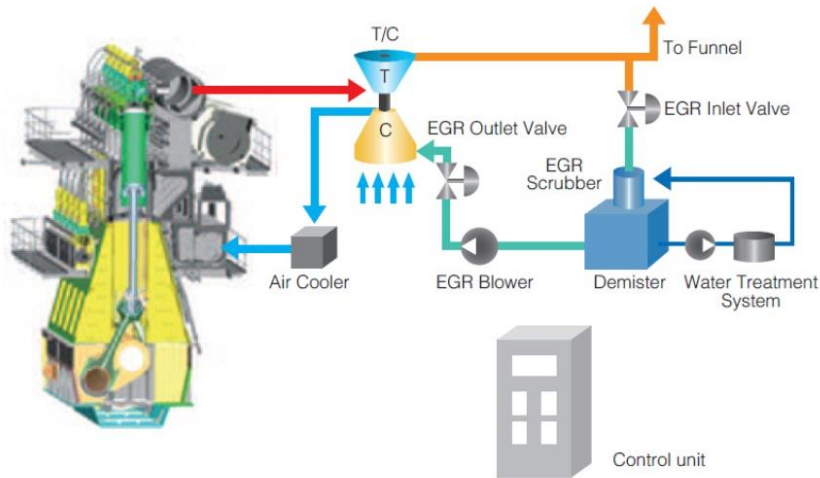


**Figure 2-9.** Diagram of low pressure IEGR low NO<sub>x</sub> combustor [123].

The ARZ hydrogen burner also presented by Huber et al. [29] aimed for 173 kW achieved NO<sub>x</sub> levels of 240 mg/Nm<sup>3</sup> at 3% O<sub>2</sub>. This burner featured IEGR at 13% to reduce the NO<sub>x</sub> levels to the ones obtained for NG of 70 mg/Nm<sup>3</sup>.

### 2.2.5 NO<sub>x</sub> reduction by impingement

Another method that studies temperature reduction to achieve lower NO<sub>x</sub> is impingement cooling against a flat wall. This technique cools the flame, which allows dropping the NO<sub>x</sub> levels. The dry-low NO<sub>x</sub> venturi combustor invented

by Walso et al. [125] featured an air-cooled annular shield to allow air/fuel mixing.

The use of impingement has also been applied for domestic fires, showing that impingement against the radiating ceramics aids in the  $\text{NO}_x$  reduction, which will be observed in Chapter 7.

### 2.2.6 $\text{NO}_x$ reduction by water injection

Water or steam injection was the first method to control  $\text{NO}_x$  in the combustion zone by removing heat from the flame. Injecting water directly into the flame creates a heat sink that lowers the flame temperature, reducing thermal  $\text{NO}_x$  formation.

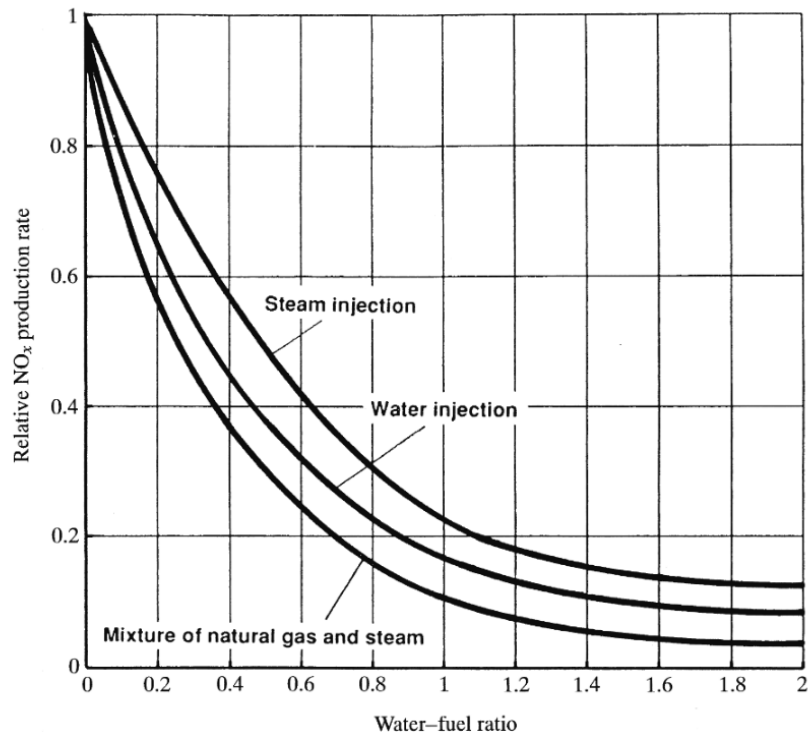


**Figure 2-10** Effect of water/steam injection over  $\text{NO}_x$  emissions [126]

Water by fuel ratios (WFR) defines the injection rates. This method adds the benefit of increasing gas turbine output since the gas mass flow increases. WFR of 1-2 can considerably reduce the  $\text{NO}_x$  emissions, as shown in Figure 2-10. However, this process requires large amounts of clean water to avoid corrosion in the turbine blades [127]. This method has been used in various works for diesel engines [128], [129]

However, this technology can bring problems such as the increase of fuel  $\text{NO}_x$ .

### 2.2.7 Premixed low-NO<sub>x</sub> combustion.

Premixed combustion occurs when the air and fuel are entirely mixed before combustion starts. On the other hand, diffusion combustion is when fuel is injected into the air and mix together after combustion [95]. Figure 2-11 illustrates the main differences between diffusion and premixed burners. More information can be found in the work of Becker and Berenbrink [130]. Premixed combustion systems in gas turbines can produce very good combustion efficiency and a low amount of pollutants. In addition, these systems can improve the combustor exit temperature, which is very useful to next-generation high-temperature turbines [21].

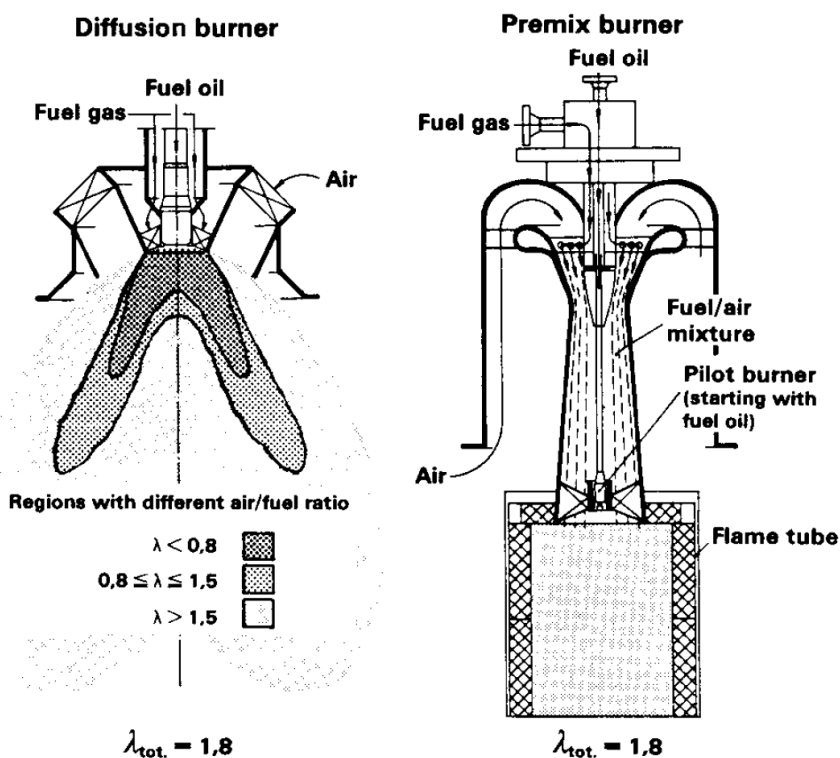


**Figure 2-11.** Comparison of diffusion and premixed burners considering an equivalence ratio of 0.55 [130].

As shown in Anderson's work, the mentioned systems allow optimal combustion efficiency and very low NO<sub>x</sub> emissions [131], [132]. Many authors explain the advantages of premixed systems and how it is possible to control pollutants' production by using the combustion of lean mixtures of fuel and air in the primary zone. To maintain the emissions down the operating conditions, it is recommended to use premixed pre-vaporized combustion by using fuel staged systems or variable geometry. This controls the reaction zone temperature, and primary zone air/fuel ratios can be maintained rich enough to prevent flame blowout [133]–[135]. Larry Thomas et al. in 2011 discussed

in their work that the Dry Low NO<sub>x</sub> (DLN) technology has helped to achieve one-digit NO<sub>x</sub> emissions in E-class industrial gas turbines [136]. In Figure 2-12 the DLN1's previous and ongoing progression to better NO<sub>x</sub> levels can be appreciated.

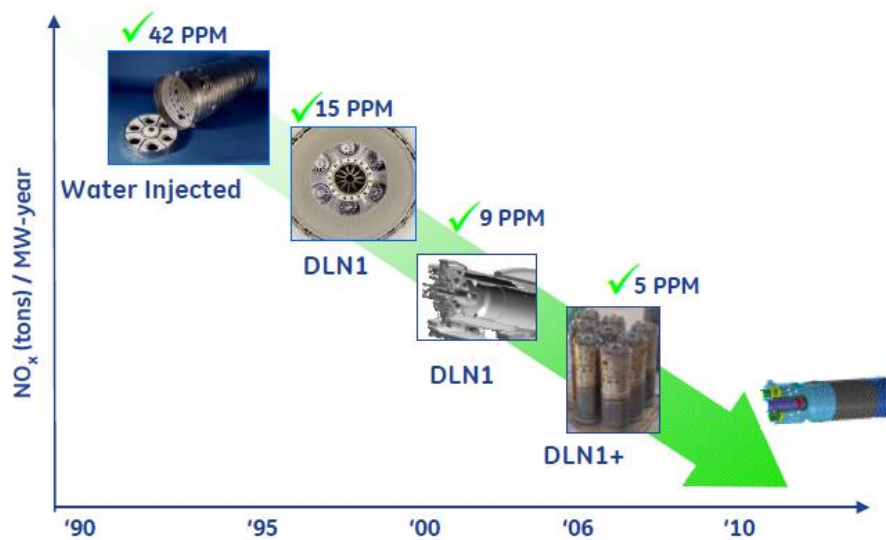


**Figure 2-12.** NO<sub>x</sub> progression with premixed systems [136].

### 2.2.8 Non-premixed low-NO<sub>x</sub> combustion.

Non-premixed or diffusion flames produce very low NO<sub>x</sub> levels for near stoichiometric mixtures [105]. In contrast to well-mixed (premixed) combustion systems, which have shown to achieve higher levels [62]. Also, diffusion flames don't feature flashback given their lack of inherent propagation speeds. Hence, non-premixed ignition is used for safety purposes [137]. However, the nature of these systems is to operate near the adiabatic flame temperature, which can result in high NO<sub>x</sub> levels unless a diluent is added to the flame. [105]

Various gas turbine technologies featuring diffusion combustion have been shown to achieve ultra-low NO<sub>x</sub> levels, and they have been widely used by some important firms. The FLOX concept mentioned in 2.2.4 [37], [41], [42] (Figure 2-13) applied to combustion systems consists of a large central burnt gas recirculation zone between an array of air holes placed on a perforated plate. The fuel is injected into the central recirculation zone, as shown in Figure 2-14. The heat release used in the FLOX burner work was 10 MW/m<sup>2</sup>bar [101]

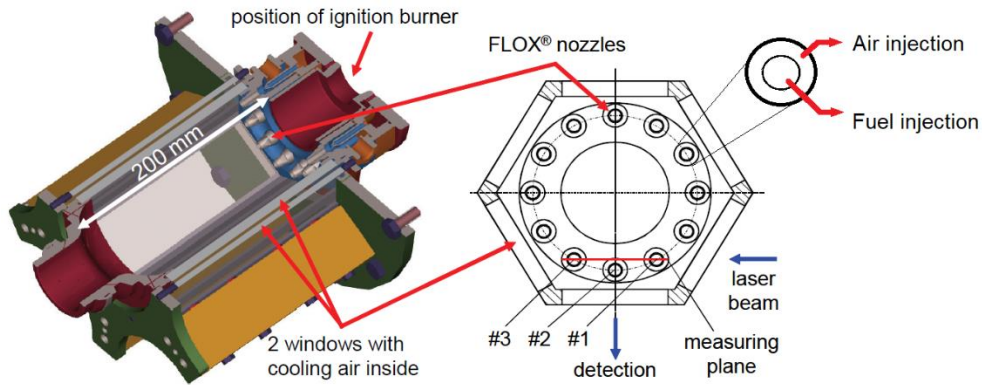


**Figure 2-13.** FLOX burner with 12 single nozzles. [37] Edited.

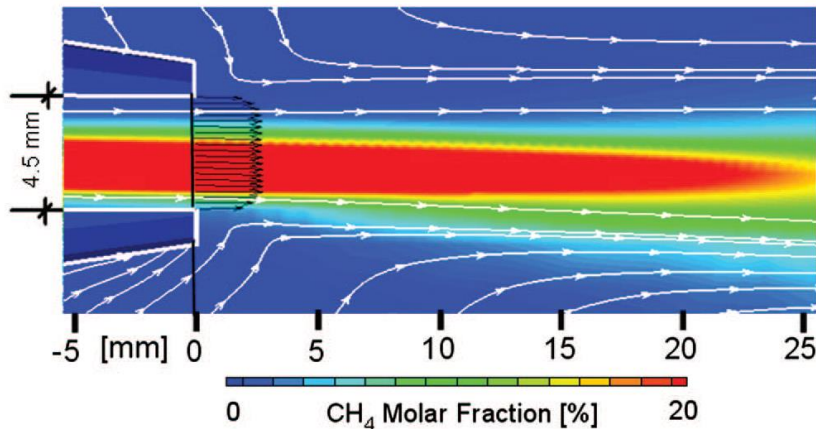
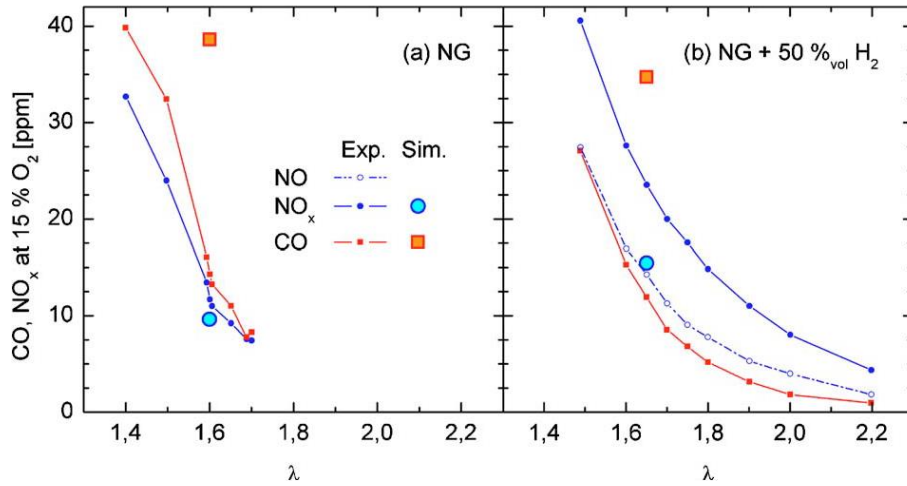


**Figure 2-14.** CH<sub>4</sub> contours obtained with CFD for FLOX burner showing recirculating flow [81]

This technique was developed for process burners that work at near stoichiometric regimes where high temperatures are achieved, and low NO<sub>x</sub> levels are produced due to IEGR. For natural gas, NO<sub>x</sub> levels of 10ppm are obtained for mixtures of  $\phi=0.61$  for an adiabatic flame temperature of 1996K, as observed in Figure 2-15.

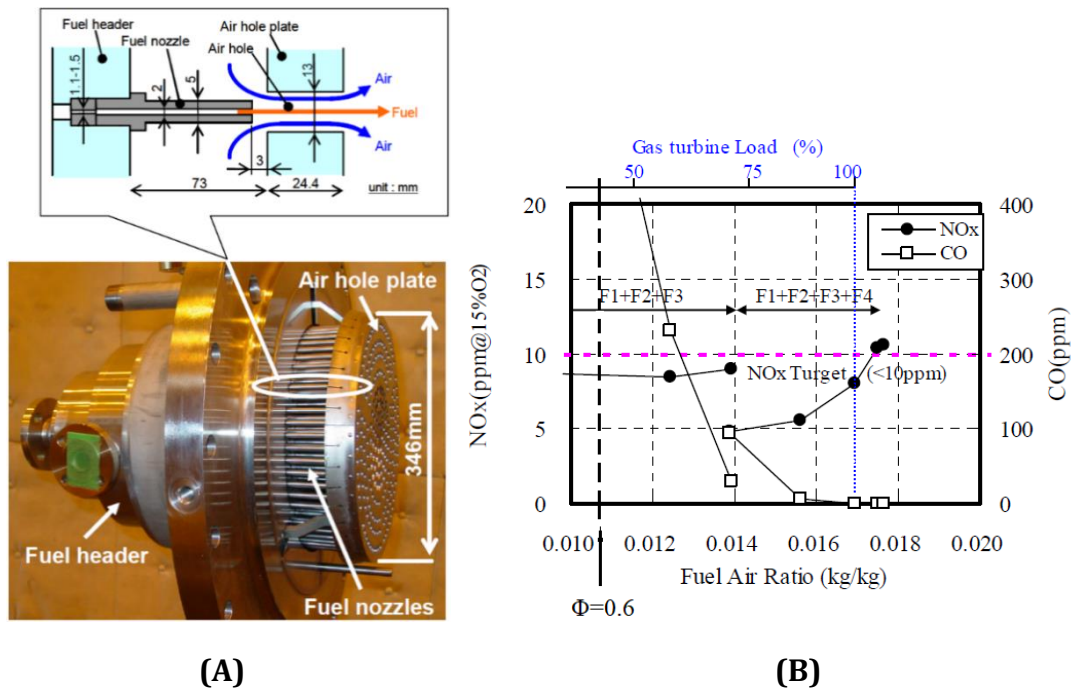
One of the main characteristics of FLOX designs is that they have widely equispaced air jets generating a large recirculation zone in the centre of the combustor, allowing the air jets to entrain the most of the recirculation gases. These air jets are located close to the combustor wall, so they only entrain air below them, which reduces the recirculation mass rate.

This technology has been studied with Computational Fluid Dynamics to improve the combustion characteristics[81]. The FLOX concept is studied in Chapter 6 for its application to the technology Grid Mix.



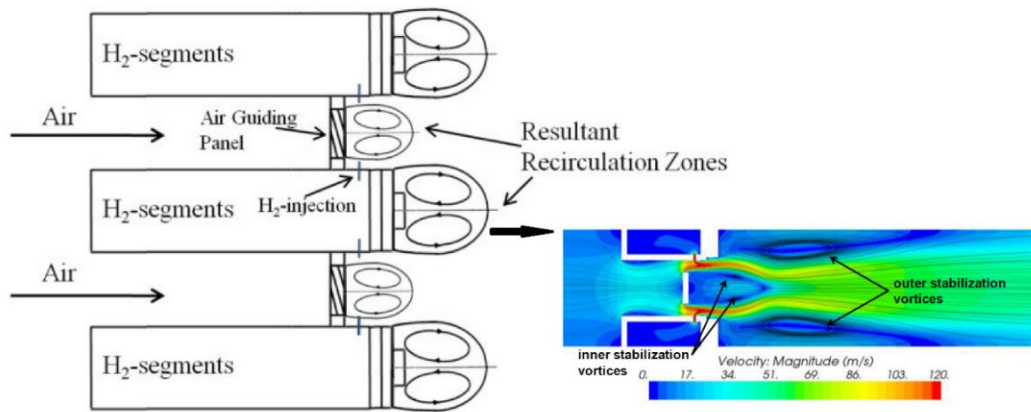
**Figure 2-15.** NO<sub>x</sub> and CO emissions for FLOX technology for two fuels [41]

Another example of diffusion flame is the Hitachi cluster nozzle burner. [138] It consists of a series of air holes installed over a thick plate featuring a small fuel nozzle in the centre of each air hole, fuelling coaxially to the air jet. Improved mixing enhances the interface distance between the fuel and air with no flashback risk due to the nozzles' reduced size. This principle is shown in Figure 2-16 A). Figure 2-16 B) indicates the NO<sub>x</sub> ppm for different fuel concentrations, the stoichiometric F/A for AHAT systems is 0.017.



**Figure 2-16.** (A) Fuel staged cluster nozzle burner of HITACHI in a 3MW Gas Turbine. (B) NO<sub>x</sub> levels at different values of A/F [138].

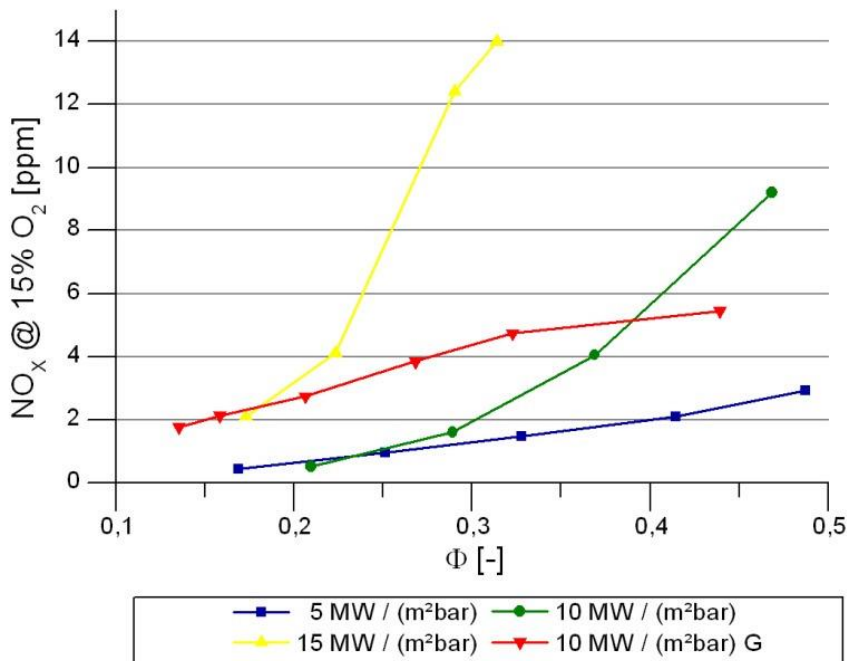
The Micromix burner [139]–[142] features a low-NO<sub>x</sub> diffusion flame implemented for H<sub>2</sub> combustion for a heat release of 15 MW/m<sup>2</sup>bar.



**Figure 2-17.** Micromix principle showing the recirculation areas inside the combustor using CFD (Edited [139], [140])

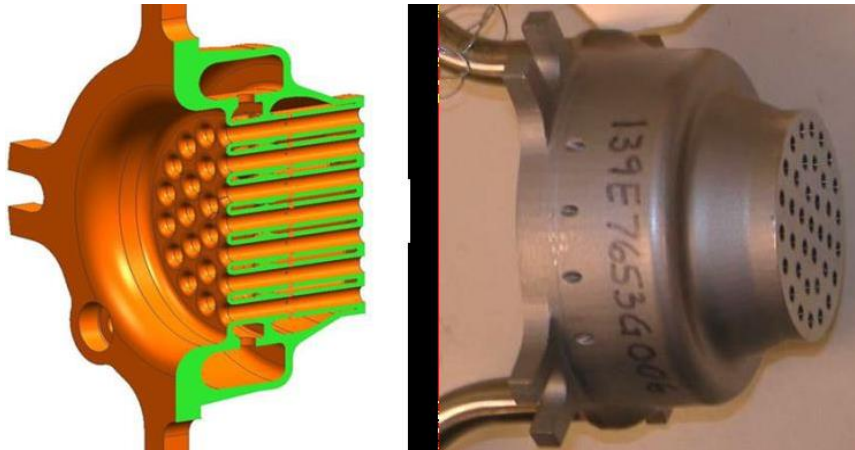
This technology's principle is to inject fuel radially into the air jets and create large recirculation zones, as shown in Figure 2-17, to enhance the mixing and reduce the NO<sub>x</sub>.

Figure 2-18. shows the NO<sub>x</sub> emissions for different combustion intensities in non-premixed systems. The NO<sub>x</sub> emissions are presented for a 15% O<sub>2</sub> in the flue.



**Figure 2-18.** NO<sub>x</sub> emissions vs  $\Phi$  for different combustors configurations. [139]

The hydrogen multi-tube mixer combustor developed by York et al. [43] resembles the Micromix since it also fuels radially but at the inlet of an array of air tubes placed on a thick plate, as shown in Figure 2-19.



**Figure 2-19.** Development and testing of a low NO<sub>x</sub> Hydrogen Combustion System for HDGT [43].

This technology benefits from the 7D stabiliser thickness to complete mixing and achieve ultra-low NO<sub>x</sub> levels, showing that a good mixing length before combustion aids in NO<sub>x</sub> production.

This technology, similarly to the Micromix described previously, features the phenomena known as jet in a crossflow which has been widely investigated and constitutes an important area in CFD aerodynamics.

All the previously mentioned diffusion low NO<sub>x</sub> technologies feature perforated or grid plates to achieve good mixing, hence good NO<sub>x</sub> levels. This technology will be described below

### **2.2.9 Hydrogen combustion**

Fuel switching from conventional fossil fuels to green hydrogen has shown to be a solution for achieving net-zero GHG emissions, and it can be produced by electrolysis of water from existing renewable power plants. Various studies have shown the advantage of producing hydrogen from electrolysis using wind energy [143]–[146],

For hydrogen energy storage, electrical power is converted into hydrogen by electrolysis. Then the hydrogen energy can be released in a combustor by using the hydrogen as fuel [147, p. 12].

However, current hydrogen combustion has some drawbacks such as the increased NO<sub>x</sub> production due to the higher peak flame temperature of hydrogen combustion on air. The industrial burner manufacturer Walter Dreizler GmbH [29] have shown in their Marathon series burners (up to 44MW in size) a NO<sub>x</sub> increase from 85 mg/m<sup>3</sup> for 100% NG to 230 mg/m<sup>3</sup> at 3% oxygen for 100% hydrogen, a factor of 2.7 increase in hydrogen. This used what

they called hollow flame technology, which was a central baffle with eight fuel injection nozzles equispaced around the baffle periphery. They also gave results for another of their burners, ARZ, for lower powers which for 173 kW gave a  $\text{NO}_x$  increase from  $70 \text{ mg/Nm}^3$  on NG to  $240 \text{ mg/Nm}^3$  at 3% oxygen on hydrogen, which was a factor of 3.4 increase in  $\text{NO}_x$ . They used external EGR at 13% with the hydrogen burner to bring the hydrogen  $\text{NO}_x$  down to the same level as NG.

Cellek and Pinarbasi [148] investigated, using CFD, a low-swirl burner and predicted an increase in the mean burner outlet  $\text{NO}_x$  from 50ppm for methane to 470 ppm for hydrogen.

These results show that solving the  $\text{NO}_x$  problem with hydrogen combustion is a critical problem area in using green hydrogen for decarbonisation.

The previously mentioned hydrogen-fuelled Micromix lean burning dry low emission (DLE), or dry low  $\text{NO}_x$  (DLN) was the first diffusion combustor using only hydrogen fuel [149]. The combustor achieves less than 2 ppm  $\text{NO}_x$  corrected to a 15%  $\text{O}_2$  exceeding the 99% combustion efficiency for gas turbine part, full and overload conditions [150]. This value has been compared with CFD simulation using the realizable k- epsilon and eddy break-up turbulent and combustion models, respectively, showing close agreement [151].

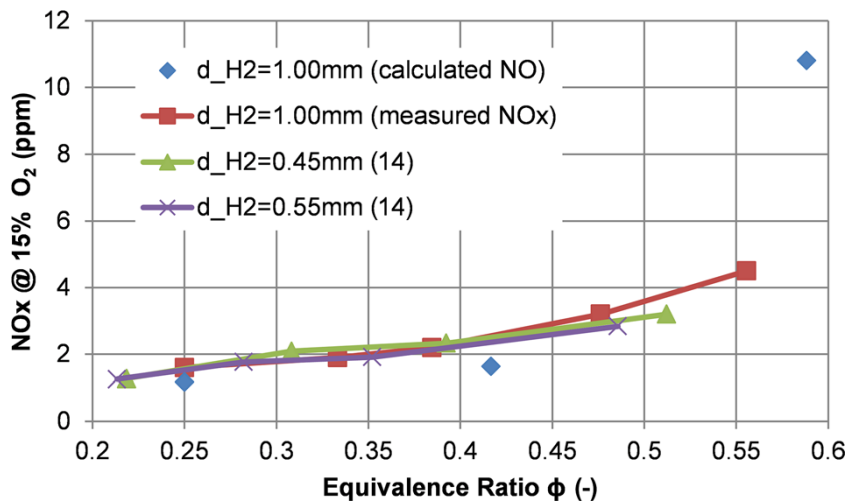


**Figure 2-20.**  $\text{NO}_x$  comparison for experimental and simulation values for Micromix hydrogen combustor [151]

The hydrogen burner developed by York et al. [43] achieves 2 ppm  $\text{NO}_x$  level at 15%  $\text{O}_2$  level, as shown in Figure 2-21.

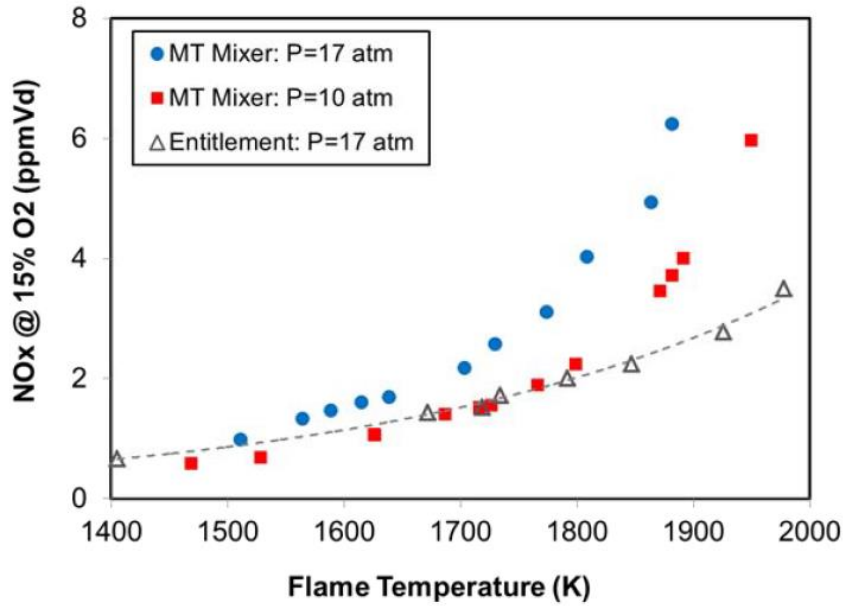


Figure 2-21. Flame temperature vs NO<sub>x</sub> levels for MT mixer [43]

### 2.2.10 Grid plate flame stabilisers

One of the most straightforward designs of low NO<sub>x</sub> flame stabilizers is a flat grid plate with an array of air holes, in which every independent hole has a separate fuel supply. These technologies, also known as perforated plates, generate a shear layer that allows fast fuel and air mixing.

Anderson was the pioneer in using grid-plate flame stabilisers for premixed flames [132]. This author demonstrated for the first time that ultra-low NO<sub>x</sub> emissions can be obtained by lean well-mixed combustion. He showed 6 ppm of NO<sub>x</sub> at 1800K in the combustor exit temperature using a 61 grid plate whose pressure was 5.5 bar using 590 and 800 K air temperature and a reference velocity of 25 m/s. Supposed gas turbine combustion was working with well fuel-and-air mixing and a lean primary zone under the maximum thermal NO<sub>x</sub> formation temperature.

Andrews et al. have studied these stabilisers for many years [21]–[25], [87], [106], [152], and they have named them Grid Mix, GM, flame stabilisers [22]. Al-Dabbagh and Andrews showed that for radial fuel injection into each air hole (GM1), the NO<sub>x</sub> emissions were as low as any in the literature [22][87] for the same flame temperature in the range 1400 – 1800K. Modern direct injection in rapid fuel and air mixing flame stabilizers showed to produce ultra-low NO<sub>x</sub> emissions even lower than for premixed combustion, given their capability to burn leaner than stable flames. The flame stabilizer geometry also considerably affects NO<sub>x</sub> production, generally due to the prompt NO<sub>x</sub> created by slow flame

development [62]. The turbulence generation by grid plates and its effects on  $\text{NO}_x$  was investigated by Phylaktou and Andrews [153].

In GM, the fuel is injected directly into the air jet shear layer. The fuel injection method for the grid plate air holes studied for Grid Mix 1 and 2 (GM1 and GM2) has been experimentally demonstrated for zero-carbon electricity to influence flame stability and  $\text{NO}_x$  emissions. The radial inward fuel injection featured in GM1 showed lower  $\text{NO}_x$  levels than GM2 but lower flame stability [152], [154] and one of the lowest  $\text{NO}_x$  in the literature. This fuel injection method has been successfully demonstrated for low  $\text{NO}_x$  burners operated by hydrogen [26], [139], [140], [155]. Current high-temperature gas turbines operate at a compressor outlet temperature of about 1800K at an overall  $\phi$  of 0.58, as shown by Ai et al. [30] by rapidly mixing fuel and air to achieve low  $\text{NO}_x$ . However, this restriction challenged the workers, pushing them to use CCGT plant using external EGR to help reduce the  $\text{NO}_x$  without passing the inlet combustor air through the stabiliser holes. The technologies investigated by Andrews et al. [25] do not need the external EGR, and are operated with inlet air at 600-400K, demonstrating 3.5 ppm of  $\text{NO}_x$  at 15%  $\text{O}_2$  for a set of adiabatic mean temperatures of 900-1900K. The internal traverses were taken at 1800K. GM1 and GM2 operated for a Mach number of 0.047, at which all the combustor air passed through the stabiliser air holes without air cooling. This results in a very high combustion heat release at 28 MW/m<sup>2</sup>bar. Only a few CFD studies have been carried out for this combustion intensities, but none at that specific heat release, which this thesis investigates.

The weak extinction  $\phi$  was 0.42 for GM1 and 0.20 for GM2. Directly fueling the shear layers improved flame stability, and both technologies could burn below the premixed flammability limit. The weak extinction for grid plates used with premixed combustion at an inlet temperature of 400K was at 1400K and  $\phi = 0.45$  for propane/air. The four holes grid plate stabilisers used for premixed combustion displayed high-velocity flows and high turbulence in the shear layer. This made them impossible to burn lower than the flammability limit of  $\phi = 0.45$ . The flame achieved with GM2 was more stable than the one obtained with GM1 since the mixing was better and the higher  $\text{NO}_x$  levels.

The GM1 technology has been applied by other combustor manufacturers like the combustor developed by the University of Aachen and Siemens in 2011 [139]. Similarly, the combustor developed by York et [43], shown in Figure 2-19, shares this principle.

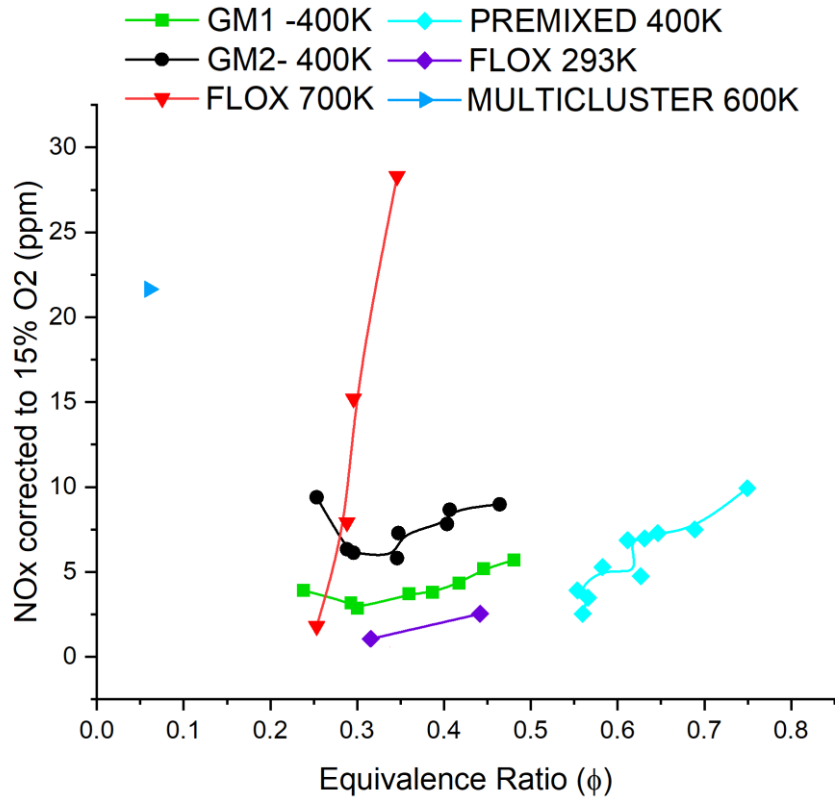


**Figure 2-22.** Comparison of NO<sub>x</sub> corrected to 15% oxygen as a function of  $\phi$  at 400K [21]-[23]

GM2 is a practical design for duct combustors like the Oxy-fuel burner employed by the Lanemark company [156].

The NO<sub>x</sub> emissions for these types of fuel injections can be viewed in Figure 2-22, which compares premixed systems and other non-premixed technologies explained before.

Despite the experimental studies available for the different fuel injection methods, no study has been developed comparing them, and GM has never been studied for hydrogen combustion.

Figure 2-23 shows some grid plate designs that have achieved lower NO<sub>x</sub> levels and better flame stability than premixed combustion showing only round hole configurations. [93].

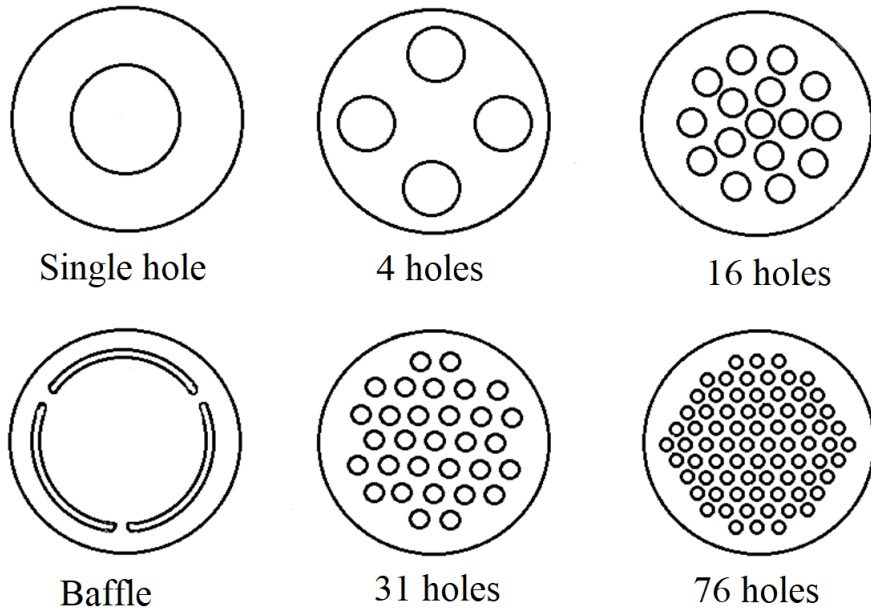


**Figure 2-23.** Plate stabilizer geometries [157]

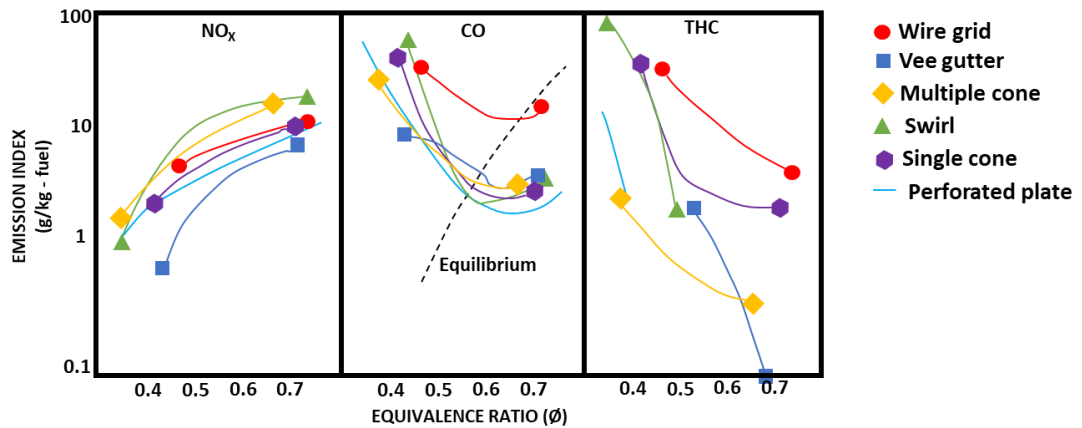


**Figure 2-24.** Emission measurements for different grid plates [158].

Figure 2-24 shows  $\text{NO}_x$ , CO and HC emissions as a function of the  $\phi$  for propane and some flame stabilizer geometries, from the work of Roffe and Venkataramani [158] considering the following conditions: a pressure of 10 bar and 800K, a reference Mach number of 0.044, reference velocity of 26 m/s, and a combustor length of 300 mm. The upper set of images of this figure shows 80% blockage, translated into a high-pressure loss of the stabilizer. Meanwhile, the lower set illustrates low-pressure loss due to 70% blockage.

A set of experiments was made by Al-Dabbagh and Andrews in 1984 [25] to achieve ultra-low  $\text{NO}_x$  levels by comparing different combustor stabilizer hole-shapes with circular holes at 740 and 600K. This showed that slot-shaped holes can produce lower  $\text{NO}_x$  emissions than circular holes due to the higher turbulence. Figure 2-25 illustrates the compared designs.

Some techniques featured in low NO<sub>x</sub> gas turbine primary zones with good flame stability were developed by Andrews et al. in 1992. These techniques use fuel injection into the base of the shear layer, demonstrating that low NO<sub>x</sub> emissions can be achieved for non-swirling jet shear layer systems for gas and liquid fuels [159].

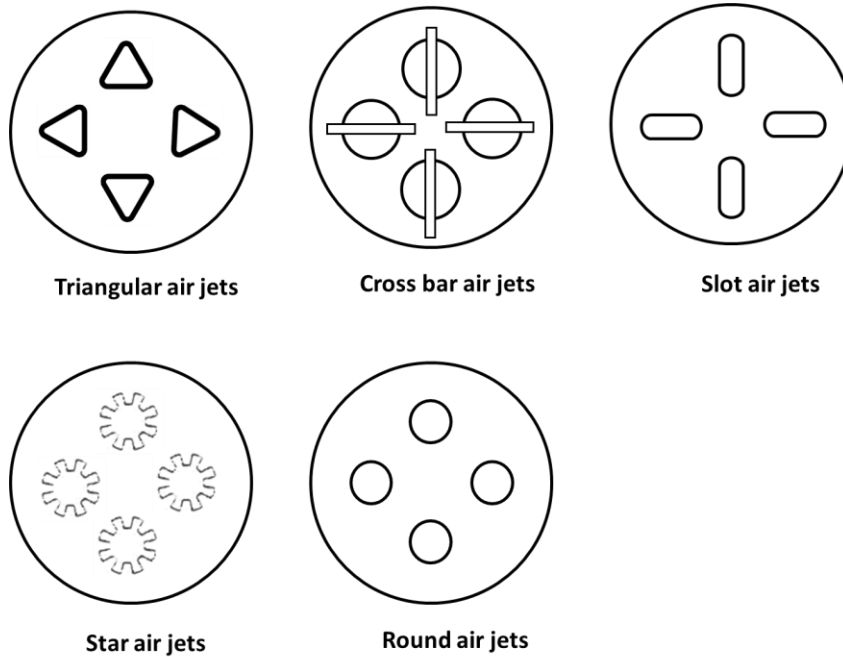


**Figure 2-25.** Four hole Grid Mix air jet configuration and jet shear layer hole shapes

Similarly, low NO<sub>x</sub> emissions have been proved for swirl stabilised systems, as mentioned in Alkabie and Andrews's work, where no influence of the swirler expansion ratio  $D/d$  was encountered for the weak extinction [160]. In contrast, fluid dynamics of non-circular jets, with and without combustion, were investigated by Schadow and Gutmark [161], showing improvements in jet mixing relative to round jets, given the additional small scale turbulence at the edges of the jets.

### 2.2.10.1 Pressure loss in grid plate flame stabilisers

Two main factors influence the pressure loss along a combustor according on Walsh and Fletcher [162]. The first is the “cold pressure drop” due to the burner’s blockage, measured as a percentage of the inlet pressure ( $\Delta P/P\%$ ). The second factor is due to the heat release in the combustion zone, commonly known as “hot pressure drop”. Usually, gas turbine combustors work for a cold pressure drop of 4 to 6% of the initial pressure [157], although some other

combustors work at higher pressure losses. Although the pressure loss can be seen as a disadvantage for the combustor, since it gives a high fuel consumption due to the reduction in the cycle network, it is also essential in the performance of the combustion of the fuel-air mixture. This is achieved by adding enough turbulence to the air/fuel mixture to achieve high-intensity combustion. An increase in pressure loss along the air holes or a smaller number of holes allows a good mixture of the combustion products with air in the dilution zone [157].

Some factors affecting the pressure loss for grid plate stabilisers [163] (orifice and perforated plates) are listed below:

- The Reynolds number affects the separation of the fluid in the upstream face of the orifice creating a small jet [164]. When the velocity increases, the jet contracts to a limited cross-sectional area known as “vena contracta”, and its ratio to the area of the orifice is known as the contraction coefficient  $C_c$ . This flow expansion due to the vena contracta is the main pressure loss factor. The orifice length affects the reattachment of the fluid to the orifice wall when expanding from the vena contracta [157].
- Porosity or flow restriction  $\beta$ . This factor is expressed as the ratio of the open area to the duct area. It mainly influences the discharge characteristic by highly affecting the contraction coefficient  $C_c$ . This has been proven theoretically for a sharp-edged orifice plate [165] and experimentally [166], [167].
- Orifice thickness/Diameter ratio ( $t/D$ ): The fluid features rely on whether the free shear layer created in the orifice inlet keeps away from the orifice wall or if it reattaches to it. Both cases are the limit flow conditions of thin orifices.
- Compressible flow. When the maximum pressure ratio value along an orifice is achieved, the pressure reductions at the opposite side of the pressure do not increase the flow discharge. This is not the case for orifice plates since the mass flow at the inlet keeps increasing even though the back-pressure decreases and the size of the vena contracta increases until its area is the same as the orifice's area.
- Discharge coefficient  $C_D$ : In a constriction such as a nozzle the discharge coefficient ( $C_D$ ) is the ratio of the actual discharge to the theoretical discharge for a fluid flow. Studies have shown how the discharge coefficient is affected by non-uniform approach velocity profiles [168].

All the flame stabiliser geometries previously mentioned exhibit an airflow in a pipe of area  $A_1$ , a total open area in the grid plate  $A_2$  and a downstream combustor area  $A_1$ . The pressure loss,  $\Delta P/P$  %, is regulated by  $A_2$  through the orifice plate flow, and when deriving from Bernoulli's equation [169], it can be expressed as in Equation (7)

$$\frac{dm}{dt} = C_D A_2 \left( 2 \rho \frac{\Delta P}{P} \right)^{0.5} \quad (7)$$

Where  $\rho$  is the upstream air density of the grid plate, expressed in  $\text{kg/m}^3$ .

The aerodynamics downstream of the combustor is crucial for predicting the discharge coefficient  $C_D$ . If  $\rho$  in Equation (7) is replaced by the gas law [170],  $\rho = P/RT$ , and the velocity is replaced by the reference Mach number,  $M_1 = U_1 / (\gamma RT)^{0.5}$  [171], then the pressure loss can be expressed as in Equation (8)

$$\left( \frac{\Delta P}{P} \right) = 0.5 \left( \frac{\gamma}{C_D^2} \right) M_1^2 \left( \frac{A_1}{A_2} \right)^2 = 0.5 \left( \frac{\gamma}{C_D^2} \right) M_2^2 \quad (8)$$

Where  $M_1$  is the reference Mach number for the combustor area  $A_1$ , and  $M_2$  corresponds to the Mach number of the mean flow in the grid plate air holes. It can be deduced from Equation (8) that the pressure loss is a function of the reference Mach number,  $M_1$ , discharge coefficient in the grid plate,  $C_D$  and the ratio of the combustor pipe area  $A_1$  with the open area of the grid plate  $A_2$ . The stabiliser blockage can be expressed as  $1 - A_2/A_1$ . Hence, the Mach number must be held constant to predict pressure loss, and the inlet temperature can be ignored.

In some works, experimental data of pressure loss has been expressed in terms of the K factor, as shown in Equation (9);, such as the work of Ward-Smith for orifice pressure loss of various geometries [164].

$$K_1 = \frac{\Delta P}{0.5 \rho U_1^2} \quad (9)$$

When using Equation (7) and expressing the mass flow rate as  $\rho U_1 A_1$  then, the  $K_1$  factor is directly related to  $C_D$ , as in Equation (10).

$$K_1 = \frac{1}{C_D^2} \left( \frac{A_2}{A_1} \right)^2 \quad (10)$$

Similarly, if the pressure loss factor is expressed in terms of the mean velocity in the grid plate holes,  $U_2$ , then:

$$K_2 = \frac{1}{C_D^2} \quad (11)$$

The area ratio in Equation (10) can be replaced with the flame stabiliser blockage  $\beta$ , as shown in Equation (12)

$$\beta = 1 - \left(\frac{A_2}{A_1}\right) \quad (12)$$

As previously mentioned, the pressure loss in grid plate flow is controlled at the sharp-edged inlet of the orifice by flow separation. The separated flow creates a vena contracta with a smaller flow area than the hole, where the ratio of this vena jet diameter to the hole diameter is the contraction coefficient,  $C_c$ . The flow expansion from the vena contracta to the downstream combustor diameter creates pressure loss.

If  $A_1$  is higher than  $A_2$ , a deduction can be made from the ideal flow theory that  $C_c = 0.61$ . If  $A_2$  is smaller than  $A_1$ , then  $C_D = C_c$  [172].

If Equation (11) is applied to this, then  $K_2$  can be related to  $C_c$  as in Equation (13).

$$K_2 = \frac{1}{C_c} - \left(\frac{A_2}{A_1}\right)^2 \quad (13)$$

$C_c$  and  $C_D$  can be related by Equation (14).

$$\frac{1}{C_D} = \frac{1}{C_c} - \left(\frac{A_2}{A_1}\right) \quad (14)$$

If the area downstream of the combustor was more significant than the upstream, then  $A_1$  in the above equations would be replaced by  $A_3$ , which is the most usual configuration in furnace burners.

A significant influence exists between the upstream pipe area  $A_1$  and the orifice area  $A_2$ , given that  $A_2/A_1$  corresponds to  $C_c$ . This has been shown by ideal fluid flow theory for the given values in Table 2-2. The most quoted value in most dynamic textbooks for an orifice with a differential area in a large downstream pipe is  $C_c = 0.611$ . This value was first computed by Kirchhoff [173]. The rest of the calculations were extended by Von Mises, considering the upstream pipe size and the dependence of  $C_c$  on  $A_2/A_1$ . For burners with a pressure loss of 2-4% and a Mach number  $M_1 = 0.047$ , the range of  $A_2/A_1$  is from about 0.26 to 0.18. Table 2-2 shows a  $C_c$  of about 0.65 with a  $C_D$  from Equation (14) for  $A_2/A_1$  of 0.26 of 0.782.

$A_2/A_1$	0	0.04	0.09	0.16	0.25	0.36	0.49	0.64
$C_c$	0.611	0.616	0.622	0.631	0.644	0.662	0.687	0.722

**Table 2-2.** Influence of  $A_2/A_1$  on the contraction coefficient  $C_c$  [173] for a sharp-edged orifice.

Most data on orifice plate pressure loss is available for a very thin plate with a sharp-edged. Hence there is an important impact of the hole thickness to hole diameter ratio on  $C_D$ . Ward-Smith [164] has correlated in Equation (15) data in the literature for orifice plate pressure loss factor  $K$  as a function of  $t/d$ .

$$K = \left[ \frac{1}{0.608\beta(1 - \beta^{2.6}) \left(1 + \left(\frac{t}{d}\right)^{3.5}\right) + \beta^{3.6}} - 1 \right]^2 \quad (15)$$

$C_c$  is also a function of  $t/d$ . As mentioned before, Phylaktou and Andrews [153] showed that an energy balance between the pressure loss and the turbulent kinetic energy for sharp-edged grid plates and experimental data for turbulent kinetic energy in the literature allowed to obtain Equation (16) for the turbulent mean fluctuating velocity,  $u'$ :

$$\frac{u'}{U_1} = \frac{0.225}{C_D} \left(\frac{A_2}{A_1}\right) = u' \frac{(\gamma RT)^{0.5}}{M_1} \quad (16)$$

Equation (16) illustrates the effect of the discharge coefficient and the upstream  $K$  factor in the produced turbulence downstream of the grid plate.

The reference Mach number,  $M_1$ , is related to the heat release (MW) per cross-sectional area,  $A_1$ , per bar by [87]:

$$\frac{MW}{PA_1} = \left( \left(\frac{\emptyset}{S}\right) M_1 CV \left(\frac{\gamma}{RT}\right)^{0.5} \right) \frac{MW}{bar \ m^2} \quad (17)$$

where  $S$  corresponds to the stoichiometric A/F by mass

$CV$  represents the calorific value of the fuel, MJ/kg<sub>fuel</sub>

Showing that the heat release is directly proportional to  $M_1$ .

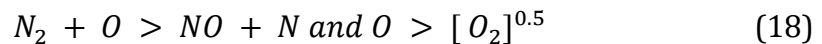
10 MW/(m<sup>2</sup>bar) corresponds to  $M_1=0.025$  if  $CV=50$  MJ/kg and the flame temperature is 1800K ( $\emptyset=0.5$  if  $T=700K$ ).

All these equations are also valid for calculating fuel injections for burner design.

### 2.2.11 Pressure dependence of NO<sub>x</sub>

There are some main independent characteristics for any combustion chamber design to consider. Some are residence time in the combustion chamber, mean air velocity and pressure loss. The residence time, as explained, is a direct function of the total length of the combustor and the reference velocity. The pressure loss is a function of the reference velocity and the inlet temperature.

Gas turbine combustors operate at high pressure, usually at 20 bar in power generation industrial gas turbines and approximately 60 bar in aero gas turbines [174]. Moreover, spark ignition and diesel engines operate up to 100 bar in the combustion zone. Pressure influences thermal NO<sub>x</sub> creation close to the stoichiometric region, and experiments [174] show that its kinetics have a square root P<sup>0.5</sup> dependence on pressure at the same peak flame temperature. This is because of the O<sub>2</sub><sup>0.5</sup> term in thermal NO<sub>x</sub> overall rate of formation as shown in Equation (18) :



The peak temperature is enhanced with pressure because products tend to dissociate at high pressure. Therefore, to eliminate thermal NO<sub>x</sub>, the pressure dependence of NO<sub>x</sub> must be eliminated. This is done by mixing air and fuel well and a primary zone temperature less or equal to 1950K. Generally, the reason to work low NO<sub>x</sub> burners at high pressure is because of NO<sub>x</sub> dependence on pressure. Nevertheless, this is very expensive, and there are some doubts regarding the impact high pressure has upon lower NO<sub>x</sub> emissions. The approach that many industrial turbines manufacturers use is that if at 1 bar of pressure, a flame stabilizer design doesn't give low NO<sub>x</sub> values, this will not give them at higher pressures. Hence, the combustor work can be done at atmospheric pressure. However, combustion efficiency may be poor in low NO<sub>x</sub> combustion tests carried out at atmospheric pressure, mainly using liquid fuels [62].

### **2.2.12 Ultra-low NO<sub>x</sub> levels by working at the lean flammability limit**

One of the main considerations for achieving low NO<sub>x</sub> levels in gas turbine combustion is to operate at lean levels, preferably at equivalence ratios below 0.6 [95].

The zone where the flow velocity is higher than the turbulent burning velocity is where the weak extinction occurs. Knowing this is useful for measuring the mean turbulent burning velocity and comparing it with experimental results. It is uncommon for low NO<sub>x</sub> combustion systems manufacturers to publish weak extinction data. However, the flame chemistry creating the weak extinction is responsible for achieving low NO<sub>x</sub> levels without creating acoustic problems, which is a big problem in almost all well mixed low NO<sub>x</sub> gas turbine combustors. These problems can often occur at an equivalence ratio of 0.65 approximately. Therefore, the laminar flame lean flammability limit has to establish the ultimate condition for weak extinction in premixed flames. It is

called the critical flame temperature to temperature of an adiabatic flame of the lean flammability limit. In the work of Andrews [99] the Gaseq flame equilibria code was considered at an initial temperature of 293K and 1 bar of pressure. Table 2-3 illustrates some calculated lean flammability limits considering methane and propane at different temperatures.

**Table 2-3.** Influence of inlet temperature on lean flammability for various critical flame temperatures for methane and propane [99]

Inlet temp (K)	1400K	1450K	1500K	1550K	1600K
<b>Methane</b>					
300	0.48	0.5	0.52	0.55	0.58
400	0.43	0.45	0.48	0.5	0.53
500	0.39	0.41	0.43	0.45	0.48
600	0.35	0.37	0.39	0.41	0.44
700	0.32	0.34	0.36	0.38	0.4
800	0.27	0.3	0.32	0.33	0.35
900	0.21	0.23	0.26	0.29	0.32
1000	0.17	0.19	0.21	0.24	0.28
<b>Propane</b>					
300	0.44	0.46	0.49	0.51	0.54
400	0.4	0.42	0.45	0.48	0.51
500	0.36	0.38	0.41	0.44	0.47
600	0.32	0.34	0.37	0.39	0.42
700	0.28	0.3	0.33	0.35	0.38
800	0.24	0.26	0.29	0.31	0.34
900	0.2	0.22	0.24	0.26	0.29
1000	0.17	0.19	0.21	0.23	0.25

Figure 2-26 shows the design of a multi-tube premixed pilot and how the diffusion pilot can be replaced, allowing this to reduce the relationship between NO<sub>x</sub> and lean stability.

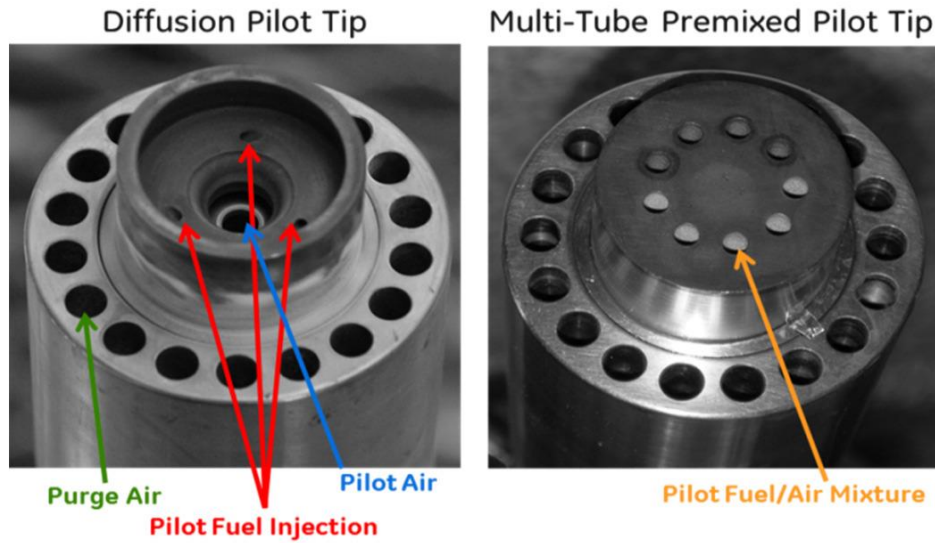


**Figure 2-26.** Photographs of a diffusion pilot tip and the multi-tube [27]

### 2.3 Computational Fluid Dynamics for turbulent combustion

The main intention of CFD is to understand the physical behaviour of fluids interacting with different objects. This behaviour is created through the effect of some phenomena such as turbulence, slip surfaces, dissipation, diffusion, convection, boundary layers and shock waves. Navier-Stokes equations govern these phenomena in the fields of aerodynamics. However, some of the fundamental characteristics of these relations are nonlinear, so there is usually no analytic solution for them [175].

Numerical methods have been used for more than 40 years to solve a variety of different problems in some disciplines of engineering using computational techniques to solve technical and scientific issues. However, up to date, no universal turbulence model clearly explains the concept of the turbulence flame available online and in the literature.

The finite volume method is a numerical method to discretize partial differential equations for mass, momentum (movement) and heat transfer (called transfer phenomena) equations by considering the conservation laws of energy, mass and momentum. This is the foundation of most commercial software to solve differential conservation equations. In the scientific community, it has been called Computational Fluid Dynamics to solve numerically the equations that describe the movement of fluid by using computers [176].

### 2.3.1 Turbulence modelling for 3D incompressible steady flows

The concept of turbulence is not fully understood and is considered the least resolved problem in physics [177]. Turbulence models have been created to help solve this problem. However, these models have advantages and disadvantages, so the user has to choose the one that better adapts their problem and discretises between computational time and accuracy level. As mentioned before, these models have been developed based on the Navier-Stokes equations to an extent. However, they also introduce hypothetical arguments that require empirical input [177]

#### 2.3.1.1 Reynolds Number

Turbulence can be determined by the Reynolds number, which is the relation of inertia forces that influence a fluid element against viscous forces and can predict whether the fluid is laminar or turbulent by Equation 19:

$$Re = \frac{UD\rho}{\eta} = \frac{UD}{\nu} \quad (19)$$

Where, U is the flow velocity, D is the section diameter or the characteristic length L,  $\rho$  is the density,  $\eta$  is the dynamic viscosity, and  $\nu$  is the kinematic viscosity. For practical pipe flow purposes, the flow is laminar if Re is less than 2000, and if Re is more than 4000, the flow will be turbulent. For those cases where Re is between 2000 and 4000, it is impossible to determine the fluid, so this zone is called the critical region[178]. Figure 2-27 shows the transition from laminar to turbulent flow and the formation of eddies [179].

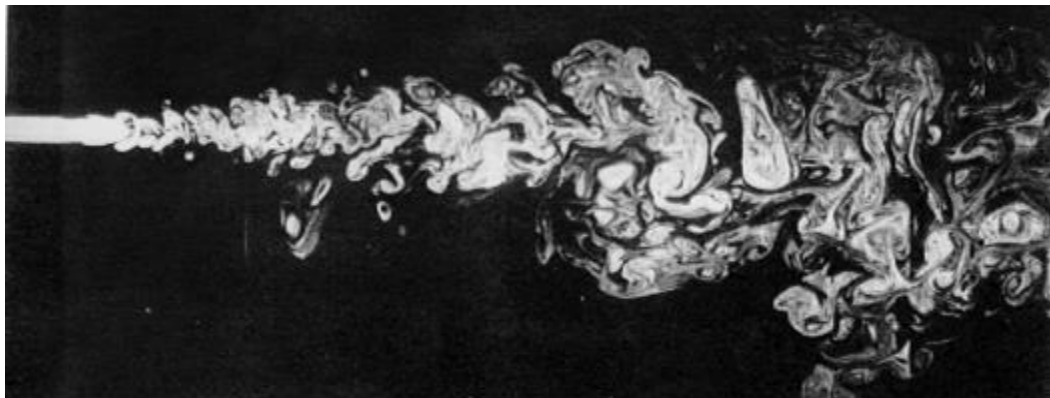


**Figure 2-27.** Free shear flow showing laminar, transition and turbulent phases [179].

### 2.3.2 Transport phenomena.

Three main topics are included in transport phenomena: fluid dynamics, heat transfer, and mass transfer. The first one deals with the transport of momentum. Heat transfer involves energy transport, and mass transfer is focused on chemical species [180]. The fluid is considered as continuum, and for the analysis of fluid flows at macroscopic length scales (usually larger than 1  $\mu\text{m}$ ) the molecular structure of the matter and molecular changes in space can be disregarded [181].

#### 2.3.2.1 Mass conservation

The equations of mass conservation (continuity equation) and momentum conservation describe the problems of relevance to the viscous flow of an isothermal flow. These equations are commonly called equations of change since they describe the change of temperature, velocity or concentration with respect to time and position within the region  $W$ .

In the Eulerian frame, the mass conservation theory must be made for a general region that is steady in space by considering the mass fluctuations in this region and the mass exchange between inside and outside of it. The conservation of mass demands that for any region  $W$ , which is fixed and within the material movement region, there must be a balance between the mass exchange rate contained in this region and the mass exchange rate through the boundary of itself [180].

Mass exchange rate contained in the  $W$  region                      =                      Mass exchange rate between the inside and outside  $W$

Then, in the Eulerian frame for any Newtonian and non-Newtonian fluids, steady or non-steady, compressible and incompressible, and one and three dimensional flows the equation of continuity on vector notation is [180]:

$$\frac{\partial \rho}{\partial t} = -\nabla \cdot (\rho \vec{v}) \quad (20)$$

The physical interpretation for both terms involving Equation (20) states that the first element  $(\partial \rho / \partial t)$  represents the rate of change of the contained mass into a very small volume element fixed  $\partial V$ , per volume unit. On the other hand, the second term  $-\nabla \cdot (\rho \vec{v})$  is the net rate of mass efflux (or divergence), by time and volume units. The continuity equation states simply that the rate of

increase of density within a differential volume element fixed in space is equal to the net rate of mass influx to the element divided by its volume.

For an incompressible flow (steady or unsteady) the density is not function of space or time , so it can be disregarded as follows

$$\frac{\partial \rho}{\partial t} = 0 \quad (21)$$

$$\nabla \cdot \vec{v} = 0 \quad (22)$$

However, the assumption of incompressibility does not impact the time dependence of the velocity.

### 2.3.2.2 Momentum conservation.

Newton's Second law of motion states the momentum principle for a collection of particles which establishes that the time rate of change of the total momentum of a given set of particles is equal to the vector sum of all the external forces that are acting on each particle of the group [182]. The law of conservation of momentum is written below.

Rate of Momentum Accumulation	=	Rate of Momentum In	-	Rate of Momentum Out	+	Sum of Forces Acting on the Control Volume
-------------------------------------	---	---------------------------	---	----------------------------	---	---

The general for of the momentum equation is given by:

$$\rho \left( \frac{D\vec{v}}{Dt} \right) = -\nabla P - [\nabla \cdot \vec{\tau}] + \rho \vec{g} \quad (23)$$

Where the first term is the mass per unit volume times the acceleration. The second term are pressure forces on element per unit volume. The third term are the viscous forces on element per unit volume. The fourth term are the gravitational forces on element per unit volume. Equation (23) is valid for any continuous medium, compressible or incompressible, steady or time-dependant, Newtonian or non-Newtonian.

Expressed in this form the equation of motion states that a differential element in movement with the fluid is accelerated due to the forces acted upon it. Or Newton's second law of motion.

$$\sum forces = mass \times acceleration$$

The momentum equation in three components including the Reynolds stresses are given in Appendix A.1

For incompressible flow the general vector form for three component is

$$\rho \left( \frac{D\vec{v}}{Dt} \right) = -\nabla P + [\mu \nabla^2 \vec{v}] + \rho \vec{g} \quad (24)$$

Which is the Navier Stokes equation first developed in France in 1822 and applies to Newtonian and non-Newtonian fluids, with constant density and viscosity.

### 2.3.2.3 Conservation of Energy.

It is usual that during combustion problems such as furnaces, power plants etc., fluid flows involve heat transfer, so to study them, it is necessary to obtain information about velocity and temperature distribution. The law of conservation of energy is derived from the first law of thermodynamics applied to a control volume. This can be seen as:

$$\begin{aligned} \text{Rate of} & & = & & \text{Total rate of heat added} & + & \text{Total rate of work made} \\ \text{increase of} & & & & \text{to fluid particles} & & \text{on fluid particles} \\ \text{energy of fluid} & & & & & & \\ \text{particle} & & & & & & \end{aligned}$$

Sometimes it is common to describe the energy of a fluid as the sum of internal, or thermal, energy  $i$ , kinetic energy  $\frac{1}{2}(u^2 + v^2 + w^2)$  and gravitational potential energy. The energy conservation of the fluid particle is described by equating the rate of change of energy of the fluid particle to the sum of the net rate of work done on the fluid particle, the net rate of heat added to the fluid and the rate of increase of energy due to sources.

So that the energy equation can be expressed as [183]:

$$\frac{\partial}{\partial t}(\rho U) = -[\nabla \cdot \rho \vec{v} U] - \nabla \cdot q - [\nabla \cdot \vec{v} P] - [\nabla \cdot (\tau \cdot \vec{v})] \quad (25)$$

Where U is the internal energy per unit mass of the fluid. The first term in Equation (25) is the rate of gain of energy. The second term is the rate of energy gain by convection by unit volume. The third term is the rate of energy gain by conduction by unit volume. The fourth term is the rate of work done on fluid by pressure forces by unit volume. The fifth term is the rate of work done on the fluid by viscous forces by unit volume.

For incompressible flow where  $i=cT$ , where  $c$  represents the specific heat and  $\nabla \cdot \vec{v}=0$ , the energy equation can be expressed in temperature terms as:

$$\rho c \frac{DT}{Dt} = \nabla(k \Delta T) + \tau_{xx} \frac{\partial u}{\partial x} + \tau_{yx} \frac{\partial u}{\partial y} + \tau_{zx} \frac{\partial u}{\partial z} + \tau_{xy} \frac{\partial v}{\partial x} + \tau_{yy} \frac{\partial v}{\partial y} + \tau_{zy} \frac{\partial v}{\partial z} + \tau_{xz} \frac{\partial w}{\partial x} + \tau_{yz} \frac{\partial w}{\partial y} + \tau_{zz} \frac{\partial w}{\partial z} + S_i \quad (26)$$

Where  $S_i$  is the internal energy expressed as  $S_i = S_E - u \cdot S_M$ . More detail can be found in Versteeg and Malalasekera [181].

#### 2.3.2.4 Chemical Species Conservation equation.

Mass transport consists of moving a chemical species from a place where concentration is very high to another where the amount is low. This occurs in a lot of chemical reactors such as combustion, distillation, gasification etc. And this can occur in two ways.

- Molecular diffusion. A random movement of single molecules in a fluid from a high concentration region to another. A molecule A follows a path to get to molecule B by diffusing through other molecules. This is modelled by the Fick's law of diffusion

$$N_{Ax} = -D_{AB} \frac{dc_A}{dx} \quad (27)$$

Where  $N_{Ax}$  is the molar rate of diffusion of constituent A per unit area,  $c_A$  is the molar concentration of constituent A, and  $D_{AB}$  is the binary diffusivity or diffusion coefficient.

On a mass basis, Equation(27) becomes [180]

$$J_{Ax} = -D_{AB} \frac{d\rho_A}{dx} \quad (28)$$

Where  $J_{Ax}$  is the mass rate of diffusion of constituent A per unit area, and  $\rho_A$  is the mass concentration of constituent A.

- Convective transport. As well as molecular diffusion transportation, mass is transported by the fluid's bulk motion. The rate at which the mass of species A is swept across a perpendicular plane of  $dA$  is

$$\rho_A v_x dA$$

Where  $v_x$  is the total mass velocity of the entire fluid.

The equation of transport of chemical species can be derived using the law of mass conservation applied to a control volume which is fixed in space

			Rate of
Rate of Mass	=	Rate of Mass A	- Rate of Mass
Accumulation		In	A Out
			+ Rate of Production of Mass A by

## Homogeneous Reaction

The species conservation equation for constant density  $\rho$  and diffusivity  $D_{AB}$  is

$$\left( \frac{\partial \rho_A}{\partial t} + v_x \frac{\partial \rho_A}{\partial x} + v_y \frac{\partial \rho_A}{\partial y} + v_z \frac{\partial \rho_A}{\partial z} \right) = D_{AB} \left[ \frac{\partial^2 \rho_A}{\partial x^2} + \frac{\partial^2 \rho_A}{\partial y^2} + \frac{\partial^2 \rho_A}{\partial z^2} \right] + r_A \quad (29)$$

Where  $r_A$  is the rate of reaction expressed in (kg A /s m<sup>3</sup>) and  $D_{ab}$  represents the components of the mass flux  $J_{AX}$  in terms of the Fick's law.

### 2.3.3 Turbulence Models

Different methods have been developed to predict turbulence. Some of them achieve perfect accuracies like Large Eddy Simulation (LES) or Direct Numerical Simulation (DNS) but require lots of computational time or the use of High-Performance Computers (HPC). These methods are usually recommended for transient-state cases or when the solution is time-dependent. Reynolds Averaged Navier Stokes (RANS) simulation has been used for decades for both steady-state and transient states giving very good accuracy without compromising the computational time. However, special attention is needed when selecting the computational models to get the best accuracy.

#### 2.3.3.1 Reynolds Average Navier Stokes (RANS) for incompressible flow

The RANS method focuses on the mean flow and turbulence effects over the flow's properties. Before applying a numerical method, the Navier Stokes equations have to be time-averaged for a steady-state. In Reynolds averaged equations, it is possible to see other terms involved with interactions with some turbulent fluctuations. These terms can be modelled with some common turbulence models, such as the  $k-\epsilon$  model [183] described in the following lines.

This method presented by Reynolds in 1895 is based on the breakdown of the flow variables <sup>2</sup>into the mean and fluctuating components, then, the complete equation gets time-averaged [184]. There are two averaging methods: Reynolds averaging and the mass-weighted averaging proposed by Favre in 1965. When there are no flow density fluctuations, the two methods are the same [185].

---

<sup>2</sup> The tensor of the viscous stresses is extended by the Reynolds-stress tensor, and the diffusive heat flux  $k\nabla T$  in the energy equation gets upgraded by the turbulent heat flux vector as explained by Blazek [184, p. 3]

The Navier Stokes equations have been already presented. And the scalar transport equation is shown in Appendix A.1

A turbulent model has to be chosen to calculate turbulent flows using the RANS equations. The most widely known RANS turbulence models are classified according to the number of equations they need to be solved [183].

### Two-equation models.

There are many turbulence models with two equations. However, all of them solve a transport equation for a turbulent velocity scale and a turbulent length scale or for the properties of these variables.

Mixing length models such as the Prandtl's model, attempt to describe the turbulence or Reynolds stresses using algebraic formulation for turbulent viscosity  $\mu_t$  in terms of the location in space. Since turbulence depends on the flow, if the turbulence gets altered it is needed to account for this within the mixing length model by modifying the length scale. The  $k-\epsilon$  on the other hand needs to solve two PDEs. The assumption for both models is that  $\mu_t$  is isotropic, which means that the ratio between the Reynolds stresses and the mean rate of deformation is identical in all directions. This hypothesis can be wrong for complex flows where the simulation can be inaccurate, so it is needed to solve additional PDEs for the actual Reynolds stresses [181].

### The $k-\epsilon$ model

The  $k-\epsilon$  model is an example of a two-equation turbulence model. It works with one transport equation that controls turbulence velocity scale ( $k$ ), and another conservation equation is related that involves a quantity which can be related to a turbulence length scale ( $\epsilon$ ) [186], [187].

The conservation equation of this model is expressed as follows.

$$\frac{\partial}{\partial t}(\rho\Phi) + \left( \frac{\partial}{\partial t}(\rho\Phi\bar{v}_x) + \frac{\partial}{\partial t}(\rho\Phi\bar{v}_y) + \frac{\partial}{\partial t}(\rho\Phi\bar{v}_z) \right) = \left[ \frac{\partial}{\partial x} \left( \frac{\mu_t}{\sigma_\Phi} \frac{\partial \Phi}{\partial x} \right) + \frac{\partial}{\partial y} \left( \frac{\mu_t}{\sigma_\Phi} \frac{\partial \Phi}{\partial y} \right) + \frac{\partial}{\partial z} \left( \frac{\mu_t}{\sigma_\Phi} \frac{\partial \Phi}{\partial z} \right) \right] + S_\Phi \quad (30)$$

Rate of change of $k$ or $\epsilon$	Transport of $k$ or $\epsilon$ by convection	Transport of $k$ or $\epsilon$ by diffusion	Source term
-------------------------------------	--	---	-------------

Where the Eddy viscosity is

$$\mu_t = \rho C_\mu \frac{k^2}{\varepsilon}$$

$C_\mu$  is the dimensionless constant, which is generally used in this model. It is called the Prandtl-Kolmogorov relationship.

$\Phi = k$  or  $\varepsilon$

$S_\Phi$  = source term of generation or elimination for  $k$  or  $\varepsilon$

This turbulence model has been the most used and validated turbulence model for more than 30 years. There have been plenty of applications in numerous fields. Some examples of these applications are: jets in stagnant surroundings and moving streams, wall jets, free and confined jets with swirl, jets in a crossflow shown in Figure 2-28, flow over surface-mounted obstacles and around objects, flows in straight pipes and ducts, and flows in sudden expansion and contraction geometries.

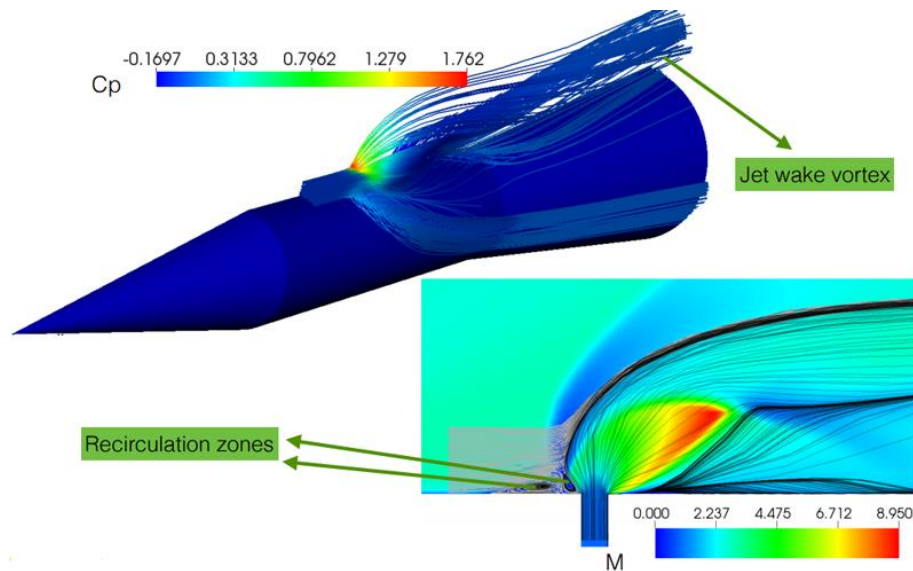


**Figure 2-28.**  $k$ - $\varepsilon$  modelling a Jet in a crossflow [188].

In addition to isothermal flows, it has been widely used to compute flows involving chemical reactions and combustion and flows that experience heat transfer.

### **Realisable $k$ - $\varepsilon$ model**

Some drawbacks have been encountered with the  $k$ - $\varepsilon$  model, such as stiffness on the numerical problem when predicting flow behaviour near the walls or working at high Reynolds numbers. To solve this problem without moving out the  $\varepsilon$  equations, some realizability constraints can be imposed on the model [189].

The realisable  $k$ - $\varepsilon$  model has been widely used over the last 20 years, given its improved performance over the standard  $k$ - $\varepsilon$  when predicting flows involving boundary layers, flow separation and recirculation zones at high velocities[190]. This model has also been reported to improve the prediction of spreading rates of round jets [191]. This is a two-equations high Reynolds number model which differs from the standard  $k$ - $\varepsilon$  in two features. First, the dissipation rate transport equation formulation is obtained from the mean-square vorticity fluctuations. And the use of the realisability constraint for the Reynolds stresses for the formulation of the eddy-viscosity [192]. In practice it means that the viscosity coefficient  $C_\mu$  is a function of local flow parameters, rather than a constant.

The model is defined by the following equations [192].

$$\frac{\partial}{\partial t}(\rho k) + \nabla \cdot (\rho u k) = \nabla \cdot \left( \rho \left\{ \frac{v_l + v_t}{\sigma_{t,k}} \right\} \nabla k \right) + \rho (P_k - \varepsilon) \quad (31)$$

$$\frac{\partial}{\partial t}(\rho \varepsilon) + \nabla \cdot (\rho u \varepsilon) = \nabla \cdot \left( \rho \left\{ \frac{v_l + v_t}{\sigma_{t,\varepsilon}} \right\} \nabla \varepsilon \right) + \rho \left( \frac{C_{1\varepsilon} S \varepsilon - C_{2\varepsilon} \varepsilon^2}{\{k + \sqrt{v_l \varepsilon}\}} \right) \quad (32)$$

$$v_t = \frac{C_\mu k^2}{\varepsilon} \quad (33)$$

$$P_k = v_t S^2 \quad (34)$$

$$S = \sqrt{2S_{ij}S_{ij}} \quad (35)$$

$$S_{ij} = 0.5 \left( \frac{\partial u_i}{\partial x_j} + \frac{\partial u_j}{\partial x_i} \right) \quad (36)$$

The model coefficients for  $C_{1\varepsilon}$  and  $C_\mu$  are computed from the equations shown in Appendix A-2. The empirical constants are defined by:

$$\sigma_{t,k}=1.0, \sigma_{t,\varepsilon}=1.2, A_0=4.04, C_{2\varepsilon}=1.9.$$

### The SST $k$ - $\omega$ model

The simple  $k$ - $\omega$  turbulent model [193] is an empirical model whose objective is to model continuity (transport) equations for turbulent kinetic energy  $k$  and the specific dissipation rate  $\omega$ , which is the same as the ratio of  $\varepsilon$  to  $k$ . This model has been modified over time, and some terms have been added to both equations, which has improved the model's accuracy in predicting free shear flows [194]. The most important characteristic of this model is that it can be applied to the boundary layer without modifying the equations[183].

Once described the advantages and applications of this turbulent model, the transport equation for the turbulent kinetic energy  $k$  and the specific dissipation rate  $\omega$  can be expressed as follows.

$$\frac{\partial}{\partial t}(\rho\Phi) + \frac{\partial}{\partial x_i}(\rho\Phi u_i) = \frac{\partial}{\partial x_j} \left( \Gamma_\Phi \frac{\partial \Phi}{\partial x_j} \right) + G_\Phi - Y_\Phi + S_\Phi \quad (37)$$

Where  $\Phi$  represents whether  $k$  as  $\omega$ .  $G_\Phi$  is the generation of  $\Phi$  due to mean velocity gradients.  $\Gamma_\Phi$  is the effective diffusivity of  $\Phi$  and  $Y_\Phi$  represents the dissipation of  $\Phi$  due to turbulence.  $S_\Phi$  represents the source terms for  $k$  or  $\omega$ .

The Shear-Stress Transport (SST)  $k$ - $\omega$  turbulence model [195] is one of the various models available for  $k$ - $\omega$ .

SST moves to  $k$ - $\epsilon$  behaviour in free-stream, avoiding the problem of  $k$ - $\omega$  of being too sensitive to inlet freestream turbulence. Additionally, it works for the continuity of the turbulence shear stress in turbulent viscosity. The mentioned features make this model more reliable when predicting adverse pressure gradient flows, behaviour in airfoils, and transonic shock waves than the other  $k$ - $\omega$  models [196]. SST has also been proved to model flow separation better than any other RANS turbulence model [197], [198]. This turbulence model has been used to study perforated plates in the work of Guo et al. [197], as shown in Figure 2-29.

The equations for the SST  $k$ - $\omega$  models are

For the turbulence kinetic energy.

$$\frac{\partial k}{\partial t} + U_j \frac{\partial k}{\partial x_j} = P_k - \beta k \omega + \frac{\partial}{\partial x_j} \left[ (v + \sigma_k \nu_T) \frac{\partial k}{\partial x_j} \right] \quad (38)$$

For the specific dissipation rate

$$\begin{aligned} \frac{\partial \omega}{\partial t} + U_j \frac{\partial \omega}{\partial x_j} = & \alpha S^2 - \beta \omega^2 + \frac{\partial}{\partial x_j} \left[ (v + \sigma_\omega \nu_T) \frac{\partial \omega}{\partial x_j} \right] \\ & + 2(1 - F_1) \sigma_{\omega 2} \frac{1}{\omega} \frac{\partial k}{\partial x_i} \frac{\partial \omega}{\partial x_i} \end{aligned} \quad (39)$$

The blending Functions  $F_1$   $F_2$  , the kinetic eddy viscosity and other can be obtained as shown in Appendix A-3.

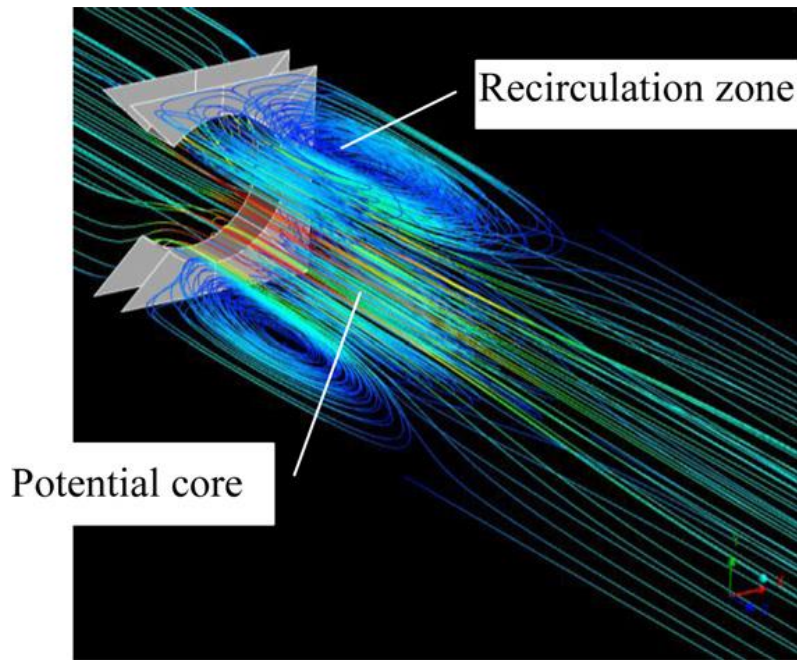


**Figure 2-29.** Gas flow streamlines in a grid plate using  $k-\omega$  SST [197].

The main drawback of this model is the missprediction of the conservation of the turbulent shear stress, and because of it there is an over prediction of the eddy-viscosity. Then, in order to obtain an accurate solution the equation of the eddy-viscosity is [199]

### **2.3.4 Mesh generation.**

In order to solve any CFD code, the domain is first divided into small control volumes, called cells or elements. It is usual to establish cells close to the edge of the domain so that the physical boundaries are the same that the control volume boundaries.

Meshes can be structured or unstructured like the ones observed in Figure 2-30A and B. The first CFD codes solved the governing equations using structured meshes, commonly used for geometries with regular domains. Structured body-fitted meshes need a blocking design that allows the structured hexahedral elements to fit inside the domain following the grid lines. However, blocking complicated irregular shapes can be very time consuming as the user needs to pay special attention to the mesh quality as well. This is why structured meshes are not suitable for irregular geometries. Unstructured meshes are commonly used for complex geometries featuring irregular shapes. The main feature of these meshes is that they don't need an implicit structure of the grid lines (or blocking). The control cells can have any shape to fit the domain. When choosing the number of cells used for the simulation, special attention is required to approach the cells to the desired cell geometrical shape.

This means that a coarse mesh features elements with irregular shapes, while a fine mesh with a large number of cells shows less skewed elements.

Structured meshes are made of hexahedrons where the elongation of the element represents the skewness as shown in Figure 2-30A and C , while unstructured meshes can feature cells with different polyhedric shapes as show in Figure 2-30B and D .

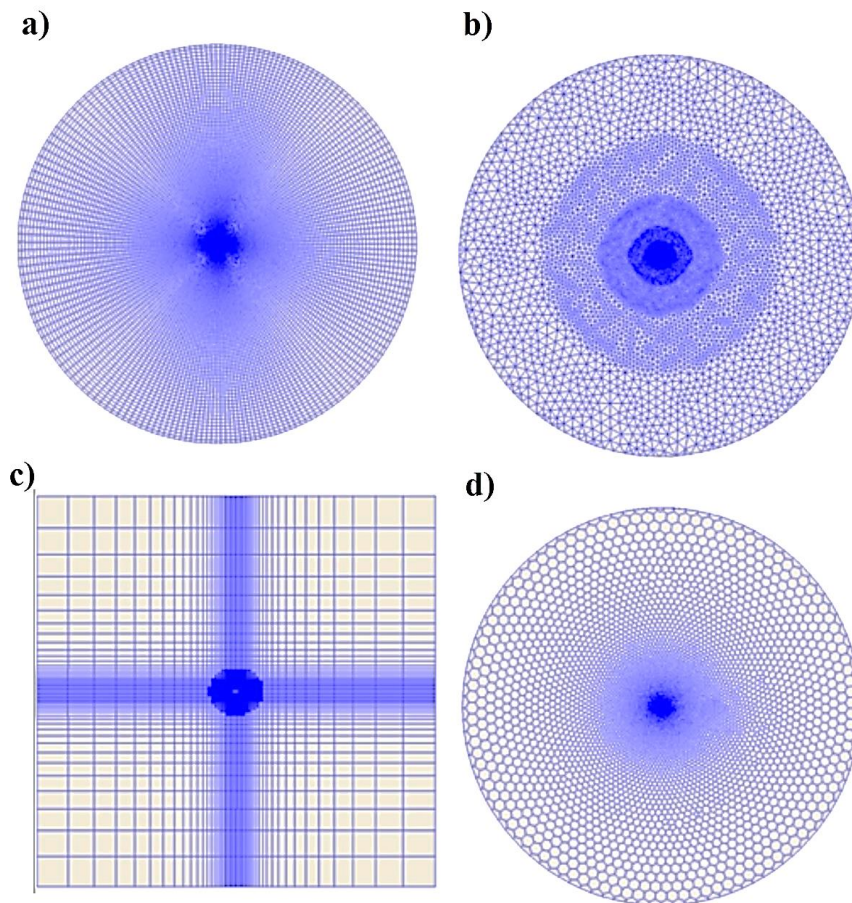


**Figure 2-30.** Different mesh types used. a) Structured with Ogrid. b) Unstructured. c) Hexahedral. d) Polyhedral

### 2.3.5 Discretisation.

The next step is the integration of the governing equations in the control volume so that every equation is discretised on every node/cell. CFD code show different discretization options.

The Semi Implicit Method for Pressure Linked Equations (SIMPLE) scheme developed by Patankar and Spalding [200] calculates the pressure basically in a guess-and-correct method [183]. If the problem is steady state and its being solved iteratively, the pressure-velocity coupling do not have to be solved. This

method solves the momentum equations to approximate the velocity field. The pressure gradient term is calculated using the pressure distribution from previous iteration by an initial approximation [181]. Then, the pressure equation is created and solved to obtain a new pressure distribution. Finally the velocity is corrected and a new flux set is calculated [201].

Momentum and corrected pressure equations are solved implicitly, while the velocity correction is solved explicitly. Hence, the name Semi-Implicit Method.

The pressure-based coupled algorithm solves the momentum and pressure-based equations together, while the segregated algorithm solves them separately. As a result, a coupled calculation allows a faster convergence than a segregated one. However, the solver is more unstable.

### **2.3.6 Solution of equations.**

The discretised equations have to be established for every node of the grid to solve the problem. In the particular case of the control volumes that are close to the domain boundaries, the general discretised equation is set up to include boundary conditions. It is then obtained a solution for the algebraic system of equations to obtain the desired property  $\Phi$  for every node. The solution of equations by using matrices is reviewed in the work of Versteeg, and Malalasekera [183].

### **2.3.7 Turbulent combustion**

Even though combustion can be found in a laminar flow field, for most industrial and technical processes it typically occurs in a turbulent flow field. This is because turbulence aids in the mixing process and consequently increases combustion. On the other hand, combustion also generates heat release, which creates gas expansion and buoyancy, bringing flow instability, allowing the transition to turbulence [177]. Combustion needs both oxidiser and fuel to be mixed at a molecular level and this depends on the turbulent mixing process. Once a set of eddies of different size has developed strain and shear between them increases the mixing.

The interaction of turbulence and combustion refutes classical scaling laws known from non reacting turbulent flows like the Reynolds number independence for free shear flows happening at the large Reynolds number limit [177]. Also, combustion involves various elementary chemical reactions occurring at diverse time scales.

Some concepts that need to be addressed related turbulent combustions are now shown.

### **Burning velocity**

Burning velocity is the speed at which a flame front propagated relative to unburnt gases. The laminar burning velocity ( $S_L$ ) corresponds to the velocity at which a laminar combustion wave propagates in relation to the unburnt gas in front of it. The turbulent burning velocity ( $S_t$ ) on the other hand surpass the laminar burning velocity to a degree depending on the scale ( $l$ ) and the turbulence intensity of the unburnt gas [202]

### **Flame speed**

The flame speeds is the measured rate of expansion of the flame front in a combustion reaction, or the speed at which a flame propagates relative to an observer [203].

Some important features must be known to correctly choose the techniques used for CFD combustion. These include the thermodynamics of combustion, the kinetics, the internal energy of formation, chemical transport processes, equilibrium in gases and adiabatic flames temperatures. Some of these subjects are too extensive to cover in this thesis. However detailed information on these processes can be found in the work of Versteeg and Malalasekera[183].

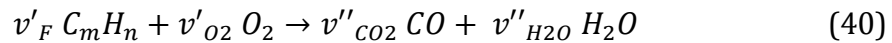
There are some requirements for turbulent burning velocity [62]:

- In order to work with ultra-low  $NO_x$ , the flame has to burn down to the lean flammability limit.
- The reference velocity in the burner after the expansion from the flame stabilizer is usually 25m/s, considering the high turbine entry temperature for low  $NO_x$  gas turbines.
- It is required that  $U_T / U_L$  (the turbulent burning velocity and the laminar burning velocity) equal to 250. However, it is better to consider the current turbulent burning velocity, where less than 25 m/s is required for a stable flame.
- Near the flammability limit where  $U_L$  is very low,  $U_T$  should be approximately  $2 u'$  (velocity of the kinetic energy of turbulent)
- It is possible to reach these conditions for flow blockages of at least 70% and a pressure drop of 2% because of the standard gas turbine burner operation.

The equations for the different premixed turbulence combustion regimes are given in Appendix A.4

### 2.3.7.1 Non premixed turbulent combustion

A crucial parameter in the description of non-premixed combustion is the mixture fraction  $Z$  which determined the flame surface. The definition of  $Z$  is as the homogenous system in the absence of diffusion. Then by writing the complete stoichiometric equation for hydrocarbons combustion  $C_mH_n$  [177]



The stoichiometric coefficients  $v'_F$  and  $v'_{O_2} = (m + n/4) v'_F$ , respectively.

In a two-feed system where subscript 1 is the fuel stream and subscript 2 is the comburent, it is possible to relate the mass fractions of fuel and oxygen to the mixture fraction as [177].

$$Z = \frac{vY_F - Y_{O_2} + Y_{O_2,2}}{vY_{F,1} + Y_{O_2,2}} \quad (41)$$

The stoichiometric mixture fraction is expressed as

$$Z_{st} = \left[ 1 + \frac{vY_{F,1}}{Y_{O_2,2}} \right]^{-1} \quad (42)$$

Then the equivalence ratio can be obtained as [204].

$$\phi = \frac{SZ}{1 - Z} \quad (43)$$

Where  $S = \frac{sY_{F,F}}{Y_{O,O}}$

$Y_{F,1}$  is the fuel mass fraction,  $Y_{O_2,0}$  is the oxidizer mass fraction

$s$  is the mass of oxygen required to burn a unit mass of fuel. For hydrogen  $s=8$

and for  $C_mH_n$  alkanes,  $s = \frac{32(m+\frac{n}{4})}{12m+n}$  [204]

The equations for the different non premixed turbulence combustion regimes are given in Appendix A.5

### 2.3.7.2 Governing equations for non-premixed combustion.

In non-premixed combustion processes like furnaces, jets of fuel and air are mixed by turbulence of the fluid so that the temperature of combustion and the concentration and distribution of species are almost completely controlled by the flow of fluid. For premixed combustion processes like spark ignition in

internal combustion engines, the turbulence, flow of fluid and turbulence are set by compression and induction processes before ignition, and they are very important in the combustion process. The governing equations for combustion can be considered as follows [181].

For continuity

$$\frac{\partial \rho}{\partial t} + \frac{\partial}{\partial x_i}(\rho u_i) = 0 \quad (44)$$

Where density in the combustion of flows depends on temperature, transport of species and pressure

For momentum

$$\frac{\partial}{\partial t}(\rho u_i) + \frac{\partial}{\partial x_i}(\rho u_i u_j) = -\frac{\partial p}{\partial x_i} + \frac{\partial \tau_{ij}}{\partial x_i} + F_i \quad (45)$$

Where  $F_i$  are the forces acting on the body, and the viscous stress tensor  $\tau_{ij}$  is

$$\tau_{ij} = \mu \left( \frac{\partial u_i}{\partial x_j} + \frac{\partial u_j}{\partial x_i} + \frac{2}{3} \delta_{ij} \frac{\partial u_k}{\partial x_k} \right)$$

For transport of species equation

$$\frac{\partial}{\partial t}(\rho Y_k) + \frac{\partial}{\partial x_i}(\rho u_i Y_k) = \frac{\partial}{\partial x_i} \left( \rho D_k \frac{\partial Y_k}{\partial x_i} \right) + \dot{\omega}_k \quad (46)$$

It can be expressed like follows

Rate of change of mass of species k	+	Total rate of decrease of mass of species k by convection	=	Total rate of increment of mass of species k by diffusion	+	Total rate of increment of mass of species k due to sources
-------------------------------------	---	---	---	---	---	---

The energy equation is

$$\frac{\partial}{\partial t}(\rho h) + \frac{\partial}{\partial x_i}(\rho u_i h) = \frac{\partial}{\partial x_i} \left[ \frac{\mu}{\sigma_h} \frac{\partial h}{\partial x_i} + \mu \left( \frac{1}{Sc_k} - \frac{1}{\sigma_h} \right) \sum_{k=1}^N h_k \frac{\partial Y_k}{\partial x_i} \right] + \frac{\partial p}{\partial t} + S_{rad} \quad (47)$$

Rate of change of mass internal energy	+	Total rate of decrease of internal energy by convection	=	Total rate of increment of internal energy by diffusion through gradients of	+	Total rate of increment of internal energy by pressure	+	Total rate of increment of internal energy by radiation
--	---	---	---	--	---	--	---	---

concentration of  
species

Where  $Sc_k$  is the species Schmidt number

$$Sc_k \equiv \mu / \rho D_k$$

And the Prandtl number  $\sigma_h$  is

$$\sigma_h = \frac{c_p \mu}{k}$$

This expresses the rate of conservation of momentum by the rate of conservation of energy

Only turbulent regimes is considered in this thesis, so laminar flows studied with CFD won't be described.

### 2.3.7.3 Combustion turbulent models for non-premixed combustion

Some combustion models have been developed due to the complexity of finding a solution for averaged species mass fraction and enthalpy equations, density and temperature changes, for realistic chemical cases, which involve many reactions and species .

#### Simple chemical reacting system model (SCRS)

This model refers to the global nature of the combustion process by considering only the final concentration of species. This process neglects its kinetics and considers combustion a one-step process with no intermediates [186]. A rapid chemical reaction of oxidants reacting stoichiometric is assumed to create products. This chemical reaction is irreversible for the Simple Chemical reacting system. For this model exists a linear relationships between species mass fractions and mixture fraction. This fact is the same for the relationship between temperature and enthalpy relationship. To calculate mean values of  $J_i$  and  $H$  we need to know the statistics of the variables  $(T, Y_i, \rho)$  as a function of  $\xi$ . [183].

#### Probability Density Function Approach (PDF)

This method involves two and three-dimensional time-dependent turbulent flows. It gives an alternative to model turbulence combustion that does not require as many assumptions as other more complex models (like the flamelet model, which will be described later), and it can be more accurate. The joint pdf

of either the scalar variables of composition that define the system's thermochemical state or the scalar compositions plus the three-velocity components are solved by this combustion method. Moreover, strongly nonlinear chemical reaction rates, pressure gradient, body forces and transport-convective problems are solved [205].

For a given variable  $\phi$ , the probability function  $F_\phi(\psi)$  is defined as [183].

$$F_\phi(\Psi) = Prob\{\phi < \Psi\} \quad (48)$$

Where  $Prob\{\phi < \Psi\}$  is the probability that  $\phi$  is smaller than the value for  $\Psi$ , and the probability density function is the derivation of the distribution function [183].

$$P_\phi(\Psi) = \frac{dF_\phi(\Psi)}{d\Psi} \quad (49)$$

### **Eddy break up, and Eddy dissipation models**

The Eddy break up model invented by Spalding (1971)[206] sets the fuel consumption rate as a function of the properties of the local fluid. The controlled mixing rate of reaction is expressed in the  $k/\varepsilon$  scale terms. This model can also adapt to reaction terms that are controlled by kinetic energy. Although the Eddy break up model achieves good predictions in CFD, the quality of the predictions relies on how well the turbulence model works because of the dependence of the fuel dissipation rate on the turbulence time scale of  $k/\varepsilon$ . If the turbulence model does not achieve good flow predictions, the combustion quality will also fail. The eddy dissipation model (EDM) was developed by Ertesvag and Magnussen in 2000 [207]. It is a modified version of the eddy break up model [183]. This model is very useful in turbulent flows when the chemical reaction rate is faster than the conservation processes of the fluid flow.

In EDM the reaction rate of fuel is defined as [208]

$$\dot{\omega}_F = -A_{edm} \bar{\rho} \beta * \omega \min \left[ \tilde{Y}_F, \frac{\tilde{Y}_O}{s}, B_{edm} \frac{\tilde{Y}_P}{s+1} \right] \quad (50)$$

Then the oxidiser and product reaction rates are calculated as:

$$\dot{\omega}_O = s \dot{\omega}_F, \quad \dot{\omega}_P = (s+1) \dot{\omega}_F \quad (51)$$

However, since the model's reaction process is not kinetically controlled, ignition and other processes involving a limit reaction by chemical kinetics can be inaccurately predicted [209]. Misprediction in combustion [210] and mixing

results [211] have been shown by various authors when studying non-premixed steady state combustion.

### Laminar flamelet model

Laminar flamelet models are considered for turbulent combustion with fast chemistry occurring in thin layers known as flamelets, incrustated in the turbulent flow [212].

This combustion model treats the turbulent flame like a crowd of stretched laminar flamelets. The turbulent flames are commonly referred to as laminar reaction sheets in movement. This model considers a great heat release in narrow zones of the surroundings of stoichiometric surfaces [183]. Some assumptions are made when studying a flamelet model. First, a two-mixture fraction flamelet model is not allowed, only one. Secondly, scalar dissipation changes and the mixture fraction following the  $\beta$ -function PDF are not considered. Lastly, empirical streams cannot be used [213]. This model has some advantages on the one hand, like the good connection between chemical reactions and molecular transport and the suitability to predict chemical non-equilibrium because of the flame aerodynamics by turbulence.

The flame structure is obtained by solving boundary layer equations developed along the stagnation streamline [214].

For non-premixed combustion them flame stretch increases the scalar dissipation rate in a turbulent flow field. If this exceed the value of  $\chi_q$  the flamelet will get consequently extinguished.

Returning to the two-feed non premixed system discussed in 2.3.8.1 , a formal asymptotic description of the flamelet structure for one-step reaction was developed retaining the time derivative term, and as a one dimensional time-dependent temperature equation [215], more detail of the model can be found in the work of Peters [216]:

$$\rho \frac{\partial T}{\partial t} - \rho \frac{\chi_{st}}{2} \frac{\partial^2 T}{\partial Z^2} = - \frac{1}{c_p} \sum_{i=1}^n h_i m_i \quad (52)$$

This model, on the other hand, has some drawbacks. For example, slow chemistry predictions such as NO<sub>x</sub> or soot are limitations for the Steady Flamelet [217]. Another disadvantage is the change of the scalar dissipation experience when transient effects occur in the turbulent flow because the flame geometry needs time to stabilize [218].

## Flamelet Generated Manifold

To reduce chemical calculations, the Intrinsic Low Dimensional Manifold (ILDM) developed by Mass and Pope considers the extensive range of chemical time scales [219], [220] from the elemental composition up to equilibrium. Then, reaction rates and species mass fractions are calculated as a function of a reduced set of variables, which measures the evolution of the reaction through a progress variable and the description of the mixture by using a mixture fraction [221]

This method is accurate when predicting high temperatures near-equilibrium but struggles to predict low-temperature zones. To solve this issue, the Flamelet Generated Manifold (FGM) was developed [222].

This concept consists of the generation of look-up tables simulating one-dimensional laminar premixed flames considering complex chemistry. Variations such as species mass fractions and reaction rates are obtained as functions of a simple set of coordinates as progress variables or mixture fractions [221].

Considering the governing transport equations of species mass transport and temperature of [223]

$$\rho \frac{\partial Y_i}{\partial t} = \frac{1}{2} \rho \chi \frac{\partial^2 Y_i}{\partial Z^2} + S_i \quad (53)$$

And

$$\rho \frac{\partial T}{\partial t} = \rho \frac{\chi_{st}}{2} \frac{\partial^2 T}{\partial Z^2} - \frac{1}{2c_p} \rho \chi \left[ \frac{\partial c_p}{\partial Z} + \sum_i c_{p,i} \frac{\partial Y_i}{\partial f} \right] \frac{\partial T}{\partial t} \quad (54)$$

The scalar dissipation  $\chi$  is then modelled across the flamelet using equation [223]

$$\chi(f) = \frac{a_s}{4\pi} \frac{\left( \sqrt{\frac{\rho_\infty}{\rho} + 1} \right)^2}{\left( \sqrt{\frac{\rho_\infty}{\rho} + 1} \right)} \exp(-2[ERZc^{-1}(ZZ)]^2) \quad (55)$$

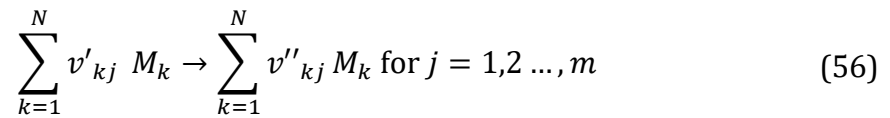
The flamelets are calculated by enhancing the scalar dissipation until it gets extinguished. Then the FGM is generated by mapping the scalar dissipation field to a progress variable. It maps the pre-tabulated chemistry to the mean mixture fraction, the mean reaction progress variable and respective variances, and the transport equation for mean enthalpy. [223]

FGM has been widely used in CFD for modelling premixed combustion and partially premixed combustion [224]–[228] and in recent years for diffusion combustion, including NO<sub>x</sub> prediction [220], [229], [230].

### 2.3.8 Reaction rates and mechanisms

In combusting flow simulation, the reactant consumption and product formation rate need to be resolved. These rates are the source terms in the transport equations for every individual species. As shown before, various equations are needed for solving combusting flows, and every species involved has a number of different reactions.

If considering a forward scheme of reactions with the stoichiometric Equation (56) [181]



Where  $v'_{kj}$  are the stoichiometric coefficients of the reactant species  $M_k$  in the reaction  $j$ .  $v''_{kj}$  are the stoichiometric coefficients in the product species in the reaction  $j$ .  $N$  is the number of species and  $m$  the number of reactions involved.

The reaction rate for Equation (56) is expressed as [231]

$$RR = \frac{d(C_{prod})}{dt} = k_f \prod_{k=1}^N (C_{M_k})^{v'_{kj}} \quad (57)$$

$k_f$  is the Arrhenius law given by

$$k_f = AT^a \exp\left(-\frac{E_a}{R_u T}\right) \quad (58)$$

Where  $A$  is the pre-exponential constant,  $a$  is the temperature exponent and  $E$  the activation energy.

The general form of the reaction progress rate for a species  $k$  in given reaction  $j$  is

$$\dot{q}_{k_f} = \frac{dC_{M_k}}{dt} \Big|_j = (v''_{kj} - v'_{kj}) \cdot \left[ k_f \prod_{k=1}^N (C_{M_k})^{v'_{kj}} - k_b \prod_{k=1}^N (C_{M_k})^{v''_{kj}} \right] \quad (59)$$

Where  $k_f$  is the forward reaction rate and  $k_b$  the backward reaction rate

Various pieces of software such as CHEMKIN [232] specialise in the development of reaction rate expressions and kinetic data.

Detailed mechanisms have been developed for a number of authors for the oxidation of various fuels and reaction rates.

The computer time for the evaluation of chemical kinetics and the equations for species transport is rather important, and it increases when the mechanisms become more complex. Hence efforts have been made to develop practical reaction schemes with

fewer reactions to represent the basis of the combustion. These are the reduced mechanisms.

### **2.3.9 NO<sub>x</sub> modelling using CFD**

Combustion systems usually produce low NO<sub>x</sub> concentrations, which have little effect on the flow behaviour, temperature and equilibrium products [233]. However, its accurate prediction is essential in the development of low-NO<sub>x</sub> systems.

An accurate NO<sub>x</sub> prediction is strongly related to the mixing and combustion simulation results. An inadequate air/fuel mixing prediction can considerably affect the NO<sub>x</sub> levels. Similarly, inaccurate temperature simulation can, in some cases, double the NO<sub>x</sub> levels [233]. Hence, critical care is needed when setting the boundary conditions, thermodynamic data and picking the suitable turbulence, combustion, and other submodels

However, current gas turbine legislation demands for NO<sub>x</sub> have pushed the industry and academia to develop more sophisticated computational methods which allow successful NO<sub>x</sub> prediction.

Some kinetic mechanisms used for PDF table creation needed by some combustion models often include NO and NO<sub>2</sub> formation. So NO<sub>x</sub> can be modelled in some cases as a preprocessing operation. However, this can result in longer computational times and not often the expected accuracy is obtained [46].

A post-processing calculation is usually undertaken for NO<sub>x</sub> prediction, which needs a converged combustion solution.

The software ANSYS FLUENT includes a NO<sub>x</sub> prediction model, which allows the modelling of prompt, thermal and flue NO<sub>x</sub> formation. De Soete and Pourkashnian et al. developed the chemical rate models [234], [235] needed for the NO<sub>x</sub> model. This model also offers the capability of N<sub>2</sub>O prediction and selective noncatalytic reduction (SNCR).

King et al. [45], [46] have used the model for NO<sub>x</sub> prediction in radial swirlers with vane passage fuel injection for gas turbines. In his work, the NO predictions with FLUENT are compared with the results obtained using a mechanism including NO<sub>x</sub>, as shown in Figure 2-31.

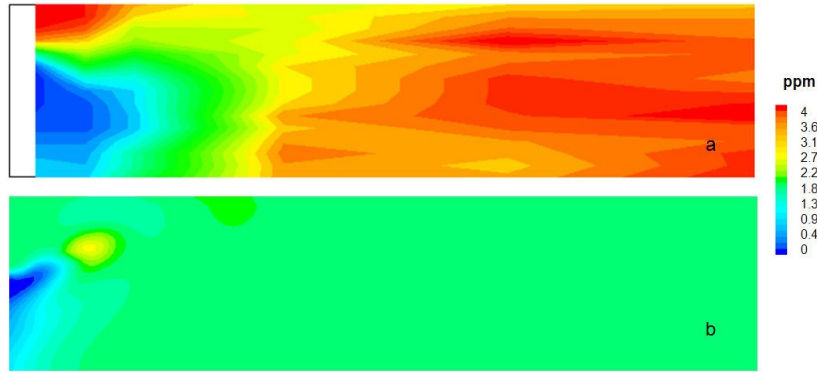


**Figure 2-31.** NO prediction comparison A) kinetic mechanism with NO, B) ANSYS FLUENT model [46].

King obtained underpredicted  $\text{NO}_x$  values compared with experimental data obtained for a Mach number of 0.05 for natural gas for a 140mm combustor [47]. He used the discretization scheme QUICK and a PDF approach.

## 2.4 Equilibrium software

Equilibria software allows the prediction of thermodynamical properties such as adiabatic flame temperature and equilibrium product composition for different fuel mixtures to improve and investigate combustion systems

Equilibrium predictions of flame composition include  $\text{NO}_x$  calculated for an infinite residence time inside the flame. In high-intensity gas turbine combustors, the residence time is approximately five milliseconds, where  $\text{NO}_x$  is not close to equilibrium [87], [236]. However, it is possible to calculate the rate of  $\text{NO}_x$  formation by obtaining the time the temperature takes to reach equilibrium. Thermal  $\text{NO}$  can be obtained for a combustion flame by estimating the adiabatic flame temperature, the approximate reaction time of the adiabatic flame gas mixture, and the equilibrium levels of  $\text{NO}$  and  $\text{O}_2$  considering the initial A/F, pressure and temperature [237]. Thermal efficiency can also be calculated with the obtention of the equilibrium fire exhaust dry oxygen for different A/F mixtures.

Different equilibria software has been developed. However, CEA [238] and Gaseq[239] have been widely used for combustion purposes [31]–[33]

The format for thermodynamic input and temperatures dependent equations used in CEA is not the same as the one used by GASEQ. For every temperature interval, CEA uses a total of nine coefficients: Seven coefficients for the specific heat  $C_p$  (a1-a7), one constant for the enthalpy  $H$  (coefficient b1), and one more coefficient for the entropy  $S$  (coefficient b2), as shown in equations (60)- (62).

$$\begin{array}{l} \text{Heat} \\ \text{Capacity} \end{array} \quad \frac{C_p^o}{R} = a_1 T^{-2} + a_2 T^{-1} + a_3 + a_4 T + a_5 T^2 + a_6 T^3 + a_7 T^4 \quad (60)$$

$$\begin{array}{l} \text{Enthalpy} \\ \text{Capacity} \end{array} \quad \frac{H^o(T)}{RT} = -a_1 T^{-2} + a_2 T^{-1} \ln T + a_3 + a_4 \frac{T}{2} + a_5 \frac{T^2}{3} + a_6 \frac{T^3}{4} + a_7 \frac{T^4}{5} + \frac{b_1}{T} \quad (61)$$

$$\begin{array}{l} \text{Entropy} \\ \text{Capacity} \end{array} \quad \frac{S^o(T)}{R} = -a_1 T^{-2} + a_2 T^{-1} + a_3 \ln T + a_4 T + a_5 \frac{T^2}{2} + a_6 \frac{T^3}{3} + a_7 \frac{T^4}{4} + b_2 \quad (62)$$

Generally, for gas species, two temperature intervals are used (minus 1000 and plus 1000), giving a total of 18 coefficients per polynomial set.

In contrast, Gaseq considers five coefficients for Cp temperature polynomial and two more constants for H and S. [240], as shown in Equations (63)-(65)

$$\begin{array}{l} \text{Heat} \\ \text{Capacity} \end{array} \quad \frac{C_p}{R} = a_1 + a_2 T + a_3 T^2 + a_4 T^3 + a_5 T^4 \quad (63)$$

$$\begin{array}{l} \text{Enthalpy} \\ \text{Capacity} \end{array} \quad \frac{H}{RT} = a_1 + a_2 \frac{T}{2} + a_3 \frac{T^2}{3} + a_4 \frac{T^3}{4} + a_5 \frac{T^4}{5} + \frac{a_6}{T} \quad (64)$$

$$\begin{array}{l} \text{Entropy} \\ \text{Capacity} \end{array} \quad \frac{S}{R} = a_1 \ln T + a_2 T + a_3 \frac{T^2}{2} + a_4 \frac{T^3}{3} + a_5 \frac{T^4}{4} + a_7 \quad (65)$$

The equilibrium codes Gaseq and CEA are based on the minimisation of the Gibbs energy. The method used by this software will not be discussed in this thesis, but a detailed explanation is provided online by Morley [239].

## Chapter 3. METHODOLOGY

The studied technologies are listed as follows, and their corresponding numerical and experimental methods will be explained in the following lines:

- The equilibrium calculations shown in Chapter 4 were performed for domestic fires in the Hy4Heat project and a glass melting factory for the project Glass Futures in 2020. The calculations were carried out for the following fuels:
  - I. Natural gas average composition from Goole glass melting plant
  - II. Pure Hydrogen (100%)
  - III. The proposed composition of hydrogen (PAS 4444)
  - IV. A blend of biodiesel
  - V. Crude glycerol
  - VI. A blend of 50% glycerol and 50% water
  - VII. UK Diesel composition
  - VIII. Pure ethanol
- CFD simulations performed for the flame stabilisers shown in Chapters 5 and 6 were carried out using ANSYS CFX and FLUENT 19.2 for RANS modelling.

Grid plate flame stabilisers (Aerodynamics)

- GM (hole diameter 19.62mm)
- GM (hole diameter 22.44mm)
- GM1 (hole diameter 19.62mm)

Grid plate flame stabilizer (Mixing and Combustion)

- I. GM1
  - II. GM2
  - III. GM3
  - IV. GM1-H2
  - V. GM1-7D
- The experiments presented in Chapter 7 for domestic fires were carried out as part of the academic team of the University of Leeds in conjunction with industrial partners for the Hy4Heat project released by BEIS in 2019. The numerical analysis for the Innovative fire was undertaken by the author of this thesis

Domestic fires

- I. Open-fronted fire
- II. Glass-fronted fire
- III. Innovative fire

### **3.1 Computational setup for thermodynamic equilibrium analysis**

Chapter 4 presents the prediction of adiabatic flame temperature and product composition for various fuels used for domestic fires and in the glass melting industry. The computations were carried out for different fuel blends using the software Gaseq [239]. Some fuels were also analysed using CEA [238].

Initially, the predictions were carried out for the product composition and adiabatic flame temperature in domestic fires for dual fuel applications for natural gas and hydrogen. Inlet temperatures up to 600K were considered for this activity, achieved from heat recovery waste gases for the glass-fronted and innovative appliances in Chapter 7. In addition, this activity was carried out to study the effect of the mixture strength at different inlet temperatures over oxygen and hydrogen levels. Natural gas and hydrogen were also investigated for a cooled flame from the NG equilibrium temperature at 300K inlet air to a cooled flame of 1850K with 1.0% excess oxygen in the exhaust. This is a condition desired in domestic fires

The equilibrium software was later used to predict product composition and adiabatic flame temperature for different green heat fuel blends used in the glass melting industry for a glass composition where heat recovery is used to preheat the combustion air up to 1000-1300K. For this activity, temperatures from 300-1600K were investigated for all the fuels at a span of equivalence ratios.

Equilibrium calculations were carried out for natural gas at 1500K inlet temperature for the combustion flame to be cooled down from its equilibria flame temperature to 1850K, considering a dry oxygen level of 1.0%, resembling existing float glass furnaces characteristics.<sup>3</sup> All the other activities involving a flame cooled down considered the equivalence ratio for an adiabatic flame temperature close to 2718K obtained with natural gas. The reason for this study of cooled products is since when cooling the flame, the reduced O and OH stops thermal NO<sub>x</sub> formation.. The same procedure applied for natural gas was followed for all the investigated fuels. For this activity, the exhaust oxygen levels were converted to wet and dry based using the predicted water content from the equilibria values for the different equivalence ratios. This enabled the prediction of the dry gas oxygen that the glass melting furnace should operate

---

<sup>3</sup> Data from existing float glass furnaces show that the optimum flue gas oxygen is from 0.5-1.5%.

on to achieve the same thermal conditions as for natural gas. The cooling process changes the oxygen levels near stoichiometric, so a range of equivalence ratios was computed to obtain the desired 1.0% dry O<sub>2</sub> at 2718K.

The software CEA was used at the beginning of this work to study a mixture of pure hydrogen/air and natural gas/air for the glass melting industry. This software allows the obtention of a single set of thermodynamic data for a specific mixture at given reactants' molar concentrations and inlet temperatures. Since most of the activities required large ranges of equivalence ratios and temperatures to be calculated, CEA was shown to be inadequate. On the other hand, Gaseq also allows the creation of mixtures using different species in a number of moles or mole fractions. One of the advantages of this software is the ability to calculate a range of equivalence ratios or given temperatures in seconds. However, Gaseq only allows setting a mixture temperature, in contrast to CEA, which allows assigning a specific temperature to each mixture species.

The adiabatic flame temperature and product composition computations were carried out at constant ambient pressure. In most simulations, a mixture of ambient air containing 78% N<sub>2</sub>, 20.95% O<sub>2</sub> and 0.96% Ar was considered the oxidiser.

To effectuate the calculations, both pieces of software require a thermodynamic file. The thermodynamic data developed by Burcat [241], containing 3746 species in their polynomial form, was used for the Gaseq calculations. All the ion elements of the Burcat's thermodynamic [241] were removed, which caused trouble in undertaking the simulations. Unfortunately, this file is too extensive to be included in this thesis.

Two kinetic mechanisms were used for the CEA calculations. The kinetic mechanisms proposed by De Vries et al.[242] for the natural gas/air and the one proposed by Skottene et al. [243] for hydrogen/air.

The mentioned modified Burcat thermodynamic file was used to study hydrogen, natural gas, ethanol, glycerol and diesel with Gaseq. In addition, a separate file was used for biodiesel as the surrogate used to replicate this fuel contained some species unavailable in the Burcat data.

Both pieces of software were compared before switching from CEA to Gaseq to evaluate the error between their thermodynamics. To obtain a set of combustion products that satisfy the equilibria for the given fuel, only species

concentrations higher than 0.1 ppm were chosen. For hydrogen, the species H, HNO, HO<sub>2</sub>, H<sub>2</sub>, H<sub>2</sub>O, H<sub>2</sub>O<sub>2</sub>, NH<sub>3</sub>, NO, NO<sub>2</sub>, N<sub>2</sub>, N<sub>2</sub>O, O, OH and O<sub>2</sub> were considered for the calculations. For methane, the predicted products were CO, CO<sub>2</sub>, H, HO<sub>2</sub>, H<sub>2</sub>, H<sub>2</sub>O, NO, NO<sub>2</sub>, N<sub>2</sub>, N<sub>2</sub>O, O, OH, O<sub>2</sub> and NH<sub>3</sub>.

The polynomials of the enthalpy of formation of equilibrium products for H<sub>2</sub> of the Burcat's and CEA thermodynamics files are illustrated in Table 3-1. An insignificant difference was encountered for all the product species between both codes.

**Table 3-1** Comparison of Burcat/CEA thermodynamic polynomials considering enthalpy of formation for H<sub>2</sub> equilibrium products at 298K

Species product	Enthalpy of formation (H) Burcat	Enthalpy of formation (H) CEA
H	8.7982080537E+01	8.7982241644E+01
HNO	4.3118975045E+01	4.1177969699E+01
HNO <sub>2</sub>	-3.1765825423E+01	-3.1665702024E+01
HO <sub>2</sub>	4.9605066163E+00	4.8491140720E+00
H <sub>2</sub>	-1.7683819351E-03	-1.7457053457E-03
H <sub>2</sub> O	-9.7602089269E+01	-9.7602089821E+01
H <sub>2</sub> O <sub>2</sub>	-5.4843220232E+01	-5.4843218541E+01
N	1.9077059732E+02	1.9077059664E+02
NH <sub>3</sub>	-1.8392762785E+01	-1.8543366662E+01
NO	3.6834058756E+01	3.6834946657E+01
NO <sub>2</sub>	1.3797984712E+01	1.3797922241E+01
N <sub>2</sub>	-1.7631669025E-03	-1.7631671159E-03
N <sub>2</sub> O	3.2931112072E+01	3.2931112184E+01
O	1.0056478365E+02	1.0056475936E+02
OH	1.5052398012E+01	1.5043533217E+01

O <sub>2</sub>	-1.7785181490E-03	-1.7785317370E-03
----------------	-------------------	-------------------

An adiabatic flame temperature calculation of a mixture of H<sub>2</sub> and air for both software pieces was undertaken to corroborate their error while predicting combustion. As a result, a neglectable difference was observed between them, as shown in Figure 3-1. This allowed switching to Gaseq and undertaking the activities quicker.

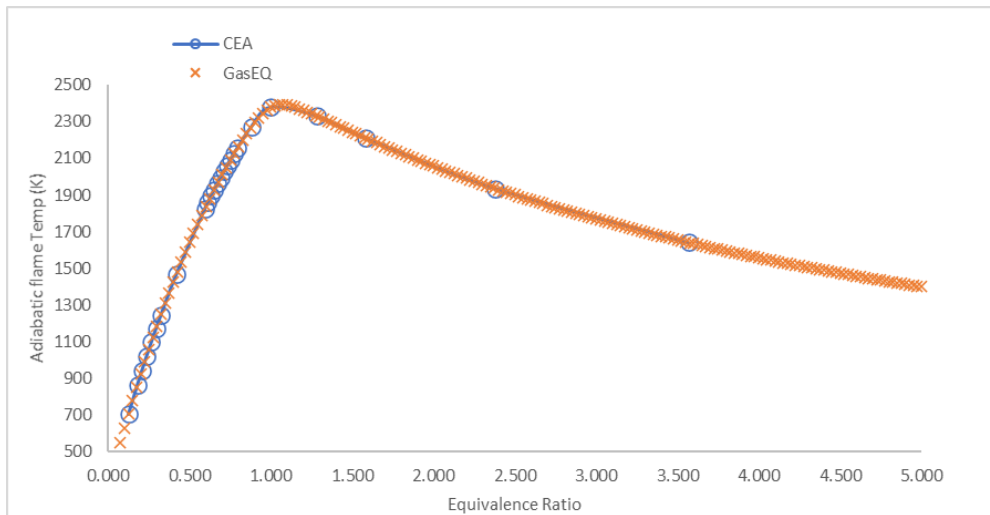


**Figure 3-1:** Adiabatic flame temperature for hydrogen flame comparison between CEA and Gaseq

The obtained results were processed, and graphs were produced using Office Excel. All runs were undertaken in a computer with the following specifications: Windows PC, an Intel® Core i7 processor, a GPU GTX 1080, 32GB 2666MHz DDR4 Non-ECC RAM, 1TB SSD, Integrated Intel HD Graphics.

### 3.1.1. Equilibrium calculations for natural gas

The activities for natural gas were undertaken considering a provided mixture of natural gas blended with air.

Natural gas is variable in its composition, and blends vary depending on the field where they are extracted. The UK imports natural gas from different countries, but its primary source is the North Sea with 48% [244]. Mike et al. show an averaged natural gas composition obtained over two days, shown in Table 3-2.

**Table 3-2:** National Grid plc averaged natural gas composition over a two days period.

	Methane	Nitrogen	Ethane	Carbon dioxide	Propane	Isobutane	Butane	Pentane	Isopentane	Neopentane	Hexane	Heptane	Octane	Nonane	Decane	Undecane	Dodecane
	%	%	%	%	%	%	%	%	%	%	mg/kg	mg/kg	mg/kg	mg/kg	mg/kg	mg/kg	mg/kg
<b>Mean</b>	92.42	3.67	3.02	0.78	0.59	0.09	0.14	0.04	0.04	0.00	409.28	540.97	184.84	14.37	0.02	1.14	0.44
<b>Median</b>	92.14	3.78	3.01	0.86	0.59	0.09	0.14	0.04	0.04	0.00	405.64	530.90	177.99	12.78	0.00	0.00	0.00
<b>Minimum</b>	90.84	2.44	2.93	0.32	0.53	0.08	0.11	0.03	0.03	0.00	355.87	492.51	150.39	7.77	0.00	0.00	0.00
<b>Maximum</b>	94.42	4.84	3.14	1.35	0.67	0.12	0.16	0.05	0.05	0.01	484.36	687.53	301.71	46.72	1.84	89.57	15.34
<b>No. of samples</b>	119	119	119	119	119	119	119	119	119	119	119	119	119	119	119	119	119

The natural gas mixture for this study was given by the glass plant of Guardian Glass in Goole, and agrees with the composition given by Table 3-2. The values provided in volume basis are as follows:

- CH<sub>4</sub>                    91.14%
- C<sub>2</sub>H<sub>6</sub>                    4.74%
- C<sub>3</sub>H<sub>8</sub>                    1.21%
- C<sub>4</sub>H<sub>10</sub> (iso + n) 0.42%
- N<sub>2</sub>                        1.18%
- CO<sub>2</sub>                      1.11%

**3.1.1.1 Equilibrium calculations for natural gas in domestic fires**

For domestic fire applications, the Goole NG composition was studied for an inlet air temperature of 300K-600K.

The mixture was then analysed for a cooled flame down to 1850K and an excess air of 1% for a room inlet temperature of 300K (26°C), which are common conditions for domestic fires.

**3.1.1.2 Equilibrium calculations for natural gas in the glass melting industry**

The activity consisted of calculating adiabatic flame temperature and product composition for inlet temperatures going up from 300K to 1600K for an equivalence ratio of Ø= 0.2-5.0. The plots for the adiabatic flame temperature and the exhaust gases are shown in Appendix B.

The Goole natural gas composition was cooled down from the adiabatic flame temperature of various values of Ø for 1500K inlet temperature to the furnace temperature of 1850K.

### 3.1.2 Equilibrium calculations for hydrogen

#### 3.1.2.1 Equilibrium calculations for hydrogen in domestic fire

These activities were carried out for inlet temperatures of 300K up to 600K for equivalence ratios going from  $\phi = 0.2$  to 6.0.

Previous calculations carried out at the University of Leeds [245] were undertaken to obtain the thermal NO levels and thermal efficiency based on exhaust equilibrium values of the corrected oxygen level on a dry basis to determine the fire A/F assuming complete combustion. The software CEA was used to calculate an inlet temperature of 295K and 1 ATM. The stoichiometric mixture of H<sub>2</sub>/air for complete combustion used the following reactant volumes: H<sub>2</sub> input volume (in %)= 29.58; O<sub>2</sub> input volume (in %)= 14.79; N<sub>2</sub> input volume (in %)= 55.63.

Therefore, the studied mixture started with an initial stoichiometric H<sub>2</sub> volume of 29.6 vol %.

The obtained results showed a peak temperature of 2378.5K at stoichiometric conditions. The peak NO was reached at  $\phi = 0.793$  for a 25% H<sub>2</sub> volume and a temperature of 2155.5K, as shown in Figure 3-2.

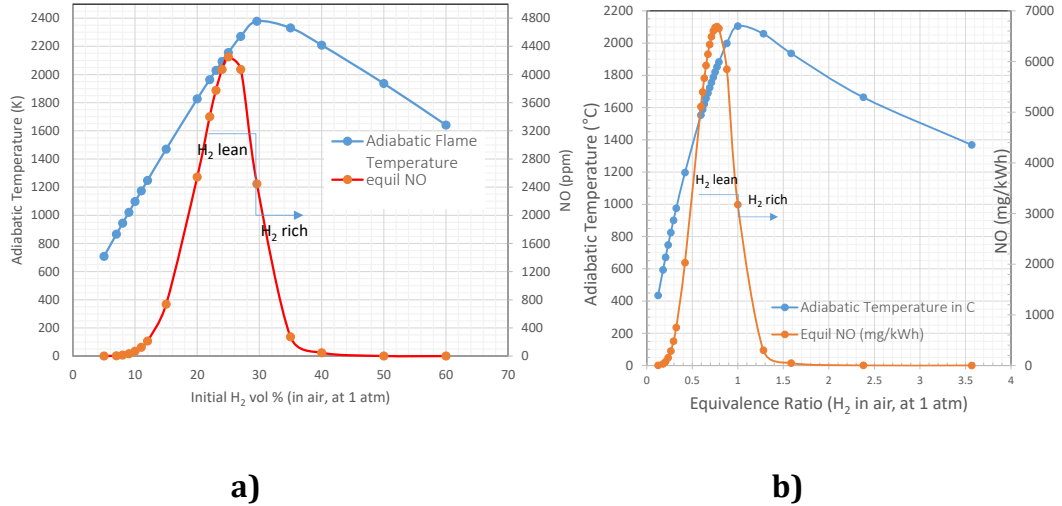


**Figure 3-2:** CEA results for an H<sub>2</sub> composition at 295K and 1 ATM. A) Adiabatic temperature in K vs initial H<sub>2</sub> in vol % in air and equilibrium NO in ppm; b) Adiabatic temperature in °C vs  $\phi$  and equilibrium NO in mg/kWh.

Thermal NO was calculated for a reaction time  $t$  of 0.1 s from the equilibrium temperature, NO and O<sub>2</sub> using Equation (66) [246].

$$\frac{[NO]}{[NO]_E} = \frac{1 - \exp^{-\alpha t}}{1 + \exp^{-\alpha t}} \quad (66)$$

$$\text{With } \alpha = \frac{2[NO]_E}{[O_2]_E^{0.5}} \times k_b$$

The results in Figure 3-3 show the thermal NO concentration levels near the Ecodesign limit of 130 mg/kWh [247] for 20-23 H<sub>2</sub> vol %.

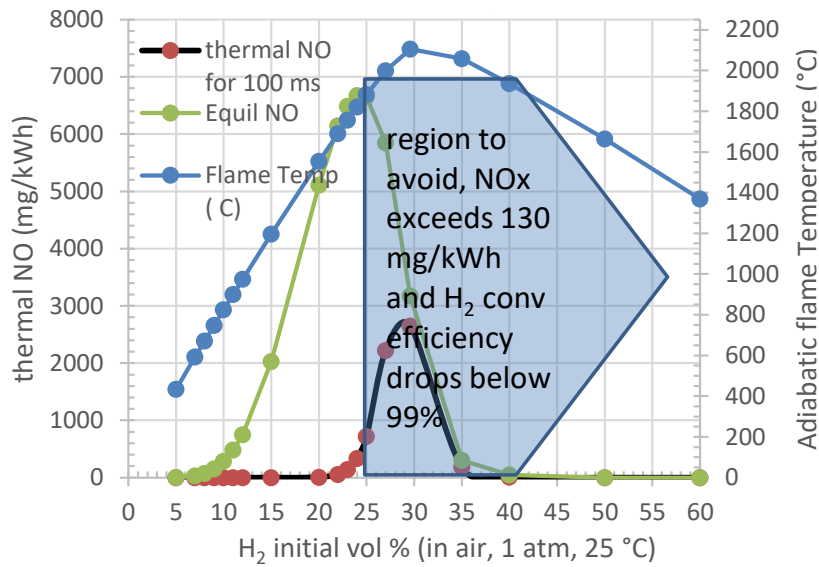


**Figure 3-3:** Thermal NO and adiabatic temperature vs H<sub>2</sub> vol% for 100 ms.

As explained before, equilibrium NO concentrations are not usually achieved in the combustion process. A long time is needed for equilibrium to occur, and real flame conditions limit the reaction time for N<sub>2</sub> and O<sub>2</sub> to dissociate recombine into NO.

This past study concluded that it is recommended to operate H<sub>2</sub> in equivalence ratios from 0.59-0.71 in air to maintain thermal NO<sub>x</sub> below 40mg/kWh, which is the limit of sustainable homes NO<sub>x</sub> emissions. This will retain the temperature flame below 1750°C for 0.03-0.1 sec reaction times.

For the present work, mixtures of hydrogen/ air for temperatures from 298-600K were investigated using Gaseq, where adiabatic flame temperatures, H<sub>2</sub>, O<sub>2</sub> and NO levels were obtained for equivalence ratios from 0.2-5.0.

A cooled flame was calculated for the H<sub>2</sub>/air mixture considering an inlet temperature of 300K and the adiabatic flame temperature obtained for the natural gas/air mixture studied for domestic fires cooling the fire temperature to 1850K below the recommended for sustainable homes.

### 3.1.2.2 Equilibria for the glass melting industry

The hydrogen mixture available in the PAS 4444 [247] was calculated and compared to a composition of 100% H<sub>2</sub>. For this study, the mixtures were simulated at 300K at atmospheric pressure calculating the adiabatic flame temperature for equivalence ratios from 0.5-5.0.

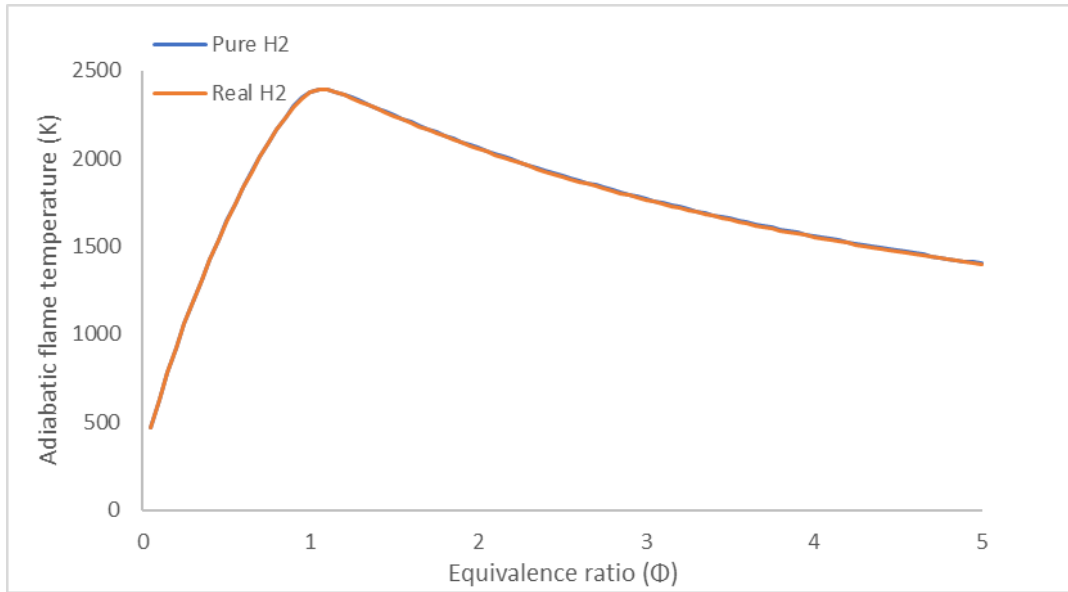
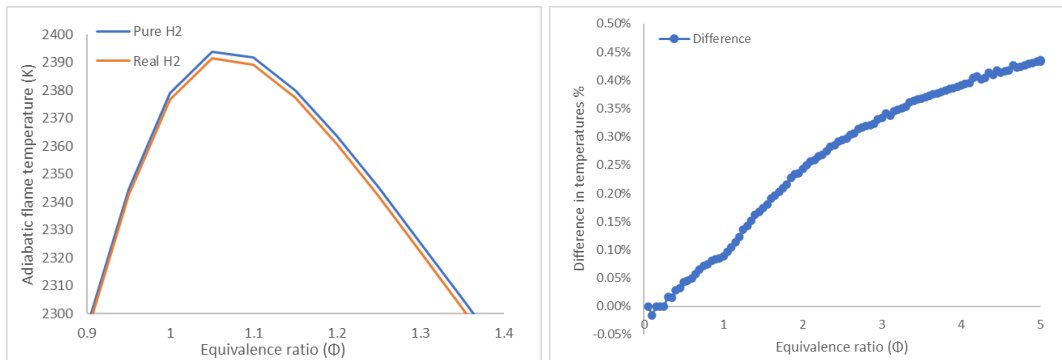


**Figure 3-4:** Comparison of adiabatic flame temperature vs  $\Phi$  for pure and real H<sub>2</sub> compositions



a)

b)

**Figure 3-5:** a) Comparison of adiabatic flame temperature vs  $\Phi$  for pure and real H<sub>2</sub> mixtures showing the error between them; b) Calculated error between both mixtures.

The obtained plots are shown in Figure 3-4, where no significant differences are observed. The error between both mixtures was calculated and shown in Figure 3-5, where the highest temperature difference was obtained at  $\Phi = 5$ . At this level, the error was 0.45%. Other inlet temperatures were also tested, showing similar results between both mixtures. Hence, it was concluded that the adiabatic flame temperature and equilibrium composition calculations for the PAS 4444 hydrogen mixture were not required, given the neglectable difference against the pure H<sub>2</sub> composition.

A hydrogen composition containing 100% H<sub>2</sub> was first studied, considering air temperatures going up to 1600K for a range of  $\Phi$  from 0.2-6.0. The adiabatic flame temperatures and exhaust levels are shown in Appendix C.

The hydrogen/air mixture was studied for a cooled flame bringing down the adiabatic temperature reached at 1% O<sub>2</sub> in the flue to the furnace temperature achieved with NG.

### 3.1.3 Equilibrium calculations con biodiesel blend for glass melting industry

A soybean FAME<sup>4</sup> based biodiesel composition obtained by Postioti et al. [249] was investigated for this study. The blend featured a carbon, hydrogen and oxygen content of 76.7%, 12.0% and 11.3%, respectively, for a composition of CH<sub>1.876</sub>O<sub>0.011</sub>.

Since the equilibria software did not allow the inclusion of species on a H/C basis, replicating the needed composition was needed using existing species in thermodynamic tables. A common way of doing this is developing surrogates that imitate the fuel composition, as shown in many works [250]–[253]. Cui et al. [253] developed a table for six different biodiesel fuel blends (BDS) obtained from the mixture of various FAMEs compounds, as shown in Table 3-3. The values for the obtention of soybean oil were approached to the blend needed for this work.

**Table 3-3:** Components of biodiesel fuels [253]

Material	Fatty acid methyl ester %									
	Caprylic acid methyl ester	Methyl decanoate	Methyl laurate	Methyl myristate	Methyl palmitate	Methyl stearate	Methyl oleate	Methyl linoleate	Methyl Linolenate	Others
	C <sub>9</sub> H <sub>18</sub> O <sub>2</sub>	C <sub>11</sub> H <sub>22</sub> O <sub>2</sub>	C <sub>13</sub> H <sub>26</sub> O <sub>2</sub>	C <sub>15</sub> H <sub>30</sub> O <sub>2</sub>	C <sub>17</sub> H <sub>34</sub> O <sub>2</sub>	C <sub>19</sub> H <sub>38</sub> O <sub>2</sub>	C <sub>19</sub> H <sub>36</sub> O <sub>2</sub>	C <sub>19</sub> H <sub>34</sub> O <sub>2</sub>	C <sub>19</sub> H <sub>32</sub> O <sub>2</sub>	C>21
Soybean					11	5	25	52	7	
Rapeseed					4	2	62	20	8	1
Palm				1	45	6	38	9		
Jatropha					15	12	71	2		
Coconut	8	8	45	18	10	2	8	2		
Cooking oil					10	3	42	35	5	

<sup>4</sup> Fatty acid methyl ester (FAME) are a type of fatty acid ester derived by transesterification of fats with methanol, They are often used to produce detergents and biodiesel. [248]

The original soybean methyl ester compounds were decomposed into their elemental values for C, H and O on a mass basis. Then, these were converted into a mole basis using Excel, obtaining a H/C of 1.84 and an O/C of 0.106, as shown in Table 3-4. These values were approached to the requested mixture using the Excel Solver, and the new composition is shown in Table 3-5.

**Table 3-4.** Original C/H and O/C composition for FAME blend for soybean oil

CALCULATION SOY BEAN BIODIESEL (SAE 2013-01-2689)												
	Element	W										
	C	12.011										
	H	1.0079										
	O	15.999										
%	C	H	O	total mass	%mass	%mass C	%mass H	%mass O	%mole C	%mole H	%mole O	
11%	17	34	2	270.4536	29.7499	22.46057	3.769546	3.51978	1.87	3.74	0.22	
5%	19	38	2	298.5072	14.92536	11.41045	1.91501	1.5999	0.95	1.9	0.1	
25%	19	36	2	296.4914	74.12285	57.05225	9.0711	7.9995	4.75	9	0.5	
52%	19	34	2	294.4756	153.1273	118.66868	17.819672	16.63896	9.88	17.68	1.04	
7%	19	32	2	292.4598	20.47219	15.97463	2.257696	2.23986	1.33	2.24	0.14	
TOTALS	100%			1452.3876	292.3976	225.56658	34.833024	31.998	18.78	34.56	2	
										H/C	O/C	Proposed fuel
										1.840256	0.106496	CH1.88 O0.11

**Table 3-5.** Approximation of the desired CHO composition for FAME blend for soybean oil

CALCULATION SOY BEAN (SAE 2013-01-2689)												
	Element	W										
	C	12.011										
	H	1.0079										
	O	15.999										
%	C	H	O	total mass	%mass	%mass C	%mass H	%mass O	%mole C	%mole H	%mole O	total %mole
32%	17	34	2	270.4536	87.02095	65.69905667	11.026239	10.295653	5.46990731	10.93981	0.643519	17.05324043
20%	19	38	2	298.5072	59.70144	45.6418	7.66004	6.3996	3.8	7.6	0.4	11.8
13%	19	36	2	296.4914	39.53219	30.42786676	4.83792	4.2664	2.53333334	4.8	0.266667	7.60000023
7%	19	34	2	294.4756	19.63171	15.21393304	2.2845733	2.1332	1.26666664	2.266667	0.133333	3.666666597
28%	19	32	2	292.4598	81.37423	63.49704391	8.9740433	8.9031476	5.2865743	8.903704	0.556482	14.74675989
TOTALS	100%			1452.3876	287.2605	220.4797004	34.782816	31.998	18.3564816	34.51019	2	54.86666694
										H/C	O/C	Proposed fuel
										1.88	0.108953	CH1.88 O0.11

The calculations were carried out using an air composition considering Ar. The adiabatic flame temperature and product composition were calculated for  $\phi = 0.025$  to 3.0. Unfortunately, higher equivalence ratios could not be studied as divergence was encountered with the software above  $\phi = 3$ . The plots for adiabatic flame temperature and flue composition are shown in Appendix D.

The biodiesel mixture was studied for a cooled temperature for various equivalence ratios going from the adiabatic temperature to the furnace operating temperature of 1850K obtained with NG.

### 3.1.4 Equilibrium calculations for glycerol for the glass melting industry

Glycerol was studied as a crude mixture of  $C_3H_8O_3$ /air.

The first activity was undertaken for inlet temperatures from 300K up to 1600K for  $\phi = 0.1$ -5.0. The adiabatic flame temperature plots and emissions are shown in Appendix E.

A cooling flame temperature was also calculated for the glycerol/air mixture for a span of equivalence ratios. The predicted adiabatic temperature at an excess  $O_2=0.01$  vol was taken down in decrements of 50K to the furnace operating temperature in NG of 1850K.

Glycerol was also studied as a mixture of 50%  $H_2O$  and 50% crude glycerol for a cooled mixture of 1850K and 1% excess  $O_2$ .

### 3.1.5 Equilibrium calculations for European diesel blend for glass melting industry

The activity was carried out for a European diesel composition [254] given as  $CH_{1.87}$  with an NCV of 43.0 MJ/kg. This mixture had a carbon content of 86.28% and 13.46% H, both on a mass basis, with a density of 834  $kg/m^3$ .

Akin to the activities carried out for the biodiesel composition, an approximation of a diesel surrogate composition to the needed C/H was undertaken.

Bai et al. [252] developed a skeletal mechanism for a tri-component diesel surrogate fuel using N-hexadecane, iso-octane and 1-methylnaphthalene. The used composition is shown in Table 3-6.

**Table 3-6.** Composition of diesel surrogate [252].

Properties	N-hexadecane	Iso-cetane	1-Methylnaphthalene
Abbr.	HXN	HMN	AMN
Mole fraction	41.3%	36.8%	21.9%
CN	100	15	0
Molar Weight	226.45	114.23	142.20
MP <sup>a</sup> (°C)	17.9	–	– 29.2
BP <sup>b</sup> (°C)	286	246.4	244.8
Density ( $Kg/m^3$ )	756	768	986
C/H ratio by weight	2.13	2.13	0.91
Lower heating value (MJ/kg)	43.952	43.4	39.259

The H/C composition was worked out using Excel on a volume basis, obtaining 1.93. The calculation is shown in Table 3-7.

The mole fractions were approached to the desired value of  $CH_{1.87}$  using the Excel Solver, as shown in Table 3-8. Then, the new mole fractions were used to create the blend in Gaseq, and the activities were developed. A mixture of air containing Ar was used for this activity.

**Table 3-7. H/C calculation for diesel surrogate**

CALCULATION DIESEL WITH SURROGATE Development of a skeletal mechanism for tri-component diesel surrogate fuel: N-hexadecane/iso-cetane/1-methylnaphthalene												
		Element	W									
		C	12									
		H	1.01									
	Mole fraction%	C	H	name	total molar weight	molar weight of sample	molar weight of C in sample	molar weight of H on sample	Moles of C in sample	Moles of H in Sample	H/C WEIGHT	LHV (MJ/kg)
	41%	16	34	HXN	226.4446	93.5216198	79.368688	14.1529318	6.608	14.042	2.125	43.952
	37%	16	34	HMN	226.4446	83.3316128	70.720768	12.6108448	5.888	12.512	2.125	43.4
	22%	11	10	AMN	142.2	31.1418	28.934499	2.207301	2.409	2.19	0.90909	39.259
TOTALS	100%				595.0892	207.9950326	179.023955	28.9710776	14.905	28.744		
											H/C MOLE	Proposed fuel
											1.92848	C H1.87

**Table 3-8. European diesel H/C approach using Excel Solver**

CALCULATION DIESEL WITH SURROGATE Development of a skeletal mechanism for tri-component diesel surrogate fuel: N-hexadecane/iso-cetane/1-methylnaphthalene												
		Element	W									
		C	12.011									
		H	1.0079									
	Mole fraction%	C	H	name	total molar weight	molar weight of sample	molar weight of C in sample	molar weight of H	Moles of C in sample	Moles of H in Sample	H/C WEIGHT	LHV (MJ/kg)
	66%	16	34	HXN	226.4446	150.0016278	127.3013921	22.70023565	10.59873384	22.5223094	2.125	43.952
	6%	16	34	HMN	226.4446	13.37848668	11.35387665	2.024610031	0.945289872	2.008740977	2.125	43.4
	28%	11	10	AMN	142.2	39.60248929	36.79550272	2.806986565	3.0634837	2.784985182	0.909091	39.259
TOTALS	100%				595.0892	202.9826037	175.4507715	27.53183224	14.60750741	27.31603556		
											H/C MOLE	Proposed fuel
											1.87	C H1.87

The adiabatic flame temperature and product composition were obtained for the blends with diesel.  $\phi$  0.125 to 6 were calculated for temperatures from 100K up to 1600K. The adiabatic flame temperatures and product compositions for the different conditions are shown in Appendix F.

The European diesel blend was studied for a cooled temperature of 1850K and 1% excess  $O_2$  for various equivalence ratios.

### 3.1.6 Equilibrium calculations for ethanol for the glass melting industry

A mixture of pure  $C_2H_5OH$  and air was studied for the obtention of adiabatic flame temperature and product composition for inlet temperatures going from 300K to 1600K, for  $\phi = 0.02-5.0$ . The obtained results are shown in Appendix G.

The ethanol/air mixture studied for a cooled temperature was approached to the glass furnace conditions achieved with NG of 1850K and 1%  $O_2$  in the flue.

### **3.2 Computational setup for gas turbine combustor flame stabilisers for high combustion intensity**

The flame stabiliser geometries numerically investigated in Chapter 5 and Chapter 6 were designed and experimentally tested by Gordon E. Andrews and Naman Al-Dabbagh [157], considering a combustor can of 76mm diameter, which was used for the simulations.

Combustion internal traverses were obtained experimentally for GM2, compared with the obtained simulation results. No internal traverses were taken for GM1. However, simulation results are compared with mean exhaust values.

The software SOLIDWORKS [255] was used to create the models for the different geometries.

Structured hexahedral and unstructured tetrahedral meshes were designed using ANSYS ICEM [256]. However, the complexity of developing the correct blocking and creating decent quality structured meshes lead to the use of unstructured polyhedral meshes for some combustion simulations. This also helped model the fuel injections quickly and vary the nozzle sizes without designing a new blocking for every new configuration. Coarser meshes were used for combustion simulations than for the study of aerodynamics to help reduce the computational time.

Polyhedral unstructured meshes were carried out with the meshing software of ANSYS FLUENT [256].

All the simulations were carried out for a steady state. ANSYS CFX was used to predict pressure loss in Chapter 5. The simulations involving combustion were initially carried out using ANSYS CFX; however, issues were encountered with opening or importing libraries for propane/air for non-premixed combustion, so it was then decided to move to ANSYS FLUENT.

All the computational runs were carried out considering a thousand iterations to allow convergence. The residuals were set to  $10^{-6}$  in all cases

The least-squares cell-based method was used for the spatial discretization gradient for the simulations carried with FLUENT.

The simulations were carried out following the procedure for FVM mentioned in Chapter 2.

NO<sub>x</sub> modelling was carried out as a post-processing operation using the NO<sub>x</sub> model included in ANSYS FLUENT. Prompt and thermal NO were simulated. As

explained in Chapter 2 prompt is crucial as it's the fact to avoid reaching zero NO values.

All runs were undertaken in a computer with the following specifications: Windows PC, Intel® Core i7 processor, a GPU GTX 1080, 32GB 2666MHz DDR4 Non-ECC RAM, 1TB SSD, Integrated Intel HD Graphics.

### 3.2.1. Grid Mix flame stabilisers

A 76mm cylindrical model with a combustion zone of roughly 4D or 330mm and an upstream length of 2D or 150mm was modelled, replicating the combustor dimensions used in the experiments. Atmospheric pressure was considered for the development of the experiments. A thermal input of 131kW and the heat release of 28 MW/m<sup>2</sup> were assumed, as mentioned in Chapter 2.

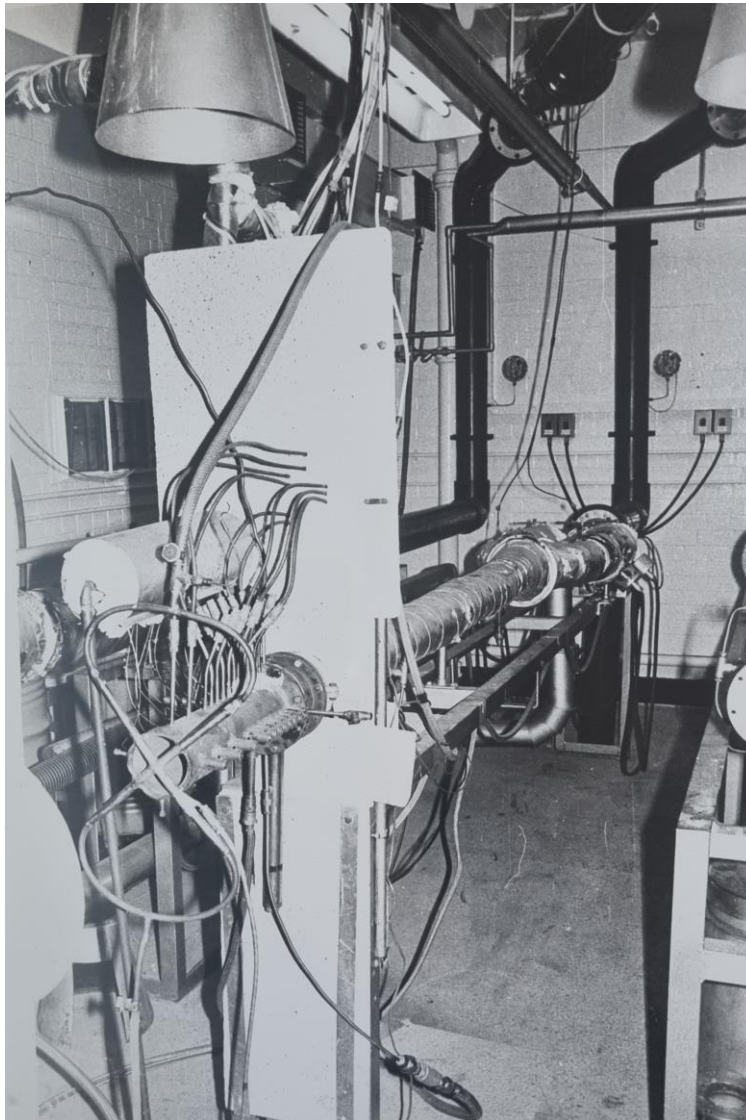


**Figure 3-6.** Experimental rig used for grid mix flame stabilisers [157].

The work was carried out at a reference Mach number of  $M=0.047$  as in the experiments. These conditions consider all the combustion air passing through the stabiliser. The airflow was considered  $0.0784 \text{ kg/s}$ . For the experimental tests, the inlet air was supplied from an air blower at  $0.1 \text{ bar}$ , and the airflow was measured using a BS1042 venturi flowmeter with a diameter of  $152 \text{ mm}$ . Then, the metered air was preheated using a  $9 \text{ kW}$  electrical heater for an inlet temperature of  $400 \text{ K}$ .

The thermal input was  $131 \text{ kW}$  and the heat release  $28 \text{ MW/m}^2$ . Industrial propane (LPG) at  $288 \text{ K}$  supplied from six cylinders of  $50 \text{ kg}$  was used for the experiments. The fuel flow rate was measured using a variable area flowmeter. The rig used for the experiments can be observed in Figure 3-6.

The experiments which this work is based on were carried out at a pressure loss of  $2.4$  and  $4\%$  for perforated plates of four holes, which gave a  $A_2/A_1$  of  $0.266$  and a  $t/d$  of  $73.4\%$ . Considering the inlet air temperature of  $400 \text{ K}$  used for the experiments, the velocity before the flame stabiliser was  $18.84 \text{ m/s}$  and the velocity at the vena contracta in the stabiliser holes was  $70.8 \text{ m/s}$ , with  $M_2 = 0.177$ . In order to stabilise a flame in a flow velocity of  $19 \text{ m/s}$  for lean low  $\text{NO}_x$  mixtures for a laminar burning velocity of  $0.15 \text{ m/s}$ , the required turbulent to laminar burning velocity had to be above  $100$ .

No film cooling air was used in the experiments as this increase the  $\text{NO}_x$  levels [257]. However reverse air flow was used for wall cooling as usually seen in industrial gas turbines. The combustor was tested in the open so the wall radiated to the environment, so the conditions were not adiabatic. However, no wall temperature profiles were measured for the conditions investigated on this thesis so no wall heat transfer was considered.

A mean gas sample probe was attached to the outlet of the experimental combustor allowing to obtain mean values for the combustion products and calculate the temperature and other combustion parameters by carbon balance. This probe was not modelled in the simulations. The combustor opening allowed to entrain cooling air into the combustor, and then the gases passed through a cone into a water-cooled exhaust.

The mean gas samples were originally obtained with a water-cooled stainless steel X probe similar to the one used by D. H Lister [258], featuring twenty gas holes of  $1 \text{ mm}$  each located on centres of equal area along with the probe. The sample flow rate was  $30 \text{ lpm}$  with a sample inlet hole velocity of  $32 \text{ m/s}$ , higher than the mean velocity in the combustor, but needed to minimise heat transfer time. Only  $5 \text{ lpm}$  were needed for the gas analysis system, the rest was dumped

before gas analysis. Gas samples were first heated at 180°C through a heated sample line and filter, and then pumped to a heated gas analysis system to measure NO<sub>x</sub> chemiluminescence using an analyser with a minimum scale of 0-4ppm and a resolution of 0.1ppm. The total hydrocarbons (THC) samples were then measured using a flame ionization detector (FID) with a resolution of 0.1ppm, oxygen levels were measured through paramagnetic analysis, and CO and CO<sub>2</sub> were obtained using a non-disperser infrared sensor (NDIS) using paramagnetic analysis. Water vapour was removed by cooling the sample prior CO, CO<sub>2</sub> and O<sub>2</sub>, while NO<sub>x</sub> and THC were measured wet. Finally, NO<sub>x</sub> was converted to dry in a post processing operation by removing the water from the equilibrium composition. NO<sub>x</sub> was obtained using a NO<sub>x</sub> analyser set for 37°C and a resolution of 0.1ppm, and a carbon molybdenum converter was used to convert NO<sub>2</sub> into NO.

The authors of the experimental work compared the obtained species product values with the calculated equilibrium composition as shown in Table 3-9 by using carbon balance and achieving sensible agreement.

**Table 3-9** Gas analysis mean exhaust concentration % compared with that for the metered mean  $\phi$  from equilibrium calculations for a metered  $\phi= 0.69$

<b>Species</b>	<b>Gas Analysis</b>	<b>Equilibrium Metered <math>\phi</math></b>	<b>Error (%)</b>
H <sub>2</sub> O	12.4	11.7	5.5
CO <sub>2</sub>	8.6	8.1	5.9
CO	0.16E+00	0.16E+00	0

The increment in gas adiabatic temperature was calculated from the equivalence ratio and corrected for the combustion efficiency obtained from the CO and THC measurements. This allowed the mean outlet temperature and the axial variation of adiabatic temperature to be obtained, for both sample probes.

Another way of obtaining the adiabatic flame temperature was using a mineral insulated type R thermocouple with grounded junction and platinum outer sheath.

The authors of the experiments calculated the increase of the adiabatic gas temperature from the equivalence ratio. They then corrected the thermal

combustion efficiency calculated from the CO and THC levels. Differences were obtained between the thermocouple measurements and the ones obtained with gas analysis, where the main ones were encountered at the stabiliser downstream face. These differences were mainly due to the probe location for the different tests and the challenge of placing them in the exact wanted position without any precision device.

Both measurements were compared with the obtained simulation results in Chapter 6.

The 15mm water-cooled gas sample probe used for obtaining the gas composition traverses for the experimental tests is shown in Figure 3-7. It featured a 1mm tip in the head, allowing the obtention of the sample gas. This sample probe provided a 3.9% blockage of the total combustor flow area for a 76mm diameter. However, thermodynamic interference produced by the device could have affected the obtained gas composition results. Thus, no exact agreement is expected with the simulation results presented in Chapter 6.

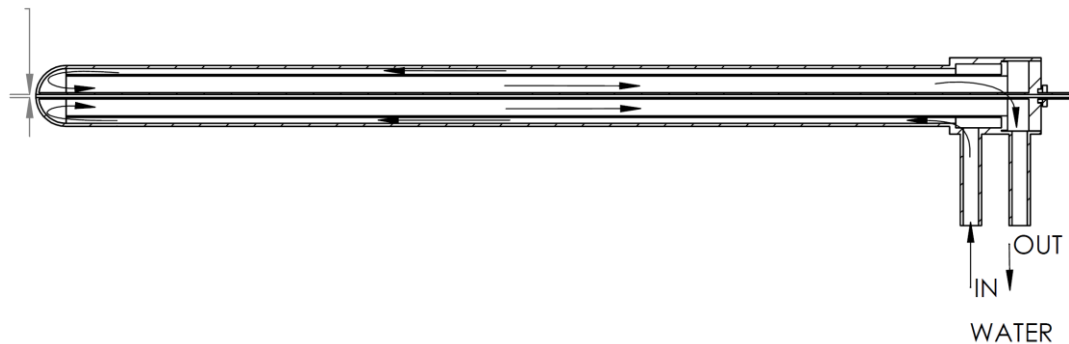


**Figure 3-7.** Internal traverse water-cooled gas sample probe 15mm OD with 1mm gas sample hole inlet

Both gas analysis probe and thermocouple were mounted in a support with 35.6mm between the two probe centrelines. Both measuring devices were traversed simultaneously. When the gas analysis probe was touching the combustor wall, and the tip was in the position 7.5mm from the wall, the thermocouple was 5.1mm offset from the combustor centreline. Once both measurements were taken in this position, the test rig was turned off, and the probes relocated. Both devices were positioned in a second arrangement, so the analysis sample probe centreline was colinear to the centre of the airhole. Thus, the thermocouple centreline was 35.6mm away from the probe inside the stabiliser holes. Therefore, when the obtained temperature was compared for both devices, they were not in the same radial flow position. The described locations were simulated and compared with the CFD results in Chapter 6.

Figure 3-8 shows the simulation arrangement for both the gas analysis probe (GA) and thermocouple (TC).

Various flame stabiliser geometries were investigated with CFD. The studied models are listed in Table 3-10 and were mentioned in 2.9. These geometries featured four air holes and a PCD of 43.2 mm, and the centre of the holes was 16.5mm from the combustor wall.

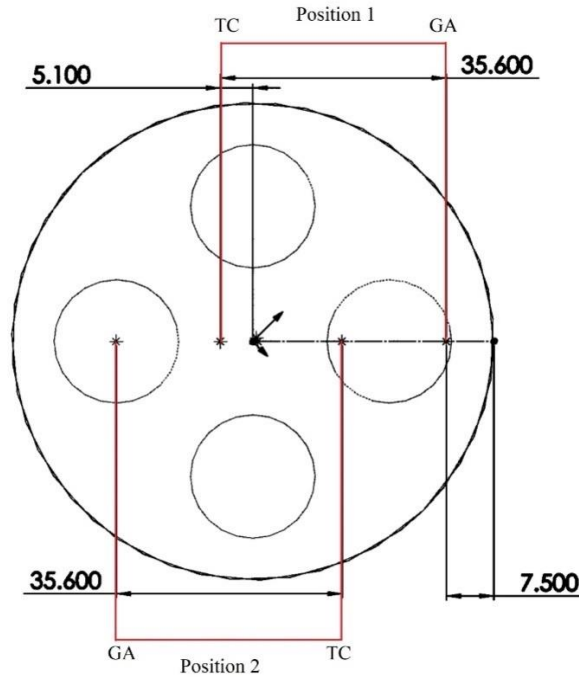


**Figure 3-8.** Traverse locations of GA and TC for 2 different positions

**Table 3-10:** Studied flame stabiliser geometries using CFD for a 76mm combustor

Name	No. air holes	Airhole size	Plate thick	Pressure loss (%)	Simulation	Fuel	Injection
Premixed	4	22.44	3.2	4	Aerod	-	-
Premixed	4	19.27	3.2	2	Aerod	-	-
GM2	4	19.62	9.53	2	Aerod/ combustion	C <sub>3</sub> H <sub>8</sub>	Axial
GM1	4	19.62/ 22.11	9.53/ 5.3	2/ 4	Combustion	C <sub>3</sub> H <sub>8</sub>	Radial

GM3	4	19.62	9.53	2	Combustion	C <sub>3</sub> H <sub>8</sub>	Axial
GM1-H <sub>2</sub>	4	19.62	9.53	2	Combustion	H <sub>2</sub>	Radial
GM1-7D	4	19.62	7D	2	Combustion	H <sub>2</sub>	Radial

Two four air-hole geometries originally used for premixed combustion were firstly investigated for pressure loss prediction. The first one featuring a hole diameter of 22.44mm was designed for  $t/d$  of 0.14 and an  $A_2/A_1$  of 0.347. The other stabilizer investigated featured an air hole diameter of 19.27mm, and it was designed for a  $t/d = 0.17$  and an  $A_2/A_1$  of 0.256, as shown in Table 2-2.

A thicker four-hole flame stabilizer was also investigated, originally termed Grid Mix 2 (GM2) and experimentally showed ultra-low NO<sub>x</sub> capabilities. This stabiliser featured an internal hollow fuel delivery plenum which made the stabiliser thicker.

These geometries were studied with no combustion, and experimental results for pressure loss are compared with simulation in Chapter 5.

The flame stabiliser GM2 featured a  $t/d$  of 0.49, giving an  $A_2/A_1$  of 0.265, as shown in Table 2-2. This geometry injected the fuel through a 0.3mm annular gap at the downstream face of the stabiliser placed 1/16" above the air hole, as shown in Figure 3-9 b). This distance corresponded to a metal ring that separated the fuel from the air, as observed in Figure 3-10.

GM1 featured eight nozzles with a 1.2mm diameter equally spaced in the inner circumferential wall of each air hole, as shown in Figure 3-11, injecting fuel radially to the air jet as shown in Figure 3-9 a).

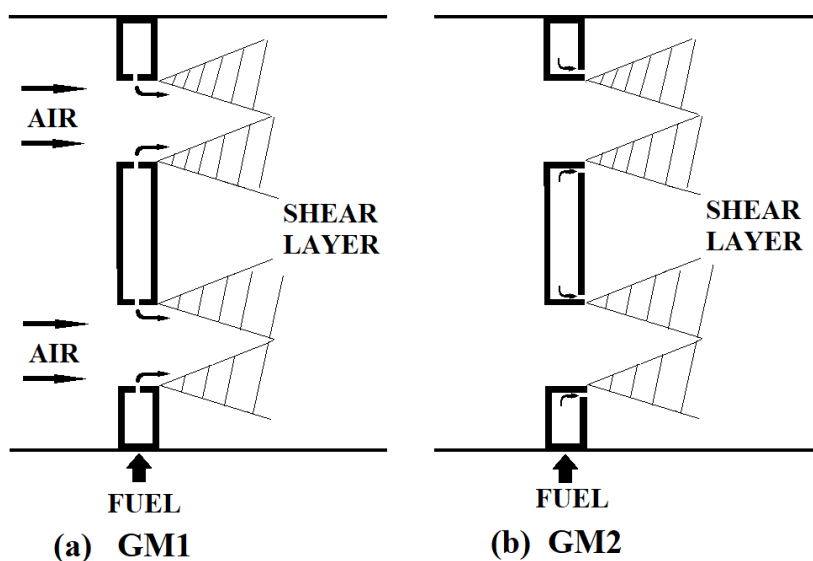


**Figure 3-9:** Fuel injection methods for a) GM1; and b) GM2

The GM1 grid plate also investigated had a hole size of 22.1mm. However, this geometry was compared to GM2 and a new addition to GM technology named GM3 to study their mixing capabilities. Hence, it was also modelled for a hole diameter of 19.62mm. Both plates, GM2 and GM1, were equally fed through four connecting pipes at the edge of the stabiliser, as shown in Figure 3-11. However, this feature was not modelled with simulation.



**Figure 3-10.** Flame stabiliser GM2 featuring an annular injection



**Figure 3-11.** Flame stabiliser GM1 featuring eight radial inward fuel nozzles per air hole

GM2 and GM1 show a welded ring near the stabiliser hole, which was how the orifice tube representing the air hole was welded to the fuel plenum. This

feature was modelled to study its effect on the aerodynamics of the flame stabiliser used for GM2.

GM3 was a new method of fuel injection imitating the concept of FLOX burners as explained in 2.2.8, applied to GM. This concept fuels at the centreline of the stabiliser airholes directly into the shear layer, as shown in Figure 3-12 a). This method is compared in Chapter 6 with GM1 and GM2 to obtain the best fuelling method. GM3 was investigated for the same injection area used for GM2 and GM1.

GM1, GM2 and GM3 were studied for a non-reacting and reacting propane/air mixture at an injection temperature of 288K.

GM1 was also investigated for dual fuel capabilities featuring hydrogen combustion. An air hole of 19.62mm was used for the simulations. The fuel nozzles were modelled as eight 1.8mm injections since velocities above 300m/s were calculated for a hydrogen flame considering the original nozzle size. The equivalence ratio of 0.55 was used for the hydrogen simulation, which is the condition needed to achieve the adiabatic flame temperature of 1800K achieved at the equivalence ratio investigated with propane. This temperature was also corroborated using the software Gaseq and CEA by comparing the adiabatic flame temperature of propane/air and calculating the needed equivalence ratio for the obtained temperature.

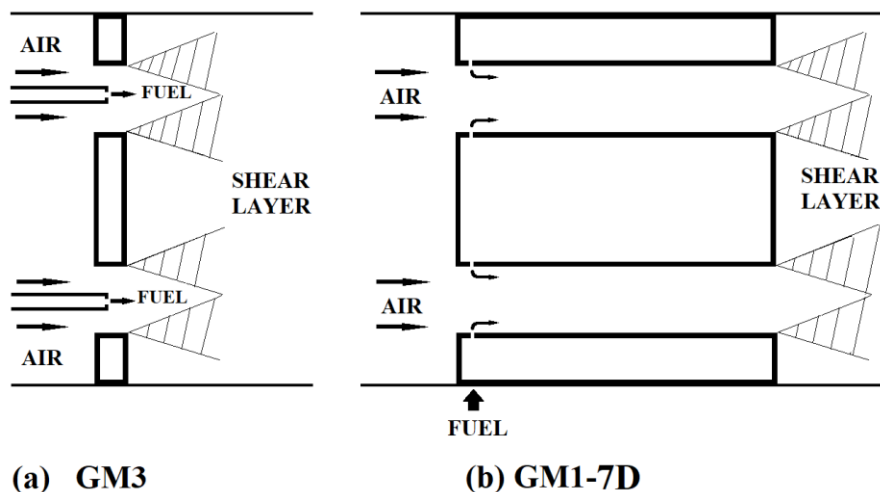


**Figure 3-12.** Fuel injection methods for a) GM3; b) GM1-GE

GM1 was lastly studied for a stabiliser thickness of 7D, similar to the work of York et al. [26] for hydrogen /air combustion mentioned in 2.2.8. as shown in Figure 3-12 b). In Yorks work, the combustion occurs after the stabilisation position with only partial flashback.

The experimental data showed that the combustor wall was only cooled by the external radiation, so adiabatic walls non-slip were considered in the simulations.

### 3.2.1.1 CFD study of aerodynamics for Grid Mix stabilisers

The pressure loss  $\Delta P/P$  %, as explained in 2.2.9.1, is controlled by the area coming through the air holes of the stabiliser.

Equation (12) was used to predict  $C_D$  from the measured  $C_c$  for the three stabilisers mentioned in Table 3-10. The obtained values traversed at the combustor wall were compared with the pressure loss CFD predictions.

The pressure loss experimental traverses were given in mm of water. These were converted to pressure coefficient  $K$  using Equation (9)

Where  $P$  is expressed in Pa,  $\rho$  is the density of the air, and  $v$  is the velocity of the fluid.

The  $C_D$  for all the simulations was calculated as the inverse of the square root of the sum of the highest value of the coefficient  $K$  recorded upstream of the combustor plus the lowest value just before the combustor outlet. Likewise, the  $C_c$  was calculated as the inverse of the square root of the subtraction of the highest value of the coefficient  $K$  recorded upstream of the combustor minus the lowest value after the flame stabiliser.

The results obtained for the thicker plate featuring an airhole of 19.62mm were compared with Equation (15), where  $\beta$  is calculated from Equation (12)

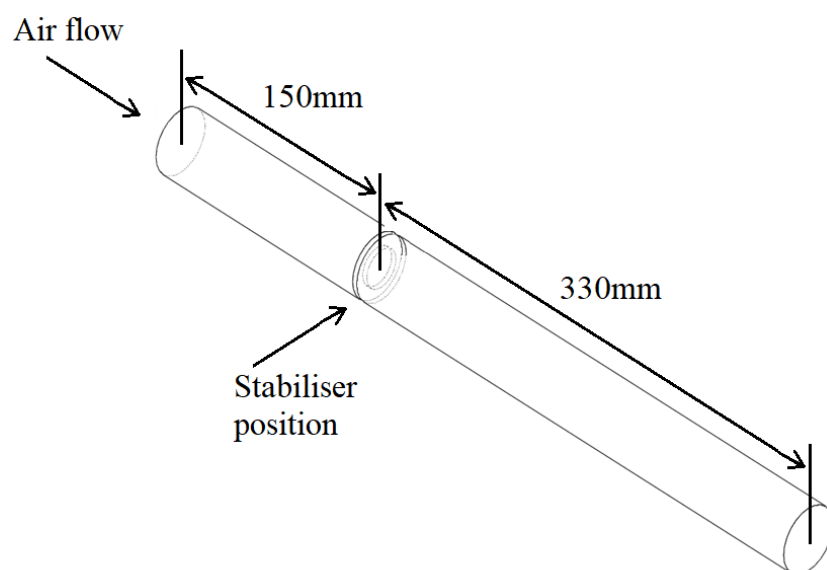


**Figure 3-13.** Computational model used for single-hole simulations (aerodynamics)

The stabilisers used for premixed combustion mentioned in Table 3-10 were firstly modelled as a single air hole of the stabiliser by simulating an octant of the air hole of the stabiliser for half of the combustor diameter (38mm), as shown in Figure 3-13 to reduce the computational time. Therefore, symmetric aerodynamic behaviour inside the combustor was assumed.

Hexahedral structured meshes were created with ANSYS ICEM, considering up to 6 million elements to verify the mesh independence.

The geometries were later evaluated for a four-hole combustor, as shown in Figure 3-14. Each model was simulated as a 90° sector of the combustor, and symmetries were used to model the four-hole mirroring the obtained simulation results. The intention of this study was to evaluate the aerodynamics effect on the combustor for a higher number of holes.

The aerodynamics of the GM2 flame stabiliser were also investigated for four mesh sizes going from 300K to 6M elements in which only air was modelled, passing through the domain under the same conditions as the other two geometries.

The discharge and contraction coefficients were obtained with simulation and compared with the available experimental data.

Inflation layers down to 0.005 mm elements were used at the walls for all cases to enhance the accuracy of the simulation and accurately predict flow separation in the region near the stabiliser. The turbulence models  $k-\epsilon$ , and the  $k-\omega$  Shear Stress Transport (SST) were compared since they have proven suitable for predicting recirculation zones and sudden contractions, as explained in 2.3.4. A pressure outlet was simulated considering 122.58 Pa for the geometries with air hole diameters of 19.27 and 19.62. The geometry featuring a 22.44 mm airhole was studied for an outlet pressure of 61.29 Pa. Both values were experimentally obtained. The discharge coefficient and contraction coefficient were calculated with the obtained traverses for the pressure loss coefficient  $K$  and compared with the experimental data. Scalable wall functions were used for the simulation as  $Y^+$  values around 30 were obtained for all the studied geometries. Figure 3-15 shows the obtained  $Y^+$  obtained for the flame stabiliser featuring an airhole of 19.27mm, and similar values were obtained for all the studied geometries.

Table 3-11 shows the boundary conditions used for aerodynamics simulations for all the studied geometries.

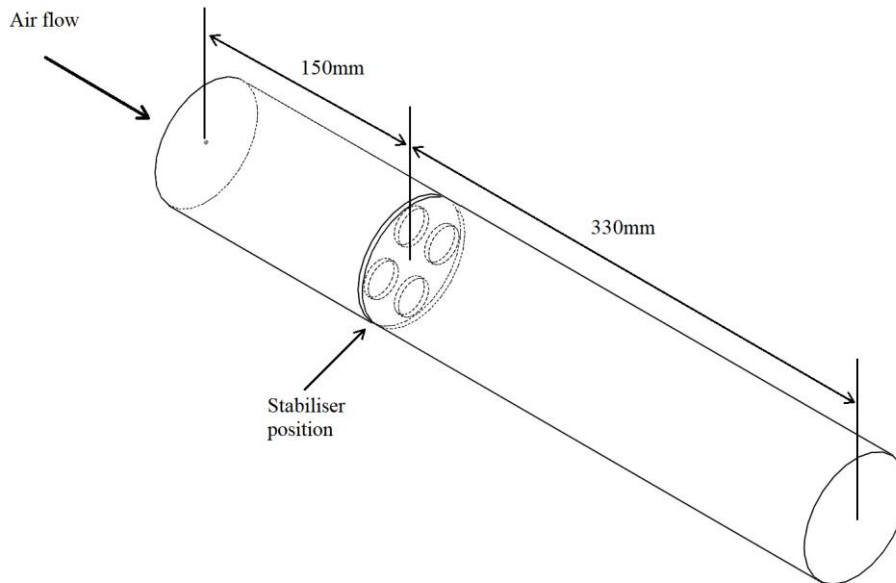


**Figure 3-14.** Computational model used for four-hole simulations

**Table 3-11.** Boundary conditions for CFD simulations of aerodynamics.

Parameter	Value
Mach number	0.047
Air inlet temperature	400°K
Air inlet mass flow rate	0.0786 kg/s
Air inlet velocity	18.84 m/s
Reference Pressure	1 ATM
Outlet pressure (19.27 & 19.62mm geometries)	122.58 Pa
Outlet pressure ( 22.44mm geometry)	61.29 Pa

As previously mentioned, the flame stabiliser experimentally used for GM1 featured a welding cord at the upstream face of the stabiliser, as shown in Figure 3-16. The air holes in this grid plate were constructed using machined cylinders, which were internally welded to the discharge face of the stabiliser but externally to the upstream face.

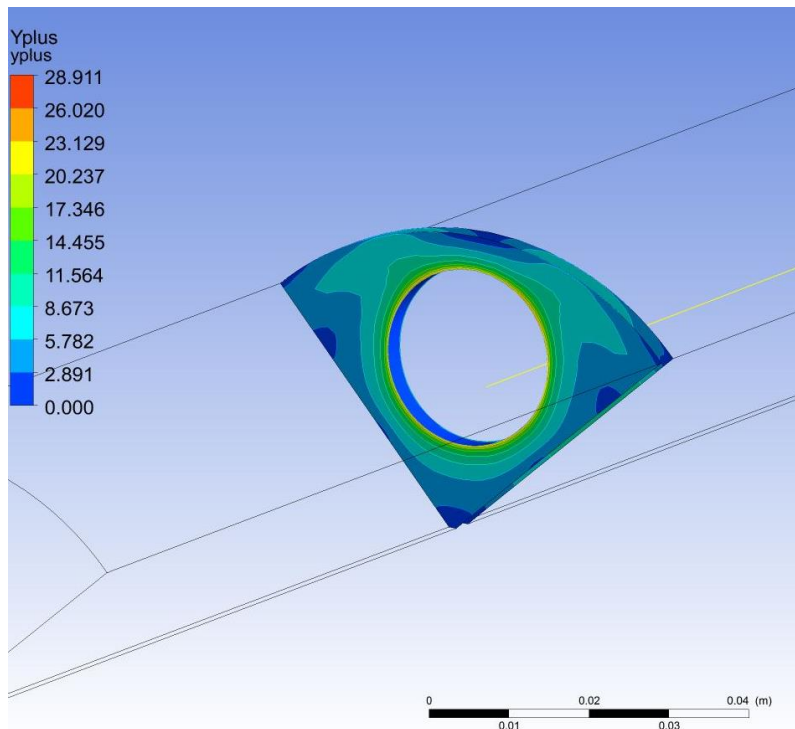


**Figure 3-15.** Y plus values for four 19.27mm hole flame stabiliser.

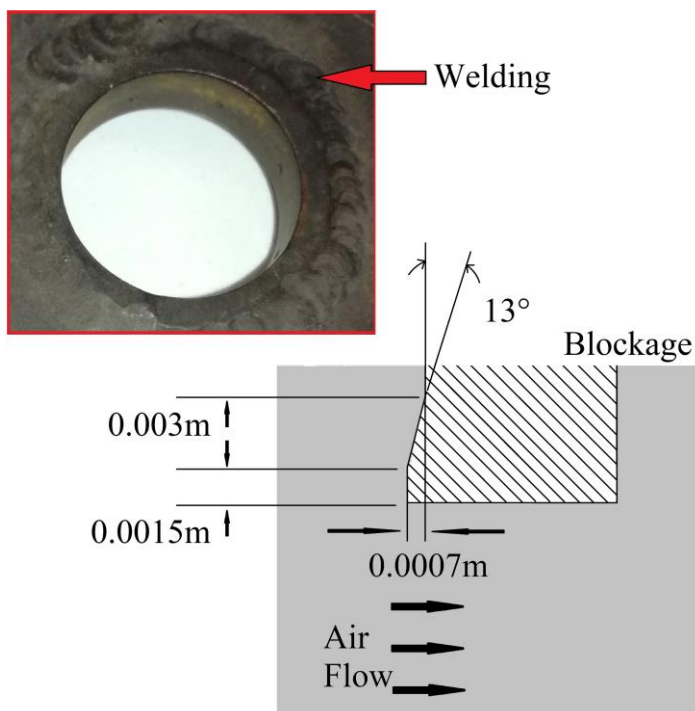


**Figure 3-16:** GM2 showing 13° weld at the stabiliser upstream air inlet

This feature was investigated to study the effect on aerodynamics. The weld was modelled as a 45° and 13° slope, as shown in Figure 3-16. A similar feature can be found at the tube entry in shell and tube heat exchangers, where the pipe inlet is welded to the rest of the device. For this study, unstructured tetrahedral meshes were created in ICEM since problems were found to simulate the slope with the blocking needed for the hexahedral mesh.

Three mesh sizes up to 2.9M elements were investigated for both angles.

The 13° welding slope at the inlet of the air holes was compared against a flat plate geometry to study the welding inlet's effect by including the fuel injection in the geometry design. Unstructured tetrahedral meshes were used, considering roughly 2M elements for both cases. For this study, GM2 was modelled featuring its fuel injection. The mesh statistics are shown in Figure 3-17, where an overall positive quality was achieved with both meshes. The turbulence model Realisable  $k-\varepsilon$  was used to model the turbulence interaction.

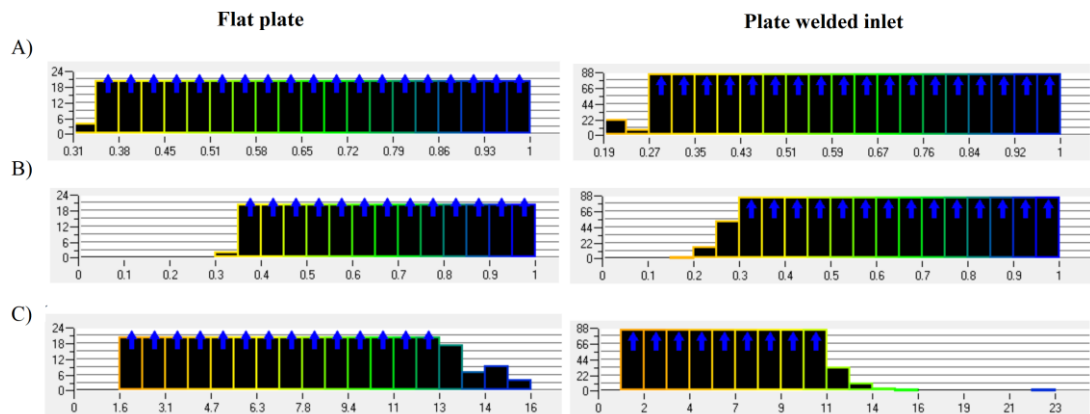


**Figure 3-17.** Mesh statistics for GM2 tetrahedral unstructured mesh: LHS) Flat plate; RHS) Welded inlet plate. A) Quality, B) Determinant, C) Aspect ratio

### 3.2.1.2 CFD study of non-reacting fuelling methods for Grid Mix flame stabiliser

Adequate and effective modelling of combustion and  $\text{NO}_x$  requires correct fuel/air mixing prediction [45]. However, sudden expansions and flow separation due to high-velocity flows can challenge the effective mixing simulation[259], as explained in 2.3.7

Three fuel injection methods were evaluated and compared using the flame stabiliser featuring four 19.62mm air holes and a stabiliser thickness of 9.53mm. The studied fuelling methods were the one featured by GM1, the annular feed of GM2 and the new addition to the GM technology GM3.

The domain for the three cases was simulated as a single hole 90° sector of the combustor using the same dimensions shown in Figure 3-14.

The computational meshes were created using ICEM ANSYS, considering a 3D domain and a structured hexahedral scheme. The geometries were initially studied using unstructured tetrahedral meshes, but issues were encountered in modelling the discrete fuel injections featured by GM2.

This study was carried out using a single mesh of around 1M elements, which was shown to obtain accurate results for the aerodynamics predictions. Hence, no mesh independence study was undertaken.

The study was carried out for a propane/air mixture using the boundary conditions shown in Table 3-12. A fuel mass flow of  $6.298 \times 10^{-4}$  kg/s was used for an equivalence ratio of 0.5. This is a usual condition for low NO<sub>x</sub> combustors [93].

All the simulations were undertaken using ANSYS CFX considering the turbulence model  $k-\epsilon$ . Steady-state adiabatic conditions at atmospheric pressure were assumed.

**Table 3-12.** Boundary conditions for CFD simulations of air/fuel mixing

Parameter	Value
Mach number	0.047
Air inlet temperature	400°K
Air inlet mass flow rate	0.0786 kg/s
Air inlet velocity	18.84 m/s
Fuel Inlet temperature	288K
Fuel inlet mass flow rate	$6.298 \times 10^{-4}$ kg/s
Equivalence ratio ( $\phi$ )	0.5
Reference Pressure	1 ATM

The runs were carried out for a first-order discretization scheme, and after convergency was achieved, they were upgraded to second order.

ANSYS CFX 19.1 did not include a straightforward way of plotting the equivalence ratio. This was calculated for an isothermal mixture using Equation (67), where the propane stoichiometric air/fuel ratio was used as 6.42. The actual A/F was calculated using Equation(68), where  $w$  is the mass fraction.

$$\phi = \frac{A/F_{Stoich}}{A/F_{Actual}} \quad (67)$$

$$\frac{A}{F_{Actual}} = \frac{\max(w \text{ Air ideal}, 0.01)}{\max(w \text{ C}_3\text{H}_8, 0.01)} \quad (68)$$

### Radial Injection (GM1)

This fuelling method GM1 was previously illustrated in Figure 3-11 A).

A mesh was created considering 1.5M elements using boundary layers of 0.01mm to successfully simulate the mixture behaviour near the walls and the fuel injection. Originally, injection points at 0.8mm cells were used to simulate

the eight fuel nozzles for a total injection area of  $4\text{mm}^2$ , considering cells of  $0.64\text{mm}^2$ . However, the mesh statistics showed a low determinant and a high aspect ratio to achieve the desired cell size, as shown in Figure 3-18. An improved mesh including a fine inflation layer for each nozzle was later developed to simulate combustion since the one used for this study was unreliable. In addition, given the geometry complexity, scalable wall functions were considered due to  $Y^+$  being less than 10 at the combustor walls. Finally, the nozzle injection velocity was calculated and set as 85 m/s.

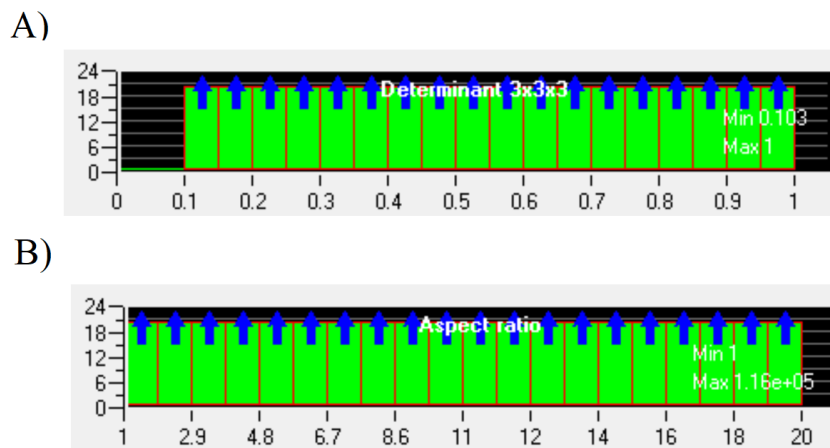


**Figure 3-18.** Mesh statistics for radial injection GM1 for 19.62mm hole stabiliser. A) determinant, B) aspect ratio

### Annular Feed (GM2)

This fuel injection method is shown in Figure 3-11 B). The size of the annular gap was set to 0.3mm, giving an injection area of  $21.7\text{mm}^2$ . A smaller 0.08mm gap was initially investigated. However, this distance was too small, and divergence was encountered with the simulation. The injection velocity was calculated to be 5 m/s for 0.3mm.

A hexahedral 1M element mesh was created for this study considering a boundary layer with a minimum element size of 0.005mm near the fuel injection and 0.01 at the walls to successfully predict fuel separation. The stabiliser hole welded inlet featured by the original design was not modelled, as the intention was to model the fluid behaviour as a flat plate.

Preliminary steady-state computations using showed divergence, so a transient simulation was carried out considering 100 timesteps for 1.0 seconds. The high-resolution advection scheme and second-order backward Euler discretization scheme were selected. The residual target for the convergence criteria was set for  $1\text{e-}6$ .

Scalable wall functions were used for this geometry as the Y+ levels were under 30.5.

The mesh statistics are shown in Figure 3-19, where the determinant was higher than 0.6, and quality of 0.28 was obtained. This mesh was later improved for the combustion runs.

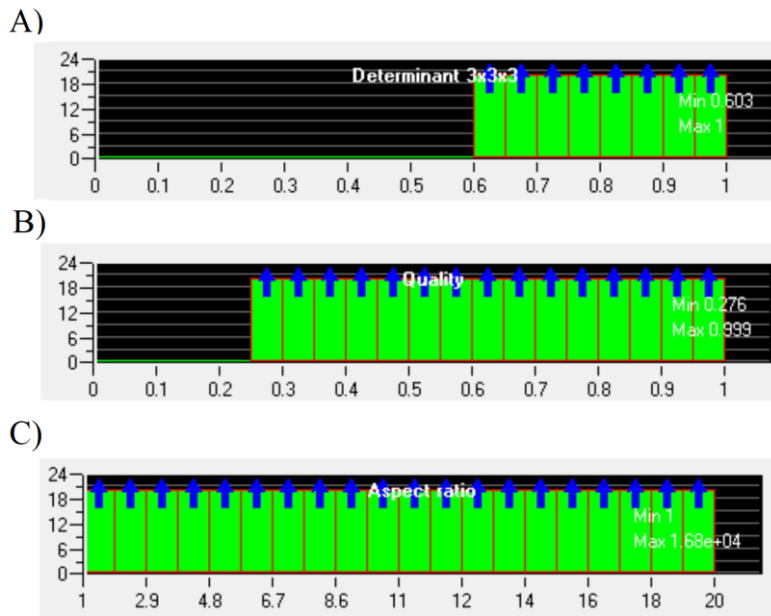


**Figure 3-19.** Mesh statistics for radial injection GM2 for 19.62mm hole stabiliser. A) determinant, B) quality, C) aspect ratio

### Centreline injection (GM3)

GM3 injects the fuel at the centreline of each air hole, as explained previously. The fuel was meant to be injected through a pipe coming from the upstream length of the combustor. However, this tube was not modelled for this non-reacting study. Instead, the fuel injection was placed midway through the stabiliser hole thickness as a single injection point, as shown in Figure 3-12 A). The sum of the eight fuel nozzle areas used in GM1 gave a total of  $4.02e^{-6} \text{ m}^2$ , which was considered for the fuel inlet in GM3, giving an injection velocity of 84.7 m/s.

A hexahedral mesh composed of 1.5M elements was used for this case. Given that the fuel injection needed a cell with a specific size in the centre of the air hole, the mesh quality was compromised, as shown in Figure 3-20. However, this issue did not affect the results. This mesh was later improved for the combustion study.

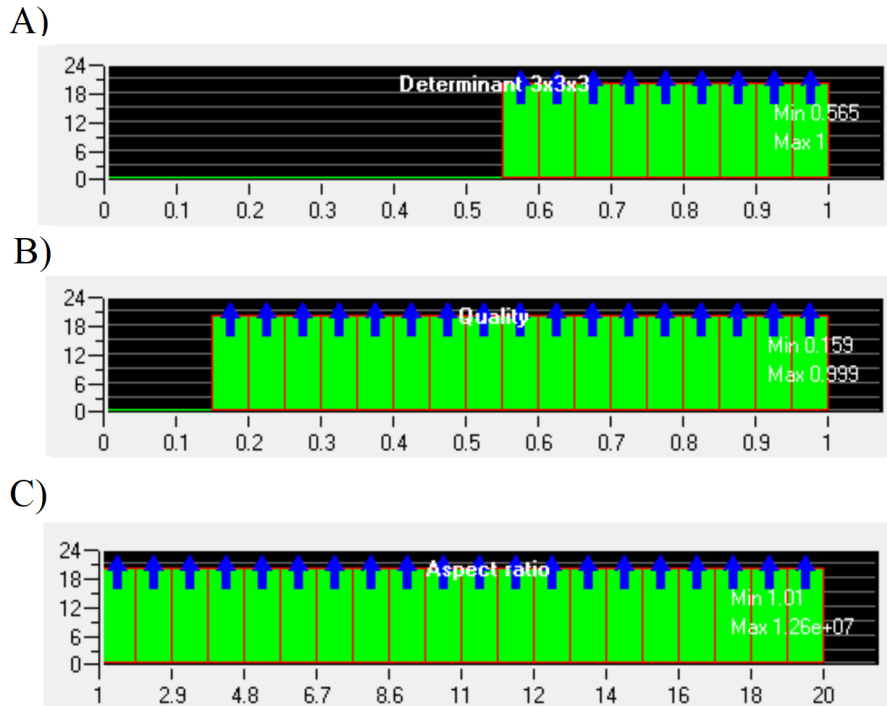


**Figure 3-20.** Mesh statistics for radial injection GM3 for 19.62mmhole stabiliser. A) determinant, B) quality, C) aspect ratio

### 3.2.1.3 CFD study of combustion for Grid Mix

As explained in the introduction of this Chapter, the software CFX was not used for the combustion simulations as the propane/air libraries needed for non-premixed combustion were not available in the software. Adding external files such as mechanisms or RIF libraries was not possible. Hence, RANS turbulence and combustion models available in ANSYS FLUENT were studied for experimental combustion results obtained for the technologies GM1 and GM2, considering the original flame stabilisers and the combustor dimensions shown in Figure 3-14. Akin to the aerodynamics and isothermal mixing studies in Chapters 5 and 6, the combustion simulations were undertaken considering 3D domains.

ANSYS FLUENT does not have the equivalence ratio as a set parameter. However, this can be obtained using the mixture fraction found in FLUENT using Equation (43)

As previously explained, the internal traverses for the experimental results were gathered for an equivalence ratio of  $\phi = 0.624$ .

Thermal efficiency was calculated using the oxygen levels as shown in Equation (69), where 100% combustion efficiency is when the measured oxygen is the

one predicted from equilibrium. The fraction of this oxygen depletion is the combustion efficiency.

$$\eta = \frac{O_{2air}\% - wO_{2actual}\%}{O_{2air}\% - O_{2eq}\%} \quad (69)$$

### 3.2.1.3.1 Validation of turbulence and combustion models for combustion for GM2 using a propane/air mixture

The original 19.62mm grid plate flame stabiliser featuring GM2 was investigated with numerical simulation. The flame stabiliser was studied using hexahedral and tetrahedral meshes. The annular gap was firstly simulated as 0.3mm as in the aerodynamics study. However, this gave an incorrect mixing and temperature distribution when using a hexahedral structured mesh, so the gap was studied as 1.0mm, showing more sensible results. Finally, the gap of 0.3mm was considered again for an unstructured hexahedral mesh used for the simulation with flamelet generated manifold.

Countless computational runs were required to find the correct parameters for this specific geometry, comparing different turbulence, combustion models, discretization schemes and solution methods. However, only the setups for the most relevant runs are described below.

The turbulence models  $k-\varepsilon$  and RNG  $k-\varepsilon$  were used for the combustion simulations. However, it was later recommended to move to Realisable  $k-\varepsilon$ , given the combustion intensity and high flows experimentally shown by GM2.

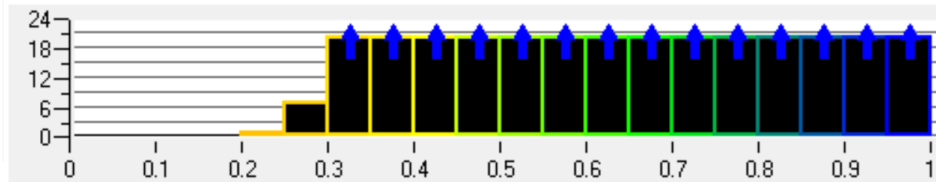
Combustion was investigated using the Eddy Dissipation Model (EDM), Chemical Equilibrium, the Steady Diffusion Flamelet (SDF) for non-premixed combustion and the Flamelet Generated Manifold for partially premixed combustion applied to diffusion combustion. Even though the Eddy Dissipation model is not recommended for diffusion flames [209], this was used as a first approach and then compared with the other models.

Adiabatic non-slip walls were used in all the simulations, given that no wall temperature profiles were taken experimentally for GM2 at the studied conditions. However, the radiation model discrete ordinates DO was used for the simulation using the EDM, Chemical equilibrium and SDF since the runs agreed better with the experiments when using radiation models.

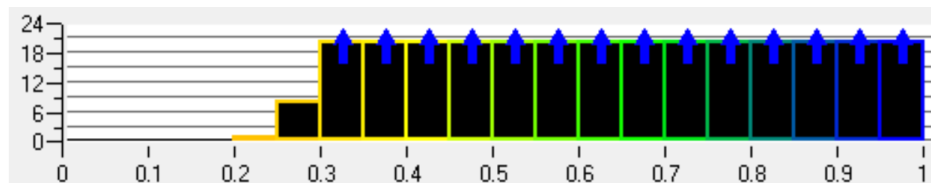
### Combustion simulations with EDM and Chemical equilibrium for non-premixed combustion

The geometry used for these simulations included the 13° welding slope investigated in Chapter 5.

A)



B)



C)

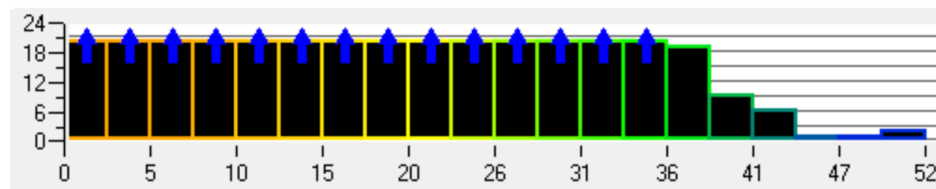


**Figure 3-21.** Statistics for unstructured tetrahedral mesh used for preliminary combustion simulations for GM2

An unstructured tetrahedral mesh of 1.7M elements was first created using ICEM for the preliminary combustion simulations for GM2 using the eddy dissipation model and chemical equilibrium for non-premixed combustion. Figure 3-21 shows the mesh statistics where quality and determinant of 0.2 were achieved. The max aspect ratio for this geometry was 52.

The turbulence model  $k-\epsilon$  was used for the EDM combustion model simulation. In addition, the turbulence model of RNG  $k-\epsilon$  with enhanced wall treatment was used for the simulations using chemical equilibrium. It was then discovered that RNG  $k-\epsilon$  [260] was suitable for rotatory flows like swirlers but not plate stabilisers.

A SIMPLE scheme of the pressure velocity coupling was used for the EDM simulation, considering a first-order upwind discretization, and then the simulations were upgraded to second order. Divergence was encountered for a Coupled scheme. This was not the case for EDM simulation, which was carried out with the Coupled method and spatial discretisation of second-order. Table 3-13 shows the under relaxation factors used for the simulations of both combustion models.

**Table 3-13.** Under-relaxation factors for combustion simulation for GM2 using EDM and Chemical equilibrium

<b>Combustion model</b>	<b>EDM</b>	<b>Chem eq</b>
<b>Solution control</b>	<b>Value</b>	<b>Value</b>
Pressure	0.3	0.5
Density	0.25	0.2
Body Forces	0.8	0.8
Momentum	0.7	0.5
Turbulence Kinetic Energy	0.8	0.75
Turbulent Dissipation rate	0.8	0.75
Turbulent Viscosity	1	1
Energy	1	0.75
Temperature	0.9	0.75
Mean Mixture fraction	0.75	0.75
Mean fraction Variance	0.75	0.75
Discrete ordinates	1	1

### **Combustion simulation with SDF for non-premixed combustion**

The lack of agreement obtained with EDM and chemical equilibrium led to the development of a hexahedral structured mesh considering the whole four-hole combustor since it was thought that the combustion was not symmetric, which probably affected the combustion results. The geometry was modelled as a flat plate.

A structured mesh was created for a whole four-hole domain using 2.8M hexahedral elements, as shown in Figure 3-22, since it was thought that the temperature distribution was not going to be uniform inside the combustor. A fine inflation layer was included near the fuel injection to allow a smooth interaction with the rest of the domain, as shown in Figure 3-23. The fuel injection was modelled using elements length up to 0.005mm. The mesh statistics are shown in Figure 3-24, where a minimum determinant of 0.62 was achieved, as illustrated in Figure 3-24A). A high aspect ratio with a maximum of

1500 was obtained (Figure 3-24B), given the nature of the geometry, which required discrete elements near the fuel injection.

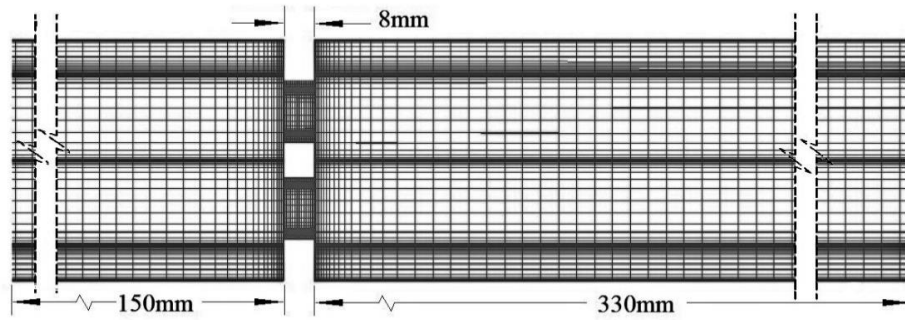


**Figure 3-22.** Hexahedral structured mesh used in combustion simulation for GM2

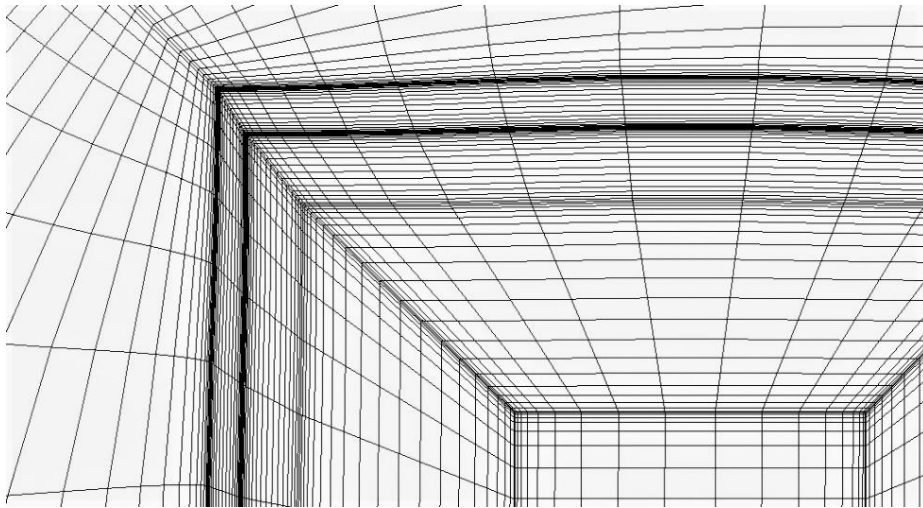
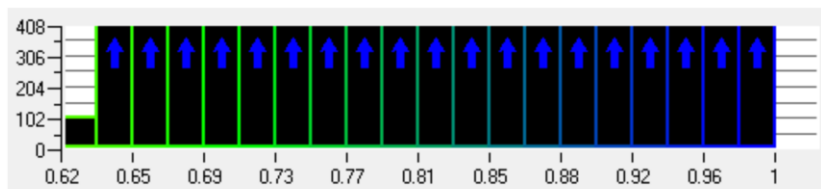


**Figure 3-23.** Inflation layer at fuel injection for hexahedral mesh used in combustion simulation with SDF for GM2

A)



B)

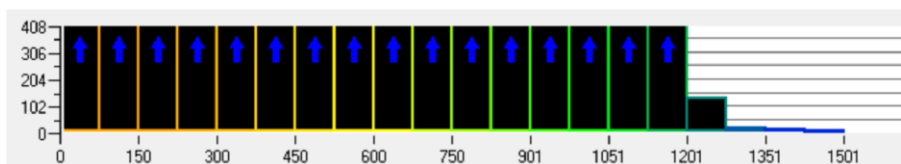


**Figure 3-24.** Statistics for structured hexahedral mesh used in combustion simulation for GM2. A) Determinant, B) Aspect ratio

The turbulence model realisable  $k-\epsilon$  was also investigated to help obtain a better turbulence interaction.

Two different kinetic mechanisms were compared for the steady diffusion flamelet (SDF) model to study the effect of chemistry on the simulation: A detailed mechanism for air/propane combustion developed by Peters [261]. composed of 107 species and 31 reactions available on the website of CERFACS. The mechanism is attached in Appendix J. And the mechanism for propane combustion available in ANSYS FLUENT, which contains 37 species [262]. Both mechanisms showed very similar results and no alterations in the temperature.

A PDF table composed of 20 species was considered for a non-adiabatic mixture, assuming a standard Schmidt number of 0.85. The radiation model Discrete ordinates DO was selected.

The SDF simulations were carried out using the SIMPLE scheme. An exhaustive search was conducted to find the best discretization scheme and solution methods. The runs were undertaken first using a first-order upwind spatial discretization, and once the solution reached convergence, the simulation was upgraded to the second order. The boundary conditions for the SDF simulations are summarised in Table 3-14.

**Table 3-14.** Boundary conditions used for combustion simulations for GM2 using SDF

Parameter	Value
Air inlet mass flow	0.0784 kg/s
Air inlet temperature	400 K
Air inlet turbulence intensity	6%
Air inlet hydraulic diameter	76mm
Fuel inlet mass flow	0.00312
Fuel inlet temperature	288
Fuel inlet turbulence intensity	10%
Fuel inlet hydraulic diameter	2mm
Walls heat flux	0 watts/m <sup>2</sup>
Pressure outlet gauge pressure	0 Pa
Pressure outlet backflow temperature	1300K

Under-relaxation values were applied to the simulations to obtain a better convergence. The values for the SDF simulations are shown in Table 3-15. In addition, the residuals monitors were set to 1e-12 for the combustion simulations using SDF.

**Table 3-15.** Under-relaxation factors for combustion simulation for GM2 using SDF

<b>Solution control</b>	<b>Value</b>
Pressure	0.2
Density	0.25
Body Forces	0.8
Momentum	0.5
Turbulence Kinetic Energy	0.8
Turbulent Dissipation rate	0.8
Turbulent Viscosity	1
Energy	1
Temperature	1
Discrete ordinates	1
Mean Mixture fraction	1
Mean fraction Variance	0.9

This simulation was also compared with the adiabatic flame temperature calculated using Gaseq for a propane/air mixture for an inlet temperature of 400K and an equivalence ratio of  $\phi=0.624$ .

NO<sub>x</sub> was calculated for SDF as a post-processing operation once the simulation converged. The options for prompt and thermal NO were selected. Considering one source of fuel injection, a carbon balance of 3 for a mixture of propane and air and an equivalence ratio of 0.624 for the prompt option. To calculate the thermal NO, a partial equilibrium for O was used. No calculation of the radical OH was carried out given its low effect in the NO<sub>x</sub> calculation. Finally, 50 PDF points were modelled considering the global maximum temperature.

#### **Combustion simulation with FGM for non-premixed combustion**

An unstructured hexahedral mesh of 1M elements and 2.6M nodes was developed for the combustion simulations using the meshing software in

FLUENT 19.2. The mesh was designed considering the element sizes shown in Table 3-16, considering a growth rate of 1.2. Five layers were used near the walls to predict fluid behaviour successfully. A 90° sector of the combustor, considering a single stabiliser hole, was used for this mesh to reduce computational time. The injection area was 73.9mm<sup>2</sup> for a propane injection of 22.1m/s.

Early results showed a miss prediction when using the quarter of the combustor. However, when moving to an unstructured polyhedral mesh, the results showed a slight difference between the full combustor and the quarter, so it was decided to model a single hole 90° sector of the combustor. This mesh was used for the simulations using the Flamelet Generated Manifold model explained in the following lines

**Table 3-16.** Element sizes used for structured hexahedral mesh used in combustion simulation with FGM for GM2

<b>Boundary</b>	<b>Cell size</b>
Wall (upstream and downstream)	1mm
Contraction wall	0.7mm
Fuel injection	0.03mm
Domain	1.5mm

Only the kinetic mechanism proposed by Peters [261] was used for the simulations using the Flamelet Generated Manifold (FGM) combustion model since it was more updated than the available in FLUENT.

The FGM simulations were undertaken using the Coupled scheme considering only first-order upwind for the spatial discretization. Upgrading the simulations to second order increased the computational time considerably and showed less agreement with the experimental data. The pseudo transient under-relaxation was used to allow convergence and for stabilisation purposes. The boundary conditions used for the simulation are shown in Table 3-17.

The values for the under-relaxation factors used in the FGM simulations are shown in Table 3-18. The residual monitors for the convergence were set to 1e-06.

**Table 3-17.** Boundary conditions used for combustion simulations for GM2 using FGM

<b>Parameter</b>	<b>Value</b>
Air inlet mass flow	0.0196 kg/s
Air inlet temperature	400 K
Air/fuel inlet turbulence intensity	5%
Air/fuel inlet turbulent viscosity ratio	10
Fuel inlet mass flow	0.00078 kg/s
Fuel inlet temperature	288
Walls heat flux	0 watts/m <sup>2</sup>
Pressure outlet gauge pressure	0 Pa
Pressure outlet backflow temperature	300K

NO<sub>x</sub> was modelled by selecting the routes of Thermal and Prompt NO. NO<sub>x</sub> reduction was not studied.

Various configurations were studied for the thermal NO<sub>x</sub> formation. The desired equivalence ratio of 0.624 and a fuel carbon number of 3 were chosen for the Prompt formation parameters. The turbulence interaction was also studied considering the mixture fraction.

**Table 3-18.** Under-relaxation factors for combustion simulation for GM2 using FGM

<b>Solution control</b>	<b>Value</b>
Pressure	0.75
Density	0.25
Body Forces	1
Momentum	0.25
Turbulence Kinetic Energy	0.75
Turbulent Dissipation rate	0.75
Turbulent Viscosity	1
Temperature	0.75

### 3.2.1.3.2 Validation of turbulence and combustion models for combustion for GM1 using a propane/air mixture

The original GM1 22.11mm hole flame stabiliser featuring a plate thickness of 5.3mm was studied with RANS CFD. Since symmetric behaviour was encountered between the air holes for simulations of GM2, the GM1 domain was modelled as a 90° sector of the combustor.

The radial fuel injections were modelled as 1.2mm diameter, placed equispaced in the periphery of the airholes midway of the stabiliser plate as for the original geometry.

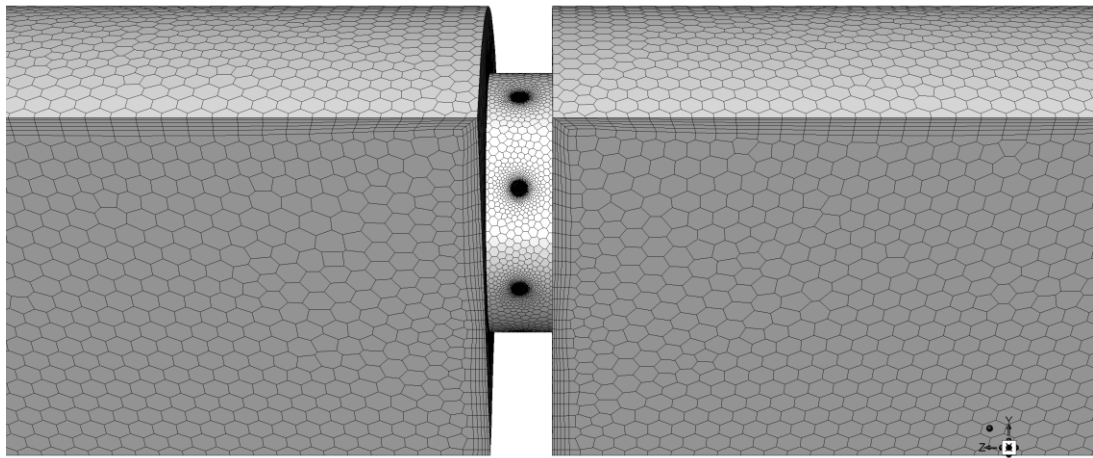


**Figure 3-25.** Hexahedral unstructured mesh used for the simulation of GM1

A hexahedral unstructured mesh was developed utilising the meshing software of ANSYS FLUENT, considering 400K elements. The mesh was modelled as shown in Figure 3-25. The mesh statistics are shown in Table 3-19, showing the cell sizes for the different boundaries. An aspect ratio of 24 and an orthogonal quality of 0.42 was achieved.

**Table 3-19.** Element sizes used for structured hexahedral mesh used in combustion simulation for GM1

Boundary	Cell size
Wall (upstream and downstream)	1.2mm
Contraction wall	1mm
Fuel injection	0.03mm
Domain	1.5mm

The simulation boundary conditions are shown in Table 3-20. The fuel injections were modelled as eight separate mass flow inlets to deliver the amount mass fraction needed for an equivalence ratio of  $\phi = 0.6$ .

**Table 3-20.** Boundary conditions used for the combustion simulation of GM1

Parameter	Value
Air inlet mass flow	0.0196 kg/s
Air inlet temperature	400 K
Air/fuel inlet turbulence intensity	5%
Air/fuel inlet turbulent viscosity ratio	10
Equivalence ratio	0.6
Single nozzle mass flow	9.6e-5 kg/s
Fuel inlet temperature	288
Walls heat flux	0 watts/m <sup>2</sup>
Pressure outlet gauge pressure	0 Pa
Pressure outlet backflow temperature	300K

The turbulence model realizable  $k-\epsilon$  was used considering enhanced wall treatment.

The simulation was carried out with the combustion model FGM. Akin to the other GM technology, a PDF table composed of 20 species was developed. An updated mechanism for propane/air combustion generated by Depcik was used [263]. This detailed kinetic mechanism has 107 reactions aimed at jet propulsion applications. Radiation was not studied for this geometry.

The simulation was carried out using the Coupled pseudo transient solver. Spatial discretization of the first order was considered. Table 3-21 shows the under-relaxation factors used for the simulation to aid convergence.

NO<sub>x</sub> was calculated as a post-processing operation for a converged solution. Prompt and thermal NO were selected. To calculate thermal NO, instantaneous O was considered. The turbulence interaction was considered for the mixture fraction.

**Table 3-21.** Under-relaxation factors for combustion simulation for GM1

<b>Solution control</b>	<b>Value</b>
Pressure	0.75
Density	0.25
Body Forces	1
Momentum	0.25
Turbulence Kinetic Energy	0.75
Turbulent Dissipation rate	0.75
Turbulent Viscosity	1
Temperature	0.75

#### **3.2.1.4 CFD study of reacting fueling methods for Grid Mix flame stabilisers**

GM1, GM2 and GM3 technologies were studied for a reacting mixture and compared to find the best fuelling method considering temperature distribution and NO<sub>x</sub>.

GM1 and GM2 were compared using hexahedral unstructured meshes using the combustion model FGM. GM3 is compared to the other two technologies using a hexahedral mesh and the combustion model SDF since attempts to use a similar mesh and the combustion model FGM for this model were unsuccessful.

The equivalence ratio used for the experiments  $\phi = 0.624$  was considered for the simulations using the boundary conditions in Table 3-17.

The GM2 technology was studied using the results obtained for the simulation with the FGM model.

#### **GM1 for combustion (19.62mm stabiliser)**

GM1 was evaluated for the same stabiliser air hole considered for GM2 of 19.62mm and a plate thickness of 5.3mm. Eight fuel nozzles of 1.9mm diameter were modelled to get a similar injection area used for the GM2 simulation of 21.8mm<sup>2</sup>. A hexahedral unstructured mesh made of 1M elements was created with the meshing software of FLUENT, considering cells of 0.03mm in the fuel injections to successfully model the fuel interaction. An orthogonal quality of 0.5 and a maximum aspect ratio of 18 were obtained for this mesh.

The turbulence model realisable  $k-\varepsilon$  was used for this simulation, considering enhanced wall functions since the minimum  $Y^+$  obtained was 50 near the stabiliser.

Combustion was modelled using FGM for diffusion combustion using a PDF table of 20 species. No radiation was modelled.

The simulation was carried out using the coupled solver for first-order upwind, a pseudo-transient scheme and the under-relaxation factors shown in Table 3-22 to aid convergence. Convergence residuals were set to  $1.0e^{-6}$

**Table 3-22.** Under-relaxation factors for combustion simulation for GM1 using FGM

<b>Solution control</b>	<b>Value</b>
Pressure	0.75
Density	0.25
Body Forces	1
Momentum	0.25
Turbulence Kinetic Energy	0.75
Turbulent Dissipation rate	0.75
Turbulent Viscosity	1
Temperature	0.75

### **GM3 for combustion (19.62mm stabiliser)**

A structured hexahedral mesh was developed for GM3 using ICEM considering 1.5M elements. The maximum orthogonal quality was 0.15, and the maximum aspect ratio was 856 obtained near the fuel injections. The fuel injections were modelled as 3.5mm diameter nozzles at the end of four long pipes coming from the inlet of the 152mm upstream length of the combustor, injecting the fuel in the centre of each stabiliser hole in the middle of the thickness of the plate.

The turbulence model realisable  $k-\varepsilon$  and enhanced wall functions were also considered for this simulation. The Max  $Y^+$  was 18 near the stabiliser and at the inlet of the injection pipes.

Combustion was modelled using the model SDF for non-premixed combustion. A PDF of 20 species was developed. No radiation models were considered.

The SIMPLE pressure-velocity coupling was selected for a first-order upwind scheme. The simulation was upgraded to second-order once convergence was achieved. The under relaxation factors shown in Table 3-23 were used to help achieve convergence. Convergence residuals were set to  $1.0e^{-6}$ .

**Table 3-23.** Under-relaxation factors for combustion simulation for GM3 using SDF

<b>Solution control</b>	<b>Value</b>
Pressure	0.2
Density	0.7
Body Forces	0.9
Momentum	0.6
Turbulence Kinetic Energy	0.7
Turbulent Dissipation rate	0.7
Turbulent Viscosity	0.9
Temperature	1

#### **3.2.1.4.1 Numerical combustion analysis for GM1 using a hydrogen/air mixture**

The GM1 concept was used in the flame stabiliser featuring a hole size of 19.62mm and a plate thickness of 9.53mm for a 76mm combustor used for GM2. This time evaluating its use in a hydrogen/air mixture for the same combustion intensity used for the experimental results of  $28\text{MW}/\text{m}^2\text{bar}$ , considering the same outlet temperature of 1800K achieved with propane. The software Gaseq was used to find the equivalence ratio needed to achieve the requested temperature. A pure  $\text{H}_2$  and air mixture composed of 21%  $\text{O}_2$  and 79%  $\text{N}_2$  was set for a product temperature of 1809K reached with the propane simulation. An equivalence ratio of 0.55 was obtained for the new mixture, which was used to compute the fuel mass fraction for the simulation boundary conditions.

The same geometry and mesh used to compare the three fuel injection methods for combustion were used for this study. The original GM1 stabiliser featured 1.2mm nozzles, too small for hydrogen combustion, giving sonic velocities for the needed equivalence ratio (360m/s). The fuel velocity for 1.8mm nozzles was 182 m/s which was still high, but it allowed more sensible results.

Table 3-24 shows the boundary conditions used for this simulation. The fuel nozzles were modelled independently, considering a hydrogen mass flow of  $3.941 \times 10^{-5}$  kg/s for a total of  $3.153 \times 10^{-4}$  kg/s.

**Table 3-24.** Boundary conditions used for combustion simulations for GM1 for a hydrogen/air flame

Parameter	Value
Air inlet mass flow	0.0196 kg/s
Air inlet temperature	400 K
Air/fuel inlet turbulence intensity	5%
Air/fuel inlet turbulent viscosity ratio	10
Equivalence ratio	0.548
Fuel mass flow	$3.153 \times 10^{-4}$ kg/s
Single nozzle mass flow	$3.941 \times 10^{-5}$ kg/s
Fuel inlet temperature	288
Walls heat flux	0 watts/m <sup>2</sup>
Pressure outlet gauge pressure	0 Pa
Pressure outlet backflow temperature	300K

The turbulence model of realisable  $k-\epsilon$  and scalable wall functions were used for the viscous model.

No radiation models were considered for the simulation since the walls were considered adiabatic.

The combustion model FGM for partially premixed combustion was utilised for a diffusion flame. The kinetic mechanism used for the development of the PDF table was developed by Konnov [264], which contains specific updates to transport data, helping improve flame calculations. A mixture of pure hydrogen and air composed of 21% O<sub>2</sub> and 79% N<sub>2</sub> was considered. Like the propane simulations, the air was modelled at 400K and fuel at 288K. Twenty species were modelled for the PDF table. This mechanism is included in Appendix I.

First-order spatial discretization for a Coupled pseudo transient pressure-velocity coupling was selected. The under-relaxation factors shown in Table

3-25 were used to help achieve convergence. Convergence residuals were set to 1.0e-12.

**Table 3-25.** Under-relaxation factors for combustion simulation for GM1 for a hydrogen/air flame

<b>Solution control</b>	<b>Value</b>
Pressure	0.75
Density	0.25
Body Forces	1
Momentum	0.25
Turbulence Kinetic Energy	0.75
Turbulent Dissipation rate	0.75
Turbulent Viscosity	1
Temperature	0.75

NO<sub>x</sub> was modelled using the FLUENT model considering Fenimore and thermal NO<sub>x</sub>. A single fuel stream of H<sub>2</sub> was selected. Thermal NO<sub>x</sub> was calculated using Instantaneous O and partial equilibrium OH. Prompt NO<sub>x</sub> was obtained for an equivalence ratio of 0.548. Lastly, the turbulence interaction was calculated with the mixture fraction of the PDF.

#### **3.2.1.4.2 Influence of a thicker stabiliser plate in NO<sub>x</sub> emissions for GM1 using a hydrogen/air mixture**

Given the high levels of NO<sub>x</sub> observed in the GM1 study for a hydrogen flame, this technology was lastly investigated for a thicker flame stabiliser. As mentioned in Chapter 2, York et al. [43], [44] developed a hydrogen combustor with a stabiliser thickness of approximately seven times the hole size diameter, which achieved ultra-low NO<sub>x</sub>. This concept was applied to GM to solve the issue of high NO<sub>x</sub> featured with a hydrogen flame, but also to test this concept at a high combustion intensity of 28MW/m<sup>2</sup>bar and a M=0.047.

The geometry was modelled for the studied 76mm combustor using the same dimensions considered for the hydrogen study of GM1, changing only the stabiliser thickness. The plate width was modelled 7D for a 19.62mm stabiliser hole diameter, so the stabiliser thickness was considered 137mm.

The injection was modelled as eight 1.8mm radial nozzles placed in the periphery of each hole 4.8mm from the stabiliser inlet face, as shown in Figure 3-12 B).

An unstructured mesh of 500K hexahedral elements was constructed using the exact element sizes for GM1 shown in Table 3-19.

The boundary conditions and simulation parameters used for the hydrogen study for GM1 were used in this one.

### **3.3 Experimental setup for domestic fires**

The experimental tests were carried out in laboratory G.03f of the Energy building at the University of Leeds for three different domestic fire appliances.

The laboratory was arranged before the tests to comply with the University's requirements for health and safety. Relevant reports and risk assessments were carried out.

All fires were investigated for dual fuel applications for natural gas and hydrogen.

The hydrogen was provided with a purity of 99.9% in 20L cylinders from external suppliers.

The University of Leeds supplied the natural gas.

#### **3.3.1 Rig concept**

The lab G.03f was conditioned accordingly before the experiments.

Hydrogen and natural gas pipes were installed in the lab following the diagrams shown in Figure 3-26. Improvements were made to the previously installed line allowing for testing of fires at plenum pressures up to 20 mbar. The removal of previously installed bayonet fittings for both H<sub>2</sub> and NG lines was required, and these were replaced by rigid piping. The bayonet fittings were easy to install, but a pressure loss was observed between the fuel manifold and the fire setup. The new piping setup was controlled by a series of valves brand Swagelok, allowing fuel gases and compressed air control.

The emissions produced for the three different fires were recorded and analysed using a HORIBA PG-350E portable gas analyser, recording every 10 sec (0.1 Hz). The device allowed the study of NO<sub>x</sub> ppm, SO<sub>2</sub> ppm, CO ppm, CO<sub>2</sub> (vol%) and O<sub>2</sub> (vol%). Then the obtained values were processed using a

Keysight Technologies U2355A data logging system, featuring 64 channels at a sampling rate of 25 kS/s.

Temperatures were measured using exposed junction 3mm type K thermocouples, and the measurements were sent to a thermocouple receiver connected to the data logger.

Then the data was sent to a computer with Intel Core-i5-8400 Processor, 8GB 2666 MHz DDR4 non-ECC RAM and processed using LabVIEW.

The NO<sub>x</sub> emissions were requested to be obtained in mg/kWh units. To convert the NO<sub>x</sub> ppm to mg/kWh at a reference oxygen level of 0%, Equation (70) was used

$$NO_x \text{ 0\% } O_2(\text{ppm}) = NO_x \text{ measured } (\text{ppm}) \times \left[ \frac{20.9\%}{20.9\% - O_2 \% \text{ actual}} \right] \quad (70)$$

The thermal efficiency was obtained following the next procedure:

First, the wet oxygen was converted into dry oxygen levels using Equation (71)

$$O_{2 \text{ dry}} = O_{2 \text{ wet}} / (1 - H_2O\%) / 100 \quad (71)$$

Then the air to fuel ratio  $A/F_{(\text{mass})}$  was obtained using Equation (72).

$$y = 0.0213 x^4 - 0.7505 x^3 + 9.3515 x^2 - 43.88 x + 105.77 \quad (72)$$

Where

$$y = A/F_{(\text{mass})}.$$

$$X = O_{2 \text{ dry}}$$

This formula was obtained from empirical data where  $R^2=0.9951 > 0.95$ .

Then the thermal efficiency can be calculated:

$$\eta_T = 1 - \left[ \left( \frac{A}{F_{\text{mass}}} + 1 \right) \left( \frac{C_p T_{\text{diff}}}{H_s} \right) \right] \quad (73)$$

Where

$C_p$  is the specific heat capacity of flue gases, 2.08 kg/°C

$T_{\text{diff}}$  was the temperature difference between ambient and ambient temperature expressed in °C.

$H_s$  is the gross calorific value, 141.8 MJ/kg [265]

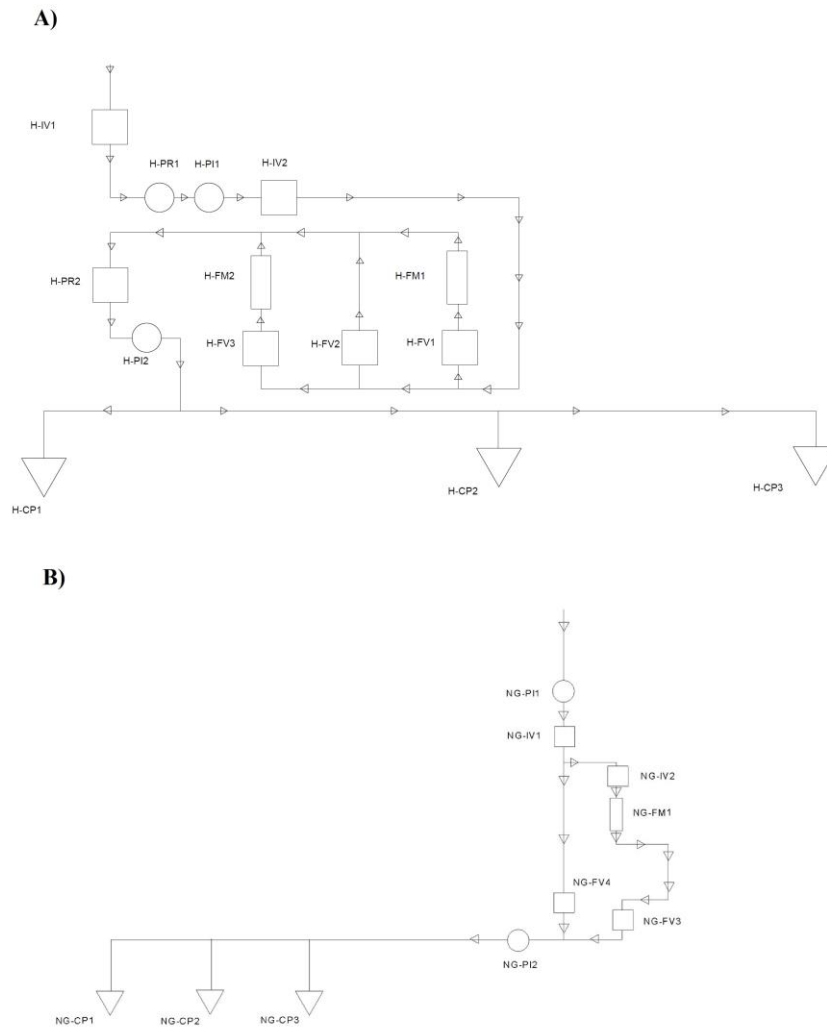


**Figure 3-26.** Schematics for: A) Hydrogen line; B) Natural gas line installed in G.03. H=hydrogen; NG=natural gas; IV=isolation valve; PR=pressure regulator; FV=flow valve; FM=flow meter

The tests were carried out by two users following the next procedure:

### Hydrogen tests

The initial setup considered all valves and hydrogen circuits closed. Next, the isolation valve H-IV1 was opened. Then, one user gradually opened the pressure regulator H-PR1 until a pressure of 2 bar was shown.

The other user then used a propane torch to ignite the fuel ports in the desired fire while the first user opened the valve H-FV2. The torch operator counted 3 seconds and confirmed ignition. The test was abandoned if the ignition was not approved, the lines were purged, the issue was investigated, and the test restarted.

If the ignition was successful, a pressure of 20 mbar should be displayed in H-P12. Then the flow meter was adjusted to the required mass flow. The flame

was left to stabilise for approximately 20 minutes. After this, measurements were recorded, and photographs were taken. To finish the test, the valves were closed in reverse order

### Natural gas tests

Akin to the hydrogen tests, the initial configuration was considering all the valves closed. Next, the main switch for the natural gas supply was activated. Then the isolation valve NG-IV1 was opened in the line. A user then ignited the torch and directed the flame to the fuel ports. Next, the other user opened the valve NG-FV4 and waited for the torch operator to confirm ignition. If the ignition was not confirmed, the valves were immediately closed, the lines purged, and the test restarted. The rest of the procedure was the same as with H<sub>2</sub>.

The lab had a ventilation opening used for a cone calorimeter, and exhaust pipes were installed in the fires to direct the exhaust gases. The lab set-up can be seen in Figure 3-27, where the three fires are shown.

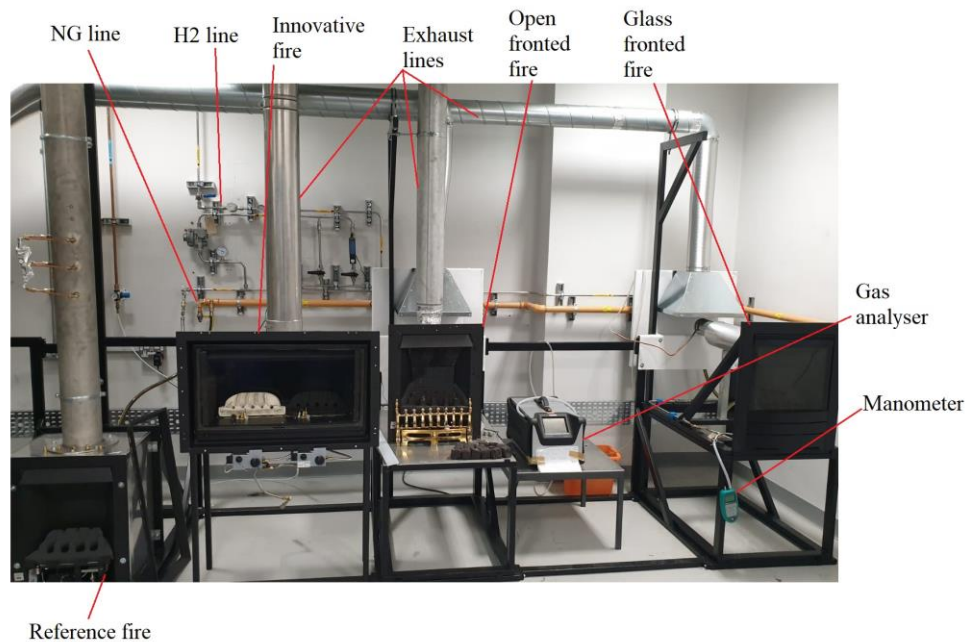


**Figure 3-27.** Rig set up in lab G.03f Energy building used in Hy4Heat project.

An additional reference open-fronted fire is shown in the picture to working only with natural gas.

The pressure in the fires was measured using a differential manometer Kane 3200 by connecting a hose to the fuel plenum in the fire burner.

The flue gas flow rate for hydrogen and natural gas was measured using a Bronkhorst mass flow meter. It was established as 0.5L/min. However, it was modified according to the requirements of the test.

Safety tests were carried out for the three fires as part of the initial procedure and according to BEIS guidelines for milestone 3 of the Hy4Heat project WP4. These tests were undertaken for leak testing, pilot ignition time, pilot thermocouple cut-off and temperature measurement on user-touchable surfaces.

### 3.3.1.1. Leak testing

One of the requirements for milestone 3 of the project was for all the gas carrying components to demonstrate a pressure tightness (leak testing) of 50 mbar of H<sub>2</sub> or 150 mbar compressed air minimum. British standards BS-7977 [266] state that every fire's volumetric leak rate must be under 100 cm<sup>3</sup> /hr to comply with the regulations. Compressed air was used for the tests.

The fuel nozzles in the burner of the fires and the pilot fuel port were covered using a mixture of adhesive foil tape and ceramic paste to test the line thoroughly. Compressed air was supplied to the fire line using the hydrogen for which the fuel was disconnected and the line completely drained. The fuel supply was isolated using a butterfly valve which allowed only the necessary amount of compressed to enter the system. Then, after leaving the pressure to settle for a minute, the test took place for 2 continuous minutes, so the volumetric leak rate could be calculated for a known volume, as shown in Equation (74). Pressure readings were taken using a KANE 3200 differential manometer connected to a pressure nipple in the fuel supply line.

$$Q_V = V \frac{dP}{P_{atm} dt} \quad (74)$$

Where  $Q_V$  is the volumetric leak rate,  $V$  is the tested volume within the line,  $dP$  is the change in pressure over a 2 minutes test period,  $P_{atm}$  is the atmospheric pressure, and  $dt$  is the change in time considered as 120 seconds. The total measured volume was considered from outside the closed valve to the fuel plenum, where all the intermediate components were tested.

### 3.3.1.2. Pilot ignition test

The requirement for passing milestone 3 according to the British standards BS-7977 was to demonstrate an interrupted flame for at least 20 seconds after half

opening the control valve<sup>5</sup> and keeping it open for half the time. If the test was successful, the valve would open fully and effectuate a “cross light” by sending the flame to the main burner.

The pilot for the open-fronted fire tests was modified to include a 3mm mineral insulated thermocouple next to the fuel port protruding approximately 45mm from the burner base, as shown in Figure 3-28. The 90° bend spark rode was moved to create an electric arc with the outside circumference of the fuel injector to achieve an effective flame. The thermocouple tip was bent several times toward the flame to obtain a successful, lasting flame. To carry out the tests, a fire was first achieved, and the control knob was left pushed open until the thermocouple tip had become hot enough to keep the magnetic valve in the pilot system open.



**Figure 3-28.** Prototype pilot used for the fires in the Hy4Heat project

A 0.05  $\Omega$  resistor was installed in series downstream of the thermocouple to aid the thermocouple cut-off safety requirement for the glass-fronted fire.

However, this reduced the thermocouple’s warm-up response, meaning that the valve had to be left open for longer before the pilot flame stayed on.

The innovative fire features two separate pilot systems for the two burners needed (this will be discussed further). This fire igniter featured the same configuration used for the glass-fronted fire, and for the tests, only one pilot was tested in two locations.

---

<sup>5</sup> The pilot knob ignited the pilot after turning it and hearing a first “click” (halfway), and another one ignited the burner (fully open)

### 3.3.1.3. Thermocouple Cut-off test

If there was an accidental flame extinction, the gas supply had to be cut off within 60 seconds after the flame blew off. For this to happen, the pilot system magnetic valve was activated by a voltage from the thermocouple when no flame was detected or when the rod was cold enough to trigger the valve. To undertake this test, the fires were operated at full pressure (20 mbar), so the temperature of the thermocouples increased to a value that allowed regular operation.

Hydrogen was used for this test. The fuel supply was instantaneously cut-off by closing the valve in the supply line, and the time from this point until the magnetic valve in the pilot was closed was taken. The moment the magnetic valve was closed was characterised by a distinctive click from the valve that could be sensed and heard.

### 3.3.1.4. User-touchable surfaces temperature tests

The last test measured the temperature for all the user-touchable surfaces in the three fires as requested in the BS-7977. The readings were obtained using a Digitron 2000T digital thermometer. The device was then held on the different surfaces to produce a temperature profile for each fire.

**Table 3-26.** Safety temperature requirements for operating surfaces for relevant materials

<b>Material</b>	<b>Temperature</b>
Metals	Tambient + 35°C
Porcelain	Tambient + 45°C
Plastics	Tambient + 60°C

**Table 3-27.** Safety temperature requirements for surfaces likely to be touched for relevant materials

<b>Material</b>	<b>Temperature</b>
Bare Metals	Tambient + 80°C
Enamelled Steel	Tambient + 95°C
Rubber, Plastics, Wood	Tambient + 100°C

The required temperatures for control surfaces and surfaces likely to be touched by an operator are shown in Tables 3-26 and 3-27, respectively.

### **3.3.2 Open fronted fire**

The reference open fronted fire was the FOCALPOINT Blenheim Slimline fire Class F. The specifications for the reference open fire are listed below, and this can be seen in Figure 3-29 A):

- Rated heat output of 3.2 kW and 1.8kW on low heat
- Heat input of 6.25 kW on a GCV basis.
- NO<sub>x</sub> emissions 128 mg/kWh at high heat
- NO<sub>x</sub> emissions 108 mg/kWh at low heat
- Net thermal efficiency: 63%
- Gross thermal efficiency: 51%

The tests aimed to produce lower NO<sub>x</sub> levels using hydrogen than those obtained with the reference fire operating solely with natural gas and achieving similar thermal efficiency. Therefore, the reference open fronted fire premixed burner was replaced with a purely diffusion type hydrogen burner featuring 4 diffusion nozzles, with no flashback risk. However, dual-fuel capabilities were demonstrated.

Different configurations were studied, considering coals and no coals. The burner was modified several times to obtain the best NO<sub>x</sub> and CO emissions by investigating single and two-staged fuel injection configurations. Different round and slot-hole sizes for the fuel nozzles in the burner were designed. The calculations for the slot and hole sizes used for the tests are shown in Appendix I. Various modifications were effectuated to the original igniter to produce a continuous and visual flame using hydrogen.

The burner for the open-fronted fire was stainless steel made, and Clean Burner Systems manufactured it. A technical drawing can be seen in Figure 3-29 B) illustrating a fuel injection configuration using slot-shaped holes.

The fire featured a 206 X 25 X 30.2mm fuel plenum where fuel was injected and distributed to the fuel nozzles located in the burner plate.

A set of fifteen ceramic bricks on top of the burner was used for the open-fronted fire. This was a series of two layers of ceramic 'coals' with the bottom layer being one casting with four large holes with the NG premixed flames emerging through these holes. The second ceramic layer was placed by hand on top of the bottom support of cubic-shaped ceramics. Minimal changes were made to the ceramics as the objective of the work was to develop a fire for hydrogen that looked similar to that on NG. The changes to the burner below

the ceramics would not be visible to the customer. Modifications were made to the bottom ceramics to adapt to the new burner design. Side, top and rear walls were also made of ceramics.

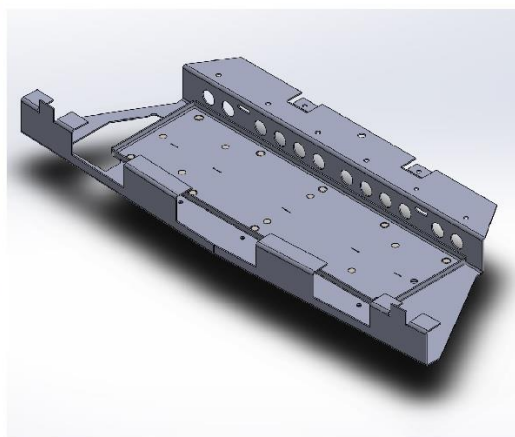
Instead of the rear ceramic wall, a black reflective glass wall was installed for two-stage combustion to produce a better-looking fire.

Single-stage combustion was first investigated to inject the fuel through the fuel nozzles in the burner plates (Figure 3-29 B).

Once the final design for single stage combustion was obtained, the fire was then investigated for double stage combustion. For this study, a primary front row of 36mm tubes was installed where the burner plate fuel nozzles; this first-stage injection provided 40% of the total fuel flow and impinged with the ceramic bricks. A secondary row of four 90mm tubes was then included at the back of the first stage injection; this second row of ceramic injected the remaining 60% of the fuel between the third row of ceramic coals, as shown in Figure 3-30. This configuration was studied to achieve a better-looking flame than the one obtained for single stage combustion. The original igniter was also configured to allow a continuous flame. The original design shown in Figure 3-28 had a deflector inside the copper pipe, allowing the fuel to stabilise. This deflector was twisted several times to keep a continuous flame that allowed a successful cross light. The fuel plenum was also modified for the second stage injection. The two-stage burner calculations and technical drawings are shown in Appendix I.2.



A)



B)

**Figure 3-29.** A) Reference open fronted fire. B) Slot-shape fuel holes burner configuration for open-fronted fire single-staged



**Figure 3-30:** Burner design for open-fronted fire two-stage injection

### 3.3.3 Glass fronted fire (LEGEND)

The reference appliance was the Legend EVORA balanced flue.

The specifications for the glass-fronted reference fire were

- Fits in a standard 16x22" opening
- 3.8kW of fire heat output
- 4.5kW gross and 4.1kW net heat input
- Thermal efficiency 84% gross
- Thermal efficiency net 93%

The original partially premixed burner operated with natural gas was replaced with a diffusion burner featuring dual-fuel hydrogen and natural gas capabilities, given the similar Wobbe index for both fuels. Airflow was similar for hydrogen and NG to deliver the same energy. Thus, this allowed the system to be used with NG. This burner showed an array of diffusion nozzles generating visible orange flames impinging on the configuration of the ceramic installed on top. In the experiments with NG (natural gas), the impingement process caused air/fuel mixing, minimising soot formation. The flue was directly discharged, and water condensation did not occur at the flue for any of the fuels. The hydrogen fire operated at the same energy input as the NG one. This featured a lean blue flame that allowed to minimise the NO<sub>x</sub> levels.

The fire burner featured a 240x37x37mm fuel plenum injecting the fuel through a burner plate featuring different hole shapes.

The burner fuel plate was studied to inject all the fuel through a set of holes located 50mm from the airholes, as shown in Figure 3-31. Eighteen different configurations of round holes and slot-like nozzles were designed, but only

some of them were investigated. It is not the intention to present all the studied configurations but only the most relevant designs producing a more attractive flame and the lowest NO<sub>x</sub>. The calculations for the fuel nozzles for the glass-fronted fire are shown in Appendix J. The work in Chapter 7 concerns the redesign of the Burner Tray Assembly and burner injector sump assembly (removed) for operation on hydrogen.

Akin to the open-fronted fire, a set of coals were placed inside the firebox to produce heat and the coal-like glowing effect. The arrangement consisted of two brick-like ceramic walls, one on each side of the burner, a rear wall, a bottom shape containing five air holes shown in Figure 3-31, and a top set of coals containing holes to allow the fuel to come through.

In the reference fire, the bottom ceramic was in two halves with a front and rear section with a gap at their junction through which the premixed NG flames emerged. The top ceramic layer was two castings that looked like 'coals' with a junction in the middle of the fire with a half left and right hand. During the project prototype, single top layer ceramics casting was used. As for the open fire, the burner changes were at the base of the fire, and there was no visible indication that the fire had a different burner, and the same ceramics were used in terms of their external visibility.

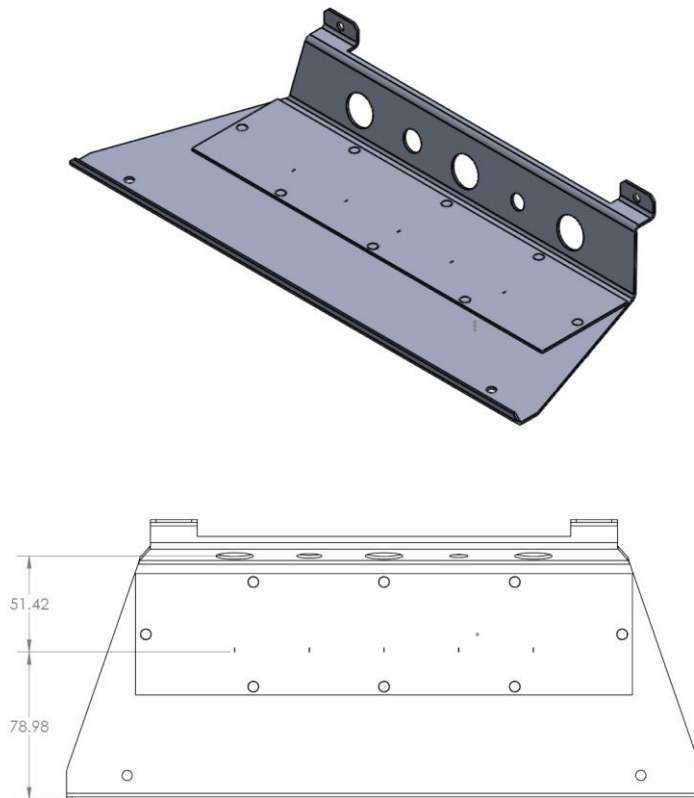


**Figure 3-31.** Location of single-stage fuel injection in the glass-fronted fire.

The fire structure is shown in Figure 3-32.

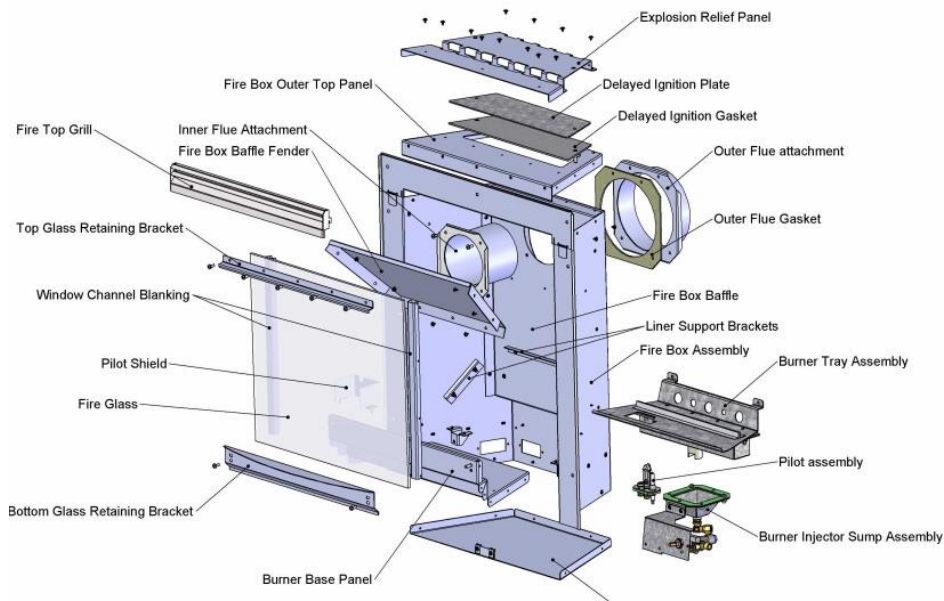


**Figure 3-32.** Construction of the Legend Glass Fronted Fire

Note the explosion protection at the top through a vent with an explosion vent cover. A weaker vent burst pressure will be fitted for hydrogen and a higher lift area.

The fire featured a double air/flue pipe on its back, as shown in Figure 3-33, where the inner pipe transported the flue gases and the exterior pipe entrained all the required air for the combustion. This figure shows the position where the thermocouple was inserted to obtain the flue temperature.

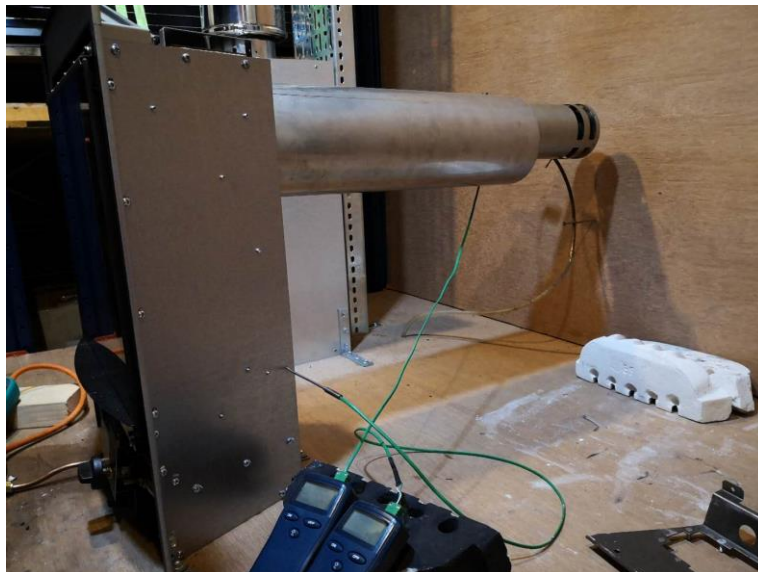


**Figure 3-33:** External flue/air pipe for the glass-fronted fire

The manual control featured two factory settings, 4.5kw high -1.5kw low or a 3:1 thermal power turndown. The remote version is also factory set (via a

modem) on the valve software, and the gas rate can be adjusted anywhere between 0kw-9kw NG.

As explained in 3.3.1, the pressure was measured using a Kane manometer connected directly to the fire fuel plenum, shown in Figure 3-34. This arrangement with a plastic hose and copper pipes was later changed to a 316L stainless steel pipe using Swagelok® fittings.



**Figure 3-34:** Manometer for plenum pressure in the glass-fronted fire.

### **3.3.4 Innovative fire**

No reference fire was considered for the innovative fire design. However, this fire was designed and manufactured for a thermal input of 7kW. The prototype was created by the University of Leeds, in conjunction with Legend burners, while Clean Burner systems and Birmingham burners manufactured the burners. The appliance featured a landscape orientation. The preliminary idea was to include a fan in the domestic fire, which would supply the air required for the combustion to occur, allowing the aerodynamics to be controlled by the air holes and fuel nozzles. The first design had a fan pressure of 5 kW, similar to the pressure used for central heating boilers. Another key feature of the innovative fire was internal gas recirculation (IEGR), as mentioned in 2.2.4, to recover heat and reduce emissions, as shown in Figure 3-35. This feature provides a significant factor in improving the fire thermal efficiency relative to the market. The intention was not to manufacture a fire to compete with the low-cost fire market dominated by "coal" or "log" like effect fires but to create a

premium appliance to provide a visually pleasing experience considering the latest regulations for NO<sub>x</sub> and CO emission levels.

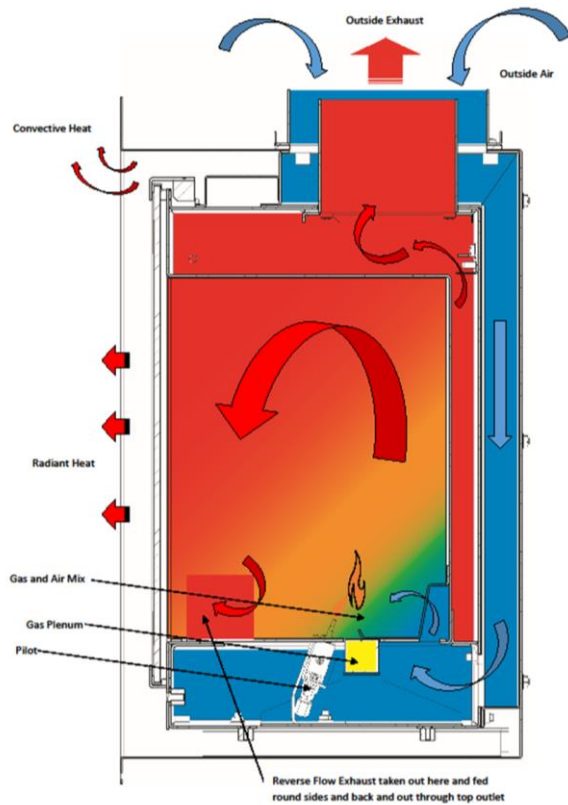


**Figure 3-35:** Innovative fire gas recirculation concept.

The original fire design was developed by the University of Leeds as a metal box that could fit in a wall, as shown in Figure 3-36. This fire featured a fuel plenum surrounded by a triple 10mm jacket for cooling purposes and IEGR.

This idea was for the fire to be enclosed in a wall with all the needed air injected through two fans, as shown in Figure 3-36. The design included an air plenum surrounded by a triple 10 mm gap jacket working as a heat exchanger, where all the incoming air was meant to be heated with the exhaust gases coming out through the other passage. The fuel was supposed to be injected through a series of nozzles in the burner plate. The outlets were slot-shaped, allowing the exhaust gases to come into one of the jackets in the box. Unfortunately, this design could not be manufactured since the industrial partners chose a less sophisticated option.

Other designs following the original one featured two of the Legend burners used for the glass-fronted fire, with two igniters to allow the crosslight of the flame. These configurations were tested with only the rear ceramics in various positions inside the box. The final design for the Innovative fire shown in Figure 3-37 was developed by Legend Fires.

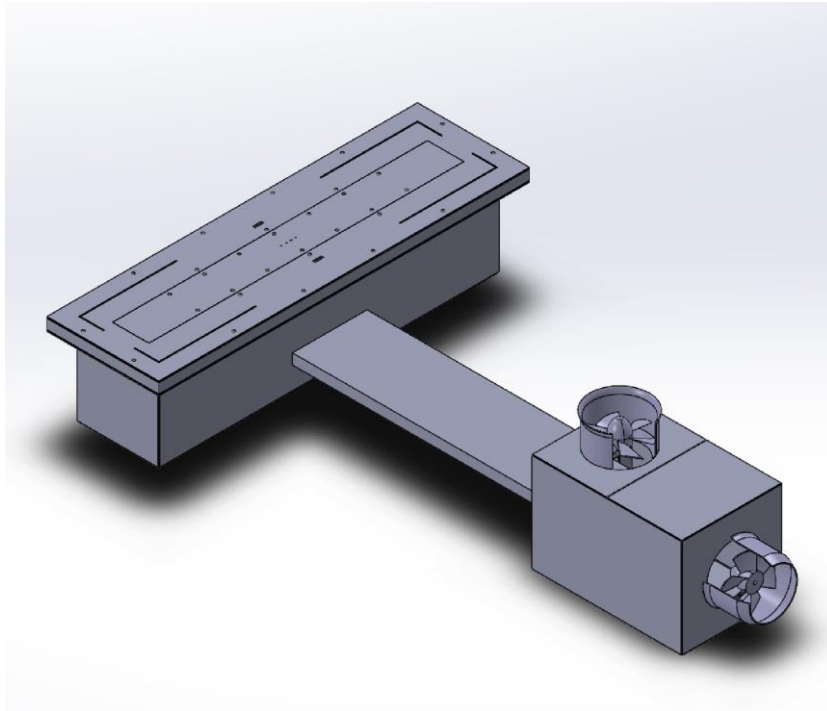


**Figure 3-36:** Preliminary prototype for Innovative fire

This prototype featured a single jacket to allow the exhaust gases to recirculate from two square outlets at the front sides of the reverse flow box. This principle is illustrated in Figure 3-35 . The design showed a double concentric pipe like the one used for the glass-fronted fire, in which the inner tube transported the exhaust gases, and the exterior pipe would bring air into the fire rear ceramic wall at different inclinations to allow flame impingement. This design had a single burner with various nozzle configurations.

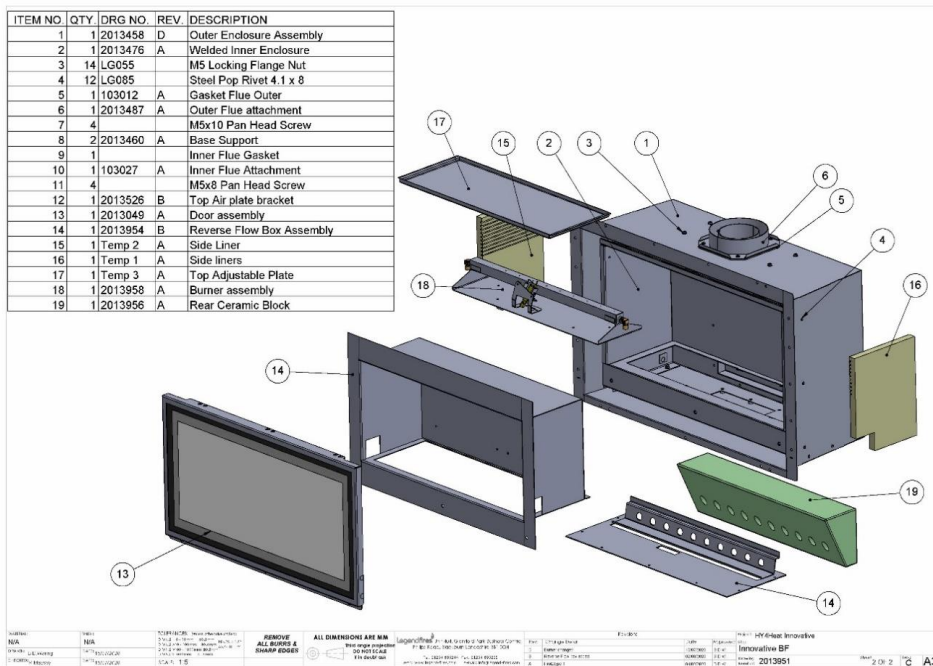


**Figure 3-37:** An approved design for Innovative fire tests

Some controversy arose in whether the flame produced for the innovative fire with LB4 and LB5 was attractive enough for the general public. This matter was discussed with members of the academic team and the industry partners, which led to the development of more tests to produce a more attractive flame.

A narrower 150mm 'letterbox' fire was used for these tests. The burner design was also modified, featuring a single plenum injecting the fuel through different size slots.

The plenum drawings and the slot sizes for the different configurations are shown in Appendix K, offering four different slot configurations. However, only the 0.1mm designs 2 and 3 were tested, and the burner designs were termed B1 and B2, respectively. The ceramic back wall of the fire was also redesigned, and the next configurations were tested:

- featuring a series of holes at the top or bottom of the block,
- The block being straight or having an inclination (C1 for 55° and C2 for 65°)
- Positioning the ceramics at different distances from the fuel injector.
- 

### **3.4 Computational setup for domestic fires**

A numerical study was undertaken for the innovative glass-fronted original prototype before the experiments to investigate the effect of the fuel hole shape on aerodynamics and emissions inside the firebox. A round hole and a slot-shaped hole were simulated and compared with an injection area of 9.6mm<sup>2</sup>. This study allowed preliminary prediction of temperatures and emission levels before the tests were undertaken. The simulations were carried out for a natural gas and air mixture.

The firebox was modelled as a rectangular domain using SOLIDWORKS with dimensions 600x240x260mm. These dimensions belonged to the first prototype of the innovative fire, later modified as the design changed. Figure 3-38 shows the CAD model of the firebox, where the four 25mm round holes in the corner illustrate the flue outlets. The air was considered to be supplied at the centre bottom of the box surrounding the fuel injection, presenting a classic example of non-premixed combustion. The original idea of this appliance was to fit in a standard domestic wall thickness, so the height of the appliance was approximately three bricks or 250mm. Later designs later changed this height to 300mm and 150mm.

ANSYS ICEM was used to create the numerical meshes for both geometries where detailed structured blockings were designed, and then the hexahedral mesh was developed.

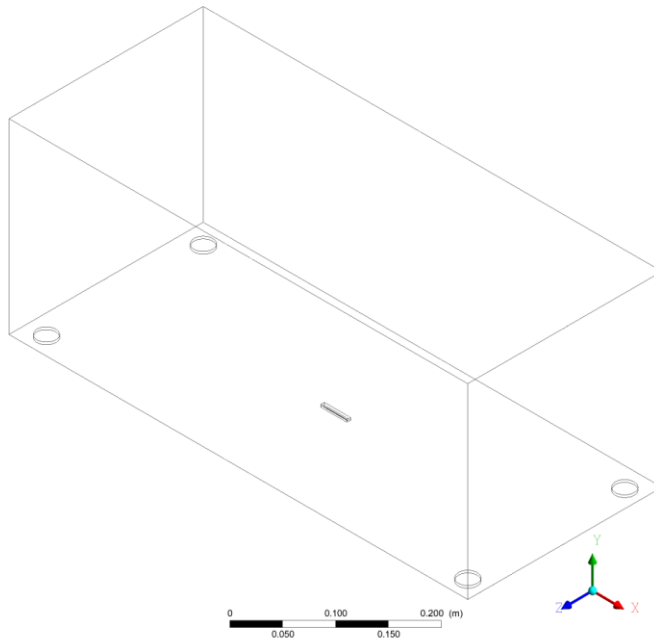


**Figure 3-38:** Innovative fire model used for the numerical analysis featuring a slot-shaped hole

ANSYS CFX was used to undertake the simulation considering the turbulence model k-epsilon and the combustion model Eddy dissipation model (EDM). The combustion model was created using a two-step PDF table for pure CH<sub>4</sub>/ O<sub>2</sub> combustion with NO formation available in the software library. Scalable wall functions and thermal energy heat transfer were used. Adiabatic walls were used for this study. Thus, no radiation models were investigated. A default inlet turbulent intensity of 5% was used for both cases.

Table 3-28 illustrates the boundary conditions used for the simulation. Only an equivalence ratio of 0.624 was studied.

**Table 3-28:** Boundary conditions for numerical study for Innovative fire.

<b>Fuel</b>	<b>Air massflow (kg/s)</b>	<b>Fuel massflow (kg/s)</b>	<b>Thermal Input (kW)</b>	<b>Inlet temperature (K)</b>	<b>Equivalence ratio (Ø)</b>
Natural gas	0.003696	0.00014	7.0	288.15	0.624

### 3.4.1 Slot-shape hole geometry

A structured hexahedral mesh was created considering 640K elements, as shown in Figure 3-39. An inflation layer of 0.05mm elements was used near the fuel injection to predict fuel separation precisely.

The slot was studied for a thickness of 0.3x32mm, and the air was injected through a 5x35mm annulus surrounding the fuel injection.

The overall quality of the mesh shown in Figure 3-40 was above 0.5, and the determinant above 0.68

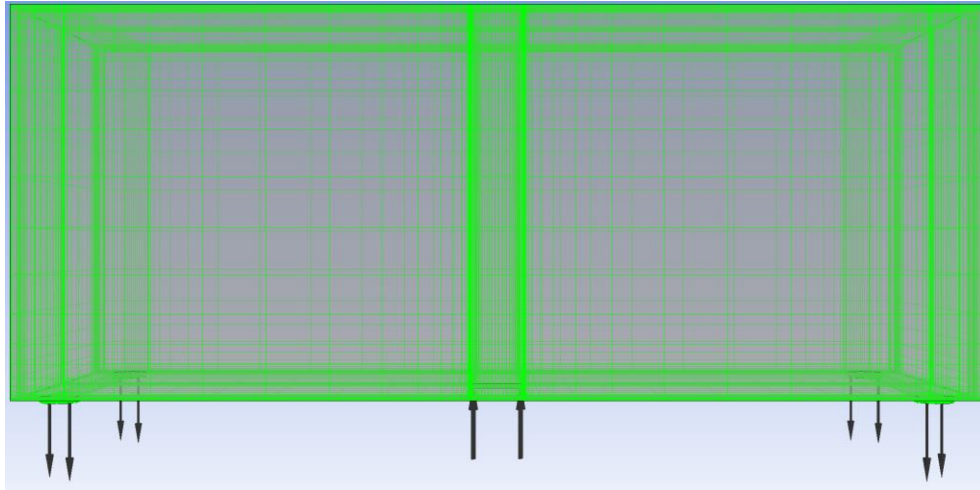


**Figure 3-39:** Mesh used for numerical analysis of Innovative fire (slot-shaped hole).

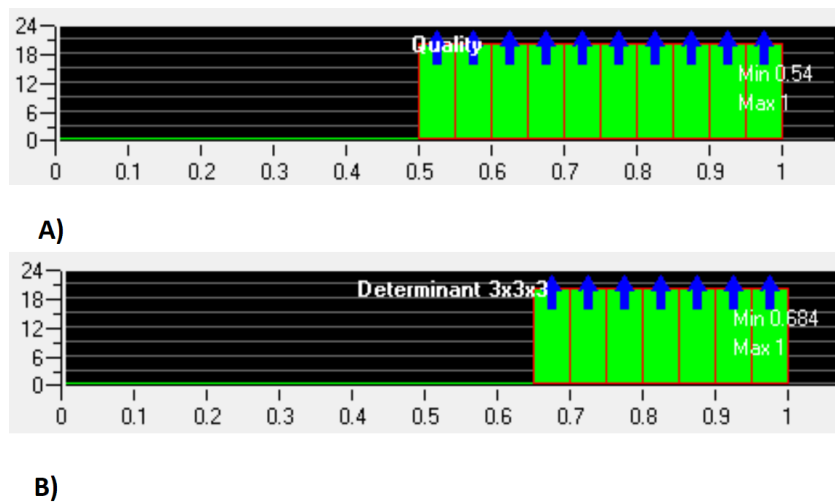
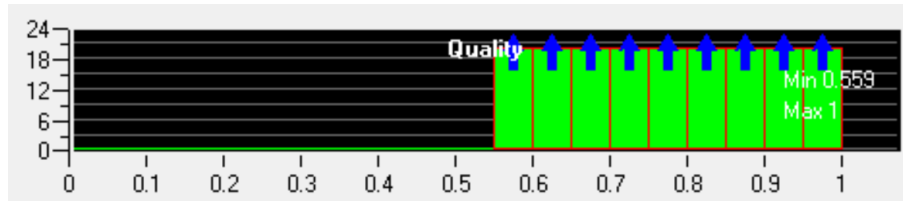


**Figure 3-40:** Mesh statistics for slot-shape fuel injection geometry of Innovative fire: a) quality; B) determinant

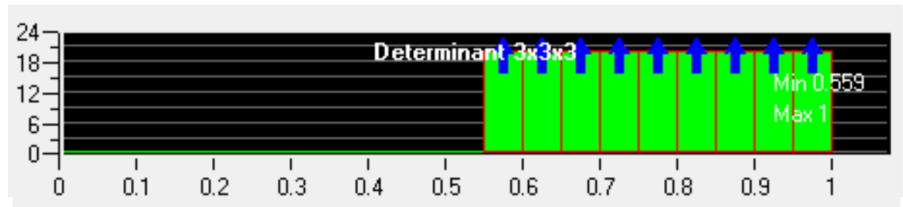
### 3.4.2 Round hole geometry

A rectangular firebox configuration was also investigated for the round hole study. The air supply was modelled as a 14.64mm diameter annulus surrounding the 3.5mm diameter fuel injection.

A hexahedral mesh of 400K elements was used for this study. Figure 3-41 shows the mesh statistics for this mesh where quality and determinant of 0.56 were achieved.



A)



B)

**Figure 3-41:** Mesh statistics for round fuel hole fuel injection geometry of Innovative fire: a) quality; B) determinant

## **Chapter 4. EQUILIBRIA AND ADIABATIC TEMPERATURE CALCULATIONS FOR VARIOUS FUELS FOR PROCESS HEATERS**

### **4.1 Introduction**

The calculation of adiabatic flame temperatures and product composition for different fuel blends used in domestic fires and glass melting float furnaces is now presented. Additionally, the equilibrium results for a cooled flame are given for the same fuels, considering the conditions achieved with NG, which are presented.

### **4.2 Equilibrium study for natural gas flame**

#### **4.2.1 Equilibrium study for natural gas for domestic fires**

The adiabatic flame temperature ( $T_{\text{adiab}}$ ) and product composition for the natural gas Goole mixture/air at 300K are shown in Table 4-1. The desired ~1% was achieved for an  $\emptyset$  of 0.95 and an adiabatic flame temperature of 2194.5K. The water vapour shows a concentration of 17.21% with a 4790 CO ppm, and 2658 NO ppm.

**Table 4-1.**  $T_{\text{adiab}}$  for NG mixture at an inlet temperature of 300K

$\emptyset$	Flame Temp K	O <sub>2</sub> wet %	O <sub>2</sub> dry%	H <sub>2</sub> O wet%	NO ppm wet	CO wet %	CO <sub>2</sub> wet %
0.8	2003.9	3.69	4.34	14.95	3103	0.06	7.95
0.825	2040.6	3.21	3.79	15.35	3187	0.08	8.15
0.85	2075.8	2.74	3.25	15.75	3219	0.12	8.33
0.875	2109.2	2.28	2.72	16.13	3191	0.18	8.50
0.9	2140.5	1.84	2.2	16.51	3092	0.25	8.65
0.925	2169.2	1.43	1.72	16.87	2916	0.36	8.76
<b>0.95</b>	<b>2194.5</b>	<b>1.06</b>	<b>1.28</b>	<b>17.21</b>	<b>2658</b>	<b>0.5</b>	<b>8.84</b>
0.975	2215.4	0.74	0.9	17.53	2319	0.69	8.85
1	2230.5	0.47	0.57	17.81	1916	0.95	8.80

### 4.2.2 Equilibrium study for a cooled natural gas flame for domestic fires

Table 4-2 shows that the desired 1% O<sub>2</sub> for a cooled flame at an inlet temperature of 300K was nearly achieved at an  $\phi$  of 0.954, indicating an T<sub>adiab</sub> of 2198K. This condition was used as a reference condition for domestic fires operated with natural gas. The H<sub>2</sub> flue levels showed 150ppm at this condition, while the NO<sub>x</sub> was 930ppm. The CO levels showed 348ppm.

**Table 4-2.** Equilibrium products for natural gas GOOLE mixture at 1.2% excess O<sub>2</sub> at 300K inlet temperature

$\phi$	Cooled Temp K	Adiab T K	$\Delta T$ K	Adiab NO ppm	Adiab CO ppm	O <sub>2</sub> wet %	O <sub>2</sub> dry %	H <sub>2</sub> O %	H <sub>2</sub> ppm	CO <sub>2</sub> % wet	CO ppm wet	NO ppm wet
0.997	1850	2229	379	1966	9128	0.11	0.54	18.36	230	9.69	1015	329
0.974	1850	2215	365	2334	6805	0.48	0.89	18.00	180	9.54	469	703
0.954	1850	2198	348	2609	5240	0.84	1.19	17.67	163	9.37	348	930
0.92	1850	2164	314	2958	3321	1.47	1.81	17.09	120	9.08	255	1232
0.89	1850	2128	278	3141	2189	2.03	2.43	16.58	98	8.81	210	1452

### 4.2.3 Equilibrium study for natural gas for the glass melting industry

The T<sub>adiab</sub> and product composition for the natural gas mixture at 1500K inlet temperature are shown in Table 4-3.

**Table 4-3:** T<sub>adiab</sub> for NG mixture at an inlet temperature of 1500K

$\phi$	Flame Temperature K	O <sub>2</sub> wet %	O <sub>2</sub> dry %	H <sub>2</sub> O wet%	NO ppm wet	CO wet	CO <sub>2</sub> wet
0.9	2702	2.84	3.29	13.70	10,940	3.19%	5.42%
0.95	2719	2.36	2.75	14.12	10,166	3.70%	5.31%
1.0	2732	1.93	2.26	14.50	9,342	4.22%	5.17%
1.05	2743	1.56	1.83	14.84	8,486	4.76%	5.00%
1.1	2750	1.24	1.46	15.13	7,619	5.31%	4.82%
1.15	2755	0.97	1.15	15.37	6,757	5.86%	4.62%
1.2	2756	0.75	0.89	15.57	5,919	6.41%	4.41%
1.25	2755	0.57	0.68	15.71	5,119	6.96%	4.19%
1.3	2751	0.42	0.50	15.80	4,371	7.51%	3.97%

The desired approximate 1.0% excess O<sub>2</sub> was achieved for a T<sub>adiab</sub> of 2755K for a Ø of 1.15.

#### 4.2.4 Equilibrium study for a cooled natural gas flame for the glass melting industry

Table 4-4 shows that the desired oxygen levels were achieved at Ø = 0.946 for the T<sub>adiab</sub> of 2718K. ΔT<sub>1</sub> is the adiabatic flame temperature difference at the specified equivalence ratio and the furnace temperature (1850K). The equivalence ratio marked with red shows a 1.0% excess O<sub>2</sub> in the flue gases or similar. This was the condition at which the rest of the fuels were studied for a cooled flame.

**Table 4-4.** Equilibrium products for natural gas GOOLE mixture at 1.0% excess O<sub>2</sub> at 1500K inlet temperature

Ø	Cooled Temp K	Adiab T K	ΔT K	Adiab NO ppm	Adiab CO ppm	O <sub>2</sub> wet %	O <sub>2</sub> dry %	H <sub>2</sub> O %	H <sub>2</sub> ppm	CO <sub>2</sub> % wet	CO ppm wet	NO ppm wet
0.976	1850	2726	876	9743	39679	0.44	0.54	18.03	229	9.55	488	676
0.96	1850	2722	872	10005	38007	0.73	0.89	17.77	176	9.42	376	868
0.946	1850	2718	868	10231	36559	0.99	1.19	17.53	149	9.30	319	1009
0.918	1850	2709	859	10669	33704	1.50	1.81	17.06	118	9.06	251	1248
0.89	1850	2698	848	11088	30915	2.03	2.43	16.58	98	8.81	210	1452
0.863	1850	2688	838	11469	28294	2.54	3.03	16.12	86	8.57	183	1626
0.836	1850	2676	826	11824	25748	3.06	3.63	15.65	76	8.32	162	1786

The predicted NO values showed considerable sensitivity to the oxygen levels. NO at 0.5% oxygen compared to 1% is roughly 30% lower with a T<sub>adiab</sub> difference of only 8K. Personal communication from Guardian Glass agreed that the amounts of CO measured were reasonable. Water content at this condition is 17.53%, and the difference between the T<sub>adiab</sub> and the furnace temperature for an NG flame was 868K

### 4.3 Equilibrium study for hydrogen flame

#### 4.3.1. Equilibrium study for hydrogen for domestic fires

The results of equilibrium calculations for a mixture considering pure hydrogen and air are now presented.

The  $T_{adiab}$  for mixtures at inlet temperatures going from 298 up to 600K is shown in Figure 4-1. The dry hydrogen flue levels for the different temperatures are shown in Figure 4-2 a), where the values changed just slightly for the different inlet temperatures. Figure 4-2 b) illustrates the NO ppm for the different inlet temperatures where the same values obtained with CEA are shown for 298K. An increase in the inlet temperature considerably affected NO production.

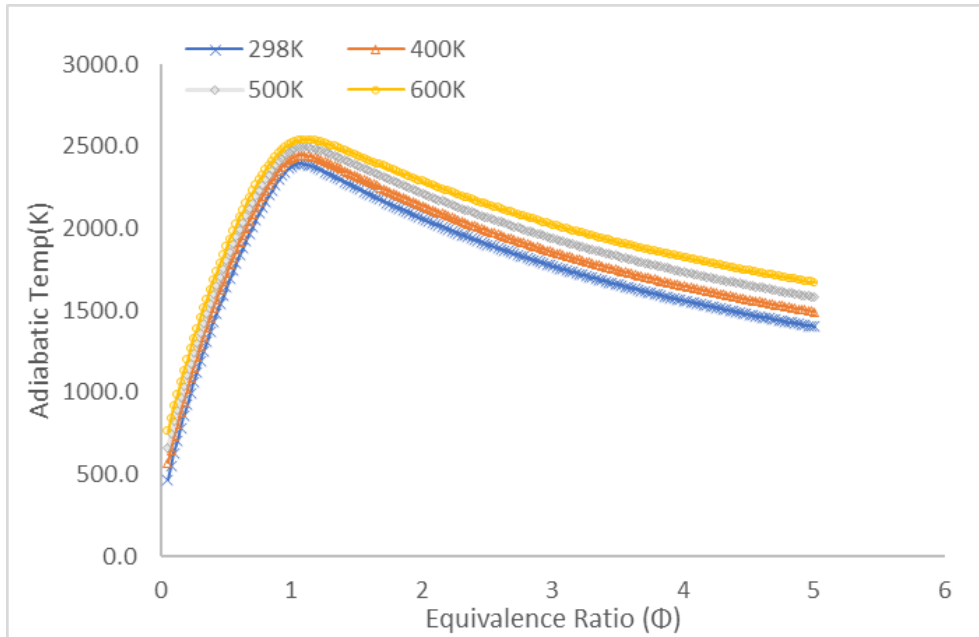


**Figure 4-1:** Adiabatic flame temperatures for H<sub>2</sub> mixture (temps 298-600K)

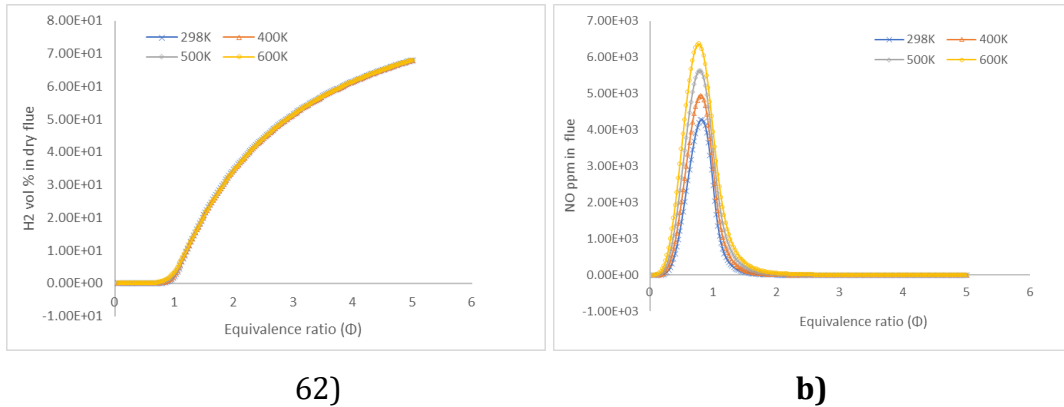


**Figure 4-2:** a) Exhaust dry H<sub>2</sub> vol % vs  $\Phi$  for H<sub>2</sub> mixture (temps (298-600K); b) NO ppm vs  $\Phi$  for H<sub>2</sub> mixture at inlet temps 298-600K

### 4.3.2. Equilibrium study for a cooled hydrogen flame for domestic fires

Table 4-5 shows the results for a mixture of pure hydrogen/air-cooled to 1850K. The mixture reached 1.11% excess O<sub>2</sub> for an  $\Phi=0.955$  and a  $T_{adiab}$  of 2349K, which is 151K higher than NG. However, lower NO<sub>x</sub> levels were

obtained for the H<sub>2</sub> flame at 300K inlet temperature. If the same flame temperature of NG was needed,  $\phi=0.822$  at a flame temperature of  $T_{\text{Adiab}}=2197\text{K}$  would have been required. However, the O<sub>2</sub> in the flue would be 4.36%.

**Table 4-5.** Equilibrium products for pure hydrogen mixture at 1.0% excess O<sub>2</sub> at 300K inlet temperature

$\phi$	Cooled Temp K	Adiab T K	$\Delta T$ K	Adiab NO ppm	O <sub>2</sub> wet %	O <sub>2</sub> dry %	H <sub>2</sub> O %	H <sub>2</sub> ppm	NO ppm wet
0.995	1850	2376	526	2563	0.10	0.16	34.43	905	313
0.967	1850	2358	508	3038	0.54	0.81	33.67	388	717
0.955	1850	2349	499	3229	0.74	1.11	33.32	328	840
0.944	1850	2339	489	3394	0.93	1.38	33.00	290	941
0.907	1850	2302	452	3855	1.56	2.30	31.92	216	1227
0.868	1850	2257	407	4164	2.25	3.25	30.75	173	1477
0.822	1850	2197	347	4297	3.08	4.36	29.36	142	1734

### 4.3.3. Equilibrium study for glass melting industry (hydrogen)

The  $T_{\text{adiab}}$  are shown in Table 4-6 for a mixture of pure hydrogen at an inlet air temperature of 1500K, where  $\Delta T$  is the difference between the  $T_{\text{adiab}}$  and the furnace temperature (1850K).

**Table 4-6:**  $T_{\text{adiab}}$  for H<sub>2</sub> mixture at 1500K inlet temp

$\phi$	Adiabatic Temp (K)	H <sub>2</sub> O wet%	$\Delta T_1$ (K)	NO ppm	O <sub>2</sub> wet%	O <sub>2</sub> dry%
0.95	2831	24.5	981	10000	1.8	2.39
0.875	2807.4	23.9	957.4	11281.2	2.4	3.16
0.85	2797.6	23.6	947.6	11700.6	2.64	2.46
0.825	2786.8	23.3	936.8	12110.0	2.9	3.78
0.8	2774.9	23.0	924.9	12505.4	3.17	4.12
0.775	2762	22.7	912.0	12882.2	3.47	4.49

0.75	2747.9	22.3	897.9	13235.5	3.79	4.88
0.725	2732.6	22.0	882.6	13560.5	4.13	5.29
<b>0.7</b>	<b>2716</b>	<b>21.6</b>	<b>866.0</b>	<b>13851.7</b>	<b>4.50</b>	<b>5.73</b>

The optimum condition for the hydrogen mixture is for a  $\Delta T = 866$ , the same as NG, for  $\phi$  of 0.70. If there was less heat transfer than NG, the flame might have to be operated leaner for the same furnace temperature.

#### 4.3.4 Equilibrium study for glass melting industry for a cooled flame (hydrogen)

The following study calculated equilibrium composition while cooling down the combustion products at an initial product composition of 1.0% excess  $O_2$ . This study was undertaken for a span of  $\phi = 0.954$  to 0.647 at constant pressure at an inlet reactant temperature of 1500K. Product composition for an inlet temperature of 1500K is shown in Table 4-7

**Table 4-7:** Equilibrium products for a mixture of pure hydrogen and air at 1.0% excess  $O_2$  at 1500K inlet temperature

$\phi$	Cooled Temp K	Adiab T K	$\Delta T$ K	Adiab NO ppm	$O_2$ wet %	$O_2$ dry %	$H_2O$ %	$H_2$ ppm	NO ppm
<b>0.954</b>	1850	2833	983	9931	0.76	1.13	33.29	324	850
<b>0.938</b>	1850	2828	978	10205	1.03	1.53	32.83	274	992
<b>0.908</b>	1850	2819	969	10719	1.55	2.27	31.95	217	1220
<b>0.879</b>	1850	2809	959	11213	2.06	2.98	31.08	183	1410
<b>0.85</b>	1850	2798	948	11701	2.57	3.69	30.21	159	1581
<b>0.822</b>	1850	2785	935	12158	3.08	4.36	29.36	142	1734
<b>0.797</b>	1850	2773	923	12552	3.53	4.95	28.59	129	1862
<b>0.772</b>	1850	2760	910	12926	3.99	5.53	27.82	118	1984
<b>0.747</b>	1850	2746	896	13276	4.46	6.11	27.04	108	2101
<b>0.722</b>	1850	2731	881	13597	4.93	6.68	26.25	100	2214
<b>0.697</b>	<b>1850</b>	<b>2714</b>	<b>864</b>	<b>13884</b>	<b>5.40</b>	<b>7.25</b>	<b>25.46</b>	<b>93</b>	<b>2324</b>
<b>0.672</b>	1850	2696	846	14131	5.88	7.81	24.66	86	2430

<b>0.647</b>	1850	2677	827	14333	6.37	8.36	23.85	80	2534
--------------	------	------	-----	-------	------	------	-------	----	------

The H<sub>2</sub> predictions showed that to achieve the same thermal conditions as for NG, a hydrogen furnace would need to operate at 7.25% dry oxygen compared to the 1.2% of NG. The prediction showed that hydrogen will not be a problem in the flue, which is lower than for natural gas

The NO levels are a problem for both fuels going above 1009 ppm for NG and 2324 ppm for H<sub>2</sub>. The water levels for a hydrogen flame are 25.5%, higher than the 17.5% obtained for NG.

If operation at 1% O<sub>2</sub> was needed, the flame would need to be 2833K, bringing the NO<sub>x</sub> lower.

#### 4.4 Equilibrium study for biodiesel composition flame

Natural gas at 1500K inlet temperature operated at 1.15% excess O<sub>2</sub> showed a T<sub>adiab</sub> of 2719K for Ø of 0.946. The biodiesel mixture was studied for the same inlet flame temperature of 1500K. The equivalence ratio and emissions are shown in Table 4-8, where Ø of 0.85 is needed to achieve the T<sub>adiab</sub> of 2710K at an oxygen flue level of 4.2%.

**Table 4-8:** T<sub>adiab</sub> for biodiesel mixture at 1500K inlet

Ø	Flame Temp K	O <sub>2</sub> wet %	O <sub>2</sub> dry%	H <sub>2</sub> O wet%	NO ppm wet	CO wet%	CO <sub>2</sub> wet%
0.75	2660.1	5.0%	5.5%	8.2%	13954	2.7%	7.5%
0.8	2687	4.4%	4.8%	8.5%	13524	3.3%	7.5%
<b>0.85</b>	<b>2710.3</b>	<b>3.8%</b>	<b>4.2%</b>	<b>8.9%</b>	<b>12985</b>	<b>3.9%</b>	<b>7.5%</b>
0.9	2730.3	3.3%	3.6%	9.2%	12358	4.6%	7.4%
0.95	2747.4	2.8%	3.1%	9.5%	11663	5.3%	7.3%
1	2761.7	2.4%	2.6%	9.7%	10916	5.9%	7.1%
1.1	2782.9	1.7%	1.8%	10.2%	9323	7.4%	6.7%

##### 4.4.1 Equilibrium study for biodiesel composition for a cooled flame

The obtained values for a cooled flame are shown in Table 4-9. An Ø of 0.95 was needed to achieve 1.0% excess O<sub>2</sub> for the biodiesel mixture. However, a leaner

condition of 0.85 would require a  $T_{adiab}$  of 2710K with an excess  $O_2$  of 3.2%. Water vapour showed levels of 11% and  $NO_x$  1742ppm higher than NG. However, CO showed to be acceptable under 300 ppm.

**Table 4-9:** Equilibrium products for a cooled mixture of biodiesel from  $T_{adiab}$  at 1.0% excess  $O_2$  at 1500K inlet temperature

$\emptyset$	Cooled Temp K	Adiab T K	$\Delta T$ K	$O_2$ wet %	$O_2$ dry %	$H_2O$ %	$H_2$ ppm	$CO_2$ wet %	CO ppm wet%	NO ppm wet
1.22	1850	2796	946	0.00	0.00	12.87	19962	9.75	60827	5
1.125	1850	2786	937	0.00	0.00	13.00	10463	11.30	36585	11
1.04	1850	2771	921	0.00	0.00	12.96	3096	12.89	12391	36
0.984	1850	2757	907	0.32	0.37	12.67	189	13.44	808	581
0.95	1850	2747	897	0.93	1.07	12.26	107	13.05	458	996
0.929	1850	2740	891	1.34	1.52	12.01	88	12.78	377	1188
0.85	1850	2710	860	2.86	3.21	11.05	55	11.78	237	1742

#### 4.5 Equilibrium study for glycerol flame

Table 4-10 shows that crude glycerol/air operation at richer levels would be needed to work at the same temperature of NG for an inlet temperature of 1500K. The oxygen levels were considerably lower than those obtained for biodiesel and closer to those obtained with natural gas with 2% at the flue.

**Table 4-10:**  $T_{adiab}$  for crude glycerol mixture at 1500K inlet

$\emptyset$	Flame Temp K	$O_2$ wet %	$O_2$ dry%	$H_2O$ wet%	NO ppm wet	CO wet%	$CO_2$ wet%
0.9	2671.9	3.19	3.75	15.07	10590	4.26	8.81
0.95	2684.6	2.76	3.26	15.55	9978	4.84	8.78
1	2694.9	2.37	2.82	16.01	9341	5.43	8.72
1.05	2702.9	2.03	2.43	16.44	8691	6.02	8.63
1.1	2709	1.73	2.08	16.85	8037	6.63	8.52
1.15	2713.1	1.46	1.76	17.22	7388	7.23	8.40

1.2	2715.4	1.23	1.49	17.57	6750	7.84	8.25
1.25	2716	1.02	1.25	17.88	6130	8.44	8.10

#### 4.5.1 Equilibrium study for glycerol flame for a cooled flame

The calculated crude glycerol mixture for a cooled flame from the  $T_{adiab}$  for some equivalence ratios to the furnace temperature of 1850 is shown in Table 4-11. An  $\phi$  of 1.43 was needed for a temperature of  $\sim 2700K$ . However, the  $O_2$  levels under these conditions were too low to be recorded. A 1.6% excess oxygen was achieved for  $\phi$  of 0.92 for a  $T_{adiab}$  of 2685K. The CO was shown to be higher than for NG, and so did the  $NO_x$ . The water content was 18.4%, also slightly higher than the 17.5% for NG.

**Table 4-11:** Equilibrium products for a cooled mixture of crude glycerol from the adiabatic flame temperature at 1.0% excess  $O_2$  at 1500K inlet temperature

$\phi$	Cooled Temp K	Adiab T K	$\Delta T$ K	$O_2$ wet %	$O_2$ dry %	$H_2O$ %	$H_2$ ppm	$CO_2$ wet %	CO ppm wet	NO ppm wet
1.43	1850	2705	855	0.00	0.00	20.26	43724	9.89	85884	4
1.26	1850	2716	866	0.00	0.00	20.34	24804	11.48	56352	6
1	1850	2695	845	0.09	0.11	19.70	561	14.66	1680	288
0.92	1850	2678	828	1.34	1.64	18.43	135	13.82	407	1127
0.87	1850	2662	812	2.30	2.79	17.49	98	13.13	295	1485

#### 4.5.2 Equilibrium study for glycerol/water composition flame

The activity considering a mixture of 50%  $C_3H_8O_3$  and 50% air at 1500K inlet temperature showed the highest flame temperature of 2669.7 at an  $\phi$  of 1.2 for an oxygen level of 1.1%, as shown in Table 4-12.

The cooled mixture shown in Table 4-13 illustrates that to achieve the required 1% excess  $O_2$ , an  $\phi=0.95$  and a  $T_{adiab}$  of 2646K would be needed. This temperature was 72K lower than for NG. CO showed higher levels than the mixture with no water and NG. However, the  $NO_x$  showed lower levels than the pure  $C_3H_8O_3$  mixture and lower than NG. This proves that water injection brings the  $NO_x$  down.

**Table 4-12:**  $T_{adiab}$  for 50% glycerol/50% water mixture at 1500K inlet temp

$\emptyset$	Flame Temp K	O <sub>2</sub> wet %	O <sub>2</sub> dry%	H <sub>2</sub> O wet%	NO ppm wet	CO wet%	CO <sub>2</sub> wet%
0.9	2635.1	3.0%	3.67%	18.5%	9490	3.7%	8.8%
0.95	2646.4	2.6%	3.17%	19.1%	8887	4.2%	8.8%
1	2655.3	2.2%	2.73%	19.7%	8266	4.7%	8.8%
1.05	2661.9	1.9%	2.33%	20.2%	7637	5.3%	8.7%
1.1	2666.5	1.6%	1.97%	20.7%	7009	5.8%	8.6%
1.15	2669	1.3%	1.66%	21.1%	6391	6.4%	8.5%
1.2	2669.7	1.1%	1.39%	21.5%	5789	6.9%	8.4%
1.25	2668.7	0.9%	1.15%	21.9%	5210	7.4%	8.3%
1.3	2665.9	0.7%	0.94%	22.3%	4659	8.0%	8.1%
1.35	2661.6	0.6%	0.77%	22.6%	4139	8.5%	8.0%

**Table 4-13.** Equilibrium products for a cooled mixture of 50% glycerol/50% water from the  $T_{adiab}$  at 1.0% excess O<sub>2</sub> at 1500K inlet temperature

$\emptyset$	Cooled Temp K	Adiab T K	$\Delta T$ K	O <sub>2</sub> wet %	O <sub>2</sub> dry %	H <sub>2</sub> O %	H <sub>2</sub> ppm	CO <sub>2</sub> wet %	CO ppm wet%	NO ppm wet
1.35	1850	2662	812	0.00	0.00	24.36	37501	10.42	64528	5
1.2	1850	2670	820	0.00	0.00	24.22	20822	11.73	40569	9
1.02	1850	2658	808	0.01	0.01	23.64	2068	13.83	4868	91
0.98	1850	2652	802	0.35	0.45	23.13	333	13.83	801	556
0.975	1850	2651	801	0.42	0.55	23.03	301	13.78	724	614
0.96	1850	2648	798	0.65	0.84	22.76	239	13.63	575	765
0.95	1850	2646	796	0.81	1.04	22.57	212	13.52	512	854

#### 4.6 Equilibrium study for European diesel composition flame

Product composition and  $T_{adiab}$  are shown in Table 4-14 for an inlet temperature of 1500K. A temperature of 2713 was achieved at  $\emptyset$  of 0.85 for an oxygen level of 4.13%.

**Table 4-14:**  $T_{adiab}$  for European diesel mixture at 1500K inlet temp

$\emptyset$	Flame Temp K	O <sub>2</sub> wet %	O <sub>2</sub> dry%	H <sub>2</sub> O wet%	NO ppm wet	CO wet%	CO <sub>2</sub> wet%
0.8	2690	4.37	4.76	8.23	14165	3.26	7.26
0.85	2713.9	3.78	4.13	8.55	13594	3.88	7.21
0.9	2734.5	3.24	3.56	8.85	12928	4.53	7.12
0.95	2752.1	2.76	3.04	9.12	12187	5.20	6.99
1	2766.9	2.33	2.57	9.38	11390	5.90	6.83
1.05	2779.2	1.95	2.16	9.61	10552	6.61	6.64
1.1	2788.9	1.61	1.79	9.81	9687	7.33	6.42

#### 4.6.1 Equilibrium study for European diesel composition for a cooled flame

Table 4-15 shows the obtained values for the cooled diesel mixture down to the furnace temperature of 1850K.

**Table 4-15:** Equilibrium products for a cooled mixture of European diesel from  $T_{adiab}$  at ~1.0% excess O<sub>2</sub> at 1500K inlet temp

$\emptyset$	Cooled Temp K	O <sub>2</sub> wet %	O <sub>2</sub> dry %	H <sub>2</sub> O %	H <sub>2</sub> ppm	CO <sub>2</sub> wet %	CO ppm wet	NO ppm wet	Adiab T K	$\Delta T$ K
1.21	1850	0.0	0.0	12.4	19260	9.5	58959	6	2802	952
1.12	1850	0.0	0.0	12.6	9668	11.1	34212	12	2791	941
1.04	1850	0.0	0.0	12.6	3124	12.5	12522	37	2777	927
0.94	1850	1.1	1.3	11.8	94	12.6	402	1169	2749	899
0.92	1850	1.4	1.6	11.6	82	12.4	352	1317	2743	893
0.88	1850	2.4	2.7	11.0	60	11.8	259	1699	2725	875
0.83	1850	3.3	3.6	10.4	49	11.2	211	1991	2705	855

The calculations showed that an  $\phi$  of 0.94 was needed to achieve an oxygen level near 1%, where the  $T_{adiab}$  was 2749K. However, the oxygen levels at the  $T_{adiab}$  of 2705K showed 3.6% for an  $\phi$  of 0.83.

#### 4.7 Equilibrium study for ethanol flame

Table 4-16 shows the  $T_{adiab}$  and product composition for near stoichiometric values where the highest flame temperature, 2749.5K, was obtained for  $\phi = 1.2$  with an excess  $O_2$  of 1.0%. The achieved  $T_{adiab}$  for the natural gas conditions was 2712.7K for a  $\phi = 0.95$ , where the exhaust  $O_2$  levels were 2.6%

**Table 4-16:**  $T_{adiab}$  for crude ethanol mixture at 1500K inlet temp

$\phi$	Flame Temp K	$O_2$ wet %	$O_2$ dry%	$H_2O$ wet%	NO ppm wet	CO wet%	$CO_2$ wet%
0.85	2679.6	3.60	4.1	13.20	11792.3	3.30	7
0.9	2697.7	3.10	3.6	13.70	11150.9	3.80	6.90
0.95	2712.7	2.60	3.0	14.10	10454.5	4.40	6.80
1	2725	2.20	2.6	14.50	9719.77	5	6.70
1.1	2742	1.50	1.8	15.20	8193.49	6.20	6.40
1.2	2749.5	1	1.2	15.80	6675.3	7.40	6
1.3	2748.3	0.60	0.7	16.20	5251.04	8.60	5.60

##### 4.7.1 Equilibrium study for ethanol/air for a cooled flame

The study for a cooled flame of an ethanol/air mixture is shown in Table 4-17. The excess flue oxygen of 1.1% was achieved at  $\phi$  of 0.95 for a  $T_{adiab}$  of 2752K. However, the closest temperature to the one achieved with NG was for  $\phi = 0.83$  with excess oxygen of 3.6%. This fuel mixture showed higher  $NO_x$  and CO levels at the exhaust than NG.

**Table 4-17:** Equilibrium products for a cooled mixture of ethanol/air from  $T_{adiab}$  at 1% excess  $O_2$  at 1500K inlet temperature

$\emptyset$	Cooled Temp K	Adiab T K	$\Delta T$ K	$O_2$ wet %	$O_2$ dry %	$H_2O$ %	$H_2$ ppm	$CO_2$ wet %	CO ppm wet	NO ppm wet
1.35	1850	2803	953	0.0	0.0	11.9	35611	7.5	90403	3
1.2	1850	2801	951	0.0	0.0	12.4	18187	9.6	56492	6
1.04	1850	2777	927	0.0	0.0	12.6	3286	12.5	13124	35
0.95	1850	2752	902	0.9	1.1	11.9	104	12.5	445	1067
0.92	1850	2743	893	1.4	1.6	11.6	82	12.4	352	1317
0.88	1850	2725	875	2.4	2.7	11.0	60	11.8	260	1699
0.83	1850	2705	855	3.3	3.6	10.4	49	11.2	211	1991

#### 4.8 Conclusions

The natural gas/air blend calculated for domestic fires to a cooled flame of 1850K showed an adiabatic temperature  $T_{adiab}=2198K$  at an equivalence ratio  $\emptyset=0.954$  and an excess air of 1.2%. The same exhaust conditions were achieved for a hydrogen flame at 2349K and  $\emptyset=0.955$ . If the same flame temperature was needed, an excess  $O_2$  of 4% would be needed. The  $NO_x$  for  $H_2$  was 840 vs 930 for NG, 90ppm lower

The adiabatic temperature ( $T_{adiab}$ ) of a natural gas /air blend was 2718K for a cooled flame temperature at 1500K inlet temperature and  $\emptyset =0.946$ , achieving excess oxygen of 1% in the flue. These are the operating conditions of the glass melting furnace.

A blend of pure hydrogen with air was compared with another one specified in the PAS4444 showing no differences in adiabatic flame temperature and product composition. The blend of pure hydrogen was studied for the furnace conditions achieved with a cooled flame for NG. The adiabatic flame temperature of  $T_{adiab} =2716K$  at  $\emptyset=0.697$  achieved 7.23%  $O_2$  in a dry condition. In order to achieve a 1%  $O_2$ , the furnace would have to burn above  $\emptyset =0.95$ , and the flame temperature would be 2831K.

The soybean biodiesel composition achieved the requested conditions at  $\emptyset=0.85$  for  $T_{adiab} =2710K$  and 3.21%  $O_2$  in the flue. The flame temperature for a 1% excess  $O_2$  was 2740 for  $\emptyset=0.95$ .

The crude glycerol blend for a cooled flame achieved the furnace conditions for natural gas at  $\phi=0.92$  and  $T_{adiab}=2678$ , which is around 40K lower than the NG flame. In order to obtain the same flame temperature this flame would have to be at  $\phi=1.26$  but showing no excess  $O_2$  in the flue.

The 50%  $C_3H_8O_3$ / 50%  $H_2O$  blend showed much lower temperatures than the furnace conditions.

The European diesel composition reached the 1.0% excess  $O_2$  at  $\phi=0.94$  showing a  $T_{adiab} = 2749K$ , which is 31K higher than the obtained with NG. A similar adiabatic temperature  $T_{adiab} = 2705$  would bring the  $O_2$  levels to 3%.

Finally, the mixture of ethanol/air for a cooled flame achieved 1.1% excess flue  $O_2$  at  $T_{adiab} = 2752K$  and  $\phi= 0.95$ . This flame would be 36K higher than NG. The same temperature conditions would be achieved at  $T_{adiab} = 2705K$  and  $\phi= 0.83$ , but for an excess  $O_2=3.3\%$ . A comparison of all the studied fuels is shown in Table 4-18. The highest adiabatic temperature achieved for the requested conditions was for ethanol at  $\phi= 0.95$  and  $T_{adiab} = 2752K$ . On the other hand, the lowest flame was achieved for glycerol at  $\phi= 0.92$  and  $T_{adiab} = 2678K$ .

**Table 4-18.** Comparison of studied fuels for glass melting furnaces (Reference NG=0.946  $T_{in}=1500K$ )

Fuel	$\phi$	Cooled Temp K	Adiab T K	$\Delta T$ K	$O_2$ wet %	$O_2$ dry %	$H_2O$ %	$H_2$ ppm	$CO_2$ wet %	$CO$ ppm wet%	$NO$ ppm wet%
NG	0.946	1850	2718	868	0.985	1.19	17.53	150	9.30	320	1010
<b>H<sub>2</sub></b>	<b>0.697</b>	<b>1850</b>	<b>2716</b>	<b>866</b>	<b>5.39</b>	<b>7.23</b>	<b>25.40</b>	<b>93</b>	-	-	<b>2310</b>
<b>B100</b>	0.85	1850	2710	860	2.86	3.21	11.05	55	11.78	237	1742
<b>C<sub>3</sub>H<sub>8</sub>O<sub>3</sub></b>	0.92	1850	2678	828	1.34	1.64	18.43	135	13.82	407	1127
<b>Diesel</b>	0.94	1850	2749	899	1.1	1.3	11.8	94	12.6	402	1169
<b>C<sub>2</sub>H<sub>5</sub>OH</b>	0.95	1850	2752	902	0.9	1.1	11.9	104	12.5	445	1067

## **Chapter 5. CFD STUDY FOR AERODYNAMICS FOR GAS TURBINE GRID PLATE FLAME STABILISERS**

### **5.1 Introduction**

The obtained simulation results for pressure loss at the combustor wall compared to the obtained experiments expressed in terms of the  $C_D$  and  $C_c$  for grid plate flame stabilisers are now presented. In grid plates, pressure loss is created from converting flow pressure energy into turbulence kinetic energy (TKE). Hence, a successful TKE prediction was needed to accurately predict the pressure loss across the combustor.

### **5.2 Modelling of pressure loss for single hole flame stabiliser**

The stabilisers study for a single hole  $45^\circ$  sector of the combustor is now presented for the grid plates featuring 22.44mm and 19.27mm air hole diameters.

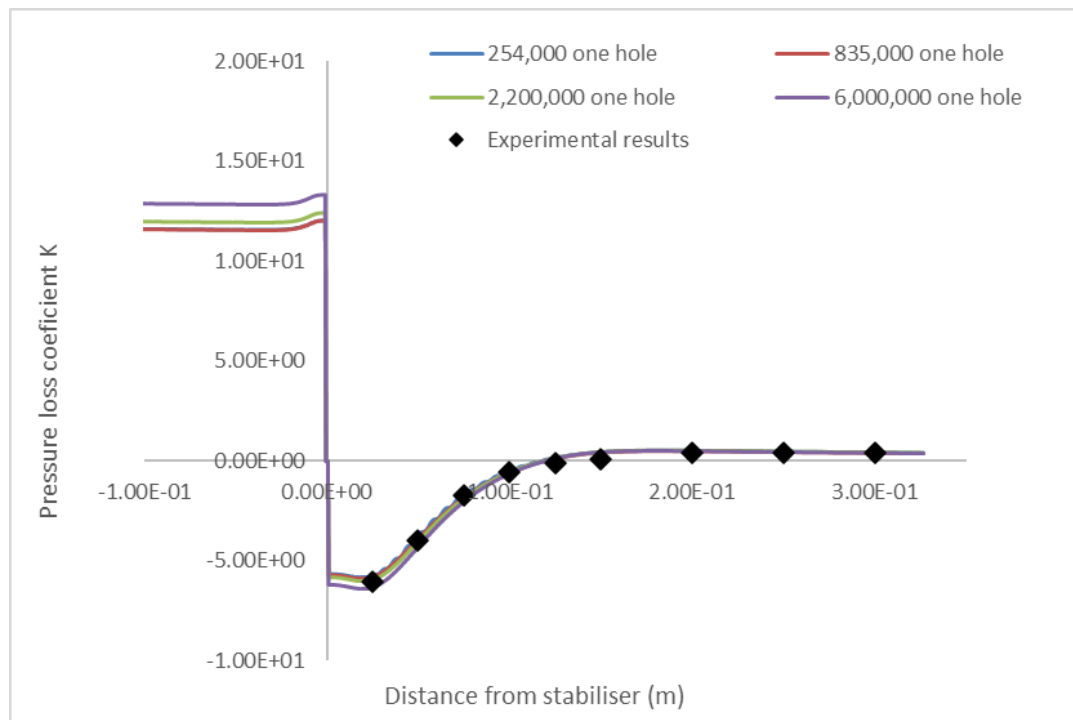
#### **5.2.1 Single air hole 22.44mm flame stabilizer**

Figure 5-1 shows a mesh independence study for the mesh sizes reported in Table 5-1 for the flame stabiliser considering a single hole with 22.44mm diameter using the turbulence model  $k-\epsilon$ . Figure 5-2 illustrates the mesh qualities studied using  $k-\omega$  SST. The graphs show the predicted pressure loss for the various mesh sizes in terms of the coefficient  $K$  vs the axial distance of the stabiliser.

The  $C_D$  and  $C_c$  results calculated from Figure 5-1 and Figure 5-2 were compared with the experimental results. Additionally, the percentual error was calculated for both values in Table 5-1. Four mesh sizes were studied using the  $k-\epsilon$  and SST turbulence models. The mesh with roughly 6 million elements showed almost perfect agreement with the experimental results for  $C_D$  and  $C_c$ , with a difference of less than 1% for both cases. The higher error was 5% for the  $C_D$  and 6% for the  $C_c$  using  $k-\epsilon$ . Divergence was encountered for the coarse mesh using SST, so no results were obtained for this quality.

A perfect agreement was achieved with the experimental results using  $k-\epsilon$ , as observed in Figure 5-1 and Table 5-1. Computational times were also considered, and it was discovered that simulations with SST took considerably longer than those using  $k-\epsilon$ . This was initially expected since  $k-\omega$  has more equations to solve than  $k-\epsilon$ , which is why this last one is usually preferred when aiming for accurate and prompt results.

The turbulence model SST  $k-\omega$  has shown to miss predict pressure gradients in sudden expansions and fuel separation [267], [268], and this was shown on this work.



**Figure 5-1.** Mesh qualities for wall pressure loss for one hole flame stabiliser 22.44mm diameter considering  $k-\epsilon$  compared with the experimental results [157]

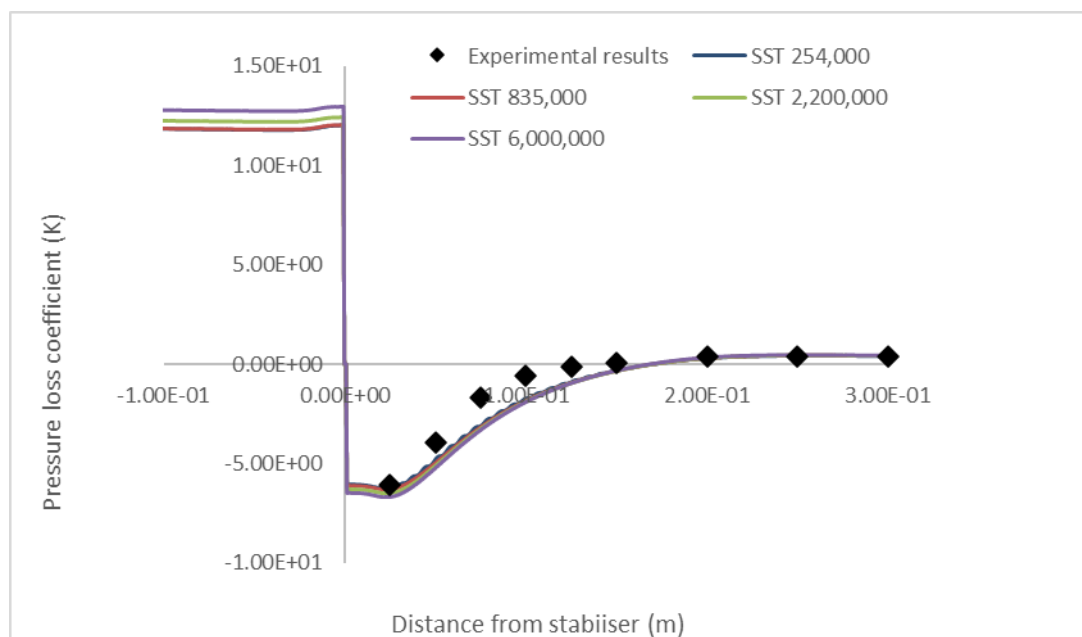


**Figure 5-2** Mesh qualities for wall pressure loss for one hole flame stabiliser 22.44mm diameter considering SST compared with the obtained experimental results [157]

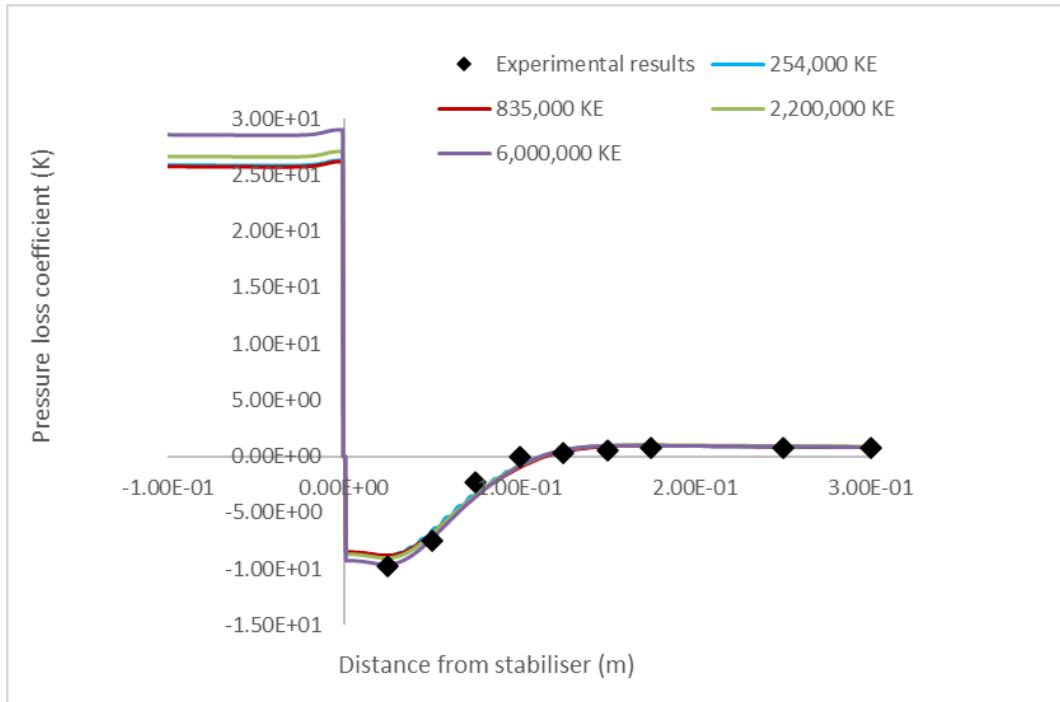
**Table 5-1.**  $C_D$  and  $C_C$  for single 22.44mm air hole flame stabilizer for the investigated mesh sizes

			Modelling		Experiment		Error %	
Turb. Model	Mesh Quality	Element No	$C_D$	$C_C$	$C_D$	$C_C$	$C_D$	$C_C$
k- $\epsilon$	Finer	5,974,098	0.815	0.656	0.818	0.65	0.37	0.92
	Fine	2,189,768	0.846	0.679	0.818	0.65	3.42	4.46
	Medium	834,828	0.861	0.688	0.818	0.65	5.26	5.85
	Coarse	254,410	0.861	0.691	0.818	0.65	5.26	6.31
SST	Finer	5,974,098	0.818	0.656	0.818	0.65	0.00	0.92
	Fine	2,189,768	0.835	0.668	0.818	0.65	2.08	2.77
	Medium	834,828	0.849	0.679	0.818	0.65	3.79	4.46

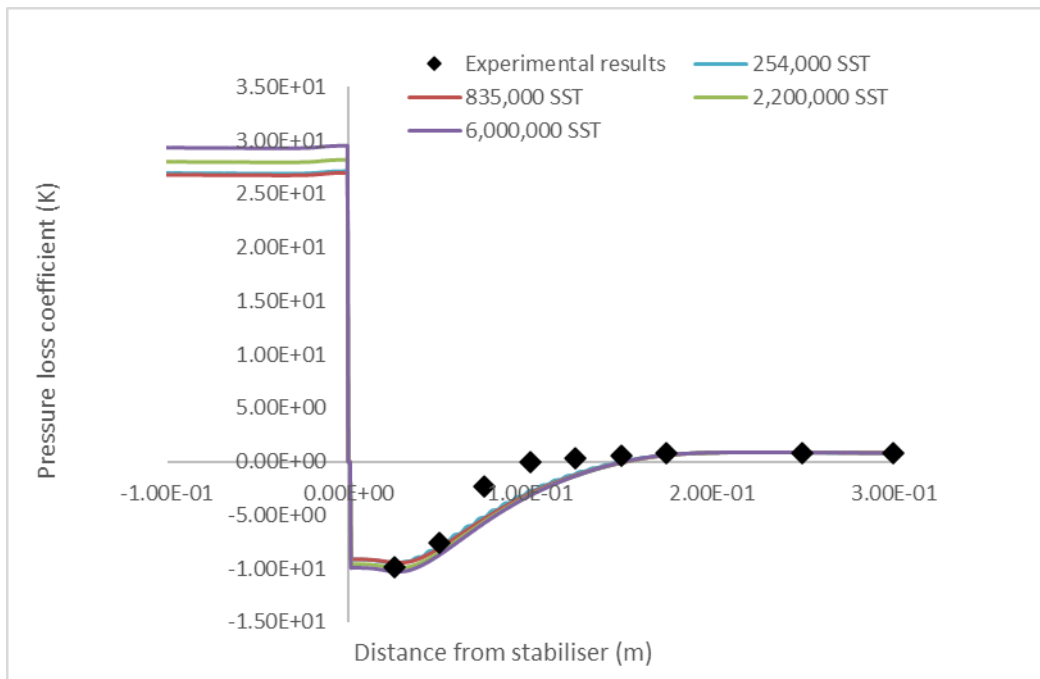
### 5.2.2 Single 19.27mm air hole flame stabiliser

Figure 5-3 shows the obtained pressure loss plots as the coefficient K along the combustor for the different mesh sizes studied using the turbulence model  $k-\epsilon$ . This mesh independence study showed no difference in the coarse and medium qualities. The 6M element mesh showed the most significant difference from the other plots. However, the calculated values for  $C_D$  and  $C_C$  for this mesh size were the closest to the experimental results shown in Table 5-2.

Figure 5-4 shows the same mesh independence study for the one hole stabiliser geometry using SST. Again, the obtained values differed from the experimental results for pressure loss. However, a slightly better agreement was achieved with this model while calculating  $C_D$  and  $C_C$  2M elements mesh size with a calculated percentual error of 0.13% for the  $C_D$  and 0.96% for the  $C_C$ .



**Figure 5-3.** Mesh qualities for wall pressure loss for one hole flame stabiliser 19.27mm diameter considering  $k-\epsilon$  compared with the obtained experimental results [157]



**Figure 5-4.** Mesh qualities for wall pressure loss for one hole flame stabiliser 19.27mm diameter considering  $SST$  compared with the obtained experimental results [157]

**Table 5-2.**  $C_D$  and  $C_c$  for single 19.27mm air hole flame stabilizer for the investigated mesh sizes

			Modelling		Experiment		Error %	
Turb. Model	Mesh Quality	Element No	$C_D$	$C_c$	$C_D$	$C_c$	$C_D$	$C_c$
$k-\epsilon$	Finer	5,881,732	0.741	0.632	0.747	0.628	0.80	0.64
	Fine	2,189,768	0.768	0.653	0.747	0.628	2.81	3.98
	Medium	834,828	0.78	0.663	0.747	0.628	4.42	5.57
	Coarse	254,410	0.78	0.665	0.747	0.628	4.42	5.89
SST	Finer	5,881,732	0.731	0.621	0.747	0.628	2.14	1.11
	Fine	2,189,768	0.748	0.634	0.747	0.628	0.13	0.96
	Medium	834,828	0.765	0.65	0.747	0.628	2.41	3.50
	Coarse	254,410	0.761	0.646	0.747	0.628	1.87	2.87

Even though the turbulence model  $k-\omega$  SST better matched the experiment in calculating the discharge and contraction coefficients, the pressure loss coefficient traverses perfectly agreed with the experimental data using  $k-\epsilon$ . Also, the simulations carried out with the  $k-\omega$  model took longer to converge. Given these reasons, the SST model was not considered for any other simulation.

### 5.3 Modelling of pressure loss for four holes flame stabilisers

The previously studied stabiliser geometries were then simulated considering a whole 76mm combustor and the actual four-hole flame stabiliser domains, and the results are now presented. All the simulations were carried out with the turbulence model  $k-\epsilon$ . The aim was to compare the aerodynamic results obtained considering a single hole stabiliser with those obtained for four-hole models. Only two mesh sizes were studied for this activity since divergence and unnecessary simulation times were encountered with meshes with more than 4 million elements.

### 5.3.1 Four 22.44mm air hole stabiliser

Figure 5-5 compares the mesh sizes studied for the four-hole flame stabiliser with an air hole diameter of 22.44mm. Table 5-3 shows the calculated values for the  $C_D$  and  $C_C$  obtained from Figure 5-5. A perfect agreement was achieved with the experimental data for the 2.7M element mesh showing a percentual error of 0.13% for the  $C_D$  and 0.73% for the  $C_C$ . These values were smaller than the 3% obtained for the single hole geometry considering a similar mesh size. Thus, better agreement with the experimental data was achieved when simulating a 90° sector of the four-hole geometry than an octant of a single hole of the same stabiliser. This was due to the effect of recirculation zones and turbulence inside the combustor, which were assumed to have a uniform behaviour for a single hole, as shown in the following lines.

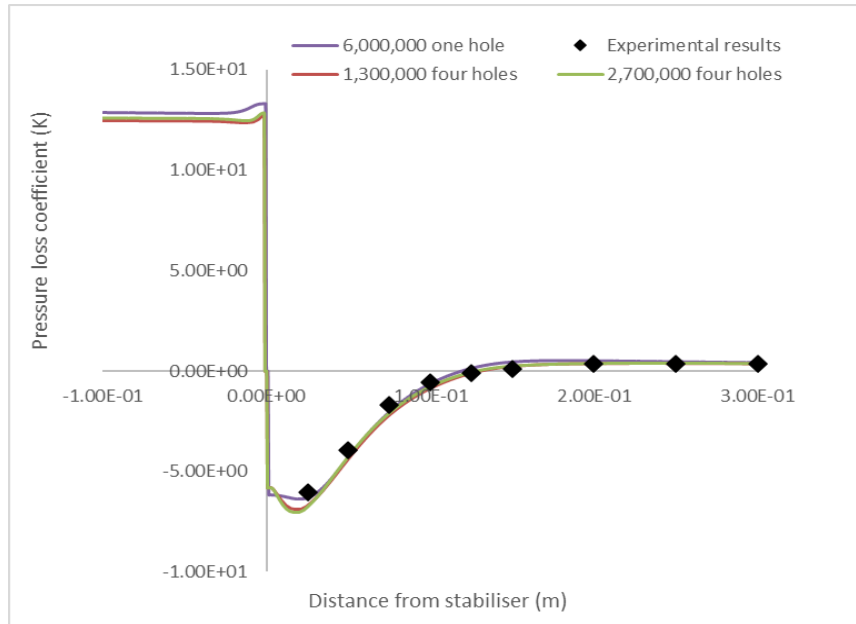


**Figure 5-5.** Mesh qualities for wall pressure loss for four hole flame stabiliser 22.44mm diameter considering  $k-\epsilon$  compared with the obtained experimental results [157].

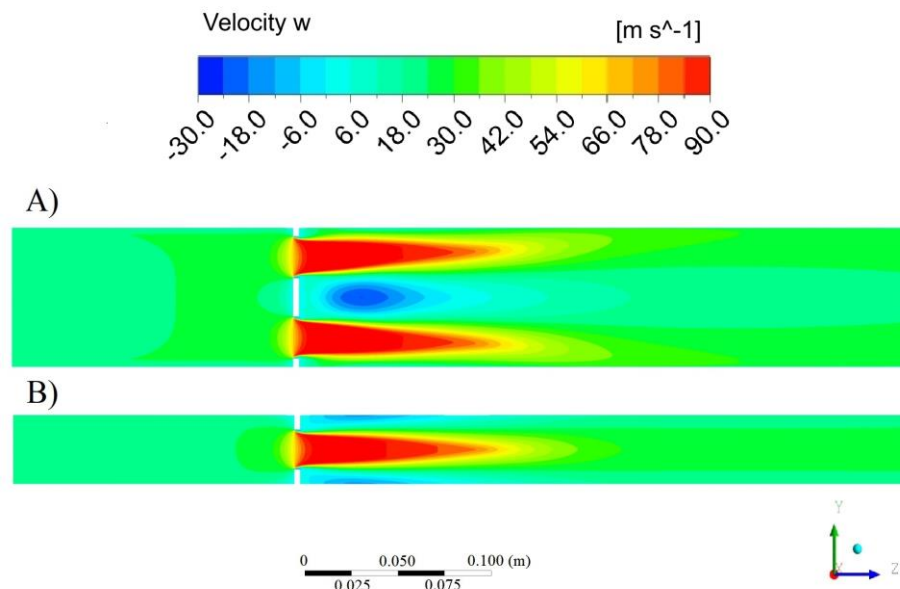
**Table 5-3.**  $C_D$  and  $C_C$  for a four 22.44mm air hole flame stabilizer for the investigated mesh sizes

			Modelling		Experiment		Error %	
Turb. Model	Mesh Quality	Element No	$C_D$	$C_C$	$C_D$	$C_C$	$C_D$	$C_C$
$k-\epsilon$	Medium	2,694,912	0.824	0.649	0.818	0.65	0.73	0.15
	Coarse	1,300,000	0.827	0.655	0.818	0.65	1.10	0.77

Equations (14) and (15) were used to calculate the  $C_D$ , where a  $C_D$  of 0.764 was obtained for this model. Unfortunately, this value was much lower than those obtained experimentally.

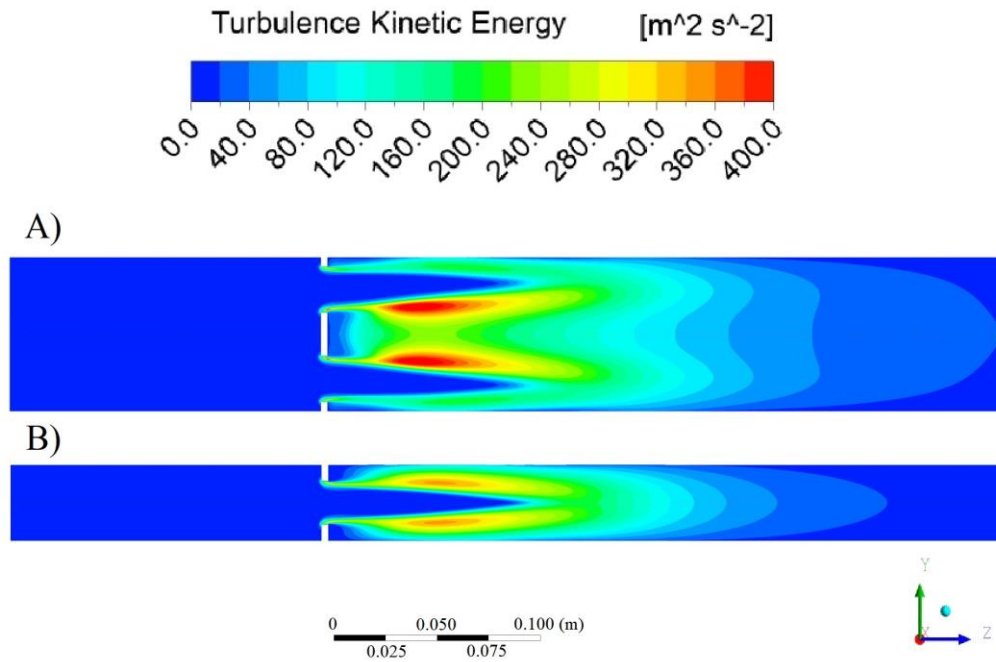
Figure 5-6 compares the obtained velocity contours for a single hole flame stabiliser with the 6M element mesh four-hole stabiliser. The air jet velocity of 84 m/s was achieved for the single hole geometry compared to 87m/s obtained with the four-hole. However, the geometry featuring a single hole showed a high-velocity shear region around the circumference of the air jet, as shown in Figure 5-6 a). In contrast, a faster shear region in between the air jets is observed for the four-hole geometry. This shear region generated a large central recirculation zone with less impact near the walls than the single hole geometry, as shown in Figure 5-6 b).

Figure 5-7 shows the turbulence kinetic energy (TKE) for the four-hole geometry compared to the single hole. Figure 5-7 a) shows a high turbulence zone of  $380 \text{ m}^2/\text{s}^2$  50mm downstream of the stabiliser, just below the vena contracta. This region corresponds to the inner recirculation side of the shear layer shown in Figure 5-6 a). In contrast, Figure 5-7 b) shows a uniform distribution of the kinetic energy with the peak of  $338 \text{ m}^2/\text{s}^2$  at the same distance relative to the stabiliser. A high turbulence zone was encountered near the wall for the single hole geometry. This high turbulence zone was not observed for the four-hole geometry, given the shape of the geometry.



**Figure 5-6.** Velocity contours for flame stabiliser 22.44mm diameter A) four holes 2.7M elements, B) one hole 6M elements

Figure 5-8 shows transversal planes with the flame stabiliser's highest predicted TKE at 55mm. Figure 5-8 a) shows three high turbulence zones surrounding each air hole of the stabiliser, whereas for the single hole geometry in Figure 5-8 b) the TKE was predicted to be totally uniform around the air jet also illustrated in Figure 5-7 b).



**Figure 5-7.** TKE contours for hole stabiliser 22.44mm diameter A) four holes, B) one hole.

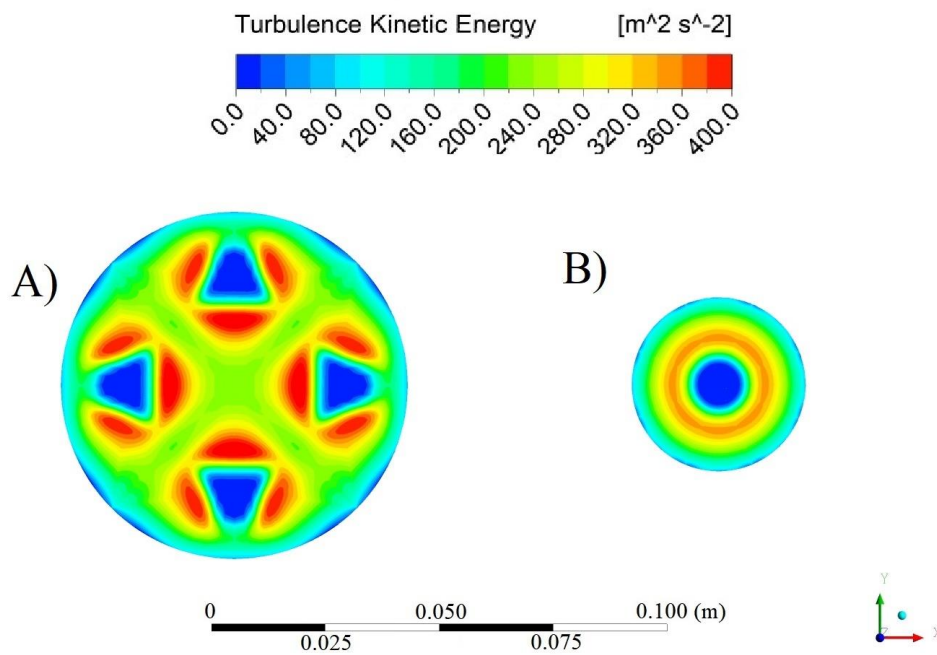


**Figure 5-8.** TKE contours 55 mm downstream the stabiliser for flame stabiliser 22.44 mm diameter. A) one hole combustor. B) 4 holes combustor.

### 5.3.2 Four 19.27mm air hole stabiliser

Akin to the previously presented geometry, only two mesh sizes were studied for the four-hole flame stabiliser with a 19.27mm air hole diameter. Figure 5-9 shows the mesh independence study of the four holes geometry compared to the most refined mesh obtained for a single hole and the experimental data for the 19.27mm air hole stabiliser. Both meshes obtained for four holes showed a higher pressure loss in the upstream length of the combustor and lower pressure loss after the stabiliser compared to the traverses obtained for a single hole. Similar to the other geometries the  $C_D$  and  $C_C$  were calculated from the obtained pressure loss coefficient  $K$  traverses and compared to the experimental values, where the same porosity of  $\beta=0.256$  used for the single hole geometry was considered for an experimental  $C_D = 0.738$ . The contraction coefficient was calculated from this value to be  $C_C=0.62$ . Both results were compared with the simulations in Table 5-4, showing the best agreement with the 2.7M element mesh. The slight disagreement for the finer mesh could be related to the high aspect ratio and the inflation layer up to 0.001mm used for the mesh of this geometry.

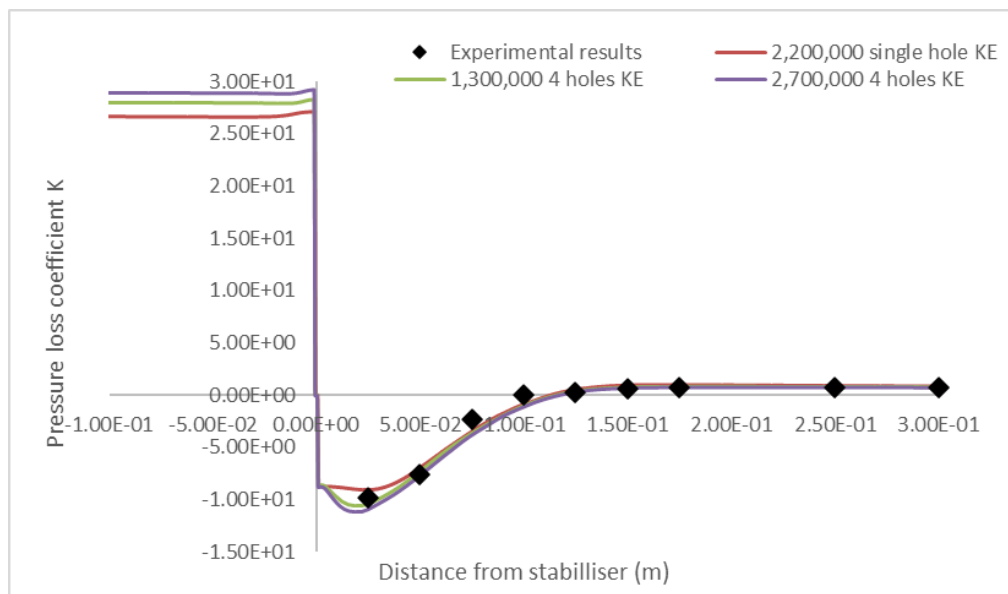


**Figure 5-9.** Mesh qualities for wall pressure loss for four hole flame stabiliser 19.27mm diameter considering  $k-\epsilon$  compared with the obtained experimental results [157].

The axial velocity contours obtained for this second four-hole geometry are compared to those obtained for the single hole in Figure 5-10. A similar velocity distribution to the one achieved for a hole diameter of 22.44mm is observed. The highest velocity of 122 m/s was obtained at the sudden contraction for the four-hole geometry, compared to the 114 m/s of the single hole stabiliser. The

main recirculation zones were located at the walls for the single geometry, where the backflow velocity was 29 m/s. Similar to the 22.44mm hole geometry, a central recirculation zone was obtained for the four-hole stabiliser under the vena contracta, where the highest backflow of 39 m/s was obtained.

**Table 5-4** .  $C_D$  and  $C_C$  for a four 19.27mm air hole flame stabilizer for the investigated mesh sizes

			Modelling		Experiment		Error %	
Turb. Model	Mesh Quality	Element No	$C_D$	$C_C$	$C_D$	$C_C$	$C_D$	$C_C$
k-ε	Medium	2,694,912	0.735	0.616	0.747	0.628	1.63	1.95
	Coarse	1,300,000	0.748	0.629	0.747	0.628	0.13	0.16

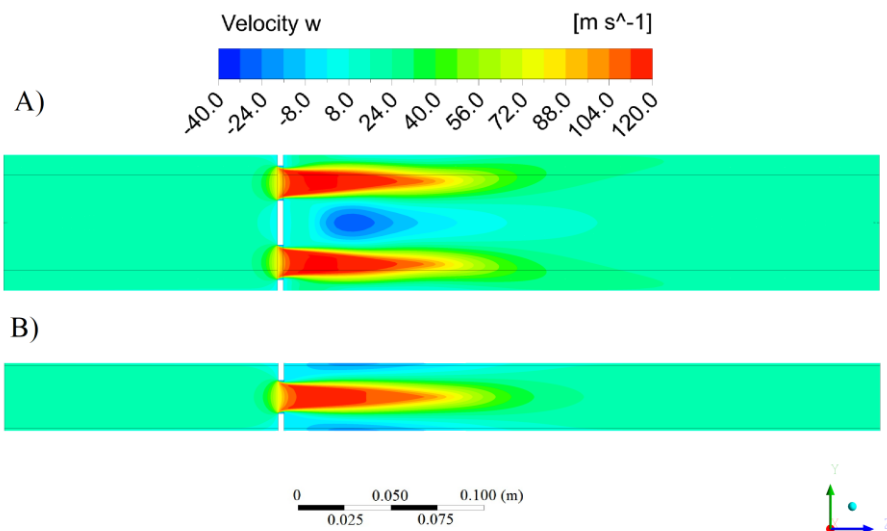


**Figure 5-10.** Axial velocity contours for flame stabiliser 19.27mm diameter. A) one hole combustor. B) 4 holes combustor

The turbulence kinetic energy contours for the four-hole geometry are compared with the obtained for a single hole stabiliser in Figure 5-11. The recirculating fluid in the central region of the combustor observed in Figure 5-10 A) produced kinetic energy peaks, in contrast to the single-hole geometry, which illustrates a perfectly uniform TKE distribution in the shear layer of the air jet. The highest turbulence peak was obtained at the stabiliser inlet at the sharp entry of the air hole. However, the second most relevant peak was obtained 60 mm downstream of the stabiliser for both cases, shown in Figure 5-12. This figure illustrates again three high turbulence zones surrounding the

air holes for the four-hole geometry, compared to the uniform energy distribution of the single hole.

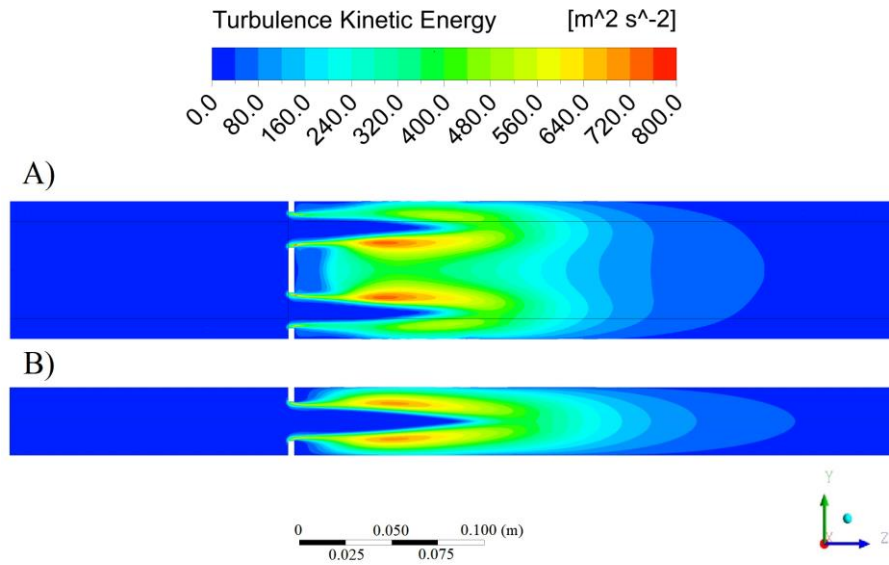


**Figure 5-11.** TKE contours for flame stabiliser 19.27mm diameter. A) one hole combustor. B) 4 holes combustor

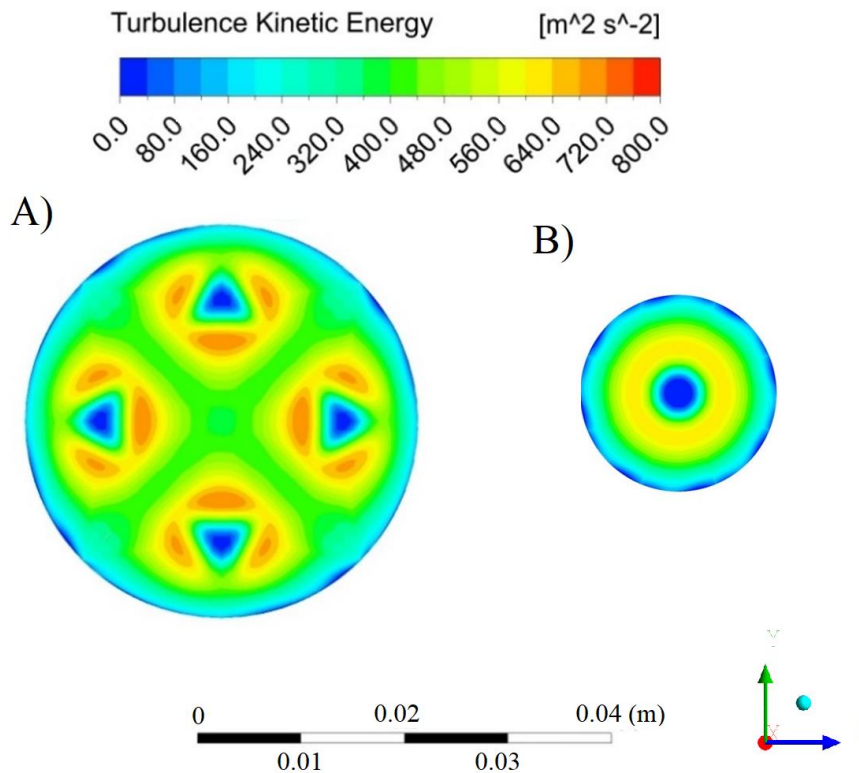


**Figure 5-12.** TKE contours 60mm downstream the stabiliser for flame stabiliser 19.27mm diameter. A) one hole combustor. B) 4 holes combustor

### 5.4 The influence of stabiliser thickness over fluid aerodynamics.

The aerodynamics of the four-hole flame stabiliser featuring the fuel injection GM2 with 19.62mm air holes and a plate thickness of 9.53mm were evaluated with CFD and compared with pressure loss experimental data, similar to the thin plates. This geometry is studied for its mixing and low NO<sub>x</sub> combustion capabilities in Chapter 6.

Figure 5-13 shows a mesh independence study for three mesh sizes used for this geometry to ensure that the results were invariant to the mesh. The obtained traverses showed to be very similar for the different sizes. However, the agreement with the experiment was not perfect as obtained with the other geometries. Figure 5-13 also compares the stabiliser with a 19.27mm airhole grid plate. Both geometries were designed for a pressure drop of 2%.

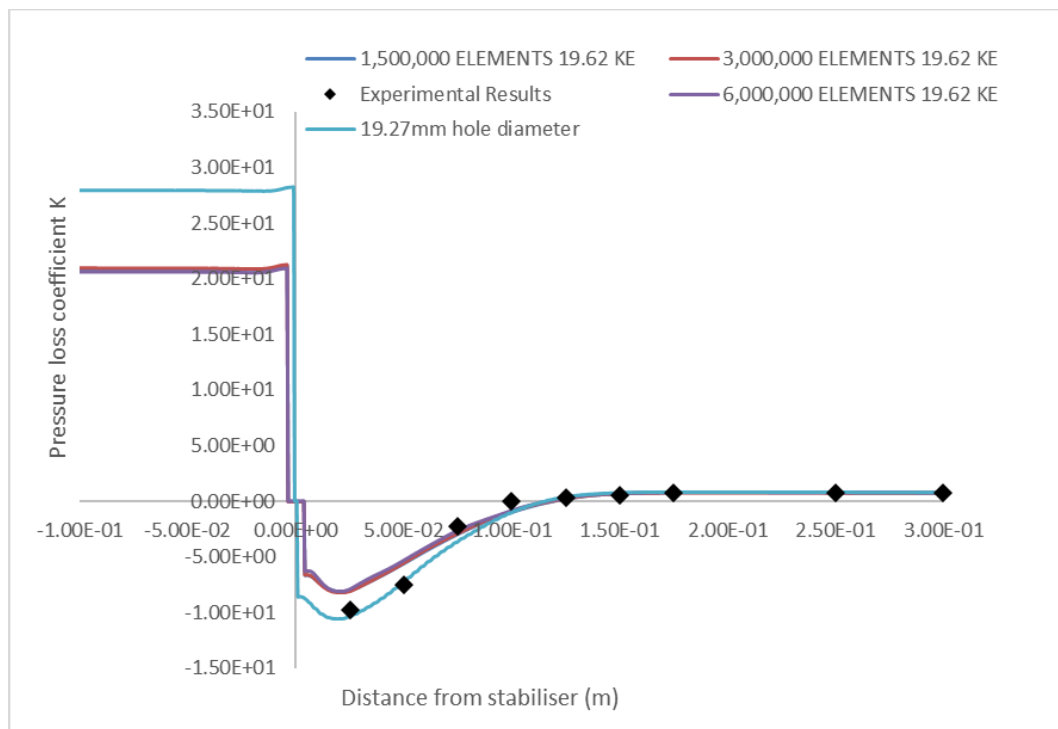


**Figure 5-13.** Mesh qualities for wall pressure loss for four-hole flame stabiliser 19.62mm diameter compared with 19.27mm stabiliser hole and the experimental results considering  $k-\epsilon$  [157].

Table 5-5 compares the obtained  $C_D$  and  $C_c$  from the pressure drop coefficient K measured in Figure 5-13 with the experimental data for a four-hole stabiliser with a pressure drop of 2%. Even though the results were very similar between the three different mesh sizes, a minimum error of 12.8% for the  $C_D$  was obtained with the experimental results for the mesh with 6M elements. As explained in Chapter 3 and shown in 5.5 this error was thought to be due to the

manufacturing of the plate which showed a welding slope at the holes inlet. However, it was later discovered that the issue was in the mesh itself. This is discussed in 5.5.

**Table 5-5.**  $C_D$  and  $C_C$  for a four 19.62mm air hole flame stabilizer for the investigated mesh sizes

			Modelling		Experiment		Error %	
Turb. Model	Mesh Quality	Element No	$C_D$	$C_C$	$C_D$	$C_C$	$C_D$	$C_C$
K-E	Fine	6,000,000	0.845	0.703	0.969	0.804	12.8	12.56
	Medium	2,700,000	0.839	0.699	0.969	0.804	13.42	13.06
	Coarse	1,300,000	0.841	0.7	0.969	0.804	13.21	12.94

The results for the effect of the area ratio in  $C_C$  showed in 2.2.9.1 Table 2-2, and the  $C_D$  values obtained using Equations (14), (15) and (9) were compared with the experimental values and illustrated in Table 5-6. An agreement was achieved for the  $C_C$  values of Table 2-2 and Equation (14) in comparison to the experimental results obtained for the flame stabiliser with a hole diameter of 19.27mm, and sensible similitude was obtained using Equations (15) and (9). On the other hand, both values for  $C_C$  and  $C_D$  disagreed with the measured results for the thicker flame stabiliser featuring 19.62mm air holes (GM2). Again, this disagreement was thought to be due to a construction feature at the inlet face of the stabiliser, where the pipe used for the air hole was welded to the stabiliser plate giving a welding slope at the air inlet instead of a sharp entry affecting the aerodynamics.

**Table 5-6.**  $C_C$  and  $C_D$  values for grid plate geometries featuring thin and thick blockages compared with the measured experimental values

Stabiliser Diameter (mm)	$A_2/A_1$	t/d	$C_C$ Table 2	$C_D$ Eq. 12	$C_D$ Eq. 13 & 7	Meas. $C_C$	Meas. $C_D$
19.27	0.256	0.17	0.65	0.78	0.673	0.628	0.747
19.62	0.265	0.49	0.66	0.80	0.800	0.804	0.969

Figure 5-14 illustrates the axial velocity contours alongside the combustor for the thin grid plate featuring air holes of 19.27mm compared to the thicker GM2 grid plate with 19.62mm air holes. No considerable effects in the velocity were observed for a thick plate apart from the lower velocity achieved at the vena contracta, given the slightly larger air hole diameter. The total mass flow for the GM2 stabiliser at 25mm downstream of the contraction was 0.026 kg/s, and the recirculating mass at the same distance was  $6.22e^{-3}$  kg/s, which corresponds to 24% of the total mass flow. This was the most significant recirculation zone in the entire domain. A small recirculation zone is shown at the contraction zone in Figure 5-14 B). For a better appreciation, Figure 5-15 shows a close up of the stabiliser region to study the fluid behaviour while impinging on the flat edge of the stabilizer. Flow separation can be observed, and the mentioned recirculation zone in the area of the stabiliser thickness.

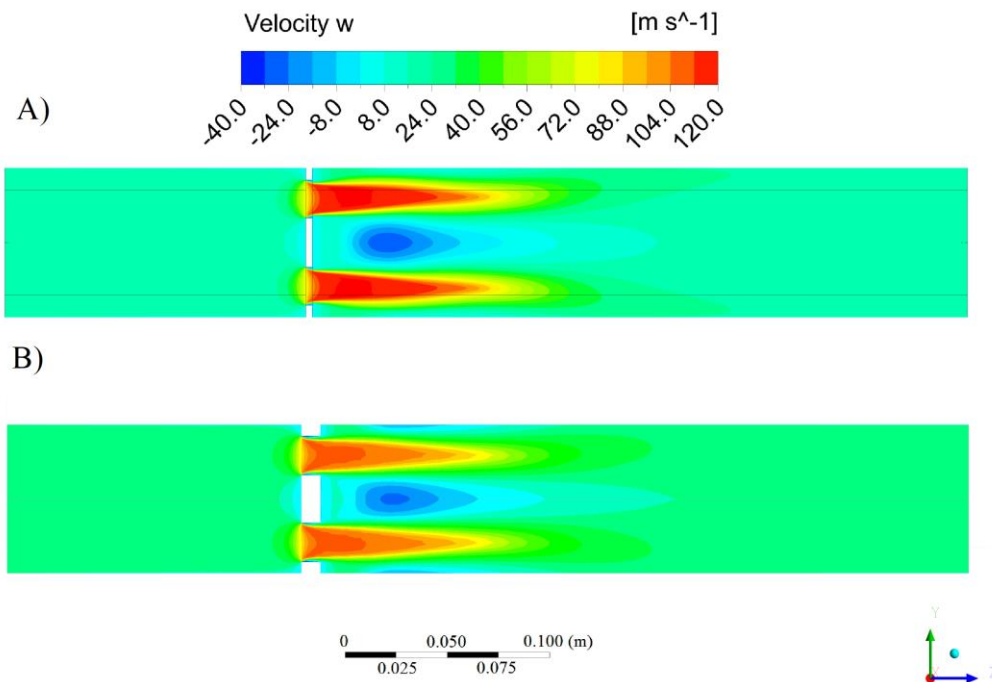


**Figure 5-14.** Axial velocity contours for four-hole flame stabiliser. A) one hole 19.27mm diameter. B) 19.62mm diameter

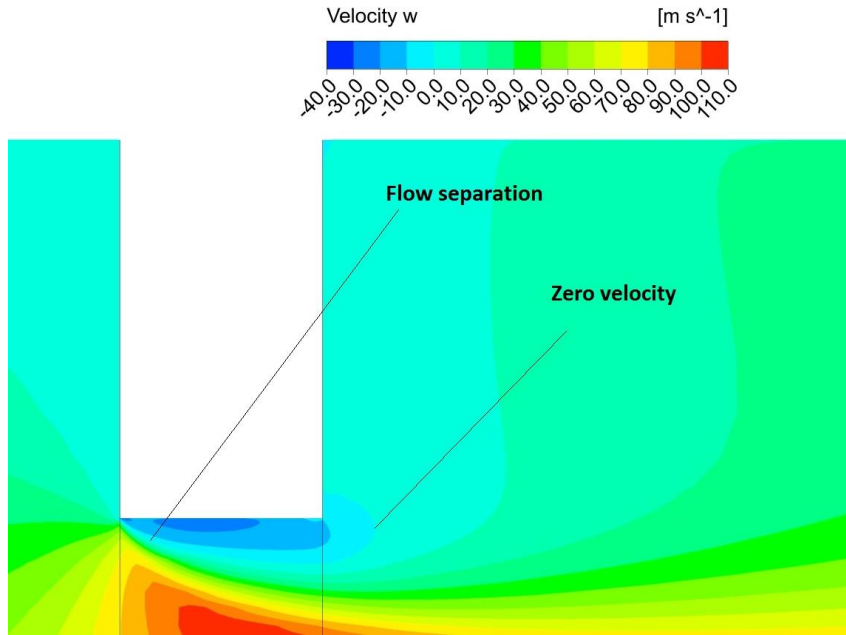


**Figure 5-15.** Closeup for stabiliser region showing the flow separation and recirculation zone.

Figure 5-16 illustrates the turbulence kinetic energy contours alongside the combustor for both stabilisers, where a considerable effect is observed for the 9.53mm plate. The larger plate thickness worked as a diffuser of the TKE as shown in Figure 5-16 B), where most of the produced energy is illustrated inside the stabiliser air-holes, in contrast to the 3.2mm plate geometry in which the peak of the TKE is 60mm downstream the stabiliser.

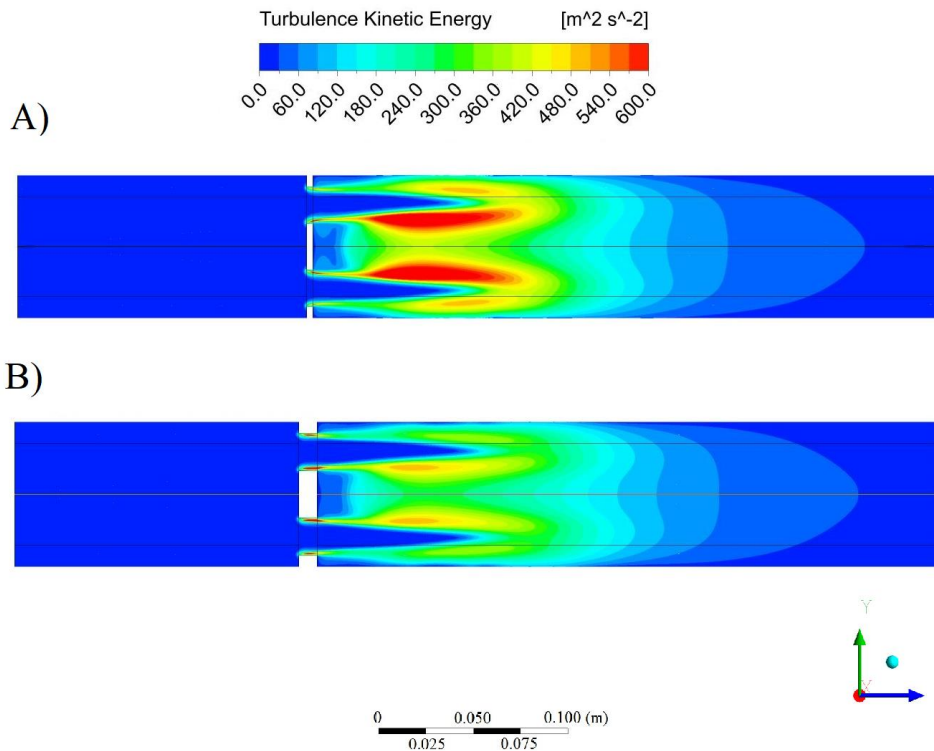


**Figure 5-16.** TKE contours for four-hole flame stabiliser. A) one hole 19.27mm diameter. B) 19.62mm diameter

### 5.5 The influence of welded inlet of grid plate flame stabiliser over fluid aerodynamics

A hypothesis was raised, given the disagreement encountered for the 19.62mm airhole grid plate flame stabiliser. The original physical plates were designed as ideal flat plates. However, the manufacturing of the model ended up with a welding slope at the stabiliser inlet. The study of the effect of the inlet weld on pressure loss and downstream aerodynamics is now presented. The weld slope was modelled at the stabiliser inlet face with a chamfer of 45 and 13 degrees to the stabiliser face, as shown in Figure 5-17.

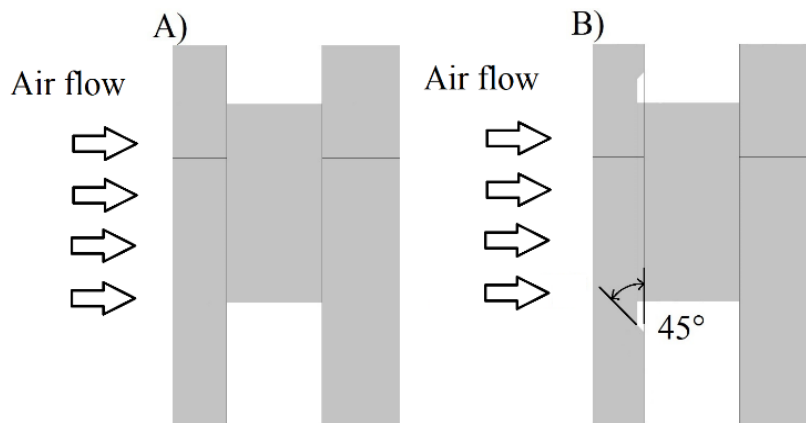


**Figure 5-17.** Enclosure of 19.62mm airhole grid plate flame stabiliser: A) Flat inlet face, B) inlet face with welding slope

The pressure coefficient  $K$  plots for both angles of the welded inlet were compared with a flat plate entry. The experimental results for 2% pressure loss in Figure 5-18, considering meshes of roughly 3M elements. The 13° slope showed an upstream pressure loss coefficient of  $K= 19$  and a minimum of  $K= - 8.3$  just after the stabiliser. The 45° slope showed a maximum  $K=18$  upstream of the stabiliser and a minimum of  $K=-6.2$  just after the contraction.

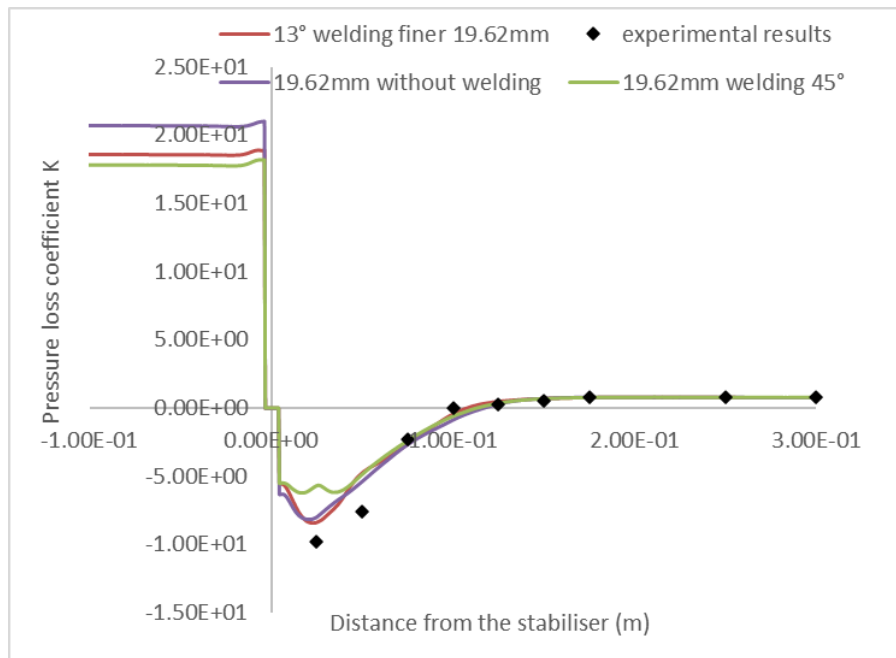


**Figure 5-18.** Mesh qualities for wall pressure loss for four-hole flame stabiliser 19.62mm diameter considering  $k-\epsilon$  comparing various plate inlet weld slopes and the experimental results [157].

The  $C_D$  and  $C_c$  were calculated from the obtained values of the pressure loss coefficient and are shown in Table 5-7

**Table 5-7.**  $C_D$  and  $C_c$  for a four 19.62mm air hole flame stabilizer featuring various plate inlet weld slopes

			Modelling		Experiment		Error %	
Plate weld slope	Mesh Quality	Element No	$C_D$	$C_c$	$C_D$	$C_c$	$C_D$	$C_c$
13° weld	Fine	2,805,401	0.914	0.77	0.969	0.804	5.68	4.23
	Medium	2,309,679	0.922	0.766	0.969	0.804	4.85	4.73
	Coarse	885,000	0.947	0.795	0.969	0.804	2.27	1.12
45° weld	Finer	2,882,000	0.893	0.726	0.969	0.804	7.84	10.2
	Fine	2,045,000	0.888	0.721	0.969	0.804	8.36	10.82
	Medium	1,020,000	0.924	0.778	0.969	0.804	4.64	3.73
	Coarse	588,000	0.936	0.765	0.969	0.804	3.4	5.34
Flat	Fine	6,000,000	0.845	0.703	0.969	0.804	12.79	12.56

	Medium	2,700,000	0.839	0.699	0.969	0.804	13.41	13.06
	Coarse	1,300,000	0.841	0.7	0.969	0.804	13.21	12.9

. The mesh independence study showed a significant effect on the mesh sizes over the results. This was expected because unstructured meshes tend to show more sensitivity to the results than structured meshes with a defined blocking. The stabiliser inlet with a slope of 45° showed a closer match with the experimental data using a mesh of 1M elements. However, the excellent agreement reached with the flat thin plates couldn't be achieved.

A considerable effect was observed in the turbulence kinetic energy contours for a welded stabiliser inlet compared to a flat plate. The slope worked as a diffuser at the stabiliser inlet, generating a shorter air jet, as shown in Figure 5-19.

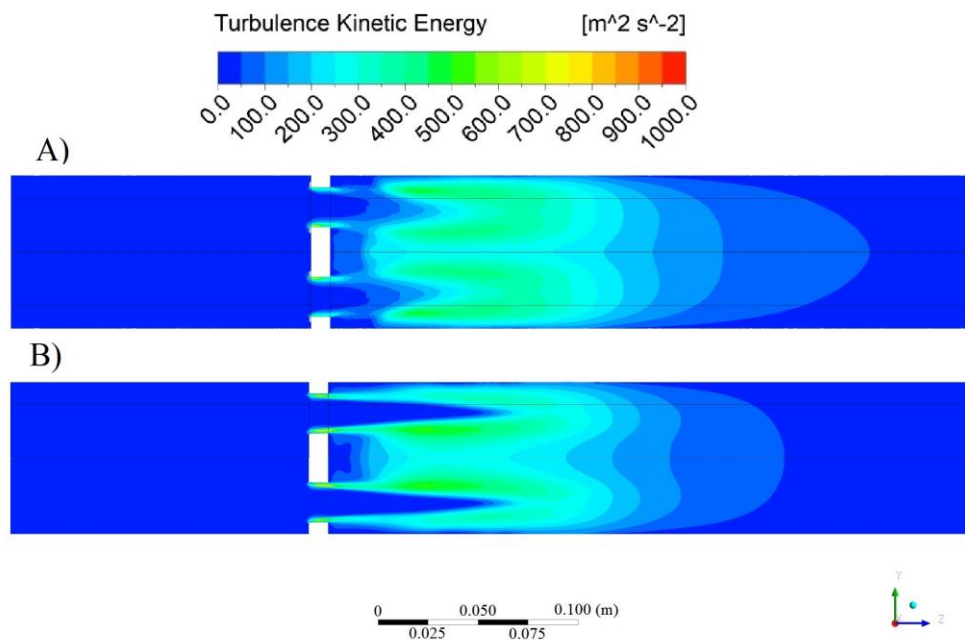


**Figure 5-19.** Turbulence Kinetic energy comparison for 19.62mm four hole flame stabiliser: A) Welded inlet. B) Flat inlet.

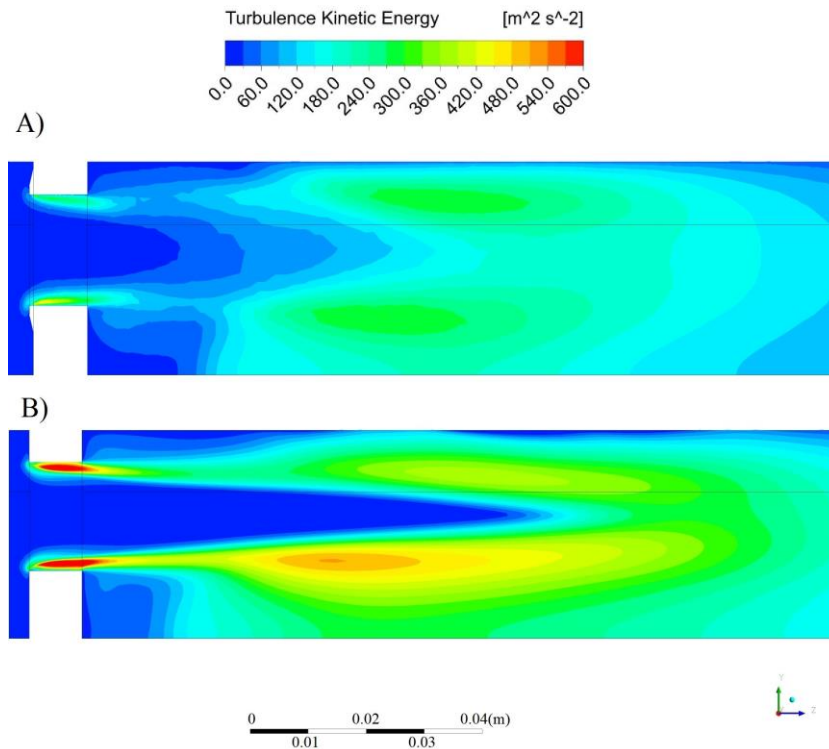


**Figure 5-20.** Closeup for stabiliser region showing the TKE for 19.62mm stabiliser hole geometry. A) Welded inlet, B) Flat inlet.

The turbulence after the air jet could allow better air/fuel mixing and benefit the  $\text{NO}_x$  levels, which will be demonstrated in Chapter 6.

Figure 5-20 shows a closeup of the stabiliser region showing the TKE contours for both  $13^\circ$  entry slope and flat plates. A considerable amount of energy is shown to be diffused at the stabiliser entry for the model with the welded entry compared to the flat geometry.

Akin to the flat geometry, the most significant recirculation zone was located 60 mm downstream of the stabiliser. This was the zone with the highest TKE.

The welding slope at the inlet of the air holes was modelled and compared to a flat plate geometry for this simulation using tetrahedral unstructured meshes to study the effect of the welding inlet over the combustion. Most aerodynamics and combustion contours showed a meaningless difference between both geometries, as observed for the TKE contours in Figure 5-21. This concluded that the differences encountered in the previous study were due to the tetrahedral mesh used to model the welding at the inlet of the air hole, not the welding itself.

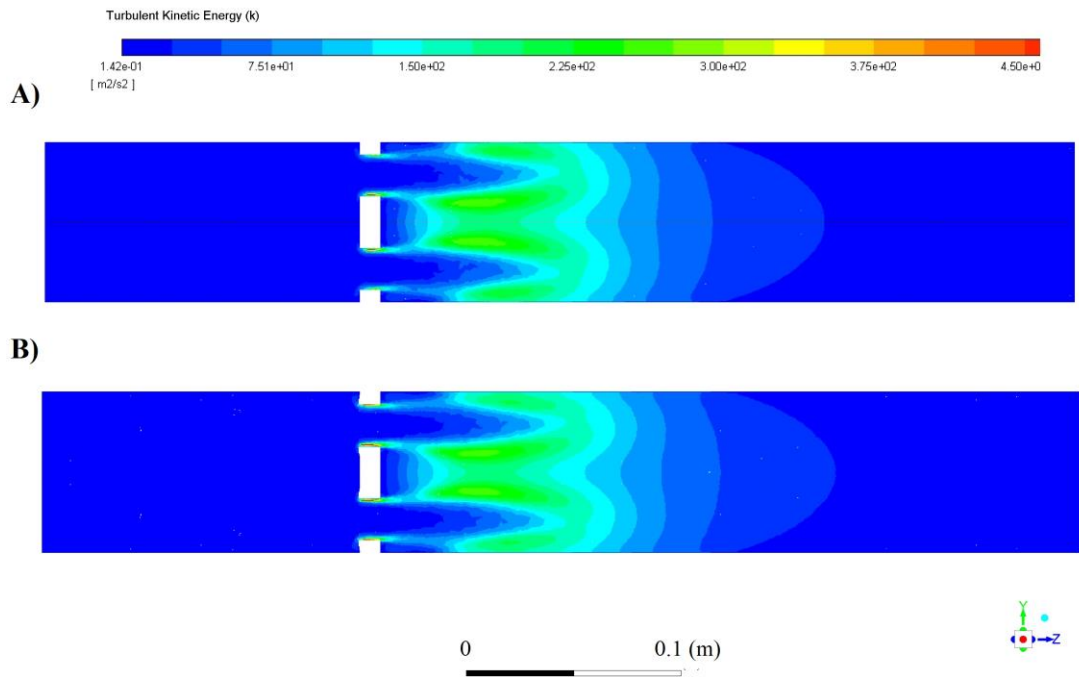


**Figure 5-21.** TKE contours for GM2 using the SDF. A) Flat plate, B) Plate with the welded inlet.

However, the study is still valid as differences were encountered for different slope inclinations, which could affect the combustion.

## 5.6 Mesh sensitivity for flame stabiliser aerodynamics

Various mesh sizes were studied for the different stabiliser geometries aiming for mesh independence from the simulation results. The most expensive evaluated meshes were composed from nearly six million elements, which for the premixed geometries showed a very good agreement. Finer meshes were not investigated since the computational time was being compromised and the desired agreement of  $>1\%$  was achieved.

### 5.6.1 Single hole geometries

The different evaluated mesh sizes for the stabiliser with a hole diameter of 22.44mm showed the best agreement with the experimental results for  $C_D$  and  $C_c$  for a single hole considering 5.97M elements. For the geometry with diameter of 19.27mm the best agreement was achieved with a mesh of 5.88M elements.

The error variance between simulation and experiment from 2.2M to 6M element meshes was 3% for the  $C_D$  and  $C_c$  considering the geometry with hole

diameter of 22.44mm and 2.5% for the one featuring a 19.27mm hole diameter for both  $C_D$  and  $C_c$  as shown in Figure 5-22.

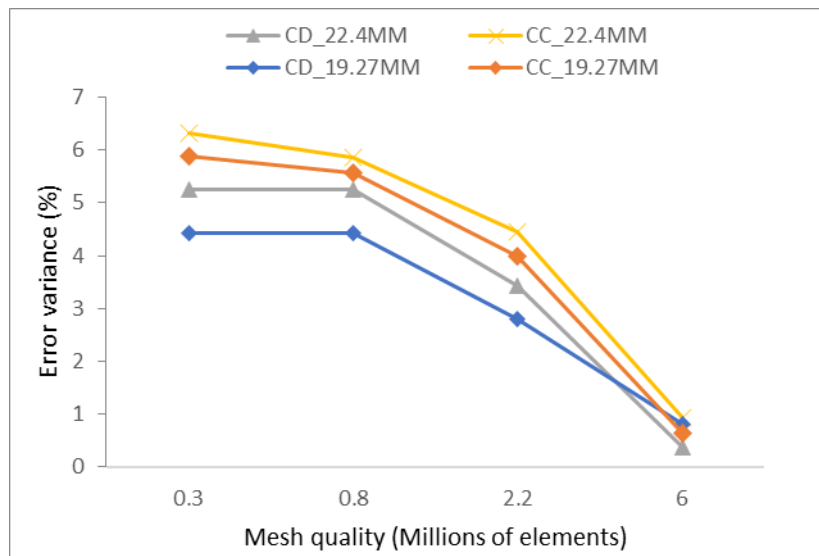


**Figure 5-22.** Simulation/experiment error variance between mesh qualities for single hole geometries

### 5.6.2 Four hole geometries

For the four-hole premixed stabilisers only two mesh sizes were investigated. As explained previously in this chapter, this was because divergence was encountered above 3M elements and the desired 1% agreement was achieved for the geometries with meshes of 2.7M elements. The simulation/experiment error variance between both mesh qualities was 0.4% for the  $C_D$  and 0.6% for the  $C_c$  for the geometry with 22.44mm hole diameter, this shows a very small variance between both results.

A better agreement between experiment and simulation was achieved with the mesh composed of 1.3M elements in comparison to the 2.7M element mesh for the geometry with a hole diameter of 19.27mm. In contrast, the error variance between simulation and experiment for the two studies meshes for the geometry featuring holes of 19.27mm diameter was 1.5% for the  $C_D$  and 1.7%, 1% higher than the 22.44mm diameter geometry. This can be seen in Figure 5-23.

As observed, better mesh sensitivity was achieved with the four-hole geometries compared to the single holes.

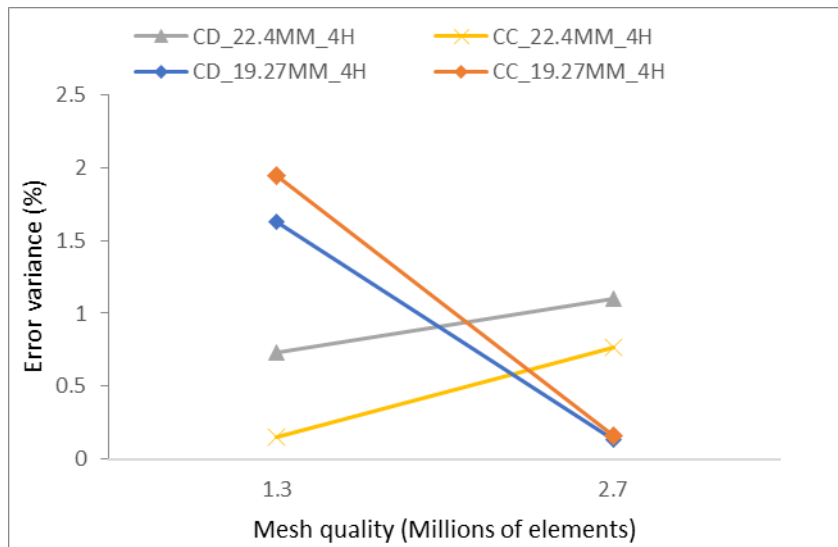


**Figure 5-23.** Simulation/experiment error variance between mesh qualities for four hole geometries

The grid mix stabiliser featuring air holes of 19.62mm could be modelled for a 6M element mesh. The simulation considering a flat inlet face of the stabiliser gave bad agreement with experiments, however there was only a variation of less of 1% between mesh sizes for both  $C_D$  and  $C_c$ .

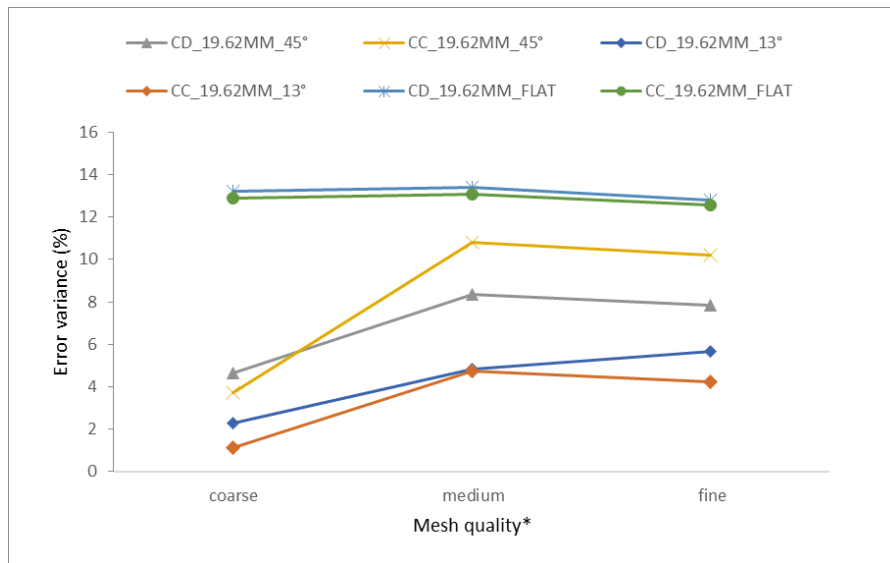


**Figure 5-24.** Simulation/experiment error variance between mesh qualities for grid mix 19.62mm geometries<sup>6</sup>.

<sup>6</sup> The number of elements varied for the flat geometry showing six million elements for its fine quality. The other two geometries featured identical mesh sizes as shown in Table 5-7.

The geometry featuring a welded slope of  $45^\circ$  showed a simulation/experiment error variation of 0.5% from the medium size mesh (2M elements) to the fine quality (3M elements) for both  $C_D$  and  $C_C$ .

The flame stabiliser model featuring a slope of  $13^\circ$  showed an error variance of 1% for the  $C_D$  and 0.5 for the  $C_C$  from the medium size mesh (2M elements) to the fine one (6M elements).

This concludes that mesh sensitivity was achieved with the simulations for the flame stabiliser used for Grid Mix featuring four air holes of 19.62mm diameter and a thicker stabiliser of 9.5mm.

## 5.7 Conclusions

The CFD predictions of premixed flame stabiliser featuring a thin grid plate of 3.2mm perfectly agreed with the experimental results for both stabiliser geometries using the turbulence model  $k-\varepsilon$  and hexahedral structured meshes up to 6 million elements considering a single and four holes. Given the better agreement between the experiments and the simulations for 19.27 and 22.44mm air hole stabilisers using the turbulence model  $k-\varepsilon$ ,  $k-\omega$  SST was not used for the 19.62mm air hole simulations.

The predicted  $C_D$  and  $C_C$  for the GM2 flame stabiliser featuring an air hole of 19.62mm and a stabiliser thickness of 9.53mm showed less agreement with the experimental results than the other studied geometries. The disagreement was thought to be due to the manufacturing of the grid plate, which featured a welding cord around the inlet air holes. This feature resulted from the flame stabiliser working as a hollow fuel plenum.

Mesh independence was achieved with the flame stabiliser used for Grid Mix showing less than 1% error variation between mesh sizes. Similarly, the thinner premixed grid plates geometries showed less than 1% simulation/experiment error variance between mesh sizes. In contrast, the geometries featuring a single stabiliser hole did not achieve mesh independence even for a 6M element.

More work must be done to achieve perfect agreement with the experimental results. The use of more sophisticated simulation methods such as LES or DNS might approach the simulation results to better match the experimental data.

## Chapter 6. CFD STUDY FOR NON-PREMIXED COMBUSTION GAS TURBINE GRID PLATE FLAME STABILISERS

### 6.1 Introduction

The isothermal mixing and combustion simulation results, including  $\text{NO}_x$  prediction, are now presented for gas turbine low  $\text{NO}_x$  grid plate flame stabilisers using turbulence and combustion models available in ANSYS FLUENT for RANS simulation.

### 6.2 Isothermal analysis of air/fuel mixing for grid plate flame stabiliser

The isothermal air/fuel mixing results are presented for the 4 hole 19.62mm diameter flame stabiliser featuring three injection methods. Figure 6-1 illustrates the  $\text{C}_3\text{H}_8$  mass fraction contours at the stabiliser fuel inlet, showing eight equally spaced nozzles for GM1, an annular injection for GM2, and a fuel injection at the centre of the air hole for GM3.

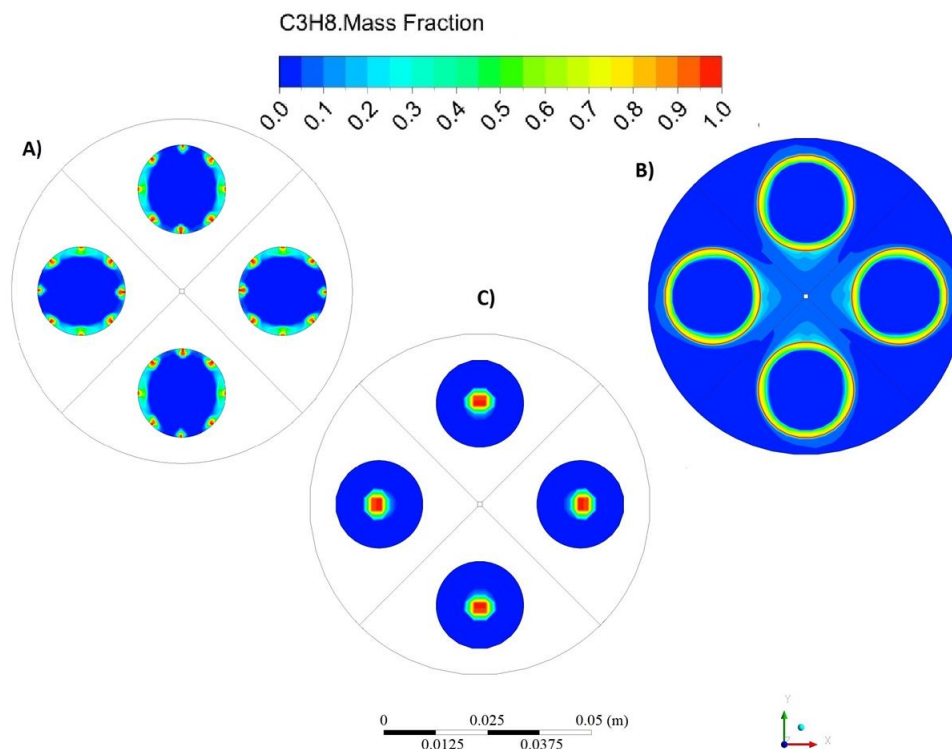


**Figure 6-1.** Simulation of fuel injection methods for A) GM1, B) GM2, and C) GM3.

The equivalence ratio contours alongside the combustor are shown in Figure 6-2 for the three cases. The most important feature observed in the simulation was that the fastest mixing was obtained with GM1, followed by GM2 and

finally GM3. The radial nozzles inside the stabiliser allowed an earlier mixing than the other two methods. Also, the jet in a crossflow generated a recirculation zone inside the stabiliser holes, which provided an extra mixing feature, as shown in Figure 6-2. GM3 showed a wider red region indicating a fuel/rich area than the other two methods. The fuel dragged up by the air jet to well after the shear layer region showed that this fuel injection method usually used by FLOX combustors might not be reliable at the presented high Mach number.

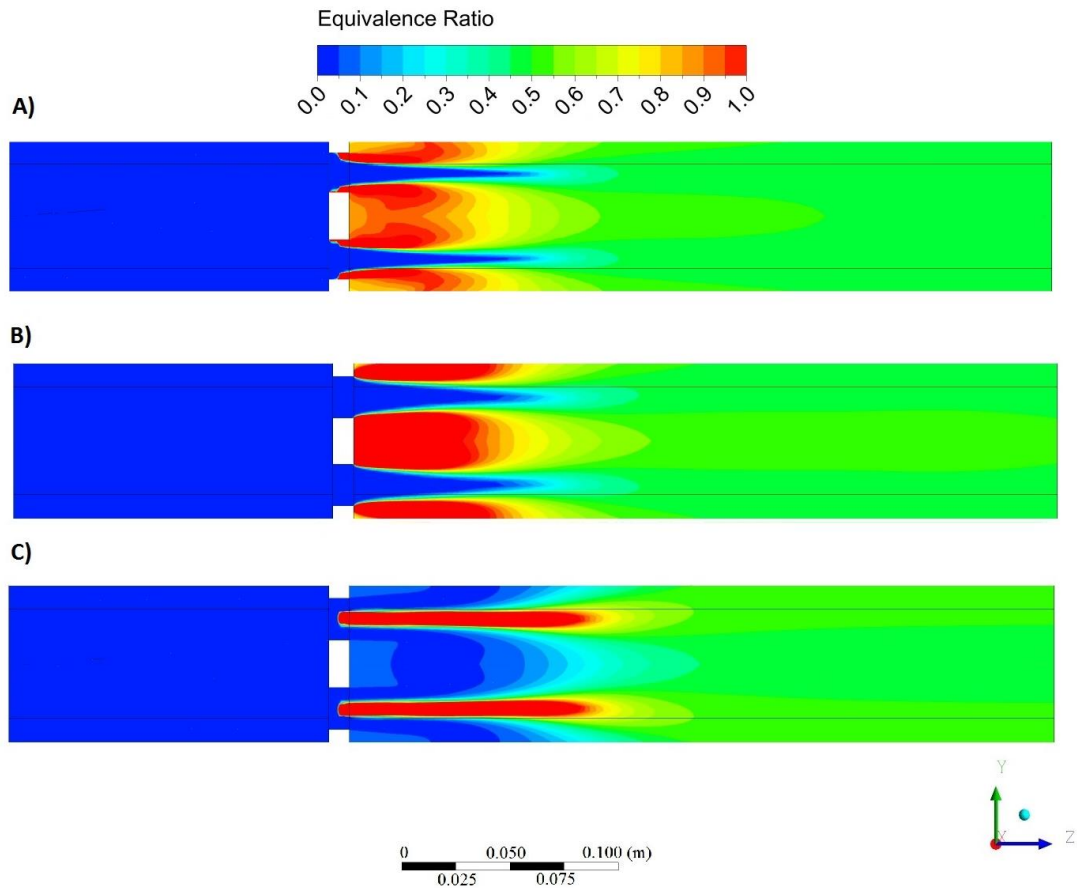


**Figure 6-2.** Equivalence ratio contours for non-reacting simulation A) GM1, B) GM2, I GM3

A more substantial fuel penetration was expected for the radial nozzles of GM1. However, the air jets velocity above 90m/s in the contraction region was higher than the 40 m/s of the fuel nozzles shown in Figure 6-3.

Figure 6-4 illustrates the equivalence ratio contours in a transversal plane 100mm downstream of the stabiliser position, where the desired  $\phi = 0.5$  was nearly obtained by GM1, followed by GM2. Contrastly, GM3 showed a rich central region surrounded by very lean regions, showing that the mixing did not develop properly.

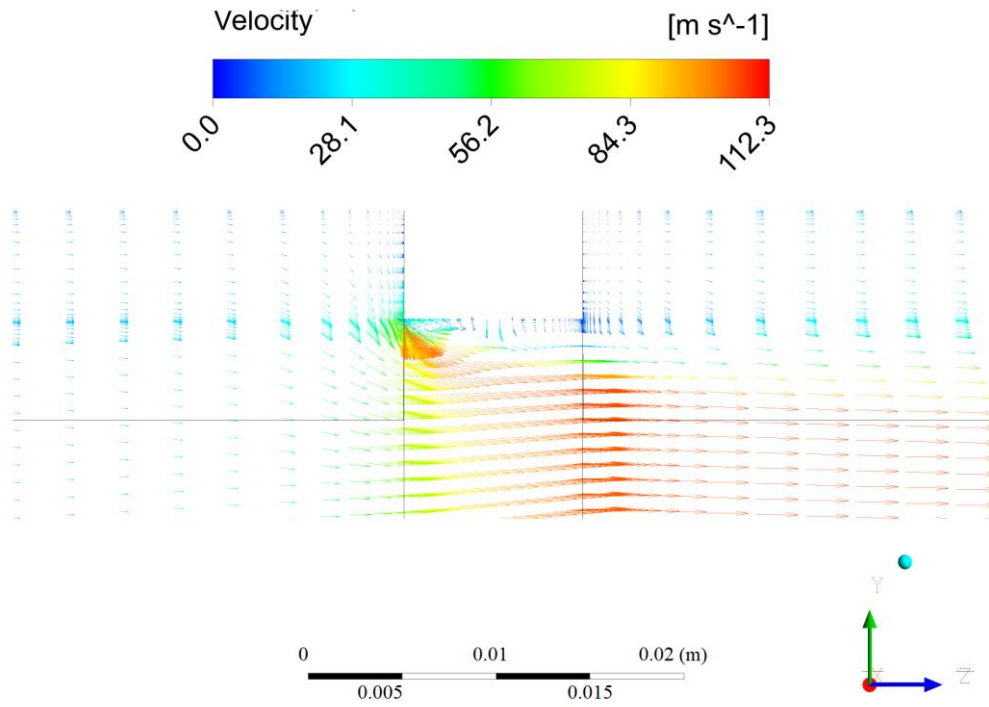


**Figure 6-3.** Closeup of grid plate air hole for GM2 showing velocity vectors

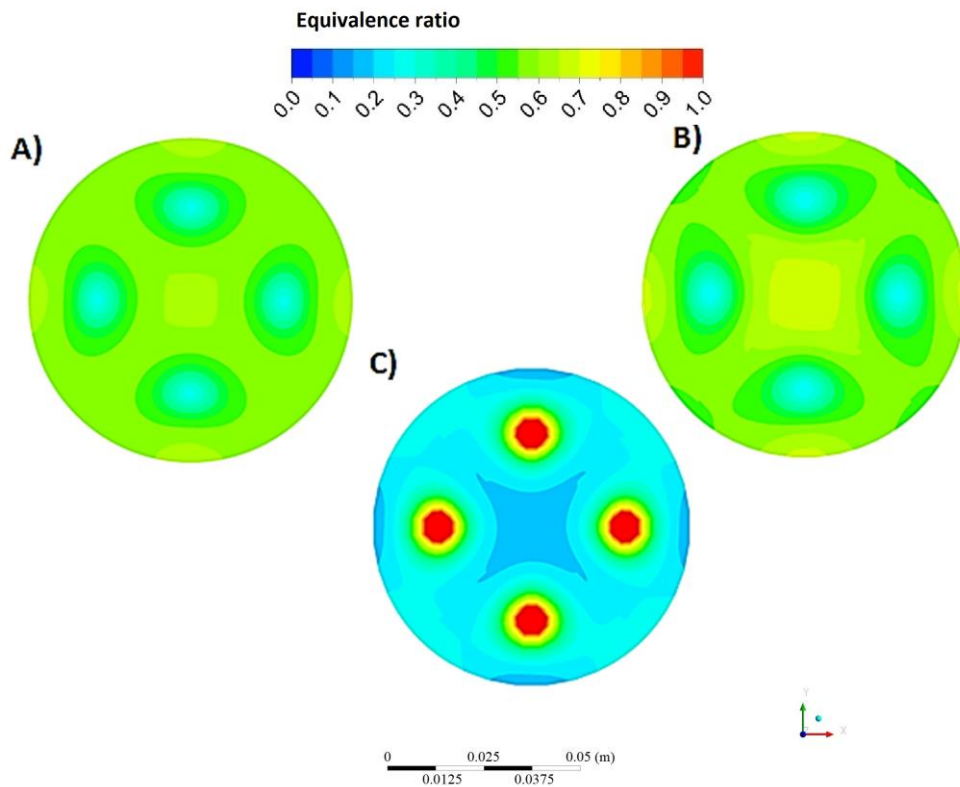


**Figure 6-4.** Equivalence ratio contours 100mm downstream of the stabiliser for a non-reacting simulation. A) GM1, B) GM2, C) GM3

These three methods are investigated for a reacting mixture and NO<sub>x</sub> further in this Chapter.

### **6.3 Combustion analysis of grid plate flame stabiliser GM2**

The results of GM2 evaluated with the various turbulence, and combustion models available for RANS simulation are now presented. The original mixture of propane/air was studied. Additionally, this technology was investigated for its use in hydrogen using the investigated combustion intensity for propane.

#### **6.3.1 GM2 studied with EDM and Chemical equilibrium combustion models**

The simulation results obtained as a preliminary study using the combustion models EDM and Chemical equilibrium for non-premixed combustion were compared with the experimental internal traverses for temperature. The following results are only presented to illustrate the preliminary combustion study for flame stabilisers. However, several assumptions were made at this stage and incorrect parameters could have been selected. As explained in Chapter 2 it has been sometimes shown that EDM might not be suitable for steady state non-premixed simulations.

The results were obtained at two positions of the gas analysis probe: At the combustor centreline and 2.6mm near the wall<sup>7</sup>. These positions were later investigated in detail and changed as described in Chapter 3. Figure 6-5 compares the simulation results with the internal traverse for the temperature at the combustor centreline. The EDM simulation reached a peak temperature of 2480K, much higher than the experimental results. The traverse 35.6mm away from the centreline is compared with simulation results in Figure 6-6, showing an over-prediction for both models.

The temperature contours are shown in Figure 6-7 for both simulations. Both simulations showed a very elongated air jet, splitting the flame into a wall region and a central one. This was thought to be due to the turbulence models used for the simulations, which might have not predicted the aerodynamics successfully. A high overprediction of the peak temperature can also be observed on the region near the wall, where temperatures higher than 2800K were obtained, this overprediction alongside with the overall high temperatures could be for the prediction of richer/than stoichiometric regions which trigger the rise of temperature, as shown by [211].

---

<sup>7</sup> These traverses are identified as centreline/zero mm and 35.6mm in the figures.

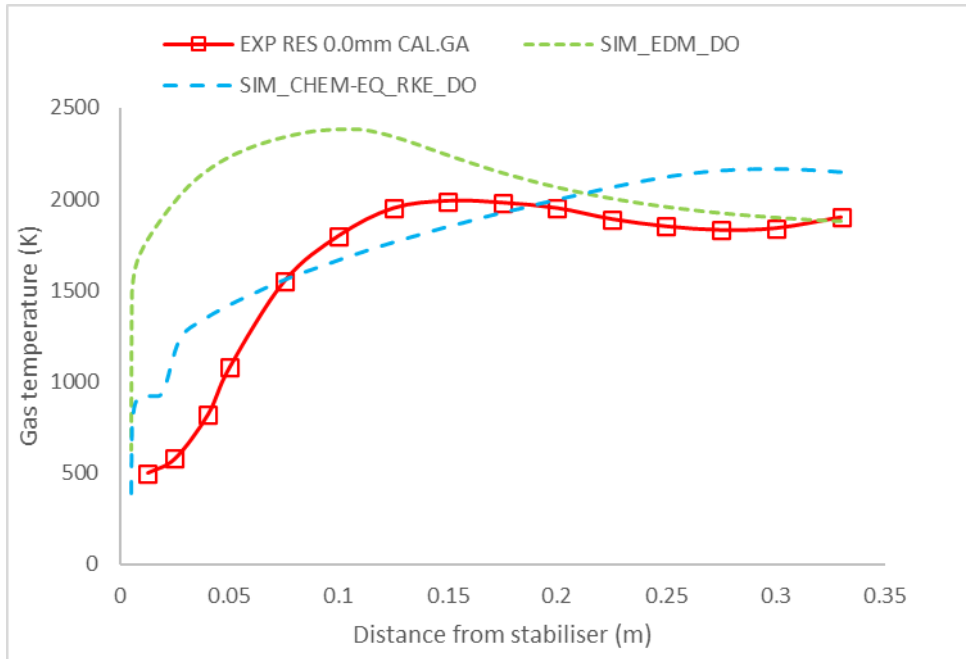


**Figure 6-5.** Comparison of temperature plot obtained with the gas analysis at the combustor centreline between experimental results [157] and simulation using EDM and chemical equilibrium

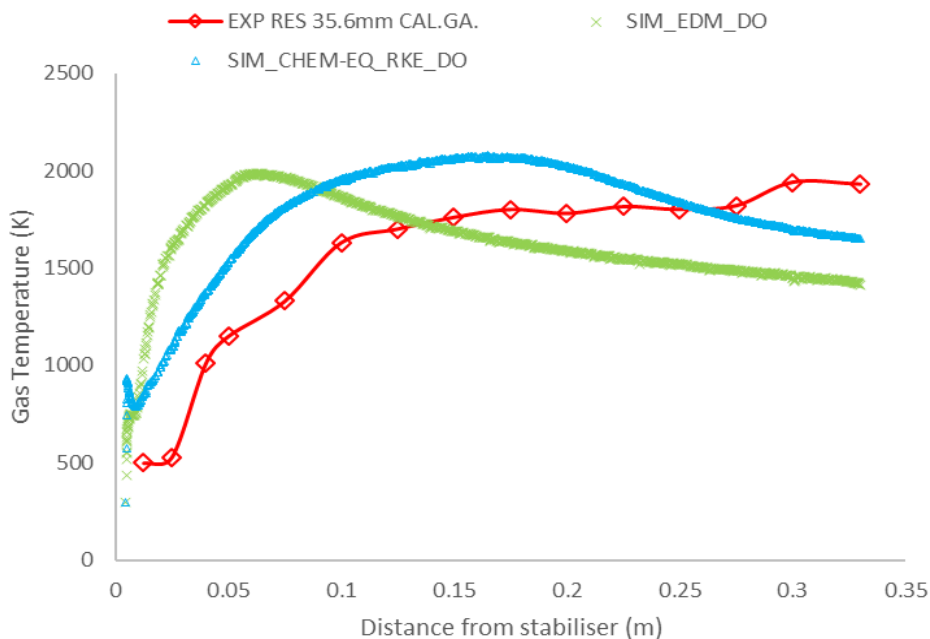


**Figure 6-6.** Comparison of temperature plot obtained with gas analysis 2.6mm from the combustor wall between experimental results [157] and simulation using EDM and chemical equilibrium

A reader might observe some results showing sensible agreement with the experimental results. However, as mentioned before, the positions of the gas analysis probe were later discovered to be incorrect, and the results were not valid. Also, the CFD contours showed a wrong temperature and mixing

distribution inside the combustor showing that the combustion model combustion models were not suitable. The turbulence model k-epsilon was used for this simulation which have also shown to perform poorly for sudden contractions and recirculation zones as explained in Chapter 2.

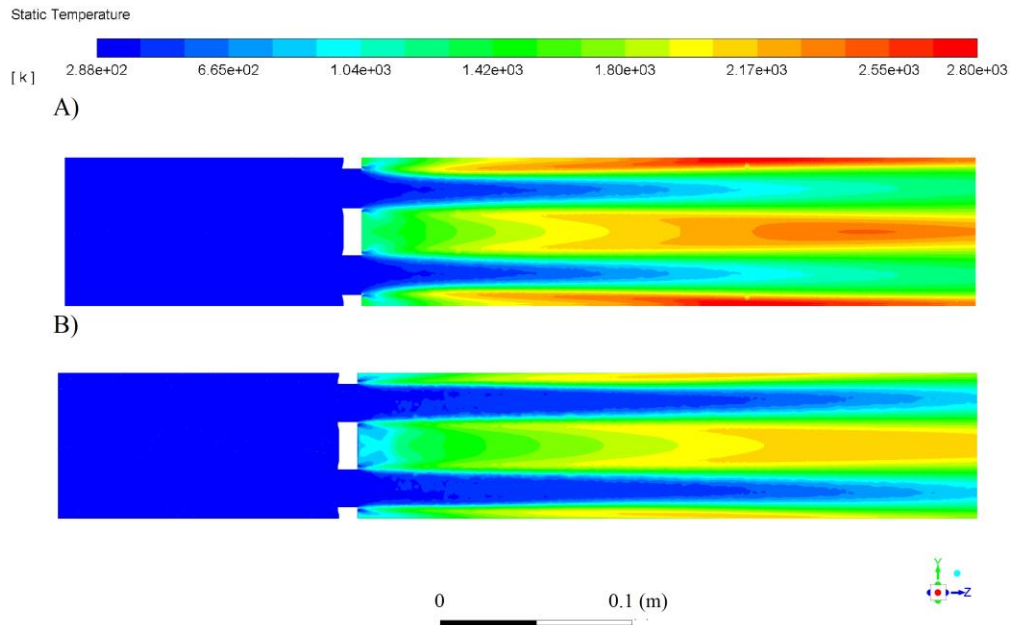


**Figure 6-7.** Temperature contours for combustion simulation for GM1. A)EMD, B) Chemical equilibrium

### 6.3.2 GM2 studied with SDF combustion model

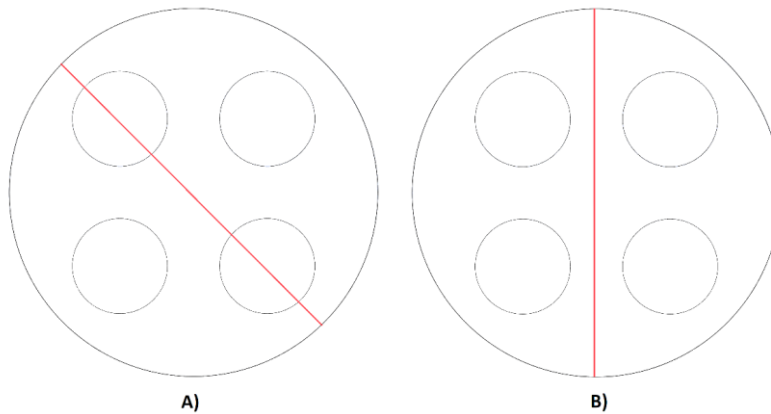
The CFD contours obtained for the Steady Diffusion Flamelet model (SDF) are shown for two orientations inside the combustor: A plane on the centreline along the combustor cutting through the middle of the stabiliser air holes and another one 45° in offset with the first orientation. Both locations are shown in Figure 6-8. The theory behind these two planes is that there was no evidence about the orientation in which the experimental data was collected.

The axial contours along the combustor of velocity, TKE, temperature,  $\phi$ , O<sub>2</sub> and CO for both orientations are shown in Figure 6-9-Figure 6-14.

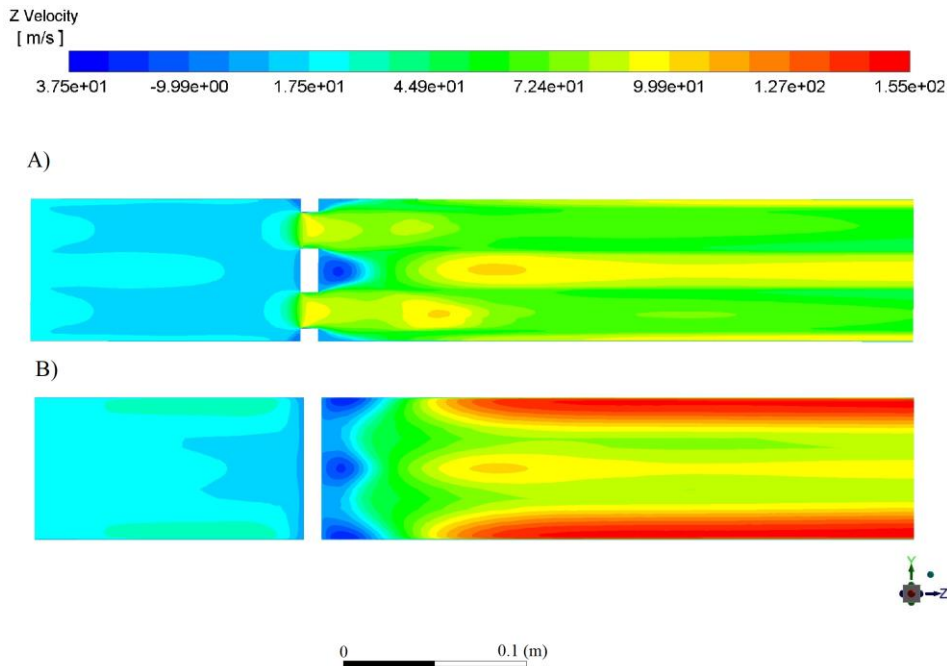
A noticeable difference can be observed between the velocity contours for both planes. A recirculating flow, represented with navy blue, was obtained just after the stabiliser position, as shown in Figure 6-9. Also, a high-velocity region near the walls, 75mm downstream of the stabiliser, is observed for the offset orientation.

Figure 6-10 shows a TKE peak at about 50-100mm from the stabiliser for both orientations. This was where the four air jets merged. No peak TKE was encountered downstream in the air shear layer formatted by the recirculating eddies.

The temperature contours in Figure 6-11 illustrate a hot central zone just after the stabiliser position due to the recirculating gases for both planes shown in Figure 6-9. This zone was not obtained with the experimental results. The wall region where the high-velocity flow was also predicted in Figure 6-9 showed a high temperature for the plane in offset with the holes.



**Figure 6-8.** Internal combustor planes used for the obtention of combustion contours using SDF for GM2 A) Inline with the holes, B) in offset with the holes.



**Figure 6-9.** Axial velocity contours for GM2 for SDF simulation. A) Inline with the holes, B) In offset with the holes.

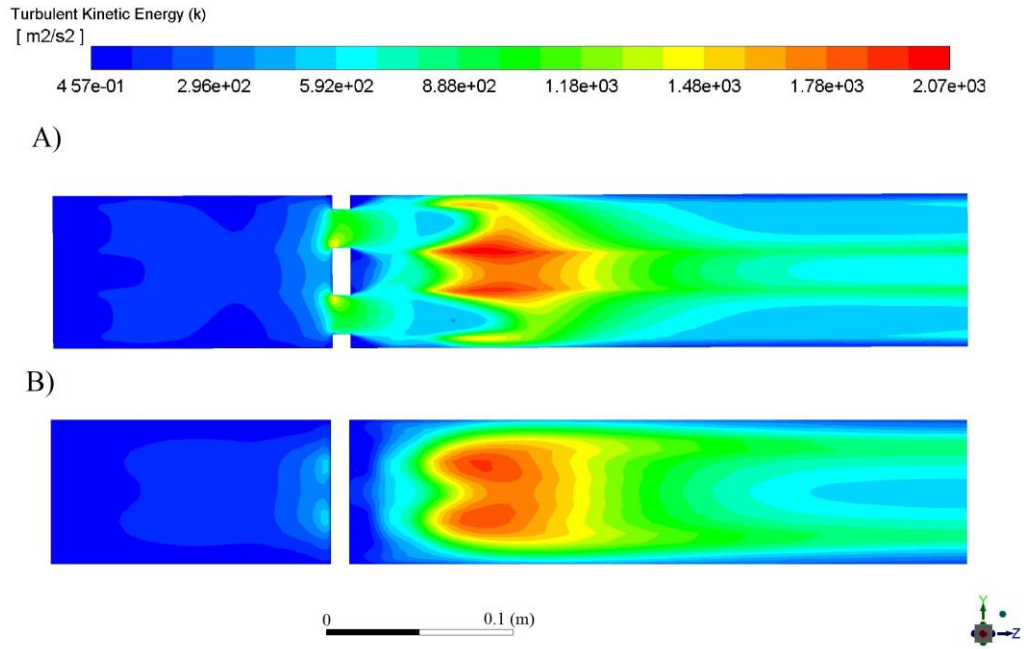


**Figure 6-10.** Axial TKE contours for GM2 for SDF simulation. A) Inline with the holes, B) In offset with the holes.

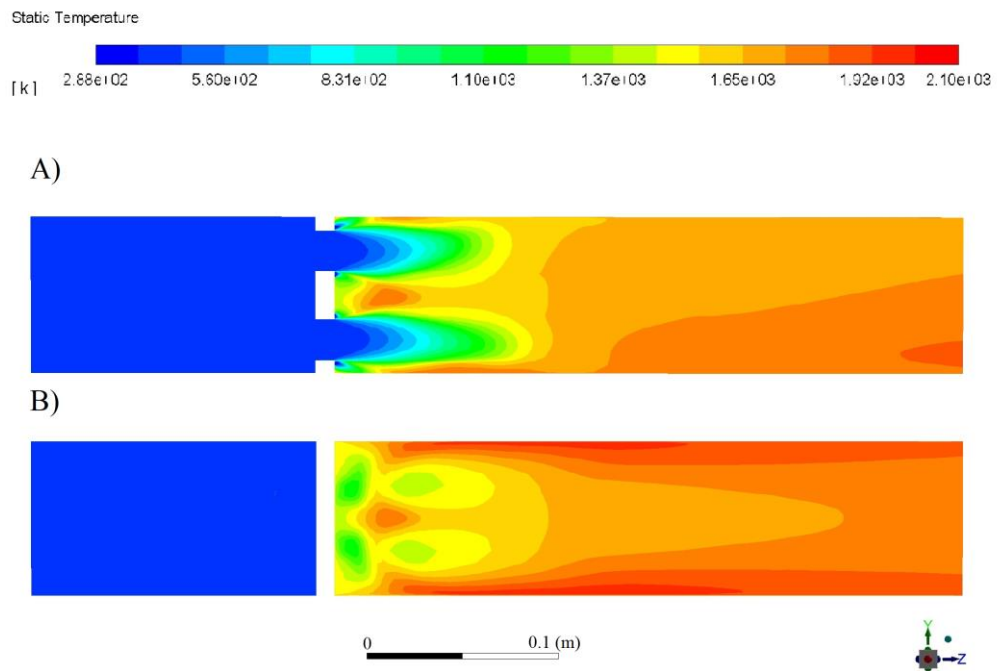


**Figure 6-11.** Axial temperature contours for GM2 for SDF simulation. A) Inline with the holes, B) In offset with the holes.

In contrast to the earlier simulations using  $k-\epsilon$  and RNG  $k-\epsilon$ , much shorter air jets were predicted with realizable  $k-\epsilon$ . The flame struggled to develop in the central high turbulence zone, and no flame was observed at the stabiliser position. Modelling the combustor as a four-hole geometry resulted in some

asymmetry at the combustor outlet. However, the rest of the combustion showed very symmetrical features for each hole.

The equivalence ratio contours in Figure 6-12 A) show a fuel-rich zone in the central recirculating region predicted in Figure 6-9 A). Figure 6-11 A) illustrates that not all the fuel burnt in this region. So the rich contours were assumed to be due to high CO and HC emissions that would need to burn downstream. The obtained rich zones show an example of rich/lean combustion, which is beneficial for NO<sub>x</sub>.

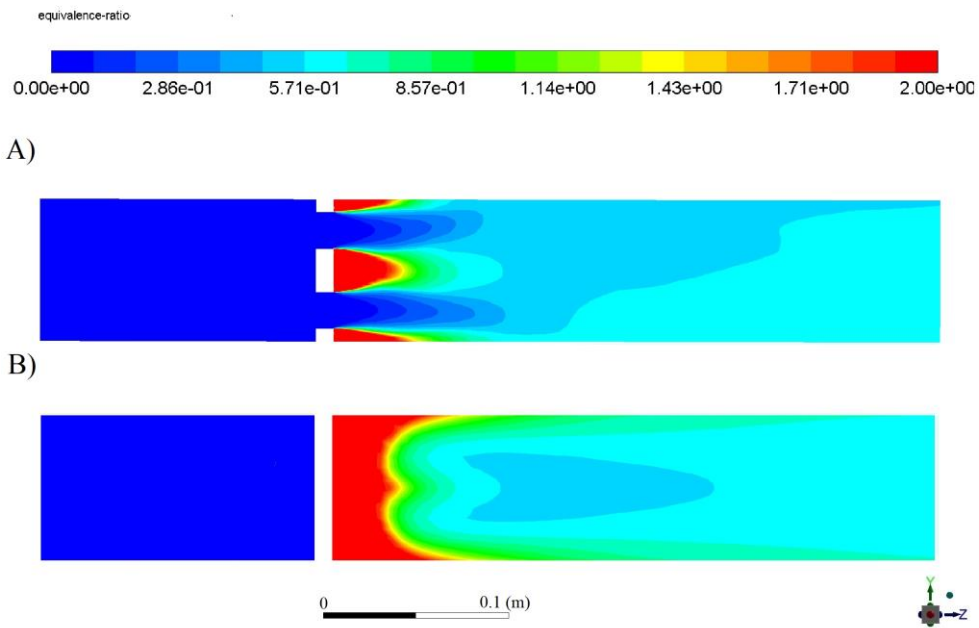


**Figure 6-12.** Axial equivalence ratio contours for GM2 for SDF simulation. A) Inline with the holes, B) In offset with the holes.

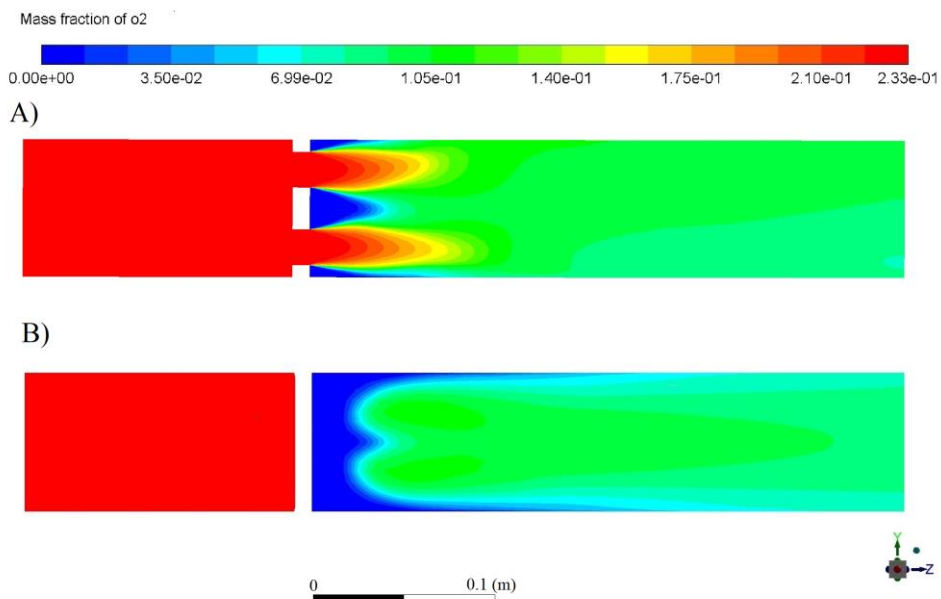


**Figure 6-13.** Axial oxygen mass fraction contours for GM2 for SDF simulation. A) Inline with the holes, B) In offset with the holes.

Figure 6-13 illustrates the oxygen mass concentration contours. The hot recirculating zone near the stabiliser region in Figure 6-11 A) consumed all the available oxygen, as shown in Figure 6-13 A), and the high temperature was due to rich combustion.

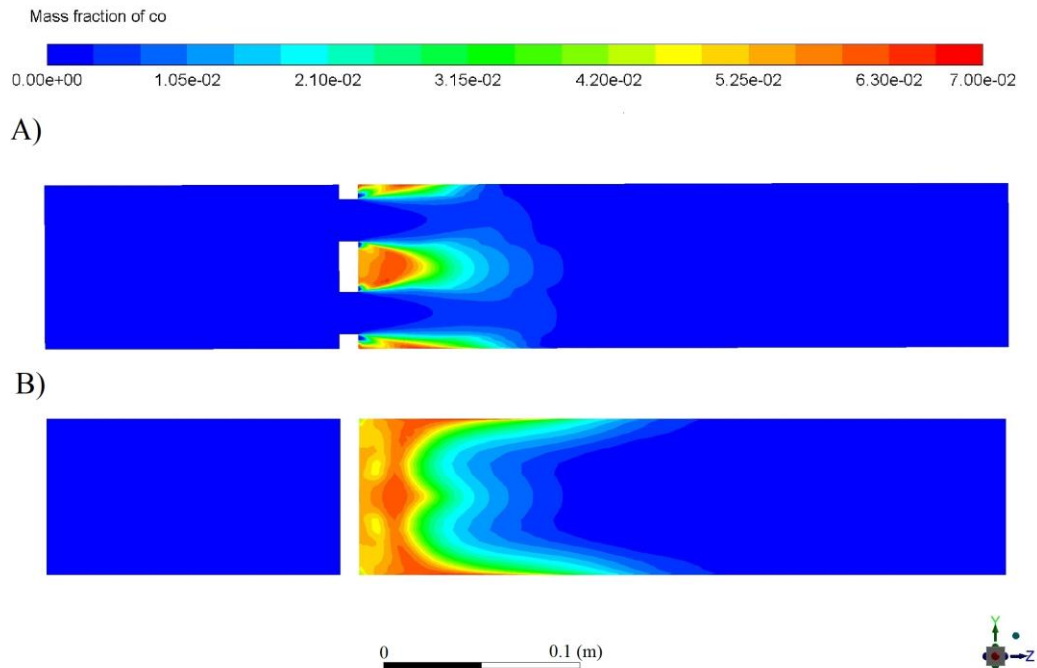
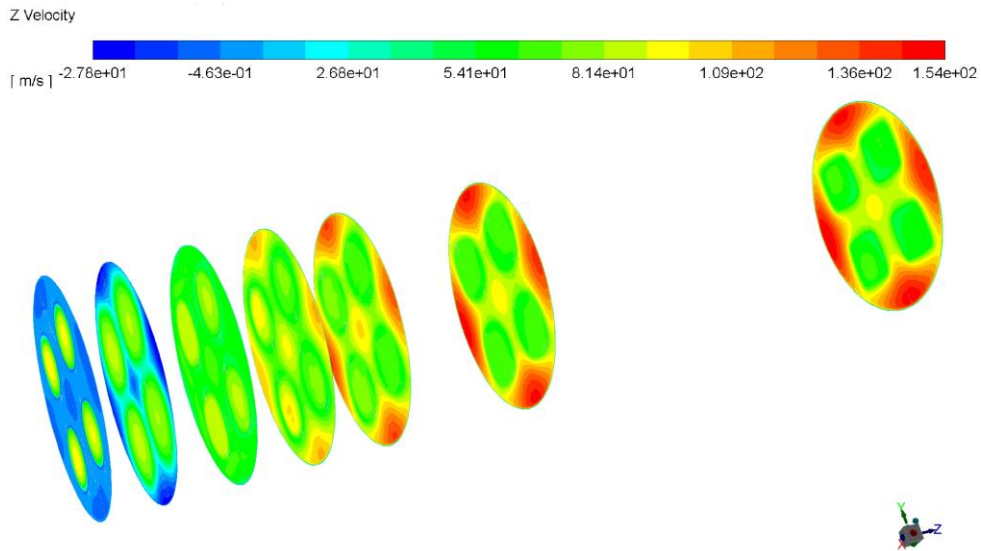


**Figure 6-14.** Axial CO mass fraction contours for GM2 for SDF simulation. A) In-line with the holes, B) In offset with the holes.

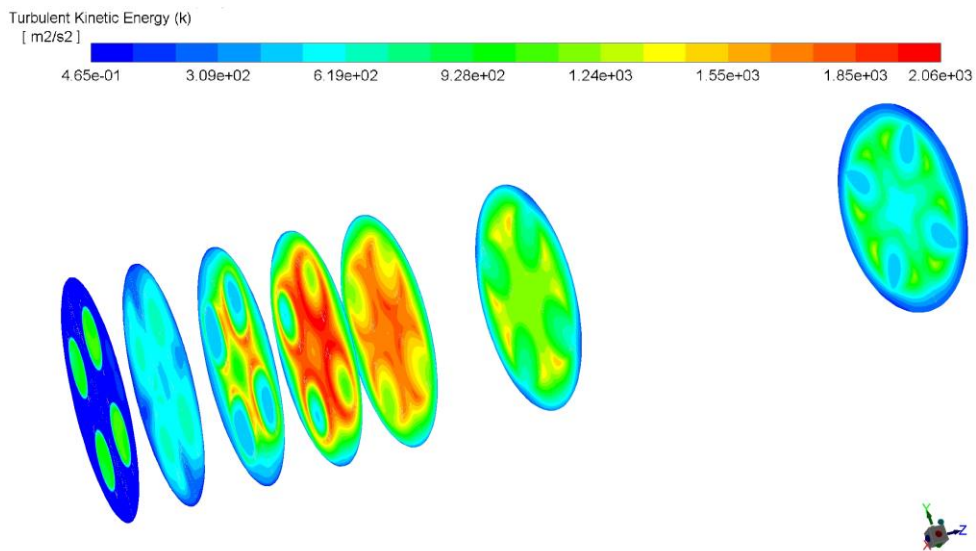
The past figures indicate that the slow velocity annular fuel injection around the air hole was being entrained into the recirculation zone on the downstream face of the stabiliser instead of being directed with the shear layer to the high turbulence region. These fuel-rich areas gave GM2 good flame stability with a much lower weak extinction than GM1 but higher  $\text{NO}_x$  levels.

CFD predictions for transversal planes 0, 25, 50, 75, 100, 150 and 300mm downstream of the flame stabilizer are shown in Figure 6-15-Figure 6-21.

Figure 6-15 and Figure 6-9 show that the recirculation zones between the air jets are still present for the plane at 25mm downstream but not for 50mm. These figures show that the recirculation zone near the stabiliser downstream face was nearly half of the combustor diameter. Figure 6-16 indicates that the TKE is concentrated mainly in the central region between the plane at 25mm and 100mm downstream. No significant turbulence was observed near the wall, despite the recirculation zones.

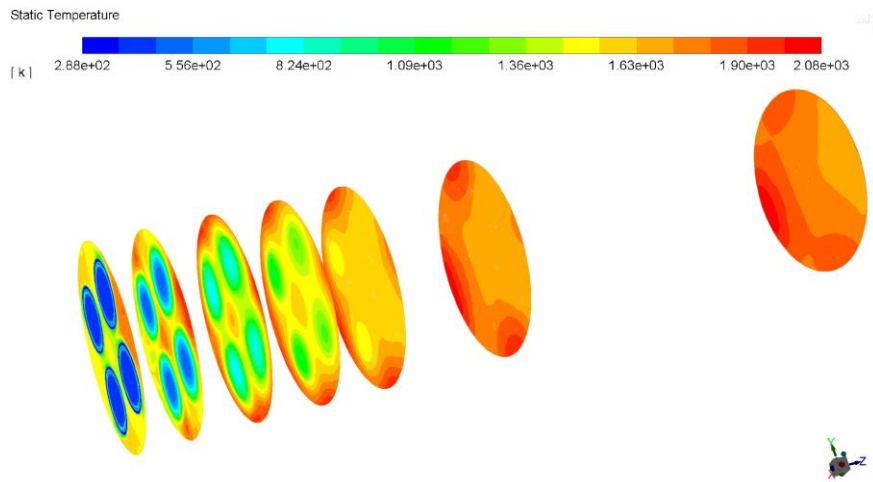


**Figure 6-15.** Z velocity contours across combustor for axial distances 0, 25, 50, 75, 100, 150 and 300mm from GM2 downstream face (SDF simulation)



**Figure 6-16.** TKE contours across combustor for axial distances 0, 25, 50, 75, 100, 150 and 300mm from GM2 downstream face (SDF simulation)

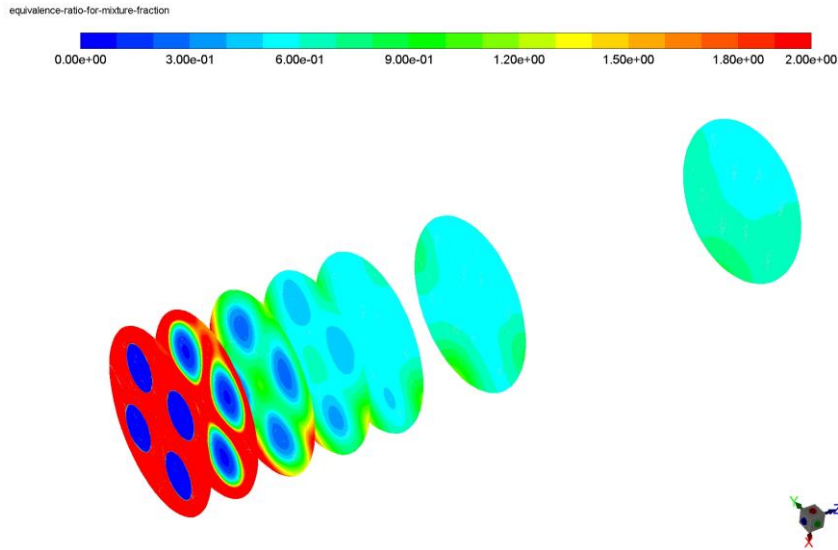
Figure 6-17 shows an initial flame development 100mm downstream with a final heat release at 300mm. Hot burnt gases were encountered in the wall region with a hot zone between the air jets near the wall. This also agreed with the experiments, which showed complete combustion by the lack of reaction zone. Experimentally, this local reverse flow region allowed the rich mixture on the stabiliser outlet face to ignite.



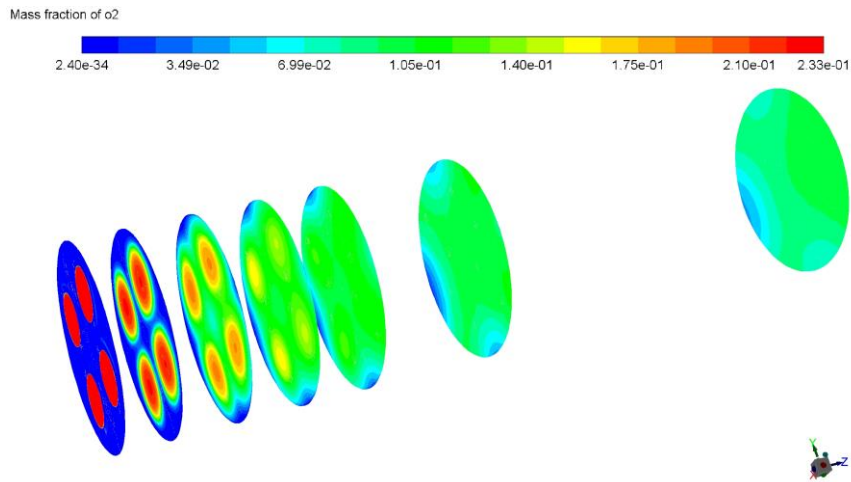
**Figure 6-17.** Temperature contours across combustor for axial distances 0, 25, 50, 75, 100, 150 and 300mm from GM2 downstream face (SDF simulation)

Figure 6-18 shows the equivalence ratio distribution. The plane at the stabiliser downstream face demonstrates levels richer than stoichiometric. The mixing was almost completed just after 50mm when the lean air jets started diffusing with the burning mixture, and they stopped at 100mm. By 200mm, the desired equivalence ratio was almost reached.

Figure 6-19 shows the oxygen predictions. The downstream face of the stabiliser shows zero levels since this is a zone richer than stoichiometric. Twenty-five mm downstream, the annular fuelling gap shows oxygen concentrations of around 10%, corresponding to the annular feed radiation zone in Figure 6-17. Some regions at the wall show zero oxygen levels due to combustion, and the CO<sub>2</sub> contours in Figure 6-20 corroborated that, showing this region filled with burnt gases. Similarly, the recirculation region at the stabiliser downstream face showed high CO<sub>2</sub> concentrations. The recirculation zone close to the flame stabilizer is also high in CO<sub>2</sub>, illustrating the presence of burnt hot gases. This zone allowed to stabilise the flame giving an  $\phi=0.2$  weak extinction. The CO predictions in Figure 6-21 show that the mentioned zone has high concentrations of CO as expected from rich combustion. However, after 100mm downstream at the primary heat release, most of the CO has been mixed with the leaner zone. These results concluded that the experimental internal traverses were potentially taken with the configuration in line with the hole(A-A) in Figure 6-8.



**Figure 6-18.** Contours of  $\phi$  across combustor for axial distances 0, 25, 50, 75, 100, 150 and 300mm from GM2 downstream face (SDF simulation)



**Figure 6-19.** O<sub>2</sub> contours across combustor for axial distances 0, 25, 50, 75, 100, 150 and 300mm from GM2 downstream face (SDF simulation)

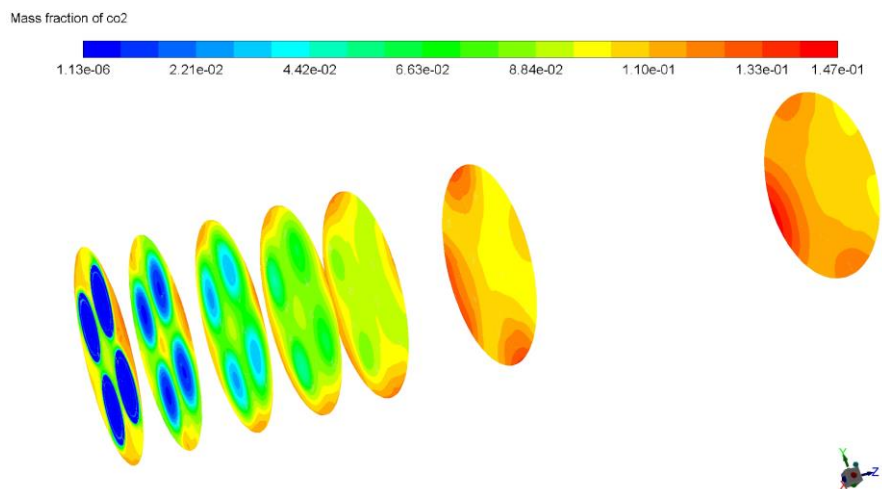


**Figure 6-20.** CO<sub>2</sub> contours across combustor for axial distances 0, 25, 50, 75, 100, 150 and 300mm from GM2 downstream face (SDF simulation)

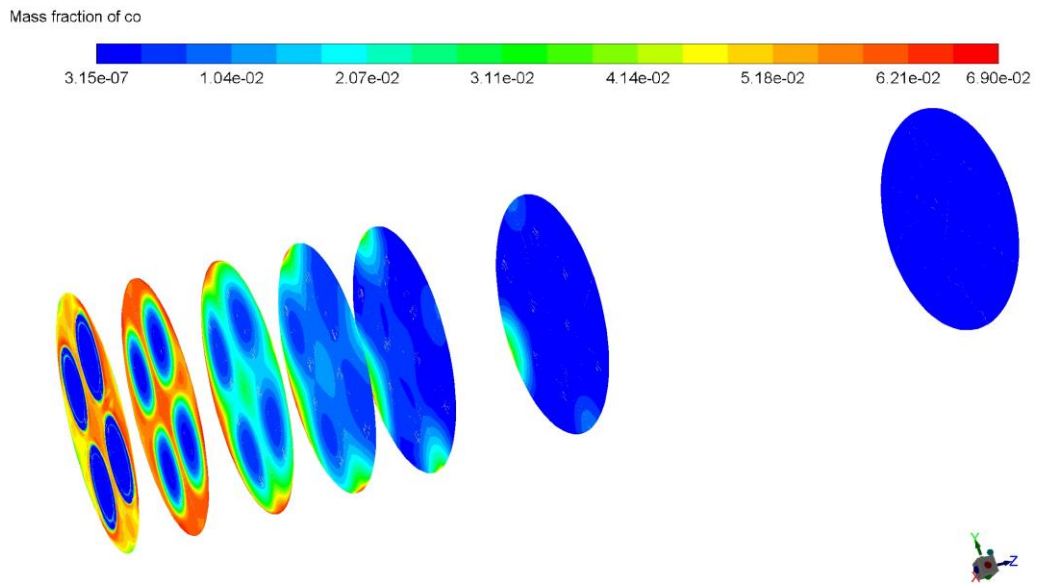
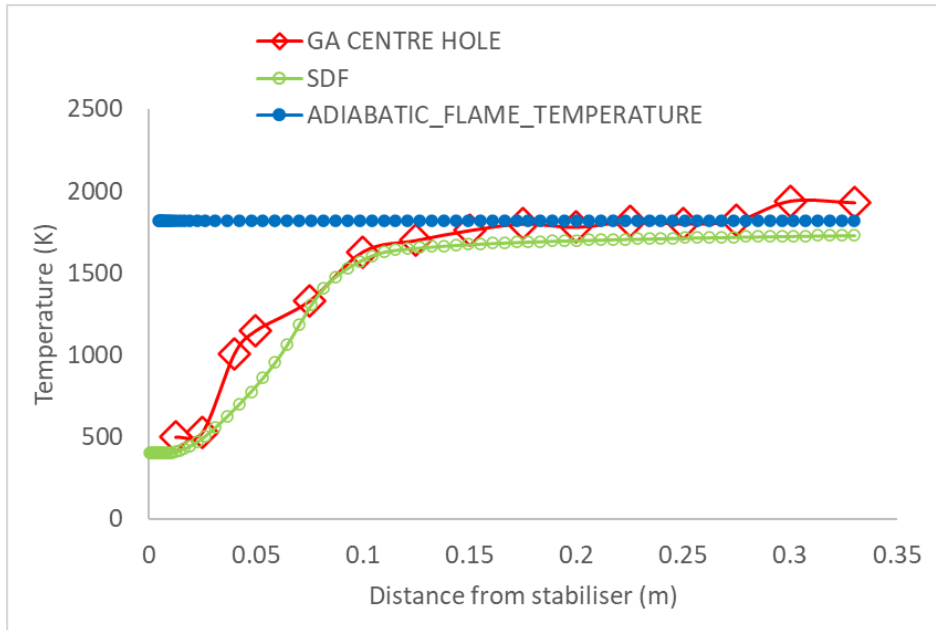


**Figure 6-21.** CO contours across combustor for axial distances 0, 25, 50, 75, 100, 150 and 300mm from GM2 downstream face (SDF simulation)

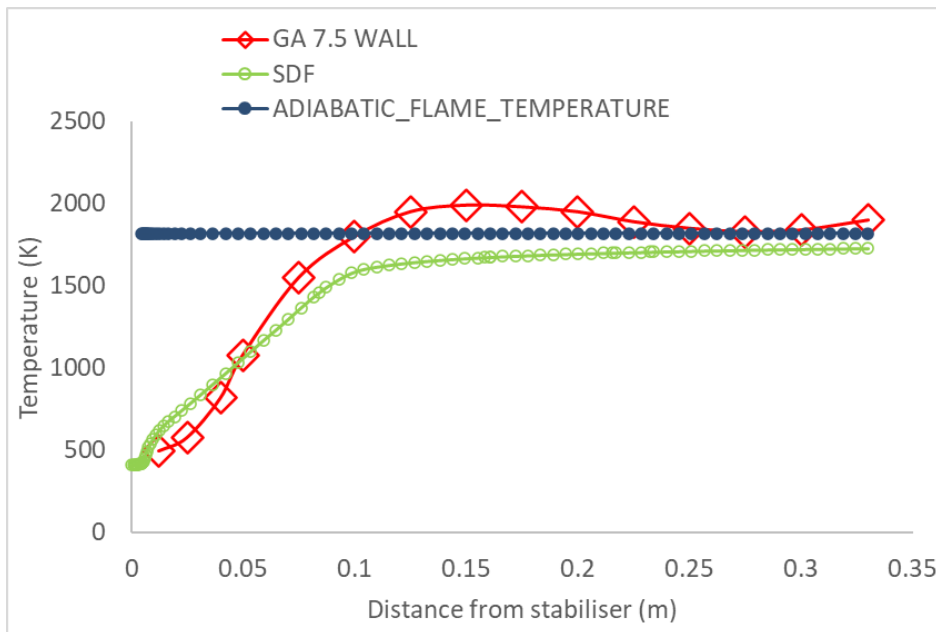
The simulation plots were compared with the experimental results obtained with gas analysis and thermocouple measurements for flame temperature in Figure 6-22-Figure 6-25, as explained in Chapter 3.

Figure 6-22 compares the temperature traverse with the gas analysis probe (GA) at the centreline of the air hole with the simulation plot obtained with SDF. Good agreement was obtained, apart from the underprediction of 200K just at the last 30mm of the downstream combustor length. However, the simulation showed the same trend of the experiments taking 100mm to reach the main heat release. The simulation was just 80K below the adiabatic flame temperature  $T_{adiab}$ .

Figure 6-23 compares the second position of the GA 7.5mm away from the wall and the SDF simulation plot, where the experimental results showed a higher temperature from 0.1-0.25, with a difference of 300K. This difference was mainly addressed to the adiabatic walls used in the simulation. The simulation reached the main heat release 0.05m before the experiments for this position. As an additional fact, the simulation was 40K below the  $T_{adiab}$  at the combustor outlet.



**Figure 6-22.** Comparison of GA based temperature [157] with simulation using SDF for GM2 for the gas analysis probe located at the combustor airhole centreline



**Figure 6-23.** Comparison of gas analysis based temperature [157] with simulation using SDF for GM2 with the probe located 7.5mm away from the combustor wall

The temperature measurements obtained with the thermocouple are compared with the simulation results in Figure 6-24 and Figure 6-25. The plot at 5 mm offset with the combustor centreline shown in Figure 6-24 featured perfect agreement for the first 50mm, then the simulation results were underpredicted by 400K. This difference was addressed to the exact position the thermocouple

was allocated to measure this traverse. However, the simulation result was only 40K under the adiabatic flame temperature at the combustor outlet. Lastly, Figure 6-25 compares the internal traverse obtained at the position 36.5mm away from the GA probe in the air hole centreline with the simulation results. An underprediction of 500K was received for the simulation just outside the stabiliser. The simulation then showed an over prediction of 200K for the rest of the downstream combustor length. However, a perfect agreement was reached with the  $T_{adiab}$  at the combustor outlet. Again, the misprediction was addressed to the TC position relative to the GA probe, which seemed to be in a hot region away from the air hole.

Predicting the adiabatic flame temperature with Gaseq gave a temperature of 1819K. The mean outlet temperature achieved with the simulations was 1806K showing almost perfect agreement with the equilibrium calculation. The CFD results for temperature could have been affected by the adiabatic walls creating a different temperature distribution inside the combustor. The experiments were carried out with no film cooling, but the walls were not adiabatic.

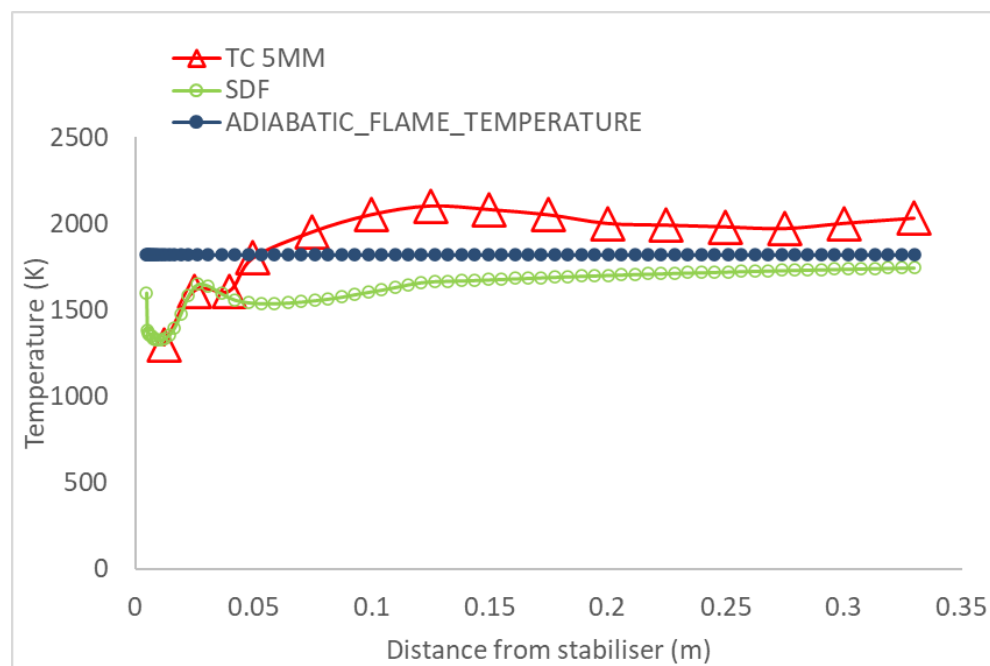


**Figure 6-24.** Comparison of thermocouple based temperature [157] with simulation using SDF for GM2 with the probe located 5mm in offset from the combustor centreline

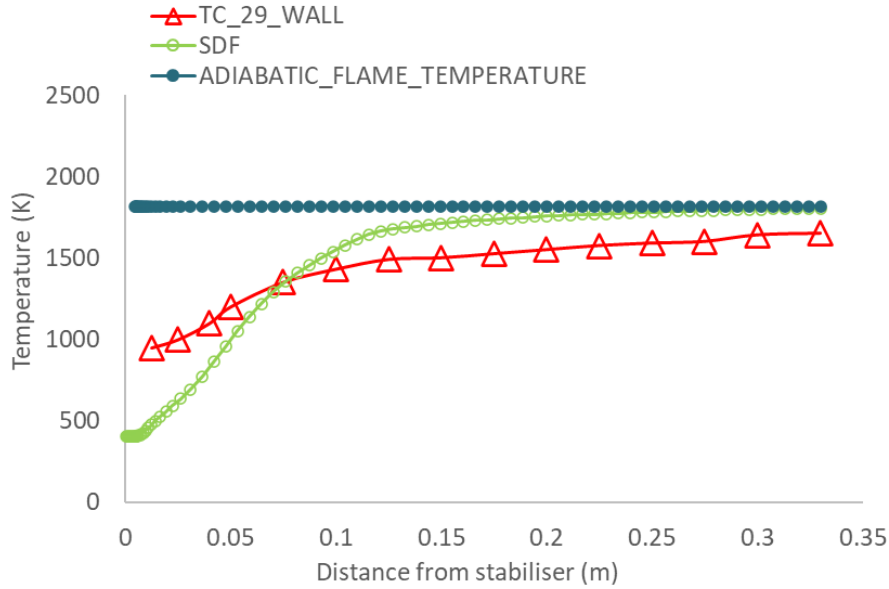


**Figure 6-25.** Comparison of thermocouple based temperature [157] with simulation using SDF for GM2 with the probe located 29mm away from the wall.

The combustion efficiency simulation results at the air hole centreline agreed with the experimental results, as illustrated in Figure 6-26. However, an earlier underprediction is observed for the simulation results. The simulation almost reached the highest efficiency faster than the experiments. The internal traverse at this position achieved 98% combustion efficiency at the outlet compared with 93% achieved with simulation.

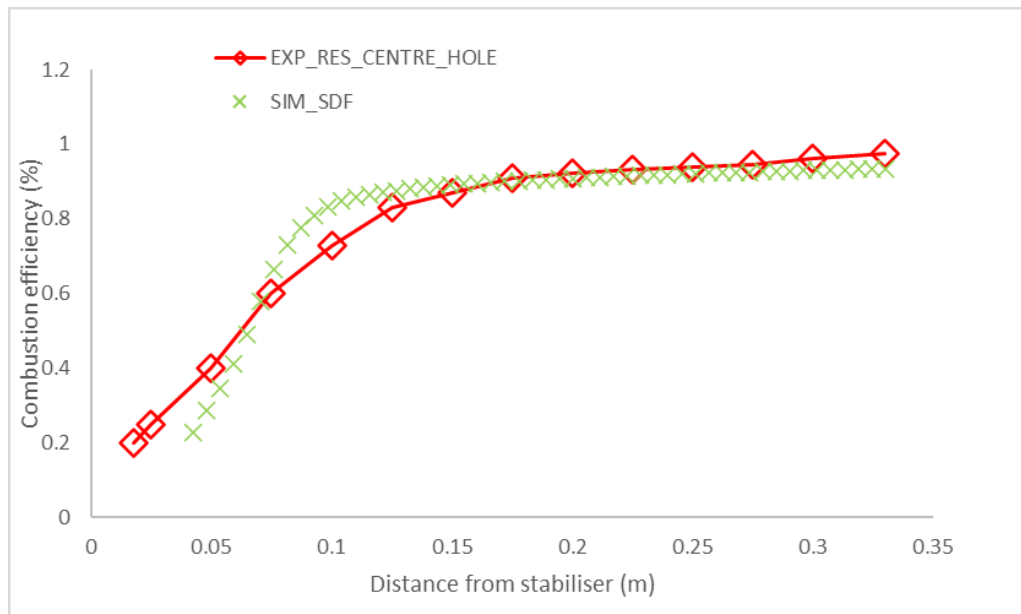


**Figure 6-26.** Comparison of combustion efficiency profiles obtained experimentally [157] and with simulation using SDF for GM2 with the gas analysis probe located at the hole centreline

Figure 6-27 shows perfect agreement between the simulation and the experimental results for the traverse taken by the GA probe at the wall. Only a slight underprediction was encountered near the stabilizer position and at the combustor outlet, where the internal traverse for the experiment showed 98% efficiency compared to 93% achieved with simulation.

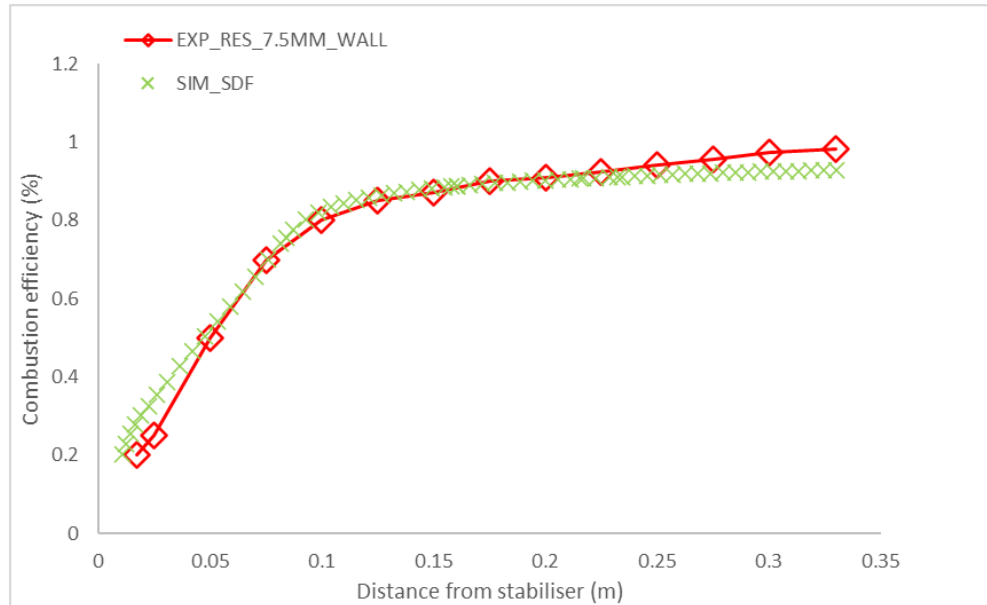
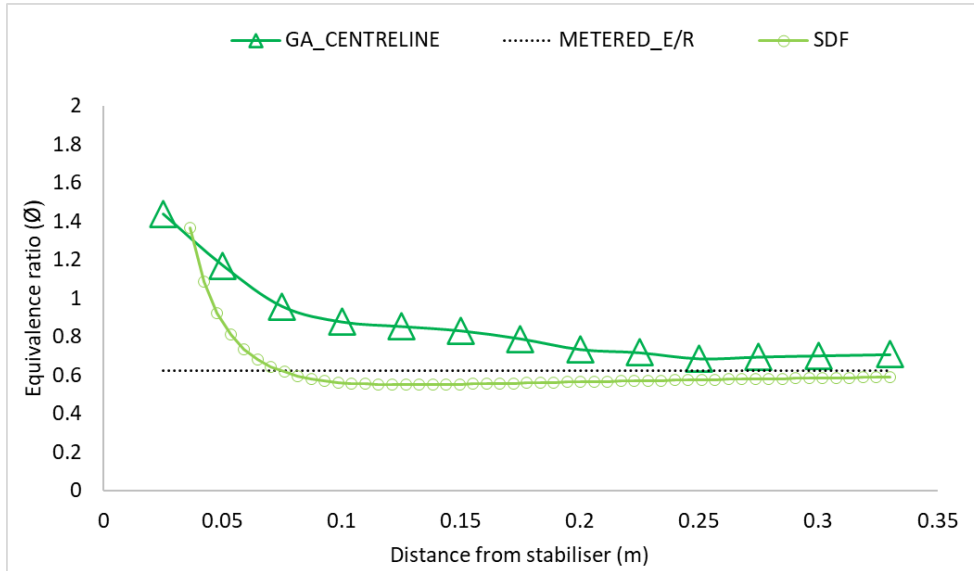


**Figure 6-27.** Comparison of combustion efficiency profiles obtained experimentally [157] and with simulation using SDF for GM2 with the gas analysis probe located 7.5mm away from the wall

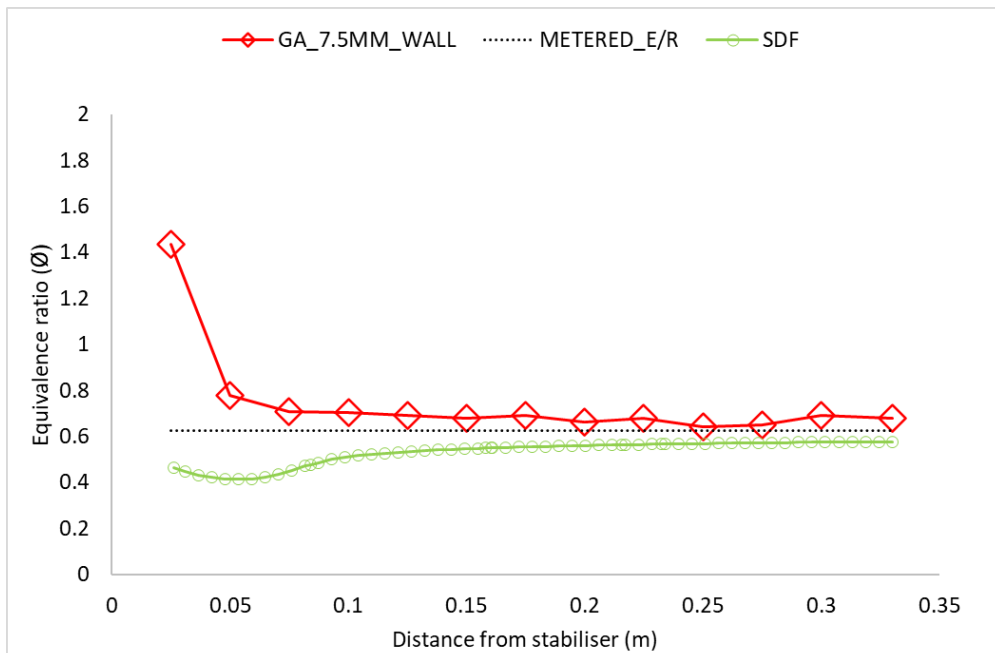
The internal traverses of the equivalence ratio were obtained at the centreline of the combustor and near the wall. The traverse measured for the centreline showed to be richer than stoichiometric in the first 50mm downstream of the combustor. This would not be possible if the traverse was taken at the hole centreline since this is a lean region. The predicted and measured equivalence ratios are compared for the two axial traverses in Figure 6-28 and Figure 6-29, where Figure 6-28 shows a faster mixing for the CFD simulation than the experimental results. The simulation predicted complete combustion 70mm after the 199tabilizer compared to the 250mm obtained with the GA. The CFD predicted thorough mixing in 80mm compared with 250mm in the measurement. However, this central region in the combustor was not critical in the simulation as the flame development occurs in the outer areas, which were well predicted.

Figure 6-28 compares the equivalence ratio traverse taken 7.5mm from the wall. The CFD simulation did not match the experiment at this location since the experimental traverse clearly shows a rich region between the annular feed and the combustor wall. In contrast, the simulation shows to be extremely lean.

Again, the experimental traverse illustrates complete combustion at 250mm compared to the 100 obtained with simulation. However, the misprediction did not affect the temperature or combustion results which agreed with the internal traverses.



**Figure 6-28.** Comparison of  $\phi$  profiles obtained experimentally [157] and with simulation using SDF for GM2 for the gas analysis probe 5mm offset from the combustor centreline



**Figure 6-29.** Comparison of  $\phi$  profiles obtained experimentally [157] and with simulation using SDF for GM2 for the gas analysis probe located 7.5mm from the wall

The simulation residuals are shown in Figure 6-30, where some divergence was encountered for the first 500 iterations using first-order upwind. In contrast, a very smooth simulation was achieved when swapping to second order. In addition, no divergence was encountered in the reports of TKE, velocity and temperature (Figure 6-31) at the combustor outlet. A converged solution was achieved at roughly 400 iterations.

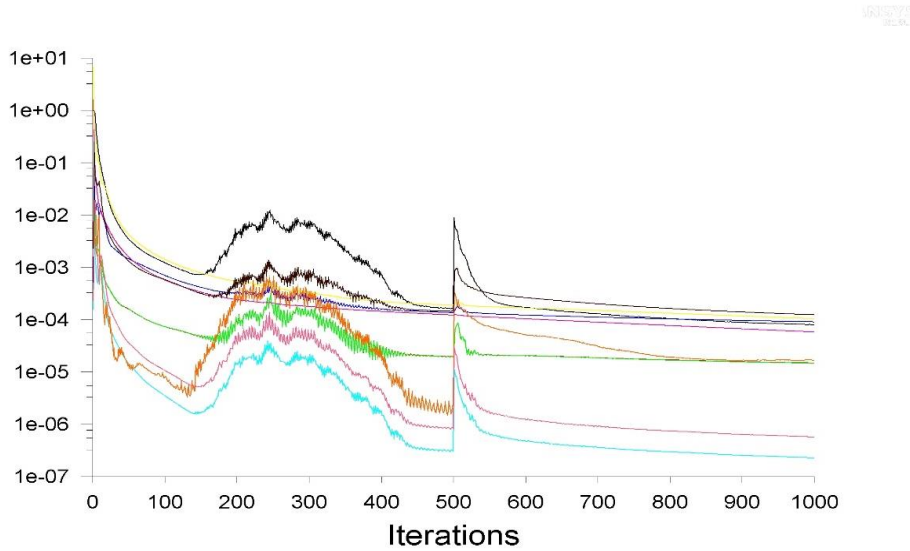


**Figure 6-30.** Residuals for SDF simulation for GM2

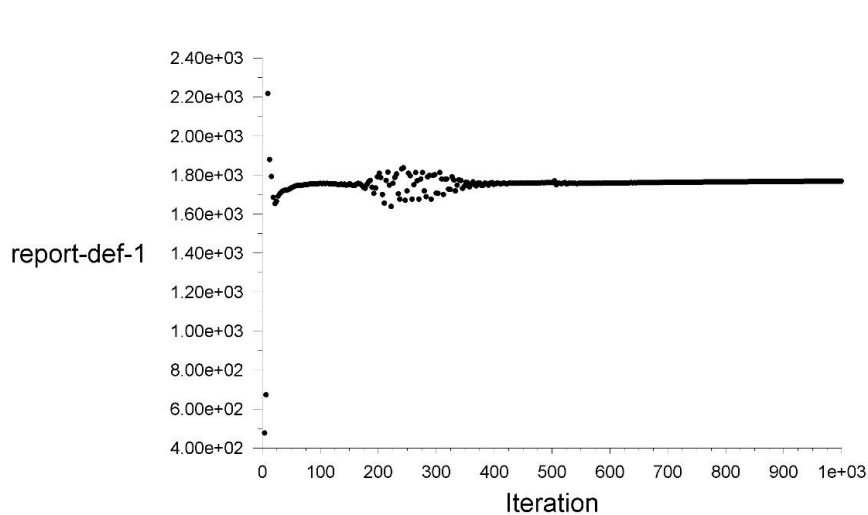


**Figure 6-31.** Temperature report definition for SDF simulation of GM2

A  $\text{NO}_x$  calculation was carried out for the simulation with SDF, and the contours are shown in Figure 6-32. The peak  $\text{NO}_x$  of 0.64 occurred at the combustor outlet. These levels were compared with the experimental results showing an underprediction of a factor of 70 for the overall combustor downstream length. The peak of  $\text{NO}_x$  formation was also miss predicted as it started 250mm downstream the stabiliser missing the high temperature zones. The thermal  $\text{NO}_x$  formation should have started just above 1800K and this was not the case

in the simulation. However as explained in Chapter 2 NO<sub>x</sub> prediction is a disadvantage of SDF, and this was proved in Figure 6-32.

It was concluded that SDF obtained an excellent agreement with the experimental results for temperature and mixing, but it was not successful for NO<sub>x</sub> prediction.

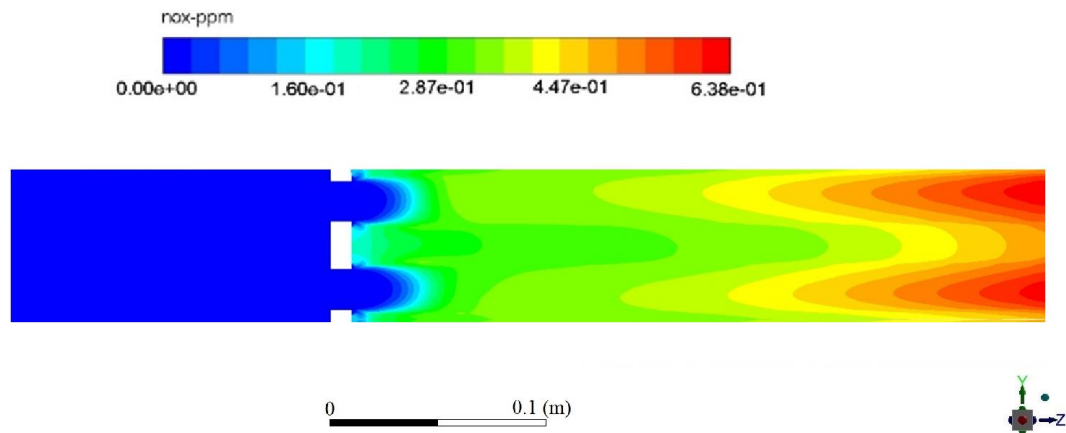


**Figure 6-32.** NO<sub>x</sub> contours for SDF simulation for GM2

### 6.3.3 GM2 studied with FGM combustion model

The aerodynamics using the FGM combustion model for an unstructured hexahedral mesh for GM2 are shown in Figure 6-33.

The velocity contours in Figure 6-33 A) obtained a peak velocity of 98 m/s in the vena contracta region downstream of the stabiliser position, higher than the inlet velocity of 71 m/s in the upstream face of the stabiliser. The higher velocity at the vena contracta was due to the sharp-edged stabiliser holes, which increased the flow velocity at a ratio of 0.72, which was close to what is expected for sharp edge short holes with a hole  $L/D = 0.485$  [164]. The inlet velocity for an  $M=0.047$  was 18.87 m/s achieved by simulation, considering a temperature rise means basis to 1800K. A mean hot gas velocity of 85 m/s was achieved. The distance for completion of these combustion velocities was between 60 and 120mm from the stabiliser position shown in Figure 6-33 A). Which gave a central heat release length of 60mm, and near the wall, this distance was 200mm, and the flame development length was around 150mm. The Initial 60mm corresponded to the inlet air-jet spreading distance, an  $X/D$  of 3 where  $D$  is the air hole diameter, similar to central regions of free jets.

A radial distance of 23.4mm between the edge of the air holes controlled the size of recirculating zones downstream of the stabiliser, which has a length of 40mm according to the zero velocity region illustrated in Figure 6-33 A). This

central zone was crucial for developing peak turbulence (Figure 6-33 B). It was one of the most critical differences between FGM simulation and SDF, which showed much higher energy in Figure 6-10 than the achieved with FGM in Figure 6-33 B). This zone was also predicted to be a high temperature and high NO<sub>x</sub> region. A non-recirculating flow was encountered at the wall region.

The turbulence peaks were obtained at the recirculation zone at the hole inlet of the stabiliser plate created by the flow separation. These high turbulence regions anchored the flame and controlled the mixture quality.

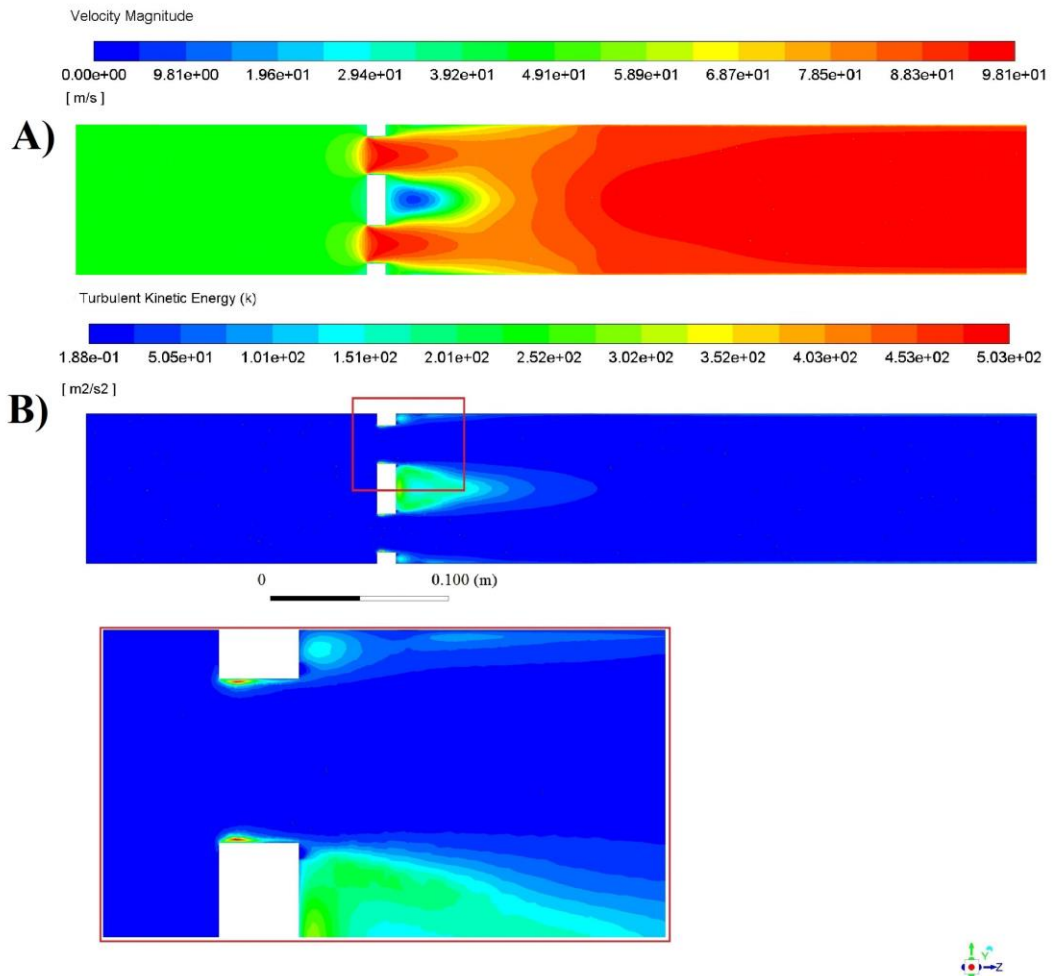


**Figure 6-33.** Simulation results for FGM and unstructured hexahedral mesh for GM2 A) Velocity contours, B)TKE contours

Figure 6-34 compares equivalence ratio contours for the simulation using FGM and the previous one undertaken with SDF. Both models showed the fuel being pushed to the wall region and the central combustor zone, where the larger recirculation zone was encountered. A slower mixing was obtained for FGM, showing a wider richer-than-stoichiometric red area than SDF. However, both simulations showed values richer than  $\phi=1.5$  in the first 25mm after the stabiliser downstream face in the high turbulence region. On the other hand,

the desired  $\phi=0.624$  was almost achieved for both simulations around 150mm downstream.

The experimental internal traverses for the equivalence ratio were compared with the plots obtained with simulation in Figure 6-35 and Figure 6-36. A perfect agreement was achieved with FGM at the combustor centreline, as shown in Figure 6-35. The complete mixing was obtained 200mm downstream from the stabiliser. Again this figure indicates that a quicker mixing was obtained with SDF.

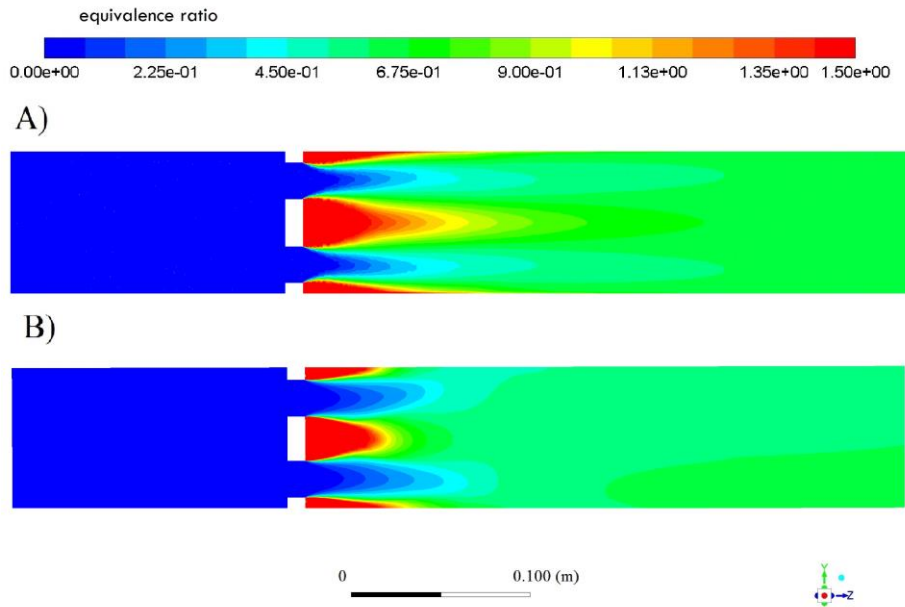


**Figure 6-34.** Comparison of equivalence ratio contours for GM2 A) FGM, B) SDF

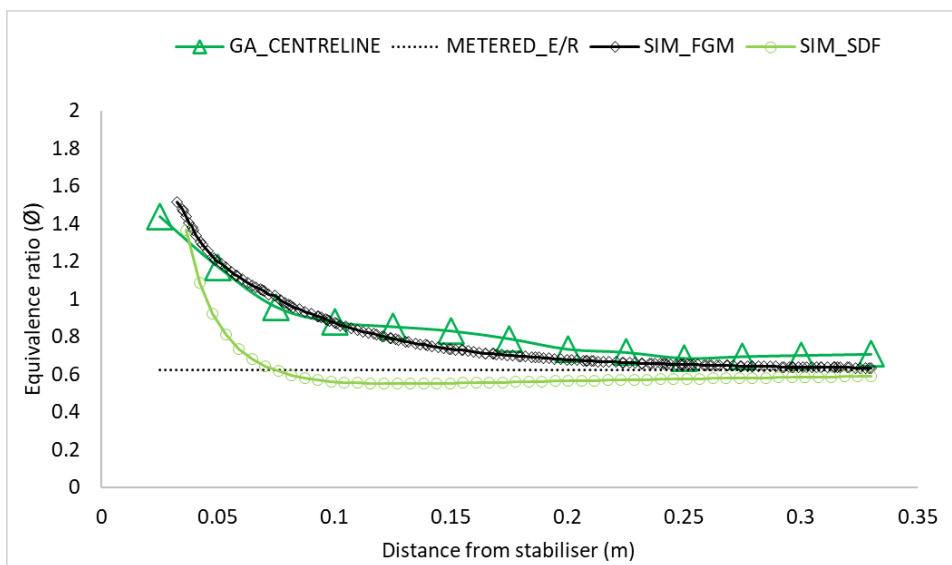


**Figure 6-35.** Comparison of  $\phi$  profiles obtained experimentally [157] and with simulation using FGM and SDF for GM2 for the gas analysis probe located 5mm in offset with the combustor centreline

Figure 6-36 compares the simulation results for FGM with SDF and the experimental internal traverse at the position near the wall, where a better agreement was achieved with the FGM simulation. However, underprediction can still be seen from the simulation, especially in the first 50mm after the stabiliser. Complete mixing was achieved at 80mm compared with the 120mm for the experimental results.

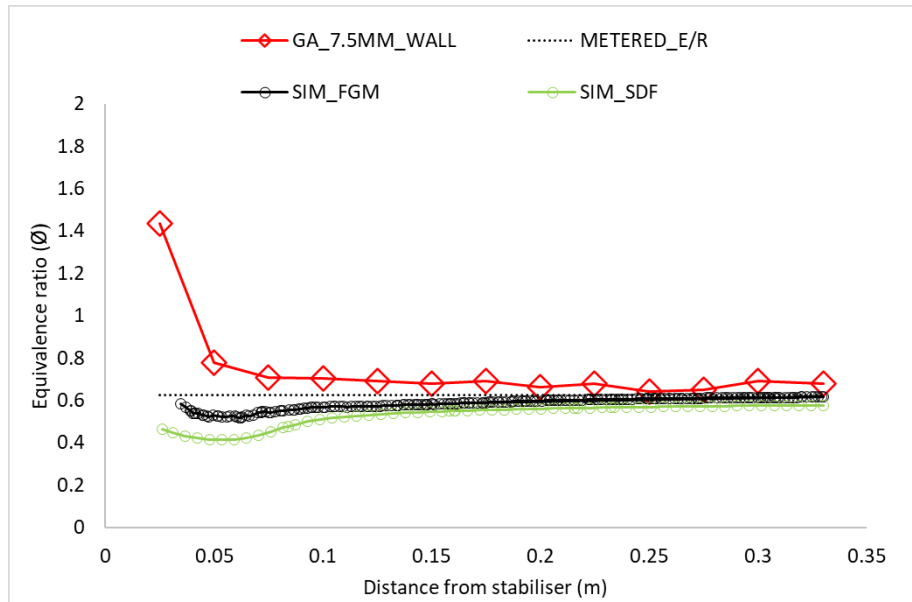


**Figure 6-36.** Comparison of  $\phi$  profiles obtained experimentally [157] and with simulation using FGM and SDF for the gas analysis probe located 7.5mm from the combustor wall

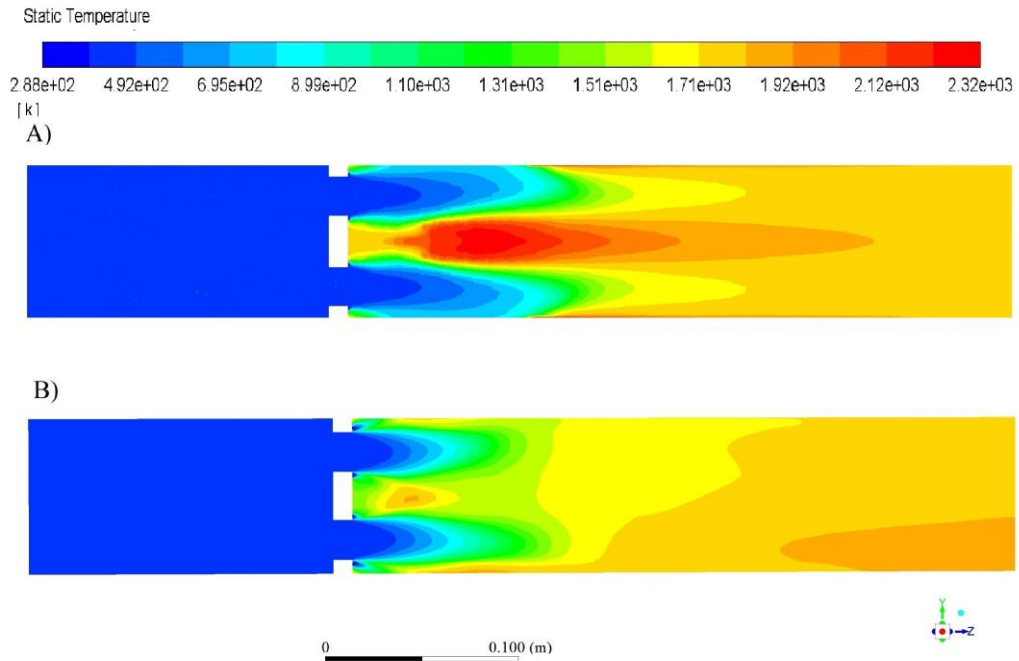
Both codes successfully achieved the desired equivalence ratio, yet the simulation with FGM reached the desired condition faster than SDF. However, as shown for SDF, a faster overall mixing was achieved.

The comparison of the temperature contours obtained with FGM and SDF is shown in Figure 6-37. The simulation with SDF predicted a slower heat release and temperature rise at the air jet outlets compared to the FGM simulation. The FGM model showed a central higher temperature zone than the SDF. This zone started 30mm from the grid plate and reached its peak 150mm downstream, which will show the highest  $\text{NO}_x$  concentration. The later combustion stages show a shorter combustion completion for SDF than FGM. A high-temperature zone was observed near the walls 80mm downstream for FGM, which was not predicted for SDF.

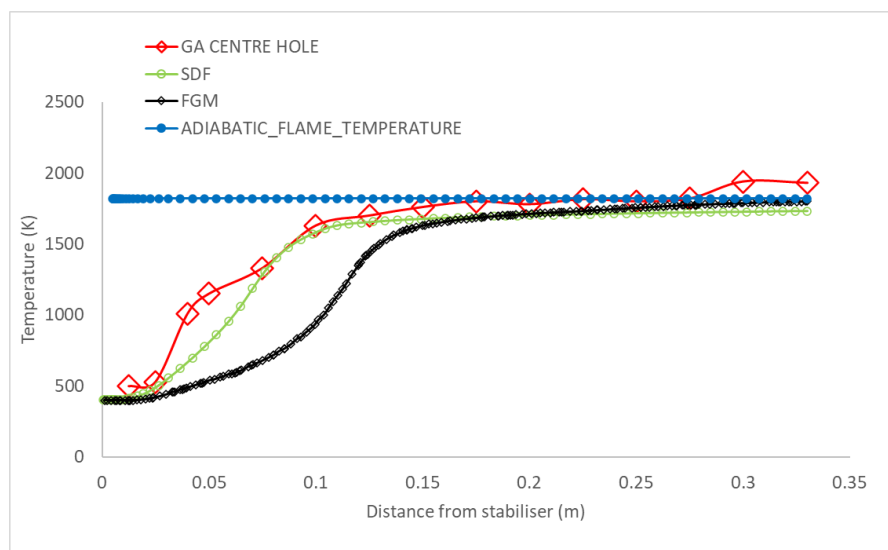
The obtained temperature plots are compared with the experimental internal traverses in Figure 6-38-Figure 6-41.

The comparison for the position of the GA at the air hole centreline in Figure 6-38 shows an early underprediction for FGM. The flame seemed to have been

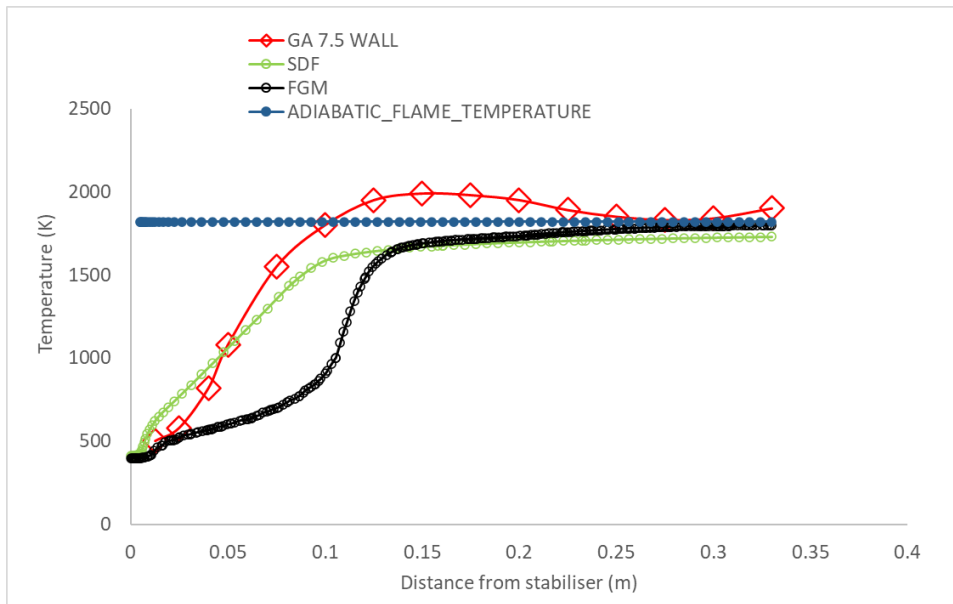
pushed back due to the more extended air jets predicted for this simulation in comparison to SDF. However, a better agreement was achieved 200mm downstream. The traverse comparison for the GA probe at the wall position showed a similar behaviour as the one obtained at the hole centreline, where the flame is pushed to 150mm downstream, unlike the SDF simulation. However, the maximum heat release was obtained at the same position as the experiments, and after this point, a better similitude was observed.



**Figure 6-37.** Comparison of temperature contours for GM2 A) FGM, B) SDF



**Figure 6-38.** Comparison of temperature profiles obtained experimentally [157] and with simulation using FGM and SDF for gas analysis probe located at the stabiliser hole centreline



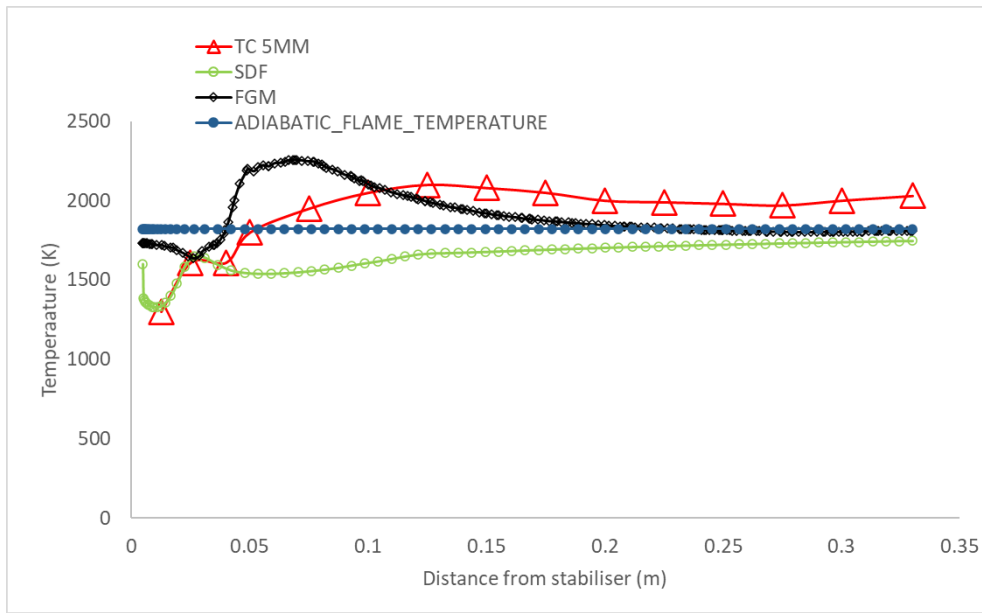
**Figure 6-39.** Comparison of temperature profiles obtained experimentally [157] and with simulation using FGM and SDF for gas analysis probe located 7.5mm away from the combustor wall

Figure 6-40 illustrates the comparison of the thermocouple position 5mm offset the combustor centreline with the simulation results for the FGM and SDF. A better match with the experiments was observed for this position. The FGM run showed an early temperature overprediction. However, after 100mm downstream, a better agreement was observed. FGM delivered more similitude to the experiments than SDF for this position.

Figure 6-41 compares the internal traverse for the thermocouple 29mm away from the combustor wall. Both simulations showed agreement with each other but a misprediction with the experimental values. An underprediction of 500K was encountered for the first 60mm and an overprediction of 200K for the rest combustor length.

The four temperature plots obtained with FGM agreed better with the adiabatic flame temperature of 1820 calculated with CEA than SDF.

The temperature contours shown in Figure 6-37 are shown in Figure 6-42 as a mean cross-sectional area-averaged temperature as a function of distance from the flame stabiliser. A flame development length of 150mm is observed, which is shown in Figure 6-33 and Figure 6-34. This characteristic of thick flames and long heat release zone are typical for a heat release of 28 MW/m<sup>2</sup> in the present work, thick flames with a long heat release zone. The total heat release in this work is 1 kW per mm axial distance.



**Figure 6-40.** Comparison of temperature profiles obtained experimentally [157] and with simulation using FGM and SDF for thermocouple located 5mm in offset from the combustor centreline

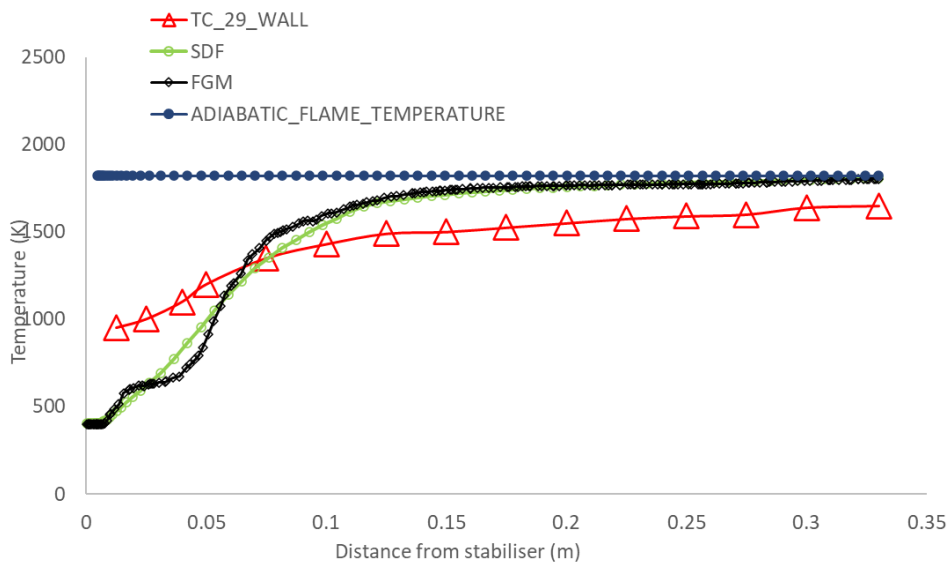


**Figure 6-41.** Comparison of temperature profiles obtained experimentally [157] and with simulation using FGM and SDF for thermocouple 29mm away from the combustor wall

The main advantage of the simulation using FGM was that it made possible the obtention of sensible  $\text{NO}_x$  levels for GM2, which was not possible with any of the other models previously studied. To do so, different thermal  $\text{NO}_x$  formation

mechanisms were investigated. However, the partial equilibrium for O instantaneous OH models showed the best agreement with the results.

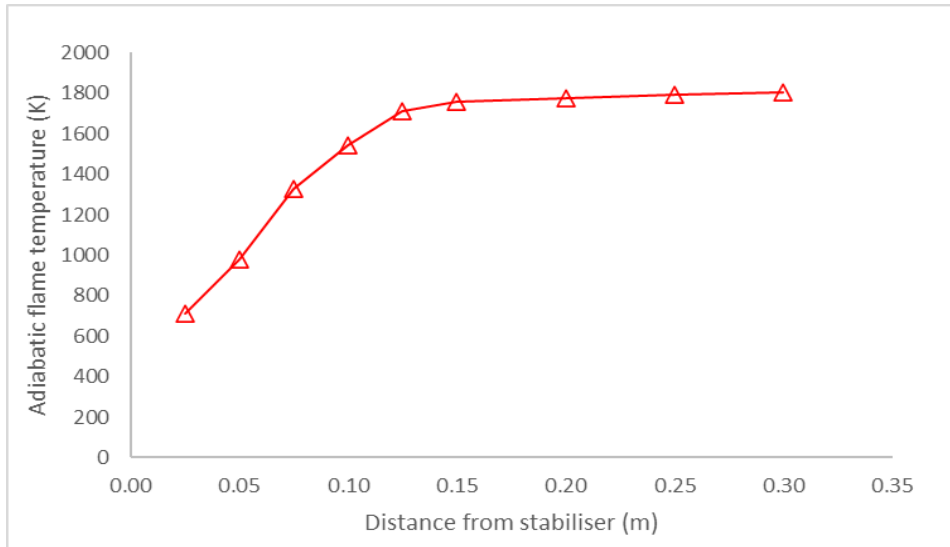


**Figure 6-42.** Cross-sectional area-averaged mean flame temperature predicted with FGM as a function of axial distance from the stabiliser position for GM2.

The NO<sub>x</sub> contours are shown in Figure 6-43, where a central region can be observed where the peak is at the main heat release shown in Figure 6-42, indicating that NO<sub>x</sub> was controlled by the thermal mechanism. The hot central region shown in Figure 6-37 showing temperatures above 2000K should be where the peak NO<sub>x</sub> is formed and this was successfully predicted. Figure 6-44 compares the results obtained by simulation with the experimental results at the centreline of the combustor since, again, it would be dubious about traversing where the air hole was.

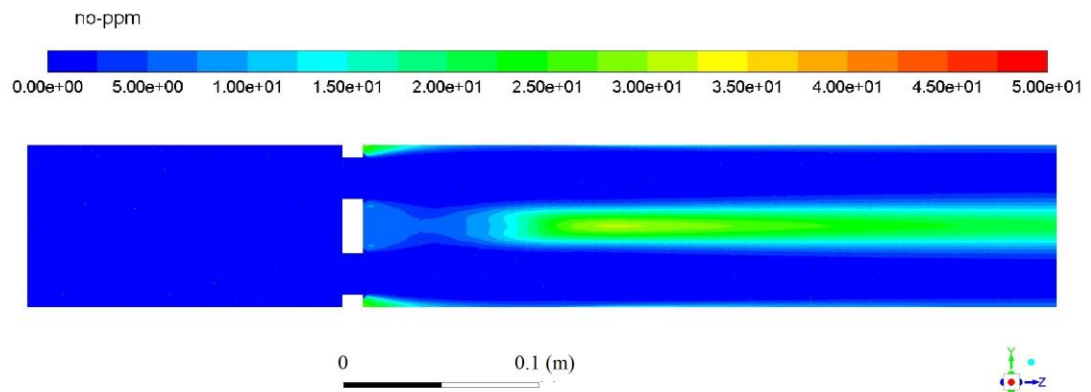


**Figure 6-43.** NO<sub>x</sub> contours for FGM simulation for GM2

Underpredicted values were obtained with the simulation showing a peak of 30ppm while the experimental result showed 42ppm. Outlet values were also underpredicted for the simulation obtaining 6ppm compared with 50 ppm for

GM2 or 2ppm compared to 10.5ppm for a corrected 15% oxygen, as shown in Table 6-1. The development of thermal NO<sub>x</sub> starts at a temperature of 1800K. Figure 6-40 showed a temperature of 1800K at 50mm downstream of the stabiliser, where the measured and predicted NO<sub>x</sub> commenced to increase in Figure 6-43.

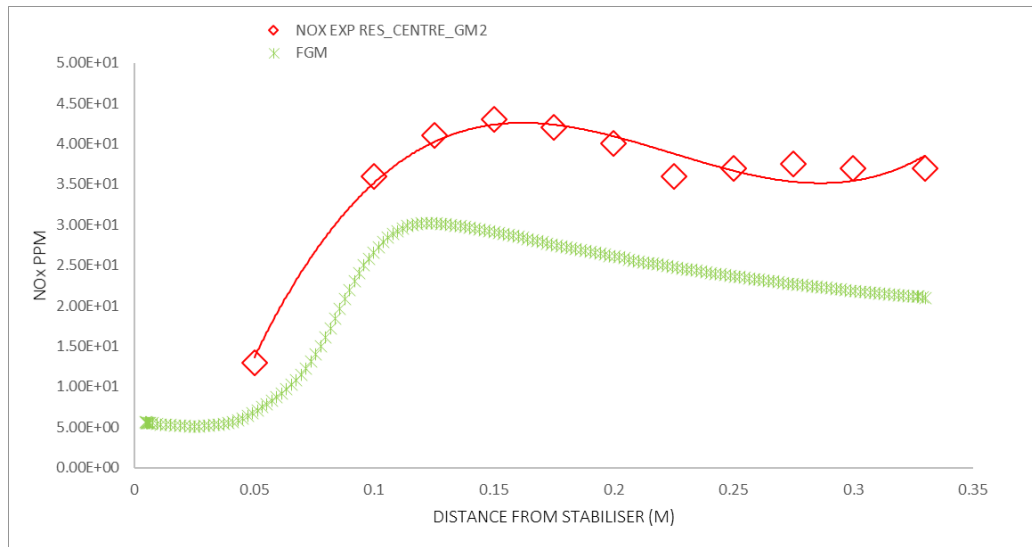


**Figure 6-44.** Comparison of NO<sub>x</sub> profiles obtained experimentally [157] and with simulation using FGM for the gas analysis probe located 5mm in offset of the combustor centreline.

**Table 6-1.** Experimental NO<sub>x</sub> results compared with simulation for GM2 Ø=0.624

<b>Experimental (ppm)</b>	<b>Simulation (ppm)</b>	<b>Experimental 15% O<sub>2</sub> (ppm)</b>	<b>Simulation 15% O<sub>2</sub> (ppm)</b>
50	6	10.5	1

One of the reasons for the NO<sub>x</sub> misprediction by the simulation was mainly the underprediction of temperature. It has been demonstrated that NO<sub>x</sub> is very dependent on the temperature results. However, the high combustion intensity used for this problem could also show that the NO<sub>x</sub> model in FLUENT could be unsuitable for such a Mach number. The residence time could be too short for the NO<sub>x</sub> to form.

Figure 6-45 shows the CO contours obtained with FGM compared with the one obtained with SDF for GM2. A high concentration was predicted at the central recirculation zone for FGM. However, the CO was thoroughly consumed when the mixing was completed, and no large concentrations were found after

130mm from the stabiliser. The simulation with SDF predicted much lower CO concentrations than FGM.

The CO<sub>2</sub> contours with FGM are compared with those obtained with SDF in Figure 6-46. Completeness of combustion for the simulation with FGM was achieved at 200mm from the stabiliser as predicted in Figure 6-37. Lower CO<sub>2</sub> levels were achieved with SDF.

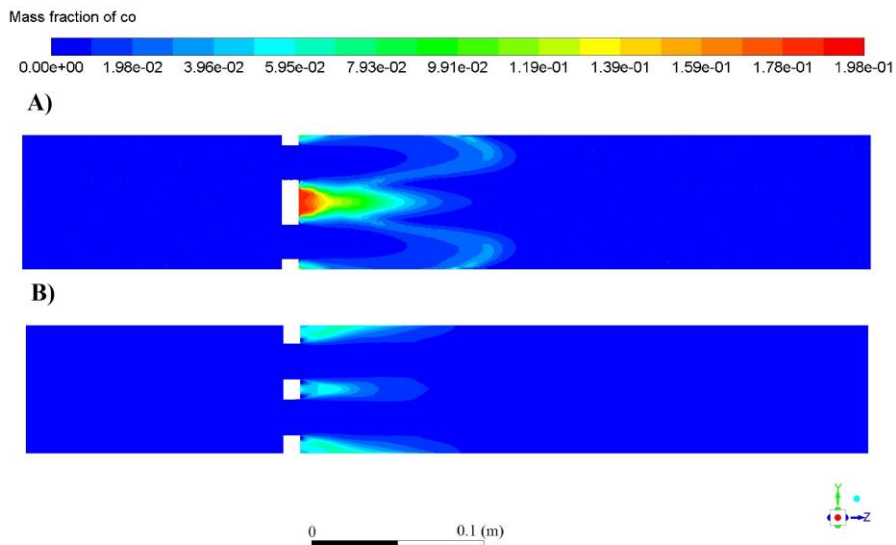


**Figure 6-45.** Comparison of CO contours for GM2 A) FGM, B) SDF

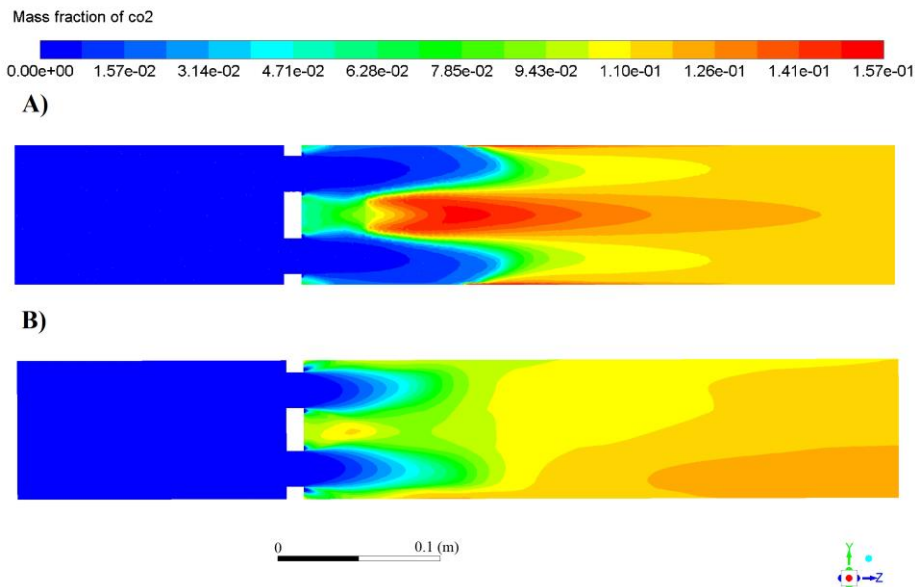


**Figure 6-46.** Comparison of CO<sub>2</sub> contours for GM2 A) FGM, B) SDF

Table 6-2 shows the obtained exit plane values with simulation for FGM compared with the equilibrium results obtained with Gaseq and CEA. Both codes predicted an adiabatic flame temperature similar to that obtained with simulation. Good agreement was also obtained for the equilibrium products.

These values show that combustion equilibrium was obtained in the 330mm combustor length. Hence, GM2 could achieve combustion in a short combustor length despite the high Mach number and high heat release.

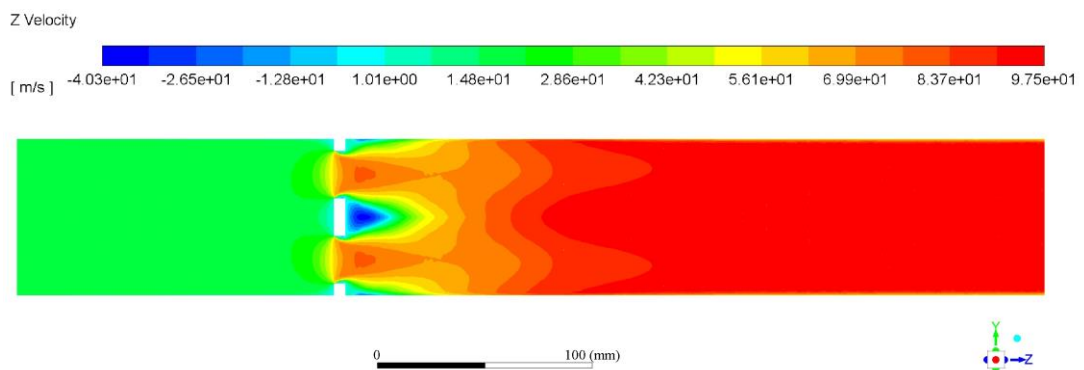
**Table 6-2.** Comparison of the CFD predicted mean composition at 330mm combustor length with two chemical equilibrium codes for GM2.

Parameter	Gaseq	CEA	FGM GM2 Simulation
Equivalence ratio	0.624	0.62	0.624
Adiabatic flame temperature	1812.59K	1820.6	1809.13K
Mean exit CO (mole fraction)	6.39e-5	6.98e-5	7.47e-5
Mean exit CH <sub>4</sub> (mole fraction)	1.41e-24	1.58e-24	2.62e-8
Mean exit O <sub>2</sub> (mole fraction)	7.3e-2	7.4e-2	7.6e-2
Mean exit CO <sub>2</sub> (mole fraction)	7.45e-2	7.46e-2	7.42e-2

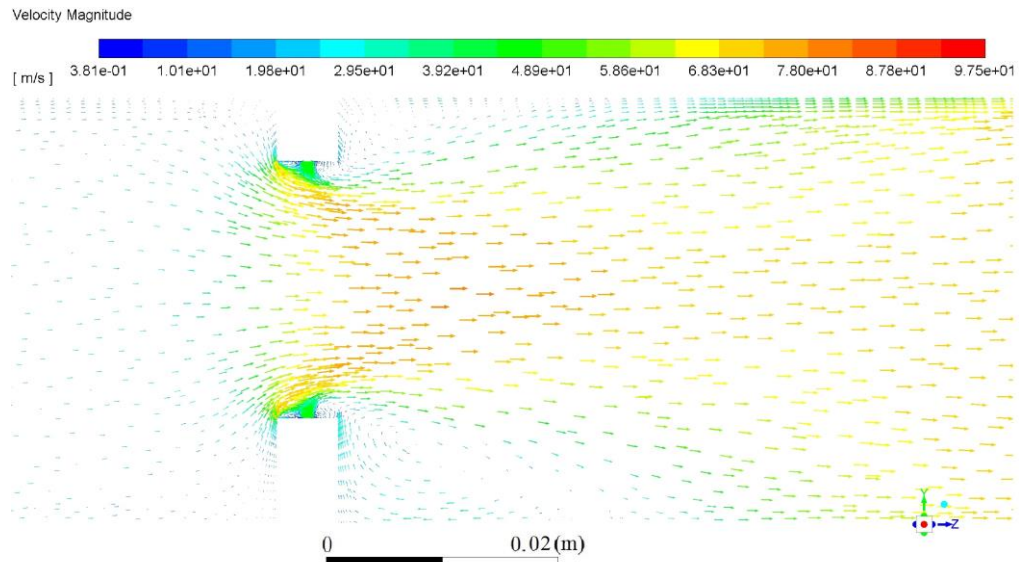
#### 6.4 Combustion analysis for GM1 grid plate flame stabiliser

Figure 6-47-Figure 6-56show contours and plots obtained for the CFD simulation undertaken for GM1 for a propane/air mixture.

Figure 6-47 shows the axial velocity contours for GM1, where a peak velocity of 98m/s was obtained at the vena contracta. A high combustion velocity can be seen at 100mm downstream of the stabiliser. Two main recirculation zones can be observed. The largest one was obtained at the centre of the combustor, and smaller ones can be seen at the wall region just 10mm after the stabiliser outlet face. Figure 6-48 shows a closeup of the stabiliser region showing the velocity vectors. The injection velocity was 48 m/s. However, not much penetration was obtained given the nozzle size and the high flow velocity in the vena contracta. Discrete recirculation zones can be observed before and after the fuel injection.

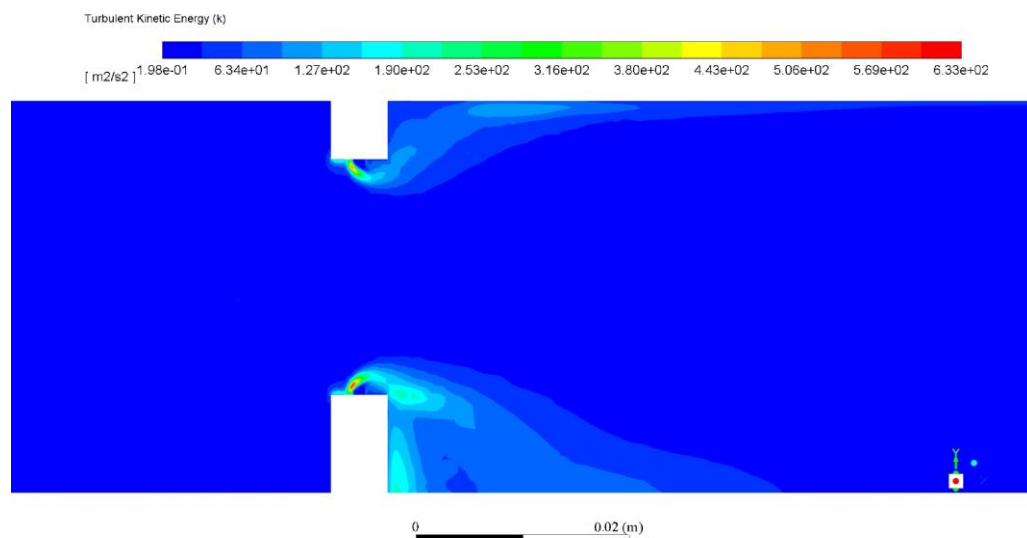


**Figure 6-47.** Axial velocity contours for FGM simulation for GM1



**Figure 6-48.** Velocity vectors for GM1 simulation

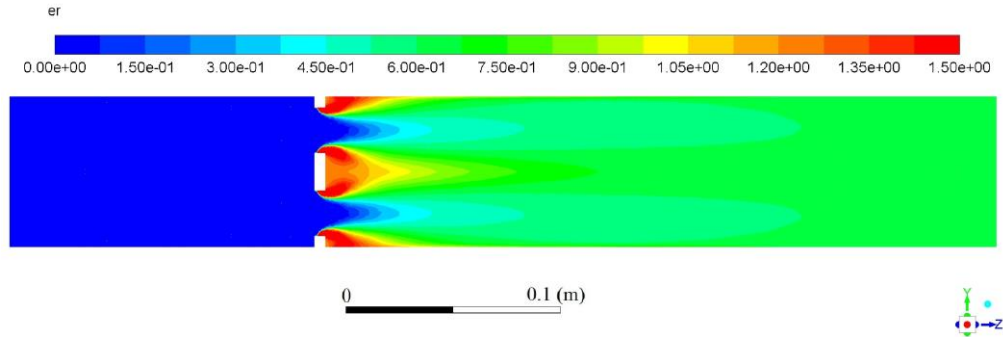
The turbulence kinetic energy contours are shown in Figure 6-49 as a closeup of the stabiliser region. The energy peaks were encountered at the fuel injection jets while being impinged by the airflow. This figure and Figure 6-48 show an interesting example of a jet in a crossflow, well predicted by Realizable  $k-\varepsilon$ , which showed a significant improvement for predicting this phenomenon compared to the previous results obtained with  $k-\varepsilon$ .



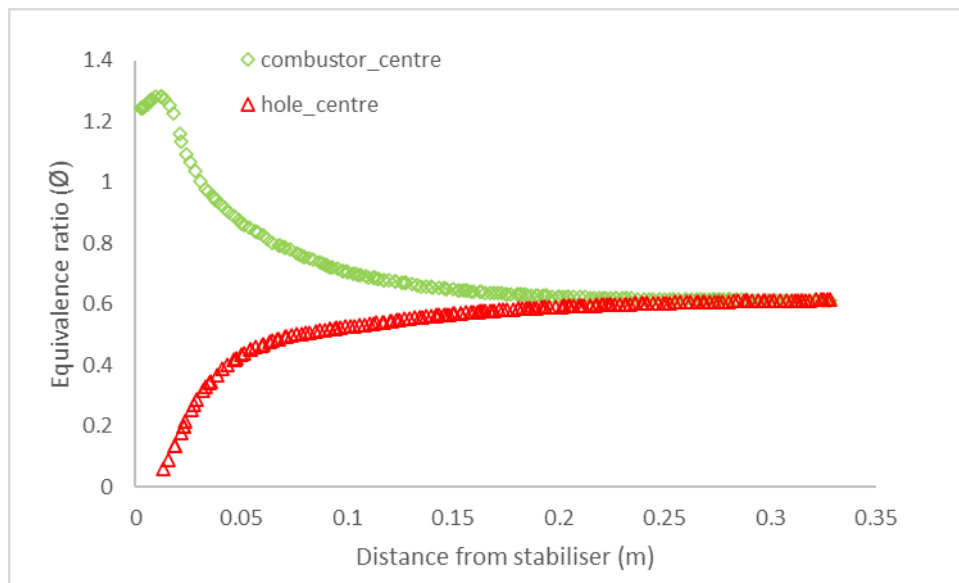
**Figure 6-49.** TKE contours for GM1 simulation

Figure 6-50 illustrates the equivalence ratio contours for GM1 where the desired condition was achieved quicker than the previously investigated GM2. The radial injections pushed the fuel to the wall region and the central area just after the stabiliser position. The region richer than stoichiometric was 50mm long, and the lean air jets were way smaller than for GM2. Figure 6-51 shows the plots of the equivalence ratio obtained at the combustor centreline and at

the centreline of the airholes. The central region after the stabiliser showed just  $\phi=1.2$ . The plot at the centreline of the hole achieved most of the mixing 50mm downstream from the stabiliser. As shown later in the text, this was the main heat release zone.

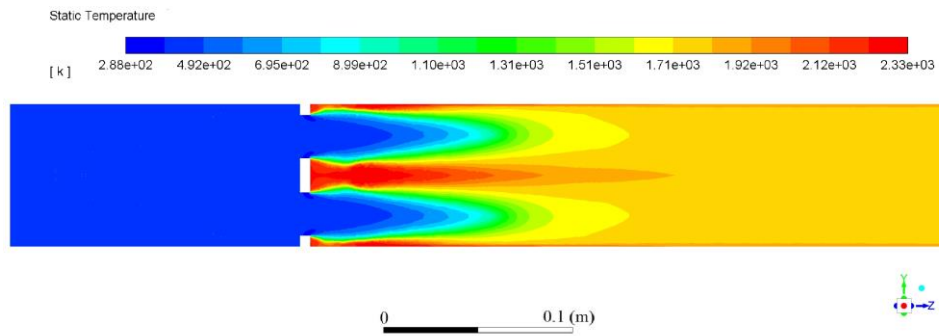


**Figure 6-50.** Equivalence ratio contours for GM1 simulation

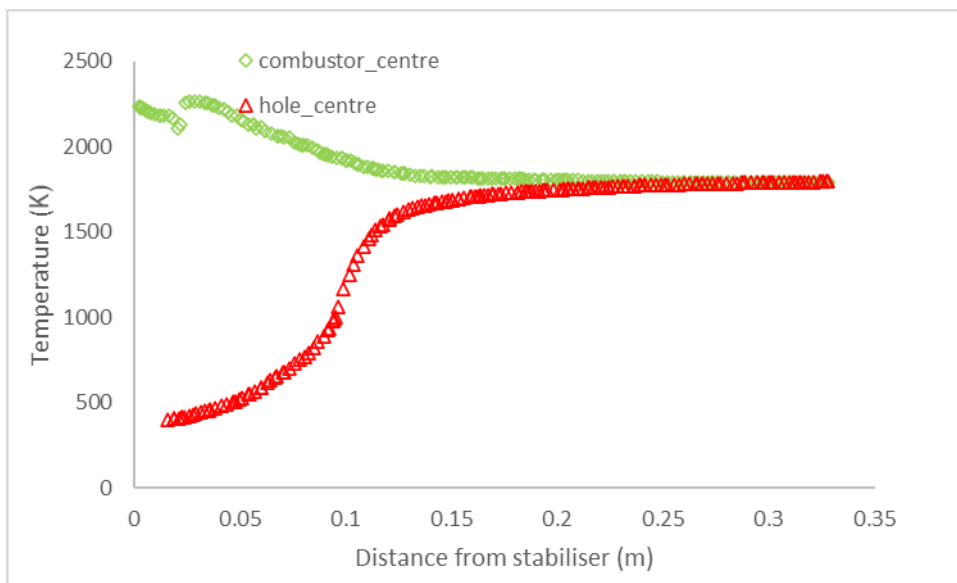


**Figure 6-51.** Equivalence ratio plots at the combustor centreline and at the centreline of the airholes for GM1.

The temperature contours are shown in Figure 6-52, where a 2200K flame was observed in the central rich region and at the walls just after the stabiliser position, where the heat release started. A high-temperature profile can be observed along the walls. Figure 6-53 shows the temperature plots for the combustor centreline and the airholes centreline. The plot at the centre of the combustor agreed with the equivalence ratio profiles in Figure 6-51, showing the main heat release around 50mm downstream of the stabiliser.



**Figure 6-52.** Temperature contours for GM1 simulation



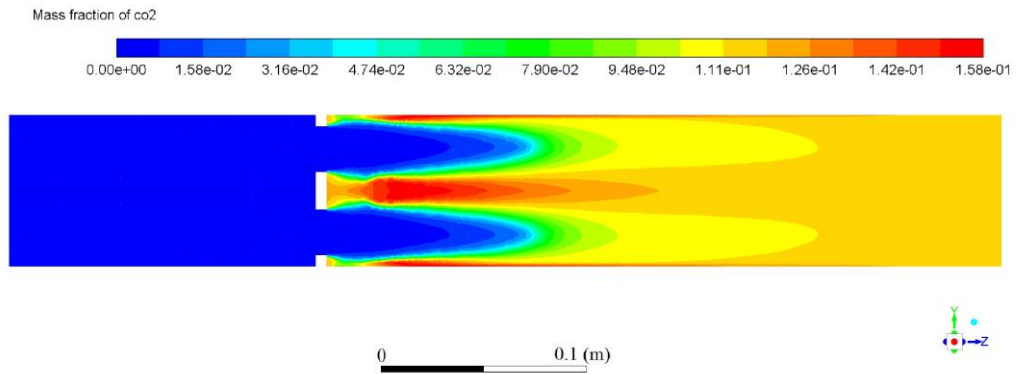
**Figure 6-53.** Temperature plots at the combustor centreline and at the centreline of the airholes for GM1.

Figure 6-54 shows the CO<sub>2</sub> contours for GM1, which shows the peak at the highest temperature region and extending along the heat release region. The CO contours show the highest peak of 0.12 at the wall region. Another high CO region is observed in the central area just at the downstream wall of the stabiliser ( Figure 6-55)

Figure 6-56 shows the NO<sub>x</sub> contours for GM1 where again a central high concentration region is observed due to the temperatures above 2000K. The peak NO<sub>x</sub> of 36ppm was obtained at 60mm downstream. Figure 6-57 shows the NO<sub>x</sub> plot 5mm offset with the centreline, as obtained for GM2. The peak of 18 was achieved at 0.75mm from the stabiliser.

The simulation means averaged at the combustor outlet was 5ppm, resulting in an underprediction compared to the experimental value of 25ppm for GM1. Or

1.2ppm compared to 7ppm for corrected oxygen at 15%, as observed in Table 6-3.



**Figure 6-54.** CO<sub>2</sub> contours for GM1 simulation

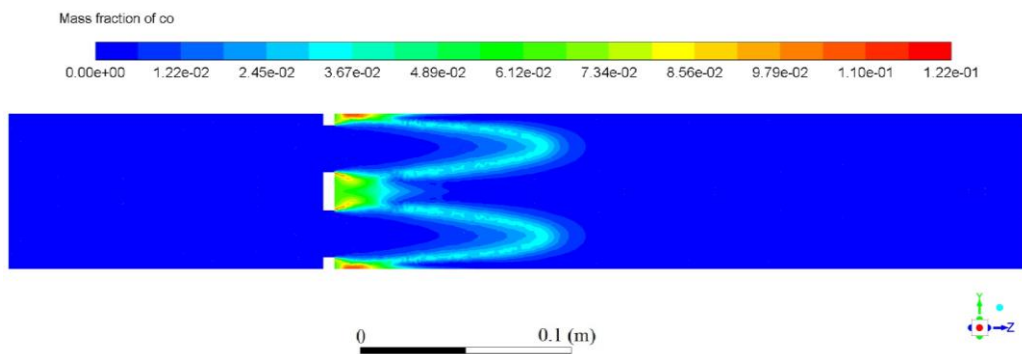


**Figure 6-55.** CO contours for GM1 simulation

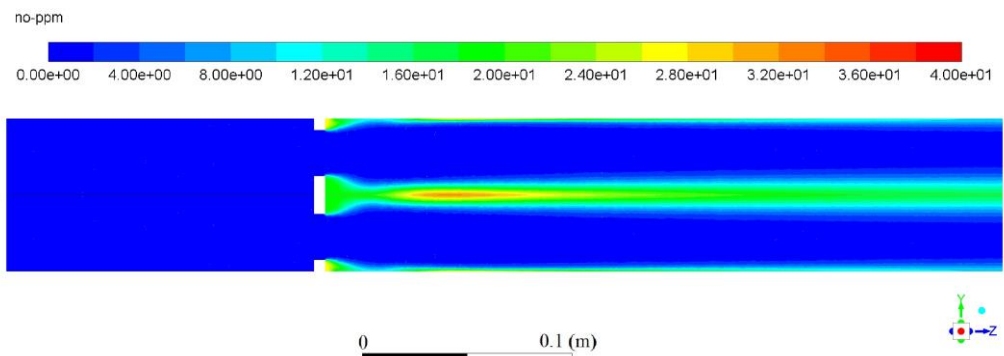


**Figure 6-56.** NO<sub>x</sub> contours for GM1 simulation

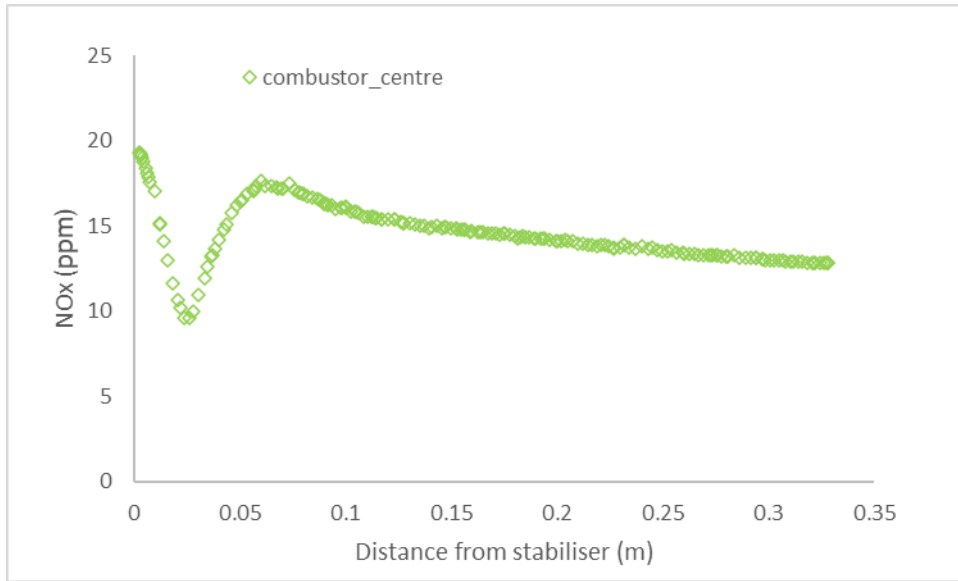


**Figure 6-57.** NO<sub>x</sub> levels for GM1 at 5mm offset of combustor centreline.

**Table 6-3.** Experimental mean exit NO<sub>x</sub> levels compared with simulation for GM1 at  $\phi=0.6$ .

<b>Experimental (ppm)</b>	<b>Simulation (ppm)</b>	<b>Experimental 15% O<sub>2</sub> (ppm)</b>	<b>Simulation 15% O<sub>2</sub> (ppm)</b>
25	5	7	2

Figure 6-59 shows a transversal plane 10mm downstream from the stabiliser showing the rich spots of the eight radial injections per air hole compared to a radial flame picture collected during the experiments for the studied conditions. The bright spots in the photograph are fuel/rich zones showing lack of reaction that resemble the eight rich red radial injections obtained with simulation.

Table 6-4 compares the simulation's average values obtained at the combustor outlet to the equilibrium values calculated with Gaseq and CEA. A perfect agreement was obtained with Gaseq for all the parameters. CEA predicted a slightly higher adiabatic flame temperature

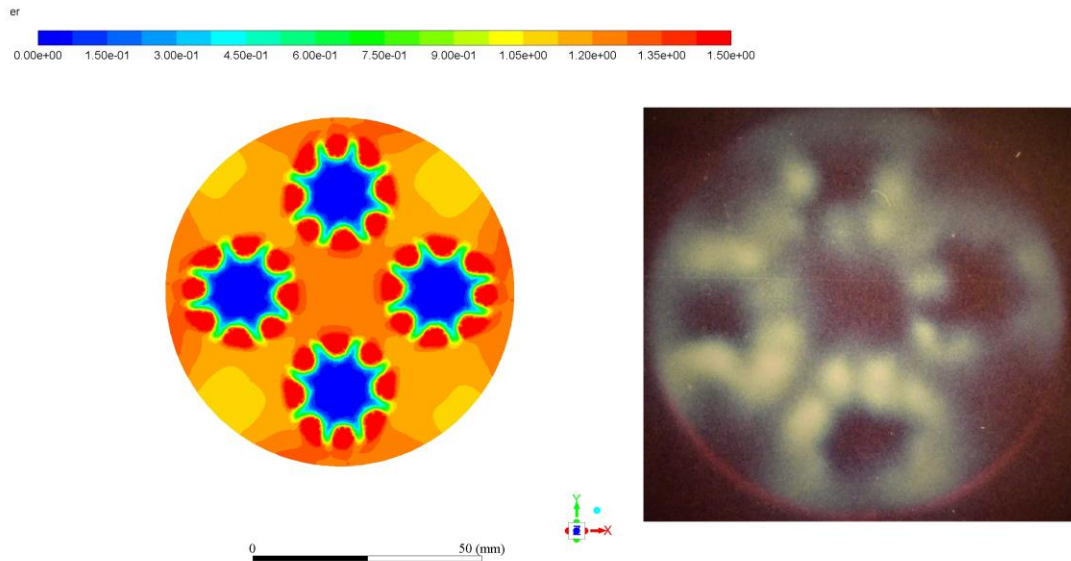


**Figure 6-58** GM1 flame at 400K,  $M=0.047$ ,  $\varnothing = 0.6$  compared with simulation

**Table 6-4** Comparison of the CFD predicted mean composition at 330mm combustor length with two chemical equilibrium codes for GM1.

Parameter	Gaseq	CEA	GM1 Simulation
Equivalence ratio	0.624	0.62	0.623
Adiabatic flame temperature	1812.59K	1820.6	1812.13K
Mean exit CO (mole fraction)	6.39e-5	6.98e-5	7.84e-5
Mean exit CH <sub>4</sub> (mole fraction)	1.41e-24	1.58e-24	6.0e-10
Mean exit O <sub>2</sub> (mole fraction)	7.3e-2	7.4e-2	7.57e-2
Mean exit CO <sub>2</sub> (mole fraction)	7.45e-2	7.46e-2	7.42e-2

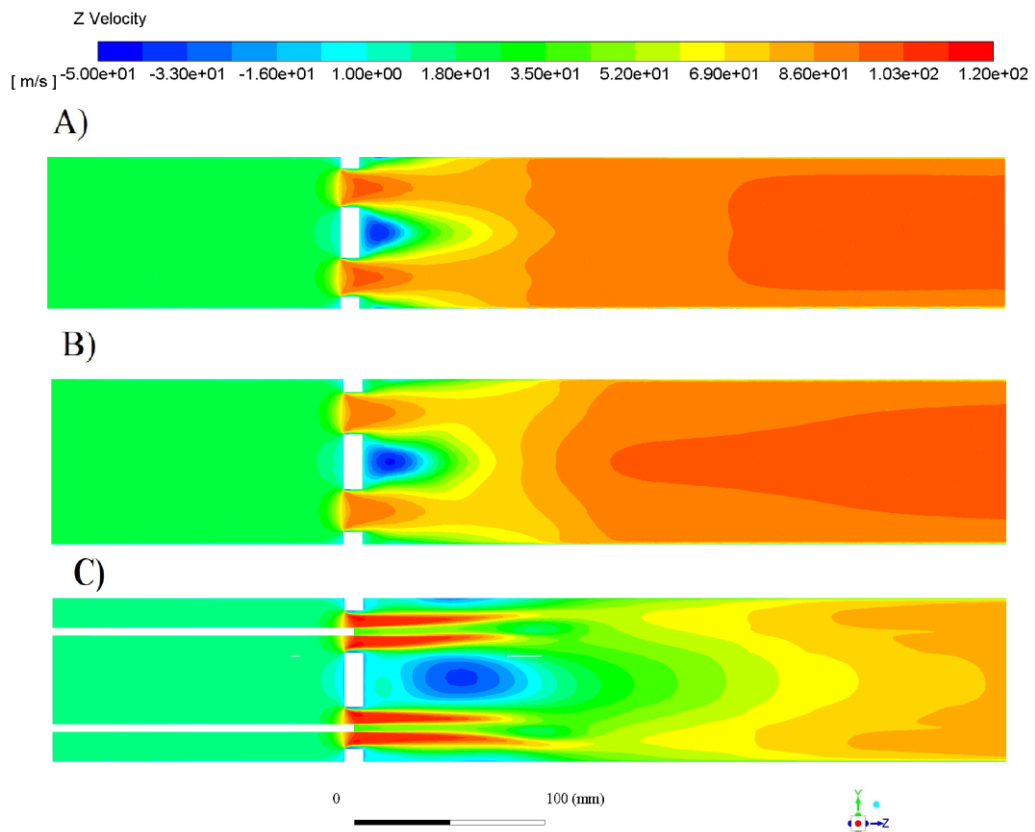
## 6.5 Combustion study for GM1, GM2 and GM3

Figure 6-59-Figure 6-63 show and compare the combustion contours obtained with simulation for the technologies GM1, GM2 and GM3.

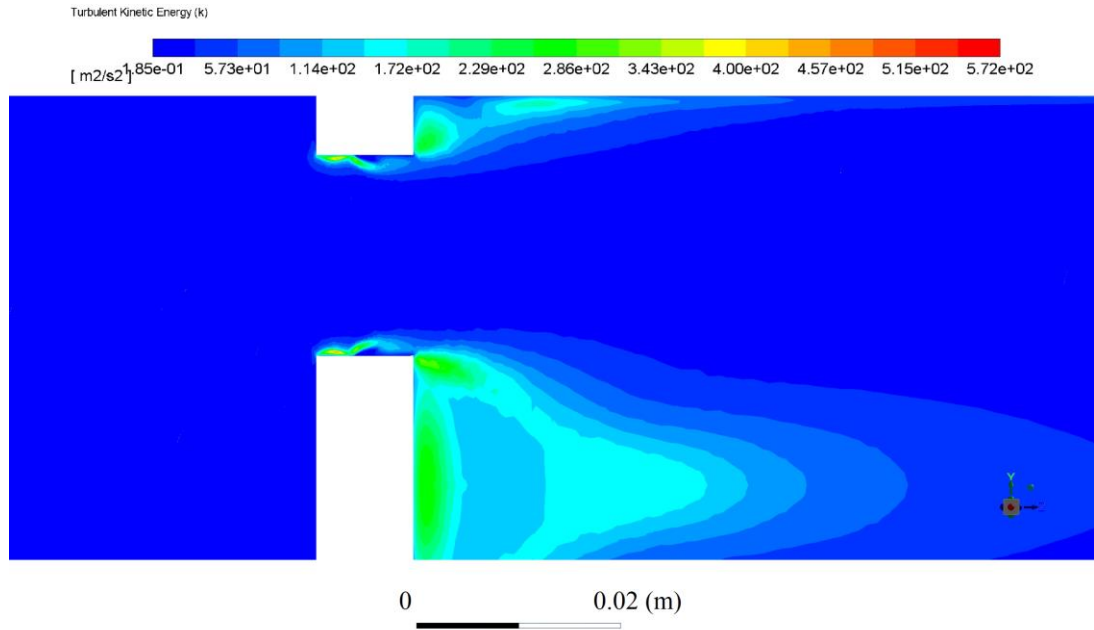
The axial velocity contours in Figure 6-59 show the highest velocity for GM3 at the stabiliser contraction area, which was 120m/s. The propane injection was 48 m/s for this technology, the highest compared to 18 m/s for each nozzle of GM1 and 19m/s for the GM2 annular feed. This high velocity was obtained due to the fuel pipes restriction at the centre of the stabiliser holes. A clear drawback of using this FLOX-like method for GM was the fuel injection getting isolated from the main recirculation areas, which has been beneficial for

mixing. Figure 6-59 C) shows more extended high-velocity jets than the other two geometries and a central recirculation zone twice the size of GM2 and four times bigger than GM1. The radial injection showed the smallest central recirculation zone. The radial nozzles fuelled the air jet directly, showing jet in a crossflow. However, no fuel penetration was observed since the fuel injection velocity was similar to the air inlet velocity of 18.8 m/s. Small recirculation zones near the wall were obtained for GM1, which could have influenced the mixing process.

A closeup of the TKE contours for GM2 is shown in Figure 6-60, showing the impingement of the air jet towards the fuel injection and producing a high energy zone. The highest energy peak was just before the fuel injection due to the sharp-edged plate. In addition, the recirculating flow in the downstream face of the stabiliser created high turbulences at the wall and the corners of the flat plate.



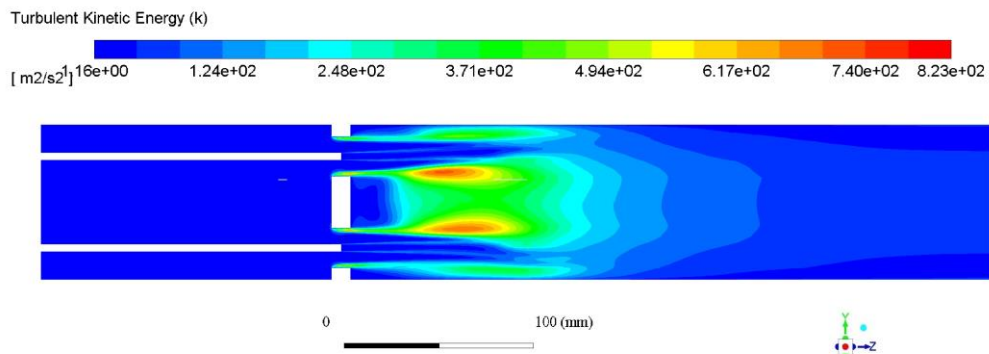
**Figure 6-59.** Comparison of axial velocity contours for reacting mixture  
A)GM1, B)GM2, C)GM3



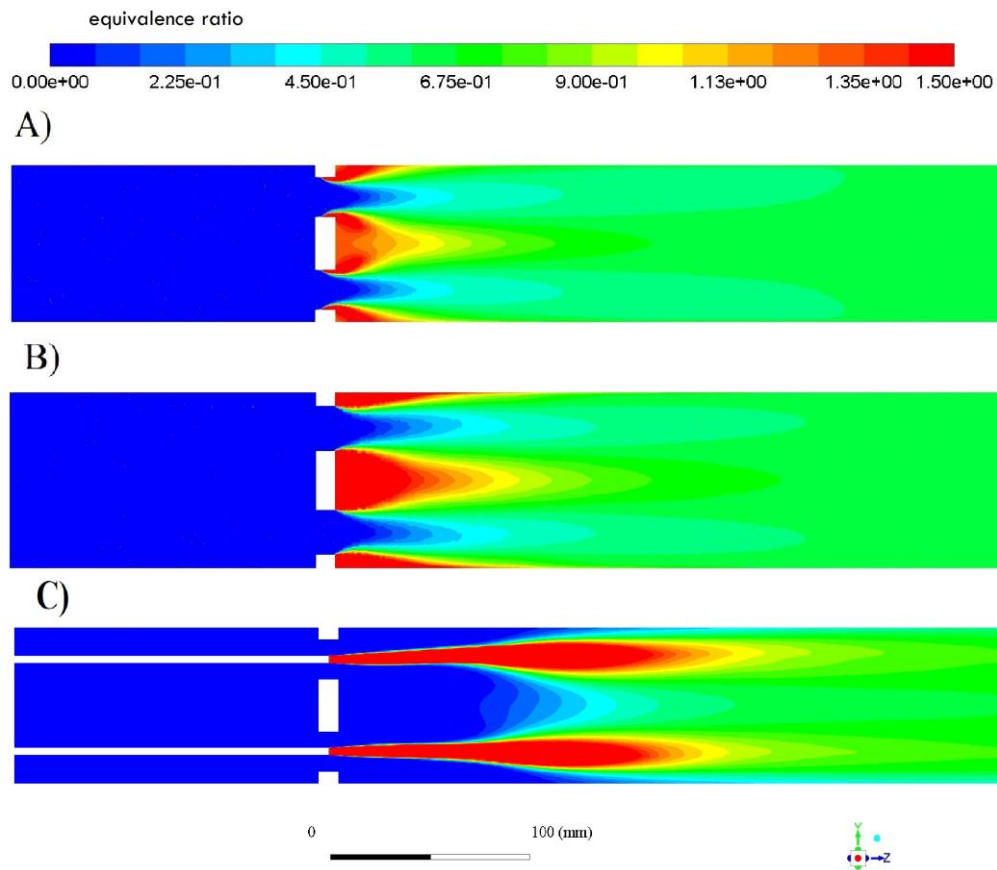
**Figure 6-60.** Closeup of TKE contours for reacting mixture for GM1 showing no fuel penetration

Figure 6-61 shows the TKE energy contours for GM3, where peak energy zones are observed in the shear layer region. However, given the high-velocity air jets, the fuel did not reach the turbulence zones until 75mm downstream of the stabiliser position.

The equivalence ratio contours in Figure 6-62 show a faster mixing for GM1 followed by GM2 and GM3. This was predicted for the isothermal mixing study for the three geometries. The three geometries achieved the desired equivalence ratio under the 330mm combustion zone length. However, as explained before, the fuel jets of GM3 took the longest to commence the mixing process, as shown in Figure 6-62C).



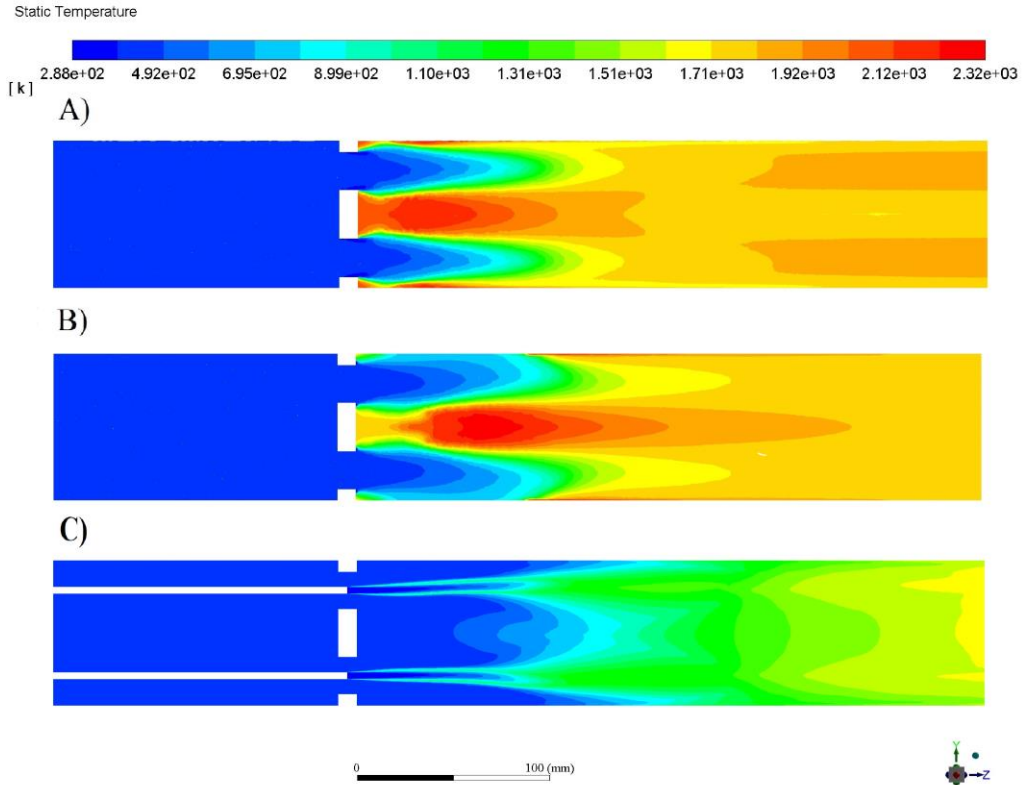
**Figure 6-61.** TKE contours for reacting mixture GM3



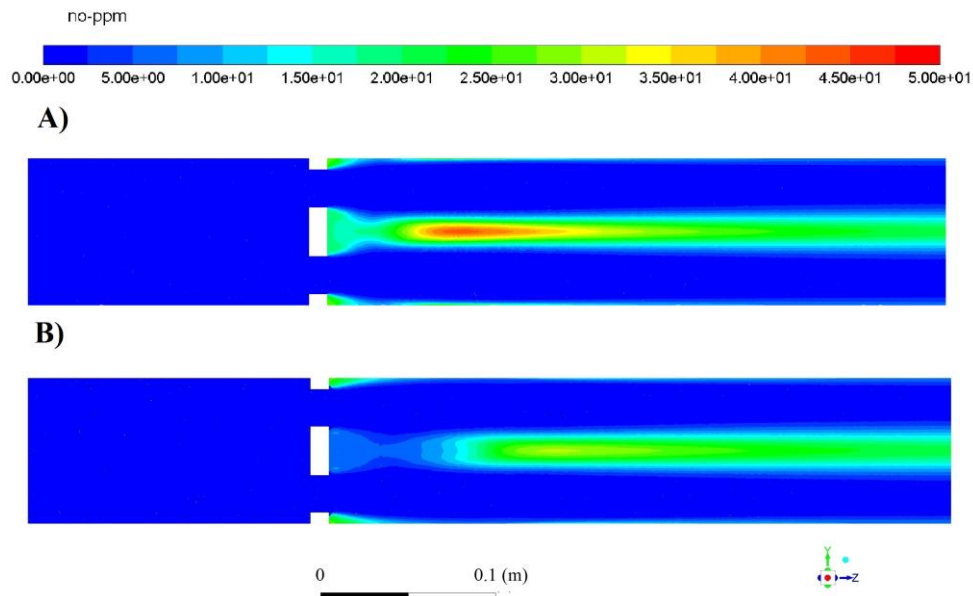
**Figure 6-62.** Comparison of equivalence ratio contours for reacting mixture A)GM1, B)GM2, C)GM3

Figure 6-62 compares the temperature contours for the three geometries. The predicted TKE at the combustor central region of GM1 anchored the flame to the stabiliser downstream face, which was not observed for GM2. High-temperature areas near the walls were obtained for GM1 due to the recirculation zones predicted in Figure 6-59 B). The maximum heat release region for GM1 was 30mm from the stabiliser compared to the 50mm of GM2. Both GM1 and GM2 achieved the peak temperature of 2320K in the centreline of the combustor.

Given the delay in mixing was predicted for GM3, the temperature development was also delayed, and it missed the central recirculation zones, which are high energy regions beneficial for flame development. Figure 6-63C) shows that the flame started developing literally at the combustor outlet. A combustor with a larger combustion zone would be needed to investigate flame development for this technology for the studied conditions.



**Figure 6-63.** Comparison of temperature contours for reacting mixture A)GM1, B)GM2, C)GM3



**Figure 6-64.** Comparison of NO<sub>x</sub> contours for reacting mixture A)GM1, B)GM2

The NO<sub>x</sub> contours for GM1 and GM2 are compared in Figure 6-64, where a faster NO<sub>x</sub> formation is observed for GM1. This was expected since the peak temperature was predicted to be closer to the stabiliser than GM2. Additionally, higher NO<sub>x</sub> levels were also obtained for GM1. Experimentally this was not the case where GM1 showed much lower levels than GM2. However, the stabiliser

air hole used for this study was smaller than the one used experimentally. Hence, the air hole influenced the pressure loss and aerodynamics, proven experimentally, and the  $\text{NO}_x$  could have been affected.

### 6.5.1 GM1 flame stabiliser for a hydrogen/air flame

The combustion aerodynamics for GM1 evaluated for a hydrogen/air flame are shown in Figure 6-65, where the axial velocity contours in Figure 6-65 A) show a high velocity for the fuel injection. The hydrogen jet velocity was 183 m/s giving a fuel/air momentum ratio of 0.25, much lower than 0.66 for propane. However, no fuel penetration was observed due to the broader air jet at the vena contracta region impinging directly on the low-density hydrogen jets. As a result, massive turbulence kinetic energy levels of  $5\text{K m}^2/\text{s}^2$  were obtained at the impingement region. However, only  $500 \text{ m}^2/\text{s}^2$  was set for this impingement in Figure 6-66 B) to capture the energy distribution for the rest of the combustor. This means that the fuel/air mixing was dominated by the turbulence generated by the airflow rather than the fuel injection momentum. A central high turbulence region is also observed for the hydrogen flame for GM1 as for propane, where it seems the high-velocity hydrogen jets impinged with the flat outlet of the stabiliser.

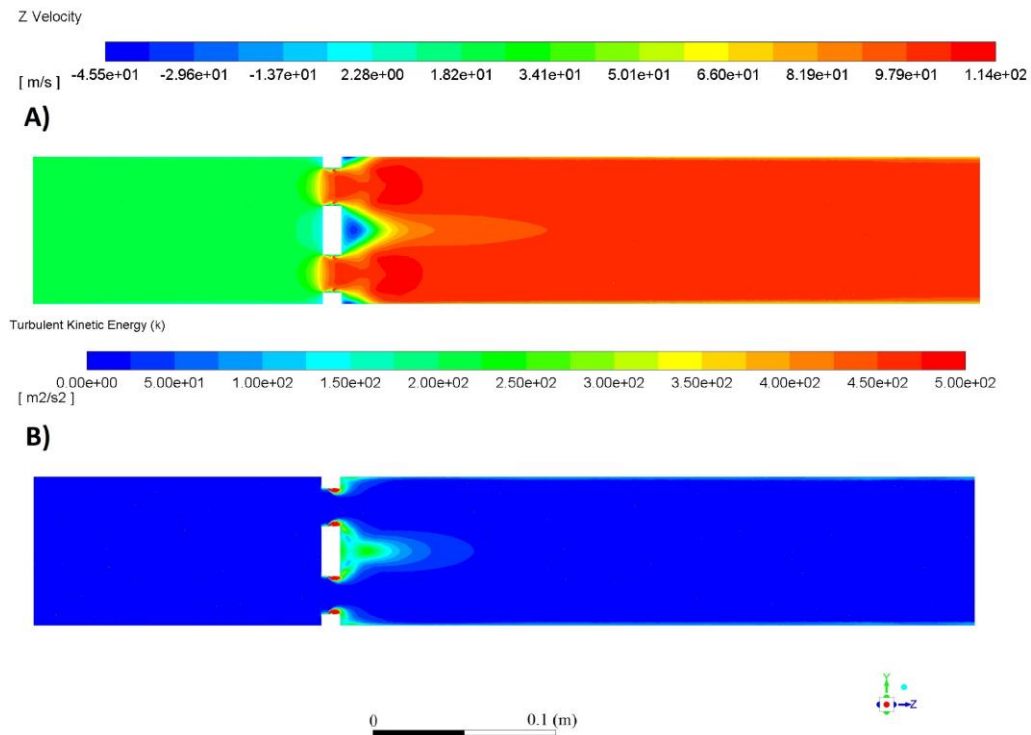


**Figure 6-65.** Flame aerodynamics for GM1 evaluated for hydrogen/air flame.  
A) Axial velocity, B) TKE

The equivalence ratio contours for GM1 for a hydrogen flame are shown in Figure 6-66. The central rich zone just downstream of the stabiliser position matched the high turbulence predicted in Figure 6-65 B). A high turbulence zone near the walls at the air hole exit was also indicated in Figure 6-65 B), which dragged the fuel from the nozzles and created a rich zone, given the 90m/s velocity air-jets and the low momentum ratio as shown in Figure 6-66. Given the low density of hydrogen, the desired equivalence ratio was achieved slower than propane.

The rich high turbulence central and near the wall zones anchored the flame to them, resulting in the peak temperatures for the wall region at the stabiliser hole exit and at the centre of the stabiliser face, as shown in Figure 6-67. The highest temperature obtained with simulation was 2434K in this region. The heat release zone was longer than propane, resembling more of the one obtained for GM2 in Figure 6-63.

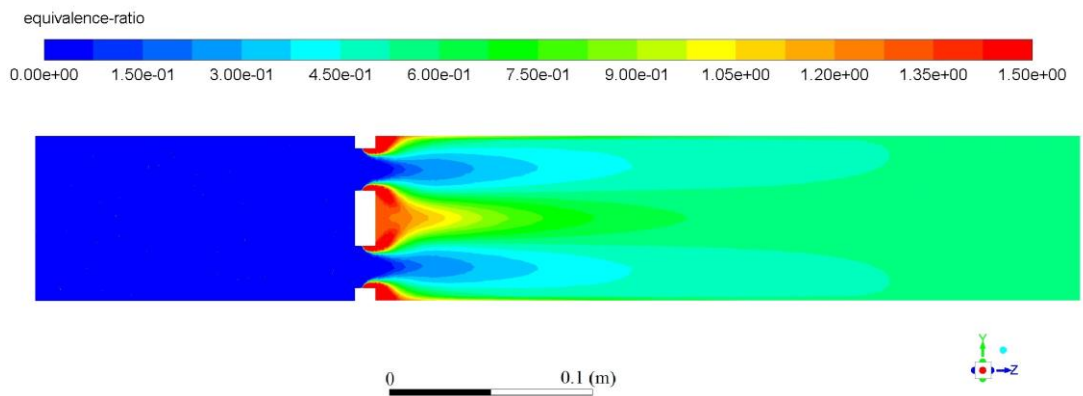


**Figure 6-66.** Equivalence ratio contours for GM1 evaluated for hydrogen/air flame

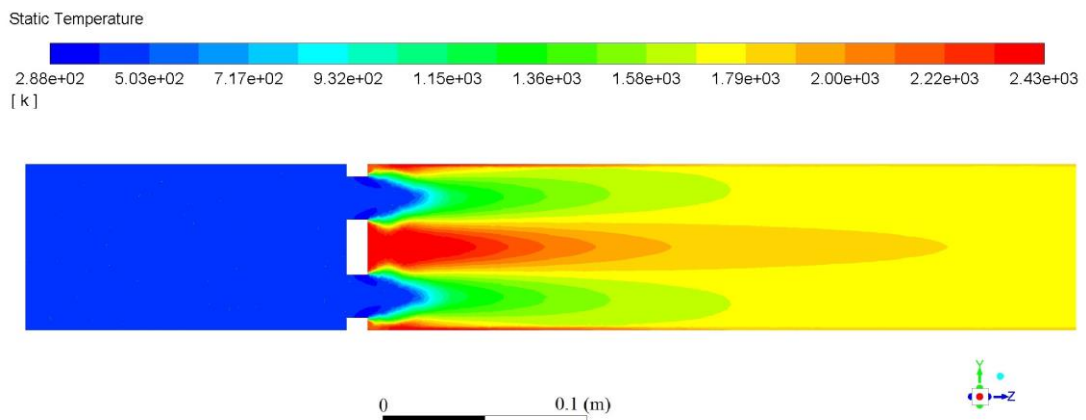


**Figure 6-67.** Temperature contours for GM1 evaluated for hydrogen/air flame

Figure 6-68 shows the oxygen levels for the simulation, which agrees with the temperature prediction. The oxygen was slowly consumed in the air jet region, and zero levels were observed for the central and wall high-temperature regions

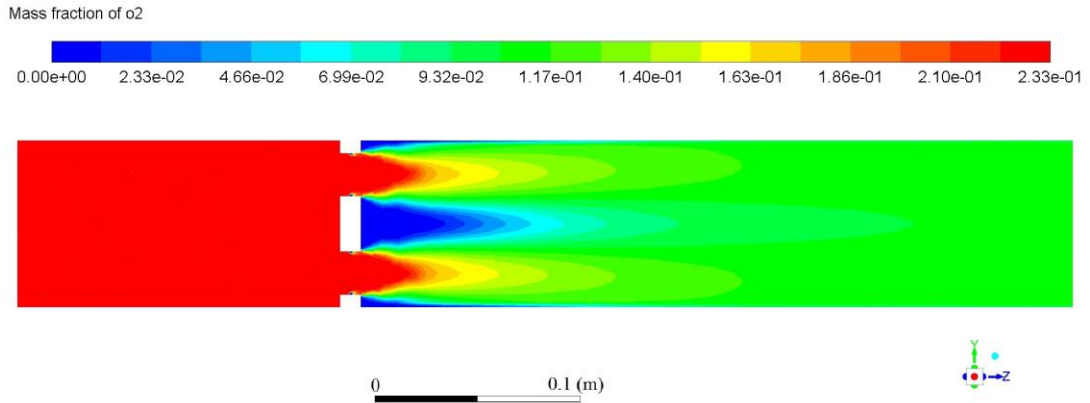


**Figure 6-68.** Oxygen contours for GM1 evaluated for hydrogen/air flame

The mean outlet levels obtained with simulation were compared with the equilibrium results obtained with Gaseq and CEA to verify the simulation validity. This comparison can be seen in Table 6-5, where a slight overprediction of the equivalence ratio was obtained with the simulation. The simulation predicted the exit means flame temperature, differing just 4K from the CEA results. The CEA calculation approached the actual studied conditions better since it allows the temperature input for the different mixture species. In contrast, Gaseq assumes a single inlet temperature for all the reactants.

**Table 6-5.** Comparison of the CFD predicted mean composition at 330mm combustor length with two chemical equilibrium codes for GM1-H2.

Parameter	Gaseq	CEA	GM1-H2 Simulation
Equivalence ratio	0.548	0.548	0.554
Adiabatic flame temperature	1819.9K	1801.6K	1805.8
Mean exit O <sub>2</sub> (mole fraction)	8.33e-2	8.36e-2	8.49e-2

The NO<sub>x</sub> contours shown in Figure 6-69 are transversal planes for the studied locations illustrated previously in Figure 6-8. Inline with the airholes and 45° offset with the first plane.

Higher NO<sub>x</sub> levels than propane were obtained for the hydrogen/air mixture. The peak was obtained 200mm from the stabiliser position in the wall region

for the plane offset with the holes in Figure 6-69B). Figure 6-69A) shows the peak of 80ppm in the central high-temperature area. The outlet means  $\text{NO}_x$  was 16.2ppm, which corrected to 15% oxygen was 7.17ppm. This indicated that using GM1 for a hydrogen/air flame obtained  $\text{NO}_x$  than for propane. Figure 6-70 compares  $\text{NO}_x$  levels at the combustor centreline for both fuels. A peak of 73ppm and an exit level of 34 was achieved with  $\text{H}_2$ . In contrast to 43 ppm and 21ppm obtained for propane

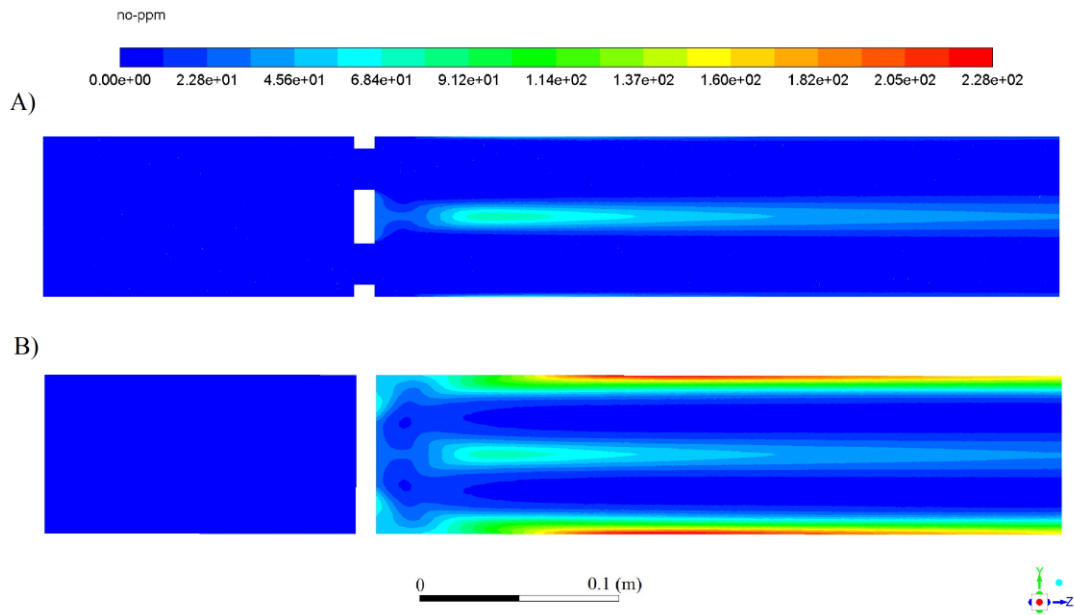


**Figure 6-69.**  $\text{NO}_x$  contours for GM1 for a hydrogen/air mixture A) Inline with the air holes B) 45° offset with the airholes

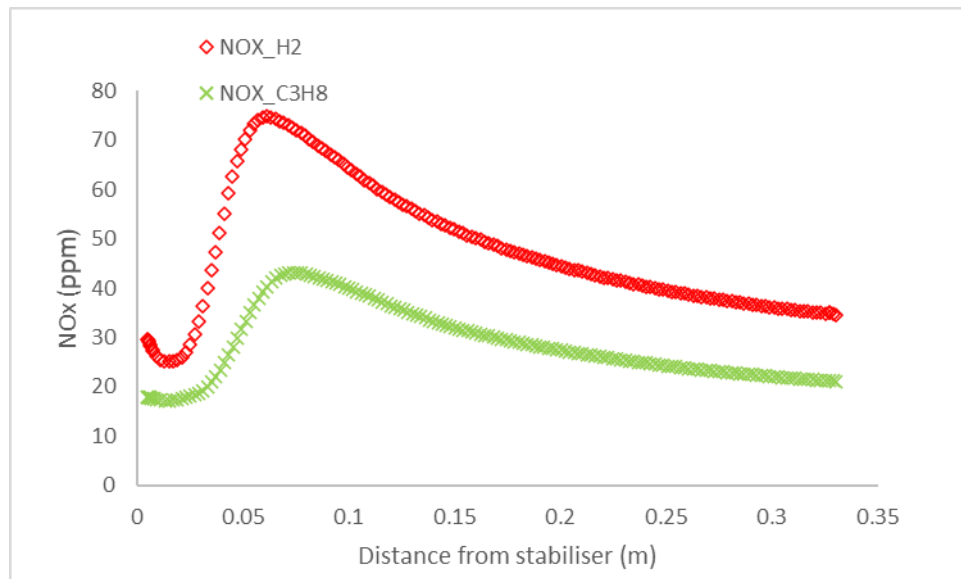


**Figure 6-70.** Comparison of  $\text{NO}_x$  levels at the combustor centreline for GM1 for a hydrogen and propane flame.

### 6.5.2 Effect of a thicker stabiliser length on NO<sub>x</sub> emissions for a hydrogen flame

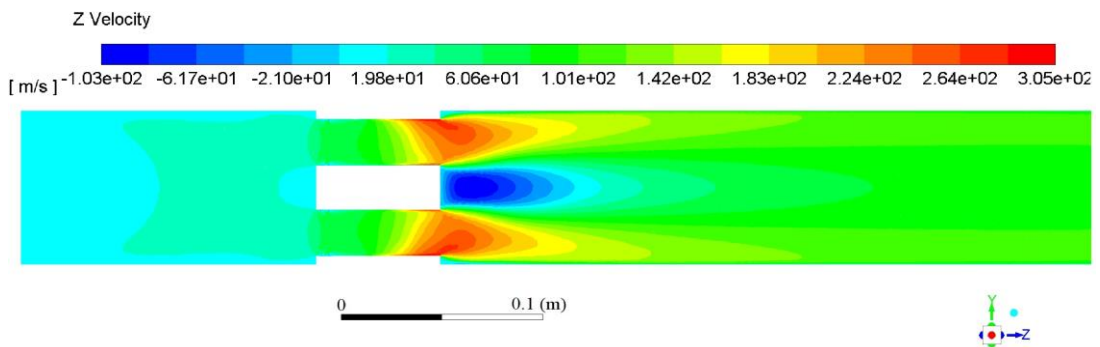
Figure 6-71 Figure 6-79 show the contours obtained for the technology GM1 evaluated for a stabiliser thickness of 7D for a hydrogen/air flame.

The velocity contours in Figure 6-71 show the same central recirculation zone after the stabiliser downstream face obtained for the past geometries. However, a more extensive area was predicted for this geometry than any of the other studied cases. The elongated thickness worked as a suction for the incoming air, which shows a higher velocity while getting closer to the stabiliser. The highest velocity was not observed at the injection points but near the outlet of the plate.

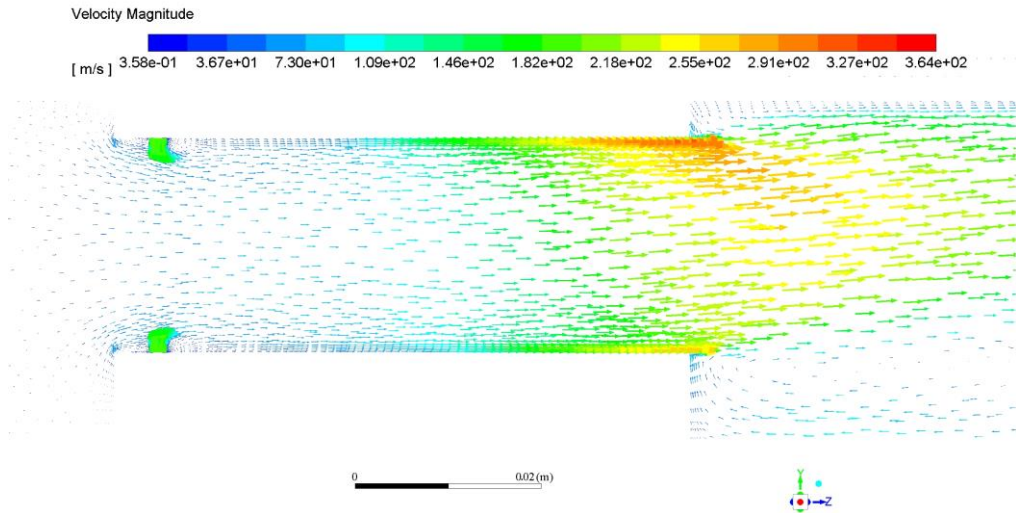
The velocity vectors at the hole region are shown in Figure 6-72. Fuel separation is observed at the sharp-edged hole inlet of the plate and then reattached to the hole wall further downstream. The calculated velocity for the injection nozzles was 182m/s. However, due to the low-density fuel, no flow penetration was encountered.

The turbulence kinetic energy contours presented in Figure 6-73 show energy peaks at the central recirculation zone featuring extremely high concentrations up to 3000 m<sup>2</sup>/s<sup>2</sup> at the lower shear layer region and just at the wall of the outlet stabiliser face.

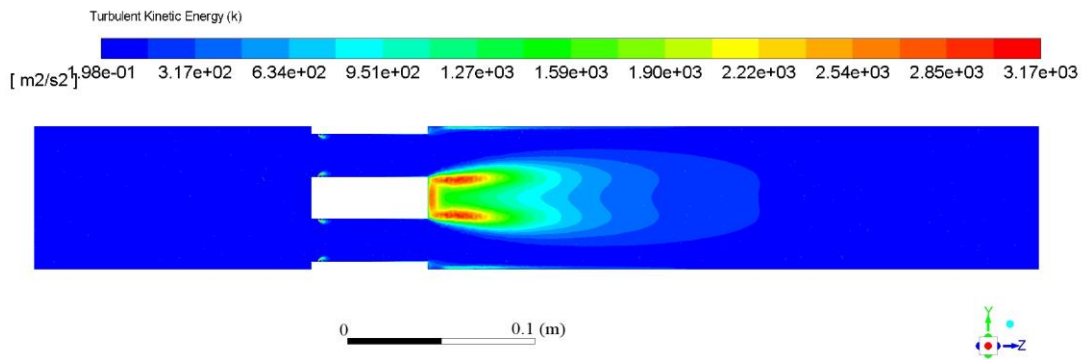
A close-up view near the region is shown in Figure 6-75, where another peak of TKE can be seen in the high-velocity fuel jets impinged by the air jet. A high energy zone can also be observed at the wall region just after the stabiliser position, which was not due to recirculation but the upper shear layer of the air jets coming out of the plate hole.



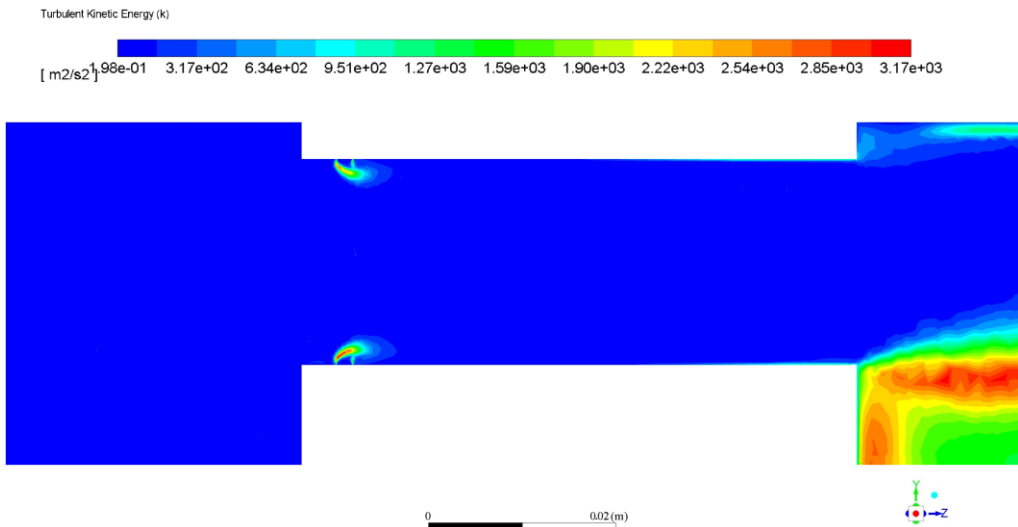
**Figure 6-71.** Axial velocity contours for GM1 with 7D stabiliser thickness for hydrogen/air flame



**Figure 6-72.** Velocity vectors at stabiliser region for GM1 with 7D stabiliser thickness for hydrogen/air flame



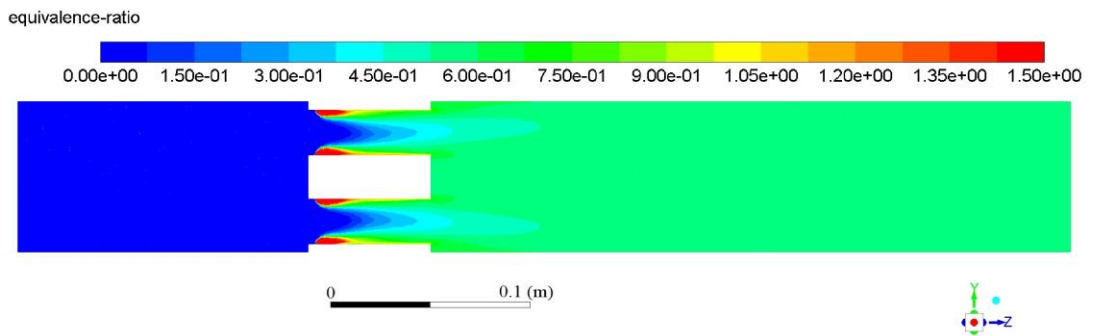
**Figure 6-73.** TKE contours for GM1 with 7D stabiliser thickness for hydrogen/air flame



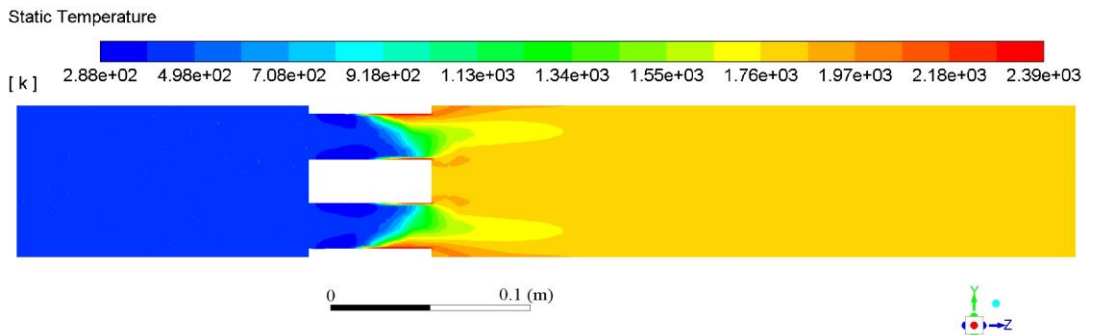
**Figure 6-74.** TKE contours at stabiliser region for GM1 with 7D stabiliser thickness for hydrogen/air flame

Figure 6-75 illustrates the equivalence ratio contours for the thicker stabiliser GM1, featuring excellent mixture qualities. Most of the fuel was mixed in the air tubes, showing fuel/rich regions only 25mm from the plate hole inlet. This was also due to the low density of hydrogen, which quickly mixed with the air jet. The desired equivalence ratio was almost achieved at the stabiliser outlet.

The highest temperature zones of 2340K were predicted at the wall region near the stabiliser exit, as shown in Figure 6-76. The flame started developing inside the stabiliser, where the equivalence ratio reached under stoichiometric levels 25mm after the stabiliser hole inlet. This was an issue reported by York et al. [27]. Most of the heat release took place inside the flame stabiliser, and it took 50mm to fully develop after the stabiliser position, where it achieved the adiabatic flame temperature. Two high-temperature regions were obtained for the high turbulence zones predicted in Figure 6-73. However, most predicted energy was not used since the mixing and flame development was mainly outside this region.



**Figure 6-75.** Equivalence ratio contours for GM1 with 7D stabiliser thickness for hydrogen/air flame



**Figure 6-76.** Temperature contours for GM1 with 7D stabiliser thickness for hydrogen/air flame

The oxygen contours are shown in Figure 6-77, where no depleted-oxygen regions are observed apart from the wall region downstream of the stabiliser thickness, where the highest temperatures were predicted.

The NO<sub>x</sub> contours are shown in Figure 6-78 and Figure 6-79, where the first one shows the values at the plane in line with the holes showing the highest levels at the combustor wall just after the stabiliser. Figure 6-79 shows the NO<sub>x</sub> contours at the wall region, which showed the highest concentrations at the exit of the stabiliser hole tube.

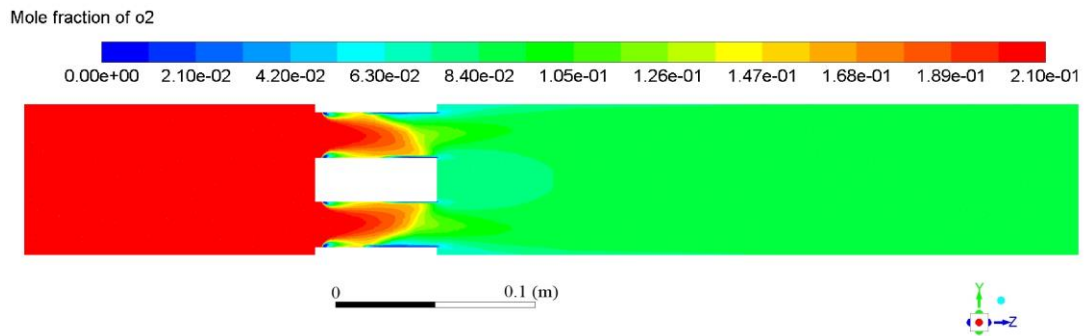


**Figure 6-77.** Oxygen mole fraction contours for GM1 with 7D stabiliser thickness for hydrogen/air flame

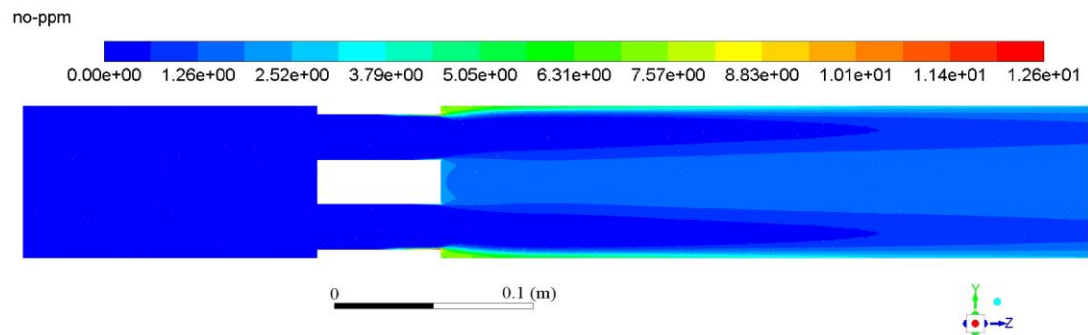


**Figure 6-78.** NO<sub>x</sub> ppm contours for GM1 with 7D stabiliser thickness for hydrogen/air flame

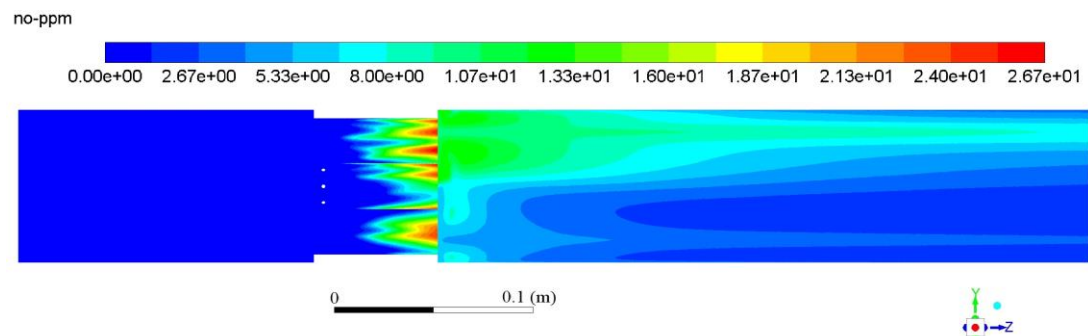


**Figure 6-79.** NO<sub>x</sub> ppm contours at wall region for GM1 with 7D stabiliser thickness for hydrogen/air flame

The highest NO<sub>x</sub> achieved for this geometry was 26.1ppm, and the mean averaged was 2ppm converted to 15% corrected oxygen was 12.4 and 1.09ppm, respectively. Table 6-6 compares the mean exit values for GM1 featuring a stabiliser thickness of 7D (GM-7D) with the thin plate geometry both operated with hydrogen. Lower levels were achieved by this geometry compared to GM1 featuring a thin plate, showing that an elongated mixing length is beneficial for NO<sub>x</sub>

A comparison between the mean exit values of GM1 with a thin plate, GM1-7D for a hydrogen flame and the results of Gaseq and CEA is shown in Table 6-7. Perfect agreement was achieved for the exit values for both geometries, which also agree with the equilibrium software values. This demonstrated that 330mm was also enough length to achieve complete combustion for a hydrogen flame with GM1

**Table 6-6.** Comparison of mean exit NO<sub>x</sub> levels between GM1-H<sub>2</sub> and GM1-H<sub>2</sub>-7D

<b>GM1-H<sub>2</sub> (ppm)</b>	<b>GM1-H<sub>2</sub> 15% O<sub>2</sub> (ppm)</b>	<b>GM1-H<sub>2</sub>-7D (ppm)</b>	<b>GM1-H<sub>2</sub>-7D 15%O<sub>2</sub> (ppm)</b>
16.2	7.17	2.21	1.09

**Table 6-7.** Comparison of the CFD predicted mean composition at 330mm combustor length with two chemical equilibrium codes for GM1-H<sub>2</sub> and GM1-H<sub>2</sub>-7D

<b>Parameter</b>	<b>Gaseq</b>	<b>CEA</b>	<b>GM1-H<sub>2</sub> Sim</b>	<b>GM1-H<sub>2</sub>-7D Sim</b>
Equivalence ratio	0.548	0.548	0.554	0.554
Adiabatic flame temperature	1819.9K	1801.6K	1805.8	1806.7
Mean exit O <sub>2</sub> (mole fraction)	8.33e-2	8.36e-2	8.49e-2	8.49e-2

## 6.6 Conclusions

The isothermal comparison of the fueling methods GM1, GM2 and GM3 showed that the technique featured by GM1 achieved the best mixing features, followed by GM2 and GM3. This was corroborated in a later combustion study for the

three geometries, where the same results were obtained. For a combustion simulation, a lower NO<sub>x</sub> was foreseen for GM1 since a faster mixing can be translated to lower NO<sub>x</sub>. This was experimentally studied and predicted [25]. However, this was not the case for the simulation.

The combustion study of GM2 showed that the steady diffusion flamelet model (SDF) achieved the best agreement with the experimental results for temperature. However, the mixing and combustion efficiency were better predicted using the Flamelet Generated Manifold (FGM) model, which also allowed the calculation of NO<sub>x</sub> for this geometry. Underpredicted values of these pollutants were obtained compared to the experiments. Hence more work needs to be done to get better accuracy for the studied conditions using RANS modelling. The mean exit values were compared with equilibria code showing that the adiabatic results obtained with simulation are valid.

The simulation for GM1 showed underpredicted NO<sub>x</sub> results compared to the experimental data using realizable  $k$ - $\epsilon$  and FGM for a propane/air flame.

Some factors are addressed that could be potential reasons for the disagreement with the experimental results:

- Some experimental parameters were assumed, such as the adiabatic walls, which could have potentially changed the temperature distribution inside the combustor.
- The physical stabiliser used for GM2 showed to have some manufacturing issues. So the fuel injection might not be uniform due to a non-uniform area of the annulus.
- The exact position where the internal traverses were obtained is dubious.
- The turbulence, combustion and NO<sub>x</sub> models could be struggling to predict NO<sub>x</sub> given the fast flows and reduced residence times.

GM1, GM2 and GM3 investigated for a reacting mixture, and the same stabiliser geometry featuring four airholes of 19.62mm showed that GM1 obtained better mixing and NO<sub>x</sub> than GM2 and much better than GM3.

The geometry featuring GM1 for the 19.62mm airhole flame stabiliser showed higher NO<sub>x</sub> levels for a hydrogen flame than propane using the FGM combustion model. This has been a concern for years for burner manufacturers when burning hydrogen. However, the geometry later investigated for an thicker stabiliser of seven times the airhole diameter showed much less NO<sub>x</sub>. This feature showed that an extended mixing length is beneficial for NO<sub>x</sub>, as

reported by York et al [27]. A comparison of simulation mean exit NO<sub>x</sub> levels for the two different studied fuels and geometries is shown in Table 6-8

**Table 6-8.** NO<sub>x</sub> level comparison for C<sub>3</sub>H<sub>8</sub> and H<sub>2</sub> for GM1

<b>GM1-C3H8 (ppm)</b>	<b>GM1-H<sub>2</sub> (ppm)</b>	<b>GM1-H<sub>2</sub>-7D (ppm)</b>
5	16.2	2.21

The mean exit values obtained for GM2 and GM1 for propane and hydrogen flames were compared with Gaseq and CEA equilibria codes, showing almost perfect agreement. This gave validation to the used simulation parameters and boundary conditions.

## **Chapter 7. EXPERIMENTAL AND CFD ANALYSIS OF DOMESTIC HEATERS**

### **7.1 Introduction**

The experimental work undertaken for three low NO<sub>x</sub> domestic fires is now presented to examine their dual fuel capabilities.

Several tests were undertaken for each fire to consistently show dual fuel capabilities for natural gas/hydrogen fuels, considering the reference NO<sub>x</sub> values of 130 mg/kWh set up by legislation. One of the main requirements of the experiments was to achieve a constantly visible flame when using hydrogen. Two of the studied fires are commercially available and are known as best selling fires, with more than 5000 units sold. The third fire consisted of a prototype glass fronted fire that showed an innovative flame, considering the requirements for emissions. This fire was studied with numerical simulation, comparing different injection shapes, and a whole set of experiments will be presented.

The three fires were studied for different coals setups by adding or removing the respective fire coals. However, the author mainly intends to show the results of the arrangement with all the coals on. Some geometries like LB17 compare the results for no coals, back coals, and all coals to show the influence of the coal arrangements over the emissions.

### **7.2 Open fronted fire**

The experimental results for the tests carried out for the Focal Point Blenheim Slimline open fronted fire for dual fuel applications for single and two-stage injection are now presented.

#### **7.2.1 Single-stage combustion**

Two main concepts were designed for the open-fronted fire burner:

- Four fuel nozzles to be in line with the air holes of the bottom ceramic coals. This concept allowed the fuel jets to thoroughly mix with the incoming air before impinging on the top ceramic coals. This feature permitted good post “coal” combustion.
- Five fuel nozzles offset to the air holes of the bottom ceramic coals. This concept illustrated the fuel nozzles impinging on the bottom ceramic structs

The designs were tested for a fuel pressure loss of 20 mbar (Design 1) and two mbar (Design 2), including a metering orifice.

The designed burners for the open-fronted fire are shown in Table 7-1, where FPB stands for Focal Point burner. However, only the geometries with round holes FPB2-FPB4 were studied since they showed very low NO<sub>x</sub> levels and a fantastic flame. All the burner plates were made of stainless steel Grade 316L.

**Table 7-1:** Studied burner configurations for the open-fronted fire

<b>Configuration</b>	<b>Description</b>	<b>Fuel hole type/orie.</b>
FPB1	Baseline reference fire 4 X 0.83mm holes	Round
FPB2	2 X 2.0mm central holes, 2 X 1.47mm end holes. 57mm equispaced	Round
FPB3	3 X 0.92mm central holes 57mm equispaced; 2 X 0.83mm end holes 92mm spaced from centre	Round
FPB4	3 X 1.63mm central holes 57mm equispaced; 2 X 1.47mm end holes 92mm equispaced from centre.	Round
FPB5	2 X (0.3 X 3.31mm) central slots 57mm equispaced; 2 X (0.3 X 1.79mm) end slots 85.5mm equispaced from centre	Slot-shape horizontal
FPB6	2 X (0.3 X 10.46mm) central slots 57mm equispaced; 2 X (0.3 X 5.67mm) end slots 85.5mm equispaced from centre	Slot-shape horizontal
FPB7	2 X (3.31 X 0.3mm) central slots 57mm equispaced; 2 X (1.79 X 0.3mm) end slots 85.5mm equispaced from centre	Slot-shape vertical
FPB8	2 X (10.46 X 0.3mm) central slots 57mm equispaced; 2 X (5.67 X 0.3 mm) end slots 85.5mm equispaced from centre	Slot-shape vertical
FPB9	2 X (0.3 X 2.21mm) central slots 57mm equispaced; 2 X (0.3 X 1.79mm) end slots 92mm equispaced from centre	Slot-shape horizontal

The designs with five nozzles assume that when impinging the fuel with the ceramic struts, it distributes equally on either side of the strut. Unfortunately, this hypothesis was incorrect as the ceramics were handmade, and some

manufacturing inaccuracies were spotted, which created some misalignment between the nozzles and the ceramic struts.

### **Configuration FPB1**

The baseline reference open fronted fire was demonstrated for NG only. The flame is shown in

Figure 7-1, where high yellow flames protrude from the ceramic coals.

The measured emissions for the reference fire were 128 mg/kWh, 60 ppm CO, and 51% thermal efficiency.

One of the requirements for the open-fronted fire designs was to achieve better light up and shut off times than the reference fire. The reference fire light up time was measured at less than 20 seconds and a shut-off time of 60 seconds.



**Figure 7-1:** Open fronted reference fire NG

### **Configuration FPB2**

The four-round hole configuration for the open-fronted fire FPB2 was tested for natural gas and hydrogen. Preliminary tests with no coals on for hydrogen showed very high levels of NO<sub>x</sub>, as shown in Table 7-2.

**Table 7-2:** Steady-state emissions for FPB2 no coals H<sub>2</sub>

<b>Pressure</b>	<b>NO<sub>x</sub> (ppm)</b>	<b>O<sub>2</sub>(%)</b>	<b>NO<sub>x</sub> (mg/kWh)</b>
13.6	27	19.3%	629

7.5	21	19.6%	674
4.8	19	19.7%	582

These high levels will later be explained due to the lack of impingement that the top coals provide to the fire and hence the flame heat removal.

Steady-state results for FPB2 for different fuel pressures and all coals are shown in Table 7-3 for NG, and Table 7-4 shows the results for H<sub>2</sub>. A considerable reduction in NO<sub>x</sub> levels is observed with the addition of the fourteen coals for the test on H<sub>2</sub>. The lowest NO<sub>x</sub> levels were achieved for NG.

The CO and NO<sub>x</sub> levels were lower than the reference fire FPB1, showing this configuration viable for dual fuel. Figure 7-2 illustrates a comparison of the NO<sub>x</sub> levels for FPB2 obtained for H<sub>2</sub> and NG

The flame for FPB2 is shown in Figure 7-3, where an intense bed burning can be seen for natural gas in Figure 7-3A), and diffusion blue flames protrude from the coals holes. It is essential to point out that flame stabilization was impossible without these top coals.

The hydrogen fire in Figure 7-3B) shows a clear flame under the ceramic coals and some small flames coming out of the ceramics.

**Table 7-3:** Steady state emissions for FPB2 all coals NG

Pressure	CO (ppm)	NO <sub>x</sub> (ppm)	O <sub>2</sub> (%)	NO <sub>x</sub> (mg/kWh)
10	70	2.8	18.85	50.2
5.7	90	2.0	19.29	45.7
4.3	136	1.3	19.42	32.3
0.9	53	2.2	20.25	124

**Table 7-4:** Steady-state emissions for FPB2 no coals H<sub>2</sub>

Pressure	NO <sub>x</sub> (ppm)	O <sub>2</sub> (%)	NO <sub>x</sub> (mg/kWh)
13.6	2.7	19.35%	64.1
9.1	2.7	19.68%	81.4
0.64	8.7	20.25%	492

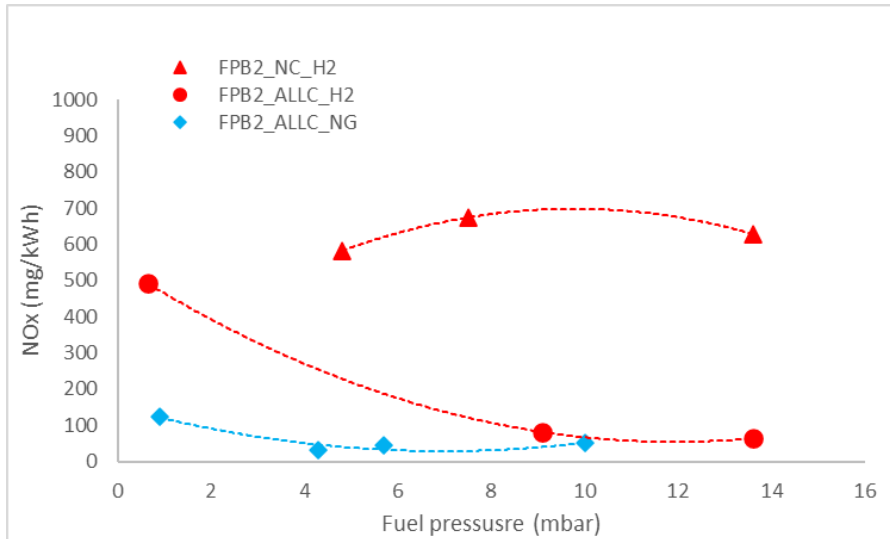


**Figure 7-2:** FPB2 burner NO<sub>x</sub> levels for H<sub>2</sub> and NG



**Figure 7-3:** Open fronted fire FPB2 10 mbar: a) NG; b) H<sub>2</sub>

### Configuration FPB3

The test results for the five-round hole FPB3 are now presented. This configuration was tested with all the ceramic coals. The emissions for NG and H<sub>2</sub> are shown in Table 7-5, where the NO<sub>x</sub> for both fuels was lower than the reference fire at high and low power. The H<sub>2</sub> test at 10 mbar showed the highest NO<sub>x</sub>, higher than FPB1. Flame photographs for NG and H<sub>2</sub> at high power are shown in Figure 7-4, where an intense glow is observed for NG in Figure 7-4 a). An excellent looking flame was achieved with the best post-coal burning during the H<sub>2</sub> test, as shown in Figure 7-4 b). Since the emissions were low enough, this configuration was considered the final design for the open-fronted fire. The emissions for FPB3 are compared with FPB2 in Figure 7-5, showing overall lower levels for FPB2. However, the flame looked better for FPB3.

**Table 7-5:** Steady-state emissions for FPB3 all coals NG and H<sub>2</sub>

Fuel	Pressure (mbar)	NO <sub>x</sub> (ppm)	NO <sub>x</sub> (mg/kWh)	O <sub>2</sub> (%)	CO (ppm)	CO <sub>2</sub> (%)
NG	15.6	3.7	94.9	19.46	252	0.65
NG	6.7	1.7	64.5	19.93	249	0.40
NG	0.4	1.2	78.8	20.34	66	0.19
H <sub>2</sub>	15	2.5	93.8	19.92	-	-
H <sub>2</sub>	10.7	3.8	151.9	19.96	-	-
H <sub>2</sub>	1.7	1.7	122.8	20.39	-	-



**Figure 7-4:** Open fronted fire FPB3 13.6 mbar: a) NG; b) H<sub>2</sub>

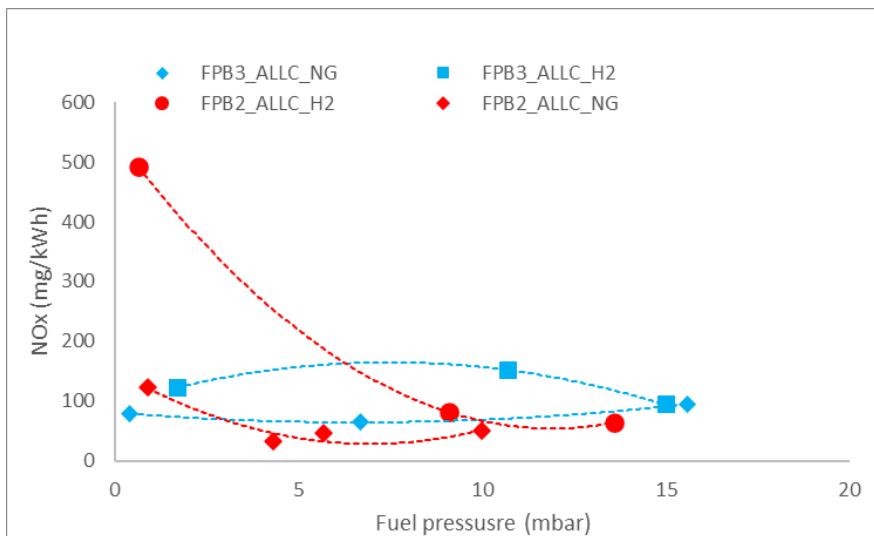


**Figure 7-5:** Steady-state emissions for FPB2 and FPB3 all coals NG and H<sub>2</sub>

### 7.2.2. Two-stage combustion

The two-stage combustor for the open-fronted fire featured the nozzle sizes for FPB3 in the first stage injection. The secondary injection was offset with the third row of top ceramic coals, meaning that the fuel was injected into the coals space. The fire was tested for hydrogen and natural gas for dual fuel applications.

#### Configuration FPB3 two-stage combustion H<sub>2</sub>

The upgraded open-fronted fire for two-stage combustion was tested at various possible power demands. The burner was designed to operate at 20 mbar at full power.

Figure 7-6 shows the burner flame at full power (20 mbar). Bright post-coal orange flames were visible. A clear reflection in the back glass wall can be seen, adding an extra aesthetic element to the fire and creating the impression of flames behind the back layer of top coals. Both angles in Figure 7-6 show the flame biased towards the fire's centre. At full power, the pilot lit successfully, and the cross light was quiet and effective.



**Figure 7-6:** Open fronted fire FPB3 for dual fuel H<sub>2</sub> 20 mbar.

Sixty-minute tests at different powers were carried out from 10-22 mbar to evaluate the NO<sub>x</sub> levels. Steady-state emissions and performance for the fire are shown in Table 7-6. NO<sub>x</sub> emissions increased until they peaked at 130mg/kWh 23 minutes after ignition. After that, they started to go down until they reached their steady state of 106 mg/kWh, as shown in Figure 7-7. These levels were well within the NO<sub>x</sub> requirement and lower than the reference open fronted fire FPB1. The oxygen levels at the exhaust were very high due to the nature of the fire design, which created a high sensitivity of the corrected NO<sub>x</sub> emissions. As a result, thermal efficiency was higher than the standard requirement of 42% and the reference fire of 51%.

**Table 7-6:** Steady-state emissions for FPB3 all coals two-stage combustion H<sub>2</sub> flame.

Plenum Pressure (mbar)	Mass Flow Rate (mg/s)	Flue O <sub>2</sub> (%)	T <sub>flue</sub> (deg. C)	NO <sub>x</sub> (mg/kWh)	Thermal Efficiency (%)
22	31	20.01	114	116	54
20	28	20.04	109	106	57
15	25	20.15	96.2	103	61
12	20	20.21	87.6	94	64
10	18	20.27	81.8	84	67

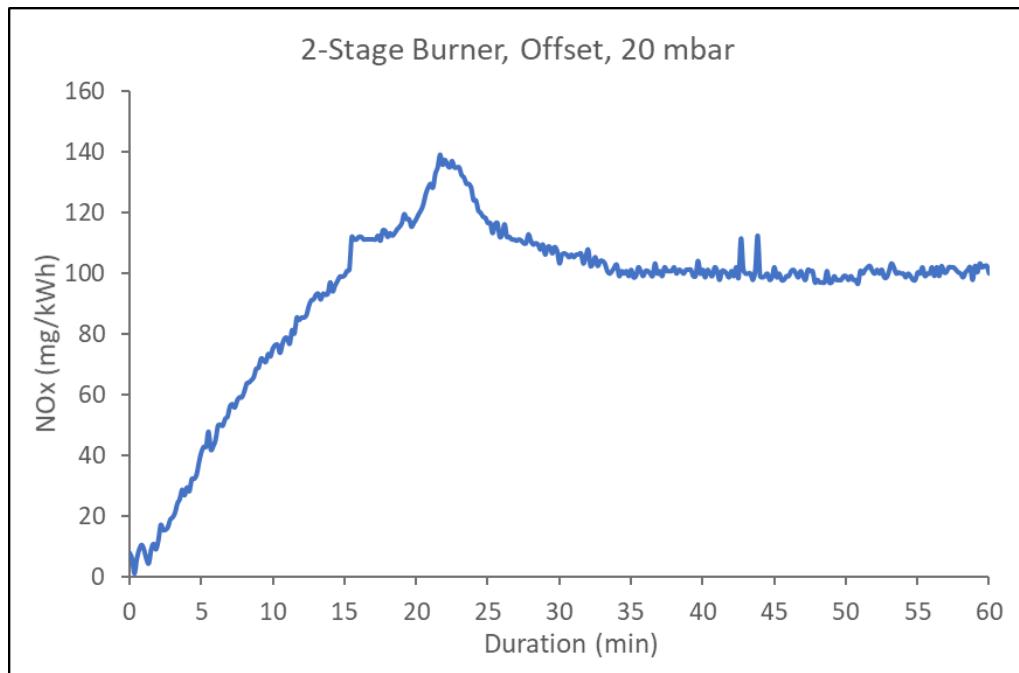


**Figure 7-7:** NO<sub>x</sub> emissions for FPB3 two-stage combustion 20 mbar, obtained in a 60 minutes test, H<sub>2</sub> flame.

Steady-state NO<sub>x</sub> results are compared with the single-stage combustion results in Figure 7-8, where the two-stage configuration showed lower values than for the single stage. However, problems were later encountered with the secondary injection pipes, which started to fall apart after several continuous tests. This was not a manufacturing issue but an actual steel composition limitation. The alloy used for these pipes included nickel to economize the manufacturing costs. Choosing an alloy without nickel would result in higher manufacturing costs, making the two-stage burner unsuitable for production.

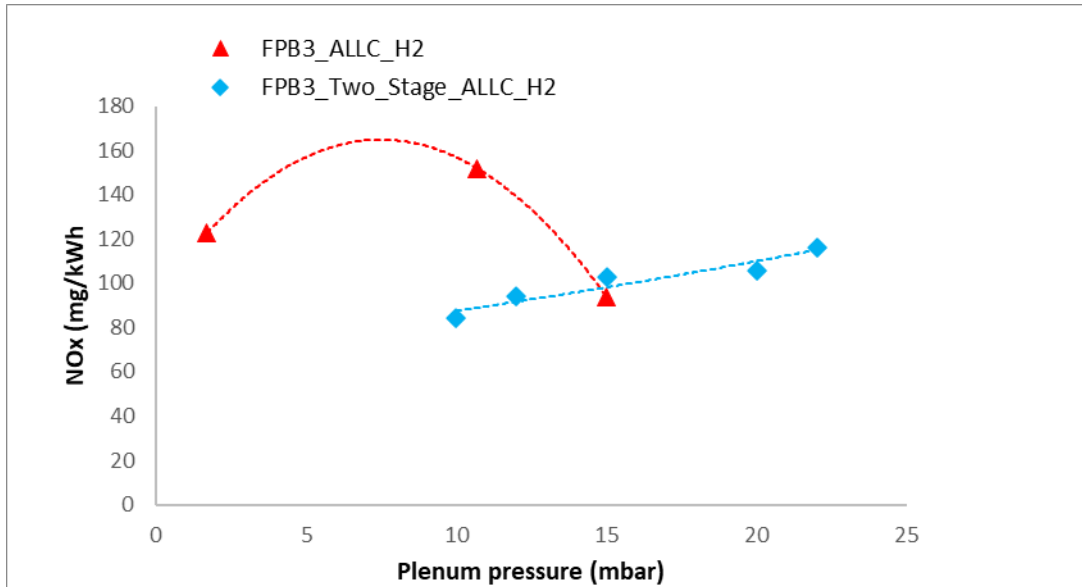


**Figure 7-8:** Steady-state NO<sub>x</sub> emissions for different powers for FPB3 for single-stage and two-stage combustion H<sub>2</sub> flame.

#### **Configuration FPB3 two-stage combustion NG**

The two-stage open fronted fire was also studied for natural gas to test its dual-fuel capabilities. Figure 7-9 shows the obtained flame at 20 mbar, where long orange central flames are observed with small blue diffusion flames coming out of the ceramics.



**Figure 7-9:** Open fronted fire FPB3 for dual fuel NG 20 mbar.

Emissions for this fire are shown in Figure 7-10, where steady-state values were obtained after 35 minutes of continuous test. After the peak values, the levels stabilised, reaching a mean NO<sub>x</sub> value of 68.05 mg/kWh. The CO levels showed a peak of 47 ppm at 10 minutes post ignition and 44ppm at a steady state. The measured oxygen was 19.2%, and the flame temperature was 158°C. The thermal efficiency was then calculated to be 59.7%.

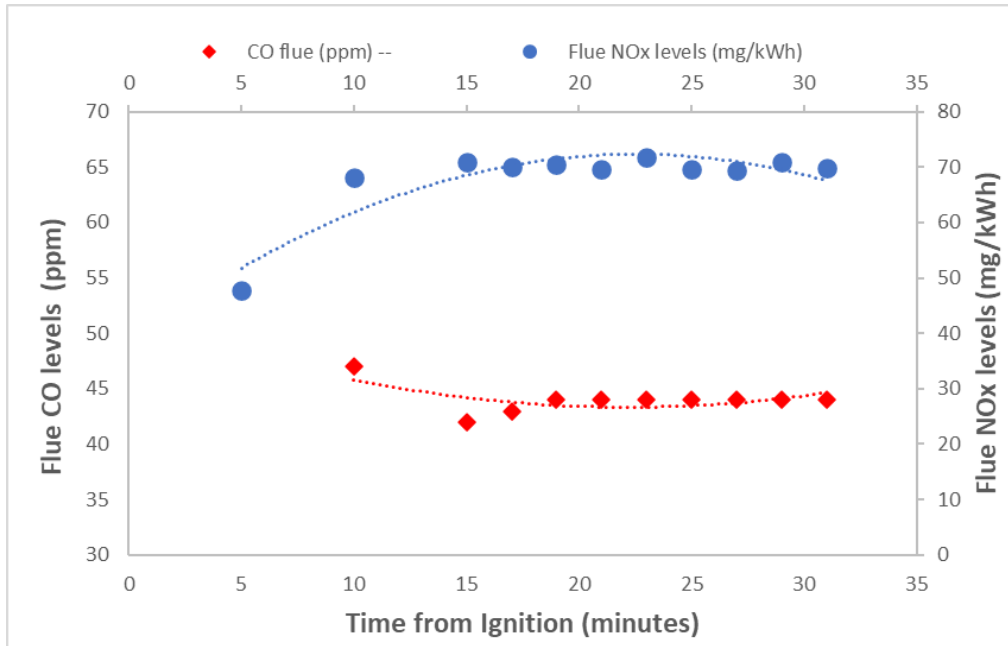


**Figure 7-10:** CO and NO<sub>x</sub> values for FPB3 two-stage burner full loading NG

No other tests for lower powers were possible since the secondary injection pipes started to fall apart after various continuous tests, as mentioned previously and shown in Figure 7-11. Soot concentrations were also observed in the fire coals.



**Figure 7-11:** Secondary injection showing cracks and notoriously worn.

### 7.3 Glass fronted fire

The reference LEGEND Evora balanced flue glass fronted fire was initially designed to operate natural gas. Upgrading this appliance to exhibit dual fuel capabilities required some essential modifications on the burner and pilot designs of the fire.

The designed burner configurations are shown in Table 7-7, where LB stands for Legend Burner. However, as mentioned in Chapter 3, only the experimental

results for the most relevant designs will be presented in this chapter. All the designs were made out of stainless steel Grade 316L.

**Table 7-7:** Studied burner configurations for the glass-fronted fire

<b>Configuration</b>	<b>Description</b>	<b>Fuel hole type</b>
LB1	Baseline reference fire	Round
LB2	5 X 0.877mm holes 40mm equispaced	Round
LB3	5 X 1.559mm holes 40mm equispaced	Round
LB4	4 X (0.3 X 2.01mm); 2 X (0.3 X 1mm) 40mm equispaced	Slot-shape
LB5	4 X (0.3 X 6.36mm); 2 X (0.3 X 3.18mm) 40mm equispaced	Slot-shape
LB6*	5 X (0.3 X 2.01mm)	Slot-shape
LB7*	5 X (0.3 X 6.36mm)	Slot-shape
LB11	4 X (0.2 X 3.02mm); 2 X (0.2 X 1.5mm) 40mm equispaced	Slot-shape
LB12	4 X (0.2 X 9.54mm); 2 X (0.2 X 4.75mm) 40mm equispaced	Slot-shape
LB13	4 X (0.1 X 6.02mm); 2 X (0.1 X 3.01mm) 40mm equispaced	Slot-shape
LB14	4 X (0.1 X 11.08mm); 2 X (0.1 X 5.54mm) 40mm equispaced	Slot-shape
LB15*	5 X (0.2 X 3.02mm)	Slot-shape
LB16*	5 X (0.1 X 9.54mm)	Slot-shape
LB17*	5 X (0.1 X 6.04mm)	Slot-shape
LB18* <sup>8</sup>	5 X (0.1 X 19.07mm)	Slot-shape

The designs LB2 and LB3 were tested at 20mbar  $\Delta P$  at the fuel jet exit

The designs LB4 and LB5 had the fuel holes in a horizontal position and midway between the back air holes in line with the ceramic ribs between the

---

<sup>8</sup> \* Gometries with asterisk had the fuel holes in offset with the top ceramic air holes.

air holes. These two designs were also reversed in the plenum chamber holder to impinge on the bottom of the bottom rear ceramics. However, in this case, the bottom rear ceramics needed a recess cut into the base to optimise an impingement gap jet. This recess cut was 10mm and common to all these impingement configurations.

Designs LB6 and LB7 featured their slots in a vertical position and located underneath the rear bottom ceramics, with an impingement gap of 10mm and in line with the centreline of the inlet air jets.

A fuel flow rate for natural gas was set to 0.139 g/s for a thermal fuel input of 6.52kW.

### **Configuration LB1**

Tests started with the reference fire LB1 to observe the flame appearance and measure the emissions. The flame appearance is shown in Figure 7-12, where a visible yellow flame is observed protruding from the ceramic holes.



**Figure 7-12:** Glass fronted reference fire LB1 natural gas

CO varied from 300 to 450 ppm, with a lower CO trend as the fire warmed up. CO<sub>2</sub> levels varied from 7.0 to 7.5%. With the CO and CO<sub>2</sub> levels obtained, the calculation of O<sub>2</sub> was possible, varying from 8.0-8.8%.

NO<sub>x</sub> levels rose from 21 ppm at idle to 38ppm as the fire warmed up. The corrected NO<sub>x</sub> to zero per cent oxygen, considering 34ppm as the average NO<sub>x</sub> and 8.4% oxygen was 57ppm.

Thermal efficiency was calculated at 73%, and exhaust temperatures varied from 420-550°C

### Configuration LB2 NG and H<sub>2</sub>

Circular hole configurations showed low NO<sub>x</sub> and CO with natural gas but very high NO<sub>x</sub> when tested with hydrogen. However, circular holes had a larger diameter than the quenching distance for hydrogen, and a popping sound was heard at ignition. This issue was due to the fuel flashback in the plenum full of air in idle conditions.

Flame visualization was effective for both fuels, as shown in Figure 7-13. However, the flames looked more interesting for natural gas (Figure 7-13 A)), where more post-coal bed combustion is observed. The hydrogen fire had lower post-coal combustion than the one for NG (Figure 7-13 B). However, a stronger glow was observed pre coal bed, looking similar to the reference fire LB1 for NG.



**Figure 7-13:** LB2 15mbar . a) Natural gas; b) Hydrogen

**Table 7-8:** Steady-state results for LB2 with all coals tested for NG and H<sub>2</sub>

Fuel	CO (ppm)	CO <sub>2</sub> (%)	O <sub>2</sub> (%)	NO <sub>x</sub> (ppm)	Converted NO <sub>x</sub> (mg/kWh)
NG	31	5.46	11.3	35.4	135.6
H <sub>2</sub>	n/a	n/a	14.0	60	320

The test results for LB2 are shown in Table 7-8: Steady-state results for LB2 with all coals tested for NG and HTable 7-8, where higher  $\text{NO}_x$  values than the reference fire were obtained for NG, and excessively high levels were obtained for hydrogen.

#### **Configuration LB5 NG**

LB5 featuring 0.3mm slots was tested for natural gas, obtaining for 20mbar a blue flame impinging on the decorative coals as shown in Figure 7-14. The measured temperature was 365°C for a thermal efficiency of 66%.



**Figure 7-14:** Glass fronted fire LB5 all coals NG 20mbar

#### **Configuration LB5 H<sub>2</sub>**

The hydrogen test was carried out at 3mbar since blow off was observed at higher powers. The results showed a visible orange flame impinging and coming out the ceramics as illustrated in Figure 7-15.



**Figure 7-15:** Glass fronted fire LB5 all coals H<sub>2</sub> 3mbar

A temperature of 374°C and 31ppm of NO<sub>x</sub> were obtained at the steady state.

#### **Configuration LB13 NG**

Design LB13, featuring 0.1mm slots, was next tested for NG. Some preliminary tests were undertaken using a layer of woven metal known as Fecralloy®. The material was placed on the fuel injectors to study the flame visualization. A visible turbulent flame was observed generated by the reduced momentum of the fuel. However, high soot levels were produced for the tests, so the material was not considered for other geometries.

The fire for natural gas at 20mbar is shown in Figure 7-16, featuring blue flames on the decorative coals but a significantly dimmed orange flame. Unfortunately, the emissions could not be recorded since they were off the scale in the analyser.

When the fuel was turned down to 5mbar an intense flame was observed impinging in the fire ceiling, as shown in Figure 7-17.



**Figure 7-16:** Glass fronted fire LB13 natural gas 20mbar



**Figure 7-17:** Glass fronted fire LB13 natural gas 5mbar

The emissions at a steady state for this last condition were:

Flue gas temperature 385°C, 300ppm CO, 1% CO<sub>2</sub>, 1ppm NO, 19.2% O<sub>2</sub>

#### **Configuration LB13 H<sub>2</sub>**

A series of tests were carried out for LB13 using hydrogen. The most relevant condition was at seven mbar, which showed a stable yellow flame after impingement on decorative coals, as illustrated in Figure 7-18.



**Figure 7-18:** Glass fronted fire LB13 H<sub>2</sub> 6mbar

The measured flue temperature and NO<sub>x</sub> vs the test duration are shown in Figure 7-19, where the peak temperature was 320°C four minutes after ignition. The NO<sub>x</sub> did not reach its steady-state after 15 minutes of the continuous test.

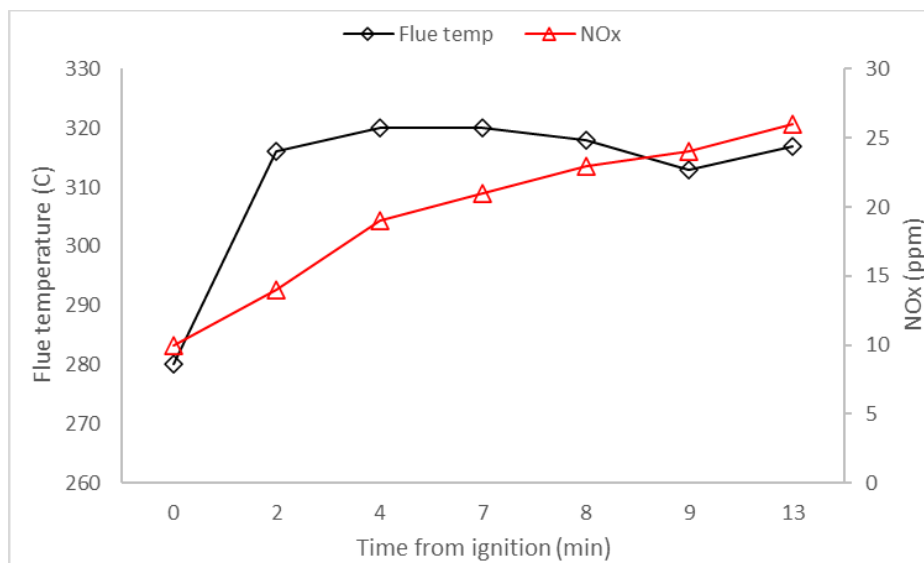


**Figure 7-19:** Temperature and NO<sub>x</sub> vs test duration for LB13 with H<sub>2</sub> 7mbar

Tests at higher pressures (10 and 12 mbar) showed excessive post-coal combustion and intense flames. In contrast, tests at lower pressures (5 mbar) did not show flame at all. The last test was carried out at six mbar once the fire was fully heated to obtain the steady-state values. A temperature of 482°C and 46ppm of NO<sub>x</sub> were recorded after roughly 20 minutes of constant operation.

A doubt arose while doing the experiments where one of the operators observed that LB5 slots looked slightly thinner than the ones featured by LB13.

This hypothesis led to a separate study to measure the slots for some configurations.

The study was carried out using the Alicona infinite focus measuring device from the Metrology lab at the University of Leeds to study the manufacturing error for the slot-shaped fuel holes. Only LB6 and LB15 were measured. The instrument measured the width and length of the plate slots, as shown in Figure 7-20, and the results were compared with the design dimensions, as shown in Figure 7-21. This study was critical since it detected a critical manufacturing inaccuracy for the experiments carried out. There was a considerable over fuelling for the designs with 0.1 and 0.2 slot widths; the injection area was in some cases double the size of the design. This problem with the slots is explained in detail in Appendix H.1.1.

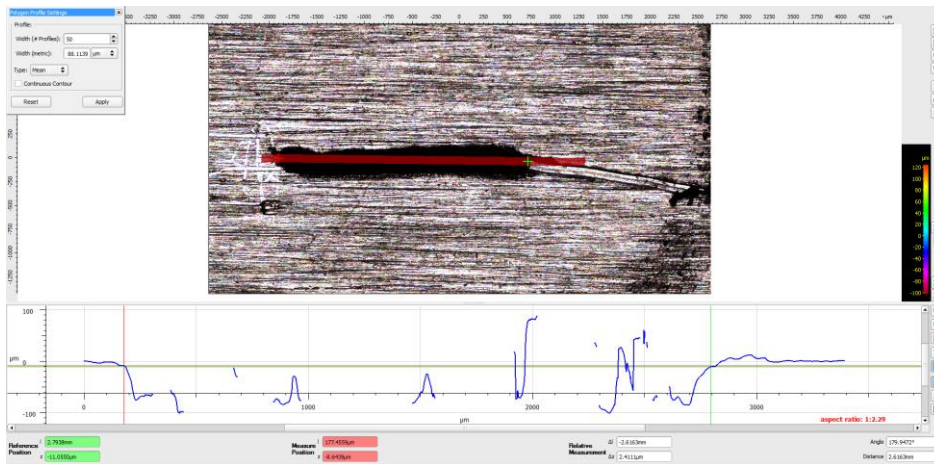


**Figure 7-20:** Measurement of burner plate LB5 slot using Alicona infinite focus

SLOT # (LHS)	LB15						LB6					
	Actual			Planned			ACTUAL			Planned		
	L mm	W mm	AREA mm <sup>2</sup>	L mm	W mm	AREA mm <sup>2</sup>	L mm	W mm	AREA mm <sup>2</sup>	L mm	W mm	AREA mm <sup>2</sup>
1	2.50	0.27	0.68	2.30	0.20	0.46	1.74	0.27	0.47	1.53	0.30	0.46
2	2.62	0.27	0.69	2.30	0.20	0.46	1.90	0.28	0.53	1.53	0.30	0.46
3	2.50	0.29	0.74	2.30	0.20	0.46	1.77	0.28	0.50	1.53	0.30	0.46
4	2.60	0.29	0.76	2.30	0.20	0.46	1.93	0.29	0.55	1.53	0.30	0.46
5	2.50	0.31	0.77	2.30	0.20	0.46	1.80	0.28	0.50	1.53	0.30	0.46
	Total		3.6435			2.3			2.559			2.295
			<b>58.4% BIGGER</b>						<b>11.5% BIGGER</b>			

**Figure 7-21:** Comparison of measured dimensions obtained with Alicona infinite focus device vs the designed dimensions for LB15 and LB6.

### Configuration LB17 NG

New burner plates were built by Clean Burner Systems (CBS) using a laser cutter, allowing up to 0.1mm slots with higher accuracy than the other plates.

The geometry LB17 was studied for different coal configurations to investigate the effect of these ceramics on the NO<sub>x</sub> and flame appearance. The tests with no ceramics were called LB17-FRONT-NC. The test with the default bottom ceramic was called LB17-FRONT-BC-D. The term “default” was used for the bottom ceramic as some other configurations were previously studied for a hole in the bottom face of the ceramics to study the influence on NO<sub>x</sub> and flame visualization. It is not intended to show the results with the modified ceramics in this thesis. In all the presented tests for LB17, the coals were placed in the front position; this means the injection burner plate was in the front position, as shown in Chapter 3 Figure 3-31. The tests featuring all the ceramics were termed LB17-FRONT-ALLC-D.

LB17 produced long and attractive flames, slightly flickering with the draft or air at full power. A flame at the right of the fire was tilting outwards, as shown in Figure 7-22 b), perhaps due to bottom coal misalignment. However, the fire still produced nice-looking flames with a well-developed post-coal burning at half power.



**Figure 7-22:** LB17-FRONT-ALLC-D-NG; a) 10 mbar, b) 20 mbar

The emissions for natural gas at full power were: NO<sub>x</sub> 48.5 mg/kWh, CO 188 ppm, O<sub>2</sub> 7.75%.

### **LB17 H<sub>2</sub>**

The cross-light ignition was considerably quieter for this fire than a traditional gas fire ignition. The pilot light time was 15-17 seconds, close to the 20 seconds time limit. This delay was due to the inclusion of a resistor in series to the thermocouple used for the igniter setup, which reduced the thermocouple cut off time for safety reasons.

Flames photographs for LB17 are shown in Figure 7-23, where Figure 7-23 b) shows still a visible, attractive flame with the laboratory lights on.



**Figure 7-23:** Glass fronted fire LB17 H<sub>2</sub> full power (3.4kW): a) lights off, b) lights on

Both images observe an intense glow below the top layer of coals. Figure 7-24 shows the flame appearance for 3.4kW where most of the burning occurs under the coals



**Figure 7-24:** Glass fronted fire LB17 H<sub>2</sub> half power (3.4kW)

Steady-state emissions for LB17 for H<sub>2</sub> at full power (3.36kW) were: NO<sub>x</sub> 305 mg/kWh, O<sub>2</sub> 14.7%. The corrected NO<sub>x</sub> emissions were far beyond the 130 mg/kWh requirement.

Figure 7-25 compares the NO<sub>x</sub> emissions for LB17 for different coal configurations. Where a considerable increase of NO<sub>x</sub> can be seen for LB17-FRONT-NC. Figure 7-26 shows the NO<sub>x</sub> levels for LB17-FRONT-BC-D and LB17-FRONT-ALLC-D for hydrogen compared to the same configurations for NG.

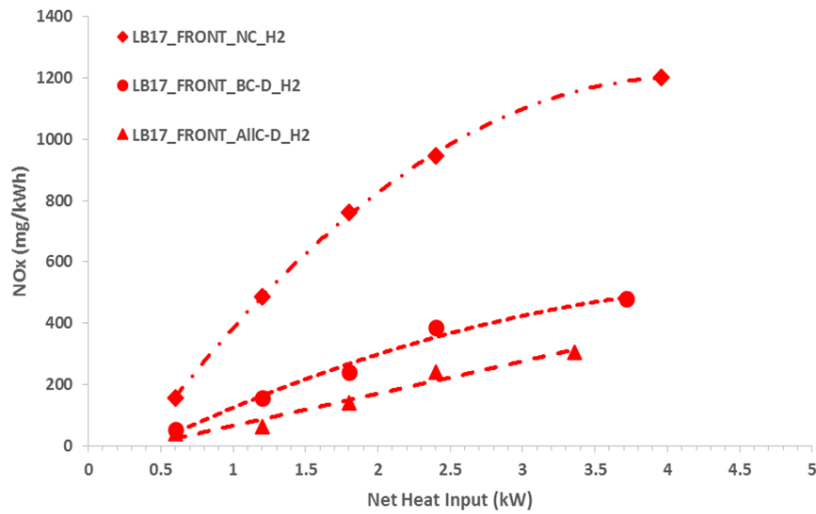


**Figure 7-25:** LB17 burner performance on hydrogen for different coal config.

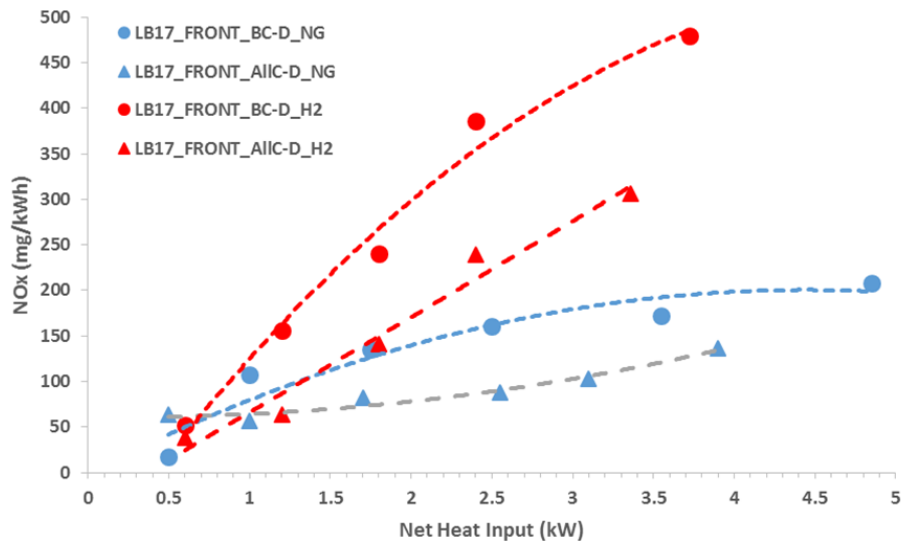


**Figure 7-26:** LB17 burner performance NO<sub>x</sub> for H<sub>2</sub> and NG

While the LB17 burner configuration, with all the default Evora ceramics, showed the most nice-looking flames of all the investigated designs, the emissions did not meet the required NO<sub>x</sub> levels below 130 mg/kWh. However, the inclusion of coals considerably improved NO<sub>x</sub> production, helping with flame stabilization.

The configuration with all coals present gave attractive post-coal flames for both fires. Although, for hydrogen, the flame was comparable to the one obtained with the reference fire. Natural gas flames appeared visible for all the heat inputs. For the hydrogen test at low power, the flames developed below the ceramic bed with only some flickering flamelets coming out of the ceramics.

## **7.4 Innovative Fire**

### **7.4.1 Numerical analysis for innovative fire**

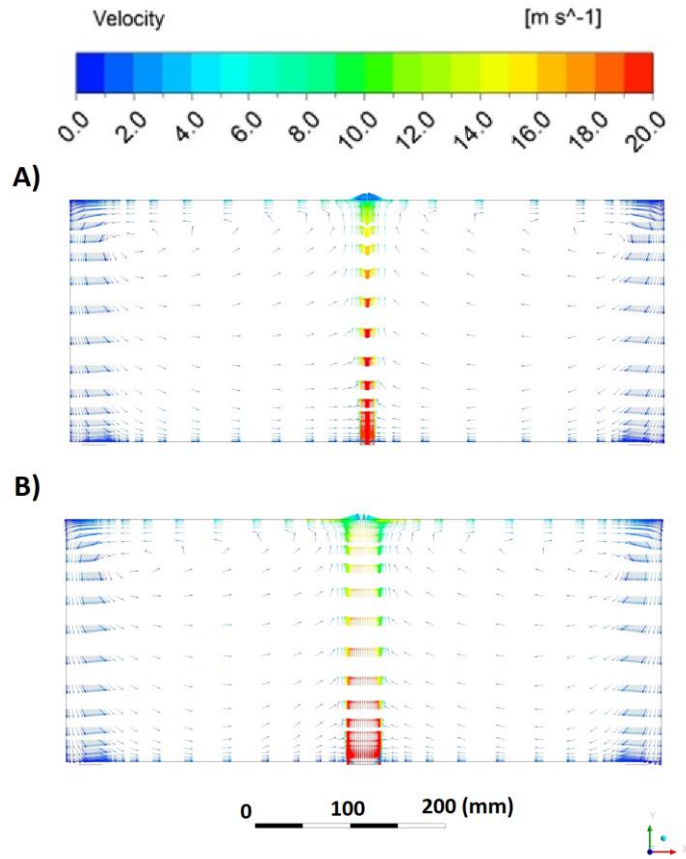
The numerical analysis results carried out for the innovative fire are now presented. This study was undertaken to compare the combustion obtained for a single round hole of the original prototype of the fire compared to a slot-shape hole. No coals were modelled during this study as the aim was to also compare the flame length and mixing characteristics for both injections.

Velocity vectors for the round hole and slot-shaped hole geometries are shown in Figure 7-27. A maximum velocity of 20 m/s was achieved for both geometries, and impingement can be observed at the top of the firebox ceiling. However, the slot-shaped hole model showed a slower injection jet which seemed to be affected by the recirculating flow inside the firebox. In contrast, the round hole geometry showed a more intense impingement in the firebox ceiling producing a higher turbulence kinetic energy at that zone, as shown in Figure 7-28, where the energy produced by the slot has a larger high turbulence zone near the firebox ceiling. The recirculation zones surrounding the hole and slot allowed in the fuel/air mixing.

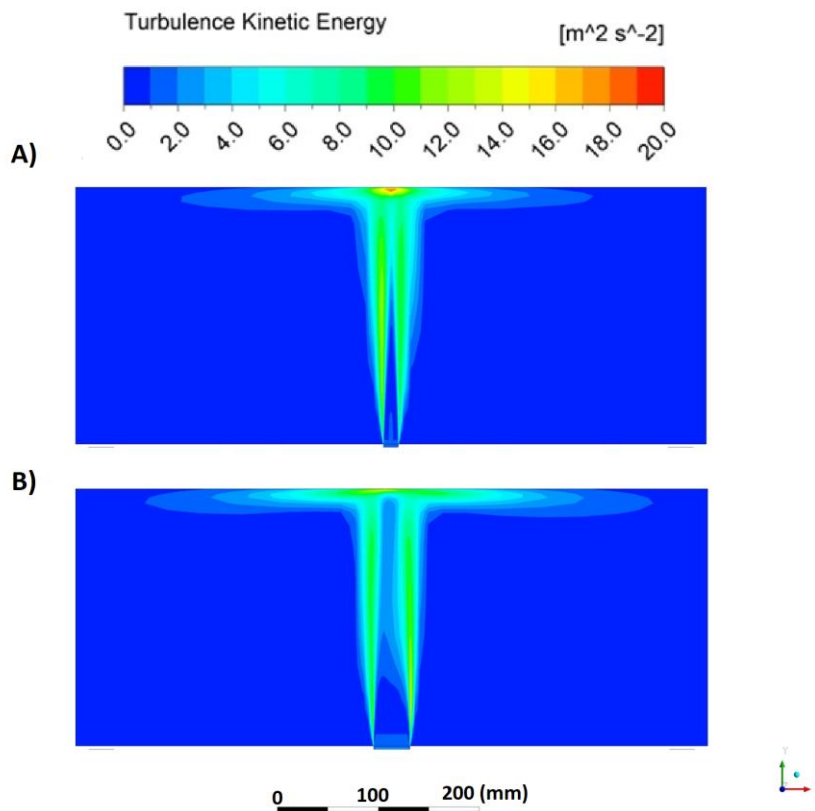
A considerable influence on the mixing quality was observed for the slot-shaped hole, as shown in Figure 7-29. Where the desired equivalence ratio was achieved first, in contrast to the high-velocity jet for the round hole. This was because the 0.3mm fuel layer got entrained by the surrounding air faster than the 3.5mm diameter hole.

Figure 7-30 shows the temperature distribution for both cases where both achieved the adiabatic flame temperature of 1700K. However, the peak flame temperature was achieved faster by the slot-shaped geometry. Showing that faster mixing influences in faster heat release as shown by the simulations of GM1 in Chapter 6.

A faster mixing and a prompt peak temperature, aided the NO<sub>x</sub> production levels, where the slot-shaped hole obtained lower NO<sub>x</sub> than the round hole as shown in Figure 7-31.



**Figure 7-27:** Velocity contours for A) Round hole; B) Slot-shaped hole for numerical analysis of Innovative fire prototype



**Figure 7-28:** Turbulence kinetic energy contours for A) Round hole; B) Slot-shaped hole for numerical analysis of Innovative fire prototype

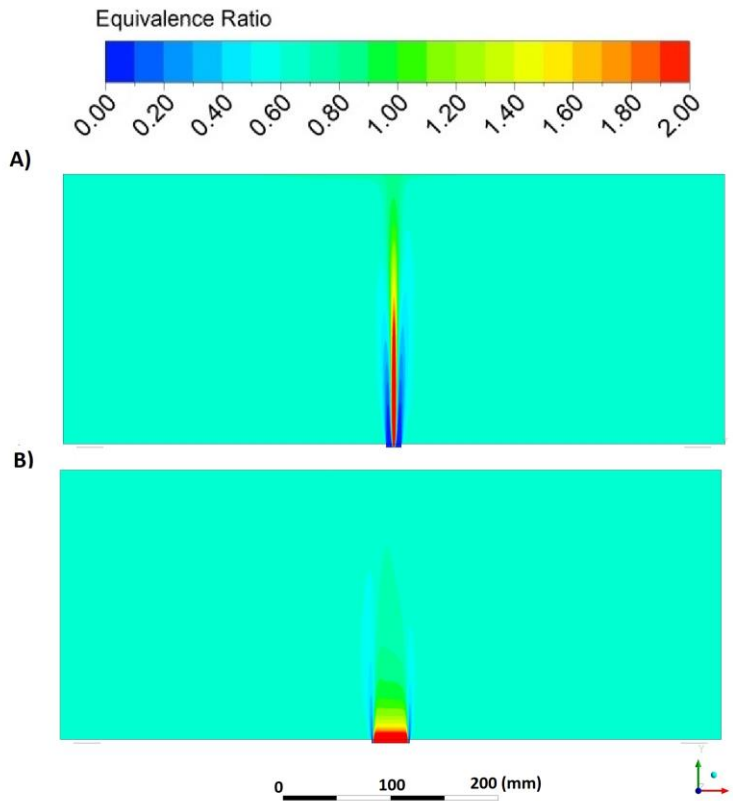


**Figure 7-29:** Equivalence ratio contours for A) Round hole; B) Slot-shaped hole for numerical analysis of Innovative fire prototype

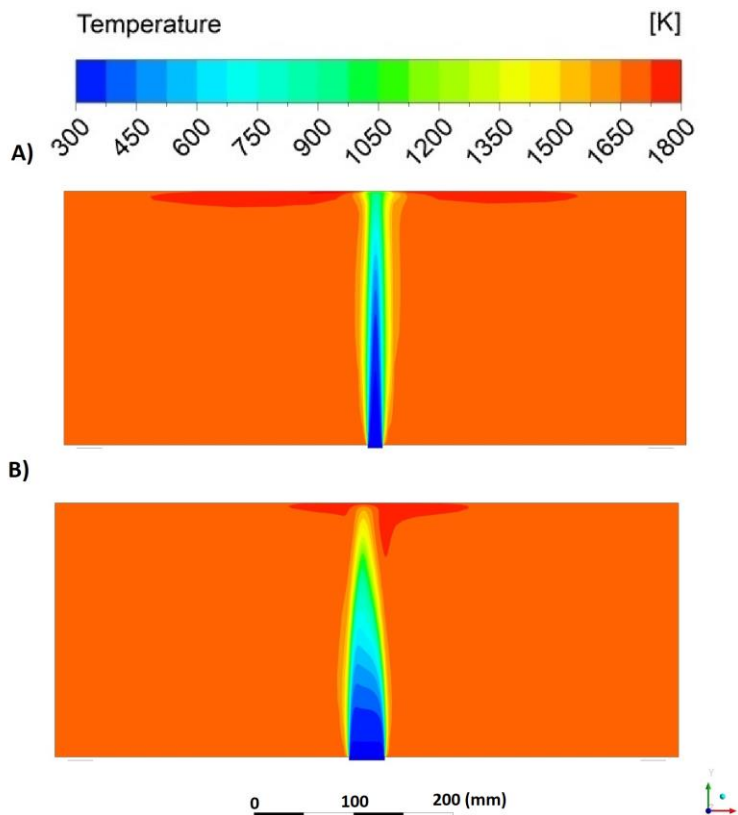


**Figure 7-30:** Temperature contours for A) Round hole; B) Slot-shaped hole for numerical analysis of Innovative fire prototype

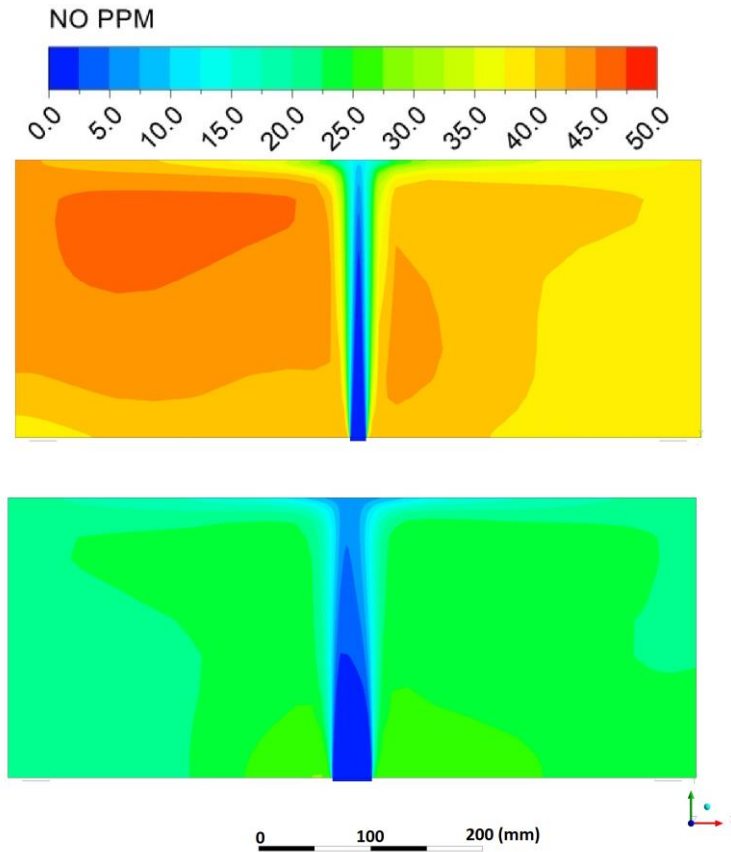


**Figure 7-31:** NO<sub>x</sub> contours for A) Round hole; B) Slot-shaped hole for numerical analysis of Innovative fire prototype

This analysis showed that slot-shaped holes would produce better NO<sub>x</sub> levels than round holes in a domestic fire. This hypothesis was validated with the experiments undertaken for the three domestic fires.

The feather like flame shown in Figure 7-30 can be compared with the flame shape obtained with no coals for LB5 for the open fire as shown in Figure 7-32, which was later used for the dual burner in the innovative fire. All the flames obtained for the different fires considering slots had the same shape as the one obtained by simulation.



**Figure 7-32.** Flame shape comparison for NG. A) Experiment; B) Simulation

## 7.4.2 Experimental tests for innovative fire

### Design 1 H<sub>2</sub> (firebox 300mm tall)

A design made of two burners in series, featuring the glass-fronted fire slot-shaped holes burners LB4 and LB5 was first tested. The 2mbar six-slot burner LB5 was positioned on the LHS of the box, while LB4 featuring six slots for an operating pressure of 20 mbar, was located at the RHS. The slot dimensions are mentioned in 6.3. As mentioned in Chapter 3, only the Legend back ceramic coal was used in these tests. This design featured the 300mm tall box shown in 3.3.4

Given the combination of 20 and 2 mbar burners, a total hydrogen mass flow rate of roughly 15 mbar was produced, giving the flame shown in Figure 7-33.



**Figure 7-33:** Flame for Innovative fire using LB4 (LHS) and LB5 (RH) 15 mbar, H<sub>2</sub>

This configuration produced aesthetically pleasing flames flickering thanks to the turbulent environment inside the fire. Additionally, LB5 flames reached the fire ceiling deflecting towards the sides creating exciting patterns. As an additional fact, the heat input of this fire was intense to the point that it was difficult to stay in front of the fire for extended periods. However, the user's touchable surface temperatures remained within the required limits.

Steady-state emissions for this configuration are shown in Table 7-9, where lower NO<sub>x</sub> values than the requirement were obtained. These values were lower than those obtained with the glass-fronted fire LB17 at 20 mbar.

**Table 7-9:** Steady-state emissions for Innovative fire featuring LB4 and LB5 burners. 15.6 mbar H<sub>2</sub>

<b>Innovative (LB4 and LB5)</b>	
NO <sub>x</sub> (ppm)	18.4
NO <sub>x</sub> (mg/kWh)	119
O <sub>2</sub> (%)	15.2
Pressure (mbar)	15.6
Mass Flow Rate (g/s)	0.08
Net Heat input (kW)	9.6

#### **7.4.2.1 M4 Design for a more attractive flame (fire box 150mm tall)**

The innovative fire with burners LB4 and LB5 was studied for another fire configuration to achieve a better-looking flame. However, the tests were only carried out for hydrogen.

Table 7-10 shows the different tests undertaken for this study. This table will now be explained fully.

B1 and B2 are designs 2 and 3 in Appendix J.1.2. C1 was a ceramic design with an equal hole size of 150mm high ceramic with a face inclination angle of 55° and featuring the air holes at the bottom. C2 was a ceramic design with an equal hole size of 150mm ceramic with a face angle of 65° and air holes at the bottom C3 was a ceramic design of 150mm ceramic with a 65° face angle in which the air hole size was proportional to the fuel hole adding 25% area to enhance IEGR and distance to the fuel hole varied. This configuration had a smile-like shape to obtain the same flame shape

Some tests were undertaken considering no ceramics. The burner performance was obtained by the ceramic impact over the flame appearance and emissions.

The ceramic air jet direction was arranged to flow downwards (down) or upwards (up). The ceramic also featured the air jets near the fuel jets (low) or at the ceiling level (high). The metering duct height of the burner air inlet was also modified to 17, 8, 5, 3, 2 and 1.2mm and this distance was set using metal shims in the gap. This is referred to as the air gap in Table 7-10.

The distance from the ceramics edge relative to the fuel holes centreline was referred to as the fuel gap and was studied from 4 – 20mm, where the optimum distance was found to be 9mm.

An assessment of the flame picture was carried out based on the height of the three flames at the centre of the fire. VS stands for “very short” where the flame did not pass the low air injection holes, about 50mm flame height. S stands for “short”, where the flame reached 50 – 100mm. M stands for “medium”, where the flame height was about 100mm but could not reach the ceiling. Finally, L stands for “long”, where the flame impinged the 150mm ceiling for the central jets.

The colour of the three over-fuelled jets were also studied where: O stands for Orange, R for red, Y for yellow, B for blue and N for none uniform, with some fuel jets not visible.

A fundamental problem in the results was that the flame was not uniform in colour or height across the 11 jets due to the intended variation of the fuel quantity per jet.

The fire shutdown time at 20 mbar steady state was also studied for each test.

A red X means that the test failed because that parameter could not meet the requirements. For example, the NO<sub>x</sub> requirement for acceptability was set at 90 mg/kWh, so there was a margin of safety in meeting the regulation, which included any differences in gas sampling procedures and gas analysis calibration.

The shutdown time requirement was set as 50 seconds. The tests marked in red were candidate designs.

The flame with the best appearance was obtained in test 31, as shown in Figure 7-34, where high yellow symmetric flames can be observed. Also, this test showed the best thermal efficiency in Table 7-10. There was no evidence of thermal damage in the reverse flow flue outlets at the base of the fire or any distortion of the heat exchanger wall where the incoming air was heated.

**Table 7-10:** Tests developed for the Innovative fire to improve the visual effect

Test No.	Burner	Ceramic	Air jet direction	Ceramic Airhole Position	Air Gap mm	Fuel Gap mm	NO <sub>x</sub> mg/kWh 0% O <sub>2</sub>	Thermal Eff. %	Shut down time secs,	Flame picture
1	B1	C1	Up	Low	Large	10	160 X	ND	33	R, S X
2	B1	C1	Up	Low	Large	10	94 X	ND	38	R, S X
3	B2	None	NA	NA	17	NA	109 X	61	34	O, N X
4	B2	None	NA	NA	7	NA	50	71	30	O, N X
5	B2	None	NA	NA	3	NA	12	80	20	O, N X

6	B2	None	NA	NA	1.2	NA	25	81	ND	N	<b>X</b>	
7	B2	None	<b>NA</b>	NA	2	NA	8	83	11	O,L,N	<b>X</b>	
<b>8</b>	<b>B2</b>	<b>C1</b>	<b>Up</b>	<b>Low</b>	<b>7</b>	<b>9</b>	<b>42</b>	<b>79</b>	<b>43</b>	<b>R, M, X?</b>		
9	B2	C1	Up	Low	17	20	4ppm*	ND	50	<b>X</b>	R, L	
10	B2	C1	Up	Low	17	1	0.8ppm*	ND	55	<b>X</b>	R, M, <b>X</b>	
11	B2	C1	UP	Low	3	9	0.5ppm*	ND	57	<b>X</b>	O VS <b>X</b>	
12	B2	C1	Up	Low	8	9	0.2ppm*	ND	43		O, N, <b>X</b>	
13	B2	C2	Up	Low	8	9	1.1 ppm	ND	65	<b>X</b>	O S N <b>X</b>	
14	B2	C2	Up	Low	8	20	6 ppm	<b>X</b>	ND	122	<b>X</b>	O M
15	B2	C2	Up	Low	5	9	15 mg	ND	129	<b>X</b>	O, S <b>X</b>	
16	B2	C1 -55°	Down	High	5	9	7 mg	ND	75	<b>X</b>	L O N	
17	B2	C1 Vertical	Down	High	5	4	13.5	80	108	<b>X</b>	L O N	
18	B2	C1 +55°	Down	High	5	9	30	82	57	<b>X</b>	YMN <b>X</b>	
<b>19</b>	<b>B2</b>	<b>C1 Vertical</b>	<b>Down</b>	<b>High</b>	<b>3</b>	<b>10</b>	<b>64</b>	<b>80</b>	<b>54</b>	<b>X</b>	<b>R L</b>	
20	B2	C1 Vertical	Down	High	3	5	7	78	60	<b>X</b>	O L N	
21	B2	C2 + 65°	Up	Low	3	20	11	ND	66	<b>X</b>	OM <b>NX</b>	
22	B2	C2 + 65°	Up	Low	17	20	195	<b>X</b>	ND	58	<b>X</b>	O VS <b>X</b>
23	B2	C2 + 65°	Up	Low	8	20	98	<b>X</b>	ND	63	<b>X</b>	O VS <b>X</b>
24	B2	C2 + 65°	Up	Low	3	9	39	ND	57	<b>X</b>	O VS <b>X</b>	
25	B2	C2 + 65°	Up	Low	5	9	43	ND	75	<b>X</b>	OVS <b>NX</b>	
26	B2	C2 + 65°	Up	Low	5	7	20	84	105	<b>X</b>	O M	
<b>27</b>	<b>B2</b>	<b>C1 + 65°</b>	<b>Down</b>	<b>High</b>	<b>5</b>	<b>9</b>	<b>60</b>	<b>78</b>	<b>50</b>		<b>O M</b>	
28	B2	C2 + 65°	Up	Low	5	9	111	<b>X</b>	80	55	<b>X</b>	OVS <b>NX</b>
29	B2	C2 Vertical	Up	High	5	10	76	ND	19		O L N <b>X</b>	
<b>30</b>	<b>B2</b>	<b>C2Vertical</b>	<b>Up</b>	<b>High</b>	<b>5</b>	<b>7</b>	<b>41</b>	<b>ND</b>	<b>20</b>		<b>Y/RL</b>	
<b>31</b>	<b>B2</b>	<b>C3Vertical</b>	<b>Up</b>	<b>High</b>	<b>5</b>	<b>7</b>	<b>66</b>	<b>93</b>	<b>17</b>		<b>Y/RL</b>	
33	B2	C3 V	Up	High	5	7	65	85	27		Y/RL	
<b>34</b>	<b>B2</b>	<b>C3 V</b>	<b>Up</b>	<b>High</b>	<b>5</b>	<b>7</b>	<b>75</b>		<b>22</b>		<b>O L</b>	
35	B2	C3 V	Up	High	3	7	75	82	ND		Y/RN	
36	B2	C3 V	Up	High	8	7	111	<b>X</b>	78	16	Y/O	
37	B2	C3 V centre 2 air holes blocked	Up	High	5	7	91	<b>X</b>	74	22 22	Y/O L N <b>X</b>	

The fire was investigated at various supply pressures going from 20 mbar to 50 mbar and closing the fuel valve down to 5mbar and a final test at 20mbar was undertaken. This, in order to study the NO<sub>x</sub> levels at the different powers. Even though the domestic gas supply is 20mbar the gas delivery in the experimental facility allowed up to 50mbar pressure delivery

The NO<sub>x</sub> levels for the different tested pressures during the test are shown in Figure 7-35, showing the peak at 30 mbar and very good levels were achieved at 20 mbar. This study showed a NO<sub>x</sub> increase as the fire heated up. The trend obtained at 20mbar at the beginning of the test was again obtained after an

hour of continuous operation. The test at 50mbar pressure loss showed the lowest NO<sub>x</sub>. However, this was an unrealistic condition for a domestic fire showing very turbulent and loud flames.

Figure 7-36 shows the gross thermal efficiency obtained at the various pressures. As observed on this graph the efficiency decreased as the supply pressure got reduced. The higher efficiency was obtained for 30mbar, again the domestic supply pressure for domestic appliances is 20mbar and this test was undertaken to study the combustion behaviour at higher pressures. The first test at 20mbar showed an overall thermal efficiency of 97% compared to the 93% after an hour of operation, this change was related to the cold condition of the fire at start-up. However, this is one of the best thermal efficiencies on the market and would make this fire a technology leader.

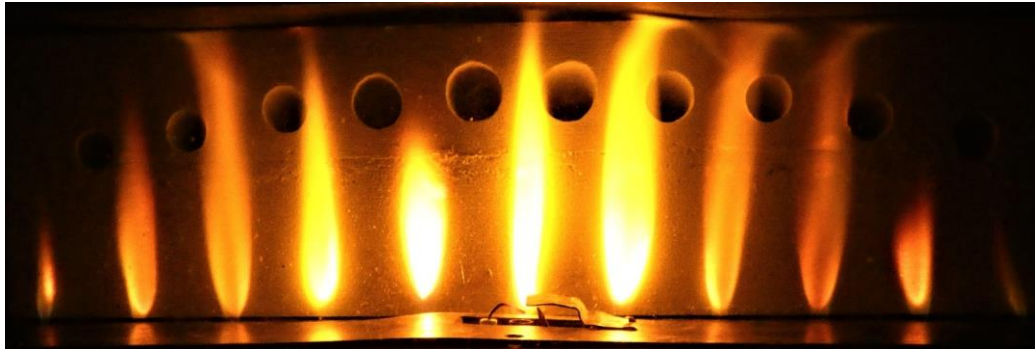


**Figure 7-34:** Test 31 Innovative fire appearance study 20 mbar

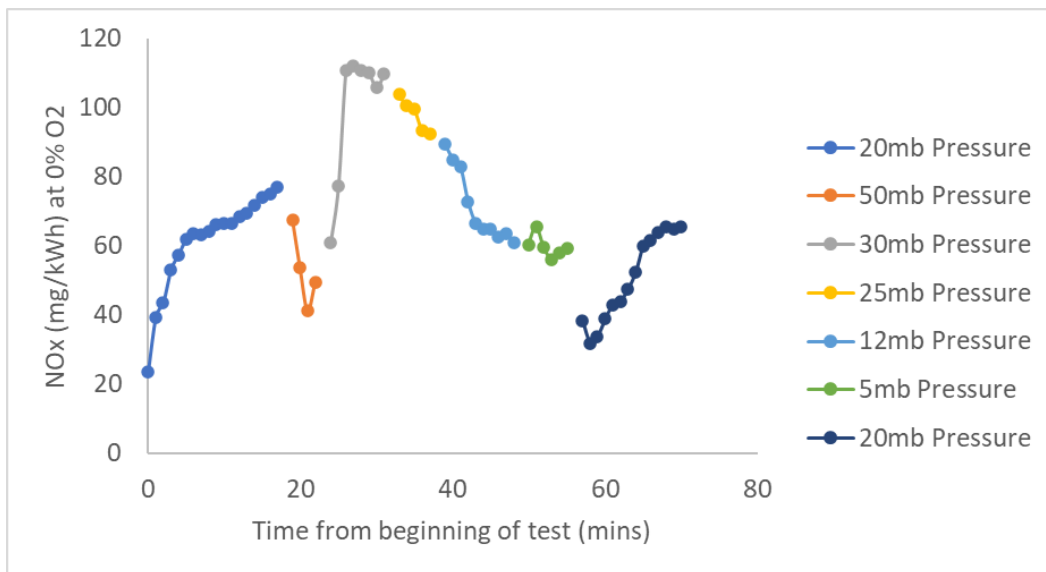


**Figure 7-35:** NO<sub>x</sub> emissions vs test duration for M6 Innovative fire test 31

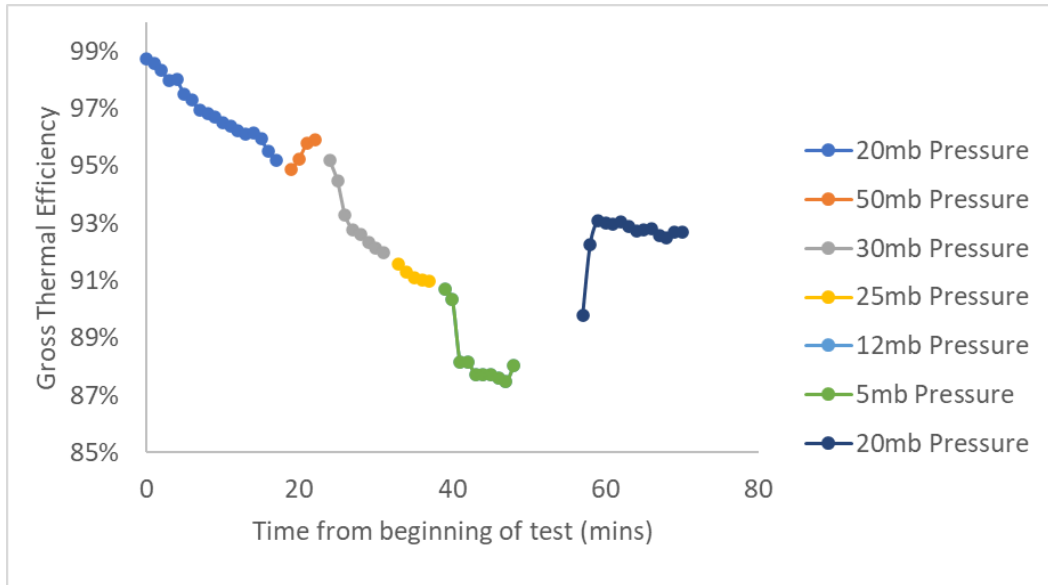


**Figure 7-36:** Thermal efficiency vs test duration for M6 Innovative fire test 31

By April 2022, the manufacturers released the innovative commercial design in Figure 7-37, where a central high flame can be observed and symmetric flames at the RHS and LHS. Unfortunately, this latest fire obtained higher  $\text{NO}_x$  than the one presented in Figure 7-34, and it could not pass the regulation.

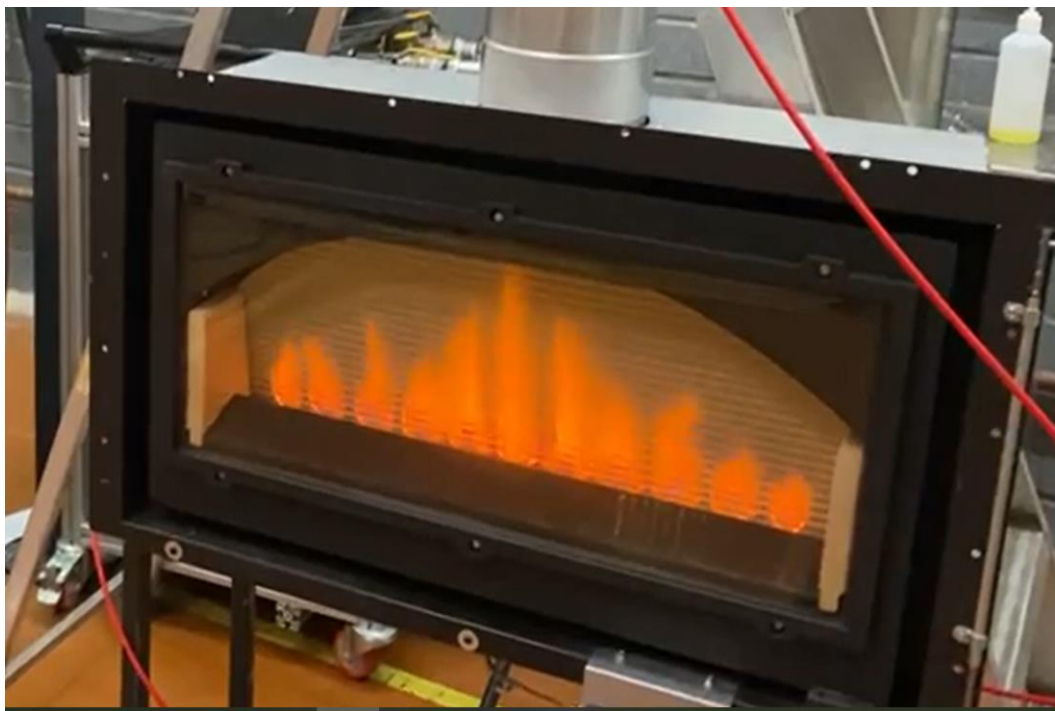


**Figure 7-37.** Final commercial design for the Innovative fire

## 7.5 Conclusions

The lowest NO<sub>x</sub> values for the single-stage injection for the open-fronted fire were obtained for FPB2 with 50.2 mg/kWh for a hydrogen flame. However, the best-looking flame was achieved with FPB3 showing 93.8 mg/kWh NO<sub>x</sub> levels.

A two-stage injection was studied for the geometry FPB3, which showed lower NO<sub>x</sub> levels than the reference fire, even at 22 mbar (116 mg/kWh for a hydrogen flame). In addition, a more exciting fire was observed than the single-stage injection. However, after several tests, the secondary injection pipes showed deterioration, making the configuration unsafe for commercialization.

The glass-fronted fire showed the most attractive flame with LB17 for hydrogen. However, the NO<sub>x</sub> was much higher than the reference fire (330 mg/kWh). In later tests developed in 2022, the NO<sub>x</sub> problem was solved, allowing this fire to pass the milestones.

The initial design of the Innovative fire proposed by the author of this thesis showed a triple jacket for IEGR and cooling purposes. However, the manufacturers did not approve this design, and a later model was investigated.

The numerical study undertaken before the experiments for the innovative fire to evaluate the combustion performance for a fuel injection featuring a round hole or a slot-shaped hole showed that the slot-shaped hole achieved lower NO<sub>x</sub>, and this was validated with the different experiments for the three fires

The burners used in the open-fronted fires LB4 and LB5 were tested for one of the designs of the innovative fire featuring a letterbox showing mesmerizing flames for hydrogen and lower NO<sub>x</sub> than the reference values (113 mg/kWh).

A final design using a single burner and a shorted firebox was investigated to improve the flame appearance, which reduced the NO<sub>x</sub> levels to 66 mg/kWh and the flame appearance satisfied the government requirements.

By 2022 this fire was developed in a design attractive to the public and passed the pollutants milestones.

The slot width showed to have a strong influence on the visibility and colour of the flame for the Innovative fire. The 0.1mm slots had poor flame visibility as they mixed too fast. On the other hand, the 0.3mm slots showed attractive, visible deep orange/yellow.

## Chapter 8. CONCLUSIONS AND FUTURE WORK

### 8.1 Equilibrium Flame Temperature and Composition

1. Equilibrium computations are helpful in computing burner operating conditions to achieve a desired flue gas composition and flame temperature. In fuel switching from NG to hydrogen or biofuels, the burner operating conditions can be determined on alternative fuels to achieve the equivalent performance on NG. For near stoichiometric combustion, the ability to fix the adiabatic composition and then cool this to predict the change in the composition of that mixture at a lower temperature is an essential capability of equilibrium codes. This was applied in the present work to fuel switching from NG to hydrogen for ambient temperature burners for fire and boiler applications and to glass melting furnaces with very high air inlet temperatures. The experimental condition on one fuel is set by the excess oxygen on a dry basis, and this is typically about 1% dry for NG. The water vapour prediction enables the wet to dry conversion for the derived operating condition that gives close to 1% oxygen dry. This is shown in Table 8-1 for NG.

**Table 8-1.** Comparison of adiabatic and cooled flame compositions for domestic heat applications for measured oxygen of about 1%

Fuel	Cond	$\phi$	Air inlet Temp K	Flame Temp K	O <sub>2</sub> wet %	O <sub>2</sub> dry%	H <sub>2</sub> O wet%	NO ppm wet	CO <sub>2</sub> wet %	CO wet %	H <sub>2</sub> ppm
NG	Adiab	0.95	300	2195K	1.06	1.28	17.21	2658	8.84	0.50	1840
NG	Adiab	0.975	300	2215K	0.74	0.90	17.53	2319	8.85	0.69	2550
NG	Cool	0.954	300	1850K	0.84	1.19	17.67	930	9.37	0.035	163
H <sub>2</sub>	Adiab	0.875	300	2266K	1.99	2.86	30.18	4100	0	0	3600
H <sub>2</sub>	Adiab	0.850	300	2234K	2.41	3.42	29.58	4200	0	0	2700
H <sub>2</sub>	Adiab	0.825	300	2200	2.85	4.0	28.95	4300	0	0	2000
H <sub>2</sub>	Cool	0.955	300	1850K	0.74	1.11	33.32	840	0	0	328
H <sub>2</sub>	Cool	0.868	300	1850	2.25	3.25	30.76	1477	0	0	173
H <sub>2</sub>	Cool	0.822	300	1850	3.08	4.36	29.36	1734	0	0	142

When cooling flames from adiabatic temperatures, the composition does not change below 1850K, as there is no dissociation below this temperature, so the composition does not change due to re-association. Thus this is the composition

at any flue gas temperature below this and above the water condensation flue gas temperature. For glass melting furnaces, the radiation heat transfer to the furnace walls reduces the gas temperature above the glass melt to 1850K. This was also the temperature used for cooling in this application.

### **8.1.1 Ambient Temperature Burner Operation for Domestic Heat Application**

The equilibrium compositions near the optimum  $\phi$  for the adiabatic temperature and a cooled flame to 1850K are shown in Table 8-1 for NG and H<sub>2</sub> for 300K air inlet temperature. The water vapour is predicted and used to convert the oxygen from a wet to a dry basis so that experimental dry oxygen measurements can be used to find the operating conditions that gave the dry oxygen measurement.

Several conclusions result from the equilibrium predictions in Table 8-1

1. For NG cooling, the cooled flame at 1850K reduces the CO and the NO, for which the CO effect is well known, but the NO reduction on cooling has not been widely recognised in the NO<sub>x</sub> literature, as it is usually stated that once formed NO cannot be destroyed. The conclusion is that by cooling the flame zone, the lower O and OH prevent thermal NO<sub>x</sub> from being created. It is well known that heat extraction from a flame zone reduces NO<sub>x</sub> formation, and this was used in domestic fires and boilers for many years with metal or ceramic inserts into the flame zone that acted as heat sinks. In Chapter 7, the interaction between the diffusion jet flames and the ceramics reduces the NO<sub>x</sub> through cooling, which shows that these equilibrium predictions are supported by experimental results. Table 8-1 also indicates that cooling increases the oxygen and decreases the hydrogen significantly, which are both a result of re-association reactions and decreased O and OH with cooling, which is why the NO is reduced.

2. For hydrogen, the adiabatic temperature increases, and if a burner is operated without heat loss, as in a gas turbine, the burner would have to work leaner with hydrogen. However, for the cooled results to 1850K, the equilibrium NO decreases significantly as the oxygen is reduced. Another effect is the very low equilibrium hydrogen, which will be the hydrogen in the flue gases (which PAS4444 requires to be below 1000ppm on hydrogen for safety and thermal efficiency reasons). Table 8-1 shows that on NG, the cooled results are similar to those for hydrogen, so if combustion is complete (has reached

equilibrium), there should not be an equilibrium hydrogen problem in using hydrogen as the fuel.

4. Table 8-1 shows that for cooling flames to 1850K or lower, hydrogen has a similar equilibrium NO to NG for the same dry excess oxygen. This has not been previously published in the hydrogen literature, where it has been assumed that hydrogen would have to burn lean to achieve low NO<sub>x</sub>. This is exploited in the 'coal-effect' open and glass-fronted fires in Chapter 7, as locally rich burning diffusion flames, are cooled by impingement onto ceramics. Very low NO<sub>x</sub> has been demonstrated on hydrogen, lower than on NG in some designs.

### 8.1.2 Glass Furnace Prediction of the Composition of the Hot Gases above the Glass in the Float Glass Process for NG and hydrogen.

The air temperature in float glass manufacture is 1200K – 1500K using regenerative burners, and results were presented for 1500K in Chapter 4. The main impact of very high air temperatures is that the equivalence ratio range, over which dissociation is important, is wider than at 300K. As the adiabatic peak temperatures are much higher at 1500K than at 300K, the impact of cooling to 1850K, which is the furnace temperature above the glass melt on NG, is much more significant than at 300K. The NG and hydrogen results at 1500K air temperature are summarised in Table 8-2

**Table 8-2.** NG and Hydrogen composition for adiabatic and cooled (1850K) flames for NG and H<sub>2</sub> at 1500K air inlet temperature.

Fuel	Ø	Condit.	Flame Temp K	O <sub>2</sub> wet %	O <sub>2</sub> dry %	H <sub>2</sub> O %	NO ppm	CO wet	CO <sub>2</sub> wet	H <sub>2</sub> ppm
NG	1.15	Adiab	2755	0.97	1.15	15.37	6,757	5.9%	4.6%	
NG	0.95	Adiab	2719	2.36	2.75	14.12	10,166	3.7%	5.3%	
NG	0.946	Cool	1850	0.985	1.19	17.53	1,010	320ppm	9.3%	150
NG	0.976	Cool	1850	0.44	0.54	18.03	680	490ppm	9.6%	230
H <sub>2</sub>	0.70	Adiab	2716	4.50	5.73	21.60	13,852	0	0	
H <sub>2</sub>	0.95	Adiab	2831	1.80	2.39	24.50	10,000	0	0	
H <sub>2</sub>	0.697	Cool	1850	5.39	7.23	25.46	2324	0	0	93
H <sub>2</sub>	0.954	Cool	1850	0.755	1.13	33.2	850	0	0	324

The measured dry oxygen for control of a glass furnace is in the range of 0.5 – 1.5%, and under adiabatic conditions, this would be achieved at Ø = 1.15. However, for cooled furnace gases by radiation heat loss to the glass melt and the ceramic walls, at 1850K, the measured dry oxygen is 1.19% at Ø = 0.946

and 0.54 at  $\phi = 0.976$ . However, the CO at 1.19% oxygen is close to the one measured on float glass furnaces under these operating conditions. So this should be the reference condition to compare with hydrogen operation. At this condition, the cooling drops the adiabatic temperature by 869K. For the same cooling for hydrogen, the adiabatic temperature should be 2719K which is achieved at  $\phi = 0.70$  and at this cooled condition, the excess oxygen would be 7.23% dry. However, if more heat transfer occurred, operation at  $\phi = 0.95$  could be possible with 1.13% O<sub>2</sub> dry, but this would require 981K cooling. As hydrogen is likely to have less radiant heat transfer due to the absence of soot radiation, the operating condition on hydrogen would likely be  $\phi=0.7$  and 7.23% O<sub>2</sub> dry.

Table 8-2 shows, as for the results at 300K in Table 8-1 that cooling the flame drastically reduces the CO emissions on NG. Also, the NO<sub>x</sub> is drastically reduced from the adiabatic conditions to 1000ppm or less, which is a factor of 10. For H<sub>2</sub>, the cooling also reduces the NO but is above that for NG. If the hydrogen flame could be operated at  $\phi=0.95$ , substantially lower NO could be achieved.

The concern in glass melting is the influence of the increase in water vapour when operating on hydrogen. Table 8-2 shows that this is quite small in the cooled condition with 17.5% H<sub>2</sub>O on NG and 25.4 on H<sub>2</sub> for the  $\phi = 0.7$  operating condition, which is a 7.9% increase in H<sub>2</sub>O (a 45% increase). Water vapour can dissolve in molten glass to give imperfections, which is undesirable. These calculations were close to the measured water vapour (using FTIR) in a burner test rig that simulated these conditions (Glass Futures, fuel switching BEIS programme, 2022).

Table 8.2 also shows that unburned hydrogen is <1000ppm in the cooled flame, which satisfies the requirement in PAS444 for unburned hydrogen to be <1000ppm.

These predictions conclude that hydrogen is a viable fuel for glass melting, and recent experimental work by Glass Futures has shown this in high-temperature testing.

### **8.1.3 Biofuels at glass melting conditions.**

The blend for soybean/air achieved a very close temperature to that of NG at 1500K inlet air temperature with the same adiabatic flame temperature as for NG with  $T_{\text{adiab}} = 2710\text{K}$  at  $\phi=0.85$ , with an excess O<sub>2</sub> of 3.2% compared with 2.75% on NG. This makes soybean biodiesel a potential replacement for NG in glass melting furnaces.

The adiabatic predictions for crude glycerol achieved the furnace conditions for NG for an excess O<sub>2</sub> at  $\phi=0.92$  and  $T_{\text{adiab}}=2678$ . This temperature is only 40K cooler than the furnace, so this fuel could be used as an alternative for the glass melting furnaces. A blend of half glycerol/ half water was also investigated for applications in future work using a distillery waste product with 90% water content. Large amounts of water would lower flame temperatures and NO<sub>x</sub> emission than the obtained with NG making this option unusable for glass melting furnaces. The 2030 diesel ban could make diesel a viable replacement for NG glass furnaces, as use for diesel production facilities would be required in the long term. However, the presented diesel blend showed that the NG conditions could be achieved at 1.0% excess O<sub>2</sub> at  $\phi=0.94$  for a flame temperature of  $T_{\text{adiab}}=2749\text{K}$ , which is close to that of NG.

## **8.2. CFD Predictions of Grid Mix Flame Stabilisers**

### **8.2.1 Prediction of Flame Stabiliser Pressure Loss and C<sub>D</sub>**

The CFD prediction of C<sub>D</sub> and C<sub>c</sub> for the four-hole premixed grid plated showed perfect agreement using the  $k-\epsilon$  turbulence model with the experimental results. The stabiliser used for GM2 showed the best agreement using a structured tetrahedral mesh. This shows that  $k-\epsilon$  is valid for studying high turbulence flows at the high  $M = 0.047$  of this work.

### **8.2.2 CFD prediction of Propane Grid Mix combustion**

The propane/air combustion results obtained with the turbulent model realisable  $k-\epsilon$  and the combustion model steady diffusion flamelet (SDF) achieved very good agreement with the experiments obtained for the flame stabiliser featuring the injection method GM2. However, SDF could not predict the NO<sub>x</sub>. In contrast, the combustion model Flamelet generated manifold (FGM) for non-premixed combustion allowed the post-processing calculation of NO<sub>x</sub> for the flame stabilisers featuring GM2 and GM1, with a reasonable agreement with the measured values. FGM better predicted mixing and combustion efficiency than the SDF model, and this helped in the NO<sub>x</sub> prediction. NO<sub>x</sub> was also underpredicted for the stabiliser featuring the fuel injection GM1, showing that this combustion model and the NO<sub>x</sub> model in FLUENT struggle to accurately predict the high combustion intensities featured by the investigated stabilisers of 400K and  $M=0.047$  for a heat release of 28 kW/m<sup>2</sup>bar. This high combustion intensity has never been modelled for gas turbines using CFD.

### **8.2.3 Prediction of the importance of fuel injection location on fuel and air mixing in Grid Mix burners**

For the study of the three fuel injection methods, GM1, GM2 and GM3, for the same flame stabiliser and same boundary conditions, GM1 showed better mixing than GM2 and much better than GM3 replicating the FLOX concept for GM. GM2 featured slightly lower NO<sub>x</sub> than GM1.

GM1 was investigated for its use on hydrogen using the optimised CFD model.

The NO<sub>x</sub> emissions were relatively high, and a method to reduce the NO<sub>x</sub>, first used by York et al. [26], [27], was extending the length of the air tube in the grid mix design. The extension of the air tube had a stabiliser thickness of 7D to allow the whole fuel to thoroughly mix before coming out of the stabiliser plate. This 7D stabiliser thickness was predicted to achieve 2 ppm NO<sub>x</sub>, lower than the 6ppm numerically predicted for the thinner plate of 16.2 ppm and for the 5mm obtained with propane.

The potential factors of disagreement between simulation and experiments were:

- The use of adiabatic walls when there was external flame tube radiation could have reduced the temperature of the burnt gases inside the combustor and could have influenced the NO<sub>x</sub> prediction.
- The large diameter gas sample probe could have disturbed the flow, which was not modelled in the CFD.
- The stabiliser plates showed manufacturing issues, such as a welding slope at the stabiliser inlet hole or a non-uniform annular gap for GM2, resulting in asymmetric holes.
- The turbulence, combustion and NO<sub>x</sub> models used for the simulations could have struggled with the high combustion intensity conditions and low residence times that were investigated.

### **8.2.4 Predicted mean burner exit conditions.**

The mean outlet values predicted for GM2, and GM1 for propane and hydrogen combustion were compared with the equilibria codes Gaseq and CEA, showing almost perfect agreement for the adiabatic flame temperature, equivalence ratio and product composition. This shows that equilibria software can also be a good tool to validate models and parameters used in CFD studies. The CFD predicted distance to the equilibrium conditions was the flame length.

### 8.3 Domestic Fires

The study was carried out for the Hy4Heat BEIS programme.

1. Hydrogen flames cannot be operated premixed, as for NG flames, as flashback will occur due to the higher reactivity of hydrogen. Diffusion flames have to be used, and  $\text{NO}_x$  is controlled using the interaction of the diffusion flames with ceramic 'coals' in the fires.

2. Hydrogen diffusion flames are visible, and no colourants are needed in domestic fire applications.

3. It was demonstrated that a hydrogen flame should be operated at equivalence ratios from 0.59- 0.71 for a flame temperature lower than 2000K. This would generate thermal  $\text{NO}_x$  levels for which the limit is at about 40mg/kWh, well inside the 130 mg/kWh Eco standard limit for coal effect fires. These conditions would keep the flame temperature under 2000K.

4. For the open-fronted fire, the impingement of diffusion jets on the bottom ceramic ribs gave good fuel and air mixing and generated four partially mixed flames that impinged on the outer ceramic coals, which achieved lower  $\text{NO}_x$  due to improved mixing and further heat losses. The configuration, FPB2, achieved  $\text{NO}_x$  levels of 50 mg/kWh for a hydrogen flame. However, the most interesting visual flame was obtained with FPB3, which showed a higher  $\text{NO}_x$  of 93.8 mg/kWh.

5. The first designs for all the fires used round hole fuel injectors with hydrogen. However, there was a 'pop' on startup, which was deemed unacceptable by the fire regulations. This was due to the fuel plenum being full of air when the fire was started so that when the fuel was introduced, there was an initial period of a few seconds with a flammable mixture in the fuel injection plenum. A flashback then occurred, making a popping noise. To avoid this happening, the round holes were replaced by thin flow holes with a width smaller than the quench distance of hydrogen (0.06mm). Fuel slot widths of 1, 2 and 3  $\mu\text{m}$  were used and manufactured using laser drilling. These had a further advantage as the long thin holes gave a wide flame at the base, and these made the flame more visible, especially for the Innovative fire. These thin slot holes were used in all the fires.

6. A problem with the thin slots was found as the slot fuel Reynolds number was a function of the hydraulic diameter, which is twice the slot width. For 1  $\mu\text{m}$  slots, this gave very low Re, which reduced the  $C_D$  for the holes, and this reduced the fuel flow. This was not realised until the fire went for a legislated test with a volumetric flow meter attached. The solution to this was to increase

the slot area by using 2 or  $w$   $\mu\text{m}$  slot widths of the same length, which increased the total flow area of the fuel slots. The CFD model of the slots also helped to explain the reduced fuel flow and predicted the measured reduced  $C_D$  for thin slot holes.

7. A two-stage injection burner was developed for the open fire, with half the fuel impinging on the bottom layer of ceramics and half on the top layer. This had excellent flame visibility and low  $\text{NO}_x$  emissions. However, the second layer fuel injectors glowed red hot and disintegrated and would have required high-temperature high, cost fuel injectors, and this was discarded as a high-cost solution that the low-cost fire market could not accommodate. The principle of fuel staging was kept in the final design with two rows of fuel injectors in the base of the fire so that one impinged on the lower ceramics and one row on the top layer of ceramics. The  $\text{NO}_x$  was higher but well below the standard. This fire was approved for use by the public and confirmed as meeting all the GAR regulations in Dec. 2021.

8. The glass-fronted fire featured the most attractive hydrogen flame for the burner design LB17. Unfortunately, the  $\text{NO}_x$  could not meet the legislation with  $\text{NO}_x$  at 330 mg/kWh. This fire would have been investigated with a two-stage injection as for the open fire. However, the fuel tube durability concerns for the open fire led to this design not being investigated for the glass-fronted fire. A design similar to that for the open fire was used with two rows of slot holes in the base of the fire, one impinging on the rear bottom ceramic with a 10mm impingement gap in the rear bottom ceramic. This entrained air into the gap and fed a flame out into the slot between the front and rear ceramics, at the same location as for the LB17 design but with half the fuel flow. This enabled the good flame visibility of LB17 to be retained, and with half the fuel used to impinge on the bottom ceramic with high heat losses, this reduced the  $\text{NO}_x$ . In addition, the flame visibility was enhanced by changing from a slot to a + shaped hole. This final design passed all the GAR tests and was approved for sale as a hydrogen ready fire in April 2022.

3.9 The innovative fire design had two innovative features that helped the flame visibility and reduced the  $\text{NO}_x$ . Firstly, the use of rich/lean combustion by placing the air jets at the top of the fire and the fuel jets at the bottom of the fire. Secondly, the fire was made with internal gas recirculation (IGR) by having the fire compartment outlet in the front of the side walls. This reverse flow meant that the diffusion flame entrained burnt gases and this IGR reduced the  $\text{NO}_x$  as no combustion occurred at 21% oxygen. Two versions of this fire were developed for the same burner: a letterbox fire with a low ceiling high and a

more standard fire with a higher ceiling and a greater distance between the fuel and air jets. The diffusion flames were placed along a nearly vertical ceramic wall to enhance the flame radiation. By changing the length of the fuel slots, the flame shape could be controlled, and an interesting curved flame was developed. This fire is currently in final development and will be sent for legislated tests in the summer of 2022.

9- The CFD study, undertaken for the innovative fire before the experiments took place, showed that slot-shaped holes achieved lower NO<sub>x</sub> levels than round holes. The successful numerical study was carried out using RANS simulation at steady-state conditions, which was also used for the combustion analysis of grid plate flame stabilisers in gas turbines. Good agreement with the experimental results was demonstrated.

10. Investigation of the NO<sub>x</sub> reduction process.

For all three fires, the diffusion flames with no ceramics in place were tested, and these always gave very high NO<sub>x</sub>. For the Innovative fire, the diffusion flames were tested with the reverse flow enclosure in place, and this reduced the NO<sub>x</sub> compared to that with free diffusion flames. The addition of the ceramics for all fires caused heat losses from the diffusion flames, and this reduced the NO<sub>x</sub> further. For the two coal effect fires, the lower and upper 'coals' were tested separately, and this showed that each layer contributed to the NO<sub>x</sub> reduction through heat losses. This is why low NO<sub>x</sub> could be achieved when high NO<sub>x</sub> was expected in hydrogen fires, which did occur with simple diffusion flames.

11. All the fires were also shown to be dual-fuel fires and could operate on NG. However, the full development of the fires on NG through to certification is for future work.

## **8.4 Future work**

### **8.4.1. Equilibrium study**

Glycerol could be investigated at various concentrations of water going from 5%-49% in order to study the effect of different H<sub>2</sub>O concentrations on the adiabatic flame temperature and product composition. This is relevant to future work on Green Distilleries, where a waste stream with 90% water and 10% flammable fluids will be used.

#### **8.4.2. Aerodynamics for grid plate flame stabilisers**

The grid mix plate flame stabilisers need to be studied with ANSYS FLUENT to compare the differences between FLUENT and CFX. Unstructured hexahedral meshes could be compared to the structured ones already designed in order to verify mesh sensitivity with the experimental results. More sophisticated computational CFD methods such as DNS or LES could be investigated to determine if a better agreement with the experimental results could be achieved.

An improved design of the welding slope at the stabiliser air hole inlet of GM2 needs to be developed to potentially improve the agreement with the experimental data.

The stabiliser plate used for GM1 needs to be studied with CFD in order to predict the experimental results obtained for a pressure loss of 4%.

#### **8.4.3 Combustion for grid plate flame stabilisers**

More work needs to be carried out to improve the agreement with the simulation and the experimental combustion results for GM2. Measured temperature profiles need to be added to the walls, and radiation models need to be revised in order to study their effect on the temperature and NO<sub>x</sub> results. This will lead to conjugate heat transfer predictions of the combustor wall temperature and the non-adiabatic features of the test facility.

More work has to be carried out for the technology GM3 in order to get a better agreement with the FLOX results, using the combustion model Flamelet Generated Manifold.

The geometry GM1 should be studied for a hydrogen flame using the original stabiliser used in the experiments featuring hole diameters of 22.11mm and a plate thickness of 5.3mm

Flame stabilisers with non-circular air holes should be investigated with CFD and compared with available experimental data at Leeds University.

#### **8.4.4 Combustion study for domestic fires on NG**

The main future work is to operate the final hydrogen design on NG and to solve any problems so that the fires can be certified for dual fuel operation. The initial work in this thesis shows that operation on NG is possible. This future work will have to determine the particulate emissions, as these are a problem with NG diffusion flames.

#### **8.4.5 The development of hydrogen process burners**

The new BEIS funding for the Green Distilleries project will involve the development of hydrogen process burners using grid type flame stabilisers. Also, we have enquires from other process industries for hydrogen burners of 30MW capacity, and the design principles in this thesis will be used.

## REFERENCES

- [1] UNFCCC (1997) Kyoto Protocol to the United Nations Framework Convention on Climate Change adopted at COP3 in Kyoto, Japan, on 11 December 1997. Japan.
- [2] S. J. Bhore, 'Paris Agreement on Climate Change: A Booster to Enable Sustainable Global Development and Beyond', *Int. J. Environ. Res. Public Health*, vol. 13, no. 11, 2016, doi: 10.3390/ijerph13111134.
- [3] J. Rockström, I. Ocko, S. Goldstein-Rose, J. C. Beard, C. Exekiel, and J. Doerr, 'Countdown at COP26', COP26, 2021. <https://blog.ted.com/jointeds-countdowncop26-three-live-streamed-events-from-november-4-6-2021/>
- [4] E. & I. S. Department for Business, 'UK energy in brief 2021', London, 2021.
- [5] IEA, 'Natural Gas-Fired Power', Paris, 2021. [Online]. Available: <https://www.iea.org/reports/natural-gas-fired-power>
- [6] Ofgem, 'Electricity generation mix by quarter and fuel source (GB)', 2021. [https://www.ofgem.gov.uk/energy-data-and-research/data-portal/all-available-charts?industry\\_sector\\_chart=1605&sort=created](https://www.ofgem.gov.uk/energy-data-and-research/data-portal/all-available-charts?industry_sector_chart=1605&sort=created)
- [7] Poyry, 'Poyry - How will intermittency change Europe's gas markets? - Point of View', 2014.
- [8] H. Government, 'UK hydrogen strategy', 2021.
- [9] E. R. Weaver, 'Formulas and graphs for representing the interchangeability of fuel gases', *J. Res. Natl. Bur. Stand.*, vol. 46, no. 3, pp. 213–245, 1951.
- [10] H. Books, 'A guide to the Gas Safety (Management) Regulations 1996', 1996.
- [11] M. Abeysekera, M. Rees, and J. Wu, 'Simulation and analysis of low pressure gas networks with decentralized fuel injection', *Energy Procedia*, vol. 61, pp. 402–406, 2014.
- [12] J. Leicher et al., 'The impact of hydrogen admixture into natural gas on residential and commercial gas appliances', *Energies*, vol. 15, no. 3, p. 777, 2022.
- [13] Y. Zhao, V. Mcdonell, and S. Samuelsen, 'Influence of hydrogen addition to pipeline natural gas on the combustion performance of a cooktop burner', *Int. J. Hydrog. Energy*, vol. 44, Apr. 2019, doi: 10.1016/j.ijhydene.2019.03.100.
- [14] H. de Vries, A. V Mokhov, and H. B. Levinsky, 'The impact of natural gas/hydrogen mixtures on the performance of end-use equipment: Interchangeability analysis for domestic appliances', *Appl. Energy*, vol. 208, pp. 1007–1019, 2017.
- [15] M. Inoue, 'Hydrogen Gas Safety Management', in *Hydrogen Energy Engineering: A Japanese Perspective*, K. Sasaki, H.-W. Li, A. Hayashi, J. Yamabe, T. Ogura, and S. M. Lyth, Eds. Tokyo: Springer Japan, 2016, pp. 385–395. doi: 10.1007/978-4-431-56042-5\_27.
- [16] M. Fukuda, K. Korematsu, and M. Sakamoto, 'On quenching distance of mixtures of methane and hydrogen with air', *Bull. JSME*, vol. 24, no. 193, pp. 1192–1197, 1981.
- [17] Y. Sato, 'Hydrogen character safety', *J Jpn Soc Saf.*, pp. 378–385, 2005.

- [18] S. Yagyu, 'Flammable limits of gas and vapor', Jpn. Soc. Saf. Eng. Tokyo, 1977.
- [19] G. Andrews and N. Ahmad, 'Counter-Rotating Axial Swirler Premixed Combustion with Low NO<sub>x</sub> Emissions at 20 MW/m<sup>2</sup>bar Combustion Intensity', presented at the Proceedings of the 10th European Conference on Industrial Furnaces and Boilers, 2015.
- [20] S. Taamallah, Z. A. LaBry, S. J. Shanbhogue, and A. F. Ghoniem, 'Thermo-acoustic instabilities in lean premixed swirl-stabilized combustion and their link to acoustically coupled and decoupled flame macrostructures', Proc. Combust. Inst., vol. 35, no. 3, pp. 3273–3282, 2015, doi: <https://doi.org/10.1016/j.proci.2014.07.002>.
- [21] N. A. ; Al Dabbagh and G. E. Andrews, 'The Influence of Premixed Combustion Flame Stabilizer Geometry on Flame Stability and Emissions', J. Eng. Power, vol. 103, no. 4, pp. 749–758, 1981, doi: 10.1115/1.3230798.
- [22] N. A. ; Al Dabbagh and G. E. Andrews, 'The influence of flame stabiliser pressure loss on mixing, combustion performance and flame stability', in International Symposium on Air Breathing Engines, 6 th, Paris, France, 1983, pp. 172–181.
- [23] N. A. Al-Dabbagh, G. E. Andrews, and R. Manorharan, 'Shear Layer Mixing for Low Emission Gas Turbine Primary Zones', no. 79481, p. V003T06A002, 1984, doi: 10.1115/84-gt-13.
- [24] G. E. Andrews and S. A. R. Ahmad, 'Noncircular jet shear layer turbulent diffusion flames for ultra-low NO<sub>x</sub> gas turbine primary zones', Conf. 8 COGEN-TURBO Power Congr. Expo. Gas Turbines Cogener. Util. Ind. Indep. Power Gener. Portland U. S. 25-27 Oct 1994 Inf. PBD 1994 Relat. Inf. Part AS, p. Medium: X; Size: pp. 411-417, 1994.
- [25] G. E. Andrews and S. A. R. Ahmed, 'Jet Shear Layer Size and Number Influences on Grid Plate Direct Fuel Injection Shear Layer Mixing Low NO<sub>x</sub> Gas Turbine Combustion With Fuel Staging for Power Turn Down', no. 43130, pp. 291–298, 2008, doi: 10.1115/gt2008-50408.
- [26] W. D. York, W. S. Ziminsky, and E. Yilmaz, 'Development and Testing of a Low NO<sub>x</sub> Hydrogen Combustion System for Heavy Duty Gas Turbines', no. 44687, pp. 1395–1405, 2012, doi: 10.1115/gt2012-69913.
- [27] W. D. ; York, B. W. ; Romig, M. J. ; Hughes, D. W. ; Simons, and J. V Citeno, 'Premixed Pilot Flames for Improved Emissions and Flexibility in a Heavy Duty Gas Turbine Combustion System', no. 56697, p. V04BT04A067, 2015, doi: 10.1115/GT2015-44102.
- [28] P. Gonzalez-Garcia, R. Ireson, A. Fuller, and R. Hulme, 'Alternative Fuel Switching Technologies for the Glass Sector: Phase 3', 2022.
- [29] A. Huber and D. GmbH, 'Impact of hydrogen and mixtures of hydrogen and natural gas on forced draught burners for gaseous fuels', 2020.
- [30] T. Ai, J. Masada, and E. Ito, 'Development of the high efficiency and flexible gas turbine M701F5 by applying "J" class gas turbine technologies', Mitsubishi Heavy Ind. Tech. Rev., vol. 51, no. 1, pp. 1–9, 2014.
- [31] A. Valera-Medina et al., 'Ammonia, methane and hydrogen for gas turbines', Energy Procedia, vol. 75, pp. 118–123, 2015.
- [32] V. Sethi, 'Advanced performance simulation of gas turbine components and fluid thermodynamic properties', 2008.

- [33] O. F. Aalrebei, A. H. Al Assaf, A. Amhamed, N. Swaminathan, and S. Hewlett, 'Ammonia-hydrogen-air gas turbine cycle and control analyses', *Int. J. Hydrog. Energy*, 2022.
- [34] M. Kaushal, S. Ahlawat, B. B. Makut, G. Goswami, and D. Das, 'Dual substrate fermentation strategy utilizing rice straw hydrolysate and crude glycerol for liquid biofuel production by *Clostridium sporogenes* NCIM 2918', *Biomass Bioenergy*, vol. 127, p. 105257, 2019, doi: <https://doi.org/10.1016/j.biombioe.2019.105257>.
- [35] U. S. E. I. Administration, 'Biofuels explained: Ethanol and the environment', 2021. <https://www.eia.gov/energyexplained/biofuels/ethanol-and-the-environment.php> (accessed Mar. 16, 2022).
- [36] N. A. AL Dabbagh G.E. Andrews, Zhao J.X., 'The prediction of premixed high intensity baffle stabilised turbulent combustion', *Elev. Symp. Turbul.*, 1988.
- [37] O. Lammel et al., 'FLOX® Combustion at High Power Density and High Flame Temperatures', *J. Eng. Gas Turbines Power*, vol. 132, no. 12, pp. 121503–121510, 2010, doi: 10.1115/1.4001825.
- [38] N. Kobayashi, H. Inoue, H. Koizumi, and T. Watanabe, 'Robust Design of the Coaxial Jet Cluster Nozzle Burner for DME (Dimethyl Ether) Fuel', no. 36851. pp. 333–338, 2003.
- [39] S. R. Hernandez, Q. Wang, V. McDonell, A. Mansour, E. Steinthorsson, and B. Hollon, 'Micro Mixing Fuel Injectors for Low Emissions Hydrogen Combustion', no. 43130. pp. 675–685, 2008.
- [40] G. E. Andrews, M. A. Altaher, and H. Li, 'Hydrogen Combustion at High Combustor Airflow Using an Impinging Jet Flame Stabiliser With No Flashback and Low NO<sub>x</sub>', no. 44687. pp. 1479–1489, 2012.
- [41] R. Lückerath, W. Meier, and M. Aigner, 'FLOX® Combustion at High Pressure With Different Fuel Compositions', *J. Eng. Gas Turbines Power*, vol. 130, no. 1, pp. 11505–11507, 2008, doi: 10.1115/1.2749280.
- [42] R. Lückerath, W. Meier, and M. Aigner, 'FLOX® Combustion at High Pressure With Different Fuel Compositions', no. 47918, pp. 241–249, 2007, doi: 10.1115/gt2007-27337.
- [43] W. D. York, W. S. Ziminsky, and E. Yilmaz, 'Development and Testing of a Low NO<sub>x</sub> Hydrogen Combustion System for Heavy Duty Gas Turbines', no. 44687, pp. 1395–1405, 2012, doi: 10.1115/gt2012-69913.
- [44] W. [General E. C. York Schenectady, NY (United States)] et al., 'Advanced IGCC/Hydrogen Gas Turbine Development', United States, 2015. doi: 10.2172/1261809.
- [45] P. T. King, N. H. Escott, G. E. Andrews, M. M. Pourkashanian, and A. C. McIntosh, 'CFD Predictions of Low NO<sub>x</sub> Radial Swirlers With Vane Passage Fuel Injection With Comparison With Internal Gas Analysis Flame Composition', 2008, vol. Volume 3:, pp. 833–846. doi: 10.1115/GT2008-51138.
- [46] P. T. King, G. E. Andrews, M. N. Kim, M. Pourkashanian, and A. C. McIntosh, 'CFD Prediction and Design of Low NO<sub>x</sub> Radial Swirler Systems'. pp. 867–876, Jun. 08, 2009. doi: 10.1115/GT2009-60107.
- [47] P. T. King, G. E. Andrews, M. M. Pourkashanian, and A. C. McIntosh, 'Nitric Oxide Predictions for Low NO<sub>x</sub> Radial Swirlers With Central Fuel

- Injection Using CFD', in Turbo Expo: Power for Land, Sea, and Air, 2012, vol. 44687, pp. 985–993.
- [48] H. Government, 'Heat and Buildings Strategy', 2021.
- [49] E. & I. S. Department for Business, 'Hy4Heat WP5: Understanding Commercial Appliances for UK Hydrogen for Heat Demonstration', 2021.
- [50] E. & I. S. Department for Business, 'DOMESTIC HEAT DISTRIBUTION SYSTEMS: EVIDENCE GATHERING', 2021.
- [51] A. R. Ltd, 'Residential Central Heating Market Report - UK 2021-2025', London, 2021.
- [52] U. Home Office, 'Detailed analysis of fires attended by fire and rescue services', 2019.
- [53] FocalPoint, 'Focal Point'.  
<https://www.focalpointfires.co.uk/product/blenheim-black-2/>
- [54] R. Kemna, M. van Elburg, W. Li, and R. van Holsteijn, 'Eco-design of CH-Boilers', Delft Van Holsteijn En Kemna, 2007.
- [55] Legendfires, 'Legend Evora'. <https://legendfires.com/collections/legend/products/evora>
- [56] A. C. Frazer-Nash, 'Appraisal of Domestic Hydrogen Appliances Prepared for the Department of Business, Energy & Industrial Strategy', 2018.
- [57] W. R. Hawthorne, D. S. Weddell, and H. C. Hottel, 'Mixing and combustion in turbulent gas jets', in Symposium on Combustion and Flame, and Explosion Phenomena, 1948, vol. 3, no. 1, pp. 266–288.
- [58] R. W. Schefer, W. D. Kulatilaka, B. D. Patterson, and T. B. Settersten, 'Visible emission of hydrogen flames', *Combust. Flame*, vol. 156, no. 6, pp. 1234–1241, 2009.
- [59] E. R. G. King's College London, 'London Air - What is Ozone?', 2018.  
<http://www.londonair.org.uk/LondonAir/Guide/WhatIsO3.aspx>
- [60] S. Sillman, '9.11 - Tropospheric Ozone and Photochemical Smog', in *Treatise on Geochemistry*, H. D. Holland and K. K. Turekian, Eds. Oxford: Pergamon, 2003, pp. 407–431. doi: <https://doi.org/10.1016/B0-08-043751-6/09053-8>.
- [61] R. J. Blaszczyk, 'Nitrogen Oxides (NO<sub>x</sub>): Why and How They Are Controlled; EPA-456/F-99-006R', 1999.
- [62] G. E. Andrews, 'Ultra low NO<sub>x</sub> Gas Turbine Combustion', 2013, vol. 1.
- [63] J. C. W. W. Carole and N. Beale, *Global climate change linkages: acid rain, air quality, and stratospheric ozone*. Springer Science & Business Media, 1989.
- [64] Y. Lu and M. A. K. Khalil, 'Methane and carbon monoxide in OH chemistry: The effects of feedbacks and reservoirs generated by the reactive products', *Chemosphere*, vol. 26, no. 1, pp. 641–655, 1993, doi: [https://doi.org/10.1016/0045-6535\(93\)90450-J](https://doi.org/10.1016/0045-6535(93)90450-J).
- [65] A. W. B. In. Faiz, 'IEA Cars and Climate Change', 1993.
- [66] P. Tikuisis, D. M. Kane, F. TM; Buick, and S. M. Fairburn, 'Rate of formation of carboxyhemoglobin in exercising humans exposed to carbon monoxide', *J. Appl. Physiol.*, p. 72, 1992.
- [67] B. Weinhold, 'Ozone Nation: EPA Standard Panned by the People', *Environ. Health Perspect.*, vol. 116, no. 7, pp. A302–A305, 2008.
- [68] F. and R. A. Department for Environment, 'National statistics Emissions of air pollutants in the UK – Nitrogen oxides (NO<sub>x</sub>)', 2022.

- [69] E. P. Agency, 'How nitrogen oxides affect the way we live and breathe'. 2008.
- [70] N. A. E. Inventory, 'Air Pollution in the UK 2020', 2021.
- [71] EEA, 'European Union emission inventory report 1990-2018', 2020. doi: 10.2800/233574.
- [72] O. Academia, 'Gases de combustión', we measure it.testo. 2010.
- [73] Ofgem, 'Ofgem's Future Insights Series The Decarbonisation of Heat', Insights Future Regul., 2016.
- [74] S. G. N. Ltd, 'Annual report and financial statements 2018', 2018. doi: 04958135.
- [75] E. & I. S. Department for Business, '2021 Government Greenhouse Gas Conversion Factors for Company Reporting', 2021.
- [76] G. E. Andrews and M. N. Kim, 'The Optimum Position of Water Heat Transfer Coils Downstream of a Radial Swirler in a 20kW Heater', in Proceedings of 13th International Conference on Heat Transfer, Fluid Mechanics and Thermodynamics (HEFAT2017), 2017, pp. 761–766. doi: 1570346302.
- [77] E. Parliament, 'Directive 2010/75/EU of the European Parliament and of the Council of 24 November 2010 on industrial emissions (integrated pollution prevention and control)', Off. J. Eur. Union, p. L–334, 2010.
- [78] F. Bonzani, C. Piana, and D. Zito, 'VeLoNOx™ Combustion System Operating Experience on Heavy Duty Gas Turbine', no. 43963. pp. 781–789, 2010.
- [79] G. E. ; Andrews and M. N. Kim, 'The Optimum Position of Water Heat Transfer Coils Downstream of a Radial Swirler in a 20 kW Heater', 13th Int. Conf. Heat Transf., pp. 761–766, 2007.
- [80] M. Klein, 'The Need for Standards to Promote Low Emission, High Efficiency Gas Turbine Facilities', no. 78606, p. V003T02A015, 1999, doi: 10.1115/99-GT-405.
- [81] H. Schütz, R. Lückerrath, T. Kretschmer, B. Noll, and M. Aigner, 'Analysis of the Pollutant Formation in the FLOX® Combustion', J. Eng. Gas Turbines Power, vol. 130, no. 1, Jan. 2008, doi: 10.1115/1.2747266.
- [82] D. Murcray, W. Williams, D. Barker, A. Goldman, C. Bradford, and G. Cook, 'Proceedings of the WMO Symposium on the Geophysical Aspects and Consequences of Change in the Composition of the Stratosphere', 1978.
- [83] P. J. Crutzen, 'The influence of nitrogen oxides on the atmospheric ozone content', Q. J. R. Meteorol. Soc., vol. 96, no. 408, pp. 320–325, 1970.
- [84] P. J. Crutzen, 'The role of NO and NO<sub>2</sub> in the chemistry of the troposphere and stratosphere', Annu. Rev. Earth Planet. Sci., vol. 7, pp. 443–472, 1979.
- [85] J. W. Chamberlain and D. M. Hunten, Theory of planetary atmospheres: an introduction to their physics and chemistry. Academic Press, 1990.
- [86] F. Kara, 'Knowledge level of prospective science teachers regarding formation and effects of acid rains on the environment and organisms', Int. J. Appl., vol. 5, no. 4, 2015.
- [87] G. E. Andrews, '16 - Ultra-low nitrogen oxides (NO<sub>x</sub>) emissions combustion in gas turbine systems A2 - Jansohn, Peter', in Modern Gas Turbine Systems, Woodhead Publishing, 2013, pp. 715–790. doi: <https://doi.org/10.1533/9780857096067.3.715>.

- [88] G. Hesselmann and M. Rivas, 'What are the main NO<sub>x</sub> formation processes in combustion plant?', in IFRF Online Combustion Handbook, vol. 1, 2001.
- [89] S. M. Correa, 'A Review of NO<sub>x</sub> Formation Under Gas-Turbine Combustion Conditions', *Combust. Sci. Technol.*, vol. 87, no. 1–6, pp. 329–362, 1993, doi: 10.1080/00102209208947221.
- [90] U. Honegger, 'Gas turbine combustion modeling for a parametric emissions monitoring system'. Kansas State University, 2007.
- [91] TMI, 'Prompt NO<sub>x</sub>, fuel NO<sub>x</sub> and thermal NO<sub>x</sub>: The DLE strategy', *Turbomachinery international*, Feb. 24, 2020. <https://www.turbomachinerymag.com/view/prompt-nox-fuel-nox-and-thermal-nox-the-dle-strategy>
- [92] J. L. Toof, 'A model for prediction of Thermal, Prompt, and Fuel NO<sub>x</sub> Emissions from Combustion Turbines', *ASME*, vol. 108, pp. 340–347, 1986.
- [93] G. E. Andrews, 'Ultra Low NO<sub>x</sub> Gas Turbine Combustion. In: Proceedings of 12th ISAIF', 12th ISAIF International Symposium on Experimental and Computational Aerothermodynamics of Internal Flows. 2015.
- [94] R. ; Miller, G. ; Davis, G. ; Lavoie, and C. Newman, 'A Super-Extended Zel'dovich Mechanism for Nox Modeling and Engine Calibration,' *International Congress & Exposition*. p. 13, 1998. doi: <https://doi.org/10.4271/980781>.
- [95] A. H. Lefebvre, *Gas Turbine Combustion*, 1st ed. Bristol, Pa.: Taylor & Francis, 1983.
- [96] R. ; Siegel and J. R. Howell, 'Thermal Radiation', *Heat Transf. Heat Mass Transf. J.*, 1997.
- [97] F. ; Maeda and Y. Iwai, 'Prediction Model of NO<sub>x</sub> for Gas Turbine Combustor with Diffusion and Lean Premixed Flames. ', *Proc. ASME Int. Gas Turbine and Aeroengine Congress 1995*. ASME, Houston , 1995.
- [98] G. E. ; Andrews, M. ; Lazim, and M. C. Mkpadi, 'Low NO<sub>x</sub> Axial Swirler with Fuel Injection into the Downstream Dump Expansion Shear Layer'. *J. Energy Inst*, 2005.
- [99] G. E. Andrews, N. T. Ahmed, R. Phylaktou, and P. King, 'Weak Extinction in Low NO<sub>x</sub> Gas Turbine Combustion', no. 48838, pp. 623–638, 2009, doi: 10.1115/gt2009-59830.
- [100] I. FUKUE, 'KS-1 Industrial Gas Turbines in a Globally Competitive Market and Environmental Regulations', in *The International Gas Turbine Congress: book of abstracts*, 1999, vol. 1999, no. 1, pp. 1–4.
- [101] E. Ito, I. Okada, K. Tsukagoshi, A. Muyama, and J. Masada, 'Development of Key Technologies for the Next Generation 1700C-Class Gas Turbine', no. 48821, pp. 919–929, 2009, doi: 10.1115/GT2009-59783.
- [102] C. Vandervort, D. Leach, H. Fujimoto, and K. Kihara, 'The role of large, dual-fuel gas turbine combined cycle, high -efficiency, reliable power generation in Asia-Pacific', in *International Gas Turbine Congress 2015*, 2015, pp. 1612–1616.
- [103] J. D. Willis, I. J. Toon, T. Schweiger, and D. A. Owen, 'Industrial RB211 dry low emission combustion', in *Turbo Expo: Power for Land, Sea, and Air*, 1993, vol. 78927, p. V03CT17A052.

- [104] S. Kajita et al., 'An Advanced Development of a Second-Generation Dry, Low-NO<sub>x</sub> Combustor for 1.5 MW Gas Turbine', in Turbo Expo: Power for Land, Sea, and Air, 1996, vol. 78743, p. V003T06A010.
- [105] J. Goldmeer, H. Fujimoto, and K. Kihara, 'Recent Advancements in Gas Turbine Fuel Flexibility', in International Gas Turbine Congress, 2015, pp. 15–20.
- [106] G. E. Andrews et al., 'High-Intensity Burners with Low Nox Emissions', Proc. Inst. Mech. Eng. Part J. Power Energy, vol. 206, no. 1, pp. 3–17, Feb. 1992, doi: 10.1243/PIME\_PROC\_1992\_206\_003\_02.
- [107] N. A. Røkke, J. E. Hustad, and S. Berg, 'Pollutant emissions from gas fired turbine engines in offshore practice: Measurements and scaling', in Turbo Expo: Power for Land, Sea, and Air, 1993, vol. 78903, p. V03AT15A021.
- [108] M. C. Mkpadi, G. E. Andrews, I. Khan, M. N. M. Jaafar, M. Pourkashanian, and Y. Yang, 'Lean/Lean Staged Low NO<sub>x</sub> Combustion for Near Stoichiometric Gas Turbine Primary Zone Conditions', ASME Turbo Expo 2001: Power for Land, Sea, and Air. Jun. 04, 2001. doi: 10.1115/2001-GT-0082.
- [109] J. Zanger, T. Monz, and M. Aigner, 'Experimental Investigation of the Combustion Characteristics of a Double-Staged FLOX®-Based Combustor on an Atmospheric and a Micro Gas Turbine Test Rig', ASME Turbo Expo 2015: Turbine Technical Conference and Exposition. Jun. 15, 2015. doi: 10.1115/GT2015-42313.
- [110] C. E. Baukal Jr, The John Zink Hamworthy Combustion Handbook: Volume 2 Design and Operations. CRC Press, 2018.
- [111] G. Goldin, F. Montanari, and S. Patil, 'A Comparison of RANS and LES of an Industrial Lean Premixed Burner', ASME Turbo Expo 2014: Turbine Technical Conference and Exposition. Jun. 16, 2014. doi: 10.1115/GT2014-25352.
- [112] R. E. Jones, 'Advanced Technology for Reducing Aircraft Engine Pollution', ASME, 1973.
- [113] E. J. Mularz, 'Results of the Pollution Reduction Technology Program for Turboprop Engines', NASA, 1976.
- [114] R. W. ; Niedzwiecki and R. E. Jones, 'The Experimental Clean Combustor Program Description and Status', NASA, 1976.
- [115] R. A. Rudley, 'Status Review of NASA programs for Reducing Aircraft Gas Turbine Engine Emissions', NASA, 1976.
- [116] H. Rohrbacher and J. Barron, 'Refurbishment of a Solar Centaur Compressor Set to Meet European Environmental Regulations', no. 78743, p. V003T07A011, 1996, doi: 10.1115/96-GT-276.
- [117] R. Puri, D. M. Stansel, D. A. Smith, and M. K. Razdan, 'Dry Ultra-Low NO<sub>x</sub> "Green Thumb" Combustor for Allison's 501-K Series Industrial Engines', no. 78804, p. V003T06A063, 1995, doi: 10.1115/95-GT-406.
- [118] H. Hermsmeyer, B. Prade, U. Gruschka, U. Schmitz, S. Hoffmann, and W. Krebs, 'V64.3A Gas Turbine Natural Gas Burner Development', no. 36061, pp. 689–695, 2002, doi: 10.1115/GT2002-30106.
- [119] G. Leonard and J. Stegmaier, 'Development of an Aeroderivative Gas Turbine Dry Low Emissions Combustion System', no. 78910, p. V03BT16A044, 1993, doi: 10.1115/93-GT-288.

- [120] J. Zachary, 'Design Challenges for Combined Cycles With Post-Combustion CO<sub>2</sub> Capture', no. 48821, pp. 881–890, 2009, doi: 10.1115/GT2009-59381.
- [121] J. Wüning, 'Flameless oxidation', 2005.
- [122] J. A. Wüning and J. G. Wüning, 'Flameless oxidation to reduce thermal NO-formation', *Prog. Energy Combust. Sci.*, vol. 23, no. 1, pp. 81–94, 1997.
- [123] N. Hiraoka, A. Miyanagi, K. Kuroda, K. Ito, T. Nakagawa, and T. Ueda, 'The world's first onboard verification test of UE engine with low pressure EGR complied with IMO's NO<sub>x</sub> tier III regulations', *Mitsubishi Heavy Ind. Tech. Rev.*, vol. 53, no. 2, p. 40, 2016.
- [124] R. B. Poola et al., 'Membrane-Based Nitrogen-Enriched Air for NO<sub>x</sub> Reduction in Light-Duty Diesel Engines'. SAE International, 2000. doi: 10.4271/2000-01-0228.
- [125] J. Waslo, M. Kuwata, and R. M. Washam, 'Impingement cooled liner for dry low NO<sub>x</sub> venturi combustor'. Google Patents, Jan. 15, 1991.
- [126] B. Schetter, 'Gas turbine combustion and emission control.VKI Lecture Series', 1993.
- [127] M. J. Moore, 'NO<sub>x</sub> emission control in gas turbines for combined cycle gas turbine plant', *Proc. Inst. Mech. Eng. Part J. Power Energy*, vol. 211, no. 1, pp. 43–52, 1997.
- [128] N. Samec, R. W. Dibble, J. Y. Chen, and A. Pagon, 'Reduction of NO<sub>x</sub> and soot emission by water injection during combustion in a diesel engine', SAE Technical Paper, 2000.
- [129] A. Parlak, H. Yaşar, C. Haşimog'lu, and A. Kolip, 'The effects of injection timing on NO<sub>x</sub> emissions of a low heat rejection indirect diesel injection engine', *Appl. Therm. Eng.*, vol. 25, no. 17–18, pp. 3042–3052, 2005.
- [130] B. Becker, P. Berenbrink, and H. Brandner, 'Premixing Gas and Air to Reduce NO<sub>x</sub> Emissions With Existing Proven Gas Turbine Combustion Chambers', no. 79306, p. V003T06A011, 1986, doi: 10.1115/86-GT-157.
- [131] D. N. Anderson, 'Effects of Equivalence Ratio and Dwell Time on Exhaust Emissions from an Experimental Premixing Prevaporizing Burner', NASA TMX-71592, 1975.
- [132] D. N. Anderson, 'Effect of Premixing on Nitric Oxide Formation', NASA TMX-68220, 1973.
- [133] A. H. Lefebvre, 'Pollution Control in Continuous Combustion Engines', Fifteenth Symposium (International) on Combustion . The Comb. Inst. Pittsburgh, 1974.
- [134] R. F. ; Sawyer, N. P. Klaypatch, and D. of M. Engineering, 'Factors Controlling Pollutant Emissions from Gas Turbine Engine', California University, Berkeley.
- [135] J. Odgers, 'Air pollution by Gas Turbines. Is Control Possible?', *Can. Aeronaut. Space J.*, pp. 339–344, 1970.
- [136] L. L. ; Thomas, D. W. ; Simons, P. Popovic, C. E. ; Romoser, D. D. ; Vandale, and J. V. ; Citeno, 'E-Class DLN Technology Advancements, DLN1+', no. 54624, pp. 835–845, 2011, doi: 10.1115/GT2011-45944.
- [137] D. Isvoranu, S. Dănilă, A. Bogoi, and C. Leventiu, 'Assessment of Chemical Time Scale for a Turbine Burner', *Transp. Res. Procedia*, vol. 29, pp. 181–190, 2018, doi: <https://doi.org/10.1016/j.trpro.2018.02.016>.

- [138] T. Koganezawa, K. Miura, T. Saito, K. Abe, and H. Inoue, 'Full Scale Testing of a Cluster Nozzle Burner for the Advanced Humid Air Turbine', no. 47918, pp. 569–576, 2007, doi: 10.1115/gt2007-27737.
- [139] H. H. W. Funke, S. Boerner, W. Krebs, and E. Wolf, 'Experimental Characterization of Low NO<sub>x</sub> Micromix Prototype Combustors for Industrial Gas Turbine Applications', no. 54624, pp. 343–353, 2011, doi: 10.1115/gt2011-45305.
- [140] H. H.-W. Funke et al., 'Experimental and Numerical Characterization of the Dry Low NO<sub>x</sub> Micromix Hydrogen Combustion Principle at Increased Energy Density for Industrial Hydrogen Gas Turbine Applications'. Jun. 03, 2013. doi: 10.1115/GT2013-94771.
- [141] A. Haj Ayed, K. Kusterer, H. H.-W. Funke, J. Keinz, C. Striegan, and D. Bohn, 'Improvement study for the dry-low-NO<sub>x</sub> hydrogen micromix combustion technology', *Propuls. Power Res.*, vol. 4, no. 3, pp. 132–140, 2015, doi: <https://doi.org/10.1016/j.jprr.2015.07.003>.
- [142] A. Horikawa et al., 'Application of Low NO<sub>x</sub> Micro-Mix Hydrogen Combustion to Industrial Gas Turbine Combustor and Conceptual Design', 2015.
- [143] M. S. Genç, M. Çelik, and İ. Karasu, 'A review on wind energy and wind–hydrogen production in Turkey: A case study of hydrogen production via electrolysis system supplied by wind energy conversion system in Central Anatolian Turkey', *Renew. Sustain. Energy Rev.*, vol. 16, no. 9, pp. 6631–6646, 2012.
- [144] G. Kakoulaki, I. Kougias, N. Taylor, F. Dolci, J. Moya, and A. Jäger-Waldau, 'Green hydrogen in Europe–A regional assessment: Substituting existing production with electrolysis powered by renewables', *Energy Convers. Manag.*, vol. 228, p. 113649, 2021.
- [145] K. Meier, 'Hydrogen production with sea water electrolysis using Norwegian offshore wind energy potentials', *Int. J. Energy Environ. Eng.*, vol. 5, no. 2, pp. 1–12, 2014.
- [146] T. Ayodele and J. Munda, 'Potential and economic viability of green hydrogen production by water electrolysis using wind energy resources in South Africa', *Int. J. Hydrog. Energy*, vol. 44, no. 33, pp. 17669–17687, 2019.
- [147] J. A. Puzskiel, J. J. Andrade-Gamboa, and F. C. Gennari, 'Chapter 12 - Recent Progress in Mg–Co–H and Mg–Fe–H Systems for Hydrogen Energy Storage Applications', in *Emerging Materials for Energy Conversion and Storage*, K. Y. Cheong, G. Impellizzeri, and M. A. Fraga, Eds. Elsevier, 2018, pp. 393–428. doi: <https://doi.org/10.1016/B978-0-12-813794-9.00012-0>.
- [148] M. S. Cellek and A. Pınarbaşı, 'Investigations on performance and emission characteristics of an industrial low swirl burner while burning natural gas, methane, hydrogen-enriched natural gas and hydrogen as fuels', *Int. J. Hydrog. Energy*, vol. 43, no. 2, pp. 1194–1207, 2018.
- [149] N. Tekin, M. Ashikaga, A. Horikawa, and Dr.-Ing. H. Funke, 'Enhancement of fuel flexibility of industrial gas turbines by development of innovative hydrogen combustion systems', Apr. 2019.
- [150] H. H.-W. Funke, N. Beckmann, and S. Abanteriba, 'An overview on dry low NO<sub>x</sub> micromix combustor development for hydrogen-rich gas turbine

- applications', *Int. J. Hydrog. Energy*, vol. 44, no. 13, pp. 6978–6990, 2019, doi: <https://doi.org/10.1016/j.ijhydene.2019.01.161>.
- [151] H. H. W. Funke et al., 'Experimental and Numerical Study on Optimizing the Dry Low NO<sub>x</sub> Micromix Hydrogen Combustion Principle for Industrial Gas Turbine Applications', *J. Therm. Sci. Eng. Appl.*, vol. 9, no. 2, Dec. 2016, doi: 10.1115/1.4034849.
- [152] N. A. ; Al-Dabbagh, A. F. ; Al-Shaikhly, G. E. ; Andrews, C. O. ; Aniagolu, and R. Manoharan, 'Shear layer combustion- Influence of the method of fuel injection on stability and emissions', in *International Symposium on Air Breathing Engines*, 9 th, Athens, Greece, 1989, pp. 325–332.
- [153] H. Phylaktou and G. E. Andrews, 'Prediction of the maximum turbulent intensities generated by grid plate obstacles in explosion induced flows', 1994.
- [154] A. F. A. Al-Shaikhly, G. E. Andrews, and C. O. Aniagolu, 'Jet Shear Layer Turbulent Diffusion Flames for Ultra-Low NO<sub>x</sub> Emissions', 1990, vol. Volume 3: doi: 10.1115/90-GT-144.
- [155] H. H.-W. Funke et al., 'Numerical and Experimental Characterization of Low NO<sub>x</sub> Micromix Combustion Principle for Industrial Hydrogen Gas Turbine Applications', 2012, vol. Volume 2:, pp. 1069–1079. doi: 10.1115/GT2012-69421.
- [156] S. Arnoux and D. Robillard, 'Oxy-fuel burner', 1997
- [157] N. A. Al-Dabbagh, 'Emissions and stability of gas turbine combustors with rapid fuel and air mixing', University of Leeds, England, 1982.
- [158] G. Roffe and K. S. Venkataramani, 'Emission measurements for a lean premixed propane/air system at pressures up to 30 atmospheres', General Applied Science Labs., Inc.; Westbury, NY, United States, United States, 1978.
- [159] U. S. ; Hussain Abdul, Gordon. E. Andrews;, and W. G. C. and A. R. Shahabadi, 'Low NO<sub>x</sub> Primary Zones Using Jet Mixing Shear Layer Combustion ', ASME, 1988.
- [160] H. S. Alkabile., G. E. Andrews, and N. T. Ahmad, 'Lean Low NO<sub>x</sub> Primary Zones Using Radial Swirlers', ASME, 1988.
- [161] K. C. ; Schadow and E. Gutmark, 'Review of passive shear-flow control research for improved subsonic and supersonic combustion', AIAA J., 1989.
- [162] P. P. Walsh and P. Fletcher, *Gas turbine performance*. John Wiley & Sons, 2004.
- [163] G. W. Hall, 'Analytical Determination of the Discharge Characteristics of Cylindrical-Tube Orifices', *J. Mech. Eng. Sci.*, vol. 5, no. 1, pp. 91–97, 1963, doi: 10.1243/JMES\_JOUR\_1963\_005\_013\_02.
- [164] A. J. Ward Smith, *pressure losses in ducted flows*. London, 1971.
- [165] H. Rouse and A.-H. ABULFETOUH, 'Characteristics of irrotational flow through axially symmetric orifices', *J. Appl. Mech.-Trans. ASME*, vol. 17, no. 4, pp. 421–426, 1950.
- [166] A. L. Jorissen and H. T. Newton, 'Discharge measurements by means of cylindrical nozzles', *Trans Amer Soc Mech Engrs*, vol. 74, p. 825, 1952.
- [167] G. W. Metger, H. T. Richards, and J. E. Rohde, 'Discharge coefficients for thick plate orifices with approach flow perpendicular and inclined to the orifice axis', 1969.

- [168] S. J. Irving, 'The effect of disturbed flow conditions on the discharge coefficient of orifice plates', *Int. J. Heat Fluid Flow*, vol. 1, no. 1, pp. 5–11, 1979, doi: [https://doi.org/10.1016/0142-727X\(79\)90019-5](https://doi.org/10.1016/0142-727X(79)90019-5).
- [169] J.-C. Han and L. M. Wright, *Experimental Methods in Heat Transfer and Fluid Mechanics*. CRC Press, 2020.
- [170] M. J. Moran, H. N. Shapiro, D. D. Boettner, and M. B. Bailey, *Fundamentals of engineering thermodynamics*. John Wiley & Sons, 2010.
- [171] NASA, 'Isentropic Flow', NASA, 2021. <https://www.grc.nasa.gov/www/k-12/airplane/isentrop.html> (accessed Aug. 31, 2022).
- [172] E. Shashi Menon, 'Chapter Twelve - Meters and Valves', in *Transmission Pipeline Calculations and Simulations Manual*, E. Shashi Menon, Ed. Boston: Gulf Professional Publishing, 2015, pp. 431–471. doi: 10.1016/B978-1-85617-830-3.00012-2.
- [173] H. Rouse, *Elementary Mechanics of Fluids*, Dover Edit. 1946.
- [174] A. Bhargava, D. W. Kendrick, M. B. Colket, W. A. Sowa, K. H. Casleton, and D. J. Maloney, 'Pressure Effect on NO<sub>x</sub> and CO Emissions in Industrial Gas Turbines', no. 78552, p. V002T02A017, 2000, doi: 10.1115/2000-GT-0097.
- [175] Z. David W., *Fundamentals of Computational Fluid Dynamics*. University of Toronto Institute for Aerospace Studies: Harvard Lomax and Thomas H. Pulliam NASA Ames Research Center, 1999.
- [176] J. ; Xamán and M. Gijón-Rivera, *Dinamica de fluidos computacionales para ingenieros (Computational Fluid Dynamics for Engineers)*. Bloomington, 2015.
- [177] N. Peters, 'Turbulent combustion: The state of the art', in *Turbulent Combustion*, Cambridge University Press, 2000, pp. 1–65. doi: 10.1017/CBO9780511612701.002.
- [178] Robert. L. Mott, *Applied Fluid Mechanics*, 6th ed. PRENTICE HALL INC., 2006.
- [179] L. C. F. D. Team, 'How does the Reynolds Number affect my CFD model?', *leap Australia Computational Fluid Dynamics (CFD)*, vol. 2018, no. June 18th. 2013.
- [180] B. Byron, S. Warren, and L. Edwin, *Transport Phenomena*, 2nd ed. United States of America: John Wiley & Sons, Inc, 2002.
- [181] H. K. ; Versteeg and W. Malalasekera, *An Introduction to Computational Fluid Dynamics*. England, 2007.
- [182] L. E. Malvern, *INTRODUCTION TO THE MECHANICS OF A CONTINUOUS MEDIUM*. New Jersey, 1969.
- [183] H. K. ; Versteeg and W. Malalasekera, *An Introduction to Computational Fluid Dynamics*. England, 2007.
- [184] J. Blazek, 'Chapter 3 - Principles of Solution of the Governing Equations', in *Computational Fluid Dynamics: Principles and Applications (Second Edition)*, Second Edition., J. Blazek, Ed. Oxford: Elsevier Science, 2005, pp. 29–75. doi: <https://doi.org/10.1016/B978-008044506-9/50005-9>.
- [185] J. C. ; Tannehill, D. A. ; Anderson, and R. H. Pletcher, *COMPUTATIONAL FLUID MECHANICS AND HEAT TRANSFER*. Bristol, PA: Taylor & Francis, 1997.
- [186] B. E. ; Launder, G. J. ; Reece, and W. Rodi, 'Progress in the Development of a Reynolds-stress Turbulence Closure', in *J. Fluid Mech*, vol. 68, 1975, pp. 537–566.

- [187] W. P. Jones and B. E. Launder, 'The prediction of laminarization with a two-equation model of turbulence', *Int. J. Heat Mass Transf.*, vol. 15, no. 2, pp. 301–314, 1972.
- [188] P. Gnemmi, R. Adeli, and J. Longo, 'Computational Comparisons of the Interaction of a Lateral Jet on a Supersonic Generic Missile', in *AIAA Atmospheric Flight Mechanics Conference and Exhibit*, American Institute of Aeronautics and Astronautics, 2008. doi: doi:10.2514/6.2008-688310.2514/6.2008-6883.
- [189] T. Avraham, 'Understanding The Realizable  $k-\epsilon$  Turbulence Model', 2018. <https://cfdisrael.blog/2018/04/23/understanding-realizability-for-the-k-epsilon-turbulence-model/>
- [190] T.-H. Shih, W. W. Liou, A. Shabbir, Z. Yang, and J. Zhu, 'A new  $k-\epsilon$  eddy viscosity model for high reynolds number turbulent flows', *Comput. Fluids*, vol. 24, no. 3, pp. 227–238, 1995.
- [191] S. Kucukgokoglan, A. Aroussi, S. J. Pickering, and M. Menacer, 'Prediction of interactions between burners in multi-burner systems', 1997.
- [192] CHAM, '3.4.8 The Realisable  $k-\epsilon$  model'. [http://www.cham.co.uk/phoenics/d\\_polis/d\\_enc/turmod/enc\\_t348.htm](http://www.cham.co.uk/phoenics/d_polis/d_enc/turmod/enc_t348.htm) (accessed Apr. 24, 2022).
- [193] D. C. Wilcox, 'Formulation of the  $k\omega$  turbulence model revisited', *AIAA J.*, vol. 46, no. 11, pp. 2823–2838, 2008.
- [194] D. C. Wilcox, *Turbulence Modeling for CFD*. La Canada, California: CW Industries, Inc, 1998.
- [195] F. Menter, 'Zonal two equation  $k\omega$  turbulence models for aerodynamic flows', in *23rd fluid dynamics, plasmadynamics, and lasers conference*, 1993, p. 2906.
- [196] F. R. Menter, 'Two-Equation Eddy-Viscosity Turbulence Models for Engineering Applications', *AIAA J.*, pp. 1598–1605, 1994.
- [197] B. Y. Guo, Q. F. Hou, A. B. Yu, L. F. Li, and J. Guo, 'Numerical modelling of the gas flow through perforated plates', *Chem. Eng. Res. Des.*, vol. 91, no. 3, pp. 403–408, 2013, doi: <https://doi.org/10.1016/j.cherd.2012.10.004>.
- [198] SIMSCALE, 'K-Omega and K-Omega SST', 2021. <https://www.simscale.com/docs/simulation-setup/global-settings/k-omega-sst/>
- [199] ANSYS, '4.4.3. Shear-Stress Transport (SST)  $k-\omega$  Model', 2015. [https://www.sharcnet.ca/Software/Ansys/17.0/en-us/help/flu\\_th/flu\\_th\\_sec\\_turb\\_kw\\_sst.html](https://www.sharcnet.ca/Software/Ansys/17.0/en-us/help/flu_th/flu_th_sec_turb_kw_sst.html)
- [200] S. V Patankar and D. B. Spalding, 'A calculation procedure for heat, mass and momentum transfer in three-dimensional parabolic flows', in *Numerical prediction of flow, heat transfer, turbulence and combustion*, Elsevier, 1983, pp. 54–73.
- [201] Alisha, 'SIMPLE algorithm', *CFD online*, 2016. [https://www.cfd-online.com/W/index.php?title=SIMPLE\\_algorithm&oldid=23531](https://www.cfd-online.com/W/index.php?title=SIMPLE_algorithm&oldid=23531)
- [202] Centre for Chemical Process Safety, 'Burning velocity', *CCPS Process Safety Glossary*, 2022. <https://www.aisc.org/ccps/resources/glossary/process-safety-glossary/burning-velocity#:~:text=Burning%20velocity%20is%20the%20speed,gas%20mixture%20ahead%20of%20it.>

- [203] X. Bao, Y. Jiang, H. Xu, C. Wang, T. Lattimore, and L. Tang, 'Laminar flame characteristics of cyclopentanone at elevated temperatures', *Appl. Energy*, vol. 195, pp. 671–680, Jun. 2017, doi: 10.1016/j.apenergy.2017.03.031.
- [204] E. M. Goodger, *Combustion calculations: theory, worked examples and problems*. Macmillan International Higher Education, 1977.
- [205] D. C. Haworth and S. H. El Tahry, 'Probability density function approach for multidimensional turbulent flow calculations with application to in-cylinder flows in reciprocating engines', *AIAA J.*, vol. 29, no. 2, pp. 208–218, 1991, doi: 10.2514/3.10566.
- [206] D. B. Spalding, 'Mixing and chemical reaction in steady confined turbulent flames', in *Symposium (International) on combustion*, 1971, vol. 13, no. 1, pp. 649–657.
- [207] I. S. Ertesvåg and B. F. Magnussen, 'The eddy dissipation turbulence energy cascade model', *Combust. Sci. Technol.*, vol. 159, no. 1, pp. 213–235, 2000.
- [208] J. Hoste, M. Fossati, I. Taylor, and R. Gollan, 'Characterisation of the eddy dissipation model for the analysis of hydrogen-fuelled scramjets', *Aeronaut. J.*, vol. 123, no. 1262, pp. 536–565, 2019.
- [209] ANSYS, '9.3. Eddy Dissipation Model', 2015.  
[https://www.sharcnet.ca/Software/Ansys/16.2.3/en-us/help/cfx\\_mod/i1309810.html](https://www.sharcnet.ca/Software/Ansys/16.2.3/en-us/help/cfx_mod/i1309810.html)
- [210] C. Schluckner, C. Gaber, M. Landfahner, M. Demuth, and C. Hochenauer, 'Fast and accurate CFD-model for NO<sub>x</sub> emission prediction during oxy-fuel combustion of natural gas using detailed chemical kinetics', *Fuel*, vol. 264, p. 116841, 2020, doi: <https://doi.org/10.1016/j.fuel.2019.116841>.
- [211] I. Zimmermann and M. Pfitzner, 'Combustion modeling of partially premixed flames', 2010, vol. 43970, pp. 335–351.
- [212] C. E. Baukal, V. Gershtein, and X. J. Li, *Computational Fluid Dynamics in Industrial Combustion*. Taylor & Francis, 2000.
- [213] U. of Chile, 'METODO DE LOS VOLUMENES FINITOS', *MODELACION NUMERICA EN INGENIERIA HIDRAULICA Y AMBIENTAL*. Chile, p. 25, 2002.
- [214] A. E. Lutz, R. J. Kee, J. F. Grcar, and F. M. Rupley, 'OPPDIF: A Fortran program for computing opposed-flow diffusion flames', Sandia National Lab.(SNL-CA), Livermore, CA (United States), 1997.
- [215] A. Linan, 'The asymptotic structure of counterflow diffusion flames for large activation energies', *Acta Astronaut.*, vol. 1, no. 7–8, pp. 1007–1039, 1974.
- [216] N. Peters, 'LAMINAR FLAMELET CONCEPTS IN TURBULENT COMBUSTION', in *Twenty-first Symposium on Combustion*, 1986, pp. 1231–1250.
- [217] F. ANSYS, 'Assumptions', 2014.
- [218] H. ; P. Pitsch N, 'Unsteady Flamelet Modelling Of Turbulent Hydrogen-Air Diffusion Flames', *Twenty-Seventh Symposium (International) on Combustion/The Combustion Institute*. pp. 1057–1064, 1998.
- [219] U. Maas and S. B. Pope, 'Implementation of simplified chemical kinetics based on intrinsic low-dimensional manifolds', *Symp. Int. Combust.*, vol. 24, no. 1, pp. 103–112, 1992, doi: [https://doi.org/10.1016/S0082-0784\(06\)80017-2](https://doi.org/10.1016/S0082-0784(06)80017-2).

- [220] U. Maas and S. B. Pope, 'Simplifying chemical kinetics: Intrinsic low-dimensional manifolds in composition space', *Combust. Flame*, vol. 88, no. 3, pp. 239–264, 1992, doi: [https://doi.org/10.1016/0010-2180\(92\)90034-M](https://doi.org/10.1016/0010-2180(92)90034-M).
- [221] T. Poinso and D. Veynante, *Theoretical and Numerical Combustion*, 2nd ed. Philadelphia, USA: R.T. Edwards, Inc., 2005.
- [222] O. Gicquel, N. Darabiha, and D. Thévenin, 'Liminar premixed hydrogen/air counterflow flame simulations using flame prolongation of ILDM with differential diffusion', *Proc. Combust. Inst.*, vol. 28, no. 2, pp. 1901–1908, 2000, doi: [https://doi.org/10.1016/S0082-0784\(00\)80594-9](https://doi.org/10.1016/S0082-0784(00)80594-9).
- [223] I. Verma, R. Yadav, P. Nakod, P. Sharkey, S. Li, and E. Meeks, 'Flamelet Generated Manifold Simulation of Turbulent Non-Premixed Bluff Body Flames', Volume 2: Combustion, Fuels, and Emissions; Renewable Energy: Solar and Wind; Inlets and Exhausts; Emerging Technologies: Hybrid Electric Propulsion and Alternate Power Generation; GT Operation and Maintenance; Materials and Manufacturing (Including Coatings, Composites, CMCs, Additive Manufacturing); Analytics and Digital Solutions for Gas Turbines/Rotating Machinery, Dec. 2019. doi: 10.1115/GTINDIA2019-2525.
- [224] H. BONGERS, J. A. V. A. N. OIJEN, L. M. T. SOMERS, and L. P. H. D. E. GOEY, 'THE FLAMELET GENERATED MANIFOLD METHOD APPLIED TO STEADY PLANAR PARTIALLY PREMIXED COUNTERFLOW FLAMES', *Combust. Sci. Technol.*, vol. 177, no. 12, pp. 2373–2393, 2005, doi: 10.1080/00102200500241198.
- [225] J. A. van Oijen, A. Donini, R. J. M. Bastiaans, J. H. M. ten Thijsse Boonkamp, and L. P. H. de Goeij, 'State-of-the-art in premixed combustion modeling using flamelet generated manifolds', *Prog. Energy Combust. Sci.*, vol. 57, pp. 30–74, 2016, doi: <https://doi.org/10.1016/j.pecs.2016.07.001>.
- [226] A. Donini, R. J. M. Bastiaans, J. A. van Oijen, and L. P. H. de Goeij, 'Differential diffusion effects inclusion with flamelet generated manifold for the modeling of stratified premixed cooled flames', *Proc. Combust. Inst.*, vol. 35, no. 1, pp. 831–837, 2015, doi: <https://doi.org/10.1016/j.proci.2014.06.050>.
- [227] P.-D. Nguyen, L. Vervisch, V. Subramanian, and P. Domingo, 'Multidimensional flamelet-generated manifolds for partially premixed combustion', *Combust. Flame*, vol. 157, no. 1, pp. 43–61, 2010, doi: <https://doi.org/10.1016/j.combustflame.2009.07.008>.
- [228] T. de Souza, R. J. M. Bastiaans, B. J. Geurts, and L. P. H. De Goeij, 'LES and RANS of Premixed Combustion in a Gas-Turbine Like Combustor Using the Flamelet Generated Manifold Approach', 2011, vol. Volume 2:, pp. 1119–1127. doi: 10.1115/GT2011-46355.
- [229] X. Liu, W. Shao, C. Liu, X. Bi, Y. Liu, and Y. Xiao, 'Numerical study of a high-hydrogen micromix model burner using flamelet-generated manifold', *Int. J. Hydrog. Energy*, vol. 46, no. 39, pp. 20750–20764, 2021, doi: <https://doi.org/10.1016/j.ijhydene.2021.03.157>.
- [230] N. Mukundakumar, D. Efimov, N. Beishuizen, and J. van Oijen, 'A new preferential diffusion model applied to FGM simulations of hydrogen flames', *Combust. Theory Model.*, vol. 0, no. 0, pp. 1–23, 2021, doi: 10.1080/13647830.2021.1970232.

- [231] K. Kuo, *Principles of Combustion*, New York., 2nd ed. New York: John Wiley & Sons, 2005.
- [232] R. J. Kee, F. M. Rupley, and J. A. Miller, 'Chemkin-II: A Fortran chemical kinetics package for the analysis of gas-phase chemical kinetics', Sandia National Lab.(SNL-CA), Livermore, CA (United States), 1989.
- [233] ANSYS, 'Fluent User's Guide', 2009.  
<https://www.afs.enea.it/project/neptunius/docs/fluent/html/ug/node643.htm>
- [234] G. G. De Soete, 'Overall reaction rates of NO and N<sub>2</sub> formation from fuel nitrogen', in *Symposium (international) on combustion*, 1975, vol. 15, no. 1, pp. 1093–1102.
- [235] G. Hand, M. Missaghi, M. Pourkashanian, and A. Williams, 'Experimental Studies and Computer Modelling of Nitrogen Oxides in a Cylindrical Furnace', in *Proceedings of the Ninth Members Conference*, 1989, vol. 2.
- [236] S. Huebner and T. Exley, 'Numerical analysis of the flows in annular slinger combustors', in *26th Joint Propulsion Conference*, 1990, p. 2164.
- [237] P.-A. Glaude, R. Fournet, R. Bounaceur, and M. Molière, 'Adiabatic flame temperature from biofuels and fossil fuels and derived effect on NO<sub>x</sub> emissions', *Fuel Process. Technol.*, vol. 91, no. 2, pp. 229–235, 2010.
- [238] B. J. McBride and Gordon. Gordon, 'Computer Program for Calculation of Complex Chemical Equilibrium Compositions and Applications II.', Ohio, 1996.
- [239] C. Morley, 'Gaseq', 2005. <http://www.gaseq.co.uk/>
- [240] W. C. Gardiner and A. Burcat, *Combustion chemistry*. Springer, 1984.
- [241] A. Burcat and B. Ruscic, *Third millennium ideal gas and condensed phase thermochemical database for combustion*. Technion-Israel Institute of Technology Haifa, Israel, 2001.
- [242] H. De Vries, O. Florisson, and G. C. Tiekstra, 'Safe Operation of Natural Gas Appliances Fuelled with Hydrogen & Natural Gas Mixtures (Progress Obtained in the Naturalhy-Project)', 2007.
- [243] M. Skottene and K. E. Rian, 'A study of NO<sub>x</sub> formation in hydrogen flames', *Int. J. Hydrog. Energy*, vol. 32, no. 15, pp. 3572–3585, 2007.
- [244] M. Bains, L. Hill, and P. Rossington, 'Material comparators for end-of-waste decisions Fuels: natural gas', 2016. doi: SC130040/R15.
- [245] V. Dupont, 'Output compositions H<sub>2</sub> flame hp cases CEA', 2019.
- [246] N. De Nevers, *Air pollution control engineering*. Waveland press, 2010.
- [247] BSI Group, 'BS PAS 4444:2020+A1:2021', 2021.
- [248] D. J. Anneken, S. Both, R. Christoph, G. Fieg, U. Steinberner, and A. Westfechtel, 'Fatty Acids', in *Ullmann's Encyclopedia of Industrial Chemistry*, John Wiley & Sons, Ltd, 2006. doi: [https://doi.org/10.1002/14356007.a10\\_245.pub2](https://doi.org/10.1002/14356007.a10_245.pub2).
- [249] L. Postrioti, M. Battistoni, C. N. Grimaldi, and F. Millo, 'Injection Strategies Tuning for the Use of Bio-Derived Fuels in a Common Rail HSDI Diesel Engine', 2003. doi: 10.4271/2003-01-0768.
- [250] E. Agbro, A. S. Tomlin, M. Lawes, S. Park, and S. M. Sarathy, 'The influence of n-butanol blending on the ignition delay times of gasoline and its surrogate at high pressures', *Fuel*, vol. 187, pp. 211–219, 2017, doi: <https://doi.org/10.1016/j.fuel.2016.09.052>.

- [251] O. Herbinet, W. J. Pitz, and C. K. Westbrook, 'Detailed chemical kinetic oxidation mechanism for a biodiesel surrogate', *Combust. Flame*, vol. 154, no. 3, pp. 507–528, 2008.
- [252] Y. Bai, Y. Wang, X. Wang, and P. Wang, 'Development of a skeletal mechanism for tri-component diesel surrogate fuel: N-hexadecane/iso-cetane/1-methylnaphthalene', *Fuel*, vol. 259, p. 116217, 2020, doi: <https://doi.org/10.1016/j.fuel.2019.116217>.
- [253] X. Cui, B. Zhou, M. Matsunaga, Y. Fujii, J. Kusaka, and Y. Daisho, 'A Numerical Study of the Effects of FAME Blends on Diesel Combustion and Emissions Characteristics Using a 3-D CFD Code Combined with Detailed Kinetics and Phenomenological Soot Formation Models'. Oct. 2013. doi: <https://doi.org/10.4271/2013-01-2689>.
- [254] A. Velaers, P. Schaberg, and A. Yates, 'Investigation of the combustion characteristics of GTL diesel fuel in a constant volume combustion chamber', SAE Technical Paper, 2007.
- [255] SOLIDWORKS [Internet], 'Support', 2018.
- [256] ANSYS [Internet], 'Support', 2018.
- [257] G. Andrews and M. Kim, 'The influence of film cooling on emissions for a low NO<sub>x</sub> radial swirler gas turbine combustor', 2001, vol. 78514, p. V002T02A038.
- [258] D. H. Lister and M. I. Wedlock, 'Measurement of Emissions Variability of a Large Turbofan Aero-Engine', 1978, vol. Volume 1A: doi: 10.1115/78-GT-75.
- [259] J. R. L. B. T.-D. in S. Allen, Ed., 'Chapter 3 An Outline of Flow Separation', in *Sedimentary Structures Their Character and Physical Basis Volume II*, vol. 30, Elsevier, 1982, pp. 101–131. doi: [https://doi.org/10.1016/S0070-4571\(08\)71013-6](https://doi.org/10.1016/S0070-4571(08)71013-6).
- [260] V. Yakhot, S. A. Orszag, S. Thangam, T. B. Gatski, and C. Speziale, 'Development of turbulence models for shear flows by a double expansion technique', *Phys. Fluids Fluid Dyn.*, vol. 4, no. 7, pp. 1510–1520, 1992.
- [261] S. Jerzembeck, N. Peters, P. Pepiot-Desjardins, and H. Pitsch, 'Laminar burning velocities at high pressure for primary reference fuels and gasoline: Experimental and numerical investigation', *Combust. Flame*, vol. 156, no. 2, pp. 292–301, 2009, doi: <https://doi.org/10.1016/j.combustflame.2008.11.009>.
- [262] C. V Naik, K. V Puduppakkam, and E. Meeks, 'A Comprehensive Kinetics Library for Simulating the Combustion of Automotive Fuels', *J. Energy Resour. Technol.*, vol. 141, no. 9, Apr. 2019, doi: 10.1115/1.4043250.
- [263] R. B. Bramlette and C. D. Depcik, 'Review of propane-air chemical kinetic mechanisms for a unique jet propulsion application', *J. Energy Inst.*, vol. 93, no. 3, pp. 857–877, 2020, doi: <https://doi.org/10.1016/j.joei.2019.07.010>.
- [264] A. A. Konnov, 'Yet another kinetic mechanism for hydrogen combustion', *Combust. Flame*, vol. 203, pp. 14–22, 2019, doi: <https://doi.org/10.1016/j.combustflame.2019.01.032>.
- [265] B. S. Institution and B. S. I. Staff, *Hydrogen-Fired Gas Appliances - Guide*. B S I Standards, 2020.

- [266] British Standards Institution, 'BS 7977-1:2009 Specification for safety and rational use of energy of . Radiant/convectors', London, United Kingdom, 2009.
- [267] A. D. Scillitoe, P. G. Tucker, and P. Adami, 'Evaluation of RANS and ZDES Methods for the Prediction of Three-Dimensional Separation in Axial Flow Compressors', Volume 2B: Turbomachinery, Jun. 2015. doi: 10.1115/GT2015-43975.
- [268] R. Fernandes, 'Investigation of pin fin cooling channels for applications in gas turbines', 2016.
- [269] R. Borghi, 'On the Structure and Morphology of Turbulent Premixed Flames', 1985.
- [270] R. G. Abdel-Gayed, D. Bradley, and A. K. C. Lau, 'The straining of premixed turbulent flames', Symp. Int. Combust., vol. 22, no. 1, pp. 731-738, 1989, doi: [https://doi.org/10.1016/S0082-0784\(89\)80081-5](https://doi.org/10.1016/S0082-0784(89)80081-5).
- [271] T. Poinso, 'Direct simulation of turbulent combustion', 1989.

## APPENDIX A.

### A.1 Navier Stokes equations

The momentum equation in three components considering the normal and shear stresses acting in a control volume is [183]:

x-component

$$\rho \frac{Du}{Dt} = \frac{\partial(-p + \tau_{xx})}{\partial x} + \frac{\partial\tau_{yx}}{\partial y} + \frac{\partial\tau_{zx}}{\partial z} + S_{Mx} \quad (75)$$

y-component

$$\rho \frac{Dv}{Dt} = \frac{\partial\tau_{xy}}{\partial x} + \frac{\partial(-p + \tau_{yy})}{\partial y} + \frac{\partial\tau_{zy}}{\partial z} + S_{My} \quad (76)$$

z-component

$$\rho \frac{Dw}{Dt} = \frac{\partial\tau_{xz}}{\partial x} + \frac{\partial\tau_{yz}}{\partial y} + \frac{\partial(-p + \tau_{zz})}{\partial z} + S_{Mz} \quad (77)$$

The pressure is expressed in negative terms since this is a compressive force, and due to the sign convention, compressive forces are expressed as negative, and tensile forces are positive [183].

To obtain the Reynolds equations, some dependent variables have to be decomposed into the mean conservation equations considering time, then to fluctuating components, and lastly, the complete equation gets time-averaged.

The Navier Stokes equations have been presented in Chapter 2.3, and the scalar transport equation is shown next

$$\frac{\partial(\overline{\rho\Phi})}{\partial t} + \nabla \cdot (\overline{\rho\Phi\vec{U}}) = \nabla \cdot (\Gamma_{\Phi}\nabla\Phi) + \left[ -\frac{\partial(\overline{\rho u'\phi'})}{\partial x} - \frac{\partial(\overline{\rho v'\phi'})}{\partial y} - \frac{\partial(\overline{\rho w'\phi'})}{\partial z} \right] + S_{\Phi} \quad (78)$$

Where the overbar means a time-averaged variable and the tilde is a Favre-averaged variable. Time average  $\Phi$  of flow property  $\phi$  is defined as

$$\Phi(t) = \frac{1}{\Delta t} \int_{t-\Delta t/2}^{t+\Delta t/2} \phi(t') dt'$$

The normal Reynolds stresses are

$$\tau_{xx} = -\overline{\rho u'^2} \quad \tau_{yy} = -\overline{\rho v'^2} \quad \tau_{zz} = -\overline{\rho w'^2}$$

And the shear Reynolds stresses

$$\tau_{xy} = \tau_{yx} = -\overline{\rho u'v'} \quad \tau_{xz} = \tau_{zx} = -\overline{\rho u'w'} \quad \tau_{yz} = \tau_{zy} = -\overline{\rho v'w'}$$

## A.2 Realisable k ε model coefficients

$$C_{1\varepsilon} = \max \left[ 0.43, \frac{\eta}{\eta + 5} \right]$$

$$\eta = S * \frac{k}{\varepsilon}$$

$$C_{\mu} = \frac{1}{\left[ A_0 + A_s * k * \frac{\hat{U}}{\varepsilon} \right]}$$

$$\hat{U} = \sqrt{S_{ij} * S_{ij} + \Omega_{ij} * \Omega_{ij}}$$

$$\Omega_{ij} = 0.5 * \left( \frac{\partial_{ui}}{\partial_{xj}} - \frac{\partial_{uj}}{\partial_{xi}} \right)$$

$$A_s = \sqrt{6} * \cos\varphi$$

$$\varphi = \cos^{-1} \left[ \max(-1, \min[\sqrt{6} * W, 1]) \right]$$

$$W = S_{ij} * S_{jk} * S_{ki} / \check{S}^3$$

$$\check{S} = \sqrt{S_{ij} * S_{ij}}$$

## A.3 SST k-ω model coefficients

$$F_1 = \tanh \left\{ \left\{ \min \left[ \max \left( \frac{\sqrt{k}}{\beta\omega y'}, \frac{500\nu}{y^2\omega} \right), \frac{4\sigma_{\omega 2} k}{CD_{k\omega} y^2} \right] \right\}^4 \right\}$$

When  $F_1 = 1$  then is inside the boundary layer. When it is 0 is in the free stream.

$$CD_{k\omega} = \max \left( 2\rho\sigma_{\omega 2} \frac{1}{\omega} \frac{\partial_k}{\partial_{xi}} \frac{\partial_{\omega}}{\partial_{xi}}, 10^{-10} \right)$$

The kinematic eddy viscosity is expressed as

$$\nu_T = \frac{a_1 k}{\max(a_1\omega, SF_2)}$$

The second blending function  $F_2$  is

$$F_2 = \tanh \left[ \left[ \max \left( \frac{2\sqrt{k}}{\beta\omega y'}, \frac{500\nu}{y^2\omega} \right) \right]^2 \right]$$

And the production limitier  $P_k$  is obtained as

$$P_k = \min \left( \tau_{ij} \frac{\partial U_i}{\partial x_j}, 10\beta k\omega \right)$$

#### **A.4 Turbulence combustion regimes for premixed combustion**

The different combustion regimes for turbulent combustion have been usually expressed in diagrams in terms of the length scale and velocity ratios. [216], [269]–[271]. A Schmidt unity number is shown in order to assume equal diffusivities for all reactive scalars

$$Sc = \frac{\nu}{D} = 1 \quad (79)$$

The flame thickness and the residence flame time are given as

$$l_F = \frac{D}{s_L}, t_F = \frac{D}{s_L^2} \quad (80)$$

Then, by considering the turbulent intensity  $\nu$  equal to the turbulent length scale  $D$ , and so the turbulent Reynolds number can be expressed as

$$Re = \frac{\nu' l}{s_L l_F} \quad (81)$$

The derivation used to show the ratio of large-scale turbulence time to the characteristic flame time known as the Damköhler number and expressed in terms of  $\nu$  can be written as

$$Da = \frac{s_L l}{\nu' l_F} \quad (82)$$

Now in turbulence, the scale Kolmogorov is known as the smallest scale that can exist without being destroyed by the viscosity and is expressed in length, time and velocity terms as:

$$\eta = \left( \frac{\nu^3}{\epsilon} \right)^{\frac{1}{4}}; \tau_\eta = \left( \frac{\nu}{\epsilon} \right)^{\frac{1}{2}}; v_\eta = (\nu\epsilon)^{\frac{1}{4}} \quad (83)$$

Then with the Kolmogorov scale is possible to obtain two Karlovitz numbers expressing the first one as:

$$Ka = \frac{t_F}{t_\eta} = \frac{l_F^2}{\eta^2} = \frac{v_\eta^2}{s_L^2} \quad (84)$$

And combining Equations 57, 58 and 60 it is possible to express the Reynolds number as

$$Re = Da^2 Ka^2 \quad (85)$$

The second Karlovitz number can be expressed in terms of the reaction zone thickness  $\delta$

$$Ka = \frac{l_\delta^2}{\eta^2} = \delta^2 Ka \quad (86)$$

### A.5 Turbulence combustion regimes for premixed combustion

In non premixed combustion there is no characteristic velocity scale or the laminar burning velocity unlike in premixed combustion. Hence there is no flame thickness describing a distinctive length scale. The strain rate  $a$ , which is the inverse of a characteristic time is locally imposed by the flow field. This parameters along with the stoichiometric Damköhler number  $D_{st}$  can define the diffusion thickness as:

$$l_D = \left(\frac{D_{st}}{a}\right)^{\frac{1}{2}} \quad (87)$$

There is also the gradient of mixture fraction field  $|\nabla Z|_{st}$ , related to the thickness  $l_D$  which is defined to a diffusion thickness  $(\Delta Z)_F$  using the following equation

$$(\Delta Z)_F = |\nabla Z|_{st} l_D \quad (88)$$

If the scalar dissipation rate  $\chi_{st}$  the following equation is obtained:

$$(\Delta Z)_F = \left(\frac{\chi_{st}}{2a}\right)^{\frac{1}{2}} \quad (89)$$

The regime diagram for non premixed turbulent combustion illustrated in shows a plot of the ratio  $Z'_{st}/(\Delta Z)_F$  versus the time scale ratio  $\chi_q/\tilde{\chi}_{st}$  where

$$Z'_{st} = \left(\widetilde{Z''^2}\right)_{st}^{\frac{1}{2}} \quad (90)$$

$\chi_q$  is the extinction (or quenching) scalar dissipation rate and  $\tilde{\chi}_{st}$  is the conditional Favre mean scalar dissipation rate. More detail can be found at Turbulent Combustion by Peters [177].

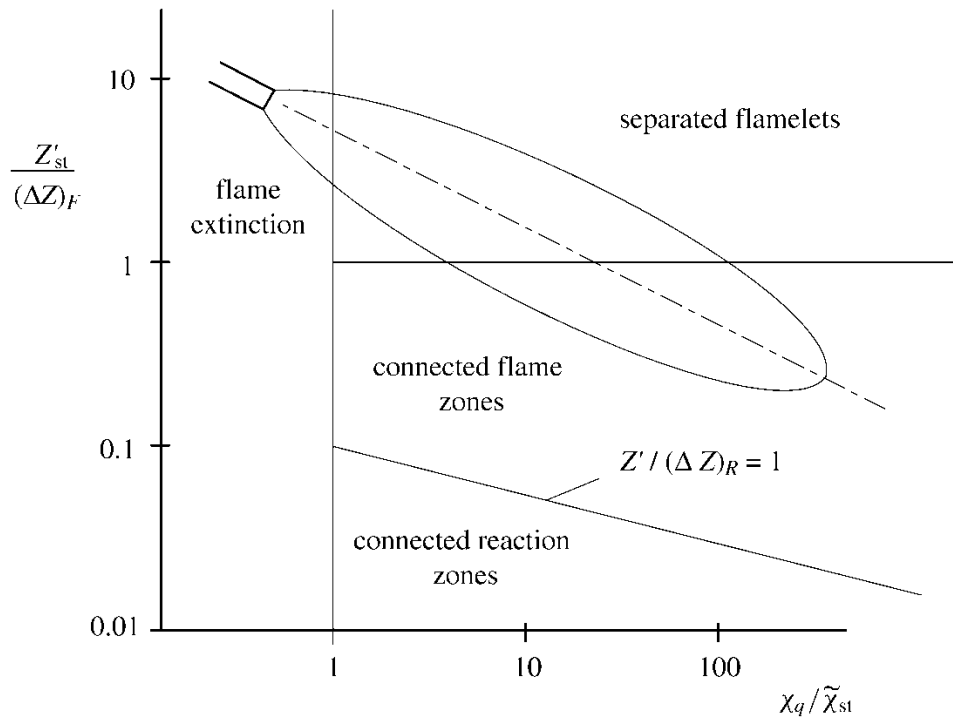


**Figure A-1.** Regimes in non-premixed turbulent combustion [177].

### APPENDIX B.

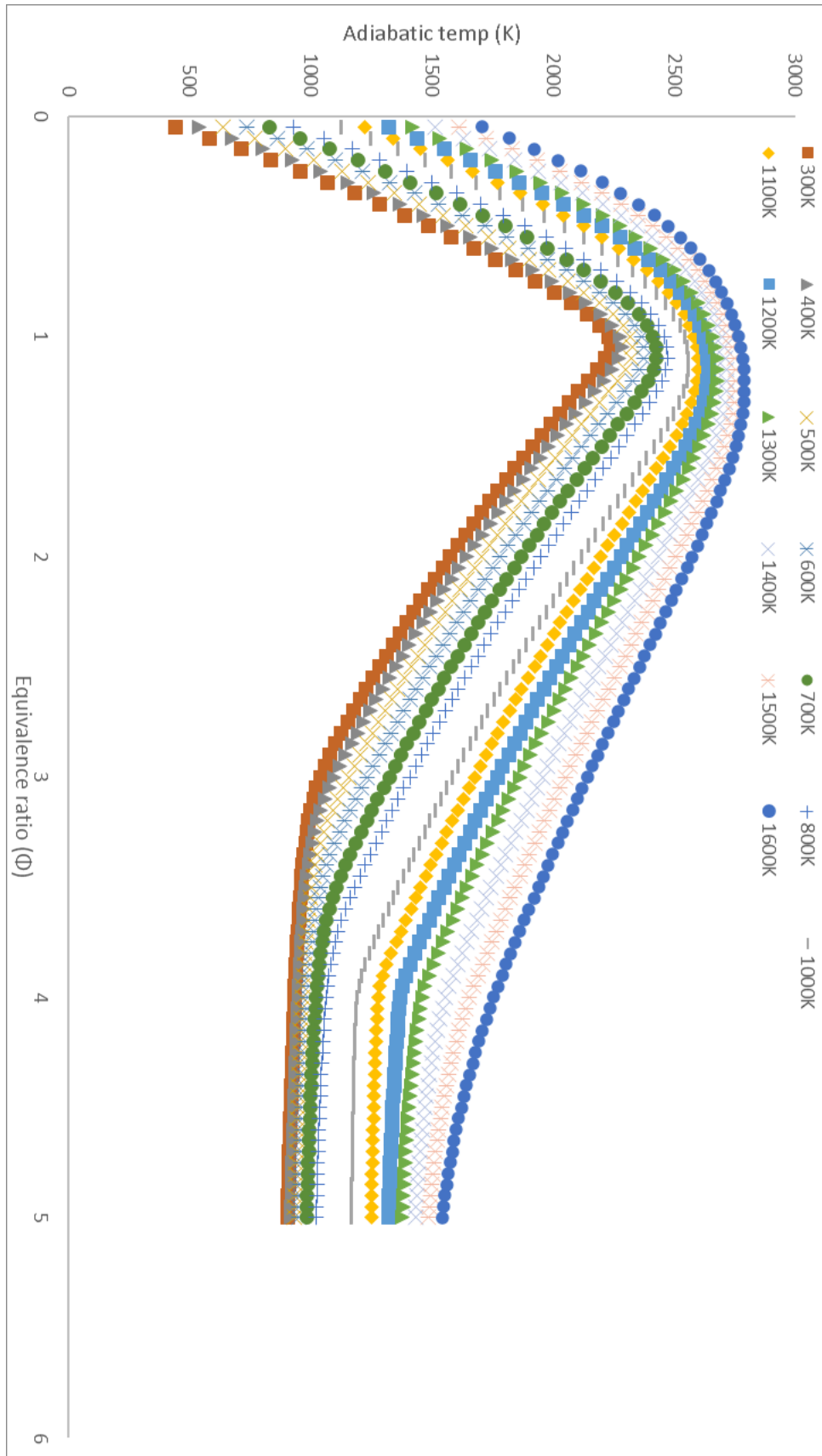


**Figure B-1.** Adiabatic flame temperature for Goole NG/air mixture (inlet temperatures 298-1600K)

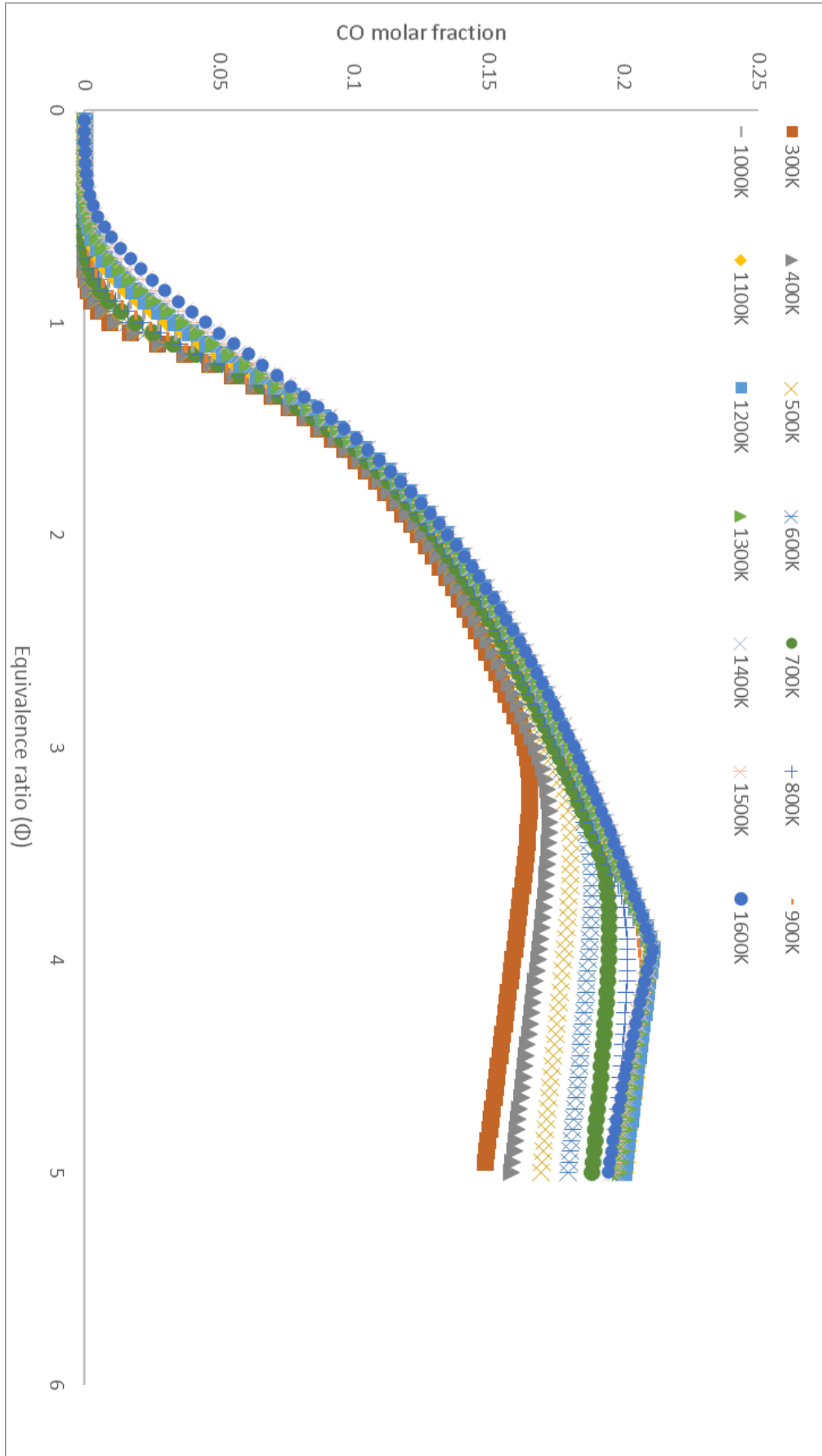


**Figure B-2.** Exhaust CO molar fraction for Goole NG/air mixture (inlet temperatures 298-1600K)

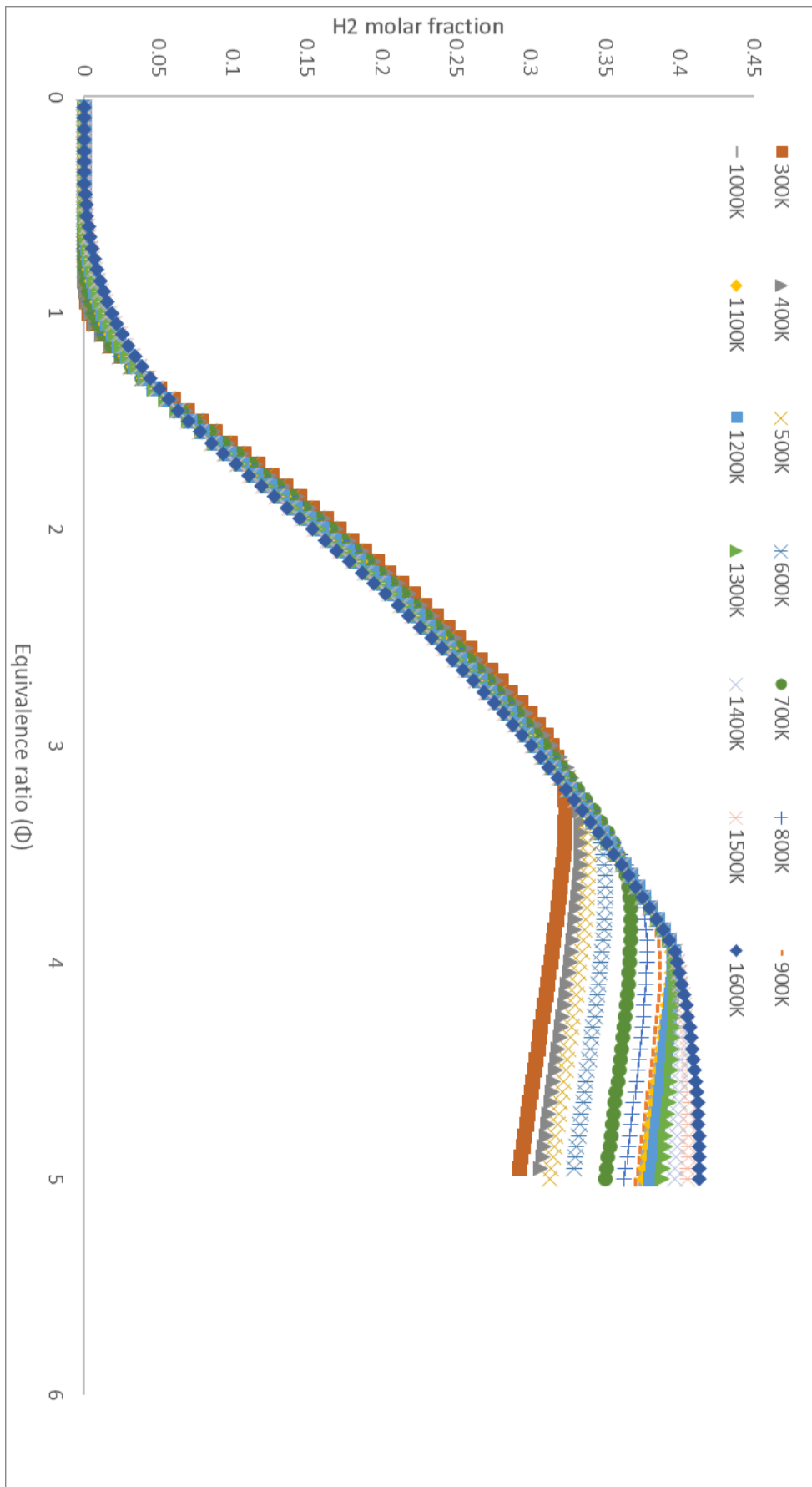


**Figure B-3.** Exhaust H<sub>2</sub> molar fraction for Goole NG/air mixture (inlet temperatures 298-1600K)

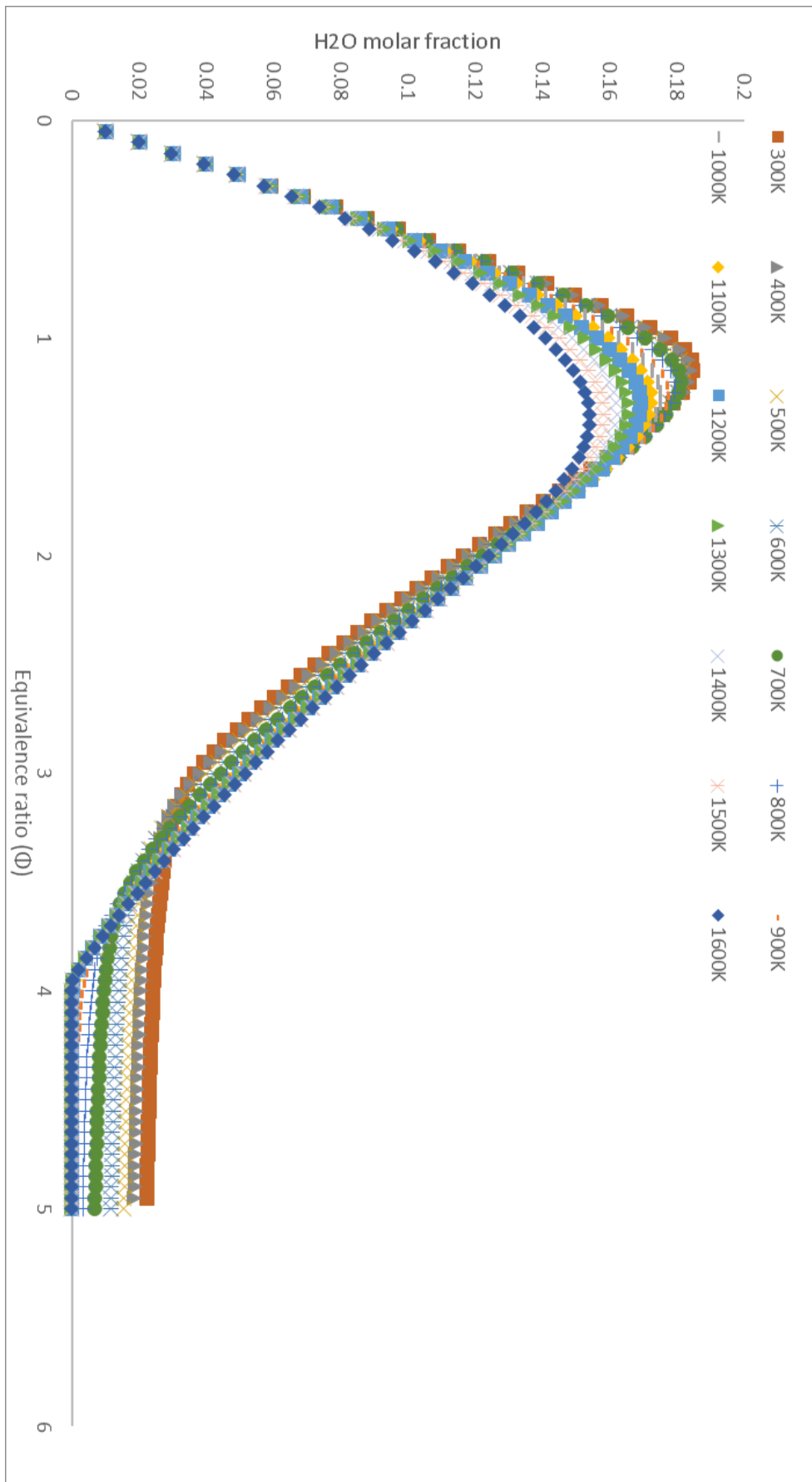


**Figure B-4.** Exhaust H<sub>2</sub>O molar fraction for Goole NG/air mixture (inlet temperatures 298-1600K)

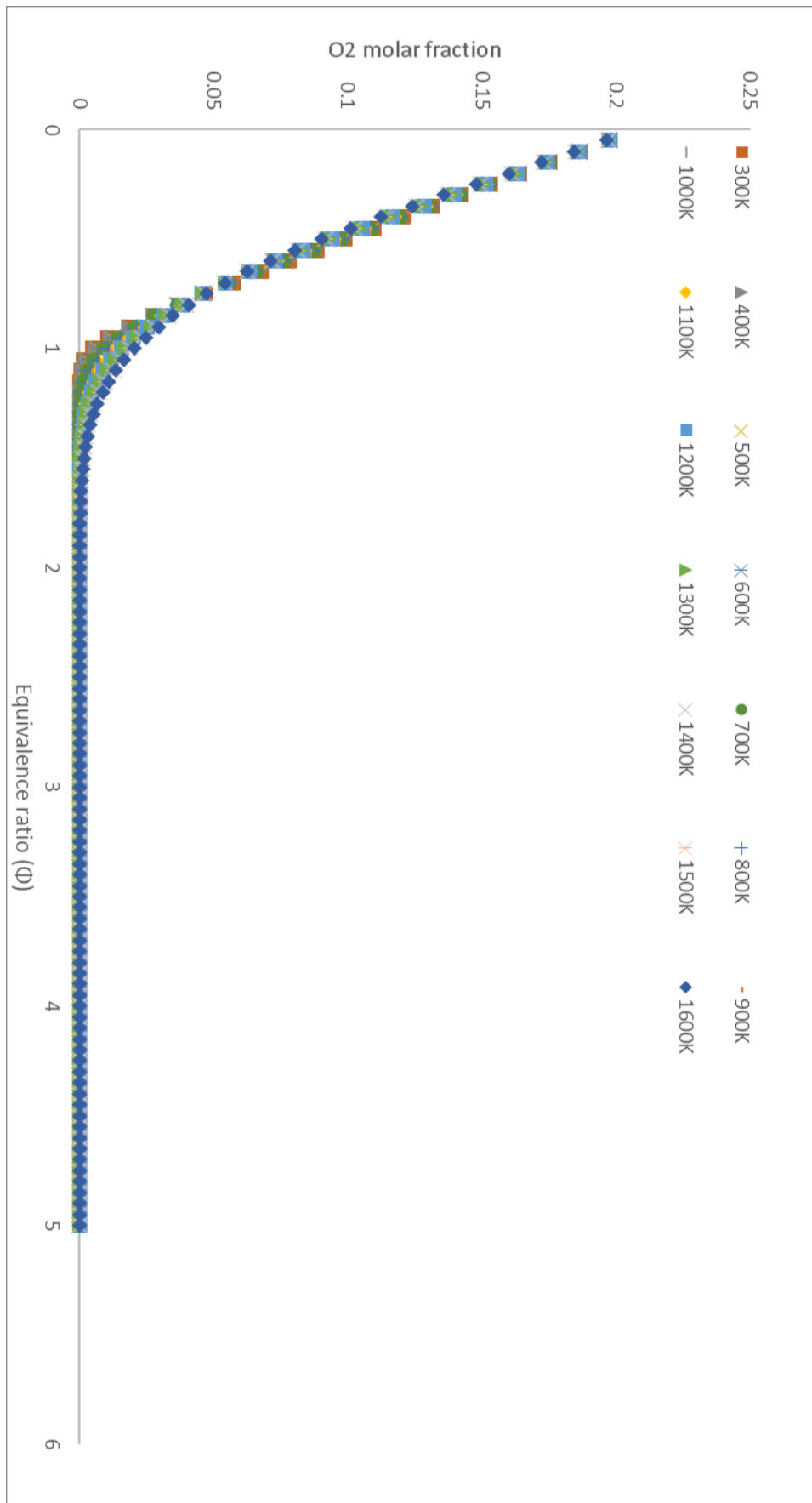


**Figure B-5.** Exhaust O<sub>2</sub> molar fraction for Goole NG/air mixture (inlet temperatures 298-1600K)

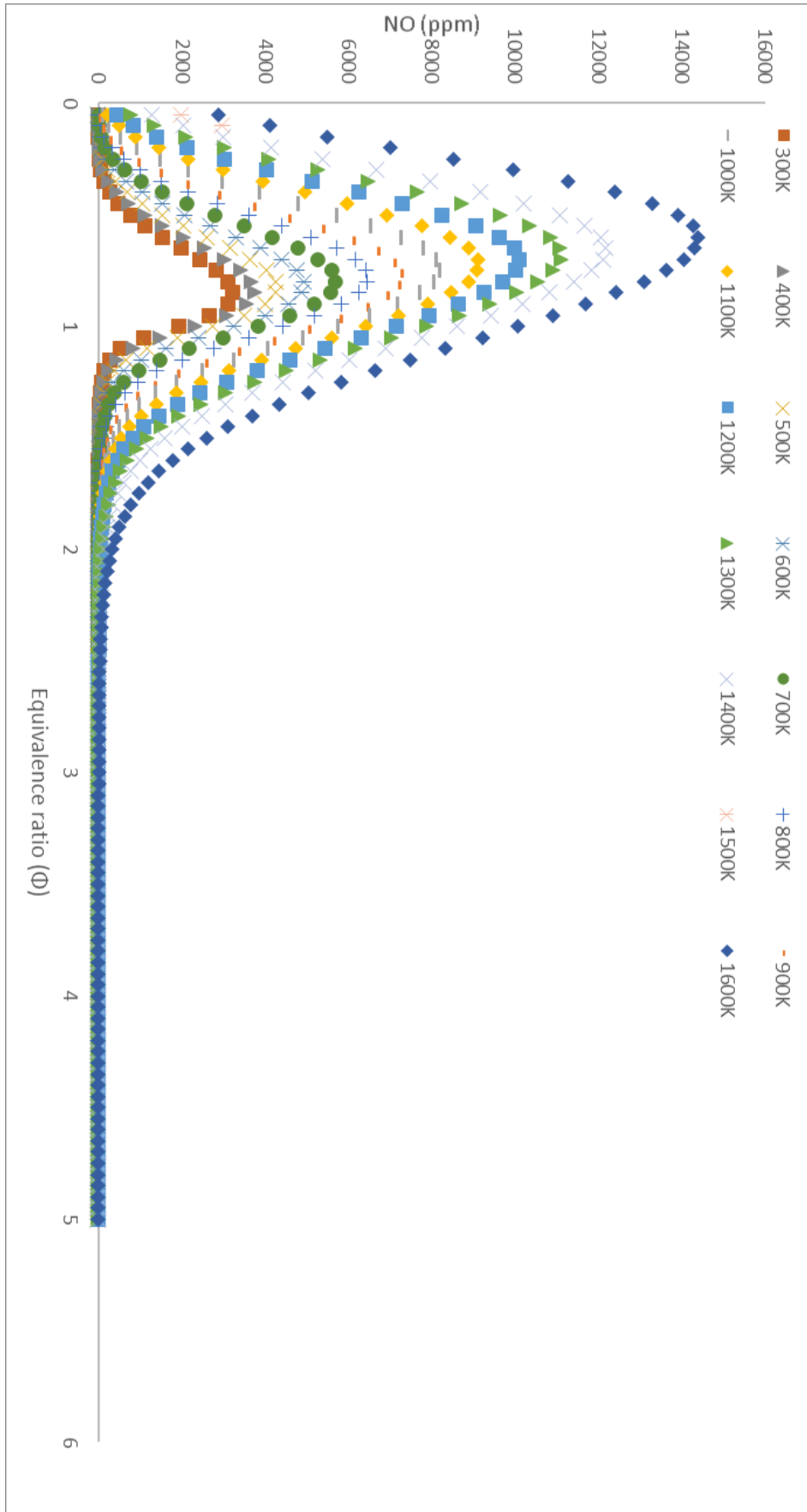


**Figure B-6.** Exhaust NO ppm for Goole NG/air mixture (inlet temperatures 298-1600K)

### APPENDIX C.

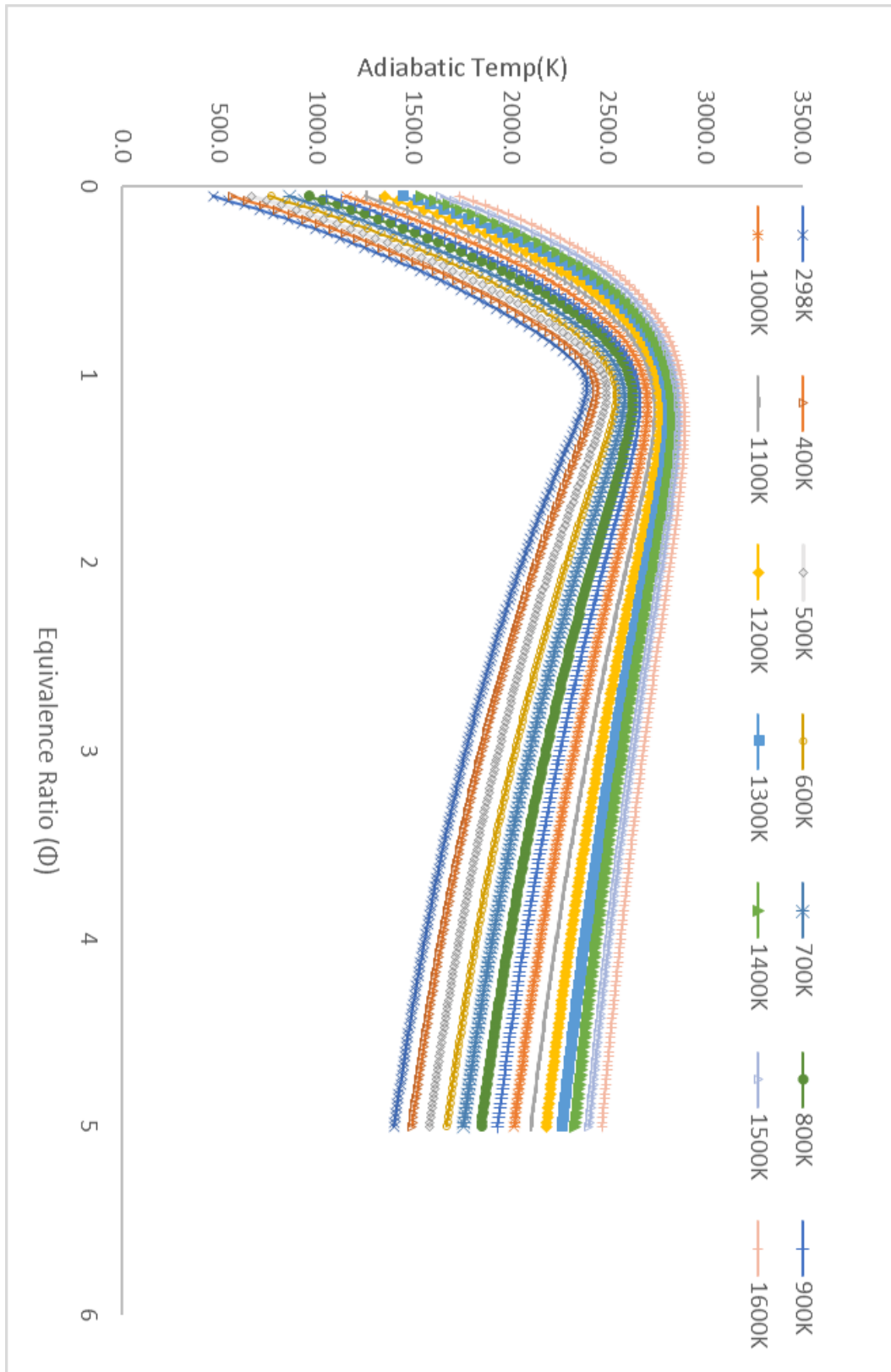


**Figure C-1.** Adiabatic flame temperature for pure H<sub>2</sub> mixture (inlet temperatures 298-1600K)

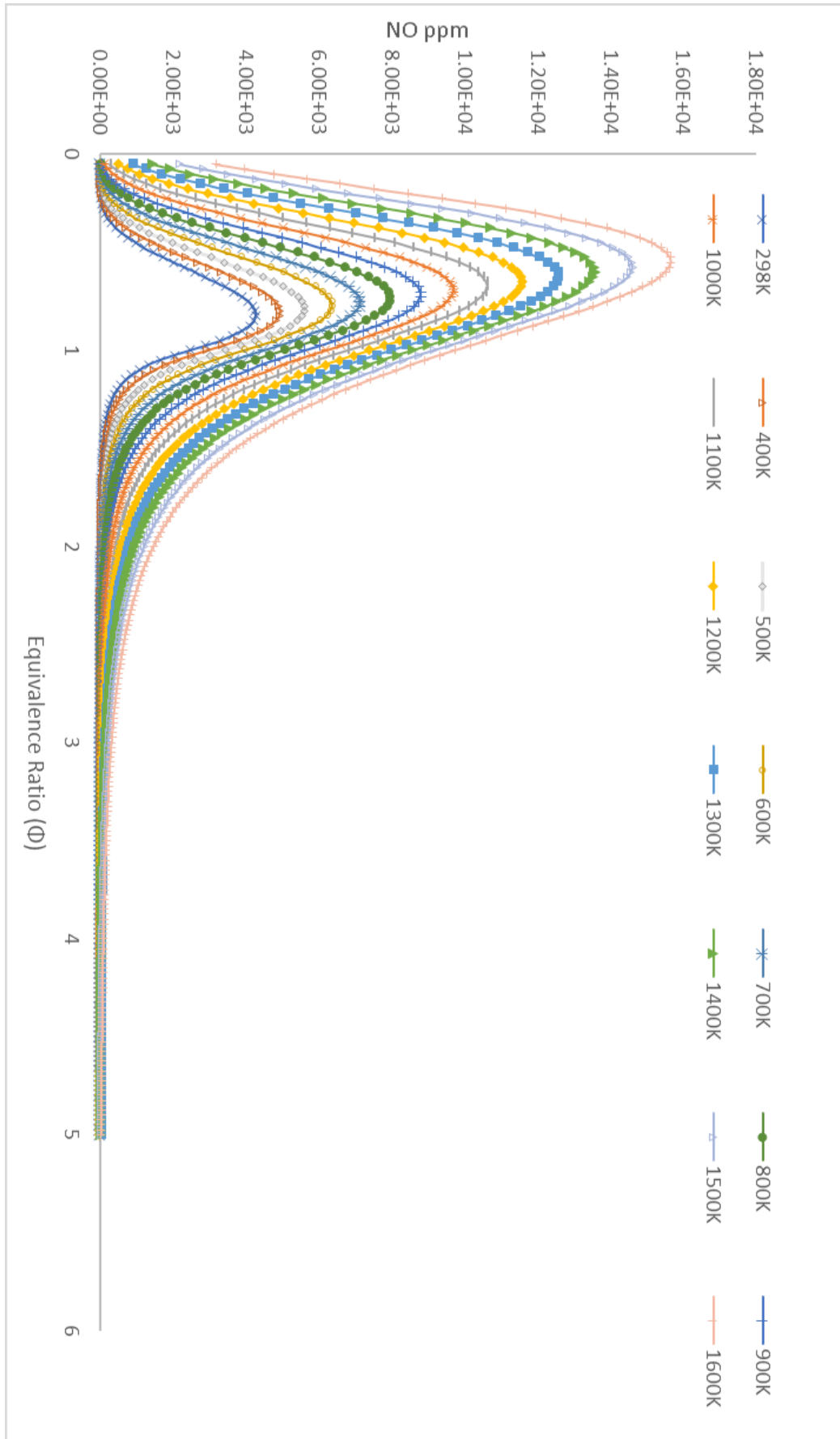


**Figure C-2.** Exhaust NO ppm for pure H<sub>2</sub>/air mixture (inlet temperatures 298-1600K)

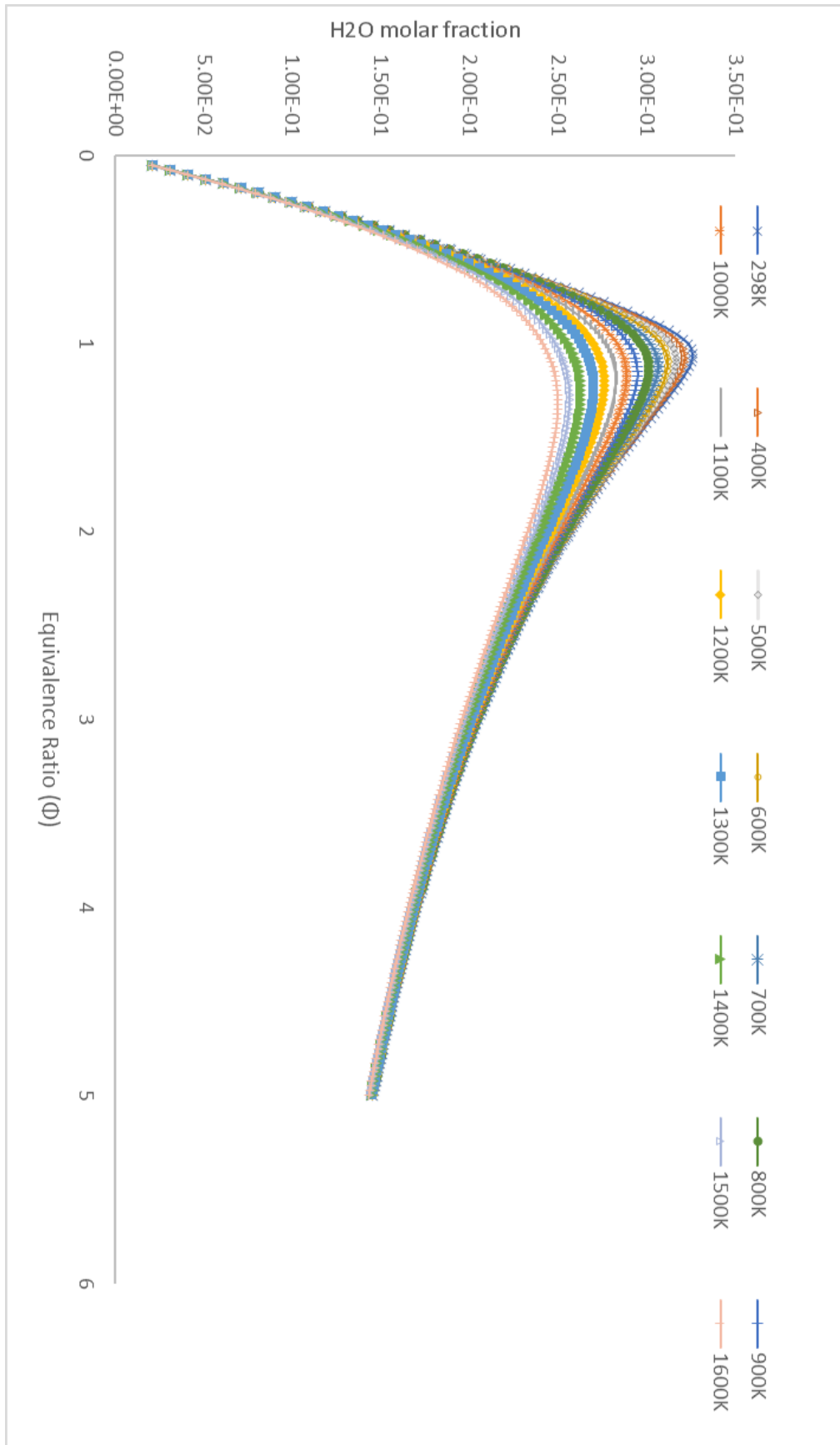


**Figure C-3.** Exhaust H<sub>2</sub>O molar fraction for pure H<sub>2</sub>/air mixture (inlet temperatures 298-1600K)

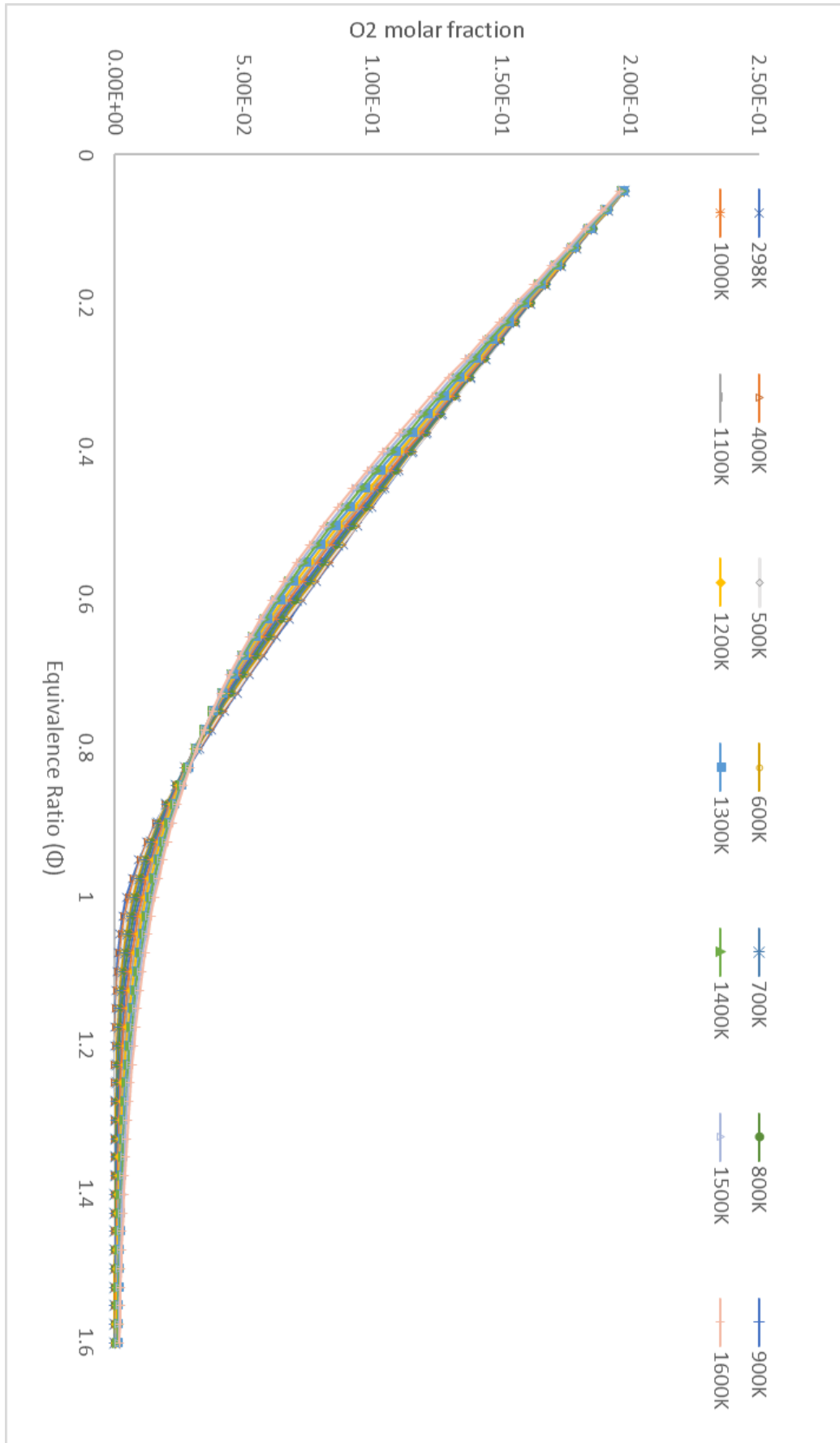


**Figure C-4.** Exhaust O<sub>2</sub> molar fraction for pure H<sub>2</sub>/air mixture (inlet temperatures 298-1600K)

### APPENDIX D.

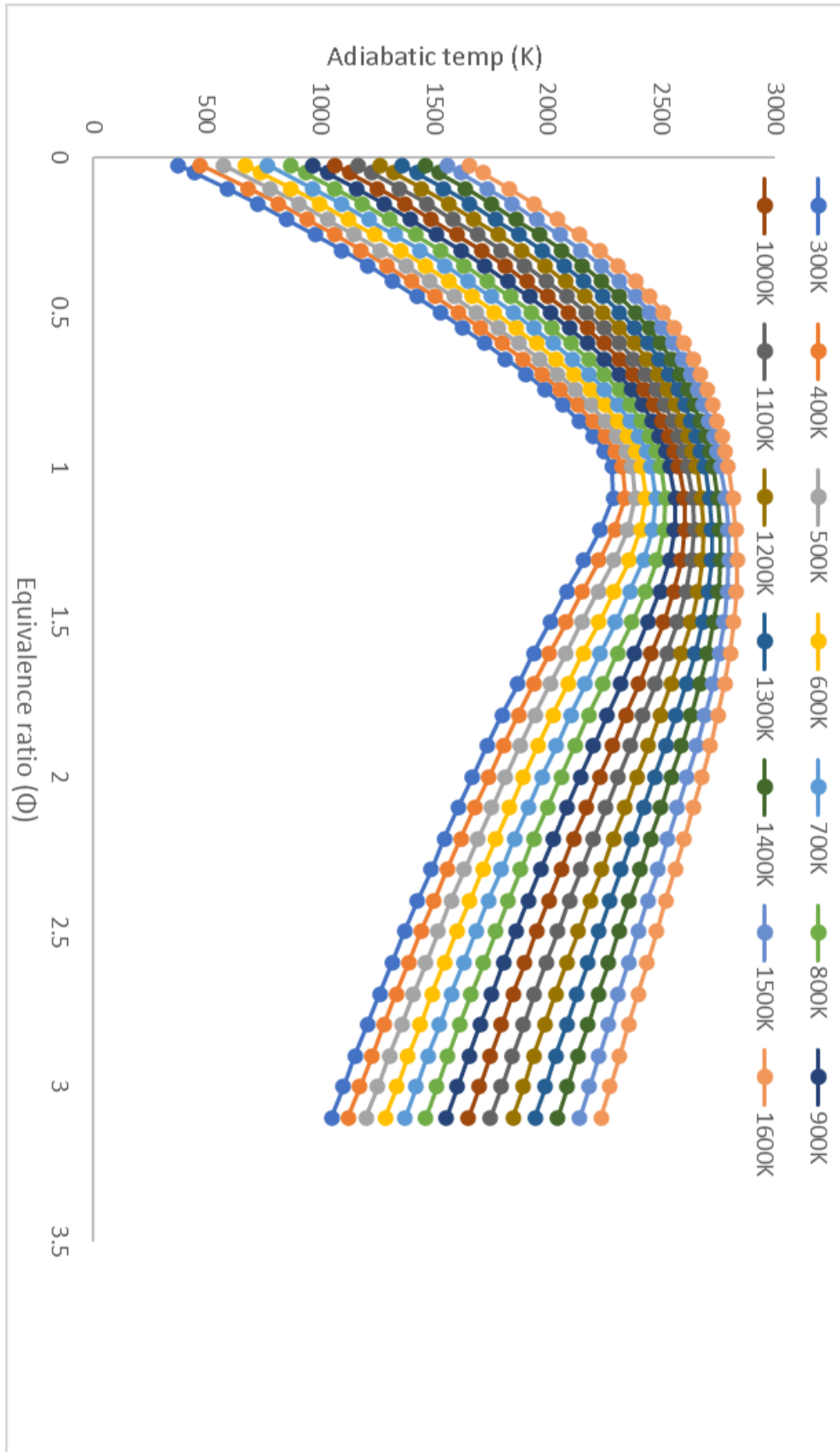


**Figure D-1.** Adiabatic flame temperature for biodiesel/air mixture (inlet temperatures 300-1600K)

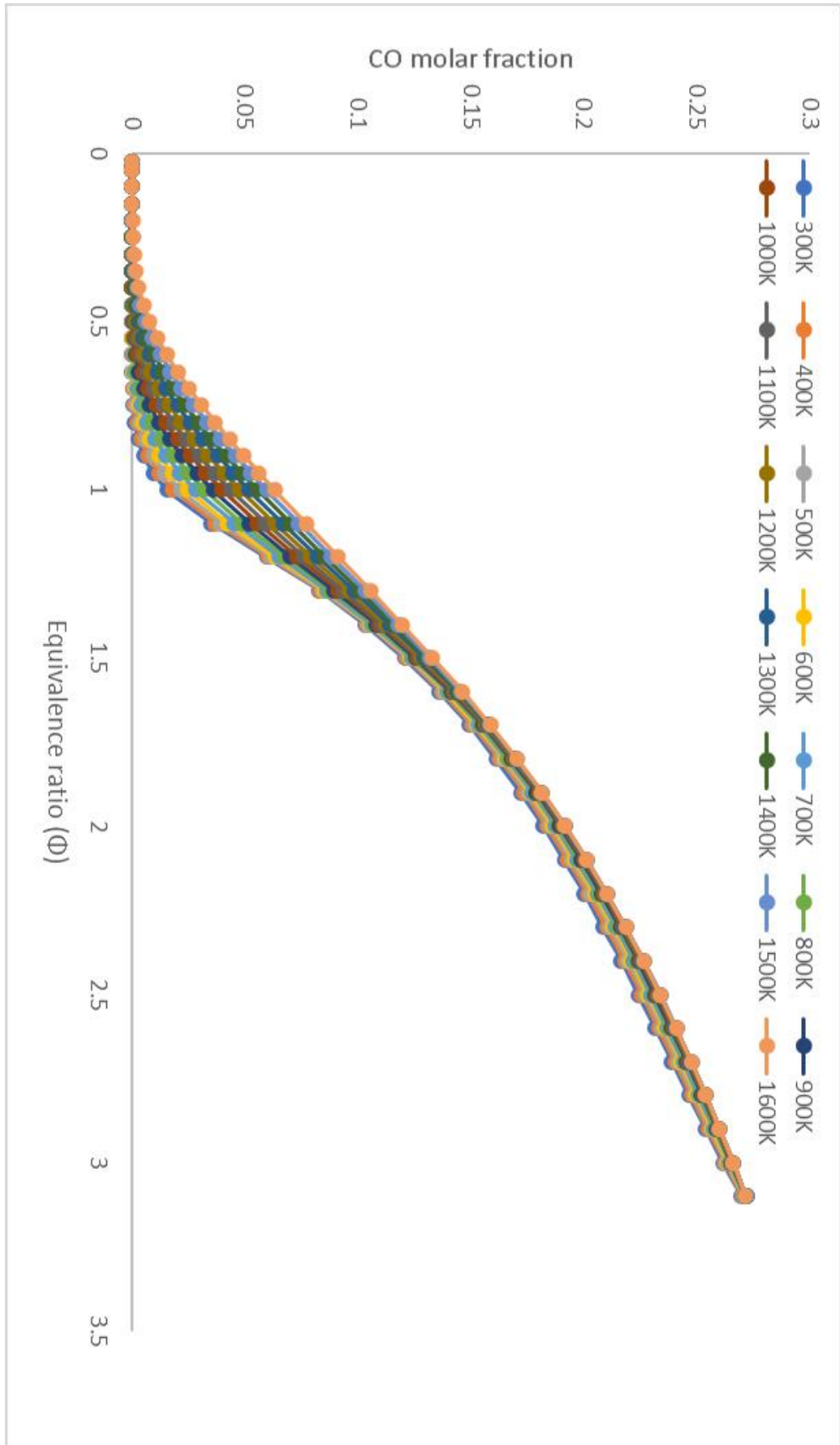


**Figure D-2.** Exhaust CO molar fraction for biodiesel/air mixture (inlet temperatures 300-1600K)

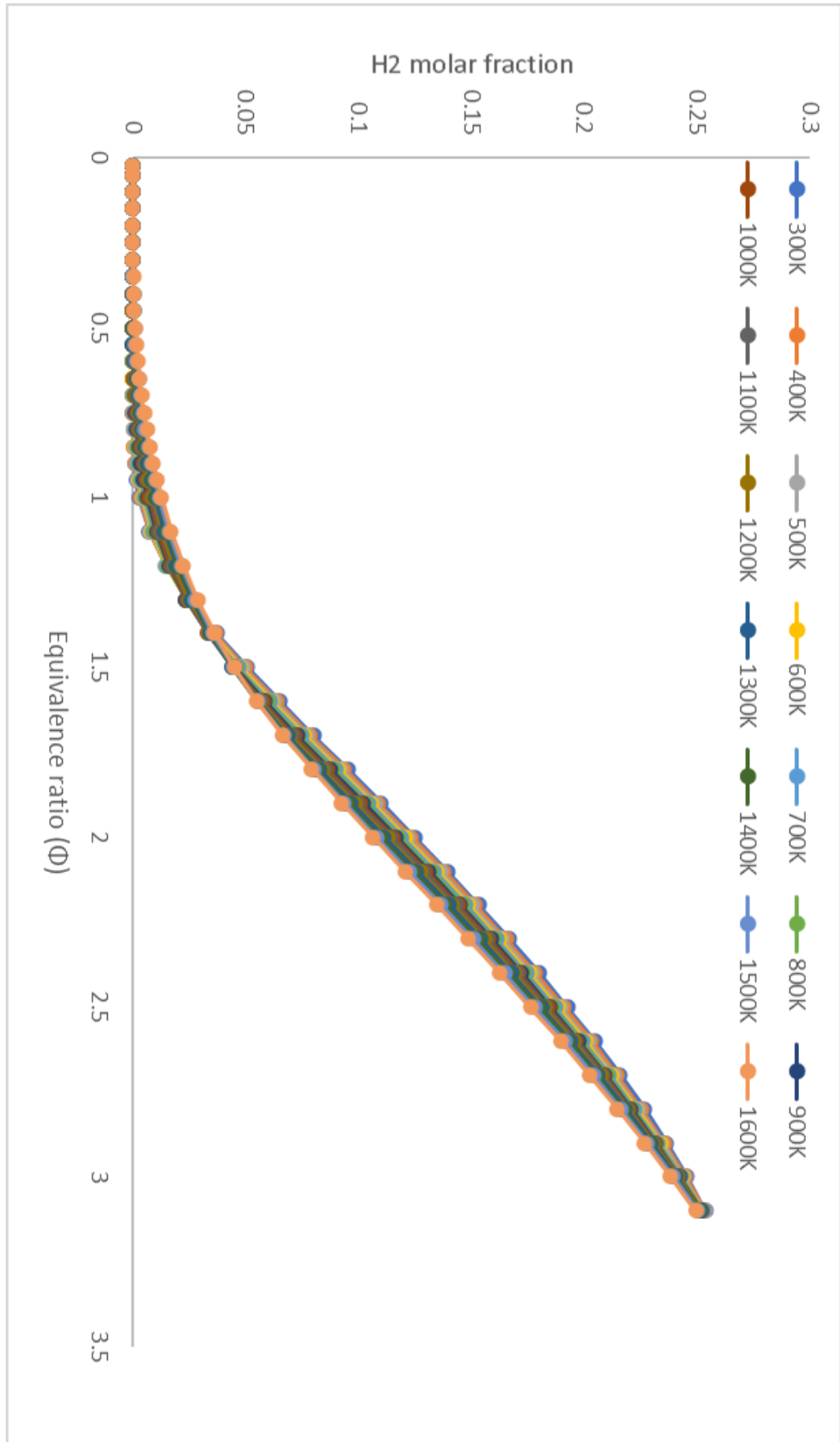


**Figure D-3.** Exhaust H<sub>2</sub> molar fraction for CH<sub>1.88</sub>O<sub>0.11</sub>/air mixture (inlet temperatures 300-1600K)

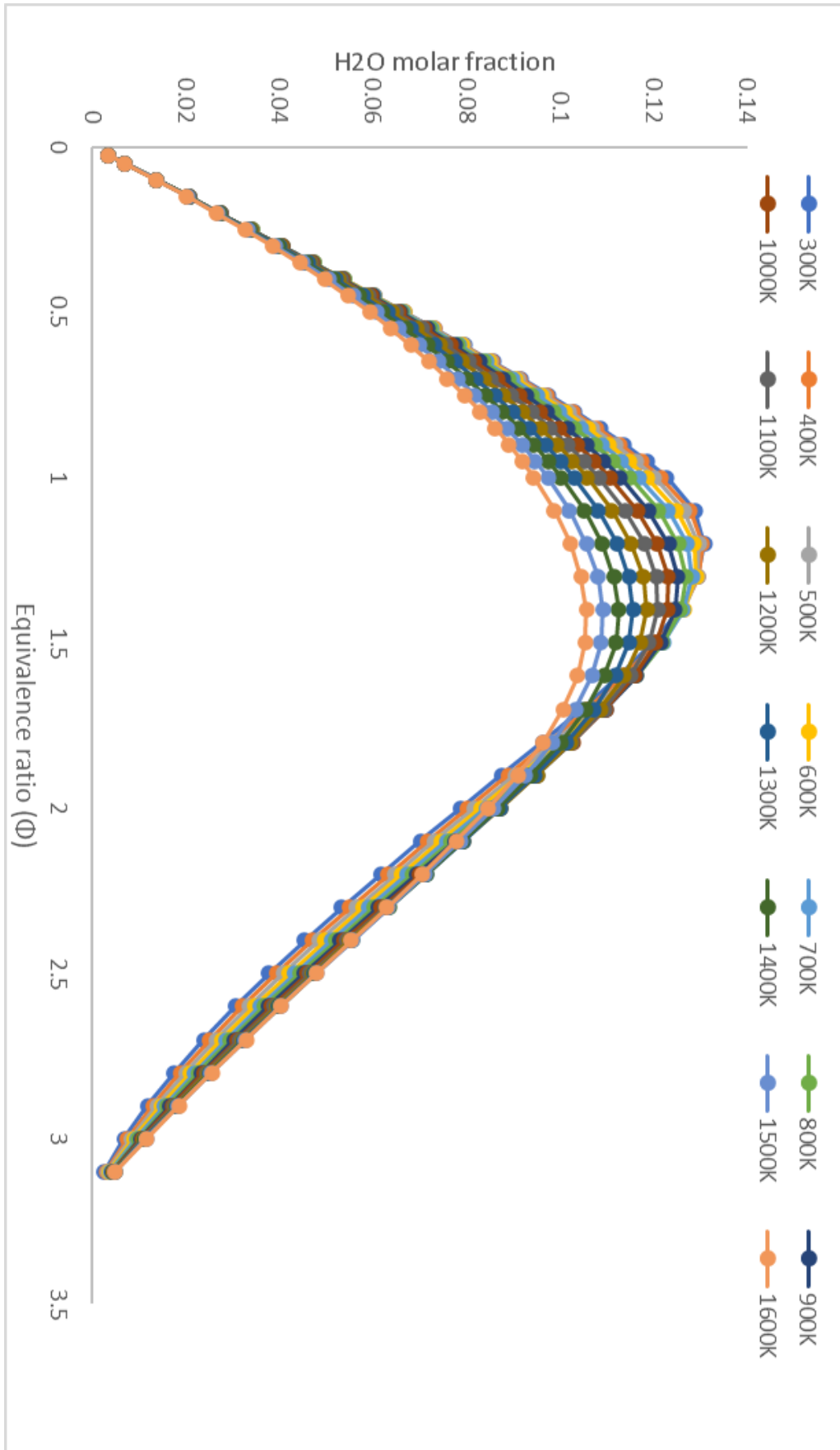


**Figure D-4.** Exhaust H<sub>2</sub>O molar fraction for CH<sub>1.88</sub>O<sub>0.11</sub>/air mixture (inlet temperatures 300-1600K)

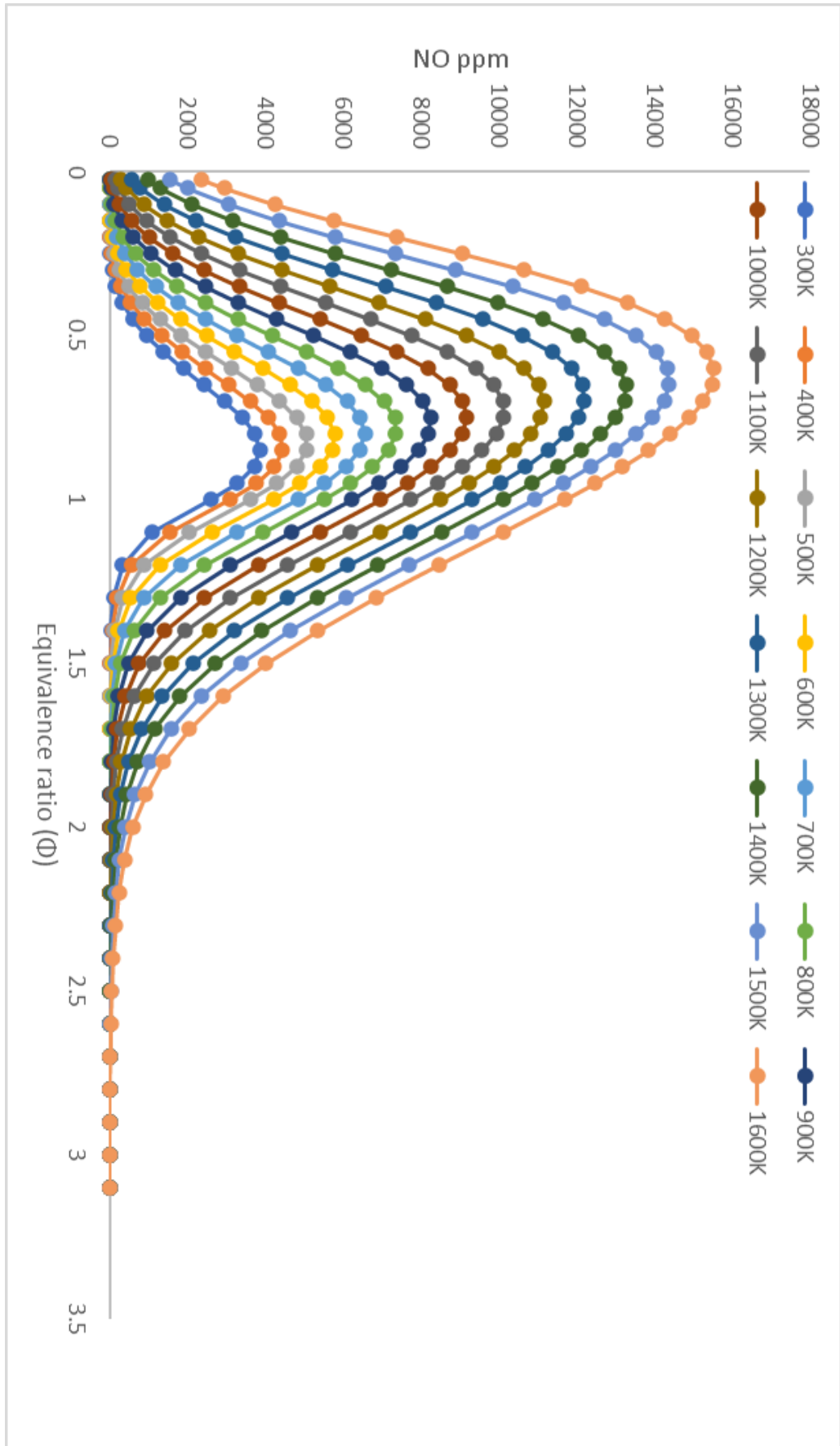


**Figure D-5.** Exhaust NO ppm for CH1.8800.11/air mixture (inlet temperatures 300-1600K)

APPENDIX E.

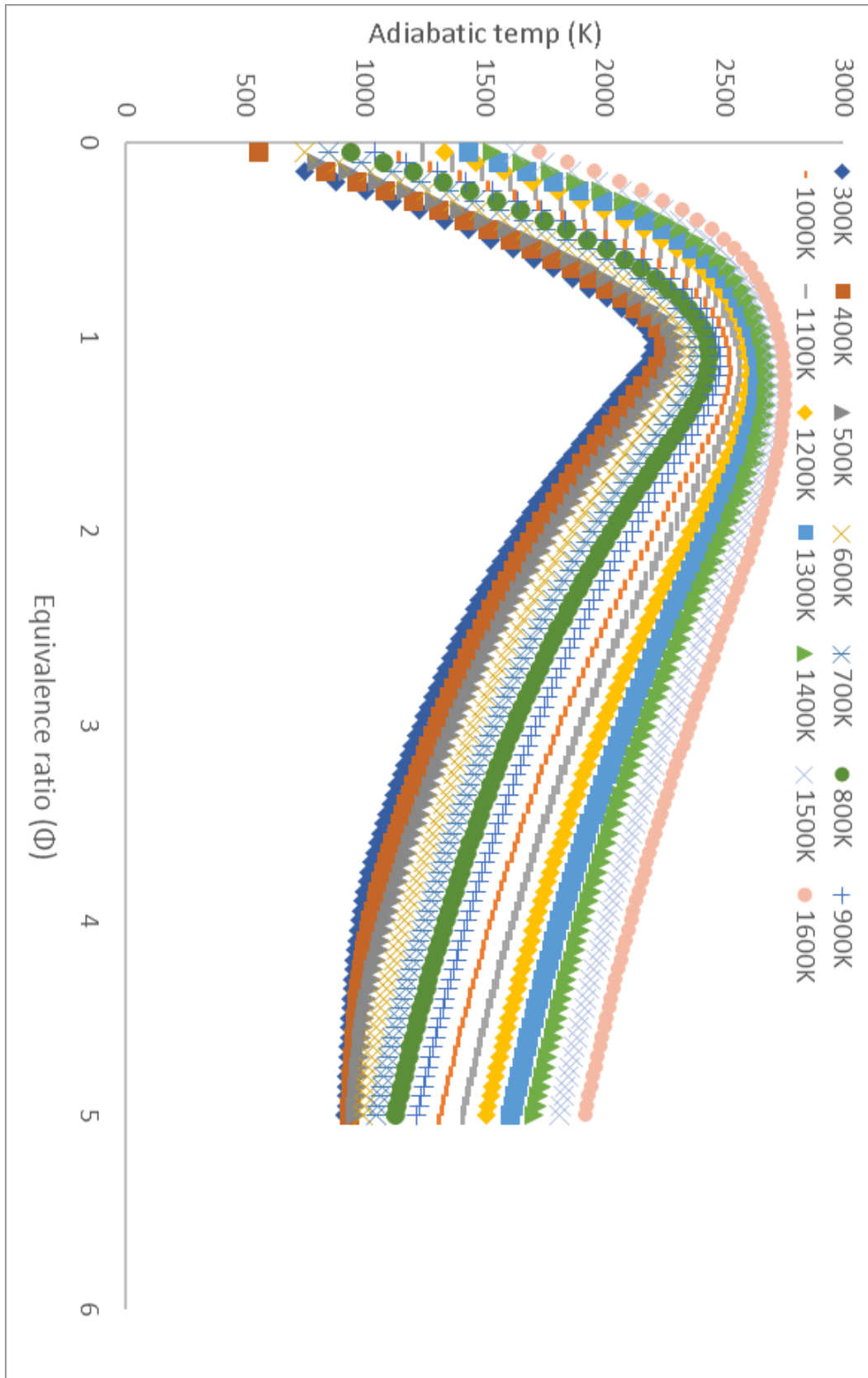
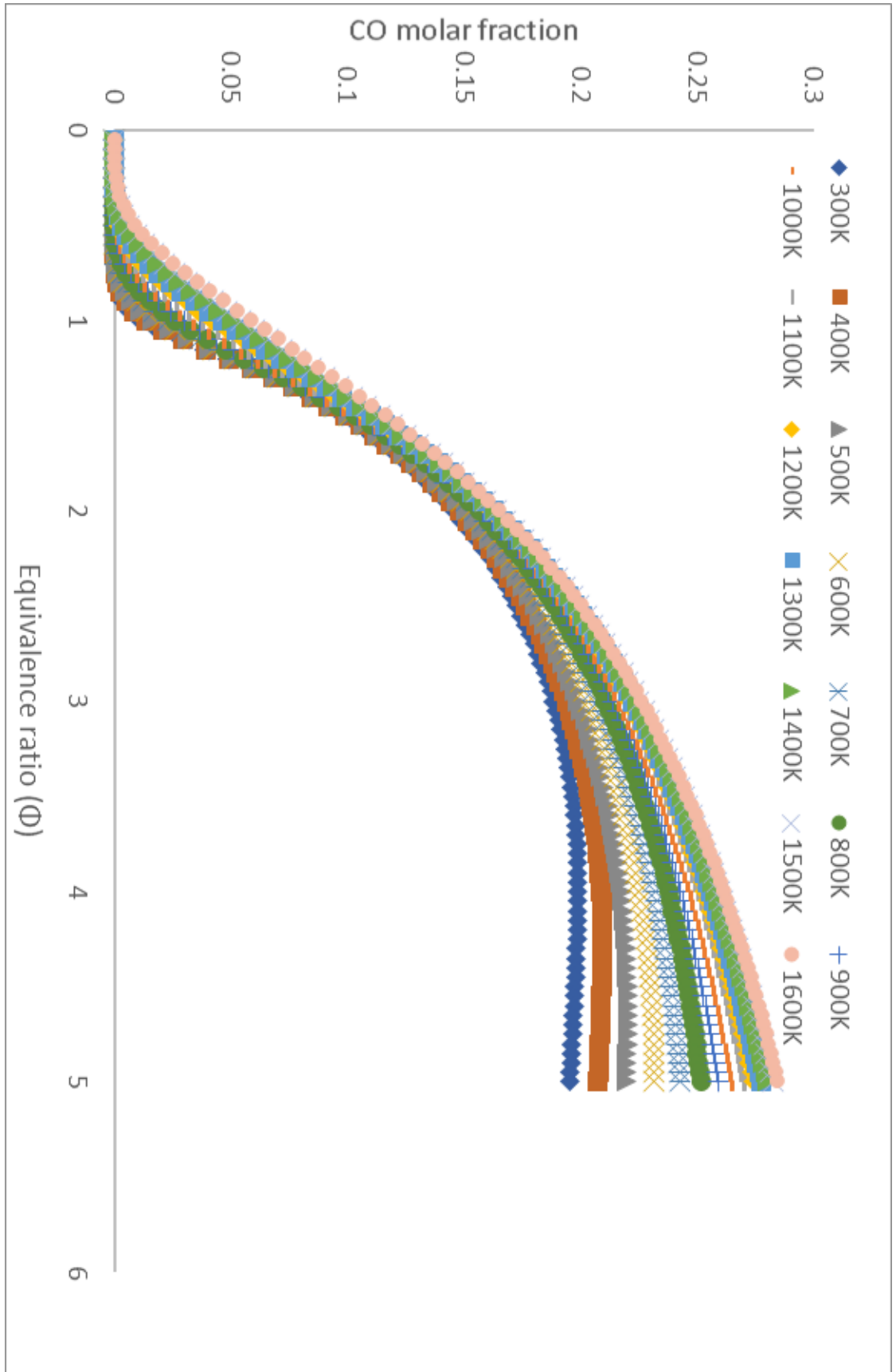
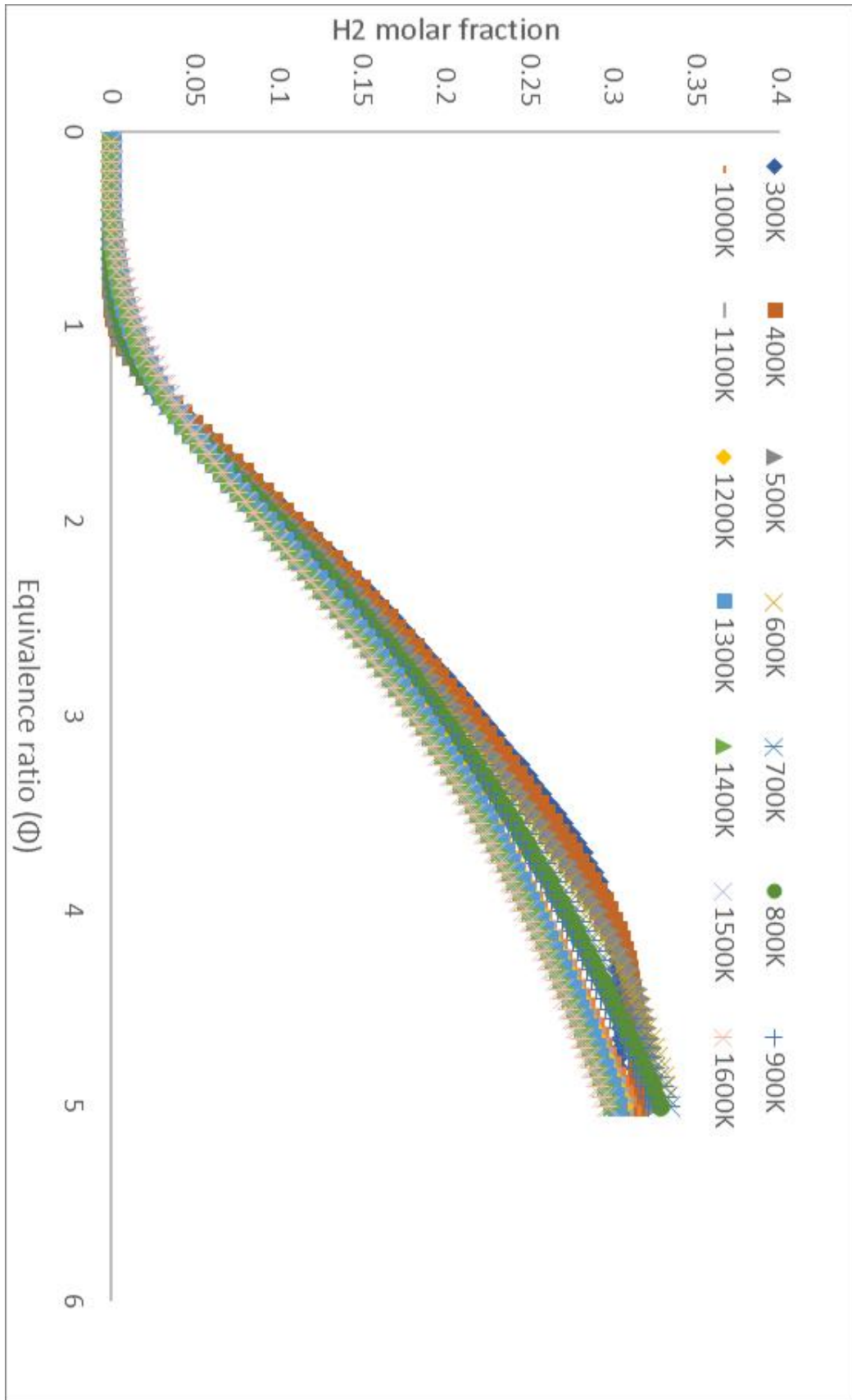


Figure E-1. Adiabatic flame temperature for pure glycerol/air mixture(inlet temperatures 300-1600K)



**Figure E-2.** Exhaust CO molar fraction for pure glycerol/air mixture (inlet temperatures 300-1600K)



**Figure E-3.** Exhaust H<sub>2</sub> molar fraction for pure glycerol/air mixture (inlet temperatures 300-1600K)

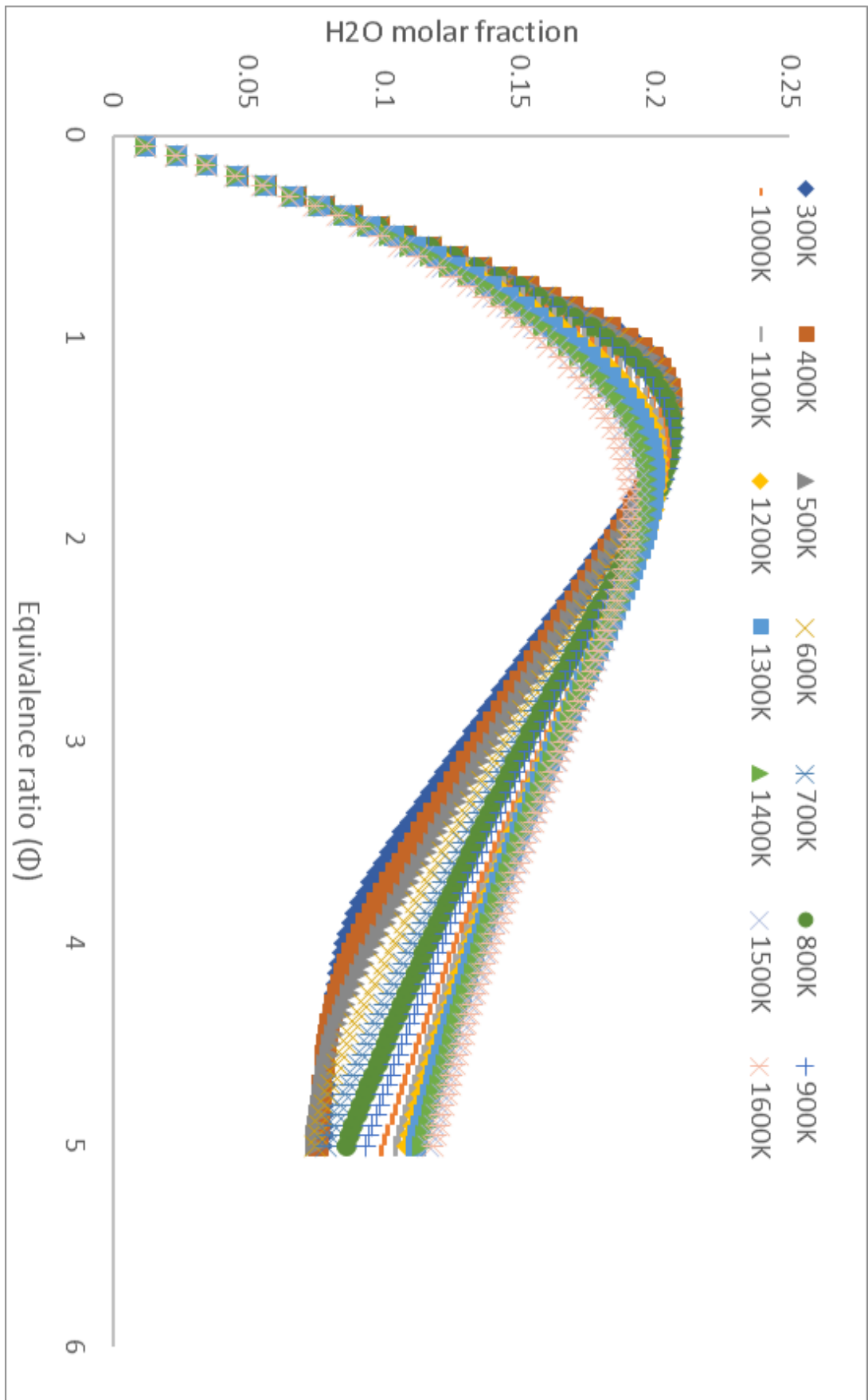


**Figure E-4.** Exhaust H<sub>2</sub>O ppm for pure glycerol/air mixture (inlet temperatures 300-1600K)

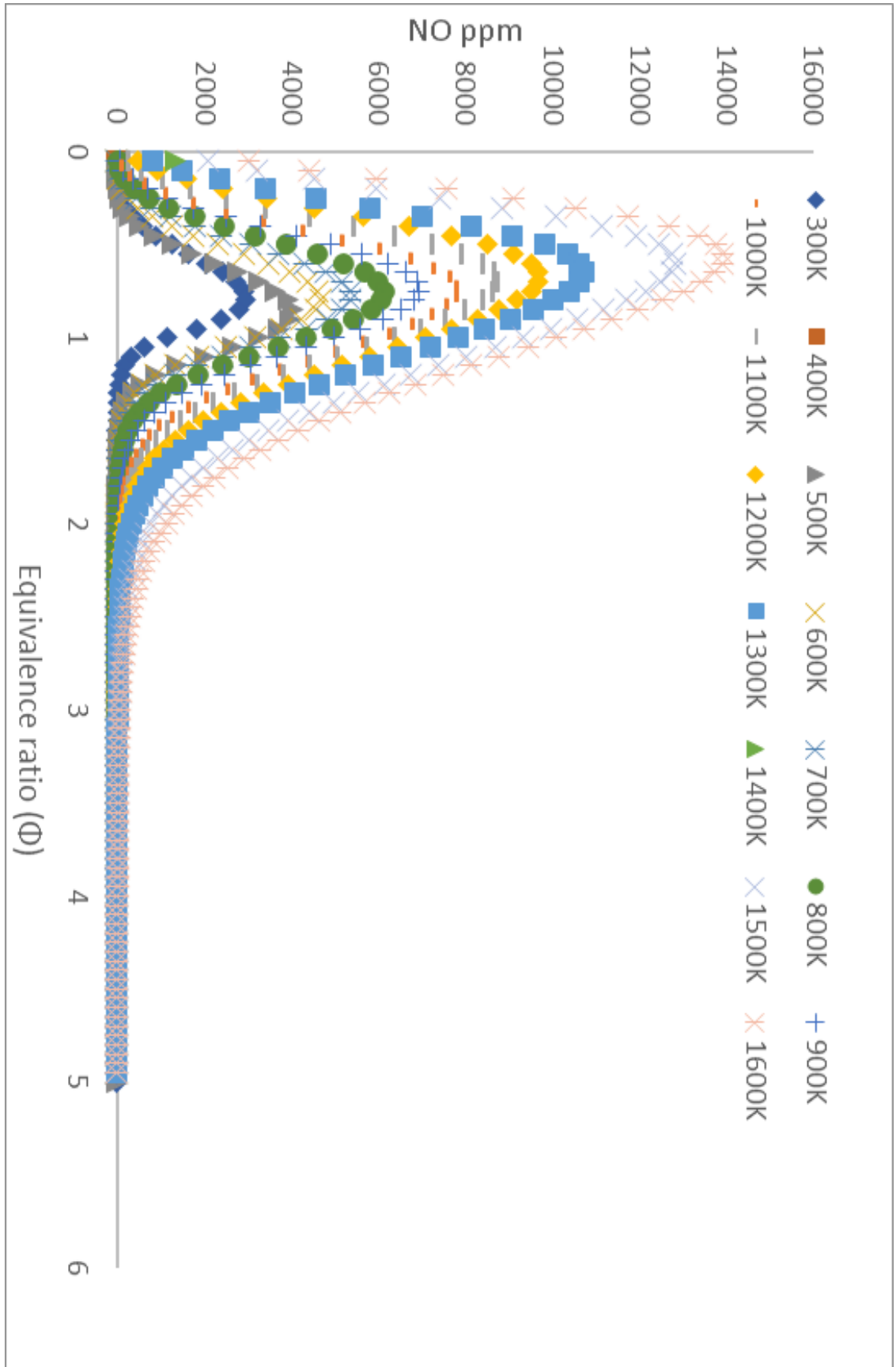


**Figure E-5.** Exhaust NO ppm for pure glycerol/air mixture (inlet temperatures 300-1600K)

### APPENDIX F.

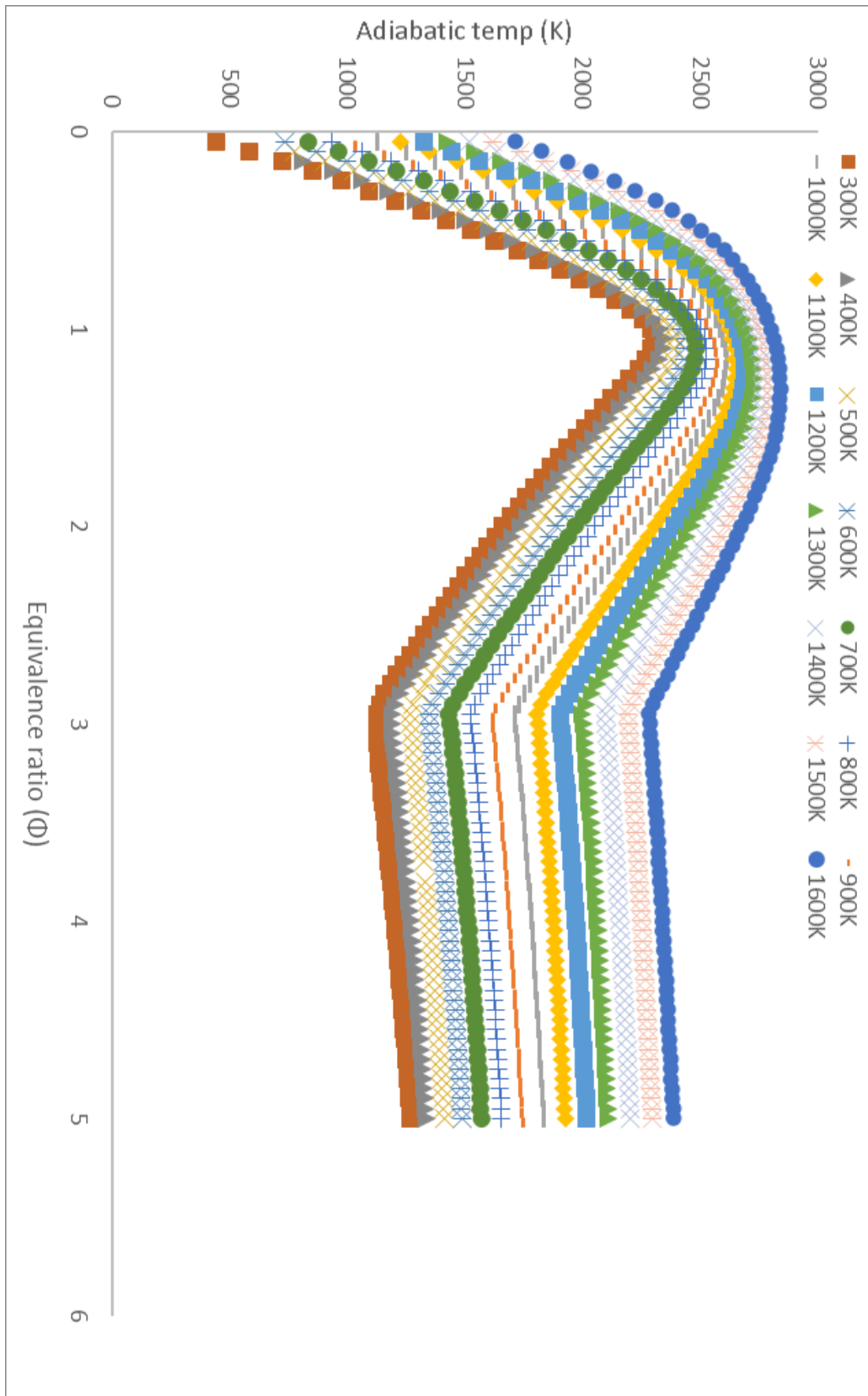


**Figure F-1.** Adiabatic flame temperature for European diesel composition/air mixture (inlet temperatures 300-1600K)

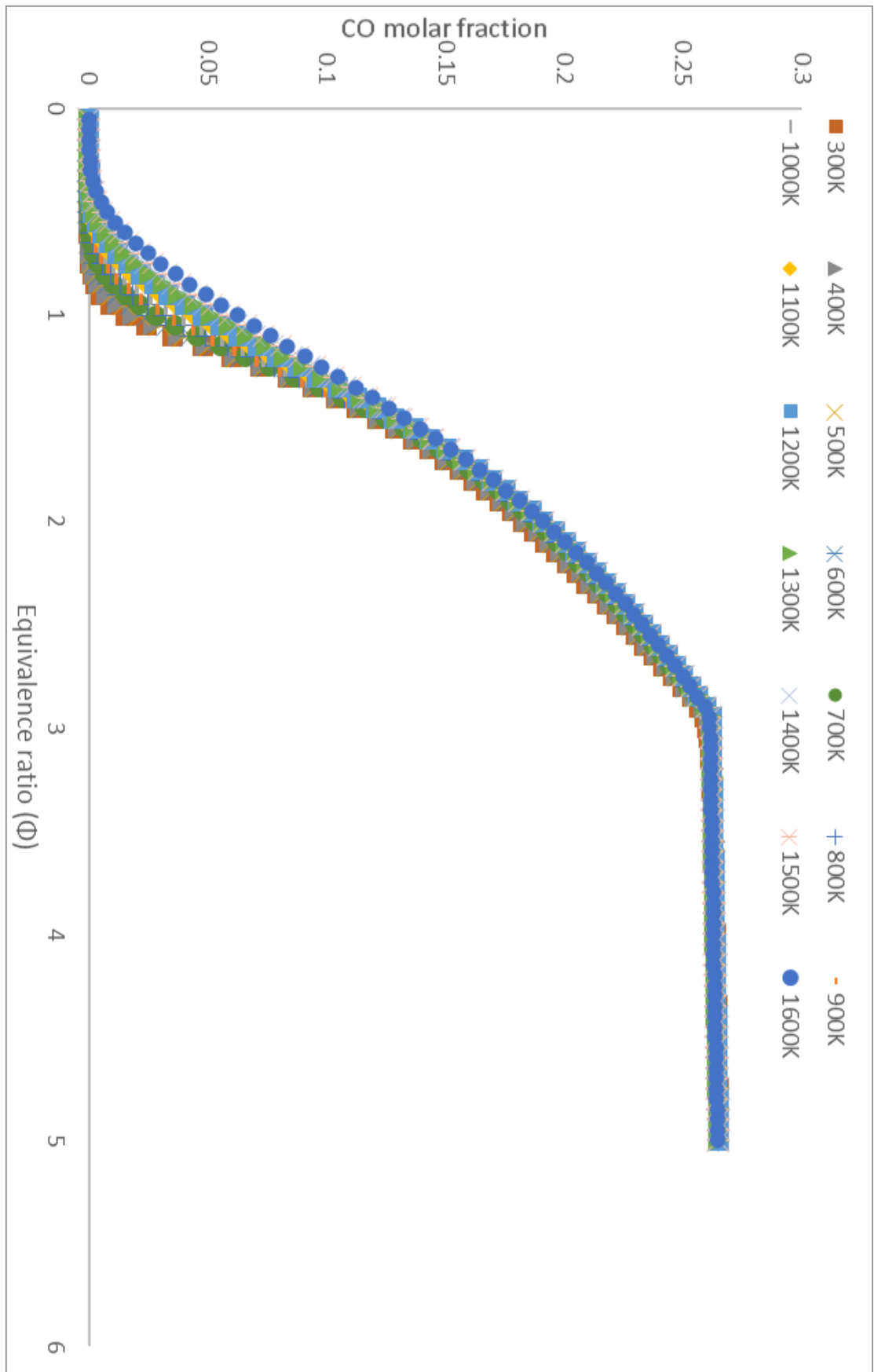


**Figure F-2.** Exhaust CO molar fraction for European diesel composition/air mixture (inlet temperatures 300-1600K)

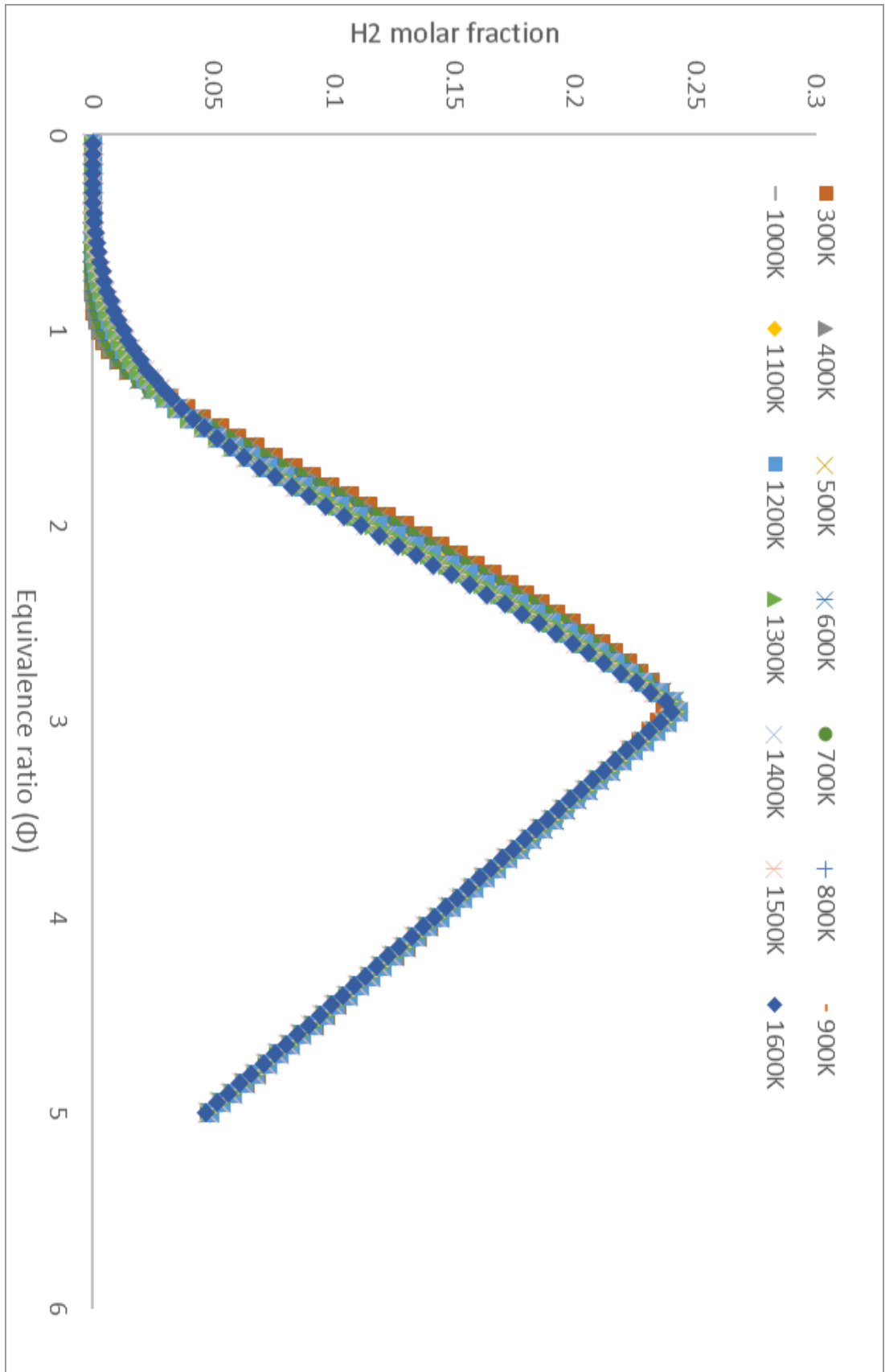


**Figure F-3.** Exhaust H<sub>2</sub> molar fraction for European diesel composition/air mixture (inlet temperatures 300-1600K)

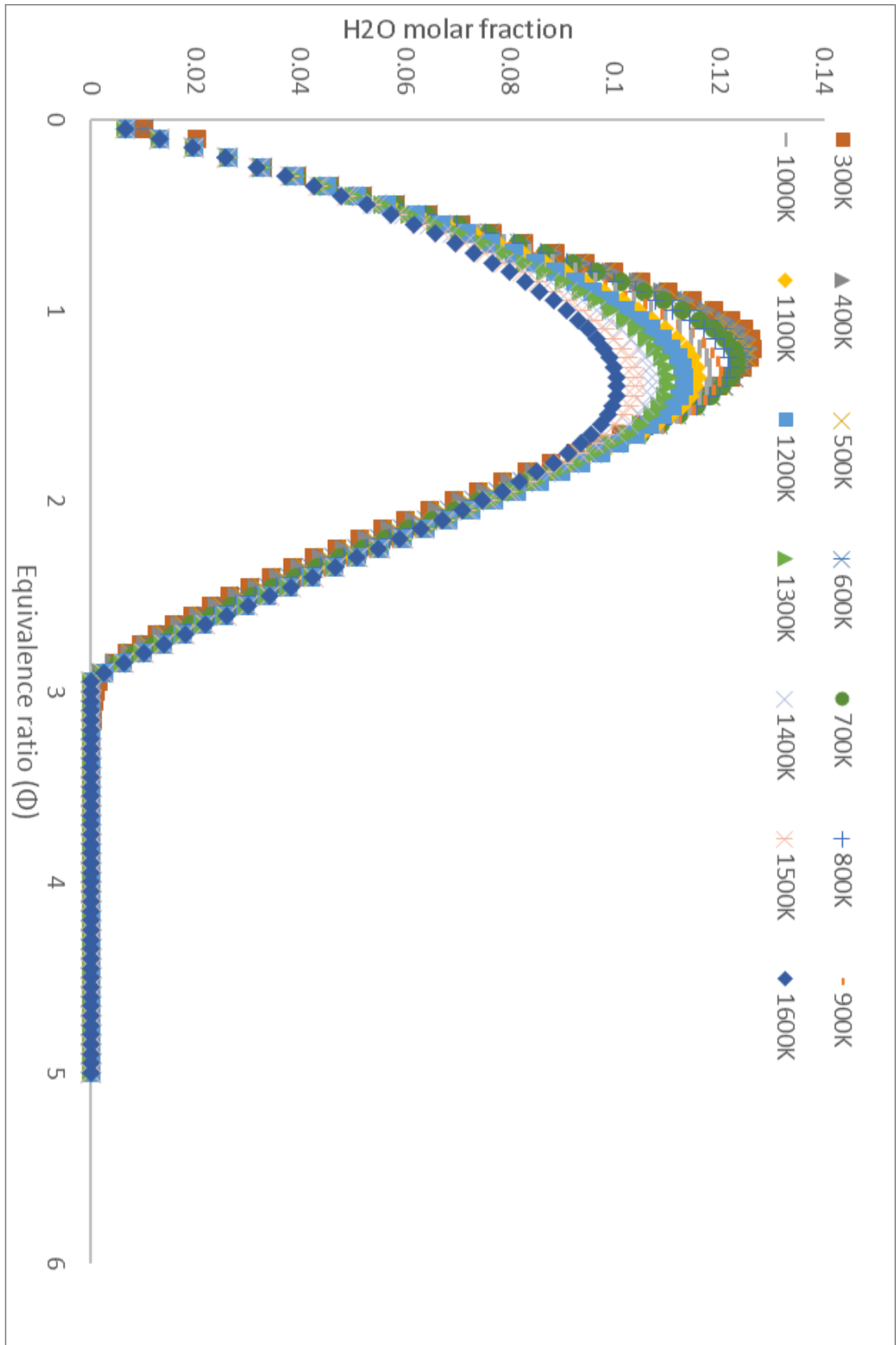


**Figure F-4.** Exhaust H<sub>2</sub>O molar fraction for European diesel composition/air mixture (inlet temperatures 300-1600K)

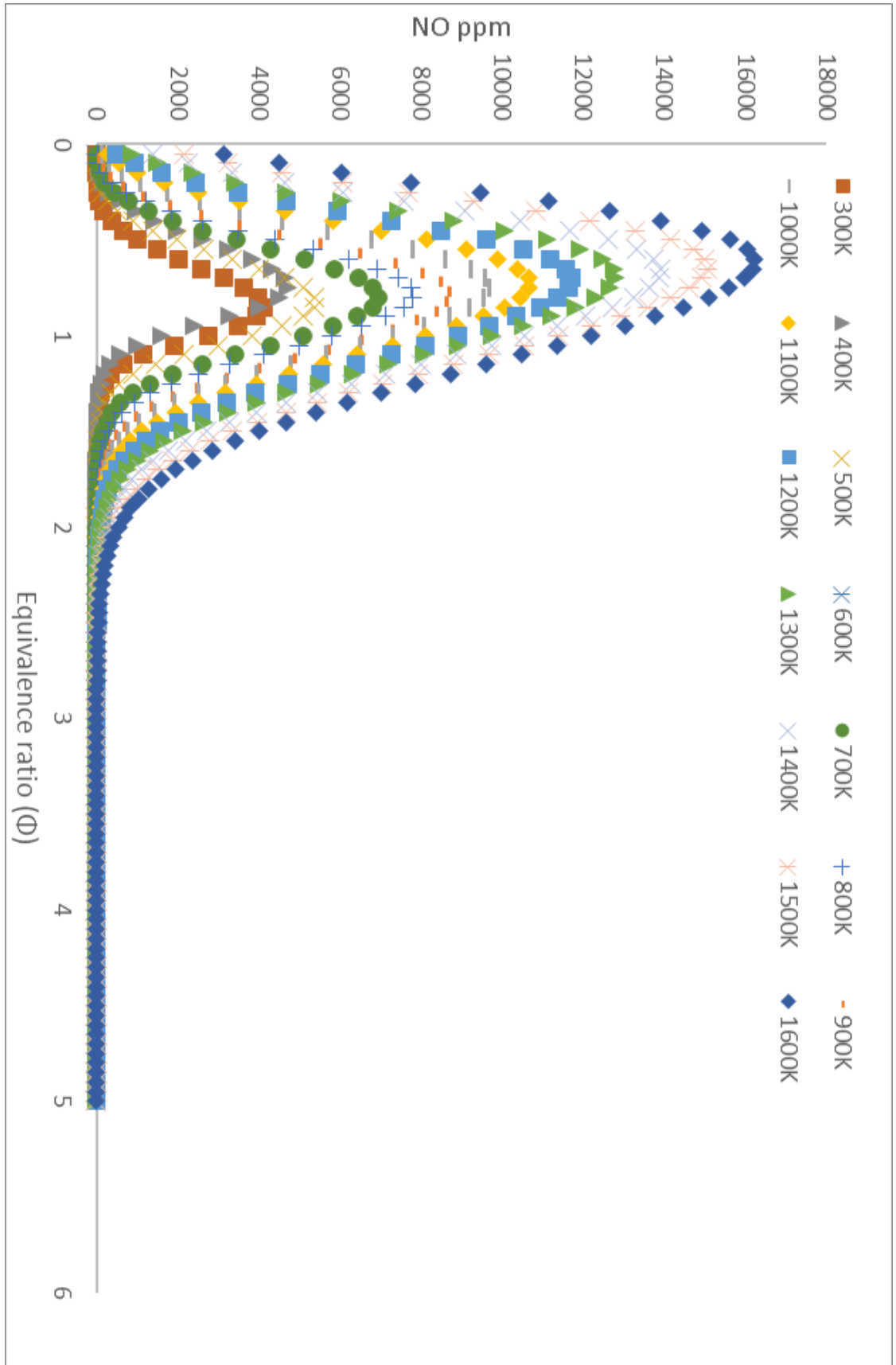


**Figure F-5.** Exhaust NO ppm for European diesel composition/air mixture (inlet temperatures 300-1600K)

### APPENDIX G.

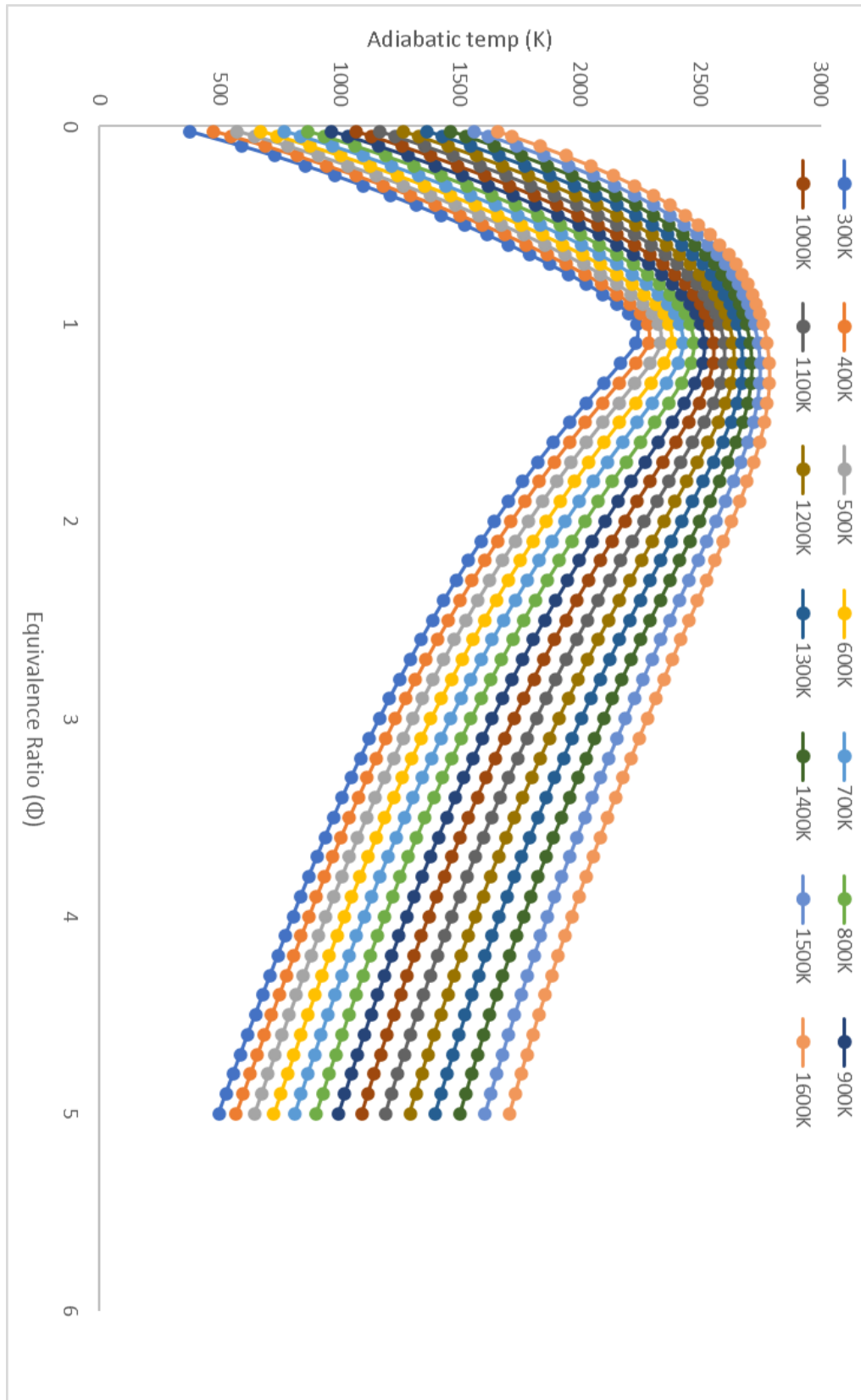


**Figure G-1.** Adiabatic flame temperature for pure ethanol/air mixture (inlet temperatures 300-1600K)

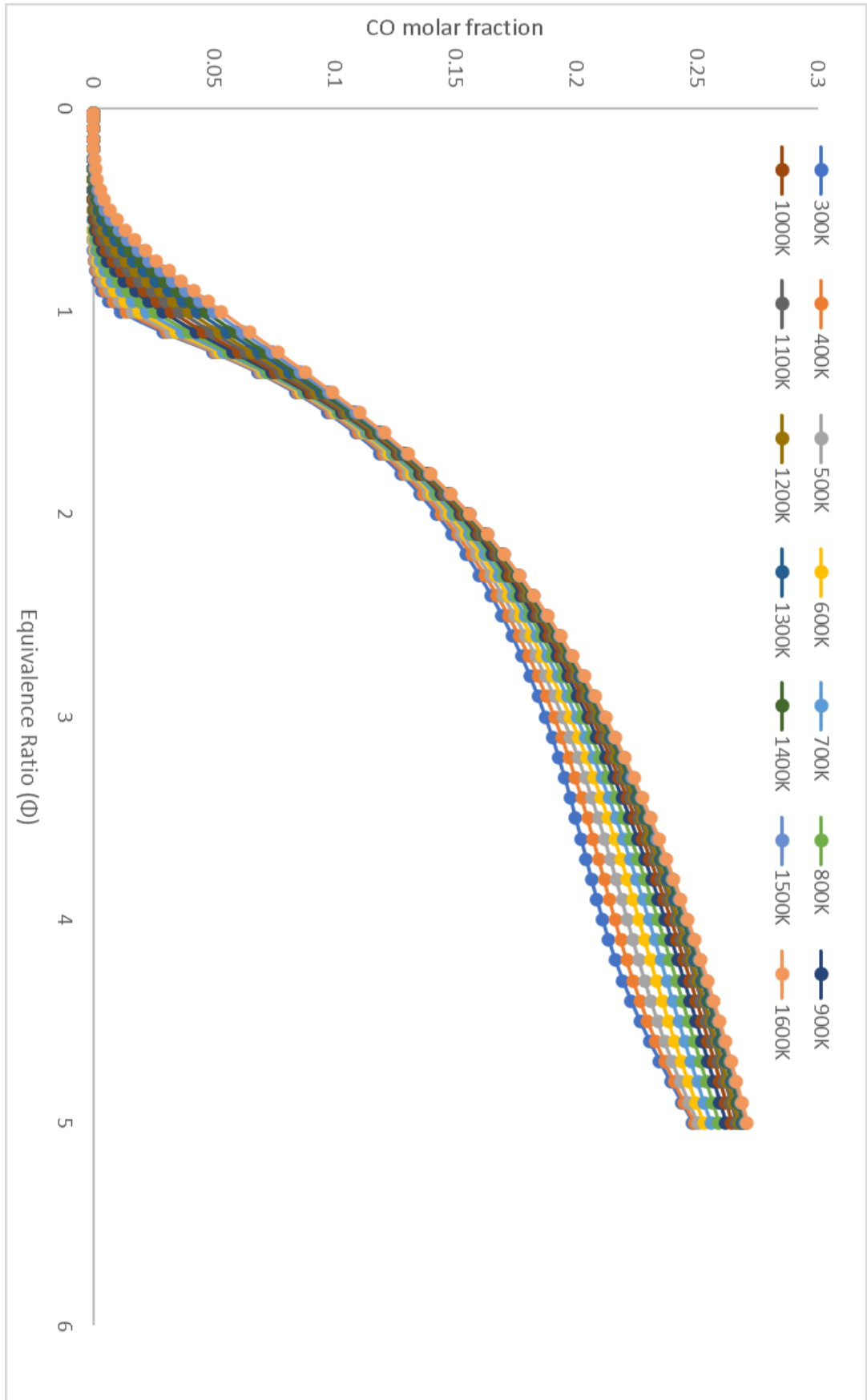


**Figure G-2.** Exhaust CO molar fraction for pure ethanol/air mixture (inlet temperatures 300-1600K)

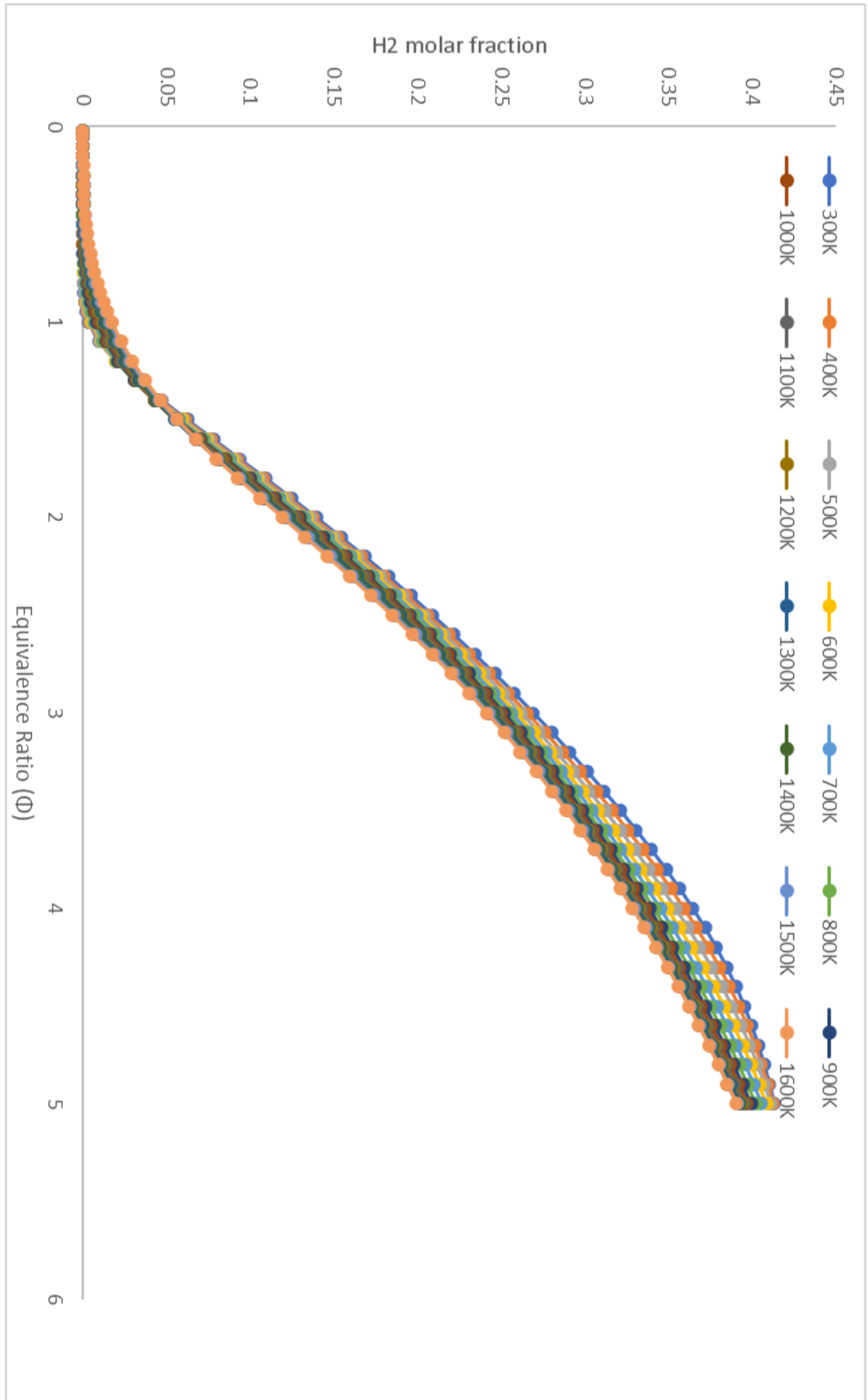


**Figure G-3.** Exhaust H<sub>2</sub> molar fraction for pure ethanol/air mixture (inlet temperatures 300-1600K)

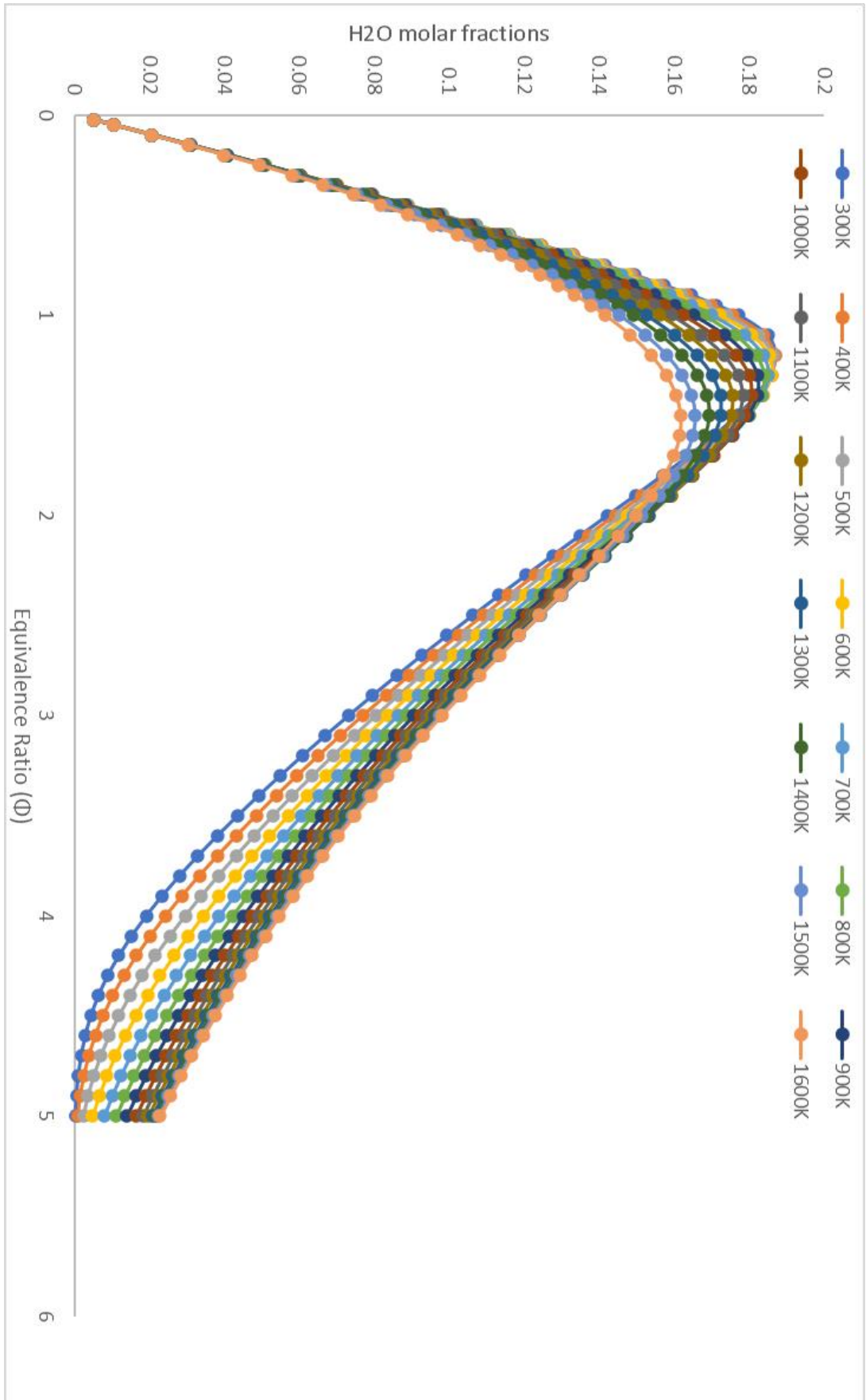


**Figure G-4.** Exhaust H<sub>2</sub>O molar fraction for pure ethanol/air mixture (inlet temperatures 300-1600K)

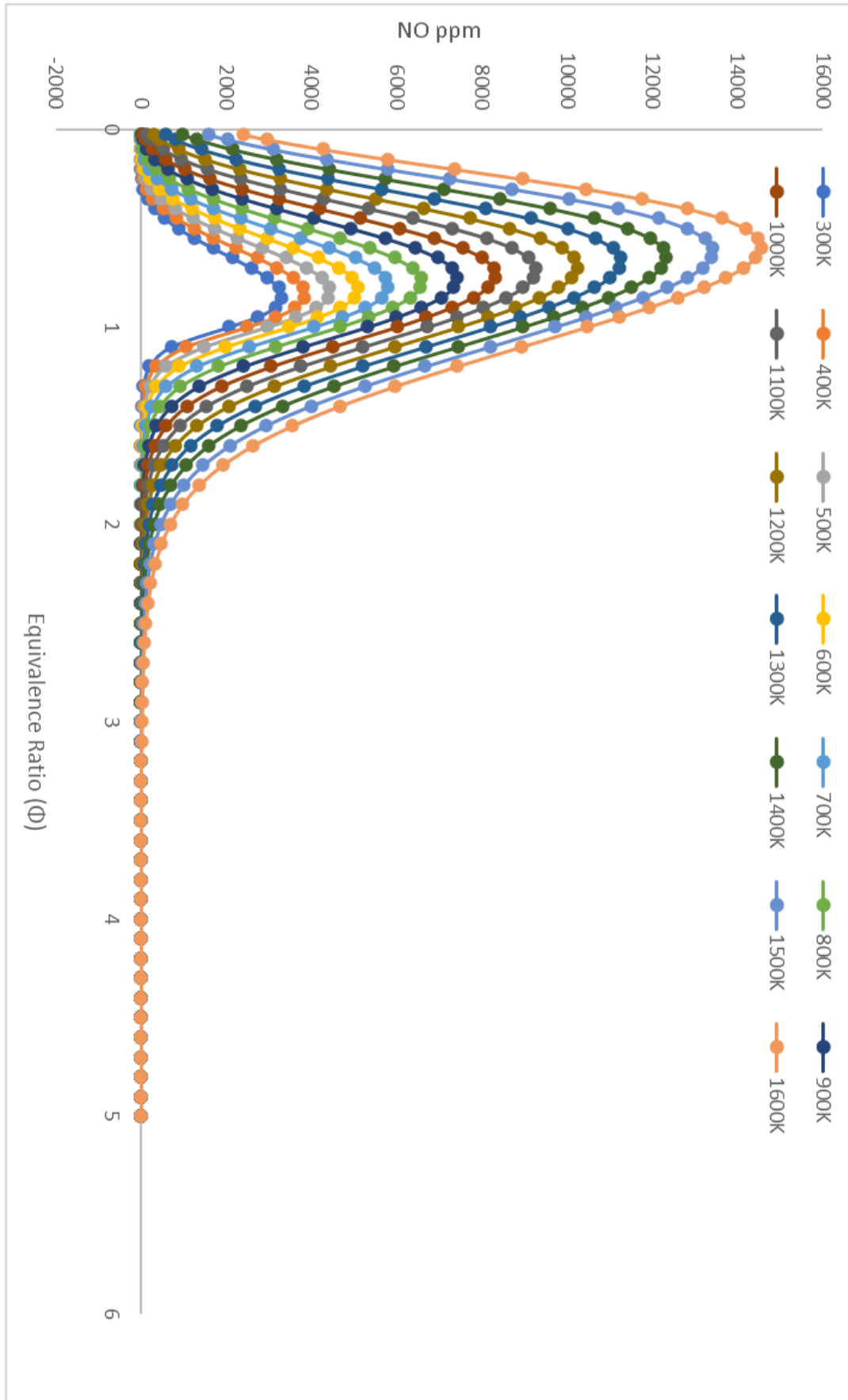


**Figure G-5.** Exhaust NO ppm for pure ethanol/air mixture (inlet temperatures 300-1600K)

## APPENDIX H.

### H.1 Detailed Mechanism developed by Peters for propane/air combustion

units(length='cm', time='s', quantity='mol', act\_energy='J/mol')

```
ideal_gas(name='gas',
  elements="O H C N",
  species="C3H8 C3H3 O H OH
  CO H2 O2 H2O HO2
  H2O2 CH CH2 CH3 CH4
  C2H C2H2 C2H3 C2H4 C2H5
  C2H6 C3H6 I*C3H7 N*C3H7 CO2
  HCO CH2O C2HO C3H4 C3H5
  N2",
  reactions='all',
  transport='Mix',
  initial_state=state(temperature=300.0, pressure=OneAtm))
```

```
#-----
# Species data
#-----
```

```
species(name='C3H8',
  atoms='H:8 C:3',
  thermo=(NASA([300.00, 1000.00],
    [8.96920800E-01, 2.66898610E-02, 5.43142510E-06,
    -2.12600070E-08, 9.24333010E-12, -1.39549180E+04,
    1.93553310E+01]),
    NASA([1000.00, 5000.00],
    [7.52521710E+00, 1.88903400E-02, -6.28392440E-06,
    9.17937280E-10, -4.81240990E-14, -1.64645470E+04,
    -1.78439030E+01])),
  transport=gas_transport(geom='nonlinear',
    diam=4.992,
    well_depth=268.5,
    rot_relax=1.0),
  note='L4/80')
```

```
species(name='C3H3',
  atoms='H:3 C:3',
  thermo=(NASA([300.00, 1000.00],
    [3.09084080E+00, 1.35495820E-02, 2.72535330E-06,
    -1.43631850E-08, 7.19814100E-12, 3.73565440E+04,
    8.49168900E+00]),
    NASA([1000.00, 5000.00],
    [5.74697260E+00, 9.61553130E-03, -3.80514910E-06,
    6.89939070E-10, -4.65615970E-14, 3.65299310E+04,
    -5.86345020E+00])),
  transport=gas_transport(geom='linear',
    diam=4.76,
    well_depth=252.0,
    rot_relax=1.0))
```

```
species(name='O',
  atoms='O:1',
  thermo=(NASA([300.00, 1000.00],
    [2.94642870E+00, -1.63816650E-03, 2.42103160E-06,
    -1.60284320E-09, 3.89069640E-13, 2.91476440E+04,
```

```
        2.96399490E+00]],
NASA([1000.00, 5000.00],
 [ 2.54205960E+00, -2.75506190E-05, -3.10280330E-09,
   4.55106740E-12, -4.36805150E-16, 2.92308030E+04,
   4.92030800E+00])),
transport=gas_transport(geom='atom',
  diam=2.75,
  well_depth=80.0),
note='J6/62')

species(name='H',
  atoms='H:1',
  thermo=(NASA([300.00, 1000.00],
    [ 2.50000000E+00, 0.00000000E+00, 0.00000000E+00,
      0.00000000E+00, 0.00000000E+00, 2.54716270E+04,
      -4.60117620E-01]),
    NASA([1000.00, 5000.00],
      [ 2.50000000E+00, 0.00000000E+00, 0.00000000E+00,
        0.00000000E+00, 0.00000000E+00, 2.54716270E+04,
        -4.60117630E-01])),
  transport=gas_transport(geom='atom',
    diam=2.05,
    well_depth=145.0),
  note='J9/65')

species(name='OH',
  atoms='H:1 O:1',
  thermo=(NASA([300.00, 1000.00],
    [ 3.83655180E+00, -1.07020140E-03, 9.48497570E-07,
      2.08435750E-10, -2.33842650E-13, 3.67158070E+03,
      4.98054560E-01]),
    NASA([1000.00, 5000.00],
      [ 2.91312300E+00, 9.54182480E-04, -1.90843250E-07,
        1.27307950E-11, 2.48039410E-16, 3.96470600E+03,
        5.42887350E+00])),
  transport=gas_transport(geom='linear',
    diam=2.75,
    well_depth=80.0),
  note='J12/70')

species(name='CO',
  atoms='C:1 O:1',
  thermo=(NASA([300.00, 1000.00],
    [ 3.71009280E+00, -1.61909640E-03, 3.69235940E-06,
      -2.03196740E-09, 2.39533440E-13, -1.43563100E+04,
      2.95553510E+00]),
    NASA([1000.00, 5000.00],
      [ 2.98406960E+00, 1.48913900E-03, -5.78996840E-07,
        1.03645770E-10, -6.93535500E-15, -1.42452280E+04,
        6.34791560E+00])),
  transport=gas_transport(geom='linear',
    diam=3.631,
    well_depth=104.2,
    polar=1.95,
    rot_relax=1.8),
  note='J9/65')

species(name='H2',
  atoms='H:2',
  thermo=(NASA([300.00, 1000.00],
```

```
[ 3.05744510E+00, 2.67652000E-03, -5.80991620E-06,
 5.52103910E-09, -1.81227390E-12, -9.88904740E+02,
-2.29970560E+00]],
NASA([1000.00, 5000.00],
 [ 3.10019010E+00, 5.11194640E-04, 5.26442100E-08,
-3.49099730E-11, 3.69453450E-15, -8.77380420E+02,
-1.96294210E+00])),
transport=gas_transport(geom='linear',
  diam=2.69,
  well_depth=99.5,
  polar=0.79,
  rot_relax=280.0),
note='J3/61')

species(name='O2',
  atoms='O:2',
  thermo=(NASA([300.00, 1000.00],
    [ 3.62559850E+00, -1.87821840E-03, 7.05545440E-06,
    -6.76351370E-09, 2.15559930E-12, -1.04752260E+03,
    4.30527780E+00]),
    NASA([1000.00, 5000.00],
    [ 3.62195350E+00, 7.36182640E-04, -1.96522280E-07,
    3.62015580E-11, -2.89456270E-15, -1.20198250E+03,
    3.61509600E+00])),
  transport=gas_transport(geom='linear',
    diam=3.382,
    well_depth=126.3,
    polar=1.6,
    rot_relax=3.8),
  note='J9/65')

species(name='H2O',
  atoms='H:2 O:1',
  thermo=(NASA([300.00, 1000.00],
    [ 4.07012750E+00, -1.10844990E-03, 4.15211800E-06,
    -2.96374040E-09, 8.07021030E-13, -3.02797220E+04,
    -3.22700460E-01]),
    NASA([1000.00, 5000.00],
    [ 2.71676330E+00, 2.94513740E-03, -8.02243740E-07,
    1.02266820E-10, -4.84721450E-15, -2.99058260E+04,
    6.63056710E+00])),
  transport=gas_transport(geom='nonlinear',
    diam=2.884,
    well_depth=583.7,
    rot_relax=4.0),
  note='J3/61')

species(name='HO2',
  atoms='H:1 O:2',
  thermo=(NASA([298.00, 1000.00],
    [ 3.24114920E+00, 3.16546230E-03, 7.38710180E-07,
    -2.36525110E-09, 9.52097990E-13, -8.58022400E+02,
    8.11793900E+00]),
    NASA([1000.00, 6000.00],
    [ 4.09799720E+00, 2.08482290E-03, -5.02545790E-07,
    5.41347180E-11, -2.23966310E-15, -1.17477800E+03,
    3.33242700E+00])),
  transport=gas_transport(geom='nonlinear',
    diam=3.458,
    well_depth=107.4,
```

rot\_relax=3.8))

```
species(name='H2O2',
  atoms='H:2 O:2',
  thermo=(NASA([300.00, 1000.00],
    [ 3.38875360E+00, 6.56922600E-03, -1.48501260E-07,
      -4.62580550E-09, 2.47151470E-12, -1.76631470E+04,
      6.78536310E+00]),
    NASA([1000.00, 5000.00],
      [ 4.57316670E+00, 4.33613630E-03, -1.47468880E-06,
        2.34890370E-10, -1.43165360E-14, -1.80069610E+04,
        5.01136960E-01])),
  transport=gas_transport(geom='nonlinear',
    diam=3.458,
    well_depth=107.4,
    rot_relax=3.8),
  note='L2/69')
```

```
species(name='CH',
  atoms='H:1 C:1',
  thermo=(NASA([300.00, 1000.00],
    [ 3.56327520E+00, -2.00313720E-04, -4.01298140E-07,
      1.82269220E-09, -8.67683110E-13, 7.04055060E+04,
      1.76280230E+00]),
    NASA([1000.00, 5000.00],
      [ 2.26731160E+00, 2.20430000E-03, -6.22501910E-07,
        6.96899400E-11, -2.12749520E-15, 7.08380370E+04,
        8.78893520E+00])),
  transport=gas_transport(geom='linear',
    diam=2.75,
    well_depth=80.0),
  note='J12/67')
```

```
species(name='CH2',
  atoms='H:2 C:1',
  thermo=(NASA([300.00, 1000.00],
    [ 3.58833470E+00, 2.17241370E-03, -1.33234080E-06,
      1.94694450E-09, -8.94313940E-13, 4.53151880E+04,
      2.26278690E+00]),
    NASA([1000.00, 5000.00],
      [ 2.75254790E+00, 3.97820470E-03, -1.49217310E-06,
        2.59568990E-10, -1.71106730E-14, 4.55477590E+04,
        6.65347990E+00])),
  transport=gas_transport(geom='nonlinear',
    diam=3.8,
    well_depth=144.0,
    rot_relax=13.0),
  note='J12/72')
```

```
species(name='CH3',
  atoms='H:3 C:1',
  thermo=(NASA([300.00, 1000.00],
    [ 3.46663500E+00, 3.83018450E-03, 1.01168020E-06,
      -1.88592360E-09, 6.68031820E-13, 1.63131040E+04,
      2.41721920E+00]),
    NASA([1000.00, 5000.00],
      [ 2.84003270E+00, 6.08690860E-03, -2.17403380E-06,
        3.60425760E-10, -2.27253000E-14, 1.64498130E+04,
        5.50567510E+00])),
  transport=gas_transport(geom='nonlinear',
```

diam=3.8,  
well\_depth=144.0,  
rot\_relax=13.0),  
note='J6/69')

species(name='CH4',  
atoms='H:4 C:1',  
thermo=(NASA([300.00, 1000.00],  
[ 3.82619320E+00, -3.97945810E-03, 2.45583400E-05,  
-2.27329260E-08, 6.96269570E-12, -1.01449500E+04,  
8.66900730E-01])),  
NASA([1000.00, 5000.00],  
[ 1.50270720E+00, 1.04167980E-02, -3.91815220E-06,  
6.77778990E-10, -4.42837060E-14, -9.97870780E+03,  
1.07071430E+01])),  
transport=gas\_transport(geom='nonlinear',  
diam=3.721,  
well\_depth=161.35,  
rot\_relax=13.0),  
note='J3/61')

species(name='C2H',  
atoms='H:1 C:2',  
thermo=(NASA([300.00, 1000.00],  
[ 2.40767980E+00, 1.01745310E-02, -1.38365310E-05,  
1.04764140E-08, -3.07593920E-12, 6.28164740E+04,  
8.71704100E+00])),  
NASA([1000.00, 5000.00],  
[ 4.56483940E+00, 2.00594610E-03, -4.93484810E-07,  
7.42849010E-11, -5.43096100E-15, 6.22823560E+04,  
-1.98727810E+00])),  
transport=gas\_transport(geom='linear',  
diam=4.1,  
well\_depth=209.0,  
rot\_relax=2.5))

species(name='C2H2',  
atoms='H:2 C:2',  
thermo=(NASA([300.00, 1000.00],  
[ 1.41027680E+00, 1.90572750E-02, -2.45013900E-05,  
1.63908720E-08, -4.13454470E-12, 2.61882080E+04,  
1.13938270E+01])),  
NASA([1000.00, 5000.00],  
[ 4.57510830E+00, 5.12383580E-03, -1.74523540E-06,  
2.86730650E-10, -1.79514260E-14, 2.56074280E+04,  
-3.57379400E+00])),  
transport=gas\_transport(geom='linear',  
diam=4.08,  
well\_depth=218.8,  
rot\_relax=2.5),  
note='J3/61')

species(name='C2H3',  
atoms='H:3 C:2',  
thermo=(NASA([300.00, 1000.00],  
[ 2.96175990E+00, 8.92724780E-03, -7.53947640E-07,  
-2.84865170E-09, 1.18926010E-12, 3.23965540E+04,  
7.92748760E+00])),  
NASA([1000.00, 5000.00],  
[ 6.14009770E+00, 3.73770940E-03, -2.70317220E-07,

```
-1.53774190E-10, 2.19529530E-14, 3.12115170E+04,  
-9.68643400E+00]],  
transport=gas_transport(geom='nonlinear',  
    diam=4.1,  
    well_depth=209.0,  
    rot_relax=2.5))
```

```
species(name='C2H4',  
    atoms='H:4 C:2',  
    thermo=(NASA([300.00, 1000.00],  
        [1.42568210E+00, 1.13831400E-02, 7.98900060E-06,  
        -1.62536790E-08, 6.74912560E-12, 5.33707550E+03,  
        1.46218190E+01]),  
        NASA([1000.00, 5000.00],  
            [3.45521520E+00, 1.14918030E-02, -4.36517500E-06,  
            7.61550950E-10, -5.01232000E-14, 4.47731190E+03,  
            2.69879590E+00])),  
    transport=gas_transport(geom='nonlinear',  
        diam=4.081,  
        well_depth=244.8,  
        rot_relax=2.0),  
    note='J9/65')
```

```
species(name='C2H5',  
    atoms='H:5 C:2',  
    thermo=(NASA([300.00, 1000.00],  
        [2.91071870E+00, 9.26902150E-03, 9.04350510E-06,  
        -1.15359640E-08, 3.27956780E-12, 1.27389830E+04,  
        7.78620670E+00]),  
        NASA([1000.00, 5000.00],  
            [3.31212810E+00, 1.39507360E-02, -5.07431880E-06,  
            8.28573100E-10, -5.02697720E-14, 1.22774910E+04,  
            4.10151290E+00])),  
    transport=gas_transport(geom='nonlinear',  
        diam=4.302,  
        well_depth=252.3,  
        rot_relax=2.0))
```

```
species(name='C2H6',  
    atoms='H:6 C:2',  
    thermo=(NASA([300.00, 1000.00],  
        [2.14157880E+00, 1.05297200E-02, 1.87302740E-05,  
        -2.66911870E-08, 1.00493320E-11, -1.14104860E+04,  
        1.16477570E+01]),  
        NASA([1000.00, 1500.00],  
            [2.15552810E+00, 1.47798610E-02, 2.33528040E-06,  
            -6.41464280E-09, 1.90369250E-12, -1.15245170E+04,  
            1.07763160E+01])),  
    transport=gas_transport(geom='nonlinear',  
        diam=4.371,  
        well_depth=241.0,  
        rot_relax=2.0),  
    note='L5/72')
```

```
species(name='C3H6',  
    atoms='H:6 C:3',  
    thermo=(NASA([300.00, 1000.00],  
        [1.49330710E+00, 2.09251750E-02, 4.48679380E-06,  
        -1.66891210E-08, 7.15814650E-12, 1.07482640E+03,  
        1.61453400E+01]),
```

```
NASA([1000.00, 5000.00],  
      [ 6.73225690E+00, 1.49083360E-02, -4.94989940E-06,  
        7.21202210E-10, -3.76620430E-14, -9.23570310E+02,  
        -1.33133480E+01])),  
transport=gas_transport(geom='nonlinear',  
                        diam=4.982,  
                        well_depth=266.8,  
                        rot_relax=1.0),  
note='T12/81')
```

```
species(name='I*C3H7',  
        atoms='H:7 C:3',  
        thermo=(NASA([300.00, 1000.00],  
                     [ 1.71329980E+00, 2.54261640E-02, 1.58080820E-06,  
                       -1.82128620E-08, 8.82771030E-12, 7.53580860E+03,  
                       1.29790080E+01]),  
                 NASA([1000.00, 5000.00],  
                     [ 8.06336880E+00, 1.57448760E-02, -5.18239180E-06,  
                       7.47724550E-10, -3.85442210E-14, 5.31387110E+03,  
                       -2.19264680E+01])),  
        transport=gas_transport(geom='nonlinear',  
                                diam=4.982,  
                                well_depth=266.8,  
                                rot_relax=1.0),  
        note='T8/81')
```

```
species(name='N*C3H7',  
        atoms='H:7 C:3',  
        thermo=(NASA([300.00, 1000.00],  
                     [ 1.92253680E+00, 2.47892740E-02, 1.81024920E-06,  
                       -1.78326580E-08, 8.58299630E-12, 9.71328120E+03,  
                       1.39927150E+01]),  
                 NASA([1000.00, 5000.00],  
                     [ 7.97829060E+00, 1.57611330E-02, -5.17324320E-06,  
                       7.44389220E-10, -3.82497820E-14, 7.57940230E+03,  
                       -1.93561100E+01])),  
        transport=gas_transport(geom='nonlinear',  
                                diam=4.982,  
                                well_depth=266.8,  
                                rot_relax=1.0),  
        note='T8/81')
```

```
species(name='CO2',  
        atoms='C:1 O:2',  
        thermo=(NASA([300.00, 1000.00],  
                     [ 2.40077970E+00, 8.73509570E-03, -6.60708780E-06,  
                       2.00218610E-09, 6.32740390E-16, -4.83775270E+04,  
                       9.69514570E+00]),  
                 NASA([1000.00, 5000.00],  
                     [ 4.46080410E+00, 3.09817190E-03, -1.23925710E-06,  
                       2.27413250E-10, -1.55259540E-14, -4.89614420E+04,  
                       -9.86359820E-01])),  
        transport=gas_transport(geom='linear',  
                                diam=3.769,  
                                well_depth=245.3,  
                                polar=2.65,  
                                rot_relax=2.1),  
        note='J9/65')
```

```
species(name='HCO',
```

```
atoms='H:1 C:1 O:1',
thermo=(NASA([300.00, 1000.00],
  [ 3.88401920E+00, -8.29744480E-04, 7.79008090E-06,
    -7.06169620E-09, 1.99717300E-12, 4.05638600E+03,
    4.83541330E+00]),
  NASA([1000.00, 5000.00],
    [ 3.47383480E+00, 3.43702270E-03, -1.36326640E-06,
      2.49286450E-10, -1.70443310E-14, 3.95940050E+03,
      6.04533400E+00])),
transport=gas_transport(geom='linear',
  diam=3.59,
  well_depth=498.0,
  rot_relax=2.0),
note='J12/70')

species(name='CH2O',
atoms='H:2 C:1 O:1',
thermo=(NASA([300.00, 1000.00],
  [ 3.79637830E+00, -2.57017850E-03, 1.85488150E-05,
    -1.78691770E-08, 5.55044510E-12, -1.50889470E+04,
    4.75481630E+00]),
  NASA([1000.00, 5000.00],
    [ 2.83642490E+00, 6.86052980E-03, -2.68826470E-06,
      4.79712580E-10, -3.21184060E-14, -1.52360310E+04,
      7.85311690E+00])),
transport=gas_transport(geom='nonlinear',
  diam=3.59,
  well_depth=498.0,
  rot_relax=2.0),
note='J3/61')

species(name='C2HO',
atoms='H:1 C:2 O:1',
thermo=(NASA([300.00, 1000.00],
  [ 2.32547510E+00, 1.57607580E-02, -1.02774140E-05,
    -3.52127740E-10, 1.79253480E-12, 1.98406020E+04,
    1.07699810E+01]),
  NASA([1000.00, 4000.00],
    [ 7.61162310E+00, 1.41202180E-03, 4.46720550E-07,
      -2.47232550E-10, 2.60930350E-14, 1.84811750E+04,
      -1.63521220E+01])),
transport=gas_transport(geom='linear',
  diam=2.5,
  well_depth=150.0,
  rot_relax=2.5))

species(name='C3H4',
atoms='H:4 C:3',
thermo=(NASA([300.00, 1000.00],
  [ 3.25857510E+00, 1.24634100E-02, 1.00955880E-05,
    -2.13096330E-08, 9.23291860E-12, 2.14665780E+04,
    7.28525930E+00]),
  NASA([1000.00, 5000.00],
    [ 5.04061860E+00, 1.25320880E-02, -4.51793050E-06,
      7.29732380E-10, -4.36503570E-14, 2.08668410E+04,
      -2.81389330E+00])),
transport=gas_transport(geom='linear',
  diam=4.76,
  well_depth=252.0,
  rot_relax=1.0))
```

```
species(name='C3H5',
  atoms='H:5 C:3',
  thermo=(NASA([300.00, 1000.00],
    [-5.41004000E-01, 2.72841010E-02, -9.63653290E-07,
    -1.91294620E-08, 9.83941750E-12, 1.51303950E+04,
    2.60673370E+01]),
    NASA([1000.00, 5000.00],
    [7.90919780E+00, 1.21152550E-02, -4.11758630E-06,
    6.15667960E-10, -3.32357330E-14, 1.23541560E+04,
    -1.96723330E+01])),
  transport=gas_transport(geom='nonlinear',
    diam=4.982,
    well_depth=266.8,
    rot_relax=1.0),
  note='U12/77')
```

```
species(name='N2',
  atoms='N:2',
  thermo=(NASA([300.00, 1000.00],
    [3.67482610E+00, -1.20815000E-03, 2.32401020E-06,
    -6.32175590E-10, -2.25772530E-13, -1.06115880E+03,
    2.35804240E+00]),
    NASA([1000.00, 5000.00],
    [2.89631940E+00, 1.51548660E-03, -5.72352770E-07,
    9.98073930E-11, -6.52235550E-15, -9.05861840E+02,
    6.16151480E+00])),
  transport=gas_transport(geom='linear',
    diam=3.632,
    well_depth=104.23,
    polar=1.76,
    rot_relax=4.0),
  note='J9/65')
```

```
#-----
# Reaction data
#-----
```

```
# Reaction 1
reaction('O2 + H => OH + O', [2.000000e+14, 0.0, 70300.0])
```

```
# Reaction 2
reaction('OH + O => O2 + H', [1.568000e+13, 0.0, 3520.0])
```

```
# Reaction 3
reaction('H2 + O => OH + H', [5.060000e+04, 2.67, 26300.0])
```

```
# Reaction 4
reaction('OH + H => H2 + O', [2.222000e+04, 2.67, 18290.0])
```

```
# Reaction 5
reaction('H2 + OH => H2O + H', [1.000000e+08, 1.6, 13800.0])
```

```
# Reaction 6
reaction('H2O + H => H2 + OH', [4.312000e+08, 1.6, 76460.0])
```

```
# Reaction 7
reaction('OH + OH => H2O + O', [1.500000e+09, 1.14, 420.0])
```

```
# Reaction 8
```

reaction('H2O + O => OH + OH', [1.473000e+10, 1.14, 71090.0])

# Reaction 9

three\_body\_reaction('O2 + H + M => HO2 + M', [2.300000e+18, -0.8, 0.0],  
efficiencies='CO2:1.5 CO:0.75 H2O:6.5 CH4:6.5 N2:0.4 O2:0.4')

# Reaction 10

three\_body\_reaction('HO2 + M => O2 + H + M', [3.190000e+18, -0.8, 195390.0],  
efficiencies='CO2:1.5 CO:0.75 H2O:6.5 CH4:6.5 N2:0.4 O2:0.4')

# Reaction 11

reaction('HO2 + H => OH + OH', [1.500000e+14, 0.0, 4200.0])

# Reaction 12

reaction('HO2 + H => H2 + O2', [2.500000e+13, 0.0, 2900.0])

# Reaction 13

reaction('HO2 + OH => H2O + O2', [6.000000e+13, 0.0, 0.0])

# Reaction 14

reaction('HO2 + H => H2O + O', [3.000000e+13, 0.0, 7200.0])

# Reaction 15

reaction('HO2 + O => OH + O2', [1.800000e+13, 0.0, -1700.0])

# Reaction 16

reaction('HO2 + HO2 => H2O2 + O2', [2.500000e+11, 0.0, -5200.0])

# Reaction 17

three\_body\_reaction('OH + OH + M => H2O2 + M', [3.250000e+22, -2.0, 0.0],  
efficiencies='CO2:1.5 CO:0.75 H2O:6.5 CH4:6.5 N2:0.4 O2:0.4')

# Reaction 18

three\_body\_reaction('H2O2 + M => OH + OH + M', [1.692000e+24, -2.0, 202290.0],  
efficiencies='CO2:1.5 CO:0.75 H2O:6.5 CH4:6.5 N2:0.4 O2:0.4')

# Reaction 19

reaction('H2O2 + H => H2O + OH', [1.000000e+13, 0.0, 15000.0])

# Reaction 20

reaction('H2O2 + OH => H2O + HO2', [5.400000e+12, 0.0, 4200.0])

# Reaction 21

reaction('H2O + HO2 => H2O2 + OH', [1.802000e+13, 0.0, 134750.0])

# Reaction 22

three\_body\_reaction('H + H + M => H2 + M', [1.800000e+18, -1.0, 0.0],  
efficiencies='CO2:1.5 CO:0.75 H2O:6.5 CH4:6.5 N2:0.4 O2:0.4')

# Reaction 23

three\_body\_reaction('OH + H + M => H2O + M', [2.200000e+22, -2.0, 0.0],  
efficiencies='CO2:1.5 CO:0.75 H2O:6.5 CH4:6.5 N2:0.4 O2:0.4')

# Reaction 24

three\_body\_reaction('O + O + M => O2 + M', [2.900000e+17, -1.0, 0.0],  
efficiencies='CO2:1.5 CO:0.75 H2O:6.5 CH4:6.5 N2:0.4 O2:0.4')

# Reaction 25

reaction('CO + OH => CO2 + H', [4.400000e+06, 1.5, -3100.0])

```
# Reaction 26
reaction('CO2 + H => CO + OH', [4.956000e+08, 1.5, 89760.0])

# Reaction 27
reaction('CH + O2 => HCO + O', [3.000000e+13, 0.0, 0.0])

# Reaction 28
reaction('CO2 + CH => HCO + CO', [3.400000e+12, 0.0, 2900.0])

# Reaction 29
reaction('HCO + H => CO + H2', [2.000000e+14, 0.0, 0.0])

# Reaction 30
reaction('HCO + OH => CO + H2O', [1.000000e+14, 0.0, 0.0])

# Reaction 31
reaction('HCO + O2 => CO + HO2', [3.000000e+12, 0.0, 0.0])

# Reaction 32
three_body_reaction('HCO + M => CO + H + M', [7.100000e+14, 0.0, 70300.0],
  efficiencies='CO2:1.5 CO:0.75 H2O:6.5 CH4:6.5 N2:0.4 O2:0.4')

# Reaction 33
three_body_reaction('CO + H + M => HCO + M', [1.136000e+15, 0.0, 9970.0],
  efficiencies='CO2:1.5 CO:0.75 H2O:6.5 CH4:6.5 N2:0.4 O2:0.4')

# Reaction 34
reaction('CH2 + H => CH + H2', [8.400000e+09, 1.5, 1400.0])

# Reaction 35
reaction('CH + H2 => CH2 + H', [5.830000e+09, 1.5, 13080.0])

# Reaction 36
reaction('CH2 + O => CO + H + H', [8.000000e+13, 0.0, 0.0])

# Reaction 37
reaction('CH2 + O2 => CO + OH + H', [6.500000e+12, 0.0, 6300.0])

# Reaction 38
reaction('CH2 + O2 => CO2 + H + H', [6.500000e+12, 0.0, 6300.0])

# Reaction 39
reaction('CH2O + H => HCO + H2', [2.500000e+13, 0.0, 16700.0])

# Reaction 40
reaction('CH2O + O => HCO + OH', [3.500000e+13, 0.0, 14600.0])

# Reaction 41
reaction('CH2O + OH => HCO + H2O', [3.000000e+13, 0.0, 5000.0])

# Reaction 42
three_body_reaction('CH2O + M => HCO + H + M', [1.400000e+17, 0.0, 320000.0],
  efficiencies='CO2:1.5 CO:0.75 H2O:6.5 CH4:6.5 N2:0.4 O2:0.4')

# Reaction 43
reaction('CH3 + H => CH2 + H2', [1.800000e+14, 0.0, 63000.0])

# Reaction 44
reaction('CH2 + H2 => CH3 + H', [3.680000e+13, 0.0, 44300.0])
```

```
# Reaction 45
falloff_reaction('CH3 + H (+ M) => CH4 (+ M)',
  kf=[2.108000e+14, 0.0, 0.0],
  kf0=[6.257000e+23, -1.8, 0.0],
  falloff=Troe(A=0.577, T3=1e-50, T1=2370.0))

# Reaction 46
reaction('CH3 + O => CH2O + H', [7.000000e+13, 0.0, 0.0])

# Reaction 47
falloff_reaction('CH3 + CH3 (+ M) => C2H6 (+ M)',
  kf=[3.613000e+13, 0.0, 0.0],
  kf0=[1.270000e+41, -7.0, 11560.0],
  falloff=Troe(A=0.62, T3=73.0, T1=1180.0))

# Reaction 48
reaction('CH3 + O2 => CH2O + OH', [3.400000e+11, 0.0, 37400.0])

# Reaction 49
reaction('CH4 + H => CH3 + H2', [2.200000e+04, 3.0, 36600.0])

# Reaction 50
reaction('CH3 + H2 => CH4 + H', [8.391000e+02, 3.0, 34560.0])

# Reaction 51
reaction('CH4 + O => CH3 + OH', [1.200000e+07, 2.1, 31900.0])

# Reaction 52
reaction('CH4 + OH => CH3 + H2O', [1.600000e+06, 2.1, 10300.0])

# Reaction 53
reaction('CH3 + H2O => CH4 + OH', [2.631000e+05, 2.1, 70920.0])

# Reaction 54
reaction('C2H + H2 => C2H2 + H', [1.100000e+13, 0.0, 12000.0])

# Reaction 55
reaction('C2H2 + H => C2H + H2', [5.270000e+13, 0.0, 119950.0])

# Reaction 56
reaction('C2H + O2 => C2HO + O', [5.000000e+13, 0.0, 6300.0])

# Reaction 57
reaction('C2HO + H => CH2 + CO', [3.000000e+13, 0.0, 0.0])

# Reaction 58
reaction('CH2 + CO => C2HO + H', [2.361000e+12, 0.0, -29390.0])

# Reaction 59
reaction('C2HO + O => CO + CO + H', [1.000000e+14, 0.0, 0.0])

# Reaction 60
reaction('C2H2 + O => CH2 + CO', [4.100000e+08, 1.5, 7100.0])

# Reaction 61
reaction('C2H2 + O => C2HO + H', [4.300000e+14, 0.0, 50700.0])

# Reaction 62
reaction('C2H2 + OH => C2H + H2O', [1.000000e+13, 0.0, 29300.0])
```

```
# Reaction 63
reaction('C2H + H2O => C2H2 + OH', [9.000000e+12, 0.0, -15980.0])

# Reaction 64
reaction('C2H2 + CH => C3H3', [2.100000e+14, 0.0, -0.5])

# Reaction 65
reaction('C2H3 + H => C2H2 + H2', [3.000000e+13, 0.0, 0.0])

# Reaction 66
reaction('C2H3 + O2 => C2H2 + HO2', [5.400000e+11, 0.0, 0.0])

# Reaction 67
falloff_reaction('C2H3 (+ M) => C2H2 + H (+ M)',
  kf=[2.000000e+14, 0.0, 166290.0],
  kf0=[1.187000e+42, -7.5, 190400.0],
  falloff=Troe(A=0.65, T3=1e+50, T1=1e-50))

# Reaction 68
falloff_reaction('C2H2 + H (+ M) => C2H3 (+ M)',
  kf=[1.053000e+14, 0.0, 3390.0],
  kf0=[6.249555e+41, -7.5, 27500.0],
  falloff=Troe(A=0.65, T3=1e+50, T1=1e-50))

# Reaction 69
reaction('C2H4 + H => C2H3 + H2', [1.500000e+14, 0.0, 42700.0])

# Reaction 70
reaction('C2H3 + H2 => C2H4 + H', [9.600000e+12, 0.0, 32640.0])

# Reaction 71
reaction('C2H4 + O => CH3 + CO + H', [1.600000e+09, 1.2, 3100.0])

# Reaction 72
reaction('C2H4 + OH => C2H3 + H2O', [3.000000e+13, 0.0, 12600.0])

# Reaction 73
reaction('C2H3 + H2O => C2H4 + OH', [8.283000e+12, 0.0, 65200.0])

# Reaction 74
three_body_reaction('C2H4 + M => C2H2 + H2 + M', [2.500000e+17, 0.0, 319800.0],
  efficiencies='CO2:1.5 CO:0.75 H2O:6.5 CH4:6.5 N2:0.4 O2:0.4')

# Reaction 75
reaction('C2H5 + H => CH3 + CH3', [3.000000e+13, 0.0, 0.0])

# Reaction 76
reaction('CH3 + CH3 => C2H5 + H', [3.547000e+12, 0.0, 49680.0])

# Reaction 77
reaction('C2H5 + O2 => C2H4 + HO2', [2.000000e+12, 0.0, 20900.0])

# Reaction 78
falloff_reaction('C2H5 (+ M) => C2H4 + H (+ M)',
  kf=[1.300000e+13, 0.0, 167000.0],
  kf0=[1.000000e+16, 0.0, 126000.0],
  falloff=Troe(A=0.5, T3=422.8, T1=422.8))

# Reaction 79
falloff_reaction('C2H4 + H (+ M) => C2H5 (+ M)',
```

kf=[2.073000e+13, 0.0, 13610.0],  
kf0=[1.594615e+15, 0.0, -27390.0],  
falloff=Troe(A=0.5, T3=422.8, T1=422.8))

# Reaction 80  
reaction('C2H6 + H => C2H5 + H2', [5.400000e+02, 3.5, 21800.0])

# Reaction 81  
reaction('C2H6 + O => C2H5 + OH', [3.000000e+07, 2.0, 21400.0])

# Reaction 82  
reaction('C2H6 + OH => C2H5 + H2O', [6.300000e+06, 2.0, 2700.0])

# Reaction 83  
reaction('C3H3 + O2 => C2HO + CH2O', [6.000000e+12, 0.0, 0.0])

# Reaction 84  
reaction('C3H3 + O => C2H3 + CO', [3.800000e+13, 0.0, 0.0])

# Reaction 85  
reaction('C3H4 => C3H3 + H', [5.000000e+14, 0.0, 37000.0])

# Reaction 86  
reaction('C3H3 + H => C3H4', [1.700000e+13, 0.0, 19880.0])

# Reaction 87  
reaction('C3H4 + O => C2H2 + CH2O', [1.000000e+12, 0.0, 0.0])

# Reaction 88  
reaction('C3H4 + O => C2H3 + HCO', [1.000000e+12, 0.0, 0.0])

# Reaction 89  
reaction('C3H4 + OH => C2H3 + CH2O', [1.000000e+12, 0.0, 0.0])

# Reaction 90  
reaction('C3H4 + OH => C2H4 + HCO', [1.000000e+12, 0.0, 0.0])

# Reaction 91  
reaction('C3H5 => C3H4 + H', [3.980000e+13, 0.0, 293100.0])

# Reaction 92  
reaction('C3H4 + H => C3H5', [1.267000e+13, 0.0, 32480.0])

# Reaction 93  
reaction('C3H5 + H => C3H4 + H2', [1.000000e+13, 0.0, 0.0])

# Reaction 94  
reaction('C3H6 => C2H3 + CH3', [3.150000e+15, 0.0, 359300.0])

# Reaction 95  
reaction('C2H3 + CH3 => C3H6', [2.511000e+12, 0.0, -34690.0])

# Reaction 96  
reaction('C3H6 + H => C3H5 + H2', [5.000000e+12, 0.0, 6300.0])

# Reaction 97  
reaction('N\*C3H7 => C2H4 + CH3', [9.600000e+13, 0.0, 129800.0])

# Reaction 98  
reaction('N\*C3H7 => C3H6 + H', [1.250000e+14, 0.0, 154900.0])

```
# Reaction 99
reaction('C3H6 + H => N*C3H7', [4.609000e+14, 0.0, 21490.0])

# Reaction 100
reaction('I*C3H7 => C2H4 + CH3', [6.300000e+13, 0.0, 154500.0])

# Reaction 101
reaction('I*C3H7 + O2 => C3H6 + HO2', [1.000000e+12, 0.0, 20900.0])

# Reaction 102
reaction('C3H8 + H => N*C3H7 + H2', [1.300000e+14, 0.0, 40600.0])

# Reaction 103
reaction('C3H8 + H => I*C3H7 + H2', [1.000000e+14, 0.0, 34900.0])

# Reaction 104
reaction('C3H8 + O => N*C3H7 + OH', [3.000000e+13, 0.0, 24100.0])

# Reaction 105
reaction('C3H8 + O => I*C3H7 + OH', [2.600000e+13, 0.0, 18700.0])

# Reaction 106
reaction('C3H8 + OH => N*C3H7 + H2O', [3.700000e+12, 0.0, 6900.0])

# Reaction 107
reaction('C3H8 + OH => I*C3H7 + H2O', [2.800000e+12, 0.0, 3600.0])
```

## APPENDIX I.

### I.1 Reduced Mechanism developed by Konnov for hydrogen/air combustion

ELEM O N AR H HE

END

SPECIES ! structure, source of thermo-data, source of transport

H ! burcat, chemkin

H2 ! burcat, chemkin

O O2 H2O OH H2O2 HO2 OX OHX O2X O3

AR ! burcat, chemkin

HE ! burcat, chemkin

N2 ! burcat, chemkin

END

REACTIONS

!\*\*\*\*\*

!

! A.KONNOV's detailed reaction mechanism h/o3 excited 2018

!

!\*\*\*\*\*

H+H+M=H2+M 7.000E+17 -1.0 0.0

H2/0.0/ N2/0.0/ H/0.0/ H2O/14.3/ ! CO/3.0/ CO2/3.0/

H+H+H2=H2+H2 1.000E+17 -0.6 0.0

H+H+N2=H2+N2 5.400E+18 -1.3 0.0

H+H+H=H2+H 3.200E+15 0.0 0.0

O+O+M=O2+M 1.000E+17 -1.0 0.0

O/28.8/ O2/8.0/ N2/2.0/ H2O/5.0/ O3/8.0/ ! NO/2.0/ N/2.0/

O+H+M=OH+M 6.750E+18 -1.0 0.0

H2O/5.0/

H2O+M=H+OH+M 6.060E+27 -3.312 120770.0

H2O /0/ H2/3.0/ N2 /2.0/ O2 /1.5/ HE /1.1/ !CH4/7/ CO2 /4/

H2O+H2O=H+OH+H2O 1.000E+26 -2.44 120160.0

H+O2(+M)=HO2(+M) 4.660E+12 0.44 0.0

LOW /1.225E+19 -1.2 0.0/

TROE /0.5 1 1E+10/

AR/0.72/ H2O/16.6/ O2/1.0/ H2/1.5/ HE/0.57/ ! CO2/3.61/ CH4/3.5/

H2O2(+M)=OH+OH(+M) 2.000E+12 0.9 48750.0

LOW /2.49E+24 -2.3 48750.0 /

TROE /0.42 1 1E+10/

H2O/7.5/ H2O2/7.7/ O2/1.2/ N2/1.5/ HE/0.65/ H2/3.7/ !CO2/1.6/ CO/2.8/

O+H2=OH+H 5.080E+04 2.67 6292.0

H+O2=OH+O 1.040E+14 0.0 15286.0

H2+OH=H2O+H 2.140E+08 1.52 3450.0

OH+OH=H2O+O 2.668E+06 1.82 -1647.0

HO2+O=OH+O2 2.850E+10 1.0 -723.9

H+HO2=OH+OH 7.080E+13 0.0 300.0

H2O+O=H+HO2 2.200E+08 2.0 61600.0

H2+O2=H+HO2 7.400E+05 2.43 53500.0

HO2+OH=H2O+O2 7.000E+12 0.0 -1093.0

DUPLICATE

HO2+OH=H2O+O2 4.500E+14 0.0 10930.0

DUPLICATE

HO2+HO2=H2O2+O2 1.030E+14 0.0 11040.0

DUPLICATE

HO2+HO2=H2O2+O2 1.940E+11 0.0 -1409.0

DUPLICATE

H2O2+H=HO2+H2 5.020E+06 2.07 4300.0

H2O2+H=H2O+OH 2.030E+07 2.02 2620.0

H2O2+O=HO2+OH 9.550E+06 2.0 3970.0

H2O2+OH=HO2+H2O	1.740E+12	0.0	318.0
DUPLICATE			
H2O2+OH=HO2+H2O	7.590E+13	0.0	7269.0
DUPLICATE			
O2+O+AR=O3+AR	4.290E+17	-1.5	0.0
DUPLICATE			
O2+O+AR=O3+AR	5.100E+21	-3.2	0.0
DUPLICATE			
O2+O+M=O3+M	6.530E+17	-1.5	0.0
AR/0.0/ O2/0.95/ O3/2.5/ O/4.0/			
DUPLICATE			
O2+O+M=O3+M	1.330E+22	-3.3	0.0
AR/0.0/ O2/1.07/ O3/2.5/ O/4.0/			
DUPLICATE			
O3+O=O2+O2	4.820E+12	0.0	4094.0
O3+O=O2X+O2	1.440E+11	0.0	4094.0
O+O+M=O2X+M	7.000E+15	-1.0	0.0
O/28.8/ O2/8.0/ N2/2.0/ H2O/5.0/ O3/8.0/ !NO/2.0/ N/2.0/			
O2X+M=O2+M	1.800E+06	0.0	400.0
O/0/ H/0/ AR/0.005/ HE/0.005/ N2/0.002/ H2O/3.3/ H2/2.5/ !CO2/0.01/ CO/5.6/			
O2X+O=O2+O	7.800E+07	0.0	0.0
O2X+H=O2+H	4.000E+13	0.0	5030.0
O2X+O+M=O+O2+M	3.600E+15	0.0	0.0
AR/0.63/			
O2X+O3=O2+O2+O	3.130E+13	0.0	5644.0
OX+O2X=O+O2	6.030E+12	0.0	0.0
OX+O2=O+O2X	1.590E+13	0.0	-139.0
OX+O2=O+O2	2.810E+12	0.0	-139.0
OX+M=O+M	4.800E+11	0.0	0.0

O2/0/ N2/0/ O/10.0/ H2O/3.0/

OX+N2=O+N2	1.260E+13	0.0	-230.0
OX+O3=O2+O+O	7.230E+13	0.0	0.0
OX+O3=O2+O2	7.230E+13	0.0	0.0
H2+O2X=H+HO2	6.160E+05	2.335	31080.0
H+O2X=OH+O	3.500E+08	1.45	4508.0
H+O2X+M=HO2+M	9.890E+09	2.03	3360.0
HO2+OH=H2O+O2X	2.140E+06	1.65	2180.0
OH+O2X=O+HO2	1.300E+13	0.0	34000.0
O3+H=OH+O2	8.430E+13	0.0	934.0
O3+OH=HO2+O2	1.000E+12	0.0	1870.0
O3+HO2=OH+O2+O2	5.850E-04	4.57	-1377.0
H+HO2=H2O+OX	2.500E+12	0.0	300.0
OX+H2=OH+H	8.100E+13	0.0	0.0
OX+H2O=OH+OH	1.000E+14	0.0	-71.0
O+H+M=OHX+M	1.500E+13	0.0	5970.0

AR/0.35/ H2O/6.5/ O2/0.4/ N2/0.4/

OHX+O2=OH+O2	8.400E+11	0.5	-482.0
OHX+N2=OH+N2	1.080E+11	0.5	-1238.0
OHX+H2O=OH+H2O	2.960E+12	0.5	-861.0
OHX+H2=OH+H2	3.540E+11	0.5	-444.0
OHX+OH=OH+OH	1.500E+12	0.5	0.0
OHX+H=OH+H	1.500E+12	0.5	0.0
OHX+O=OH+O	1.500E+12	0.5	0.0
OHX+AR=OH+AR	2.170E+10	0.5	2060.0
OHX+H2=H2O+H	2.600E+12	0.5	-444.0
OHX+O2=O3+H	2.520E+11	0.5	-482.0
OHX+O2=HO2+O	1.008E+12	0.5	-482.0
OHX+H2O=H2O2+H	2.960E+12	0.5	-861.0

$\text{OHX}=\text{OH}+\text{h}\nu$	1.400E+06	0.0	0.0
$\text{H}+\text{O}_2+\text{H}=\text{H}_2+\text{O}_2$	8.800E+22	-1.835	800.0
$\text{H}+\text{O}_2+\text{H}=\text{OH}+\text{OH}$	4.000E+22	-1.835	800.0
$\text{H}+\text{O}_2+\text{O}=\text{OH}+\text{O}_2$	7.350E+22	-1.835	800.0
$\text{H}+\text{O}_2+\text{OH}=\text{H}_2\text{O}+\text{O}_2$	2.560E+22	-1.835	800.0

END

## APPENDIX J.

### J.1 Thin slots for dual fuel applications

Dual fuel is not related to the fuel hole shape but to the similarity of the Wobbe Index. If two fuels share a similar Wobbe index, then the same energy will pass through a gas hole metering orifice for the same gas supply pressure. However, the hole shape affects the  $C_D$  mainly through the Reynolds number. For example, for slot-shaped holes, the fuel is laminar due to the width of the slot controlling the hydraulic diameter, resulting in a reduced flow capacity and thermal power of the test.

The controlling equation is the orifice flow equation that can be derived from Equation (7) as:

$$m'f = C_D A_f (2\rho \Delta P)^{0.5}$$

The fuel density  $\rho$  varies by a factor of 8 difference between methane and hydrogen. In domestic fires  $\Delta P$  is 20 mbar

It was decided to consider  $A_f$  as the injector outlet flow area for Design 1, but also in Design 2, it was decided to have a dual restrictor with two fuel orifices, one for metering the flow, and another one for the fuel hole outlet area. For Design 2, 90% of the pressure loss was at the metering orifice and 10% at the fuel injector. If the burners didn't feature a metering hole, they would have passed 3.16 more gas flow or energy flow if  $C_D$  did not change.

If  $C_D$ ,  $A_f$  and  $\Delta P$  were constant and the fuel mass flow was only in function of the density the other parameters could be a constant  $C_1$ . Then

$$m'f = C_1 \rho^{0.5}$$

Suppose the mass flow rate is treated as burner power  $B_H/GCV_H$  for  $H_2$  and  $B_{NG}/GCV_{NG}$  for NG. Both expressed in kg/s, and the GCV in MJ/kg<sub>f</sub> (140 and 50 respectively) and the density ratio is treated as a MW ratio. Then when ratio both powers a similarity of 95% can be seen.

$$\frac{B_H}{B_{NG}} = \left[ \frac{\rho_H}{\rho_{NG}} \right]^{0.5} \left[ \frac{GCV_H}{GCV_{NG}} \right] = 0.95$$

This shows that a dual fuel burner operating with NG would give 5% less energy on hydrogen, which would not be notorious by the customer.

This is where the Wobbe Index comes from, but is confused by the tradition of the gas industry in working in volume units and not mass.

$GCV\rho_f^{0.5}$  = Wobbe Number for GCV in MJ/kg

or  $GCV\rho_f^{0.5} = \text{Wobbe Number for GCV in MJ/m}^3$

Another method of expressing the Wobbe number in volumetric terms is the Wobbe Index, which uses the gas density relative to air<sup>9</sup>

Some reasons for using thin slot fuel holes instead of round holes are listed below:

- Prevention of flashback

At start-up conditions, the fuel line is full of air. When fuel is injected, the fuel/air mixture generates a small explosion which is not desired. In order to avoid this, the fuel hole nozzle should be smaller than the quench distance, which is 2.4mm for CH<sub>4</sub> and 0.6 for H<sub>2</sub>. Burners operating at less 7kW have hole sizes below 2.4mm. On the other hand, hydrogen would not be able to work at the same hole size, or flashback would occur. To stop this a larger number of smaller holes could be used or switching to thin slots with a width less than 0.6mm.

The problem of multiple small holes is that the produced flames would be much smaller, making flame visualization for H<sub>2</sub> more difficult. The investigated 0.1, 0.2 and 0.3mm laser cut slots had the same area of the round holes, and successfully avoided start-up flashback. The flame showed to be proportional to the slot length and was more visible than for round holes.

- Lower NO<sub>x</sub> due to improved fuel/air mixing by increasing the shear layer surface area

The shear layer controls the mixing of high-velocity fuel jets with the low velocity surrounding air. Thin slot shear layers are longer than round holes, considering the same injection area, and this can be shown by comparing the hole circumference ratio to the hole area  $\frac{4\pi D}{\pi D^2} = 4D$  with the slot length and thickness for the same area  $\frac{8(L+t)}{\pi D^2} = \frac{8L}{2Lt} = \frac{4}{t}$ , where the shear layer increases with the reduction of the thickness  $t$  relative to the round hole with the same area. This was the reason for investigating 0.1mm slots

- Flame appearance due to slot width

A longer flame was assumed for a long thin slot compared to round holes. However, flame impingement with the top ceramics resulted in very fast mixing and consequently poor post flame visibility.

---

<sup>9</sup> The same as the MW ratio for the same P and T conditions

### **J.1.1 Flow characteristics for thin slots**

A problem encountered when doing the experiments was the influence of flow rate due to the pressure loss. It was observed that slot holes passed less flow than round holes with the same area and gas supply pressure. Which showed that it was erroneous to consider  $C_D$  as constant.

The thin slots were laser made for the same area as round jets. However, manufacturing thin slots is complicated to keep a uniform area. An irregular slot area was obtained for the different configurations, which was a problem.

Round holes of around 2mm diameter drilled in a 2mm sheet metal gave an  $L/D$  near 1, and the  $C_D$  for a sharp entry was taken as 0.84. On the other hand, slot holes were 0.1-0.3mm laser cut in the same 2mm sheet metal, which gave a larger  $L/D$  of about 20 for 0.1mm and 8 for 0.3mm slots. For round holes the pressure loss increases with the jet length as well as the slot  $L/D$  decreasing  $C_D$ .

Both investigated  $C_D$  values 0.84 and 0.74 consider a turbulent flow in the holes, assuming that  $C_D$  is constant and independent for turbulent flows. In contrast, slot holes have the hydraulic diameter  $D_H$  being two times the slot width if the slot is very long relative to the width as for this work. As  $t$  was reduced, so did the Reynolds number, transitioning from turbulent to laminar, where the  $C_D$  was smaller and the pressure higher. This resulted in a mass flow and thermal power reduction for the same supply pressure.

By reducing the fuel delivery by about 50%, Reynolds stays about 2000. When using 0.3 slots  $Re$  is three times higher than the one for 0.1mm slots for the same fuel supply. This issue made the 0.3mm a better choice than 0.1.

## APPENDIX K.

### K.1 Open fronted fire single-stage injection calculations

The following calculations were carried out for a hydrogen flame. The design principle was the hydrogen diffusion jets impinging with the top ceramics to resemble the reference partially premixed NG burner.

Hydrogen was used for a GCV of 142MJ/kg and an NCV of 120MJ/kg, with a density  $\rho=0.08464 \text{ kg/m}^3$  at an ambient temperature of 15°C.

The non-condensing domestic burner design was aimed for a hydrogen flame. The differences between NCV and GCV for H<sub>2</sub> showed that it was more appropriate to design for the net fuel energy (NCV) input for H<sub>2</sub> as for NG.

The thermal fuel input of the reference open fronted fire was 6.25kW on a GCV basis or 5.6kW on an NCV for H<sub>2</sub>. The flow rate was 0.044 g/s for a GCV basis and 0.0467 g/s for an NCV basis.

The open-fronted fire premixed design featured a large linear array of holes fed from a plenum air chamber. The hole sizes were: Hole 1 8mm diameter; Hole 2 3.5mm; Hole 3 1.6mm.

For the first design, hydrogen holes were not meant to be used for NG. Two designs were manufactured: Full hydrogen metering pressure loss of 20mbar in the fuel plenum. A pressure loss of 2mbar in the fuel plenum. The orifice plate flow Equation (7) was used for a  $C_D$  of 0.83

-Design 1. For 20mbar, the total fuel hole area was 3.058mm<sup>2</sup>. The design featured two hole sizes passing 17.55% through 0.537mm<sup>2</sup> and the other two passing 32.45% through 0.992mm<sup>2</sup>. The hole diameters were 0.827mm and 1.124mm, respectively. The holes were spaced 57mm, and the first hole was 13mm from the end of the fuel tube. For a 0.3mm slot, the slot length was 1.79mm for the smaller injection and 3.307mm for the large one. The jet velocity was aimed for 180 m/s

-Design 2. For 2mbar pressure loss, the metering fuel hole area was 3.22mm<sup>2</sup> for a hole diameter of 2.025mm. The total outlet area was 9.67mm<sup>2</sup>. The two fuel hole sizes were 1.7mm<sup>2</sup> for a hole diameter of 1.471mm, delivering 17.55% of the fuel, and 3.138mm<sup>2</sup> for a hole diameter of 2mm, delivering 32.45%. For 0.3mm slots, the smaller one was 5.67mm length; the larger slot was 10.46mm.

The fuel jet Reynolds number was given by Equation (19) which can be expressed as:

$$Re = 4 m'_f / \pi d \mu \quad (91)$$

Where  $d$  is the hole diameter,  $m'_f$  is the flow mass flow, and the viscosity  $\mu$  for  $H_2$  was  $0.84 \times 10^{-5}$  Ns/m<sup>2</sup>

Design 1 for a hydrogen flame had a  $Re=1502$  for the small hole and  $Re=2044$  for the large one. Design 2 a  $Re=845$  for the small hole and  $Re=1156$  for the larger hole.

## K.2 Open fronted fire two-stage design

The Reference fire Thermal output was 3.2kW at full power and 1.8kW at low power. The design was based on the NCV as explained in I.1<sup>10</sup>. The designs were aimed for full thermal operation power and lower powers were achieved using the valve IV in Figure 3-26.

A new  $C_D$  of 0.74 was used for this design using deductions of Equation (14). The slots were manufactured in sheet metal with 1.5mm thickness. This gave an  $L/D$  of 15 and a  $L/D_h$  of 7.5.

The work for a single-stage showed that impingement into the ceramic ribs gave the best  $NO_x$  and good thermal efficiency for Design 1. Hence, only one design was studied for two-stage combustion.

Design 1. Fuel plenum pressure loss of 15mbar. The  $H_2$  mass flow was 0.0467 g/s at full power. The fuel total area was 3.96mm<sup>2</sup> for density of  $\rho=0.08464$ . From the obtained  $C_D$  and total fuel area the effective design area was 2.93mm<sup>2</sup>

$$C_{DA} = m'_f / (2\rho P)^{0.5} \quad (92)$$

Where the  $C_{DA}$ = design effective area;  $m'_f$ = mass flow rate  $\rho$ =density;  $P$ = gas supply pressure.

A fuel split 60% to the primary fuel impinging into the bottom ceramics, and 40% to the secondary axially staged fuel impinging into the top ceramics were used. The fuel flow area for the primary fuel injection was 2.38mm<sup>2</sup> and 1.58mm<sup>2</sup> for the secondary injection. The slot area was first calculated for a

---

<sup>10</sup> The reasons for working at NCV are:

1. It requires a high fuel mass flow so would be conservative
2. Open fronted fires are not condensing and so to get sufficient energy out it would be more sensible to design on a NCV basis.

0.1mm width. However, this resulted in a higher  $C_D$  for the required Reynold. So the slots were changed to a width of 0.2mm, where the total hole length was 23.8mm for the primary injection and 15.8mm for the secondary injection.

The Reynolds number for a conventional hole can be calculated as in Equation (93)

$$Re = \rho u L / \mu \quad (93)$$

Where  $u$  is the fuel velocity and  $L$  is the slot dimension for this work.

The hydraulic diameter  $D_H$  was considered twice the slot width for this work, 0.4mm. The hydrogen viscosity was considered as  $0.88 \times 10^{-5}$  Ns/m<sup>2</sup> at 293K.

The methane viscosity was considered as  $1.10 \times 10^{-5}$  Ns/m<sup>2</sup> at 293K.

The massflow rate is obtained from Equation

$$m' = \rho u A \quad (94)$$

There  $A$  is the flow area of the nozzle. For a 1.2mm slot this was 7.92mm<sup>2</sup>.

Then  $Re$  can be calculated as in Equation (95)

$$Re = \frac{m' D_H}{A \mu} \quad (95)$$

The fuel mas flow rate for 6.2 kW at GCV is 0.0934 g/s for H<sub>2</sub> and 0.1532 g/s for methane

For hydrogen  $Re$  was 539. For methane  $Re$  was 703.

The burner design for the two-stage injection is shown in Figure K-1, where the primary injections are shown for a vertical arrangement. In contrast, the secondary back injection shows the holes parallel to the burner length edges in a horizontal position.



## APPENDIX L.

### L.1 Flow calculations for glass-fronted fire

The same fuel hole size was calculated for natural gas and hydrogen because of the requirement of dual-fuel capabilities of the fire, given the similar Wobbe Index for both fires. British Natural gas was used for an NCV of 45 MJ/kg, a molecular weight of 18 and a density of 0.8 kg/m<sup>3</sup>. Condensation was not studied for the fire, so it was sensible the use NCV, which differs considerably from the GCV (50 MJ/kg). The thermal fuel input of 6.25kW was considered for a NG flow rate of 0.125 g/s in a GCV basis, and 0.139 g/s in a NCV.

The designs used four diffusion jets aligned from the fuel bar, so they were on the centreline between the airholes. Impingement was expected with the top ceramic coals. The distance between the holes was 40mm and so the separation between the 4 fuel holes centreline. The fuel was 400mm long with the first fuel hole 110mm from the closed end.

Design 1 was manufactured for a fuel supply pressure loss of 20mbar without metering holes. The orifice plate flow Equation (7) gave a  $C_D$  of 0.83, a 4-hole design with 0.03125 g/s on a GCV basis and 0.03475 g/s on an NCV basis. This gave four 0.929mm and four 0.98mm, respectively, and an area of 0.569mm<sup>2</sup> per hole.

Design 2 was manufactured for a pressure loss of mbar at the distribution pipe inlet featuring four holes of 1.908mm diameter considering the GCV and 2.012mm for the NCV. The design featured a fuel pipe inlet hole working as a metering hole in addition to the 4 outlet holes AT 200Pa pressure loss. The holes were 1.653mm in diameter on a GCV basis and 1.774mm for an NCV. Which gives an area of 2.472 mm<sup>2</sup> per hole

Design 1 gave a NG jet velocity of 60 m/s, and 15.7 m/s for Design 2. For hydrogen the two velocities will be 539 m/s and 143 m/s. The fuel jet Reynolds numbers were obtained by Equation (93) as 3,300 for NG and 4,322 for H<sub>2</sub>. Where the NG viscosity is  $1.10 \times 10^{-5}$  Ns/m<sup>2</sup>, and  $0.84 \times 10^{-5}$  NS/m<sup>2</sup> for H<sub>2</sub>.

Design 2 Reynolds numbers were 2216 for H<sub>2</sub> and 1732 for NG.

The round hole sizes above were greater than the quench distance for hydrogen (0.3 – 0.5mm depending on the data source).

Design 1 slot- Considering the quench distance as 0.3mm, this gave a slot length of 1.90 mm. The slots were aligned with the ceramic struts.

Design 2 slot- Considering the quench distance as 0.3mm, the slot length was 8.24mm aligned with the ceramic struts.

## APPENDIX M.

### M.1 Flow calculations for the Innovative fire

The innovative design was manufactured for a thermal input of 7kW using a GCV of 50kW/kg for NG and 142kW/kg for H<sub>2</sub>. The NG density was considered as 77 kg/m<sup>3</sup> and a molecular weight of 18. The reason for working with the GCV was that the idea was to design a condensing boiler.

The burner design was the same for H<sub>2</sub> than for NG. This is a fuel mass flow rate of 0.14 g/s for NG and 0.0493 g/s for H<sub>2</sub> for 7kW. A wall thickness of 1.5mm and a C<sub>D</sub> of 0.83 was considered.

The Innovative design had several changes in air and fuel holes. It is not the intention to explain all the tested configurations. Only the configurations with the best NO<sub>x</sub> and flame appearance will be described.

#### M.1.1 First fire configuration (LB4-LB5)

Design 1- This was for NG at a fuel pressure loss of 20mbar. The fuel velocity was 59.8 m/s which was 1/3 of the hydrogen velocity of 170 m/s. The same orifice plate flow equation was considered for both fuels and the same fuel mass flow.

The total hole area was 3.04mm<sup>2</sup> from Equation (7), which gave a single round hole of 1.97mm diameter. For a single slot with 0.3mm width, the slot length was 10.13mm. The 1 kW design featured 7 holes of 0.74mm diameter. The 0.3mm slot design for the same 1kW was 7 slots with a length of 1.45mm.

Design 2- This was for NG at a fuel pressure loss of 2mbar. The fuel velocity was 18.9 m/s for NG and 53.8 m/s for H<sub>2</sub>.

Equation (7) gave a total hole area of 9.61mm<sup>2</sup>. This was 3.5mm diameter for a round hole and 32mm slot length for a 0.3mm slot. The 1 kW design featured 7 holes of 1.32mm diameter. The 0.3mm slot design for the same 1kW was 7 slots with a length of 4.6mm.

The air holes were designed for 60% excess air with NG for low NO<sub>x</sub>, and the same airflow was considered for H<sub>2</sub>. The stoichiometric A/F of 16.5 gave an  $\phi = 0.625$  for NG for 60% excess air. This provided an airflow of 3.696 g/s and a fuel flow of 0.14 g/s.

#### M.1.2 Second fire configuration (Long burner)

Design 1. 20mbar fuel pressure loss at the discharge hole. An area of 3.62mm<sup>2</sup> for a 0.1mm slot with a length of 36.2mm

Design 2. 2mbar pressure loss at the discharge hole. An area of 11.45mm<sup>2</sup> for a 0.1mm slot with a length of 1145mm.

Design 1 with 0.3mm slot width

Design 2 with 0.3mm slot width. This design showed the most exciting flame

For a 10 air hole design, 9 fuel jets were offset, the airholes and two half-size end ones, for a total of 11 fuel nozzles, as shown in Figure M-1

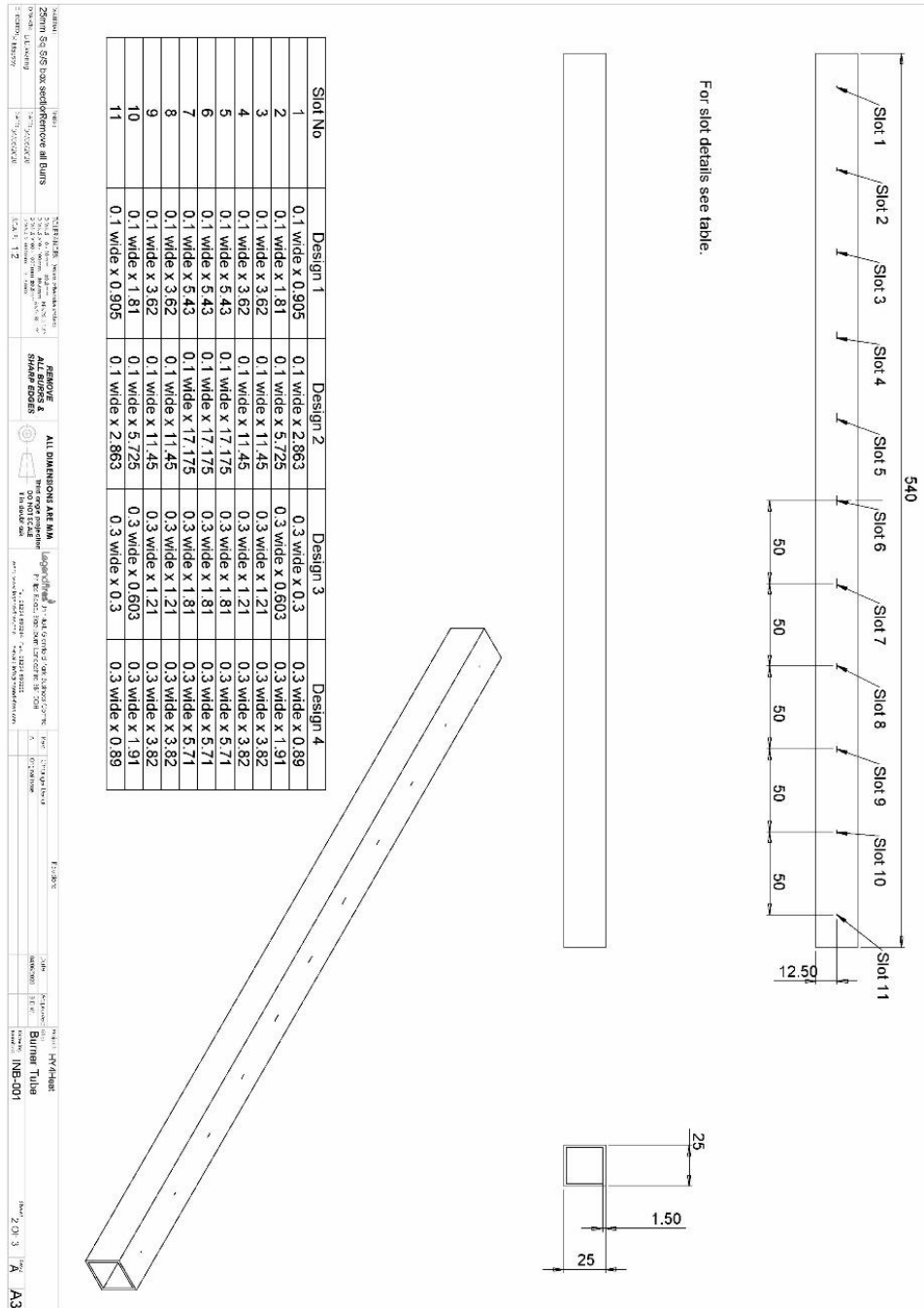


Figure M-1. Fuel plenum with different slot sizes used for the innovative fire tests featuring a single burner.